

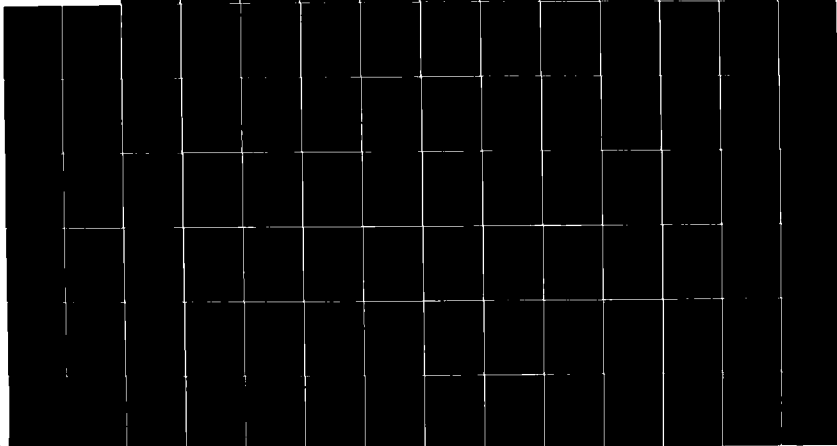
AD-A084 937

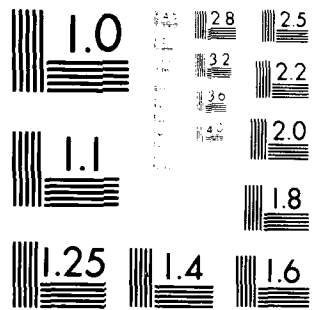
PENNSYLVANIA STATE UNIV UNIVERSITY PARK APPLIED RESE--ETC F/6 20/1  
AN EXPERIMENTAL ANALYSIS OF THE BASIC PHENOMENA INVOLVED IN MOD--ETC(U)  
JAN 80 M S LANG  
ARL/PSU/TH-80-43  
N00024-79-C-6043  
NL

UNCLASSIFIED

1 of 5

AD  
A084937





MICROCOPY RESOLUTION TEST CHART  
NATIONAL BUREAU OF STANDARDS 1963-A

ADA 084937

LEVEL

(12)

AN EXPERIMENTAL ANALYSIS OF THE BASIC  
PHENOMENA INVOLVED IN MODERN  
DIFFRACTION THEORIES

Mark Stiles Lang

Technical Memorandum  
File No. TM 80-43  
January 21, 1980  
Contract No. N00024-79-C-6043

Copy No. //

The Pennsylvania State University  
Institute for Science and Engineering  
APPLIED RESEARCH LABORATORY  
Post Office Box 30  
State College, PA 16801

DTIC  
ELECTE

APPROVED FOR PUBLIC RELEASE  
DISTRIBUTION UNLIMITED

NAVY DEPARTMENT

NAVAL SEA SYSTEMS COMMAND

80 5 30 028

FILE COPY

UNCLASSIFIED

SECURITY CLASSIFICATION OF THIS PAGE (When Data Entered)

REPORT DOCUMENTATION PAGE		READ INSTRUCTIONS BEFORE COMPLETING FORM
1. REPORT NUMBER TM 80-43/	2. GOVT ACCESSION NO. AD-A034937	3. RECIPIENT'S CATALOG NUMBER
4. TITLE (and Subtitle) AN EXPERIMENTAL ANALYSIS OF THE BASIC PHENOMENA INVOLVED IN MODERN DIFFRACTION THEORIES.		5. TYPE OF REPORT & PERIOD COVERED PhD Thesis, May 1980
7. AUTHOR(s) Mark Stiles/Lang		6. PERFORMING ORG. REPORT NUMBER TM 80-43
9. PERFORMING ORGANIZATION NAME AND ADDRESS The Pennsylvania State University Applied Research Laboratory / P. O. Box 30, State College, PA 16801		8. CONTRACT OR GRANT NUMBER(s) N00024-79-C-6043/
11. CONTROLLING OFFICE NAME AND ADDRESS Naval Sea Systems Command Department of the Navy Washington, DC 20362		10. PROGRAM ELEMENT PROJECT, TASK AREA & WORK UNIT NUMBERS
14. MONITORING AGENCY NAME & ADDRESS (if different from Controlling Office)		12. REPORT DATE January 21, 1980
		13. NUMBER OF PAGES 452 pages & figures
		15. SECURITY CLASS. (of this report) Unclassified, Unlimited
		15a. DECLASSIFICATION DOWNGRADING SCHEDULE
16. DISTRIBUTION STATEMENT (of this Report) Approved for public release, distribution unlimited, per NSSC (Naval Sea Systems Command), 4/18/80 H-1/PS4/1		
17. DISTRIBUTION STATEMENT (of the abstract entered in Block 20, if different from Report)		
18. SUPPLEMENTARY NOTES		
19. KEY WORDS (Continue on reverse side if necessary and identify by block number)		
20. ABSTRACT (Continue on reverse side if necessary and identify by block number) This study utilizes direct experimental techniques to analyze the basic scattering mechanisms that are important to modern diffraction theories. The efforts are intended to supplement and guide the development of theoretical models by exploring parameter ranges and configurations that are intuitive extensions of the cases handled by current prediction techniques. A broad program of experimental investigation of rigid three-dimensional scatterers is presented. The thin prolate spheroids is used as a basic model for scattering from smoothly curved bodies. Baffles, cylinders, cones, and		

DD FORM 1 JAN 73 1473

EDITION OF 1 NOV 65 IS OBSOLETE

UNCLASSIFIED

SECURITY CLASSIFICATION OF THIS PAGE (When Data Entered)

391001



UNCLASSIFIED

SECURITY CLASSIFICATION OF THIS PAGE(When Data Entered)

20. ABSTRACT (continued)

cone variants serve for an examination of edges and tips of various orders. In addition to standard pulse measurements with gated receivers, some data are obtained by a holographic imaging technique.

The results show that the backscattered pressure from smoothly curved bodies is determined almost exclusively by specular effects, even at wavelengths that are relatively large compared to the appropriate dimensions of the scatterers. Small changes in or additions to the smooth surface, however, modify both the amplitude and directivity of the scattering. Evidence of surface fields very close to smoothly curved scatterers is also observed. These phenomena can, in general, be identified with Franz-type creeping waves. However, they appear to depend only loosely on the shape of the scatterer's surface, and a prominent wave-type effect is noted at the antipole. Other data show that very small discontinuities in the shape of a model's surface can be prominent scattering sources, while discontinuities in only the surface's slope or curvature scatter much less. The form of the edge on a baffle is seen to be an important scattering parameter for finite edges with thicknesses as small as a quarter of a wavelength. Furthermore, moderate surface damping on a flat baffle appears to significantly attenuate the diffracted field propagating at a grazing angle along the baffle.

Finally, because of a weakness in the current literature, the Freedman theory of echo formation is carefully derived, and its predictions are compared with applicable experimental results. The technique is found to be an exact (i.e., not asymptotic) variant of physical optics that produces a reasonably good model of scattering from baffles but that exhibits serious errors in cases involving three-dimensional bodies.

Accession For	
NTIS	<input checked="checked" type="checkbox"/>
DDC TAB	<input type="checkbox"/>
Unannounced	
Justification	
By	
Distribution/	
Availability Codes	
Dist	Avail and/or special
A	

UNCLASSIFIED

SECURITY CLASSIFICATION OF THIS PAGE(When Data Entered)

## ABSTRACT

This study utilizes direct experimental techniques to analyze the basic scattering mechanisms that are important to modern diffraction theories. The efforts are intended to supplement and guide the development of theoretical models by exploring parameter ranges and configurations that are intuitive extensions of the cases handled by current prediction techniques.

A broad program of experimental investigation of rigid three-dimensional scatterers is presented. The thin prolate spheroid is used as a basic model for scattering from smoothly curved bodies. Baffles, cylinders, cones, and cone variants serve for an examination of edges and tips of various orders. In addition to standard pulse measurements with gated receivers, some data are obtained by a holographic imaging technique.

The results show that the backscattered pressure from smoothly curved bodies is determined almost exclusively by specular effects, even at wavelengths that are relatively large compared to the appropriate dimensions of the scatterers. Small changes in or additions to the smooth surface, however, modify both the amplitude and directivity of the scattering. Evidence of surface fields very close to smoothly curved scatterers is also observed. These phenomena can, in general, be identified with Franz-type creeping waves. However, they appear to depend only loosely on the shape of the scatterer's surface, and a prominent wave-type effect is noted at the antipole. Other data show that very small discontinuities in the shape of a model's surface can be

prominent scattering sources, while discontinuities in only the surface's slope or curvature scatter much less. The form of the edge on a baffle is seen to be an important scattering parameter for finite edges with thicknesses as small as a quarter of a wavelength. Furthermore, moderate surface damping on a flat baffle appears to significantly attenuate the diffracted field propagating at a grazing angle along the baffle.

Finally, because of a weakness in the current literature, the Freedman theory of echo formation is carefully derived, and its predictions are compared with applicable experimental results. The technique is found to be an exact (i.e., not asymptotic) variant of physical optics that produces a reasonably good model of scattering from baffles but that exhibits serious errors in cases involving three-dimensional bodies.

## TABLE OF CONTENTS

	<u>Page</u>
ABSTRACT.....	iii
LIST OF FIGURES.....	viii
LIST OF TABLES.....	xxiv
LIST OF SYMBOLS.....	xxv
ACKNOWLEDGEMENTS.....	xxx
1. INTRODUCTION.....	1
1.1 Background and Objective.....	1
1.2 Scope of the Study.....	3
1.3 Review of Related Work.....	5
1.3.1 Eigenfunction Method.....	6
1.3.2 Watson Transformation.....	8
1.3.3 Integral Solutions.....	9
1.3.4 Asymptotic or Approximate Solutions.....	10
1.3.5 Geometrical Optics.....	11
1.3.6 Lundeburg-Kline Expansion.....	11
1.3.7 Kirchhoff Approximation.....	13
1.3.8 Freedman Method of Echo Formation.....	14
1.3.9 Keller's Geometrical Theory of Diffraction.....	16
1.3.10 Ufimtsev's Method of Boundary Waves.....	25
1.3.11 T-Matrix or Extended Boundary Condition.....	27
1.3.12 Experimental Work.....	28
2. FREEDMAN THEORY OF ECHO FORMATION.....	31
2.1 Derivation of the Basic Integral Expression.....	32
2.2 Integral Evaluation by Discontinuities in $W(r)$ .....	37
2.3 Extension of Results to Narrow-Band Pulses.....	46
2.4 Examples of Some Simple Bodies.....	50
2.4.1 Sphere Example.....	50
2.4.2 Circular-Disk Example.....	54
2.4.3 Rectangular-Plate Example.....	59
2.4.4 Finite-Cylinder Example.....	62
2.4.5 Finite-Cone Example.....	64
2.4.6 Modified Cone Examples.....	69
3. EXPERIMENTAL SETUP FOR GATED-PULSE MEASUREMENTS.....	79
3.1 Measurement Chamber.....	79
3.2 Measuring Equipment.....	82
3.3 Models.....	86
3.4 Techniques.....	93

	<u>Page</u>
4. SMOOTH-BODY DIFFRACTION MEASUREMENTS.....	97
4.1 Geometry of the Prolate Spheroid.....	98
4.2 Backscattering from Prolate Spheroids.....	101
4.2.1 Backscattered Frequency Response from a Prolate Spheroid.....	101
4.2.2 Backscattered Directivity from a Prolate Spheroid...	103
4.2.3 Backscattered Directivity from Partially Damped Spheroids.....	105
4.2.4 Geometric Calculations for a Prolate Spheroid.....	115
4.3 Prolate Spheroid with Small Surface Discontinuities.....	123
4.3.1 Effect of Surface Imperfections.....	123
4.3.2 Effect of Thin Band Obstructions.....	126
4.4 Prolate Spheroid with Cylinder Obstructions.....	137
4.4.1 Total Backscatter from Cylinders and Spheroid.....	138
4.4.2 Effect of Cylinder Location.....	140
4.4.3 Effect of Spheroid Incidence Angle.....	148
4.4.4 Effect of Spheroid on Cylinder's Bistatic Scattering.....	156
4.4.5 Effect of Hole in Surface of Spheroid.....	161
4.5 Bistatic Scattering from Prolate Spheroids.....	164
4.6 Creeping Waves.....	174
4.6.1 Creeping Waves on Smooth Spheres and Spheroids.....	175
4.6.2 Creeping Waves on Spheres with Bands.....	184
4.6.3 Creeping Waves on Flattened Spheres.....	196
5. EDGE DIFFRACTION MEASUREMENTS AND THE FREEDMAN THEORY.....	206
5.1 Scattering at the Edge of a Plane Baffle.....	207
5.1.1 Angular Distribution of the Field.....	207
5.1.2 Field Along the Shadowed Side of the Baffle.....	218
5.2 Backscattering from Rounded and Square Edges.....	242
5.3 Backscattering from Small Cylinders.....	252
5.4 Scattering from Cones and Modified Cones.....	274
5.4.1 General Discussion of Experimental Concerns.....	276
5.4.2 Backscattering at Axial Incidence.....	280
5.4.3 Scattering by a Normal Cone.....	294
5.4.4 Scattering by Cones with Spherical and Hemispherical Caps.....	308
5.4.5 Scattering by Cones with Terminations.....	329
6. HOLOGRAPHIC IMAGING TECHNIQUES.....	342
6.1 Theoretical Basics.....	343
6.2 Experimental Apparatus.....	356
6.3 Experimental Results.....	364
6.3.1 Backscattering at a Flat Baffle.....	365
6.3.2 Backscattering at Spheres of Different Sizes.....	370
6.3.3 Backscattering at a Prolate Spheroid.....	375
6.3.4 Backscattering at a Finite Cone.....	378
6.4 General Conclusions About the Technique.....	384

Page

7. SUMMARY AND CONCLUSIONS.....	385
REFERENCE LIST.....	394
APPENDIX A: DERIVATION OF THE KIRCHHOFF SCATTERING INTEGRAL.....	404
APPENDIX B: RECEIVER-GATE MODULE.....	415

## LIST OF FIGURES

<u>Figure</u>		<u>Page</u>
1.1	Ray tube of geometrical optics. A caustic occurs at those points where one or both of the radii of curvature of the wavefront vanish.....	12
1.2	Geometric description of the three new types of diffraction rays proposed by Keller, including (a) edge rays, (b) vertex rays, and (c) surface rays.....	18
2.1	Definition of the geometry for backscattering showing the locations of the transducers and scatterer, a strip along the scatterer between ranges $r$ and $r+dr$ , an area $dS$ , and the surface normal $\underline{n}$ .....	33
2.2	Approximate values of the solid angle $W(r)$ versus range $r$ for a body with a portion of its surface parallel to the incident wavefront.....	38
2.3	Approximate values of the projected area $A(r)$ and its derivatives for a sphere.....	51
2.4	Approximate values of the projected area $A(r)$ and its derivatives for a circular disk at nonaxial incidence.....	55
2.5	Geometry utilized in calculation of the scattering from a circular disk.....	57
2.6	Approximate values of the projected area $A(r)$ and its derivatives for a rectangular plate at nonaxial incidence.....	60
2.7	Geometry used for calculation of backscattering from a finite cylinder.....	63
2.8	Approximate values of the projected area $A(r)$ and its derivatives for a finite circular cone at axial incidence.....	65
2.9	Geometry used for calculation of backscattering from a finite cone at nonaxial incidence.....	68
2.10	Geometry used for calculation of backscattering from a cone-sphere at axial incidence.....	70
2.11	Geometry used for calculation of backscattering from a spherically capped cone at axial incidence.....	73
2.12	Geometry used for calculation of backscattering from a hemispherically capped cone at axial incidence.....	76

<u>Figure</u>	<u>Page</u>
3.1 Photograph of the measurement chamber with the 28-inch prolate spheroid in position.....	80
3.2 Block diagram of the measurement chamber (in plan view) and the associated electronic equipment.....	83
3.3 Photograph of the prolate-spheroid models.....	88
3.4 Photograph of the special cone model, including its various spherical and hemispherical caps and terminations.....	90
3.5 Oscilloscope trace of the backscattered returns from (A) a length of 25-pound-test fishing line and (B) a thin prolate spheroid at $30^\circ$ incidence.....	92
4.1 Geometry used to describe prolate spheroids, including (a) the dimensions of the ellipse of revolution and (b) the associated orthogonal coordinate surfaces.....	99
4.2 Backscatter versus normalized frequency from the 42-inch prolate spheroid at several incidence angles.....	102
4.3 Directivity of the backscatter from the 28-inch prolate spheroid for normalized $h\xi_0$ values of 130, 195, and 261.....	104
4.4 Test of the backscattering properties of the corduroy damping material in two orientations, as applied to a flat rectangular baffle at 34.3 kHz.....	107
4.5 Photograph of the 28-inch prolate spheroid with a portion of its surface covered in a corduroy damping material.....	108
4.6 Directivity of the backscatter from plain, end-damped, and totally damped prolate spheroids. ( $h\xi_0 = 223$ ).....	110
4.7 Directivity of the backscatter from a prolate spheroid with various degrees of damping material applied at both ends. ( $h\xi_0 = 223$ ).....	111
4.8 Directivity of the backscatter from plain, center-damped, and totally damped prolate spheroids. ( $h\xi_0 = 223$ ).....	113
4.9 Directivity of the backscatter from a prolate spheroid with various degrees of damping material applied at the center. ( $h\xi_0 = 223$ ).....	114
4.10 Geometry used for the calculation of backscattering from a prolate spheroid.....	116



<u>Figure</u>	<u>Page</u>
4.11 Backscattered directivity from the 28-inch prolate spheroid at 27 kHz compared to a simple geometric calculation. ( $h\xi_0 = 176$ ).....	120
4.12 Backscattered directivity from the 42-inch prolate spheroid compared to a simple geometric calculation. ( $h\xi_0 = 261$ ).....	122
4.13 Backscattered directivity from the 28-inch prolate spheroid at 34.3 kHz with both a good nose and a slightly dented nose illuminated. ( $h\xi_0 = 223$ ).....	125
4.14 Backscattered directivity from a prolate spheroid with a band of corduroy damping material around the nose. ( $h\xi_0 = 223$ ).....	127
4.15 Backscattered directivity from a prolate spheroid with a smoothly preceded cloth band around the nose. ( $h\xi_0 = 223$ ).....	128
4.16 Backscattered directivity from a prolate spheroid with a sloped clay band around the nose. ( $h\xi_0 = 223$ ).....	130
4.17 Backscattered directivity from a prolate spheroid with and without a thin rubber band around its nose. ( $h\xi_0 = 264$ ).....	131
4.18 Backscattered directivity from a prolate spheroid with and without medium-thick rubber bands around its nose. ( $h\xi_0 = 264$ ).....	132
4.19 Backscattered directivity from a prolate spheroid with and without various thick rubber bands around its nose. ( $h\xi_0 = 264$ ).....	133
4.20 Backscattered directivity from a prolate spheroid with and without a thin rubber band around its center. ( $h\xi_0 = 264$ ).....	135
4.21 Backscattered directivity from a prolate spheroid with various rubber bands around its center. ( $h\xi_0 = 264$ ).....	136
4.22 Backscatter versus angle of incidence from a prolate spheroid with 3/4-inch-diameter cylinders on top at its center. ( $h\xi_0 = 150$ , $\lambda = .6$ inch).....	139
4.23 Backscatter from 3/4-inch-diameter cylinders along the top of the 28-inch prolate spheroid (axial incidence) compared to backscatter from the cylinders suspended alone. ( $h\xi_0 = 150$ , $\lambda = .6$ inch).....	141

<u>Figure</u>	<u>Page</u>
4.24 Plot of the actual backscatter from a 3/4-inch-diameter by 1/2-inch-tall cylinder versus distance compared to the geometric computation. ( $\lambda = .6$ inch).....	143
4.25 Backscatter from 1/4-inch-diameter cylinders along the top of the 28-inch prolate spheroid (axial incidence) compared to backscatter from the cylinders suspended alone. ( $h\xi_0 = 150$ , $\lambda = .6$ inch).....	144
4.26 Backscatter from 3/4-inch-diameter cylinders along the top of the 28-inch prolate spheroid ( $20^\circ$ incidence) compared to the backscatter from the cylinders suspended alone. ( $h\xi_0 = 150$ , $\lambda = .6$ inch).....	146
4.27 Backscatter from a 3/4-inch-diameter by 1/2-inch-tall cylinder along the top of the 42-inch prolate spheroid (axial incidence) compared to backscatter from the cylinder suspended alone. ( $h\xi_0 = 225$ , $\lambda = .6$ inch).....	147
4.28 Backscatter from 3/4-inch-diameter cylinders centered on the 28-inch prolate spheroid versus spheroid incidence angle compared to backscatter from the cylinders suspended alone. ( $h\xi_0 = 150$ , $\lambda = .6$ inch).....	149
4.29 Backscatter from 1/4-inch-diameter cylinders centered on the 28-inch prolate spheroid versus spheroid incidence angle compared to backscatter from the cylinders suspended alone. ( $h\xi_0 = 150$ , $\lambda = .6$ inch).....	150
4.30 Backscatter from 3/4-inch-diameter cylinders on the 28-inch prolate spheroid 7 inches forward of center versus spheroid incidence angle compared to backscatter from the cylinders suspended alone. ( $h\xi_0 = 150$ , $\lambda = .6$ inch).....	152
4.31 Backscatter from 1/4-inch-diameter cylinders on the 28-inch prolate spheroid 7 inches forward of center versus spheroid incidence angle compared to the backscatter from the cylinders suspended alone. ( $h\xi_0 = 150$ , $\lambda = .6$ inch).....	153
4.32 Backscatter from 3/4-inch-diameter cylinders on the 28-inch prolate spheroid 7 inches back of center versus spheroid incidence angle compared to the backscatter from the cylinders suspended alone. ( $h\xi_0 = 150$ , $\lambda = .6$ inch)....	154
4.33 Backscatter from 1/4-inch-diameter cylinders on the 28-inch prolate spheroid 7 inches back of center versus spheroid incidence angle compared to the backscatter from the cylinders suspended alone. ( $h\xi_0 = 150$ , $\lambda = .6$ inch)....	155

<u>Figure</u>	<u>Page</u>
4.34 Bistatic scattering from 3/4-inch-diameter cylinders centered on top of the 28-inch spheroid (axial incidence) compared to that from the cylinders alone. ( $h\xi_0 = 150$ , $\lambda = .6$ inch).....	157
4.35 Bistatic scattering from 1/4-inch-diameter cylinders centered on top of the 28-inch prolate spheroid (axial incidence) compared to that from the cylinders alone. ( $h\xi_0 = 150$ , $\lambda = .6$ inch).....	158
4.36 Bistatic scattering from 3/4-inch-diameter cylinders centered on top of the 28-inch prolate spheroid ( $20^\circ$ incidence) compared to that from the cylinders alone. ( $h\xi_0 = 150$ , $\lambda = .6$ inch).....	159
4.37 Bistatic scattering from 3/4-inch-diameter cylinders centered on top of the 28-inch prolate spheroid ( $45^\circ$ incidence) compared to that from the cylinders alone. ( $h\xi_0 = 150$ , $\lambda = .6$ inch).....	160
4.38 Backscatter from 3/4-inch-diameter cylinders along the top of the 28-inch prolate spheroid (axial incidence) with a hole at its center compared to the same case without the spheroid hole. ( $h\xi_0 = 150$ , $\lambda = .6$ inch).....	162
4.39 Backscatter from 1/4-inch-diameter cylinders along the top of the 28-inch prolate spheroid (axial incidence) with a hole at its center compared to the same case without the spheroid hole. ( $h\xi_0 = 150$ , $\lambda = .6$ inch).....	163
4.40 Backscatter from a cylinder along the top of the 28-inch prolate spheroid (axial incidence) with both 1/2-inch- and 3/4-inch-deep holes at its center. ( $h\xi_0 = 150$ , $\lambda = .6$ inch).....	165
4.41 Backscatter at various spheroid incidence angles from 3/4-inch-diameter cylinders on the 28-inch prolate spheroid just behind the center, both with and without a hole at the spheroid's center. ( $h\xi_0 = 150$ , $\lambda = .6$ inch)....	166
4.42 Backscatter at various spheroid incidence angles from 1/4-inch-diameter cylinders on the 28-inch prolate spheroid just behind the center, both with and without a hole at the spheroid's center. ( $h\xi_0 = 150$ , $\lambda = .6$ inch)....	167
4.43 Bistatic scattering from a prolate spheroid at axial incidence. ( $h\xi_0 = 166$ , $\lambda = 1/2$ inch).....	169
4.44 Bistatic scattering from a prolate spheroid at broadside incidence in the plane of its axis. ( $h\xi_0 = 166$ , $\lambda = 1/2$ inch).....	170

<u>Figure</u>	<u>Page</u>
4.45 Bistatic scattering from a prolate spheroid at $10^\circ$ and $20^\circ$ incidence in the plane of its axis. ( $h\xi_0 = 166$ , $\lambda = 1/2$ inch).....	171
4.46 Bistatic scattering from a prolate spheroid at $30^\circ$ , $40^\circ$ , $50^\circ$ , and $60^\circ$ incidence in the plane of its axis. ( $h\xi_0 = 166$ , $\lambda = 1/2$ inch).....	172
4.47 Bistatic scattering from a prolate spheroid at $70^\circ$ , $80^\circ$ , and $90^\circ$ incidence in the plane of its axis. ( $h\xi_0 = 166$ , $\lambda = 1/2$ inch).....	173
4.48 Oscilloscope trace of the backscattering from a sphere at $ka = 6$ , including (a) the incident pulse at the sphere and (b) the specular and creeping-wave returns.....	176
4.49 Plot of the specular (X) and creeping-wave (O) returns in the backscatter from a sphere normalized to the pulse incident on the sphere.....	178
4.50 Plot of the bistatic specular and creeping-wave returns from a sphere at $ka$ 's of 6 and 12 normalized to the pulse incident on the sphere.....	179
4.51 Oscilloscope trace of the backscattered specular and creeping-wave returns from a 2:1 prolate spheroid ( $h\xi_0 = 13.5$ ) at (a) axial and (b) broadside incidence.....	180
4.52 Comparison of the bistatic specular and creeping-wave returns from a 2:1 prolate spheroid ( $h\xi_0 = 13.5$ ) and a similar sphere ( $ka = 6$ ).....	182
4.53 Oscilloscope traces of (a) the incident pulse and (b) the backscattered returns from a 7:1 prolate spheroid and surrounding room reflectors at $h\xi_0 = 38$ .....	183
4.54 Oscilloscope trace of the backscattered (a) specular and (b) creeping-wave returns from a 7:1 prolate spheroid at $h\xi_0 = 38$ .....	185
4.55 Bistatic specular and creeping-wave returns from a 7:1 prolate spheroid. ( $h\xi_0 = 38$ ).....	186
4.56 Oscilloscope trace of the backscattered specular and creeping-wave returns from a sphere at $ka = 6$ with bands having thicknesses of (a) $.03\lambda$ and (b) $.13\lambda$ oriented along the source/receiver axis.....	187
4.57 Bistatic specular and creeping-wave returns from a plain sphere and a sphere with two thicknesses of rubber bands around its surface in the source/receiver axis. ( $ka = 6$ )...	189

<u>Figure</u>		<u>Page</u>
4.58	Oscilloscope trace of the backscattered specular and creeping-wave returns from a sphere at $ka = 6$ with a band oriented (a) in the source/receiver axis and (b) $10^\circ$ off the source/receiver axis.....	190
4.59	Bistatic specular and creeping-wave returns from a sphere with a band around its surface slightly out of the source/receiver axis compared to the returns from a plain sphere. ( $ka = 6$ ).....	191
4.60	Oscilloscope trace of the backscattered returns from (a) a plain sphere and (b) a sphere with a band along the source/receiver axis open slightly at the antipole. ( $ka = 6$ ).....	192
4.61	Oscilloscope trace of the backscattered specular, band, and creeping-wave returns from a sphere at $ka = 6$ with bands having thicknesses of (a) $.03\lambda$ and (b) $.13\lambda$ oriented perpendicular to the source/receiver axis.....	194
4.62	Bistatic specular and creeping-wave components from a sphere with various circumferential bands oriented parallel to the incident wavefront.....	195
4.63	Oscilloscope trace of the backscattered returns from a flattened sphere with two different degrees of flatness. ( $ka = 6$ ).....	197
4.64	Bistatic specular and creeping-wave components from a slightly flattened sphere with the flat oriented at the front and back relative to the microphone. ( $ka = 6$ ).....	198
4.65	Bistatic specular and creeping-wave components from a moderately flattened sphere with the flat oriented at the front and back relative to the microphone. ( $ka = 6$ ).....	199
4.66	Bistatic specular and creeping-wave returns from a deeply flattened sphere with the flat oriented at the front and back relative to the microphone. ( $ka = 6$ ).....	200
4.67	Effect of a small band at the surface focus point on the bistatic specular and creeping-wave components from a deeply flattened sphere with its flat oriented opposite the microphone. ( $ka = 6$ ).....	202
4.68	Bistatic specular and creeping-wave returns from a slightly flattened sphere with the flat oriented at the left and right relative to the microphone. ( $ka = 6$ ).....	203
4.69	Bistatic specular and creeping-wave returns from a moderately flattened sphere with the flat oriented at the left and right relative to the microphone. ( $ka = 6$ ).....	204

<u>Figure</u>		<u>Page</u>
4.70	Bistatic specular and creeping-wave returns from a deeply flattened sphere with the flat oriented at the left and right relative to the microphone. ( $ka = 6$ ).....	205
5.1	Angular distribution of the field scattered by the edge of a baffle into the incident half-space at a distance of 10 inches from the edge. ( $\lambda = .643$ inch).....	209
5.2	Angular distribution of the field scattered by the edge of a baffle into the incident half-space at a distance of 18 inches from the edge. ( $\lambda = .643$ inch).....	210
5.3	Angular distribution of the field scattered by the edge of a baffle into the incident half-space at a distance of 30 inches from the edge. ( $\lambda = .643$ inch).....	211
5.4	Angular distribution of the field scattered by the edge of a baffle into the incident half-space at distances of 10, 18, and 30 inches from the edge. ( $\lambda = .643$ inch).....	212
5.5	Total received field angularly distributed about the edge of a rectangular baffle in the forward half-space at 10 inches from the edge, both with and without damping material on the shadowed side of the baffle. ( $\lambda = .643$ inch).....	214
5.6	Total received field angularly distributed about the edge of a rectangular baffle in the forward half-space at 18 inches from the edge, both with and without damping material on the shadowed side of the baffle. ( $\lambda = .643$ inch).....	215
5.7	Total received field angularly distributed about the edge of a rectangular baffle in the forward half-space at 30 inches from the edge, both with and without damping material on the shadowed side of the baffle. ( $\lambda = .643$ inch).....	216
5.8	Total received field angularly distributed about the edge of a rectangular baffle in the forward half-space at 10, 18, and 30 inches from the edge with damping material on the shadowed side of the baffle. ( $\lambda = .643$ inch).....	217
5.9	Field measured parallel to a rigid finite baffle for grazing incidence.....	219
5.10	Field measured parallel to a rigid finite baffle at a distance of $1/2$ inch for several angles of incidence on the edge.....	220

<u>Figure</u>	<u>Page</u>
5.11 Field measured parallel to a rigid finite baffle at a distance of 2 inches for several angles of incidence on the edge.....	221
5.12 Field measured parallel to a rigid finite baffle at a distance of 6 inches for several angles of incidence on the edge.....	222
5.13 Field measured parallel to a rigid finite baffle at a distance of 12 inches for several angles of incidence on the edge.....	223
5.14 Field measured parallel to a rigid finite baffle at a distance of 18 inches for several angles of incidence on the edge.....	224
5.15 Field measured parallel to both rigid and damped baffles at a distance of 1/2 inch for grazing incidence.....	226
5.16 Field measured parallel to both rigid and damped baffles at a distance of 1 inch for grazing incidence.....	227
5.17 Field measured parallel to both rigid and damped baffles at distances of 2, 4, and 6 inches for grazing incidence....	228
5.18 Field measured parallel to both rigid and damped baffles at a distance of 1/2 inch for 120° incidence.....	230
5.19 Field measured parallel to both rigid and damped baffles at a distance of 1 inch for 120° incidence.....	231
5.20 Field measured parallel to both rigid and damped baffles at a distance of 2 inches for 120° incidence.....	232
5.21 Field measured parallel to both rigid and damped baffles at a distance of 6 inches for 120° incidence.....	233
5.22 Field measured parallel to both rigid and damped baffles at a distance of 12 inches for 120° incidence.....	234
5.23 Field measured parallel to both rigid and damped baffles at a distance of 18 inches for 120° incidence.....	235
5.24 Field measured parallel to a damped baffle at a distance of 1/2 inch for incidence angles of 60°, 90°, and 120°.....	236
5.25 Field measured parallel to a damped baffle at a distance of 1 inch for incidence angles of 60°, 90°, and 120°.....	237
5.26 Field measured parallel to a damped baffle at a distance of 2 inches for incidence angles of 60°, 90°, and 120°.....	238

<u>Figure</u>	<u>Page</u>
5.27 Field measured parallel to a damped baffle at a distance of 6 inches for incidence angles of $60^{\circ}$ , $90^{\circ}$ , and $120^{\circ}$ .....	239
5.28 Field measured parallel to a damped baffle at a distance of 12 inches for incidence angles of $60^{\circ}$ , $90^{\circ}$ , and $120^{\circ}$ .....	240
5.29 Field measured parallel to a damped baffle at a distance of 18 inches for incidence angles of $60^{\circ}$ , $90^{\circ}$ , and $120^{\circ}$ .....	241
5.30 Comparison of the backscattered directivities from a square edge, a rounded edge, and a cylinder with a 1/8-inch width. ( $\lambda = 1/2$ inch).....	244
5.31 Comparison of the backscattered directivities from a square edge, a rounded edge, and a cylinder with a 3/8-inch width. ( $\lambda = 1/2$ inch).....	245
5.32 Comparison of the backscattered directivities from a square edge, a rounded edge, and a cylinder with a 2-inch width. ( $\lambda = 1/2$ inch).....	246
5.33 Comparison of the backscattered frequency response from a half-cylinder-capped board and a cylinder for cylinder diameters of 1/8, 3/8, and 2 inches.....	247
5.34 Backscattered directivity from a 1/8-inch edge, as measured experimentally and as computed using the Freedman method.....	249
5.35 Backscattered directivity from a 3/8-inch edge, as measured experimentally and as computed using the Freedman method.....	250
5.36 Backscattered directivity from a 2-inch edge, as measured experimentally and as computed using the Freedman method....	251
5.37 Backscatter from a thin edge at various frequencies.....	253
5.38 Directivity of the backscatter from 3/4-inch-diameter cylinders with lengths of 1/8 and 1 inch. ( $\lambda = 1/2$ inch)...	255
5.39 Directivity of the backscatter from 3/4-inch-diameter cylinders with lengths of 1/4, 1/2, and 3/4 inch. ( $\lambda = 1/2$ inch).....	256
5.40 Directivity of the backscatter from 1/2-inch-diameter cylinders with lengths of 1/8 and 1 inch. ( $\lambda = 1/2$ inch)...	258
5.41 Directivity of the backscatter from 1/2-inch-diameter cylinders with lengths of 1/4, 1/2, and 3/4 inch. ( $\lambda = 1/2$ inch).....	259



<u>Figure</u>	<u>Page</u>
5.42 Directivity of the backscatter from 1/4-inch-diameter cylinders with lengths of 1/4 and 1 inch. ( $\lambda = 1/2$ inch)...	260
5.43 Directivity of the backscatter from 1/4-inch-diameter cylinders with lengths of 1/2 and 3/4 inch. ( $\lambda = 1/2$ inch).....	261
5.44 Directivity of the backscatter from 1/8-inch-diameter cylinders with lengths of 1/4 and 1 inch. ( $\lambda = 1/2$ inch)...	262
5.45 Directivity of the backscatter from 1/8-inch-diameter cylinders with lengths of 1/2 and 3/4 inch. ( $\lambda = 1/2$ inch).....	263
5.46 Directivity of the backscatter from 1-inch-long cylinders with diameters of 1/8, 1/4, 1/2, and 3/4 inch. ( $\lambda = 1/2$ inch).....	265
5.47 Directivity of the backscatter from 1/4-inch-long cylinders with diameters of 1/8, 1/4, 1/2, and 3/4 inch. ( $\lambda = 1/2$ inch).....	266
5.48 Comparison of measured and predicted values for the backscattered directivity from a 3/4-inch-diameter by 1-inch-long cylinder. ( $\lambda = 1/2$ inch).....	267
5.49 Physical-optics computation for the backscattered end and side contributions from a 3/4-inch-diameter by 1-inch-long cylinder. ( $\lambda = 1/2$ inch).....	268
5.50 Comparison of measured and predicted values for the backscattered directivity from a 1/4-inch-diameter by 1-inch-long cylinder. ( $\lambda = 1/2$ inch).....	270
5.51 Physical-optics computation for the backscattered end and side contributions from a 1/4-inch-diameter by 1-inch-long cylinder. ( $\lambda = 1/2$ inch).....	271
5.52 Comparison of measured and predicted values for the backscattered directivity from a 3/4-inch-diameter by 1/4-inch-long cylinder. ( $\lambda = 1/2$ inch).....	272
5.53 Comparison of measured and predicted values for the backscattered directivity from a 1/4-inch-diameter by 1/2-inch-long cylinder. ( $\lambda = 1/2$ inch).....	273
5.54 Frequency dependence of all the returns backscattered by the cone model at axial incidence.....	277
5.55 Frequency response of the backscattered return from the cap joint of the the cone model, both before and after smoothing with modeling clay.....	279

<u>Figure</u>	<u>Page</u>
5.56 Directivity of the backscatter from the cap joint of the cone model, both before and after smoothing with modeling clay.....	281
5.57 Frequency response of the backscatter from the smoothed cap joint of the cone model with several different caps attached.....	282
5.58 Frequency response of the backscattered returns from the cone model.....	284
5.59 Frequency response of the backscattered returns from the cone with a spherical cap of 1/2-inch radius.....	285
5.60 Frequency response of the backscattered returns from the cone with a spherical cap of 1-inch radius.....	286
5.61 Frequency response of the backscattered returns from the cone with a spherical cap of 2-inch radius.....	287
5.62 Frequency response of the backscattered returns from the cone with a hemispherical cap of 2-inch radius.....	289
5.63 Frequency response of the backscattered returns from the cone with a hemispherical termination.....	290
5.64 Frequency response of the backscattered returns from a cone with a smooth spherical termination.....	292
5.65 Frequency response of the backscatter from the rear edge of the cone model with no termination, a hemispherical termination, and a smooth spherical termination.....	293
5.66 Directivity of the backscatter from the 18-inch cone model at 10 kHz. ( $kh = 84$ ).....	295
5.67 Directivity of the backscatter from the 18-inch cone model at 20 kHz. ( $kh = 168$ ).....	296
5.68 Directivity of the backscatter from the 18-inch cone model at 30 kHz. ( $kh = 251$ ).....	297
5.69 Directivity of the backscatter from the 18-inch cone model at 40 kHz. ( $kh = 335$ ).....	298
5.70 Directivity of the backscatter from the rear disk of the 18-inch cone model at 10 kHz. ( $kr = 30$ ).....	299
5.71 Directivity of the backscatter from the rear disk of the 18-inch cone model at 20 kHz. ( $kr = 61$ ).....	300

<u>Figure</u>	<u>Page</u>
5.72 Directivity of the backscatter from the rear disk of the 18-inch cone model at 30 kHz. ( $kr = 91$ ).....	301
5.73 Directivity of the backscatter from the rear disk of the 18-inch cone model at 40 kHz. ( $kr = 122$ ).....	302
5.74 Bistatic scattering from the 18-inch cone model for axial incidence at 10 kHz. ( $kh = 84$ ).....	304
5.75 Bistatic scattering from the 18-inch cone model for axial incidence at 20 kHz. ( $kh = 168$ ).....	305
5.76 Bistatic scattering from the 18-inch cone model for axial incidence at 30 kHz. ( $kh = 251$ ).....	306
5.77 Bistatic scattering from the 18-inch cone model for axial incidence at 40 kHz. ( $kh = 335$ ).....	307
5.78 Bistatic scattering from the 18-inch cone model for $20^\circ$ incidence at 20 kHz. ( $kh = 168$ ).....	309
5.79 Bistatic scattering from the 18-inch cone model for $20^\circ$ incidence at 40 kHz. ( $kh = 335$ ).....	310
5.80 Bistatic scattering from the 18-inch cone model for $45^\circ$ incidence at 20 kHz. ( $kh = 168$ ).....	311
5.81 Bistatic scattering from the 18-inch cone model for $45^\circ$ incidence at 40 kHz. ( $kh = 335$ ).....	312
5.82 Directivity of the backscatter at 10 kHz from the cone model with a spherical cap of 1/2-inch radius. ( $\lambda = 1.35$ inch).....	314
5.83 Directivity of the backscatter at 10 kHz from the cone model with a spherical cap of 1-inch radius. ( $\lambda = 1.35$ inch).....	315
5.84 Directivity of the backscatter at 10 kHz from the cone model with a spherical cap of 2-inch radius. ( $\lambda = 1.35$ inch).....	316
5.85 Directivity of the backscatter at 20 kHz from the cone model with spherical caps having radii of 1/2, 1, and 2 inches. ( $\lambda = .675$ inch).....	318
5.86 Directivity of the backscatter at 30 kHz from the cone model with spherical caps having radii of 1/2, 1, and 2 inches. ( $\lambda = .45$ inch).....	319

<u>Figure</u>	<u>Page</u>
5.87 Directivity of the backscatter at 40 kHz from the cone model with spherical caps having radii of 1/2, 1, and 2 inches. ( $\lambda = .34$ inch).....	320
5.88 Bistatic scattering at 10 kHz from the cone model with spherical caps having radii of 1/2, 1, and 2 inches. ( $\lambda = 1.35$ inch).....	321
5.89 Bistatic scattering at 10 kHz from only the tip of the cone model with a spherical cap of 1/2-inch radius. ( $\lambda = 1.35$ inch).....	322
5.90 Bistatic scattering at 20 kHz from the cone model with spherical caps having radii of 1/2, 1, and 2 inches. ( $\lambda = .675$ inch).....	324
5.91 Bistatic scattering at 30 kHz from the cone model with spherical caps having radii of 1/2, 1, and 2 inches. ( $\lambda = .45$ inch).....	325
5.92 Bistatic scattering at 40 kHz from the cone model with spherical caps having radii of 1/2, 1, and 2 inches. ( $\lambda = .34$ inch).....	326
5.93 Directivity of the backscatter at 10 kHz and 20 kHz (-10 dB) from the cone model with a 2-inch hemispherical cap. ( $\lambda = 1.35, .675$ inch).....	327
5.94 Directivity of the backscatter at 30 kHz and 40 kHz (-10 dB) from the cone model with a 2-inch hemispherical cap. ( $\lambda = .45, .34$ inch).....	328
5.95 Bistatic scattering from the cone model with a 2-inch hemispherical cap at frequencies of 10 kHz, 20 kHz (-5 dB), 30 kHz (-10 dB), and 40 kHz (-15 dB).....	330
5.96 Directivity of the backscatter at 10 kHz from the cone model with a hemispherical termination.....	332
5.97 Directivity of the backscatter at 20 kHz from the cone model with a hemispherical termination.....	333
5.98 Directivity of the backscatter at 40 kHz from the cone model with a hemispherical termination.....	334
5.99 Directivity of the backscatter at 10 kHz from the cone model with a spherical termination.....	336
5.100 Directivity of the backscatter at 20 kHz from the cone model with a spherical termination.....	337

<u>Figure</u>	<u>Page</u>
5.101 Directivity of the backscatter at 40 kHz from the cone model with a spherical termination.....	338
5.102 Bistatic scattering from the cone model with a hemispherical termination at 10, 20, and 40 kHz.....	339
5.103 Bistatic scattering from the cone model with a spherical termination at 10, 20, and 40 kHz.....	340
6.1 Basic geometry used for the wavefront-reconstruction derivation.....	346
6.2 Block diagram of the control and data-acquisition electronics used for recording acoustic holograms.....	359
6.3 Photograph of the microphone scanning system used for holographic measurements.....	360
6.4 Block diagram of one channel of the high-speed amplitude/phase detection system.....	362
6.5 Reconstruction of a 12-inch square baffle at 8 kHz taken with a continuous source.....	366
6.6 Reconstruction of a 12-inch square baffle at 8 kHz taken with a pulsed source.....	367
6.7 Reconstruction of a 12-inch square baffle at 8 kHz after modifying the phase-error electronics.....	369
6.8 Reconstruction at 17 kHz of two spheres of different diameters in the same object plane.....	371
6.9 Reconstruction (side view) at 17 kHz of two spheres of different diameters in the same object plane.....	372
6.10 Reconstruction (side view) at 17 kHz of two unequal spheres in different object planes, as viewed in the plane of the closest sphere.....	373
6.11 Reconstruction (side view) at 17 kHz of two unequal spheres in different planes, as viewed in the plane of the furthest sphere.....	374
6.12 Reconstruction at 17 kHz from a 7:1 prolate spheroid for broadside incidence.....	376
6.13 Reconstruction at 17 kHz from a 7:1 prolate spheroid at axial incidence, viewed in the plane of the tip.....	377

<u>Figure</u>	<u>Page</u>
6.14 Reconstruction at 17 kHz from a 7:1 prolate spheroid at axial incidence, viewed in the plane at the spheroid center.....	379
6.15 Reconstruction at 17 kHz from a finite cone, viewed in the plane of the tip.....	380
6.16 Reconstruction at 17 kHz from a finite cone, viewed in the plane of the rear edge.....	381
6.17 Reconstruction at 17 kHz from a spherically capped cone, viewed in the plane of the tip.....	382
6.18 Reconstruction at 17 kHz from a spherically capped cone, viewed in the plane of the rear edge.....	383
A.1 Geometry showing a rigid body subjected to an incident acoustic wave from a point source at $\underline{r}_2$ , as viewed at a field point at $\underline{r}$ .....	407
A.2 Scattering of a plane wave at a plane boundary.....	412
B.1 Schematic of the preamplifier and full-wave rectifier elements of the receiver-gate module.....	416
B.2 Schematic of the peak detector, log convertor, and sample-hold elements of the receiver-gate module.....	418
B.3 Schematic of the timing elements of the receiver-gate module.....	419

## LIST OF TABLES

<u>Table</u>		<u>Page</u>
1.1	Comparison of Levy & Keller's (1959) and Pathak & Kouyoumjian's (1974) GTD Diffraction and Attenuation Coefficients for Variable Radius-of-Curvature, Impedance Surfaces.....	23
2.1	Freedman Discontinuity Data for a Sphere of Radius $a$ .....	53
2.2	Freedman Discontinuity Data for the Rectangular Plate of Figure 2.6.....	61
2.3	Freedman Discontinuity Data for the Finite Cone at Axial Incidence.....	67
2.4	Freedman Discontinuity Data for the Cone-Sphere.....	71
2.5	Freedman Discontinuity Data for a Spherically Capped Cone...	74
2.6	Freedman Discontinuity Data for a Hemispherically Capped Cone.....	77
B.1	List of Semiconductor Components Used in the Receiver-Gate Module.....	420

## LIST OF SYMBOLS

$a, b, c', d, m$	dimensions of a particular scattering body
$A(r)$	projection toward the transducers of that part of a scattering body within range $r$
$A_i, A'_i$	Airy function and its derivative in Pathak and Kouyoumjian's (1974) notation
$A_{LK}, A'_{LK}$	Airy function and its derivatives in Levy and Keller's (1959) notation
$c$	sound velocity in the medium
CMOS	complementary metal-oxide semiconductor
$D$	size of the discontinuity in $W(r)$ at a specific range; also denotes distance between the hologram plane and object plane
$D(W, g, n, \omega)$	magnitude of the discontinuity in $W(r)$ of order $n$ at point $r_g$ for the frequency $\omega$
$D_n$	GTD diffraction coefficient defined by Pathak and Kouyoumjian (1974)
$D_n^{LK}$	GTD diffraction coefficient defined by Levy and Keller (1959)
$E(g, n)$	Freedman backscattering contribution associated with a single discontinuity in $W(r)$ of order $n$ at range $r_g$
$E_g$	Freedman backscattering contribution associated with all discontinuities in $W(r)$ and its derivatives at range $r_g$
$f(r)$	any continuous function of a parameter $r$
$f(\theta, \phi)$	backscattering form function
$F(r, \theta)$	function that defines a three-dimensional surface in the form $\phi = F(r, \theta)$
FET	field-effect transistor
$G$	Gaussian curvature
$G(r), G(\underline{r}, \underline{r}')$	Green's function
$G_n(r)$	normal derivative of the Green's function



GTD	geometrical theory of diffraction (Keller theory)
$h$	normalized spheroidal frequency (defined in Section 4.1); also denotes height of cone
$i$	positive square root of $-1$
$I(r)$	indefinite integral defined by Equation 2.17
$I_+(r_g), I_-(r_g)$	antiderivatives associated with $W_+(r_g)$ and $W_-(r_g)$ , respectively
$I_f$	intensity of the scattered field
$I_s$	intensity of the surface field
$j_0$	spherical Bessel function of order zero
$J_0$	Bessel function of order zero
$J_1$	Bessel function of order unity
$k$	wave number
$k'$	wave number of reflected wave
$k_x, k_y, k_z$	spatial wave numbers in the $x$ , $y$ , and $z$ directions, respectively
$K$	spatial wave number in a plane, $K = (k_x^2 + k_y^2)^{1/2}$
$\ell$	length of a cylinder
$M$	incident wave constant defined as $M = P \exp(-i2kr_1)$
$\hat{n}$	unit normal vector
$\underline{n}$	normal vector
$P_i$	incident pressure
$P_s$	scattered pressure
$P$	constant that specifies the pressure from a source in the form $P[\exp(-ikr)/r]$

$q_n$	root of the GTD impedance equation defined by Pathak and Kouyoumjian (1974)
$q_n^{LK}$	root of the GTD impedance equation defined by Levy and Keller (1959)
$r, \theta, \phi$	spherical coordinates
$r_f$	range from the origin of coordinates to the furthest illuminated part of a scattering body
$r_g$	range from the origin of coordinates to a specific discontinuity on a scatterer
$r_m$	mean range from the origin of coordinates to a scattering body
$\hat{r}_0$	Fourier-transformed coordinate, $\hat{r}_0 = (k_x, k_y, z)$
$r_l$	range from the origin of coordinates to the nearest part of a scattering body
$R$	constant range parameter used in several examples, usually denoting the range from the center of an object to the transducers
$R_H, R_O$	distances from the center of coordinates to points on the hologram or object, respectively
$R_s$	distance from the center of coordinates to a source point
$dS$	incremental element of surface area
$t$	time coordinate
$T$	delayed time coordinate, $T = t - (2r_g/c)$
$\underline{u}$	acoustic particle velocity
$u_i$	component of the acoustic particle velocity that is incident on a body in the direction of propagation
$V$	velocity potential; also used to represent the voltage waveform of a pulse
$W(r)$	total solid angle subtended by the portion of a scattering body within range $r$
$W_+(r_g), W_-(r_g)$	continuous quantities that represent $W(r)$ at ranges following or preceding, respectively, a discontinuity at $r_g$

$x', y', z'$	rectangular coordinates
$x_H, y_H, z_H$	rectangular coordinates in the hologram plane
$x_0, y_0, z_0$	rectangular coordinates in the object plane
$z_H, z_0$	distances along the z-coordinate axis to the hologram plane and the object plane, respectively
$\alpha_n$	GTD attenuation coefficient defined by Pathak and Kouyoumjian (1974)
$\alpha_n^{LK}$	GTD attenuation coefficient defined by Levy and Keller (1959)
$\epsilon$	half-angle of a cone
$\lambda$	wavelength of sound in the medium
$\xi, \eta, \phi$	spheroidal coordinates (defined in Section 4.1)
$\rho, \rho_0$	density of the medium
$\rho', \phi, z$	cylindrical coordinates
$\rho_g$	radius of curvature of a surface in the plane containing the propagation path
$\rho_1, \rho_2$	principal radii of curvature of a surface at a given point
$\rho_*$	variable radius of curvature of an impedance surface
$x_{LK}, \chi$	dummy integration parameters used in the definition of the Airy function
$\psi$	angle between the radius vector and the normal to a surface
$\omega$	harmonic wave frequency
$\omega_0, \lambda_0, k_0$	mean frequency, wavelength, and wave number in a frequency band
$\Delta\omega$	bandwidth
$\nabla$	vector gradient operator
$\nabla^2$	Laplacian operator

- \* convolution operator
- ^ denotes a vector of unit magnitude; also denotes the result of a two-dimensional Fourier transform
- (underscore) denotes a vector quantity

## ACKNOWLEDGEMENTS

The author wishes to express his deepest gratitude to Professor Eugen J. Skudrzyk, thesis advisor, for his continuing guidance and support throughout this study. Appreciation is also expressed to Professors Francis H. Fenlon, Sabih I. Hayek, Jiri Tichy, and William Thompson, Jr. for their instruction and active participation in the author's doctoral committee.

The author wishes to thank Dr. Robert L. Cohen and Mr. Kent E. Eschenberg for their substantial contributions to the acoustical-holography efforts. Appreciation is also expressed to Mr. Lynn A. Poole for his assistance in the design of the electronic equipment. Finally, the assistance of Mr. Frederick R. Stocker in introducing the author to computer graphics is acknowledged.

This research was supported under the Exploratory and Foundational Research program directed by Dr. M. T. Pigott of the Applied Research Laboratory under contract with the U. S. Naval Sea Systems Command. Additional support was also received from the Office of Naval Research, Code 464.

1

CHAPTER 1  
INTRODUCTION

1.1 Background and Objective

Considerable effort has historically been expended to model the diffraction of wave fields using asymptotic and approximate methods. Over 130 references are cited in this report, and they represent only a fraction of the total number in the literature. However, due to the complexity of the phenomena, fundamental questions remain to be solved.

Even the most respected diffraction theories exhibit some dramatic failures in surprisingly simple cases. For example, the Freedman (1962a, 1962b) theory provides a method for resolving backscattered echos in time and space that has been considered important enough to be included in Albers' (1972, pp. 246-268) collection of benchmark papers in underwater acoustics. However, the theory includes some questionable mathematical developments that have not been critically examined, and the few existing comparisons between prediction and experiment (Dunsiger, 1968, 1970) are inconclusive at best. As a second example, the Keller extended-geometrical prediction for backscattering from a thin spheroid is incorrect by at least one order of magnitude for reasons that are unresolved. This has led to a loss of confidence in the otherwise successful geometrical methods. A final example concerns Franz-type creeping waves. This surface-wave phenomenon attracted considerable attention that apparently led to conclusive explanations approximately 10 years ago. However, because creeping waves have been observed so rarely, serious doubts about the concept have arisen.

The problems with modern diffraction theories illustrated by these examples can be traced to a common cause: insufficient knowledge about the basic physics of diffraction. Thus, while mathematical techniques can be used to accurately model a given set of observed characteristics, misleading or nonphysical conclusions are frequently drawn when the predictions are analytically extrapolated (i.e., with no additional knowledge of the physics) to slightly different conditions. The likelihood that a given analytic model will be improperly interpreted is enhanced by the complexity of the required analytic techniques and the tendency of professionals to restrict their interests to either theoretical or experimental research. In any case, before one develops a diffraction model, a clear understanding of the basic physical phenomena (i.e., physical intuition) should first be established.

For this study, the urge to develop new diffraction theories has been avoided. Instead, the objective is to analyze the basic physical phenomena on which existing theories are based. Thus, the present work first identifies and then critically examines the problems and assumptions of today's dominant diffraction theories. The approach used for this examination involves careful, physical observation of basic experiments designed specifically to aid in the development of physical intuition. The procedure is a form of experimental analysis in which the results of simple experiments are used to formulate further experiments in an iterative fashion until an intuitive understanding of the particular phenomenon is reached.

## 1.2 Scope of the Study

The first task of this study was to review the popular diffraction theories in order to isolate points that needed further clarification. This was accomplished primarily by an extensive literature review that is summarized in Section 1.3. For the Freedman theory, however, a detailed analysis of the derivation was required because such an evaluation does not appear in the literature. That theoretical analysis is presented in Chapter 2. The second and larger task was to devise and perform a series of experiments that would serve as informative test cases for the problems and weaknesses identified in the first task. The prolate spheroid served as a basic model for diffraction from smooth surfaces. The effects examined include the origin and angular dependence of the scattering components, the significance and nature of the creeping waves, and the influence and interaction with small obstructions on the smooth surface (Chapter 4). Other types of models were used to examine both the directivity and frequency response of edges and tips of various orders. These models included baffles, cylinders, cones, and cone variants (Chapter 5). Finally, to complete the analysis of the Freedman theory begun in Chapter 2, the cylinder and cone data in Chapter 5 were compared with equivalent theoretical predictions.

The experimental analysis has been limited to a subset of acoustic-wave scattering (mostly backscattering) effects demonstrated by bodies of convex geometry in an air medium. Thus, the scattered fields observed are singly diffracted and scalar in nature, and all scattering bodies are essentially rigid. Because of practical limitations,



4

farfield conditions for diffraction effects could not be obtained. The source and receiver were always far enough from the scatterer to assume that any local, exponentially decaying fields had died out (i.e., in the acoustic farfield). However, the wavefronts could not be considered as planar, and differences in propagation-path losses between different models or different parts of the same model occasionally had to be taken into account.

Two different measurement techniques were used. Most of the results are standard gated-pulse measurements, i.e., a transmitted tone burst of finite length is scattered by a body and then measured during a known time window with a gated receiver. The second measurement technique is a long-wavelength imaging technique similar to standard holography. In this technique, the monofrequency pressure field (either pulsed or continuous) scattered by a body is measured at many points within a large, rectangular aperture, and the originating field at the surface of the scatterer is then reproduced by a numerical wave-reconstruction process. Because the results of this new imaging technique must be interpreted carefully, they are all presented separately in Chapter 6 along with an explanation of the theoretical basis for the technique and the required experimental equipment.

Some comments about the selection of experiments and presentation of results are in order. First, because the goal of this study was to understand rather than to verify hypotheses, each individual test was preceded by a series of "insight experiments." These experiments involved such simple techniques as manually positioning a model and associated microphone while concurrently observing the results on an

oscilloscope (see Section 3.4). Then, configurations that looked interesting were examined more closely, and data were recorded for analysis and presentation. Many of the final results presented in this document were preceded by weeks or months of preliminary investigations. Second, the individual data curves are presented in a form as close to the original as possible. This has been done because the small oscillations, asymmetries, etc. that occur in the data frequently provide either insights into the phenomena or indications of the confidence that should be accorded to the data. The frequency-response plots could not be preserved in this form because they had to be manually adjusted to compensate for the loudspeaker's response. Third, as a further interpretive aid, each plot contains a small figure intended to describe unambiguously the configuration used in that particular experiment. Thus, the results of this thesis have been organized and presented to support both a broad reading to develop insights and a more detailed examination of any cases of interest to the particular reader.

### 1.3 Review of Related Work

Before the results of this work are discussed, it should be informative to review from a broad perspective some of the major theoretical and experimental developments in the study of diffraction. The literature on the subject is too voluminous to permit a complete review in this introduction; therefore, the description will be limited to an outline of the past developments that were considered when formulating the experiments for this study. For additional information,

2

major works of a summary nature have been written by Bowman, Senior, and Uslenghi (1969); James (1976); New, Andrews, Brill, Eisler, and Ueberall (1974); Skudrzyk (1971); and Uslenghi (1978).

The study of diffraction can be traced back to observations made many centuries ago about the propagation of light and sound. Even the formal study of this phenomenon was evident as early as the 17th century when Huyghens proposed the famous principle of wavefront construction that bears his name. As early as 1881, Rayleigh applied the classical normal-mode solution to the scattering from an infinite cylinder; in 1908, Mie applied the solution to a sphere. Since then, much progress has been made toward improving both the applicability and numerical suitability of various methods. The advent of radar and its attendant problems in the period from 1940 to 1945 provided a significant boost to the level of effort devoted to scattering problems, and this effort has largely continued to the present day. Nevertheless, the fact that scattering from very simple shapes still receives a lot of attention is a good indication of the complexity of the subject.

#### 1.3.1 Eigenfunction Method

Some of the earliest formal diffraction solutions were derived using the method of eigenfunctions or normal modes. This method (as applicable here) involves expressing the problem in a coordinate system where the three-dimensional wave equation separates into three ordinary differential equations, solving the three equations independently for the characteristic modes, and forming the solution as a sum of these modes. As already mentioned, the solutions for the infinite cylinder

7

and sphere were formulated very early by Rayleigh (1881) and Mie (1908), respectively. Spence (1948) derived an equivalent expansion for a circular aperture as a limiting case of the oblate spheroid, and he later evaluated the eigenfunction solution for a prolate spheroid (Spence & Granger, 1951). At about the same time, Horton and Karal (1950) worked out the solution for a paraboloid of revolution. Shortly thereafter, Siegel, Crispin, and Schensted (1955) derived the normal-mode solution for the semi-infinite cone, while that for the elliptic cylinder was not seriously studied until 1963 by Barakat.

An observation of the dates on which these eigenfunction solutions were derived provides an indication of the relative benefits and drawbacks of this method. The procedure is formally straightforward and rigorous, but it is applicable only to bodies that are coordinate surfaces in one of the eleven separable coordinate systems (only nine of these are separable for vector problems). In addition, the separation constants that are formed in the procedure appear simultaneously in more than one of the "independent" solutions for all but the rectangular, circular-cylindrical, and spherical coordinate systems. This fact, coupled with the relatively slow convergence of the resulting series, severely limits the practicality of eigenfunction solutions for numerical analysis. The relative complexity and the series form of the wave functions also make it difficult to draw physical conclusions about the results without extensive numerical computations.

Despite the difficulties, numerical analysis of eigenfunction solutions has provided much useful data where exact solutions were required or other solutions were not available. For example, Hickling

(1958) used this procedure to show that the backscatter from similar-sized bodies of various shapes (sphere, prolate spheroid, and circular cylinder) is dependent on the body geometry even at relatively low frequencies. The advent of desk calculators and, later, computers was responsible for making these results feasible although time consuming. Hickling (1962, 1964) used the same method to evaluate some of the earliest results of scattering from an elastic sphere. These results included a very interesting theoretical study of pulse scattering derived by Fourier transforming the eigenfunction solution. Most of the reliable results for scattering from the prolate spheroid are also based on eigenfunction techniques applied either directly or through asymptotic evaluation of the mode functions (Andebura & Ostashevskii, 1974; Kleshchev & Sheiba, 1970; Lauchle, 1975a, 1975b; Senior, 1966).

#### 1.3.2 Watson Transformation

An interesting and numerically useful result can be obtained from the eigenfunction solution when the Watson (1918) transformation is applied. This transformation involves representing the modal terms of the solution as poles inside the contour of a complex integral, then shifting the contour to produce a solution in terms of a new series of poles that yields better convergence properties. Franz (1954) showed that this transformation produces terms in the solutions for the sphere and cylinder that can be interpreted as waves traveling around the bodies on their surface: the "creeping waves" (see also Deppermann & Franz, 1954; Franz & Deppermann, 1952; Uberall, Doolittle, & McNicholas, 1966). This new wave phenomenon has received considerable attention in

the literature, and it is discussed in more detail in this introduction in conjunction with Keller's geometrical diffraction theory. The Watson transformation has been applied, with similar results, to the eigenfunction solutions for the elliptic cylinder (Leppington, 1967) and, for one order of summation, to the prolate spheroid (Kleshchev, 1974).

### 1.3.3 Integral Solutions

In addition to the eigenfunction solution, another technique that formally produces exact solutions is direct application of the well-known Helmholtz-Huyghens radiation integral (see, for example, Skudrzyk, 1971, pp. 489-494). Utilization of this technique leads to an integral equation that relates the wave amplitude at a field point to the amplitude and normal derivative of the wave field along any closed boundary that envelopes the point. The method is rigorous, but it can be solved directly only in very rare cases. Techniques for solving the integral equation numerically by breaking the integral up into a finite number of sums and solving the resulting system of equations on a computer have been studied (see, for example, Copley, 1968; Schenck, 1968). However, this method is most important as the starting point for many approximate, numerical methods, especially those that are concerned with surface fields or currents on the body of a scatterer (see, for example, Hong, 1967).

#### 1.3.4 Asymptotic or Approximate Solutions

Because the exact formulations of the diffraction problem are generally not suitable for obtaining quantitative results at any but the lowest  $kL$  values (where  $L$  is a characteristic length), considerable effort has been devoted to determining approximate solutions to the problem. One of the most straightforward methods uses normal-mode solutions with one or more terms replaced by numerically simpler forms that are analytically valid at designated limiting values of the parameter. Other methods proposed exhibit considerable diversity and ingenuity, but they have certain common features. The techniques often begin with an exact formulation in either eigenfunction or integral form. In addition, they may assume relationships based on heuristic or formal representations of well-known solutions. For example, one often sees the phase relationship in a solution assumed a priori to correspond to geometric paths in an otherwise rigorous treatment in order to obtain the solution in a form such as  $U(r) = \exp(ikr) I(r)$  (see, for example, Brown, 1966; Hong, 1967). Because of the necessarily strong ties to known results and methods, most of the asymptotic solutions given in the literature apply to the same simple cases as do the more formal solutions (although the practicality or applicable parameter range is generally expanded). The heuristic assumptions sometimes make it difficult to estimate convergence criteria and ranges of applicability. Finally, it is not at all uncommon to find that different solutions are required for different aspect angles, frequency ranges, shapes, etc. In short, the asymptotic methods may require considerable ingenuity and skill for their application to obtain a reliable prediction, but their

accuracy can be surprisingly good in certain, sometimes unpredictable, cases.

#### 1.3.5 Geometrical Optics

Perhaps the most obvious first approximation for short wavelengths is classical geometrical optics (Born & Wolf, 1959, pp. 108-131). This well-known method is based on the concept of rays with propagation described by shortest-distance paths according to Fermat's principle and conservation of energy within tubes of rays (see Figure 1.1). It is very useful when dealing with the short wavelengths encountered in optics, but its usefulness is more limited for acoustics and radar applications where the size of the wavelengths encountered are of the same order of magnitude as the scattering objects.

#### 1.3.6 Lundeburg-Kline Expansion

Lundeburg and Kline (see Kline, 1951) developed an asymptotic-series solution in powers of  $1/k$  in an attempt to assess the magnitude of error involved in the geometrical-optics approximation. This technique is especially appreciated, because it includes the geometrical-optics solution as its first term and goes on to provide a formal, rigorous procedure for deriving additional terms in the solution. Keller, Lewis, and Seckler (1956) applied this basic method to a wide variety of scattering problems in a paper that is frequently referenced for accurate representations of specular scattering mechanisms. They noted, however, that even this simple expansion is difficult and lengthy to apply in many applications. An interesting



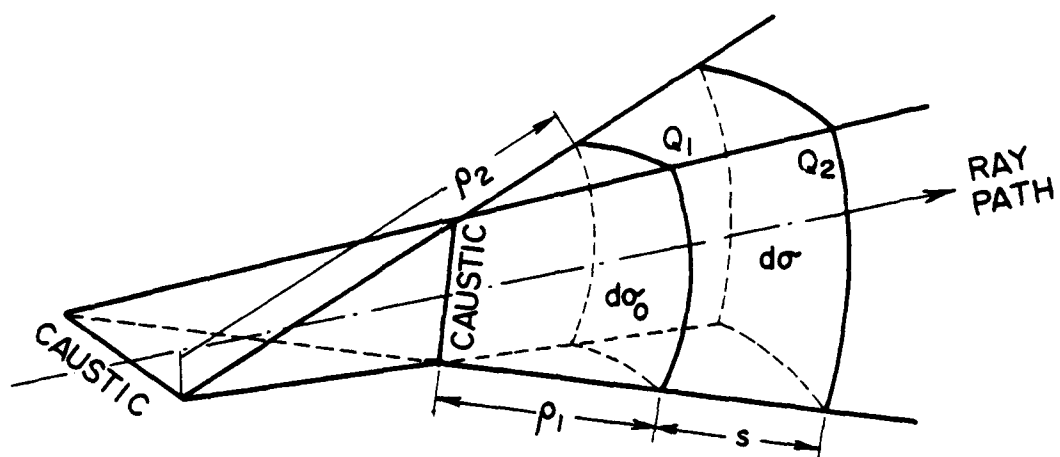


Figure 1.1 Ray tube of geometrical optics. A caustic occurs at those points where one or both of the radii of curvature of the wavefront vanish.

result relating to this method was obtained by Darling and Senior (1965). They found that the radius of convergence of this series approximation for a thin spheroid is larger than that for the similar sphere--a result that is contrary to assumptions commonly made.

#### 1.3.7 Kirchhoff Approximation

One of the earliest and most important examples of approximate diffraction techniques is based on assumptions first proposed by Kirchhoff in the late 19th century (see, for example, Skudrzyk, 1971, pp. 517-519). According to Kirchhoff, the field behind an aperture in a plane (shadowed side) can be computed by means of an integral over the aperture only. It must be assumed that (1) the field and its normal derivative vanish behind the screen, and that (2) the field and its normal derivative in the aperture are both identical with those for the undisturbed incident field at the location of the aperture. This approach was later modified by Rubinowicz (1924) to represent the diffracted field as a line integral over the edge of the aperture (see Skudrzyk, Hayek, & Stuart, 1973). The Kirchhoff method can also be formulated for scattering from three-dimensional bodies, where it is known as physical optics. In the latter case, each point on the diffracting object is assumed to act as a small volume source in an infinite plane baffle, where it scatters with a known reflection factor into a space angle of  $2\pi$ .

The applicability of the Kirchhoff-Rubinowicz method has been studied fairly extensively. Theoretical analyses (Leitner, 1949; Spence, 1949) and experimental analyses (Wiener, 1949) have both shown

that the field near the edge of an aperture differs considerably from that assumed by Kirchhoff. However, they also show that the physical-optics expressions work surprisingly well in their prediction of the field at great distances from an aperture, although the accuracy is degraded in some cases at angles away from the direct forward or backward direction (Ross, 1966). The accuracy of the physical-optics predictions for three-dimensional scatterers is more variable. Good agreement has been reported for scattering from the tip of a semi-infinite, electromagnetic cone (Siegel, Crispin, & Scensted, 1955) and the curvature discontinuity of a cone-sphere (Senior, 1965), despite the fact that the original assumptions are of questionable validity in these cases. However, results from similar acoustic scatterers reported in Chapter 5 exhibit much poorer agreement between theory and experiment. In general, the Kirchhoff method is considered to be an improvement over geometrical optics, and Leizer (1966) has reported some limited success in attempting to formulate a procedure for suitably modifying geometrical-optics results with physical-optics corrections. This approximate method must be used judiciously, though, because it is known to predict contributions from the shadow boundary in cases where none have been observed with either exact-theoretical or experimental procedures.

#### 1.3.8 Freedman Method of Echo Formation

A modified form of the Kirchhoff method was used by Freedman (1962a, 1962b) in a study of the shapes of backscattered acoustic pulses, a problem that is very important for target identification.

Freedman's results show that an echo is composed of a number of discrete "images" of the incident pulse. Using an analysis with coincident source/receiver transducers at the origin of the coordinates, an individual image pulse is generated wherever there is a discontinuity with respect to range in the solid angle subtended by the scattering body at a given range. An approximate procedure for evaluating this type of solution as a sum of discrete area segments was proposed by Neubauer (1963), and the original procedure was used by Gatkin, Paramonova, and P'yanov (1972) to approximate the scattering by a rigid spheroid. Freedman (1970a, 1970b, 1971, 1972, 1977) later generalized the basic technique to handle transient radiation problems.

The Freedman method is of particular interest because of its easily evaluated results and its prediction of scattering mechanisms based on a formal analytical procedure. However, it does not seem to have been quantitatively analyzed to any significant extent in the literature (see, however, Dunsiger, 1968, 1970). Thus, the method has received further study in this thesis. The qualitative descriptions of scattered pulse shapes provided by Freedman (1962a, 1962b, 1964) make interesting reading, especially for those persons unfamiliar with the complex forms encountered in experimental work. Similar analyses of echo shapes based on exact theoretical studies (Hickling, 1962, 1964; Rudgers, 1969) and experimental studies (for example, Barnard & McKinney, 1961; Hampton & McKinney, 1961) have also been reported.

### 1.3.9 Keller's Geometrical Theory of Diffraction

Perhaps the most promising and ingenious approach to the problem of high-frequency asymptotic solutions for complex scattering objects was developed by J. B. Keller in the mid-to-late 1950's (Keller, 1956, 1957, 1958, 1962; Levy & Keller, 1959). In discussing this technique, it is important to separate the method itself from the actual implementation that is continually evolving. The method is based on two assumptions: (1) wave-propagation properties at a given point are determined solely by the properties of the medium and the structure of the field in an arbitrarily small neighborhood of the point; and (2) all fields, no matter how they were produced, must have the same local structure, i.e., that of a plane wave (Keller, 1962). Having made these assumptions, one can construct a solution for any complex shape by first breaking the scattering object into a sufficient number of simple structures whose properties are known and then matching the field between regions. The solution in the locality of the simple structures is obtained from "canonical" problems, which are defined as the simplest boundary-value problems that have the same local properties (field, media, geometry) as the given structure. Keller and his colleagues have tried to develop this concept into a complete method that is both formal and rigorous rather than heuristic.

Keller's implementation of these assumptions is based directly on the principles of geometrical optics with the addition of diffraction rays. He defines three new laws associated with edge, vertex, and grazing-surface diffraction. Thus, an incident ray striking an edge is reflected in a manner similar to reflection from a plane but spreading

in a complete arc around the edge to form a cone of rays (see Figure 1.2a). A similar result is postulated to occur at a vertex, where rays now spread in a complete spherical pattern (Figure 1.2b). Note that the terms edge and vertex refer not only to appropriate discontinuities in a surface or edge but also to discontinuities in their derivatives. The last diffraction ray is a surface ray that forms whenever an incident ray impinges tangent to the scatterer surface. It then propagates along the surface, continually directing new rays into the medium in a direction tangent to the current path (Figure 1.2c). The ray paths assumed for both the geometrical and diffracted rays are shortest paths based on an extended concept of Fermat's principle, with the addition of certain specified phase discontinuities (for example, at a caustic). The edge and vertex rays are subjected to a multiplicative diffraction coefficient at their formation but are otherwise described by geometrical optics. The surface rays are described by three parameters: a multiplicative diffraction coefficient at the points of formation and reradiation, an exponential attenuation factor accounting for loss of energy due to reradiation, and a factor to account for spreading on the surface. All of these coefficients are determined by comparison with an appropriate canonical problem.

Several general conclusions can be drawn about Keller's geometrical theory of diffraction (GTD). One primary advantage is the fact that it does not possess any case-limiting associations such as a requirement for separation of variables. This gives GTD the very important benefit of being applicable to an object of any shape; however, in practice, the separation from specific simple geometries is not complete because of

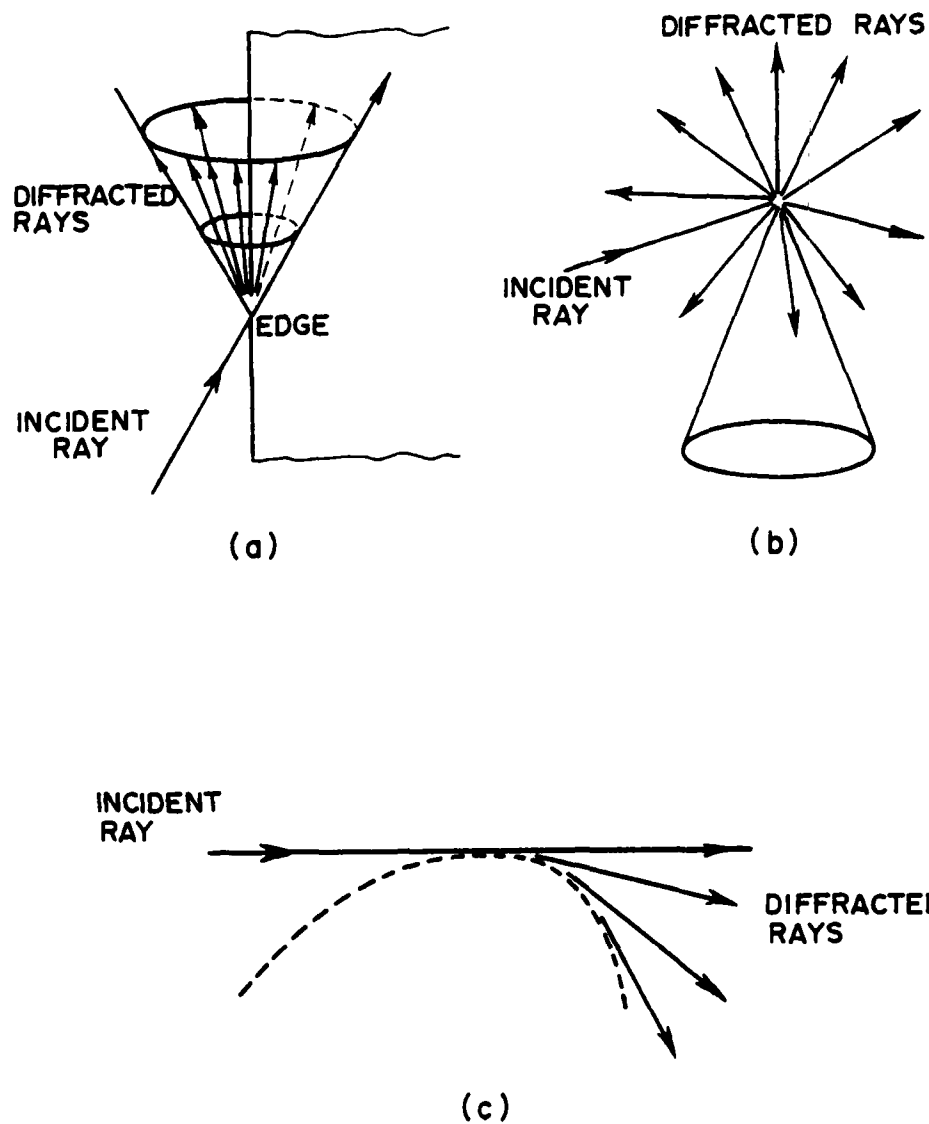


Figure 1.2 Geometric description of the three new types of diffraction rays proposed by Keller, including (a) edge rays, (b) vertex rays, and (c) surface rays.

the requirement for applicable canonical problems. Furthermore, solutions have been derived only for relatively simple objects because of the complicated geometrical relations that are required to model more complex shapes. Confidence in the method is aided by the extensive efforts of Keller and his colleagues to show that the GTD solutions agree with the solutions of other formal methods in the asymptotic limit. But, one must remember that some of this agreement is enforced by the canonical construction process. (The determination of coefficients by comparison with canonical problems is usually made in the asymptotic limit.) In addition, although the nature of the method implies greater accuracy as the wavelength decreases in proportion to the scatterer size, the heuristic construction process, which gives the method its versatility, also exhibits the absence of rigorous criteria for error analysis as well as the lack of a formal application procedure. Thus, one must have at his command a large catalog of individual coefficients and local solutions, and one must apply considerable skill in constructing the total solution. Finally, the complete method, as presently implemented, is based on geometrical optics. This dependence brings along all the problems of the latter method at caustics (Figure 1.1) and shadow boundaries.

In addition to the general considerations listed previously, the accuracy of geometrical-diffraction-theory solutions is heavily influenced by the applicability of the canonical problems used. The construction procedure guarantees a match with the canonical problems in the asymptotic limit. Thus, the total solution can also be expected to match in the asymptotic limit to at least the degree that the local-



mechanism assumption is valid if the solution is derived with adequate care and precision. However, the solution can be expected to be optimum when the assumptions made about the propagation mechanisms correspond to actual physical processes. This last conclusion should encourage careful analytical and experimental consideration of the processes involved.

The edge problem is probably the best understood of the Keller canonical problems. The diffraction coefficients can be determined from Sommerfeld's exact solutions for the half-plane or wedge (see Keller, 1962). Alternately, if impedance boundary conditions are desired, the wedge solution of Malyughinets (1960) or the impedance-edge solution of Kendig (1977) may be employed. Keller and Hansen (1965) have summarized these results and compared them with some experimental results and with other analytic formulations. This comparison generally confirms the validity of the Keller edge solution--at least in those problems where it has been utilized (see also Keller, 1961; Ross, 1966). The cone of rays postulated to emanate from an edge has also been observed experimentally (Senior & Uslenghi, 1972). Finally, higher-order coefficients have been obtained for the edge at a discontinuity in curvature (Albertsen & Christiansen, 1978; Senior, 1972; Weston, 1962, 1965), but these coefficients are based on canonical solutions that are approximate rather than exact, as was the case for the previously mentioned edge coefficients.

The canonical problems for corners and vertices are not nearly as well developed as those for the edge. Kraus and Levine (1961) obtained an eigenfunction solution for the elliptic cone that is capable of

producing a solution of the quarter-plane problem, but no diffraction coefficients have been derived. The results that are available for the vertex problem are also limited. The semi-infinite cone problem has been evaluated, for example, by Siegel, Crispin, and Schensted (1955). However, most of the geometrical-diffraction-theory results in the literature either treat the vertex contribution as negligible in comparison to more prominent ones (for example, scattering from the base of a finite cone) or utilize a physical-optics approximation at the vertex (Bechtel, 1965; Keller, 1960; Senior, 1965).

The surface rays postulated in the Keller geometrical theory of diffraction were formulated based on the creeping waves of Franz (1954). In this case, three characteristic parameters must be determined: the diffraction coefficients, the attenuation factor, and the surface spreading factor. In Keller's implementation, the diffraction coefficients at formation and reradiation are assumed to be functionally identical due to reciprocity, and both the diffraction and the attenuation coefficients are assumed to depend to a first-order approximation solely on the surface radius of curvature along the direction of propagation. Thus, these coefficients are obtained from the two-dimensional cylinder problem (Keller, 1956; Levy & Keller, 1959). It is important to note that the exponential decay represented by the attenuation coefficient is attributed to reradiation energy loss (not surface damping), although the derivation of the appropriate canonical solution does take the impedance of the surface into account. Higher-order diffraction and attenuation coefficients, which also depend on the first and second derivatives of the curvature and sometimes also

the curvature transverse to the propagation path, have been derived by Franz and Klante (1959), Keller and Levy (1959), and Voltmer (1970). The surface spreading factor is determined from geometrical considerations rather than from a canonical solution because the appropriate canonical solution for all problems solved up to this time would be virtually identical with that of the original problem.

The properties attributed to the Keller surface rays and the general notion of creeping waves have probably been the most controversial aspects of the Keller theory, despite the fact that there is some experimental evidence of creeping waves (Harbold & Steinberg, 1969; Neubauer, 1968). This controversy has been aided by the fact that Kouyoumjian, who has published extensively on the Keller method, uses a different definition of the Airy function than does Keller in his derivation of the surface-ray coefficients. A comparison between the coefficients used by the two different researchers is shown in Table 1.1, which was made available to the author by Dr. Francis H. Fenlon. Keller provided GTD solutions involving surface rays for the sphere and the cylinder (Levy & Keller, 1959) and for the spheroid (Levy & Keller, 1960), and he showed that they matched the eigenfunction solutions in the asymptotic limit. However, a numerical evaluation of Keller's results for thin spheroids (that uses the first-order surface-wave coefficients) by New, Andrews, Brill, Eisler, and Uberall (1974) indicates that these results are in error by at least one order of magnitude at low and even mid frequencies. In addition, Leppington (1967) found that successive terms representing creeping waves in the Watson-transformed eigenfunction solution for an elliptic cylinder do

Table 1.1

Comparison of Levy & Keller's (1959) and Pathak & Kouyoumjian's (1974)  
Diffraction and Attenuation Coefficients for Variable  
Radius-of-Curvature, Impedance Surfaces

	Levy & Keller (1959)	Pathak & Kouyoumjian (1974)
Airy Function	$A_{LK}(-\chi_{LK}) = \int_0^{\infty} \cos(t^3 - \chi_{LK}t) dt$	$A_i(-\chi) = \frac{1}{\pi} \int_0^{\infty} \cos(\frac{t^3}{3} - \chi t) dt$
Square of Diffraction Coefficient	$(D_n^{LK})^2 = \frac{\pi^{3/2} 2^{-1/2} - 1/3 k^{-1/6} \rho_g^{1/3} e^{-i\pi/12}}{3 A_{LK}'^2(-q_n^{LK}) + q_n^{LK} A_{LK}^2(-q_n^{LK})}$	$D_n^2 = \frac{\pi^{3/2} 2^{-1/2} - 5/6 k^{-1/6} \rho_g^{1/3} e^{-i\pi/12}}{A_i'^2(-q_n) + q_n A_i^2(-q_n)}$
Attenuation Coefficient	$\alpha_n^{LK} = (q_n^{LK}/\rho_*) (k\rho_*/6)^{1/3} e^{i\pi/6}$	$\alpha_n = (q_n/\rho_*) (k\rho_*/2)^{1/3} e^{i\pi/6}$
Roots	$q_n^{LK}$	$q_n = q_n^{LK/3}$

not necessarily decrease as had previously been assumed. (They do decrease for the circular cylinder.) Finally, studies of the surface fields on curved bodies such as spheroids by other asymptotic methods, such as those of Chen and Pao (1977), Goodrich and Kazarinoff (1963), and Kazarinoff and Ritt (1959), generally support the possible interpretation of surface-wave effects on these bodies; but they further indicate that Keller's analytic description of surface rays may not adequately describe the phenomenon. Kazarinoff and Ritt indicate that surface-wave propagation throughout the body may depend to second order on the radius of curvature at the irradiated tip for axial incidence--a conclusion that would void the local-mechanism assumption of Keller. Note that when elastic bodies are considered, an additional type of creeping wave, much more prominent than the Franz-type wave, is found traveling in the elastic surface (see Doolittle, McNicholas, & Uberall, 1967; Dragonette, 1978; Goodman, Bunney, & Marshall, 1967).

The last group of canonical solutions for the Keller theory to be considered here result from the inaccurate representations given by geometrical optics near caustics and shadow boundaries. Since geometrical optics predicts an infinite field at a caustic, Kay and Keller (1954) have derived a finite solution for a caustic point and line; and Levy and Keller (1959) have shown how these results can be applied as a canonical solution to problems utilizing the geometrical theory of diffraction. The discontinuities predicted by geometrical optics at shadow boundaries have been analyzed by Buchal and Keller (1960) as a boundary-layer problem. A boundary layer is defined as a thin layer in which a function varies rapidly with respect to a

parameter (such as caustics and shadow boundaries). Buchal and Keller showed how an asymptotic solution that is valid in the boundary layer could be used to correct the field at surface edges. Brown (1966), Fock (1965), and Ludwig (1969) have studied the corresponding problem for convex bodies. In a somewhat more elegant approach, Kouyoumjian and Pathak (1974) have used a more general canonical solution to derive diffraction coefficients at edges involving Fresnel integrals. This method, which is often called the uniform theory of diffraction, derives additional terms that add to the geometrical-diffraction-theory solution to control the problems of the latter solution in the boundary layer (see also Lee, 1978). However, the problem of caustics in the field is not aided by this method.

Without going into detail, it should be mentioned that the Keller theory has been extended for use with elastic bodies (Keller, 1958) and with bodies that can support surface waves (Keller & Karal, 1960; Karal & Keller, 1964). In the latter case, complex rays are introduced. New canonical solutions are also under constant development. For example, Pathak and Kouyoumjian (1974) have derived coefficients to describe the launching of surface rays from the edge of an aperture in a curved surface.

#### 1.3.10 Ufimtsev's Method of Boundary Waves

The idea of constructing a solution from a number of canonical solutions with an assumption of localized diffraction mechanisms is not unique to Keller. At about the time of Keller's proposals, Ufimtsev (1958, 1969) proposed a similar technique based on physical optics. In

his method, the surface field predicted by a Kirchhoff approach, which is known to be in error near edges and shadow boundaries, is corrected by the addition of a nonuniform edge component or "boundary wave." Then, the farfield solution is determined by integrating the surface field. The boundary wave is derived using a canonical solution such as that for a wedge or half-plane. Although a complete series of canonical solutions is formally feasible, Ufimtsev has only derived relations for the case of edges.

The Ufimtsev method has been compared with other methods by Knott and Senior (1974), and Senior and Uslenghi (1971). They show that the Ufimtsev method is correct only to first order for the strip and the disk, but that its numerical estimates for these cases are reasonably close to those obtained by Keller's method. They also note that Ufimtsev does not actually evaluate the surface terms; rather, he uses their formation to construct an equivalent group of half-planes whose scattering solutions are then summed. In general, the Ufimtsev method has been in the shadow of the Keller method since its inception because of its dependence on integral formulations and because it has not been as extensively developed. Because physical optics offers an improvement over geometrical optics, it would at first appear to hold more promise than the Keller method. However, its strong association with the very complex fields on the surface of a body (as opposed to those some distance away) makes its practical implementation extremely complicated and its solutions difficult to evaluate.

### 1.3.11 T-Matrix or Extended Boundary Condition

The final theoretical method to be considered is based on the extended boundary condition formulated by Waterman for electromagnetics (1965) and acoustics (1969). The method makes use of the Helmholtz integral formula and expansions of the incident, scattered, and surface fields in terms of orthogonal basis functions. The actual relationships among the expansion coefficients are too complex to explain in detail here. However, in general, two sets of equations are derived: (1) the Helmholtz integral outside the scatterer is used to relate the coefficients of the scattered wave to those for the surface fields; and (2) the Helmholtz integral evaluated for a point inside the body, where the field is everywhere zero, is used as an extended boundary condition to relate the incident-wave coefficients to those for the surface-field components. Finally, a transition (T) matrix that directly relates the incident-wave and scattered-wave expansion coefficients is derived. The Helmholtz integral evaluation inside the body is called the extended boundary condition because the condition is forced throughout an entire volume. The basic method has also been extended to cover scattering from elastic bodies by V. V. Varadan (1978), V. V. Varadan and V. K. Varadan (1979), and Varatharajulu and Pao (1976).

A numerical evaluation of the Waterman (T-matrix) method has been performed by Bolomey and Wirgin (1974). Although it is an integral method, they show that the Waterman method is significantly more efficient in a numerical sense than the direct integral methods discussed in Section 1.3.3. The method is generally valid for all types of scattering bodies, but it is currently restricted by computational



complexity to low frequencies and to roughly spherical (i.e., not elongated) bodies. In general, a judgment of the usefulness of this relatively new method must await its further development. The heavy reliance on matrix techniques makes it very difficult to draw physical conclusions about the results of a T-matrix solution without extensive numerical evaluation, but the method could prove to be extremely useful in the modern computer age.

#### 1.3.12 Experimental Work

Because the study reported in this thesis is primarily experimental in nature, a review of past experimental results is of interest. An overall historical trend in the use of experiment seems to be indicated. Early work in wave propagation and diffraction depended very heavily on experimental results to "show the way." Rayleigh (1945) made extensive use of simple experiments to aid the development of his monumental work on acoustics first published in 1894. Becknell and Coulson (1922) first determined that the caustic in the shadow behind a disk is the evolute (i.e., locus of the center of curvature) of the scattering edge by means of diffraction experiments with visible light. As interests later turned toward longer-wavelength effects in the acoustics and microwave range, organized scientific development began to depend more heavily on theoretical developments. While experimental data were still used directly for certain specialized applications, the developmental studies began to use experiments primarily as direct confirmation of theoretical results. The apparent transition in research methods seems to result from the highly developed, complex theoretical methods that have been

formulated. The resulting specialization of personnel in either theory or experiment has made the cross fertilization of these two complementary methods more difficult.

When examining the literature for experimental results, one is generally disappointed by the relatively small amount of data available (or at least published in the open literature). The bodies that have received the most attention are the simplest shapes: the sphere and the cylinder. For examples in acoustics, Foxwell (1970) and Weiner (1947) examined the field near the surface of rigid spheres and/or cylinders. The scattering from elastic spheres has also received a lot of attention (Freedman, 1964; Hampton & McKinney, 1961; Newbauer, Vogt, & Dragonette, 1974). In fact, because the analytical solution for a sphere is so well understood, this body is frequently used as a calibration standard for other experiments.

Another shape that has received a fair amount of attention in electromagnetics is the finite cone and the related cone-sphere, the latter because of its importance as a radar target. Wiener (1948) included the cone among the bodies on which he performed surface measurements. Hong and Borison (1968) and Keys and Primich (cited in Keller, 1961) provided farfield scattering results for the cone. The cone-sphere was examined, for example, by Blore (1963), Kennaugh and Moffatt (1962), and Senior (1965). In addition, the acoustic field of a prolate spheroid, both on the surface (Blake & Wilson, 1977) and in the farfield (Bayliss & Maestrello, 1978), was recently measured.

One interesting result in which experiment has played a major role is the discovery of creeping-wave effects. Franz and Depperman (1952)

were attempting to explain results of Limbach when they first postulated the existence of creeping waves. Barnard and McKinney (1961) later interpreted their measured results for elastic spheres in water in terms of those creeping waves. However, Doolittle, McNicholas, and Uberall (1967) showed that Barnard and McKinney actually observed (and thus discovered) Rayleigh-type creeping waves, which exist in an elastic surface. Identification of Franz-type creeping waves was reported by Harbold and Steinberg (1969) and Neubauer (1968), but a large degree of doubt as to the validity of the Franz-wave assumptions still exists.

The techniques used in experimental scattering have remained relatively static for many years. Virtually all measurements are made in acoustic or microwave test ranges by irradiating objects with continuous or pulsed wave fields and detecting the scattered result at desired locations with appropriate receivers. The technique has been extended somewhat for the determination of target shape (inverse scattering) by recording the scattering of pulses in two or more directions and mapping the time relationships in two dimensions (for example, Dunsiger, 1968, 1970). In addition, Dardy, Bucaro, Schuetz, and Dragonette (1977) have reported a technique whereby the frequency response of a body is determined by Fourier transforming the scattering from short pulses (see also Moore, 1974) in near real time.

## CHAPTER 2

## FREEDMAN THEORY OF ECHO FORMATION

When acoustic waves are incident upon a body of given shape and acoustic properties, complicated spatial distributions of both farfield and surface pressure result. Much effort by many researchers has been devoted to the development of new and refined techniques for predicting these distributions to greater and greater precision and over wider parameter ranges. However, when the wavelength is sufficiently small in terms of the scattering-body dimensions and when the observation point is sufficiently far from the scatterer, it is possible to make assumptions that simplify the prediction techniques to a significant degree. One appealingly simple method that attempts to capitalize on this last fact is the Freedman (1962a, 1962b) theory of echo formation. Unfortunately, unlike other frequently referenced methods such as the Keller theory, the Freedman theory has not been critically evaluated in the literature--even though its derivation is based on a Taylor expansion of questionable validity. Consequently, a complete analysis of the Freedman method has been included here.

The Freedman technique utilizes a physical-optics approach based on the Kirchhoff assumptions (modified for three-dimensional scattering) to predict the backscattering from a rigid, convex body. In general, it shares the advantages and limitations of the physical-optics approach, although additional mathematical complications are introduced for bodies whose shadow projected in the direction of the incident field takes the form of an ellipse. However, the Freedman method is formulated in a

manner that is more useful for physical interpretation of backscattering results for both continuous waves and narrow-band pulses. The value and appeal of this last benefit has attracted much attention to this method, especially in the field of underwater acoustics. Unfortunately, results of this study show that the physical interpretations provided by the method are sometimes erroneous.

The derivation presented here generally follows that of Freedman (1962a). However, certain complications, such as nonuniform source/receiver directivities, have been omitted to prevent them from clouding the interpretation of the results. Some additional remarks and conclusions about the method and its results have also been included. In the last part of this chapter, the Freedman method is applied to several examples, including spheres, cylinders, finite baffles, cones, and modified cones. These examples are intended both to point out important analytic features of the method and to show the computations that have been used for comparison with experiment. Discussions of the agreement between theory and experiment are found with the experimental results in Chapter 5.

### 2.1 Derivation of the Basic Integral Expression

The general case to be considered is that of backscattering from a rigid object insonified by a continuous, single-frequency source. The geometry is shown in Figure 2.1. The transmitter/receiver pair acts as a point element located at the origin of a spherical coordinate system in an unbounded, nondissipative, homogeneous, isotropic, fluid medium. The scattering body is assumed to be both rigid and convex. Its surface

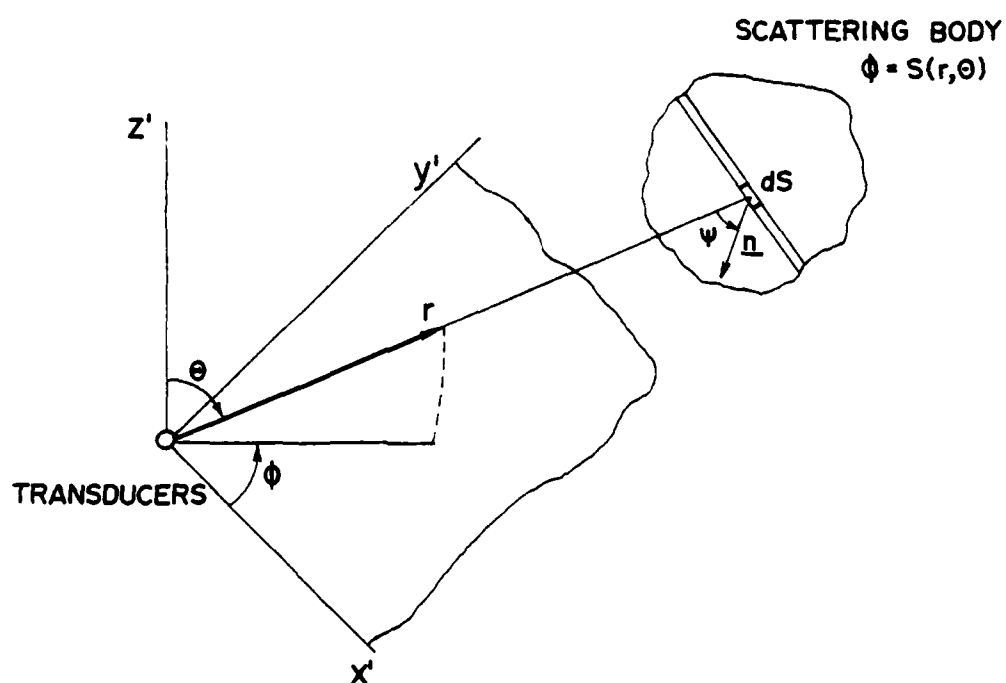


Figure 2.1 Definition of the geometry for backscattering showing the locations of the transducers and scatterer, a strip along the scatterer between ranges  $r$  and  $r+dr$ , an area  $dS$ , and the surface normal  $\underline{n}$ .

is represented by an equation of the form  $\phi = S(r, \theta)$ , which may be multivalued. A surface element of area  $dS$  and outward normal  $\underline{n}$  exists at every point  $(r, \theta)$  on the body surface  $S$ .

Assuming that the scattering body is far enough from the transmitter for the inverse-range law to hold, the pressure incident on an element of body surface  $dS$  at a distance  $r$  from the source is given by

$$p_i = \frac{P \exp(-ikr)}{r} \quad (2.1)$$

Here  $k = 2\pi/\lambda$  is the wave number,  $\lambda$  is the wavelength in the fluid medium, and  $P$  is the strength of the source. A harmonic time dependence of  $\exp(i\omega t)$  has been suppressed. The particle velocity of the wave incident at  $dS$  can be obtained from the corresponding pressure by the relation (Skudrzyk, 1971, p. 280)

$$\underline{u} = \left(\frac{i}{k\rho c}\right) \nabla p \quad (2.2)$$

where  $\rho$  is the density of the medium and  $c$  is the sound velocity in the medium. (Note the use of an underscore to represent a vector quantity.) Substituting Equation 2.1 into Equation 2.2, one obtains for the velocity incident on  $dS$  in the direction of propagation

$$u_i = \left(\frac{P_i}{\rho c}\right) \left(1 - \left(\frac{i}{kr}\right)\right) \quad (2.3)$$

Since the scattering body is rigid, the component of the net velocity normal to the surface must be zero on the surface. Thus, each element

$dS$  must act as a source of volume velocity  $-u_i \cos \psi dS$  to cancel the normal component of the incident velocity.

At this point, the Kirchhoff approximations are introduced. Kirchhoff assumes that each area element in the illuminated region acts as if it were imbedded in an infinite plane baffle, thus radiating equally over a solid angle of  $2\pi$ . In addition, the field in the shadowed region is assumed to be identically zero. The pressure  $dp_s$  back at the receiver due to the radiation of a source element of volume velocity  $-u_i \cos \psi dS$  is given by (see Skudrzyk, 1971, p. 348)

$$dp_s = \left(\frac{-iP}{\lambda}\right) \left(1 - \left(\frac{i}{kr}\right)\right) \left(\frac{\exp(-i2kr)}{r^2}\right) \cos \psi dS \quad (2.4)$$

If one assumes that the range is large enough for terms of order  $(1/r^3)$  to be neglected compared to those of order  $(1/r^2)$ , this equation reduces to

$$dp_s = \left(\frac{-iP}{\lambda}\right) \left(\frac{\exp(-i2kr)}{r^2}\right) \cos \psi dS \quad (2.5)$$

The total pressure  $p_s$  at the receiver due to backscattering from the body is obtained by integration over the illuminated surface:

$$p_s = \left(\frac{-iP}{\lambda}\right) \iint_S \left(\frac{\exp(-i2kr)}{r^2}\right) \cos \psi dS \quad (2.6)$$

This is just the Kirchhoff integral expression for the backscattering from a rigid body. The same relation can be derived by more formal means, as is shown in Appendix A.



In order to further evaluate the Kirchhoff expression (Equation 2.6), the projected area  $\cos \psi dS$  can be specified in the form

$$dS \cos \psi = F(r, \theta) dr d\theta \quad . \quad (2.7)$$

This allows Equation 2.6 to be written as

$$p_s = \left(\frac{-iP}{\lambda}\right) \int_0^{\infty} \left\{ \exp(-i2kr) \int_r \left(\frac{F(r, \theta)}{r^2}\right) d\theta \right\} dr \quad , \quad (2.8)$$

where the inner integral is applied over the range of  $\theta$  appropriate for each constant value of  $r$ . The kernel of the  $\theta$  integral is noted to be the differential element of solid angle (see Spiegel, 1959, pp. 124-125). The total solid angle subtended by the portion of the scattering body within range  $r$  is thus given by

$$W(r) = \int_0^r \left\{ \int_r \left(\frac{F(r, \theta)}{r^2}\right) d\theta \right\} dr \quad . \quad (2.9)$$

The derivative with respect to range of  $W(r)$  matches the inner integral of Equation 2.8, allowing that equation to be written in the form

$$p_s = \left(\frac{-iP}{\lambda}\right) \int_0^{\infty} \left(\frac{dW(r)}{dr}\right) \exp(-i2kr) dr \quad (2.10)$$

[assuming that  $W(r)$  is continuous]. Thus, the Kirchhoff scattering expression can be formulated in terms of the derivative of the solid angle subtended by the portions of the scattering body within range  $r$ . Note that the integral now takes the form of a Fourier transform. Note

also that, as  $r$  becomes large enough for the variation in  $(1/r^2)$  over the extent of the scattering body to be neglected,  $w(r)$  may be replaced by

$$W(r) = \frac{A(r)}{r_m^2} \quad (2.11)$$

Here  $A(r)$  is the projection toward the transducers of that part of the scattering body within range  $r$ , and  $r_m$  is some mean range to the body.

## 2.2 Integral Evaluation by Discontinuities in $W(r)$

The derivation of the scattering equation up to this point has differed little from common implementations of the Kirchhoff method. However, Freedman makes a significant departure from earlier practice by evaluating the modified Kirchhoff integral (Equation 2.10) in terms of the discontinuities in  $W(r)$  and its derivatives with respect to range. The effect of this last procedure is to divide the integral into a series of contributions that can be related to various physical features of the scatterer.

Let  $r_l$  denote the range to the nearest part of the scattering body, and let  $r_f$  denote the range to the furthest part of the body in the illuminated zone. In general, the total solid angle  $W(r)$  will be zero for ranges up to  $r_l$ , will increase continuously from range  $r_l$  until it reaches a maximum at range  $r_f$ , and then will remain at that maximum value out to range infinity. Consider, however, the example illustrated in Figure 2.2. In this case, a portion of the scatterer surface at range  $r_g$  is parallel to the incident wavefront, causing a discontinuous

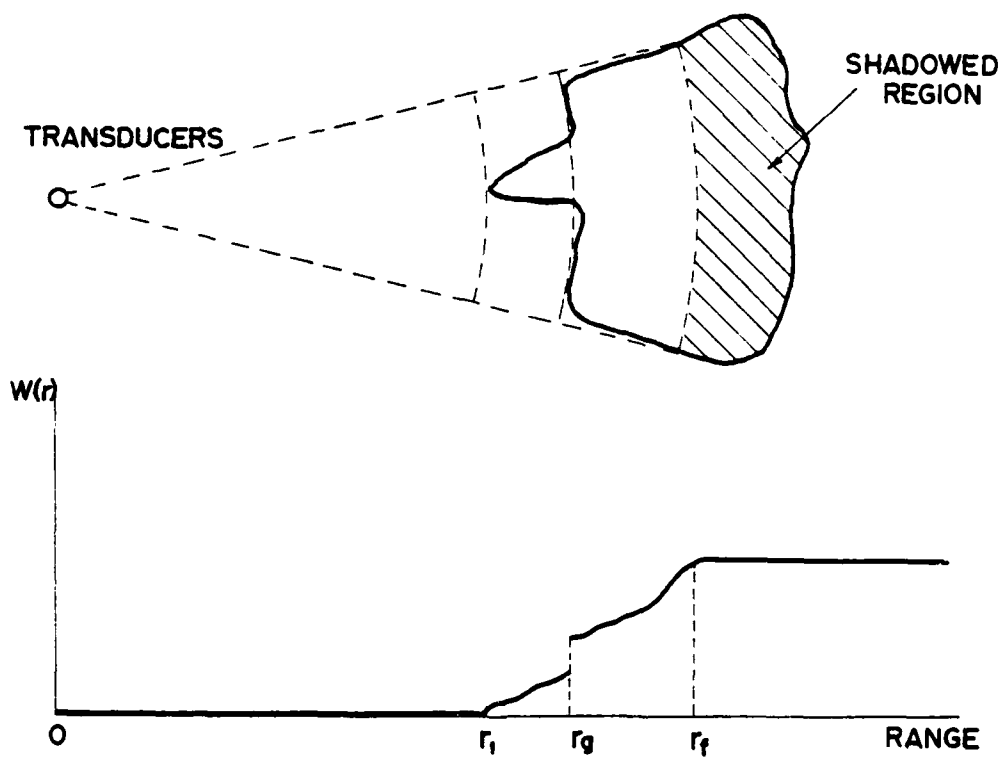


Figure 2.2 Approximate values of the solid angle  $W(r)$  versus range  $r$  for a body with a portion of its surface parallel to the incident wavefront.

jump in  $W(r)$  at that point. Equation 2.10 can be evaluated for this example if the function  $W(r)$  is continuous over the remaining portions of the range (or else further subdivision must take place) and if the derivative  $dW(r)/dr$  is modified to account for the discontinuity.

Still referring to the example in Figure 2.2, let  $W_-(r)$  be a continuous quantity that represents  $W(r)$  from range zero to range  $r_g$ . The continuity at  $r_g$  means that the single-sided limit of the function  $W_-(r)$  as  $r$  approaches  $r_g$  exists and that the value assigned to the function at  $r_g$  is this limit. Similarly, let  $W_+(r)$  be a continuous quantity that represents  $W(r)$  from range  $r_g$  out to range infinity. Finally, let the size of the discontinuity at  $r_g$  be denoted by  $D$ , where

$$D = W_-(r_g) - W_+(r_g) \quad (2.12)$$

The function  $W(r)$  can be represented as

$$W(r) = \begin{cases} W_-(r) & 0 < r < r_g \\ W_+(r) + D & r_g < r < \infty \end{cases} - DH(r - r_g) \quad (2.13)$$

where  $H(r-r_g)$  represents a Heaviside step function. Since the result will eventually be integrated, one can differentiate Equation 2.13 to obtain

$$\frac{dW(r)}{dr} = \begin{cases} \frac{dW_-(r)}{dr} & 0 < r < r_g \\ \frac{dW_+(r)}{dr} & r_g < r < \infty \end{cases} - D\delta(r - r_g) \quad (2.14)$$

Here  $\delta(r-r_g)$  is a Dirac delta function. If Equation 2.14 is substituted

into Equation 2.10, three integrals result: the two continuous integrals on either side of  $r_g$  and the delta function contribution at  $r_g$ . The latter contribution is just

$$\int_0^{\infty} D\delta(r - r_g)\exp(-i2kr)dr = D \exp(-i2kr_g) \quad (2.15)$$

Since  $dW(r)/dr$  is zero for  $r < r_l$  and  $r > r_f$ , the value of the integral over the full range becomes

$$\begin{aligned} \int_0^{\infty} \left(\frac{dW(r)}{dr}\right)\exp(-i2kr)dr &= \int_{r_l}^{r_g} \left(\frac{dW_{-}(r)}{dr}\right)\exp(-i2kr)dr \\ &+ \int_{r_g}^{r_f} \left(\frac{dW_{+}(r)}{dr}\right)\exp(-i2kr)dr \\ &- (W_{-}(r_g) + W_{+}(r_g))\exp(-i2kr_g) \quad (2.16) \end{aligned}$$

These results can be extended to include cases where more than one discontinuity exists in  $W(r)$  by further dividing the range into subdivisions between each discontinuity.

The preceding analysis shows how the modified Kirchhoff scattering integral (Equation 2.10) is related to discontinuities in the solid angle  $W(r)$  subtended by the scattering body. However, the solutions over the continuous ranges of the function are still in integral form.

To evaluate these continuous integrals, the indefinite integral or antiderivative given by

$$I(r) = \int \left( \frac{dW(r)}{dr} \right) \exp(-i2kr) dr \quad (2.17)$$

must be examined. If the integrand is continuous over the range of integration  $r_1 \leq r \leq r_f$ , then the value of the integral can be determined solely by the antiderivatives at the end points. In this case,

$$\int_{r_1}^{r_f} \left( \frac{dW(r)}{dr} \right) \exp(-i2kr) dr = I(r_f) - I(r_1) \quad (2.18)$$

Using this notation and the range subdivision of Equation 2.16, Equation 2.10 can be written in the form

$$p_s = \left( \frac{-iP}{\lambda} \right) \sum_{g=1}^f \{ (I_-(r_g) - I_+(r_g)) - (W_-(r_g) - W_+(r_g)) \exp(-i2kr_g) \} \quad (2.19)$$

where  $I_-(r_g)$  and  $I_+(r_g)$  refer to the antiderivatives of the continuous integrals involving  $dW_-(r)/dr$  and  $dW_+(r)/dr$ . This relation is valid when the summation includes  $r_1$ ,  $r_f$ , and range points in between them where discontinuities in  $W(r)$  occur. [Recall that  $I_-(r_1) = I_+(r_f) = 0$ .] However, in order to support the next step in the Freedman procedure,

the summation is extended to include points where discontinuities in derivatives of  $W(r)$  occur. This extension does not affect the result of Equation 2.19, and it will be used in the following discussion to express the value of  $p_s$  solely in terms of discontinuities in both  $W(r)$  and its derivatives.

A further evaluation of the indefinite integral (Equation 2.17) can be performed by noting that it is of the form

$$I(r) = \int f(r) \exp(-i2kr) dr \quad . \quad (2.20)$$

If this equation is integrated iteratively by parts  $m$  times, the solution becomes

$$I(R) = -\exp(-i2kR) \sum_{n=1}^m \left(\frac{-i}{2k}\right)^n f^{(n-1)}(R) + R_m \quad , \quad (2.21)$$

where

$$R_m = (i2k)^{-m} \int_R f^{(m)}(r) \exp(-i2kr) dr \quad (2.22)$$

and

$$f^{(m)}(r) = \left(\frac{d^{(m)}}{dr^m}\right) f(r) \quad . \quad (2.23)$$

Finally, by replacing  $f(r)$  with its actual form from the modified

Kirchhoff integral (Equation 2.10), one obtains

$$I(R) = -\exp(-i2kR) \sum_{n=1}^m \left( \frac{W^{(n)}(R)}{(i2k)^n} \right) + R_m \quad (2.24)$$

In his derivation, Freedman draws the tempting additional conclusion that Equation 2.24 can be treated as an asymptotic, series representation of  $I(r)$  for large values of  $kr$  by letting  $m$  tend to infinity. This would require that

$$\left( \frac{1}{2k} \right)^m \int_R |W^{(m+1)}(r)| dr \rightarrow 0 \quad \text{as } m \rightarrow \infty \quad (2.25)$$

However, there is no justification for making this assumption. Furthermore, as is shown later for the example of a circular disk, this series representation fails completely with many useful scatterer shapes because of the unbounded behavior of  $dW(r)/dr$  and its derivatives at crucial ranges. Since the disk example can be solved by direct application of the Kirchhoff integral (in the form of Equation 2.6), the difficulty clearly lies with the solid-angle interpretation of the Freedman method. Having expressed that conclusion for the general case, it should also be mentioned that there are useful examples where the integration-by-parts procedure terminates naturally after a few terms (the sphere, for example). Thus, the Freedman technique is useful if its application is restricted to problems where the series of integrations does terminate. From that point of view, this procedure should be considered a formal solution technique for the Kirchhoff integral expression rather than an asymptotic approximation of it.



Keeping the reservations mentioned in the preceding paragraph in mind, substitution of the integration-by-parts expression of Equation 2.24 into one term of Equation 2.19 yields

$$\begin{aligned} & (I_-(r_g) - I_+(r_g)) - (W_-(r_g) - W_+(r_g)) \exp(-i2kr_g) \\ &= -\exp(-i2kr_g) \sum_{n=0}^N \left\{ \frac{(W_-^{(n)}(r_g) - W_+^{(n)}(r_g))}{(i2k)^n} \right\} . \end{aligned} \quad (2.26)$$

Note that  $N$  is large enough to guarantee that higher-order derivatives of  $W_+(r)$  are identically zero. The quantity  $[W_-^{(n)}(r_g) - W_+^{(n)}(r_g)]$  represents the magnitude of the discontinuity in the  $n$ th derivative of  $W(r)$  with respect to range. Let it be denoted by  $D(W, g, n)$ . The total expression for the backscattered pressure from Equation 2.19 can then be written as

$$p_s = \sum_{g=1}^f E_g , \quad (2.27)$$

where

$$E_g = \left( \frac{iP}{\lambda} \right) \exp(-i2kr_g) \sum_{n=0}^N \left( \frac{D(W, g, n)}{(i2k)^n} \right) . \quad (2.28)$$

The quantity  $E_g$  represents the scattering contribution due to all discontinuities in different orders of  $W^{(n)}(r)$  at range  $r_g$ , and the sum of these contributions at all appropriate ranges  $r_g$  is the total

backscattered pressure  $p_s$ . At large ranges, the solid angle  $W(r)$  can be replaced by the normalized area (Equation 2.11) to obtain

$$E_g \approx \left( \frac{iP}{\lambda r_m^2} \right) \exp(-i2kr_g) \sum_{n=0}^N \left( \frac{D(A,g,n)}{(i2k)^n} \right), \quad (2.29)$$

where

$$D(A,g,n) = A_-^{(n)}(r_g) - A_+^{(n)}(r_g). \quad (2.30)$$

Before proceeding further, a few comments about the general techniques just described should be reviewed. First, consider the introduction of discontinuities in the zeroth and first order of  $w^{(n)}(r)$ . When solving the Kirchhoff integral (Equation 2.6) directly, one finds that it is necessary to split the range of integration precisely as is done in the Freedman method because of either a piecewise-continuous kernel or a surface parallel to the incident wavefront. Solving each of the resulting continuous integrals will then yield the same final solution as Freedman obtains, but the solution will be perceived as arising from the integration between discontinuities instead of the change of value at each discontinuity. From an intuitive point of view, it is natural to expect some physical response to arise at the point where a jump in a function that is otherwise continuous occurs. However, the quantitative values associated with the discontinuities are suspect because the surface field predicted by Kirchhoff methods is known to be erroneous at edges (Wiener, 1949). In fact, the accuracy of the Kirchhoff method is usually attributed to its

integration over a few Fresnel zones without seriously violating the assumption of a planar neighborhood. As a second comment, the higher-order discontinuities in the Freedman method arise from a valid solution technique in those cases where the integration-by-parts series terminates. These discontinuities do not explicitly appear when performing the Kirchoff integration directly. However, at points where only a second- or higher-order discontinuity is found, the direct integration method will be required to split the range of integration exactly as does Freedman because of a change in the functional form of the integrand (such as occurs at the rear joint of a cone-sphere). Finally, note that the form of the function  $W(r)$  [or  $A(r)$ ] must be known explicitly in order to determine the values of the various discontinuities. In addition, when the functional form is known, it frequently exhibits essential discontinuities in its derivatives. Any further evaluation of the Freedman method is best performed by comparison with experiment, as has been done in Chapter 5 of this document.

### 2.3 Extension of Results to Narrow-Band Pulses

Under the assumption of narrow-band pulses and idealized transmitting and receiving systems, the results of Section 2.2 for continuous, monofrequency scattering can be extended to include pulsed signals. Let  $V(T)$  represent the waveform of the incident pulse on a time scale where

$$T = t - \left(\frac{2r}{c}\right) \quad . \quad (2.31)$$

The bandwidth of the pulse is assumed to be sufficiently limited for  $V(T)$  to be represented as

$$V(T) = V'(T)\exp(i\omega_0 T) \quad , \quad (2.32)$$

where  $\omega_0$  is the center frequency of the pulse's spectrum. This is true, for example, with a gated sine burst for which the gating envelope includes several cycles of the sine wave. Consideration of the waveform shape is based on the following Fourier transform pair:

$$v(\omega) = \left(\frac{1}{2\pi}\right) \int_{-\infty}^{\infty} V(T)\exp(-i\omega T)dT \quad (2.33)$$

and

$$V(T) = \int_{-\infty}^{\infty} v(\omega)\exp(i\omega T)d\omega \quad . \quad (2.34)$$

Note that the factor  $1/2\pi$  has been assigned to the forward transform to simplify the following discussion.

The previously derived solution at each frequency, Equation 2.28, can be separated into components from each order of discontinuity as

$$E(g,n) = \left(\frac{iP}{\lambda}\right)\exp(-i2kr_g) \left(\frac{D(W,g,n)}{(i2k)^n}\right) \quad . \quad (2.35)$$

Inserting the  $\exp(i\omega t)$  time dependence (which has been suppressed) and

rearranging to see the dependence on  $\omega$ , this equation becomes

$$dE(g,n) = \left(\frac{i\omega v(\omega)}{2\pi c}\right) \exp\left(i\omega t - i\omega\left(\frac{2r_g}{c}\right)\right) \left(\frac{c}{i2\omega}\right)^n D(W,g,n,\omega) d\omega \quad (2.36)$$

The left-hand side of Equation 2.36 has been designated  $dE(g,n)$  because it now represents one frequency component in the spectrum. Note that the wave constant  $P$  has been replaced by the appropriate spectrum coefficient  $v(\omega)$ , and the frequency dependence of  $D$  has been explicitly denoted. The total response is obtained by integrating over all frequencies to obtain

$$E(g,n) = \left(\frac{i}{2\pi c}\right) \left(\frac{c}{i2}\right)^n \int_{-\infty}^{\infty} \omega^{1-n} v(\omega) \exp(i\omega T) D(W,g,n,\omega) d\omega \quad (2.37)$$

The spectrum of the transmitted pulse is assumed to be zero outside a band of

$$\omega_0 - \left(\frac{\Delta\omega}{2}\right) < \omega < \omega_0 + \left(\frac{\Delta\omega}{2}\right) \quad (2.38)$$

Equation 2.37 then becomes

$$E(g,n) = \left(\frac{i}{2\pi c}\right) \left(\frac{c}{i2}\right)^n \int_{\omega_0 - (\Delta\omega/2)}^{\omega_0 + (\Delta\omega/2)} \omega^{1-n} v(\omega) \exp(i\omega T) D(W,g,n,\omega) d\omega \quad (2.39)$$

Now assume that  $\omega^{1-n} D(W, g, n, \omega)$  is slowly varying over the bandwidth of integration. Thus,

$$E(g, n) \approx \left( \frac{i}{\lambda_0} \right) \left[ \frac{D(W, g, n, \omega_0)}{(i2k_0)^n} \right] \int_{\omega_0 - (\Delta\omega/2)}^{\omega_0 + (\Delta\omega/2)} v(\omega) \exp(i\omega T) d\omega \quad , \quad (2.40)$$

where

$$\omega_0 = k_0 c = \frac{2\pi c}{\lambda_0} \quad . \quad (2.41)$$

Since  $v(\omega)$  is band-limited, the integral in Equation 2.40 is just the transform of Equation 2.34. As a result,

$$E(g, n) \approx \left( \frac{i}{\lambda_0} \right) V(T) \left( \frac{D(W, g, n, \omega_0)}{(i2k_0)^n} \right) \quad . \quad (2.42)$$

Finally, using the form of  $V(T)$  given in Equation 2.32, one obtains

$$E(g, n) \approx \left( \frac{i}{\lambda_0} \right) V'(T) \exp(i\omega_0 t - i2k_0 r_g) \left( \frac{D(W, g, n, \omega_0)}{(i2k_0)^n} \right) \quad . \quad (2.43)$$

Note that this equation has exactly the same form as that for the continuous-wave case, Equation 2.35, with the frequency and wavelength parameters replaced by mean values.

In physical terms, Equation 2.43 indicates that a sine-burst pulse of sufficient length and sufficiently smooth envelope will act approximately like the continuous-excitation case for the pulse's mean

frequency. Each backscattered contribution will be an approximate image of the incident pulse, and the total solution can be found by vectorially summing the components. This last result is the reason for denoting the Freedman technique as an echo formation method.

## 2.4 Examples of Some Simple Bodies

Probably the best way to gain insight into the Freedman method is through examples that are solved and compared with other results. The following sections discuss solutions for the sphere, the circular disk, the square plate, the finite cone, and cone variants. Comparison of these results with experimental values is presented in Chapter 5. Note that the circular disk is a case where the Freedman method breaks down but a direct solution of the Kirchhoff integral yields a valid prediction.

### 2.4.1 Sphere Example

The sphere has been studied as a diffraction target probably more than any other body. However, this fact makes it an excellent first choice when evaluating a new scattering method. Computing the backscattering from a rigid sphere at large range by the Freedman method rests almost completely upon determination of the ranges and values of the discontinuities in the projected area  $A(r)$ . A qualitative plot of these functions with the associated geometry is given in Figure 2.3. The only discontinuities lie at the specular reflection point and the shadow boundary (i.e., at the closest and furthest illuminated points). A tabulation of the values of these discontinuities is given in Table

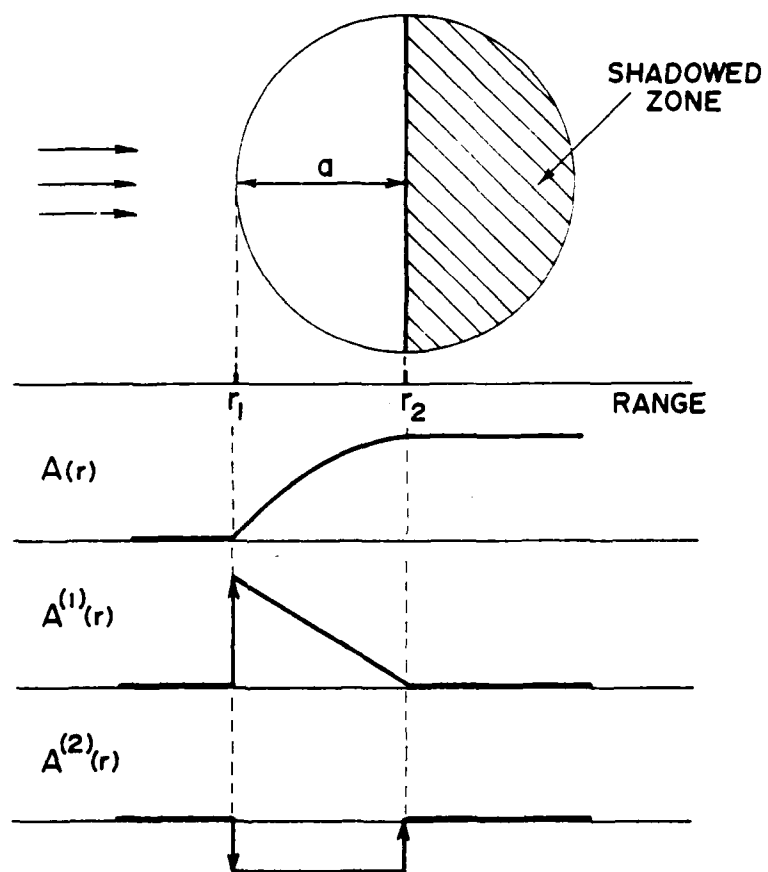


Figure 2.3 Approximate values of the projected area  $A(r)$  and its derivatives for a sphere.



2.1. Note that derivatives of  $A(r)$  of third or higher order are identically zero except for delta functions, which have been considered separately in the derivation of the solution technique.

Substituting the discontinuity values of Table 2.1 into Equation 2.29, one finds for the components from ranges  $r_1$  and  $r_2$ :

$$E_1 = \left( \frac{iM}{r_m} \right) \left( \frac{a}{2} \right) \left( 1 + \left( \frac{1}{2ka} \right) \right) \quad (2.44)$$

and

$$E_2 = \left( \frac{iM}{r_m} \right) \left( \frac{1}{4k} \right) \exp(-i2ka) \quad , \quad (2.45)$$

where

$$M = P \exp(-i2kr_1) \quad . \quad (2.46)$$

The first term of the  $E_1$  component corresponds to that for geometrical optics, while the second term is presumably a correction to that result.  $E_2$  is a component arising at the shadow boundary.

The Kirchhoff integral in the form of Equation 2.10 can be solved directly in this example by substituting for  $dA(r)/dr$ . Since the integrand is continuous, the process involves solving the expression

$$\int_{r_1+a}^{\infty} \left( \frac{1}{r} - \frac{1}{r-r_1} \right) \exp(-i2kr) dr \quad (2.47)$$

Table 2.1

Freedman Discontinuity Data for a Sphere of Radius  $a$ 

$n$	$A^{(n)}(r)$	$D(A,1,n)$	$D(A,2,n)$
0	$\pi a^2 \left\{ 1 - \left[ \left( a - (r - r_1) \right) / a \right]^2 \right\}$	0	0
1	$2\pi (a - (r - r_1))$	$-2\pi a$	0
2	$-2\pi$	$2\pi$	$-2\pi$
3	0	0	0

formally and evaluating it at the two endpoints. The resulting contributions at each end of the integration range correspond precisely to the previous expressions given in Equations 2.44 and 2.45. This is not surprising since the Freedman results are based on the same procedure except that the integration is done formally by parts before substitution of the actual quantities. Note that one may have difficulty attributing a physical significance to the discontinuities with an order of greater than one in the Freedman solution because they arise solely as intermediate results of the integration by parts. However, the Freedman formulation replaces the integration required in the evaluation of the solution with a series of simpler differentiations.

#### 2.4.2 Circular-Disk Example

The circular disk is interesting from the point of view of the Freedman method because it is one of the simplest examples for which the method breaks down. Figure 2.4 is a plot of the geometry and the relative values of  $A(r)$  and its derivatives. At nonaxial incidence, the projected area takes the form of an ellipse. The area of the ellipse subtended as a function of range  $r$  can be computed by integrating a strip parallel to the axis of rotation to obtain

$$A(r) = a^2 \cos \theta (R(1 - R^2)^{1/2} + \arccos(R)) \quad , \quad (2.48)$$

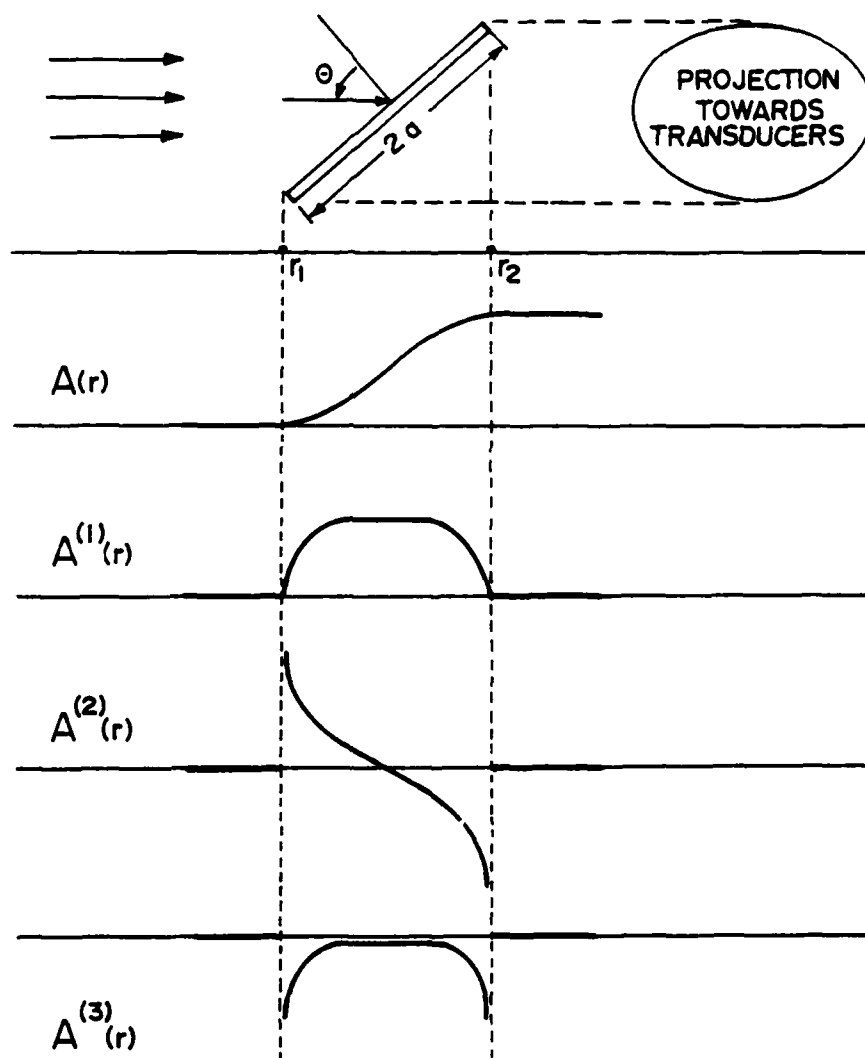


Figure 2.4 Approximate values of the projected area  $A(r)$  and its derivatives for a circular disk at nonaxial incidence.

where

$$R = \frac{a \sin \theta - (r - r_1)}{a \sin \theta} , \quad (2.49)$$

$a$  is the radius of the disk, and  $R$  varies between 1 at  $r_1$  and -1 at  $r_2$ . The term  $(1-R^2)^{1/2}$  causes the breakdown of the Freedman formulation, as is easily seen by differentiating Equation 2.48 to obtain

$$\frac{dA(r)}{dr} = a^2 \cos \theta \left( \frac{1 + R}{(1 - R^2)^{1/2} a \sin \theta} + (1 - R^2)^{1/2} \right) . \quad (2.50)$$

This expression and all further derivatives tend to either negative or positive infinity at both endpoints of the range. Thus, the Freedman solution reduces to a summation of infinite discontinuities at both  $r_1$  and  $r_2$ .

The problem of infinite discontinuities is based on the behavior of the area expression (Equation 2.48) as a function of range. The initial (zero) and final (maximum) values are approached smoothly with greater and greater slope. Since the form of  $dA(r)/dr$  is troublesome, direct evaluation of the modified Kirchhoff expression (Equation 2.10) is not possible. However, the difficulty is, in fact, solely attributable to the interpretation of the scattering process in terms of the area derivative with respect to range. A continuous integrand can easily be derived using the geometry of Figure 2.5. Note that, in this case, the origin of the coordinates is placed at a convenient point on the scatterer instead of a point on the transducers to simplify the analysis. Substituting into the original Kirchhoff integral of Equation

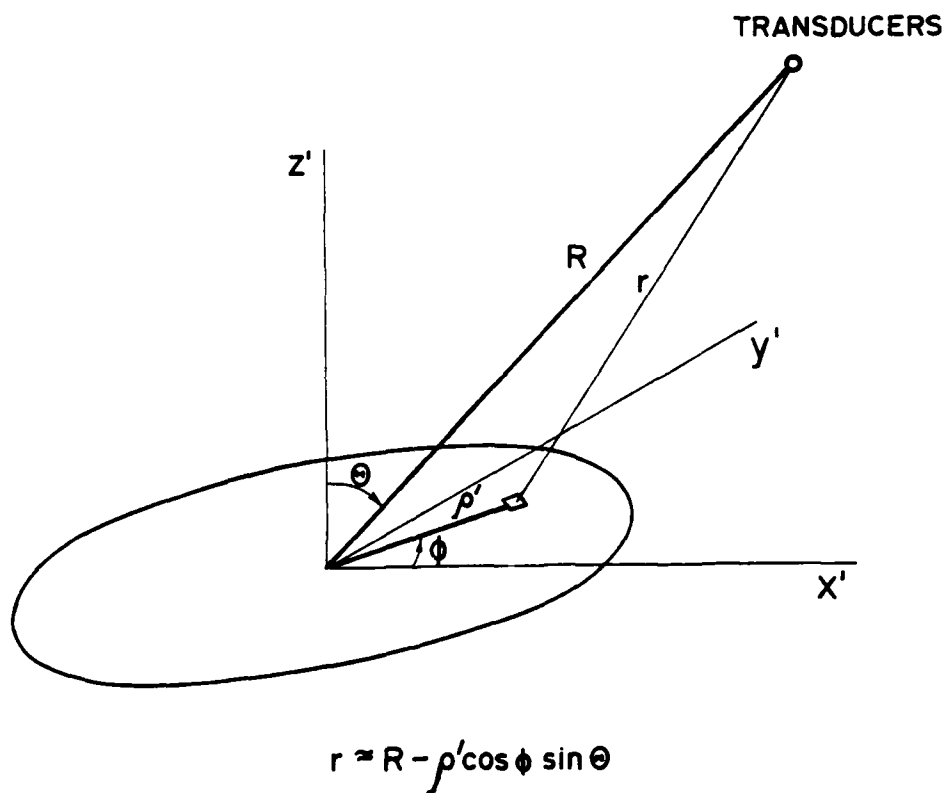


Figure 2.5 Geometry utilized in calculation of the scattering from a circular disk.

2.6 and assuming that the range is large, one obtains

$$p_s = \left( \frac{-iP}{\lambda R^2} \right) \exp(-i2kR) \int_0^a \int_0^{2\pi} \exp(ik\rho' \cos \phi \sin \theta) \cdot \cos \theta \rho' d\phi d\rho' , \quad (2.51)$$

which can be evaluated using the formula (Skudrzyk, 1971, p. 697)

$$J_m(x) = \left( \frac{1}{2\pi i^m} \right) \int_0^{2\pi} e^{ix \cos \phi} e^{im\phi} d\phi \quad (2.52)$$

to yield

$$p_s = \left( \frac{-ikP \exp(-i2kR)}{R^2} \right) a^2 \cos \theta \left( \frac{J_1(2ka \sin \theta)}{2ka \sin \theta} \right) . \quad (2.53)$$

This expression can also be utilized at normal incidence by taking the limit as  $\theta \rightarrow 0$  to yield

$$p_s(\theta = 0) = \left( \frac{-ikP \exp(-i2kR)}{R^2} \right) \left( \frac{a^2}{2} \right) . \quad (2.54)$$

These last results show that the problems encountered with the circular disk are due to the Freedman interpretation and not the Kirchhoff formulation itself. The particular geometry that precipitates the difficulties (the projected ellipse) also occurs with other simple objects such as finite cylinders and cones. From a qualitative point of view, the Freedman prediction of returns from ranges  $r_1$  and  $r_2$  appears to have validity based on physical intuition, and this correctly

corresponds to observed data (see Section 5.4.3). However, the direct Kirchhoff result obtained in this case does not separate into individual components like the Freedman result would do because the integral was recognized as a form of the Bessel function.

### 2.4.3 Rectangular-Plate Example

The geometry for the rectangular plate is shown in Figure 2.6. Although it appears to be similar to that for the circular disk, the projected-area function  $A(r)$  in this case approaches the endpoints at a constant rate. Thus, the derivatives of  $A(r)$  are well behaved and truncate at the second order, as is shown in Table 2.2. Substitution into the Freedman equation (Equation 2.29) yields the following components at  $r_1$  and  $r_2$ :

$$E_1 = \frac{-Mb \cot \theta}{2\pi r_m^2} \quad (2.55)$$

and

$$E_2 = \left( \frac{Mb \cot \theta}{2\pi r_m^2} \right) e^{-i4ka \sin \theta} \quad (2.56)$$

The magnitude of the sum is

$$|P_s| = |E_1 + E_2| = \left( \frac{P2kab \cos \theta}{\pi r_m^2} \right) \left( \frac{\sin(2ka \sin \theta)}{2ka \sin \theta} \right) \quad (2.57)$$

As in Section 2.4.1, the same result is obtained by direct integration of the Kirchhoff integral expressed in terms of the area derivative



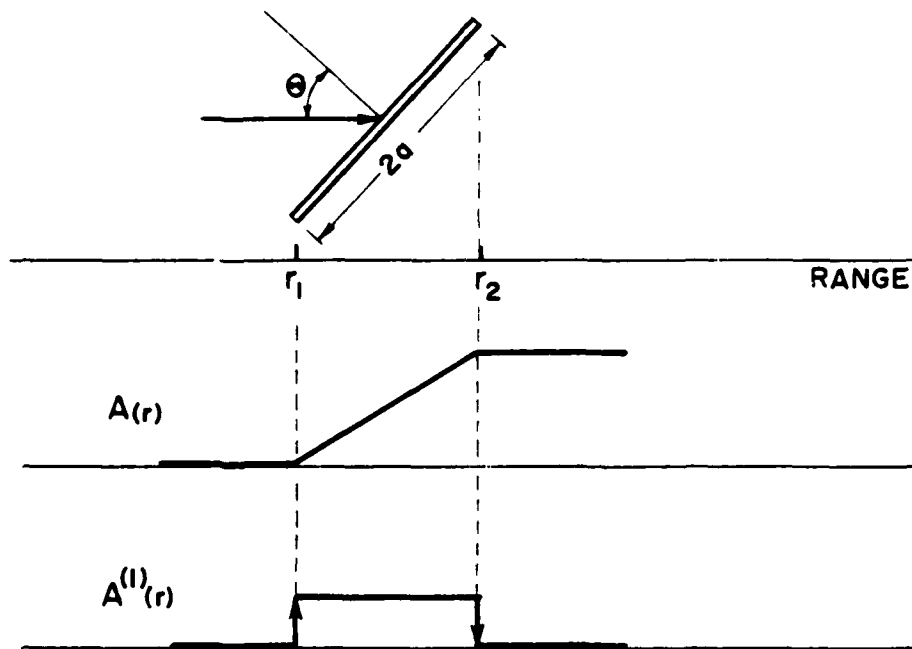


Figure 2.6 Approximate values of the projected area  $A(r)$  and its derivatives for a rectangular plate at nonaxial incidence.

Table 2.2

Freedman Discontinuity Data for the Rectangular  
Plate of Figure 2.6

$n$	$A^{(n)}(r)$	$D(A,1,n)$	$D(A,2,n)$
0	$(2b/\tan \theta)(r - r_1)$	0	0
1	$(2b/\tan \theta)$	$-(2b/\tan \theta)$	$(2b/\tan \theta)$
2	0	0	0

(Equation 2.10), with the two components ( $E_1$  and  $E_2$ ) arising from the integral evaluation at the two endpoints.

#### 2.4.4 Finite-Cylinder Example

The solution for backscattering from a finite circular cylinder at nonaxial incidence includes contributions both from the disk at the illuminated end and the side. The cylinder end is essentially the same as the circular disk, and the Freedman summation breaks down in the same manner as has been shown for the disk (see Section 2.4.2). This summation also breaks down for the side component. However, the Kirchhoff result can again be obtained directly.

Refer to the geometry of Figure 2.7. Calculation of the contribution from the endcap follows closely that shown in Section 2.4.2 for the circular disk, with

$$r \approx R - \rho' \cos \theta \sin \theta + \ell \cos \theta \quad (2.58)$$

assumed at large range. The result is

$$p_s(\text{top}) = \left( \frac{-ikPe^{-i2kR}}{R^2} \right) a^2 \cos \theta e^{-i2k\ell \cos \theta} \left( \frac{J_1(2ka \sin \theta)}{2ka \sin \theta} \right), \quad (2.59)$$

which is the same as that for the disk except for the additional phase factor involving the half-length  $\ell$  of the cylinder. Computation of the side contribution is somewhat more involved. Assuming that

$$r \approx R - z \cos \theta + a \cos \phi \sin \theta, \quad (2.60)$$

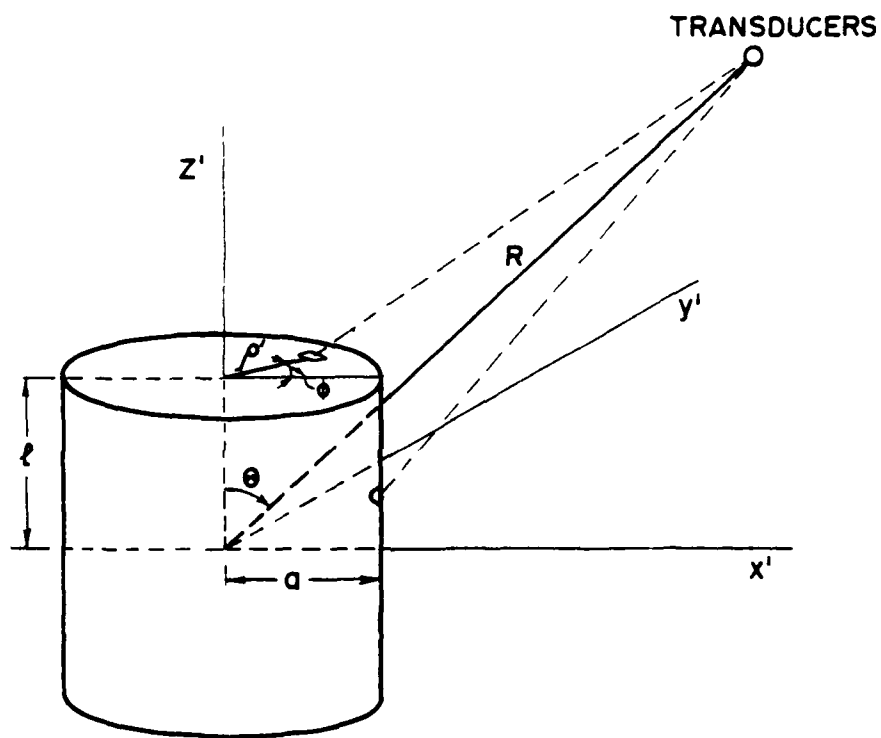


Figure 2.7 Geometry used for calculation of backscattering from a finite cylinder.

the Kirchhoff integral becomes

$$p_s(\text{side}) = \left( \frac{-iPe^{-i2kR}}{\lambda R^2} \right) \int_0^l \int_0^{2\pi} e^{-i2ka \cos \phi \sin \theta} \cdot e^{i2kz \cos \theta} \cos \phi \sin \theta a d\phi dz \quad (2.61)$$

This integral can be evaluated using a modified form of the Bessel-function relation in Equation 2.52 to obtain

$$p_s(\text{side}) = \left( \frac{-k^2 Pe^{-i2kR} (4a^2 l \sin^2 \theta)}{R^2} \right) \left( \frac{J_1(2ka \sin \theta)}{2ka \sin \theta} \right) \cdot j_0(2kl \cos \theta) \quad (2.62)$$

Equation 2.62 exhibits an angular dependence similar to that of the end component multiplied by a  $j_0(x) = \sin x / x$  term that depends on the length of the cylinder. Finally, in situations where the end and side components interfere, the magnitude of their vector sum becomes

$$|p_s| = \left( \frac{ka^2}{R} \right) \left( \frac{J_1(2ka \sin \theta)}{2ka \sin \theta} \right) \left\{ \cos^2 \theta + \frac{(16k^2 l^2 \sin^2(2kl \cos \theta))}{(2kl \cos \theta)^2} \right. \\ \left. \cdot \sin^2 \theta (\sin^2 \theta - \cos^2 \theta) \right\}^{1/2} \quad (2.63)$$

#### 2.4.5 Finite-Cone Example

The finite cone will first be considered for axial incidence only. The geometry and behavior of the discontinuities are shown in Figure 2.8, and the quantities required for the Freedman solution are listed in

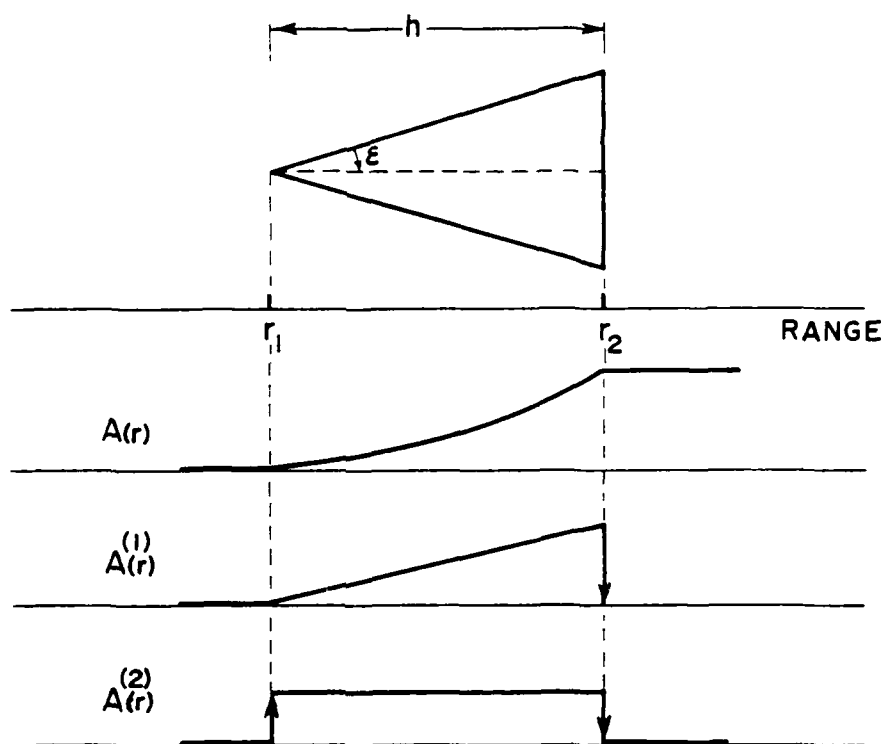


Figure 2.8 Approximate values of the projected area  $A(r)$  and its derivatives for a finite circular cone at axial incidence.

AD-A084 937

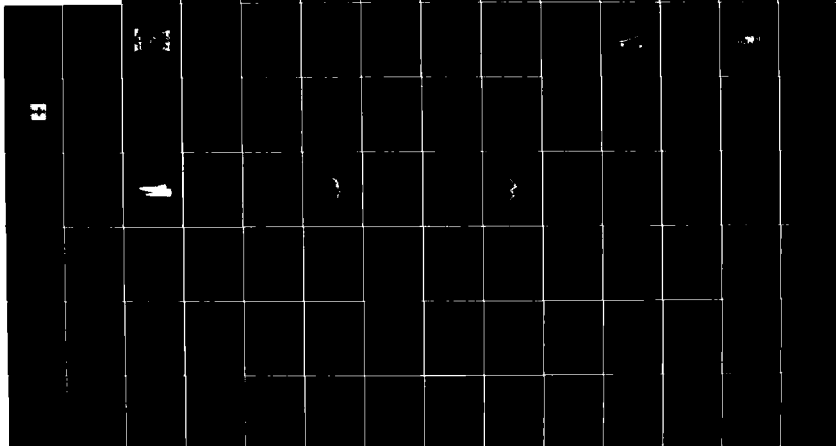
PENNSYLVANIA STATE UNIV UNIVERSITY PARK APPLIED RESE--ETC F/G 20/1  
AN EXPERIMENTAL ANALYSIS OF THE BASIC PHENOMENA INVOLVED IN MOD--ETC(U)  
JAN 80 H S LANG  
UNCLASSIFIED ARL/PSU/TN-80-43

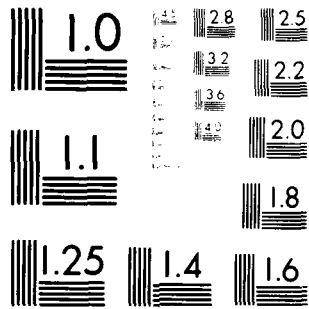
N00024-79-C-6043

HL

2 of 5

All Rights Reserved





MICROCOPY RESOLUTION TEST CHART  
 NATIONAL BUREAU OF STANDARDS-1963-A



Table 2.3. The evaluation yields for the component returns from the tip

$$E_1 = \left(\frac{iM}{2}\right) \left(\frac{1}{4k}\right) \tan^2 \epsilon \quad (2.64)$$

and from the rear

$$E_2 = \left(\frac{M}{2r_m}\right) \exp(-i2kh)h \tan^2 \epsilon \left(1 - \left(\frac{i}{2kh}\right)\right) \quad (2.65)$$

The magnitude of the sum becomes

$$|p_s| = |E_1 + E_2| = \left(\frac{M \tan^2 \epsilon}{2r_m}\right) \left\{1 - \left(\frac{\sin 2kh}{kh}\right) + \left(\frac{\sin^2 kh}{(kh)^2}\right)\right\}^{1/2} \quad (2.66)$$

The finite cone at nonaxial incidence presents some difficulty. Depending on the relative values of the cone half-angle and the angle of incident radiation, a number of individual cases must be considered. For incidence at an angle less than the cone half-angle (i.e.,  $\theta < \epsilon$  in Figure 2.9), all of the cone except the base is irradiated. However, for  $\epsilon < \theta < \pi/2$ , a shadow boundary is formed on the side of the cone. Evaluation of the Freedman discontinuity data shows that, like the circular disk and the side of the circular cylinder, the expressions break down as a result of infinite discontinuities. A direct evaluation of the Kirchhoff integral (Equation 2.6) can be constructed in this case. However, the integration cannot be carried out analytically except in the special case of axial incidence, for which one obtains the same result as that of the Freedman method.

Table 2.3

Freedman Discontinuity Data for the Finite  
Cone at Axial Incidence

$n$	$A^{(n)}(r)$	$D(A,1,n)$	$D(A,2,n)$
0	$\pi(h - (r_2 - r))^2 \tan^2 \epsilon$	0	0
1	$2\pi(h - (r_2 - r)) \tan^2 \epsilon$	0	$2\pi h \tan^2 \epsilon$
2	$2\pi \tan^2 \epsilon$	$-2\pi \tan^2 \epsilon$	$2\pi \tan^2 \epsilon$
3	0	0	0

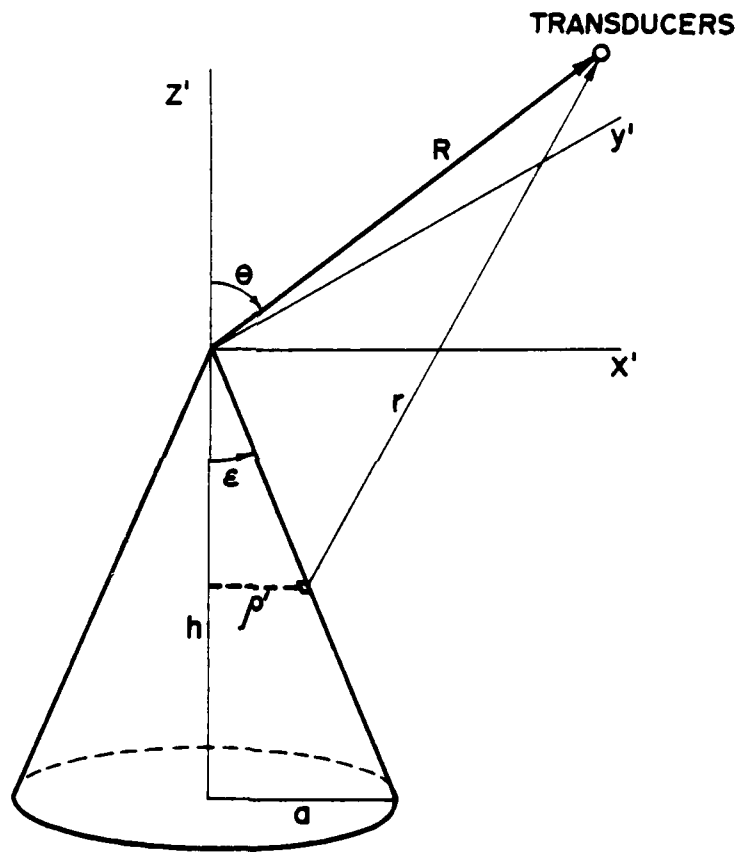


Figure 2.9 Geometry used for calculation of backscattering from a finite cone at nonaxial incidence.

#### 2.4.6 Modified Cone Examples

Variants of the finite cone are very useful for studies of scattering from surface discontinuities. Comparisons of diffraction from tips, first-derivative (slope) discontinuities, and second-derivative (curvature) discontinuities can be made by joining portions of spheres to the basic cone shape in the required manner. The Freedman prediction method is well suited for this type of backscattering problem because the solution can be constructed by joining the solutions of the basic constituent shapes with the correct phase factors. At the same time, studies of discontinuities on the surface of modified cones represent a good test of the quantitative values for edge-type scattering predicted by the Freedman theory (and hence physical optics), at least for axial incidence where this theory is valid. Thus, computations have been made for three selected cases: (1) a cone-sphere, where a sphere is joined to the rear of a cone smoothly in both cross-section and surface slope; (2) a spherically capped cone, where a sphere is joined to the tip of a cone smoothly in both cross section and slope; and (3) a hemispherically capped cone, where a hemisphere is joined to the front of a cone smoothly in cross section only.

A representation of the geometry for the cone-sphere appears in Figure 2.10. The spherical termination reduces the severe discontinuity at the rear of the cone (whose contribution dominates the backscattering) to a discontinuity in curvature only. The values of the resulting Freedman discontinuity data are presented in Table 2.4. Substitution of these data into the Freedman relation (Equation 2.29)

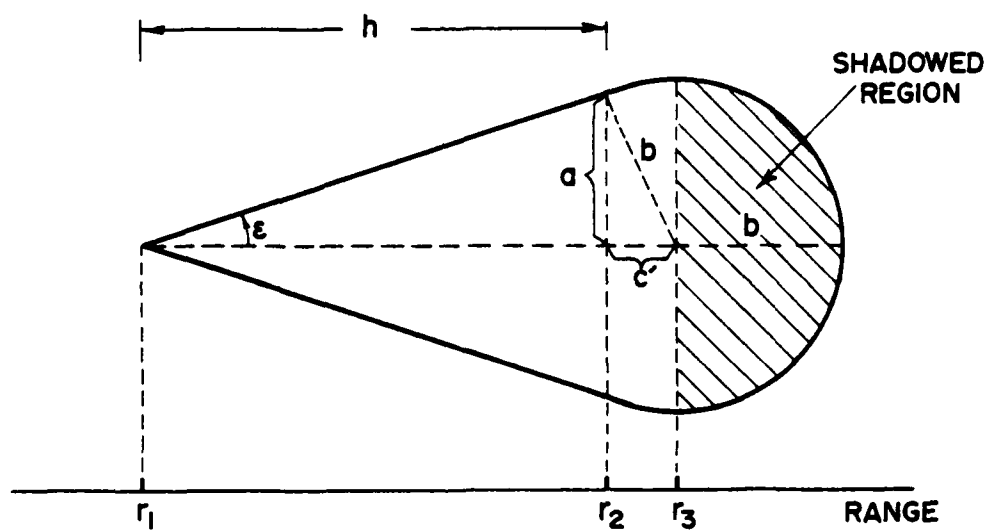


Figure 2.10 Geometry used for calculation of backscattering from a cone-sphere at axial incidence.

Table 2.4  
Freedman Discontinuity Data for the Cone-Sphere

n	$A^{(n)}(r)$		$D(A,1,n)$	$D(A,2,n)$	$D(A,3,n)$
	$r_1 < r < r_2$	$r_2 < r < r_3$			
0	$\pi(h - (r_2 - r))^2 \tan^2 \epsilon$	$\pi(b^2 - (c' - (r - r_2))^2)$	0	0	0
1	$2\pi(h - (r_2 - r)) \tan^2 \epsilon$	$2\pi(c' - (r - r_2))$	0	0	0
2	$2\pi \tan^2 \epsilon$	$-2\pi$	$-2\pi \tan^2 \epsilon$	$2\pi(1 + \tan^2 \epsilon)$	$-2\pi$
3	0	0	0	$= 2\pi/\cos^2 \epsilon$	0

yields for the scattering components:

$$E_1 = \left( \frac{iM}{2} \right) \left( \frac{1}{4k} \right) \tan^2 \epsilon \quad , \quad (2.67)$$

$r_m$

$$E_2 = \left( \frac{-iM}{2} \right) e^{-i2kh} \left( \frac{1}{4k} \right) (1 + \tan^2 \epsilon) \quad , \quad (2.68)$$

$r_m$

and

$$E_3 = \left( \frac{iM}{2} \right) e^{-i2kh(1+\tan^2 \epsilon)} \left( \frac{1}{4k} \right) \quad . \quad (2.69)$$

$r_m$

As expected, the contributions from the closest ( $E_1$ ) and furthest ( $E_3$ ) ranges are equivalent to those from the cone and sphere, respectively, modified by the proper phase relationships for the new geometry. The contribution  $E_2$  from the cone-to-sphere joint region, which has the same frequency dependence as that from the tip ( $E_1$ ) but is much stronger, is a new result.

To compare the scattering from a curvature discontinuity with that from the abrupt rear edge of a cone, a spherically capped cone is used. The geometry is shown in Figure 2.11, and the Freedman discontinuity data are listed in Table 2.5. The values have been computed by specifying the radius  $b$  of the spherical nose and then determining the shortening parameter  $m$  that will match the surface slope at the joint.

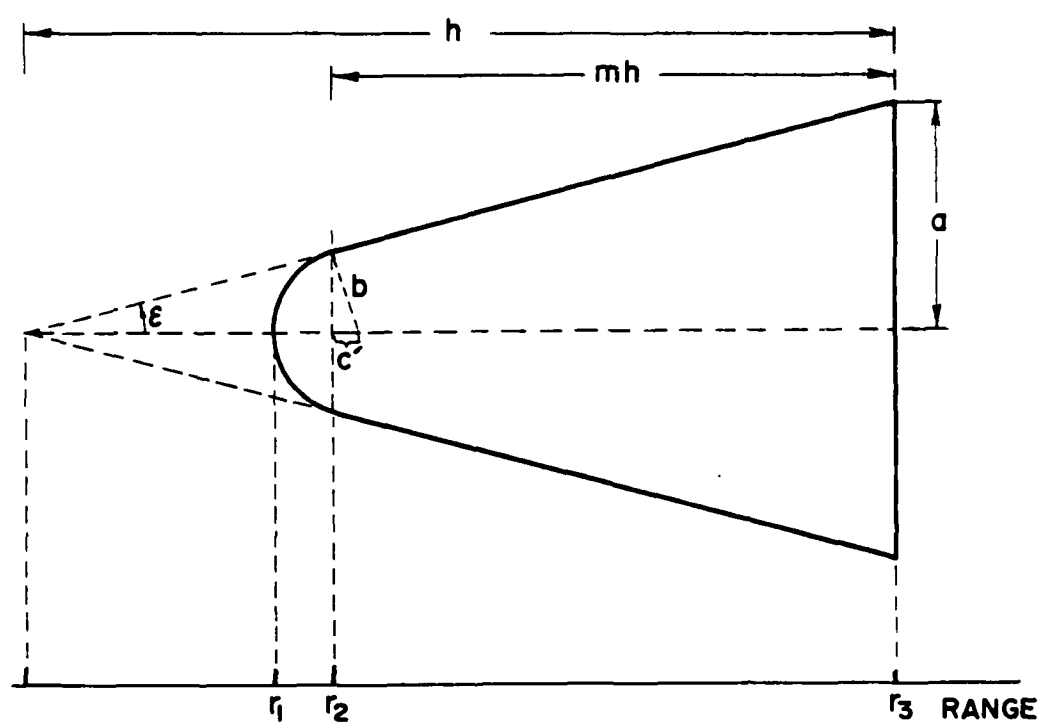


Figure 2.11 Geometry used for calculation of backscattering from a spherically capped cone at axial incidence.



Table 2.5  
Freedman Discontinuity Data for a Spherically Capped Cone

n	$A^{(n)}(r)$		$D(A,1,n)$	$D(A,2,n)$	$D(A,3,n)$
	$r_1 < r < r_2$	$r_2 < r < r_3$			
0	$\pi\{b^2 - (b - (r - r_1))^2\}$	$\pi(h(1 - m) + (r - r_2))^2$ $\cdot \tan^2 \epsilon$	0	0	0
1	$2\pi(b - (r - r_1))$	$2\pi(h(1 - m) + (r - r_2))$ $\cdot \tan^2 \epsilon$	$-2\pi b$	0	$2\pi h \tan^2 \epsilon$
2	$-2\pi$	$2\pi \tan^2 \epsilon$	$2\pi$	$-2\pi(1 + \tan^2 \epsilon)$ $= -2\pi/\cos^2 \epsilon$	$2\pi \tan^2 \epsilon$
3	0	0	0	0	0

The pressure components from the three discontinuities are

$$E_1 = \left(\frac{-M}{r_m}\right) \left(\frac{b}{2}\right) \left(1 + \left(\frac{i}{2kb}\right)\right) , \quad (2.70)$$

$$E_2 = \left(\frac{iM}{r_m}\right) e^{-i2kb(1-\sin \epsilon)} \left(\frac{1}{4k}\right) (1 + \tan^2 \epsilon) , \quad (2.71)$$

and

$$E_3 = \left(\frac{M}{r_m}\right) e^{-i2k(b(1-\sin \epsilon)+mh)} \left(\frac{h \tan^2 \epsilon}{2}\right) \left(1 - \left(\frac{i}{2kh}\right)\right) . \quad (2.72)$$

These expressions, with the exception of the geometry-related phase factor, correspond to the specular sphere component ( $E_1$ ), the cone-sphere joint ( $E_2$ ), and the cone termination ( $E_3$ ), respectively.

Finally, in order to note the difference between a discontinuity in curvature and that of slope, the cone can be capped with a true hemisphere whose radius is the same as that of the cone at the joint (see Figure 2.12). The Freedman discontinuity relations for this case are summarized in Table 2.6. The only change in this table from that of the spherically capped cone (Table 2.5) is the additional discontinuity at  $r_2$  in the first derivative, although the phases involved in the resulting pressure terms also differ slightly. The pressure

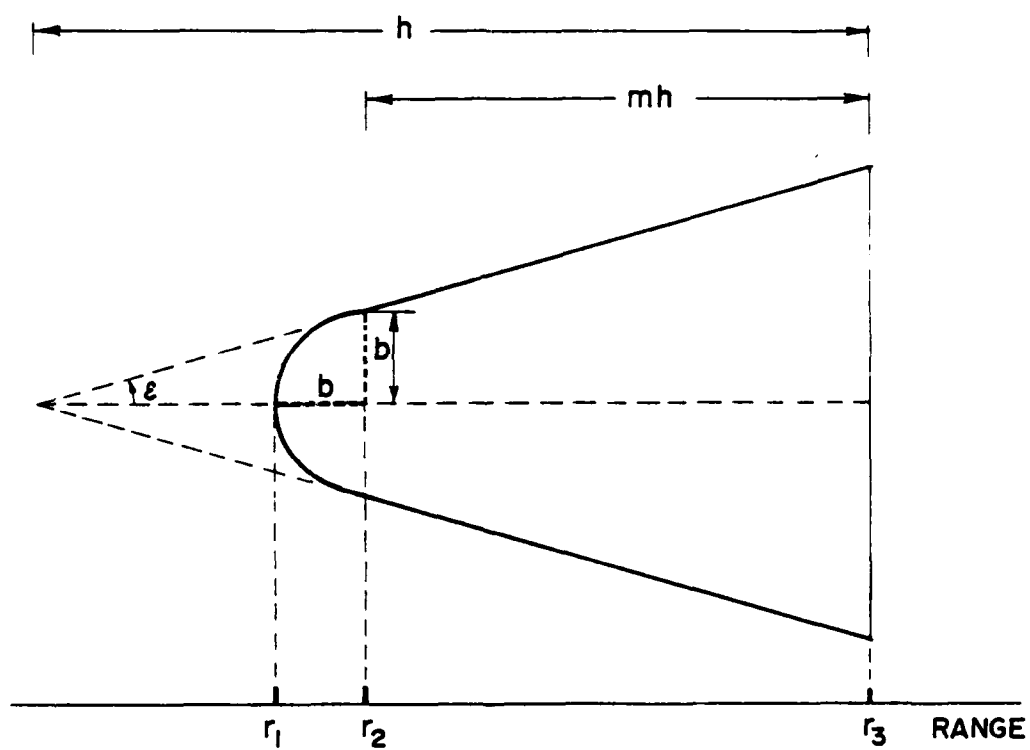


Figure 2.12 Geometry used for calculation of backscattering from a hemispherically capped cone at axial incidence.

Table 2.6  
Freedman Discontinuity Data for a Hemispherically Capped Cone

n	$A^{(n)}(r)$ $r_1 < r < r_2$	$A^{(n)}(r)$ $r_2 < r < r_3$	$D(A,1,n)$	$D(A,2,n)$	$D(A,3,n)$
0	$\pi(b^2 - (b - (r - r_1))^2)$	$\pi(h(1 - m) + (r - r_2))^2$	0	0	0
		$\cdot \tan^2 \epsilon$			
1	$2\pi(b - (r - r_1))$	$2\pi(h(1 - m) + (r - r_2))$	$-2\pi b$	$-2\pi b \tan \epsilon$	$2\pi h \tan^2 \epsilon$
		$\cdot \tan^2 \epsilon$			
2	$-2\pi$	$2\pi \tan^2 \epsilon$	$2\pi$	$-2\pi(1 + \tan^2 \epsilon)$	$2\pi \tan^2 \epsilon$
3	0	0	0	0	0

contributions from each point of discontinuity in the range are

$$E_1 = \left( \frac{-M}{r_m} \right) \left( \frac{b}{2} \right) \left( 1 + \left( \frac{i}{2kb} \right) \right) , \quad (2.73)$$

$$E_2 = \left( \frac{-Me^{-i2kb}}{r_m} \right) \left( \frac{b}{2} \right) \left\{ \tan \epsilon + \left( \frac{i(1 + \tan^2 \epsilon)}{2kb} \right) \right\} , \quad (2.74)$$

and

$$E_3 = \left( \frac{Me^{-i2k(b+mh)}}{r_m} \right) \left( \frac{h \tan^2 \epsilon}{2} \right) \left( 1 - \left( \frac{i}{2kh} \right) \right) . \quad (2.75)$$

The contribution at the joint ( $E_2$ ) in this case includes a frequency-dependent curvature quantity along with an additional frequency-independent quantity related to the discontinuity in slope.

## CHAPTER 3

## EXPERIMENTAL SETUP FOR GATED-PULSE MEASUREMENTS

This chapter contains a description of the measurement chamber, the transmitting and receiving apparatus, and most of the scattering models used for gated-pulse measurements in this study. In addition, there is an explanation of some points of technique that should be of interest, such as the actual pressure component that is plotted in the results. Because the reliability of the data and conclusions presented in this document is based on the apparatus and the procedure utilized in the investigations, the description in this chapter is both necessary and important. However, most of the information is not required for an intuitive overview. The delineation of the signal-detection procedure in Section 3.4 is an exception; it should be reviewed so that the plots appearing in later chapters can be correctly interpreted.

3.1 Measurement Chamber

All experiments in this study that involve gated-pulse techniques were performed in the small anechoic chamber pictured in Figure 3.1. The chamber, which has been described in detail by Berger and Ackerman (1956), is located in the basement of Osmond Laboratory (Physics Department) at The Pennsylvania State University's main campus. The 12 x 8 x 6 foot inside dimensions of the room make it fairly small, but it has true fiberglass wedges backed by a cavity on all wall, floor, and ceiling surfaces. Because this facility is used for psychoacoustic work involving human subjects, the room contains a heavy metal grating that



Figure 3.1 Photograph of the measurement chamber with the 28-inch prolate spheroid in position.

serves as a floor. Sections of this grating that lie under the scattering object are sometimes removed during diffraction experiments to eliminate the associated reflections, and all remaining floor sections are always covered with a lightweight, unbacked fiberglass (Owens-Corning R13).

Tests show that the measurement chamber is qualified for acoustic measurements from at least 1 kHz to more than 50 kHz, based on the standard inverse-square-law propagation criteria for a small source. However, this verification procedure is of little value for diffraction measurements. A spurious reflection reaching a microphone in the chamber at a level 10 dB or more below the direct signal will have no noticeable effect on the total received signal. Thus, the propagation loss measured for the given source/receiver path will not differ from that obtained under free-field conditions. On the contrary, the same spurious reflection may completely obscure returns from a scatterer, which are frequently 20 - 40 dB lower in amplitude than the incident pulse. A better indication of the chamber's suitability for scattering measurements was obtained by measuring the backscattered return from a small spherical scatterer at different ranges. As expected, the latter test did point out some inaccuracies caused by spurious reflections in the chamber at all but the highest frequencies examined. Thus, although the reduced amplitude of the wall reflections in an anechoic chamber is helpful, diffraction measurements in this type of chamber must still utilize gated-pulse techniques, and the researcher must use skill when placing measuring equipment and models in the chamber to minimize spurious reflections.



The measurement chamber was modified slightly for this study. A suspension point in the form of a 5-inch-diameter disk with hooks along its perimeter was installed between two wedges in the ceiling. This support can be electrically rotated in either direction at about 1/2 r.p.m., and it includes a precision potentiometer that develops a voltage proportional to the rotational position. Directly below the ceiling support is the pivot point of a short rotating boom that can be mounted just above the grating (floor). This boom, which also contains a potentiometer for position indication, is used to rotate the microphone about the scatterer for collection of bistatic scattering data.

### 3.2 Measuring Equipment

A block diagram of the measurement apparatus, including a plan view of a chamber setup and the associated electronic equipment, is shown in Figure 3.2. The transmitting equipment consists of a Spectral Dynamics SD104A-5 sweep oscillator, a General Radio 1396-A tone-burst generator, a Dynaco Mark III power amplifier, and a suitable loudspeaker. A separate oscillator drives the timing input of the tone-burst unit to permit pulses of constant length. (Pulse timing is based on cycle count in the GR unit.) Because the tone-burst generator attenuates the output signal by only about 40 dB in the off state, a passive thresholding circuit consisting of two parallel diodes has been inserted at the output of the generator. This circuit adds a small amount of distortion to the signal near zero volts, but it improves the off-state attenuation by at least 40 dB. The power amplifier has sufficient drive capability

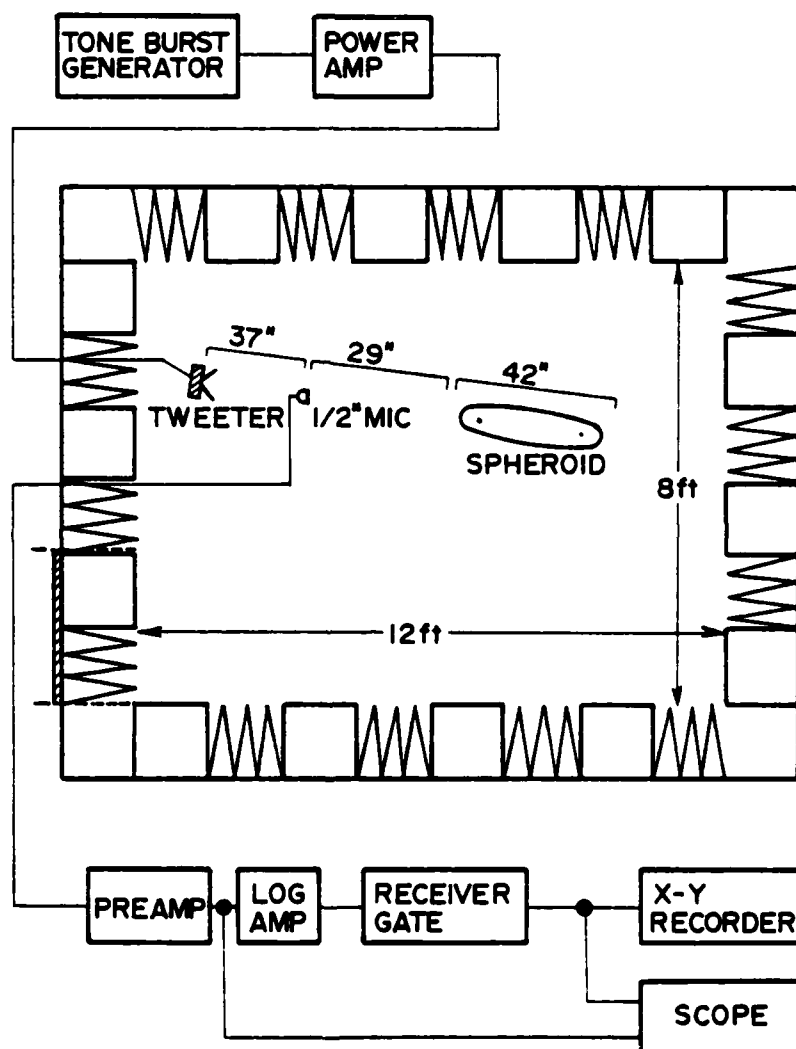


Figure 3.2 Block diagram of the measurement chamber (in plan view) and the associated electronic equipment.

to apply a 60-volt (peak-to-peak), short-duration pulse to a loudspeaker with an impedance of 8 - 16 ohms.

The selection of suitable loudspeakers for this study was one of the more difficult tasks. The size of the models and characteristics of the measurement chamber dictate a frequency range of about 10 - 50 kHz. In addition, a good pulse response is required. Three different tweeter units have been used throughout the study in a roughly chronological sequence. The first is an inexpensive piezo-bender horn loudspeaker manufactured by Motorola (Super Horn, Model No. 50D59067A01). This tweeter provides a reasonably flat output over the frequencies of 10 - 40 kHz. However, asymmetries occur in its directivity pattern at angles small enough to influence the scattering from the larger models. The Motorola tweeter also has a low power-handling capacity, which mandates a low repetition rate for the pulses. The second tweeter is a dynamic horn loudspeaker with a titanium diaphragm manufactured by Technics (Model No. EAS-9HH42). This unit has a very smooth directivity curve and a large (20 watts continuous) power-handling capability. However, it has no useful output at frequencies above about 25 kHz, and the mass of its coil assembly degrades the transient response. The best tweeter that has been found is a magnetic-ribbon unit also manufactured by Technics (Model No. EAS-10TH1000). This loudspeaker has a usable output from about 5 kHz to at least 50 kHz. It also has both a wide, uniform directivity pattern and excellent transient characteristics. Unfortunately, the ribbon tweeter is very expensive and somewhat difficult to obtain.

The receiving equipment used for gated-pulse measurements in this study consists of a Bruel and Kjaer 1/2-inch condensor microphone (Model 4133) with associated cathode follower and power supply, an Ithaco Model 435 adjustable-gain preamplifier, an 18 - 24 dB/octave filter (either an SKL 302 or an Ithaco 4302), a Tektronix 561B oscilloscope, a special receiver-gate module, and a Mosley Model 135 X-Y plotter. The excellent (although insensitive) response of the condensor microphone at frequencies up to 40 kHz made selection of this critical transducer much easier than that for the loudspeaker. The filter is used only for suppression of residual hum components from the microphone and associated cables. The oscilloscope is used to monitor spurious returns and to observe pulse shapes. (The waveform of the scattered returns frequently conveys useful information about the physical scattering mechanism.) Finally, the plotter is used to make graphs of selected returns as a function of either the appropriate rotation-position signal from the chamber or a ramp voltage proportional to frequency from the sweep oscillator.

The heart of the receiving system is the receiver-gate module. Although commercial units exist, the module used in this study was constructed as part of this project to reduce the required expenditure. The device performs the following functions: (1) full-wave rectifies the input signal; (2) measures the peak value on a logarithmic scale; and (3) samples and holds the peak value received in a preset time window until the next pulse. In application, the width and time delay of the sampling window are adjusted to include the desired returns, and a continuous plot (actually updated at every pulse) is made of the

amplitudes of the returns. The circuit designed for this project can provide a dynamic range of about 40 dB (60 dB if carefully adjusted). Because of its usefulness and relatively small cost, a complete schematic of the device is included as Appendix B. Note that a version of this device used for some of the earlier data drifted in calibration over time by as much as 2 - 3 dB, which meant that the calibration had to be checked frequently to insure reasonable accuracy. The final version (described in Appendix B) appears to be stable within at least 1 dB over a period of weeks.

### 3.3 Models

Several experimental models have been either acquired or built for this study, including prolate spheroids, cylinders, spheres, and finite cones. Most of the models are made of wood, although the selection of a construction material is not critical in most cases. The high ratio of characteristic impedance between the model material and surrounding medium that is required to consider a scatterer as a rigid body is easily satisfied for experiments in air. A soft wood such as pine has an impedance that is almost 4000 times that of air. Even a soft rubber has an impedance 160 times that of air. For this reason, all the scatterers and surface obstructions used in this study are considered as ideally rigid except the cloth damping material used in several experiments.

The assortment of spherical models allows scattering data to be collected over a range in  $ka$  ( $a$  = radius,  $k = 2\pi/\lambda$ ) of about .6 - 120 for a frequency range of 10 - 40 kHz. The largest spheres are spun-

aluminum shells of 6- and 12-inch diameters. The smallest spheres are steel ball bearings having 1/2- and 1/4-inch diameters. The validity of the data obtained from the two smallest spheres (i.e., for  $ka < 6$ ) is somewhat questionable, however, because almost any form of suspension scatters more than these spheres. Standard pool balls, 2-1/4 inches in diameter, also make excellent models. Because of their easy availability, these balls have been used wherever the models have been modified in a destructive manner.

Cylindrical models appropriate for both finite and infinite examples have been utilized. The "infinite" cylinders are aluminum tubes that are at least 6 feet long and have 6-, 1-1/4-, and 3/4-inch diameters. This translates roughly into a  $ka$  range of 2 - 60. The models used as finite cylinders, however, are concentrated in a lower  $ka$  (frequency) range of .3 - 7. These small cylinders were machined from solid drill rod in all combinations of the lengths of 1, 3/4, 1/2, 1/4, and 1/8 inch and diameters of 3/4, 1/2, 1/4, and 1/8 inch. The 20 cylinders were used both individually and as obstructions placed on a spheroid.

Figure 3.3 shows the spheroidal models used. There are three prolate spheroids with a length-to-width ratio of 7:1 and major axes of 42, 28, and 14 inches. These thin spheroids were originally constructed for hydrodynamic tests, and they are made of solid wood that is heavily varnished. Using the radius of the spheroid at the tip as the characteristic dimension  $a$ , the range in  $ka$  covered is about .7 - 7. If the normalized spheroidal coordinates (see Section 4.1) are considered, the range of the parameter  $h\xi$  covered is about 30 - 390. A less

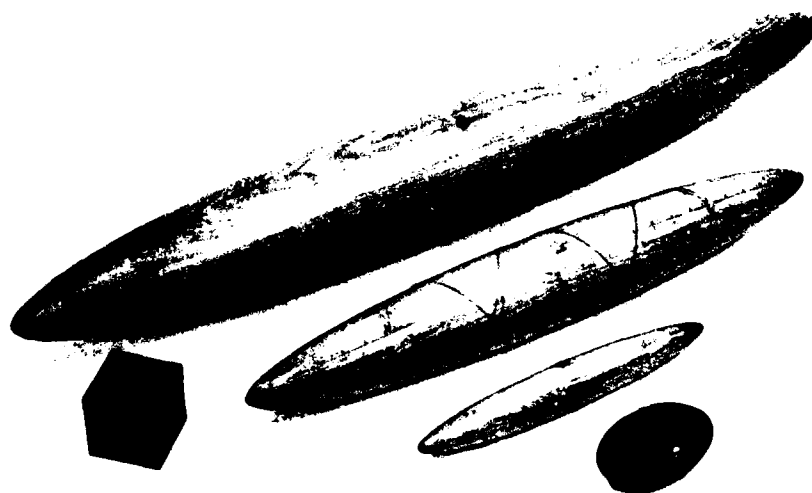


Figure 3.3 Photograph of the prolate-spheroid models.

eccentric, wooden (unvarnished) spheroid with dimensions of 3 x 5 inches was obtained for the creeping-wave measurements. For this spheroid, the parameter  $h\zeta$  varies over a range of about 12 - 48.

Figure 3.4 shows the special cone model that was constructed for a series of tests on edge diffraction. The basic shape is that of an 18-inch-long cone with a  $20^\circ$  half-angle made of uncoated wood. If  $b$  is the radius of the base (which, in this case, is just over 6-1/2 inches), the range of  $kb$  covered is about 28 - 112. This translates to a range in  $kh$  of 85 - 335, where  $h$  is the cone length. The tip of the cone was constructed as a separate section and then attached to the point on the cone body at which the radius of the cone is 2 inches (i.e., about 5-1/2 inches from the tip). This tip section can be removed and replaced by one of several caps that form specular regions and/or edges on the surface. The caps include portions of spheres that join the cone outline smoothly in both cross section and slope to produce nose radii of 1/2, 1, and 2 inches (C, D, and on cone in Figure 3.4), respectively. There is also a hemispherical cap with a 2-inch radius (A in Figure 3.4) that is continuous only in surface cross section at the union between the hemisphere and the cone. In addition to the various caps, the base of the cone contains a threaded fixture countersunk into its surface so that special terminations can be mounted. The two terminations used include a hemisphere with a radius equal to that of the cone base and a large spherical section that preserves both the slope and cross section of the cone outline at the joint (cone-sphere). The cone and all of its caps and terminations were machined precisely out of solid wooden blocks on a tracing lathe using numerically generated patterns. Despite this



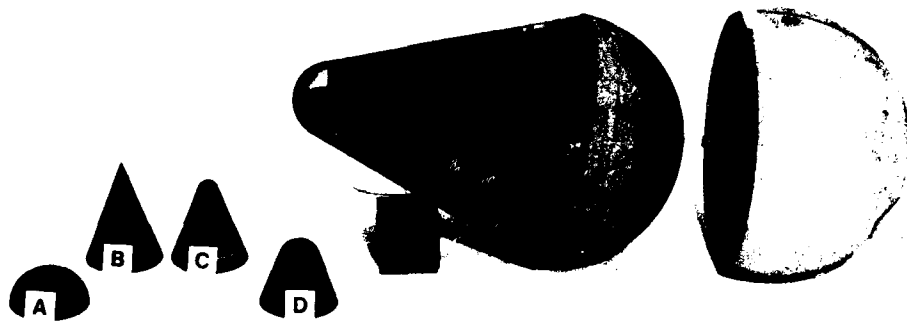


Figure 3.4 Photograph of the special cone model, including its various spherical and hemispherical caps and terminations.

care, the line on the surface of the cone at which the caps join with the basic model generated scattering returns of its own (see Section 5.4.1). Note that the line where the spherical sections of the caps join geometrically with the cone outline is not the same as the physical joint between the cap and the basic model except for the 2-inch caps.

In addition to the basic shapes already mentioned, several models were constructed to test specific conditions. These models include half-planes, planes terminated in half-cylinders, and modifications of the basic spherical shape. The models are described in detail in later sections along with the corresponding experimental results. Note that commonly available items, such as rubber bands and modeling clay, were also used extensively to patch or distort the basic models. This procedure permitted experiments to be interactively modified using the guidance of current results without waiting for additional models to be constructed.

The support mechanism for all the models proved to be a major problem. Early experiments showed that a 3/4-inch-diameter support rod scatters virtually as much as the 42-inch spheroid at broadside incidence. The implied requirement for very small vertical suspensions is evident in the trace of Figure 3.5. The scattered return (B) in the figure is from the 28-inch spheroid at 34.3 kHz for incidence  $30^\circ$  from the axial direction; the return (A) is from a length of braided fishing line (25-pound test) hanging vertically just in front of the spheroid nose. Problems with undesired suspension echoes are greatest for spheroids and small spheres, whose scattered returns are very small; however, these problems must be given careful attention when using any

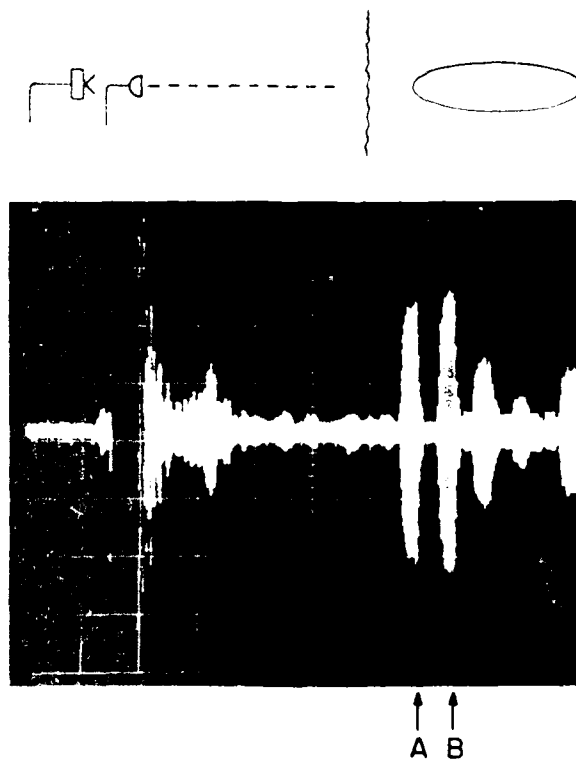


Figure 3.5 Oscilloscope trace of the backscattered returns from (A) a length of 20-pound-test fishing line and (B) a thin prolate spheroid at  $30^\circ$  incidence.

of the models described here. The suspension-echo problems can be partially alleviated by mounting the support strings at an angle to the vertical line in order to direct any scattered return away from the receiver. For example, the two large returns following return (B) in Figure 3.5 are from the fishing lines (also 25-pound test) that support the spheroid in this manner. However, in order to provide completely satisfactory results, a tempered steel wire, only about .007 inch in diameter and attached to hooks countersunk completely into the models' surface, was used for all models that this wire could support.

### 3.4 Techniques

The basic procedure for using pulsed sources and gated receivers in scattering measurements is so commonly known that it requires no further explanation. However, some discussion is important for a proper interpretation of the results of this study. First, one must know which property of the received signal was detected. Second, many of the major intuitive keys described in this document were discovered by using methods and data that are not revealed in the plots that are presented. Thus, understanding the general procedures that were followed is useful in order to place the results in perspective.

One important decision that must be made by all experimentalists involves the quantitative values assigned to the returned signals. The waveforms scattered by even simple shapes can have very strange envelopes that vary with time as different scattering mechanisms interact. To eliminate any confusion about what part of a received pulse to measure, this author chose, unless otherwise specified, to use

a pulse that was short enough to isolate all independent scattering mechanisms and then to detect the largest return. Thus, the window on the receiver gate was set to include all desired returns from the model, and the gate detected and plotted the peak value of the largest signal in that window. A particular plot may be dominated by two or more different mechanisms at different parameter ranges if the returns attributed to these mechanisms alternately assume the maximum value in the window. To supplement these total results, the individual returns were isolated in the window for separate plots whenever there were two or more distinct returns visible. The time-delay setting of the window was placed on a large dial so that it could be manually manipulated to track a particular return when necessary.

Most of the final experimental plots included in this document are traced directly from the recorded results after shifting the vertical scale for proper normalization. Although much of the fine structure that is visible is not significant, it does give the researcher an idea of the variability in the data and thus the level of confidence that can be assumed. Much of the information learned from the experiments does not appear explicitly in the plotted results. For example, the almost total specular dependence of the backscattering from a prolate spheroid was indicated by the scattered pulse envelope for relatively long pulses being virtually identical to that of the incident pulse. Careful observation of such details from even a simple experiment was found to be an efficient method for developing intuition about the scattering process that could be used to target future experiments.

One common (but somewhat unorthodox) procedure involved the author manipulating the various elements in an experiment from inside the chamber while observing the resulting effects on an oscilloscope placed within view. This technique can be used, for instance, to quickly determine the origin of observed pulses by moving objects and placing small pieces of damping material within various possible acoustic paths until a change is noted. The sensitivity of the data to scatterer position can also be examined by forcing the scatterer slightly away from its stationary position. In general, this quick-look approach, combined with careful observation, has been used extensively to develop intuition and understanding of the mechanisms at work. Accurate quantitative plots of the noted effects can then be interpreted and extrapolated more effectively.

In many cases, it was found that judicious experimental procedures allowed useful data to be obtained in an apparently hopeless situation. For example, Figure 4.53b (on page 183) shows the scattered returns obtained in a search for creeping waves on a thin prolate spheroid. Return (SP) is the specular echo, and return (CRP) is the creeping-wave echo; all other returns are from the chamber surfaces, microphone, etc. The spurious echoes are obviously large enough to obscure the desired data. However, by observing which returns moved in time with the body and by rearranging the equipment to get these returns in a relatively clear area of the trace, accurate quantitative information has been obtained. The improvement is, unfortunately, limited to a single frequency per arrangement because the spurious returns generally change when the frequency is varied. This fact is the most important reason

why few continuous frequency-response plots are presented in this study. Directive sources can be used to some advantage against this problem, but a compromise is required between irradiating the entire scatterer uniformly (to simulate farfield conditions) and not irradiating the walls of the chamber (to minimize spurious reflections).

Finally, one should note that the data do not represent truly farfield diffraction measurements. The transducers are not much more than one body length from the model for the large scatterers. Thus, the exponentially decaying field near the scatterer has decayed adequately to meet the conditions for the acoustic farfield, and higher inverse powers of the range are beginning to get small. However, the scattered wavefront must travel much further to reach an essentially plane-wave condition.

#### CHAPTER 4

##### SMOOTH-BODY DIFFRACTION MEASUREMENTS

This chapter discusses the results of an investigation into the scattering from smooth convex bodies and smooth bodies with small obstructions on their surface. The physical phenomena are probably some of the simplest of all those in the broad area of diffraction. Despite that fact, the geometrically simple body chosen as the basis for most of the experiments, the thin prolate spheroid, continues to prove troublesome in both theoretical and experimental work. The shape is useful as a model of objects from ship and airplane bodies to finite wires. In addition, it represents a very fundamental example (i.e., dual radii of curvature) that must surely be understood before moving to more complex bodies.

A variety of simple experiments were either selected or evolved for this investigation. First, a study of both the directivity and frequency response of the backscatter from a prolate spheroid was carried out. This effort included tests of spheroids that were damped at selected areas on their surface as a means of locating the origin of the primary scattering sources. The results checked closely with simple geometric calculations. Then, the sensitivity of the backscattering to small changes in the smooth curvature of the spheroid was examined. This work looked at small surface imperfections, holes in the body, and both bands and cylinders placed on the surface of the models. The cylinders, in particular, proved very informative, demonstrating the effect of surface fields near the spheroid that modify the scattering by



objects in that vicinity. These experiments also showed the dramatic change that occurs when moving from a doubly curved body to a body that is flat in one dimension. Finally, a detailed examination of the Franz-type creeping waves was performed. These studies verified the existence of some scattering component that appears to circumnavigate both spheres and spheroids. However, they also revealed additional properties that point to a much more complicated phenomenon than traditional creeping waves.

#### 4.1 Geometry of the Prolate Spheroid

The prolate spheroid is a cigar-shaped body formed by rotating an ellipse, such as that of Figure 4.1a, about its major axis. For purposes of discussion, it is convenient to define a set of nondimensionalized coordinates by choosing

$$\xi = \frac{r_1 + r_2}{d}, \quad (4.1)$$

$$\eta = \frac{r_1 - r_2}{d}, \quad (4.2)$$

and  $\phi$  as the angle of rotation about the major axis. The resulting coordinate surfaces for a constant  $\xi$  and  $\eta$  at a given  $\phi$  are ellipses and hyperbolas, respectively (see Figure 4.1b). A particular model with a given length-to-width ratio corresponds to a coordinate surface  $\xi_0$ .

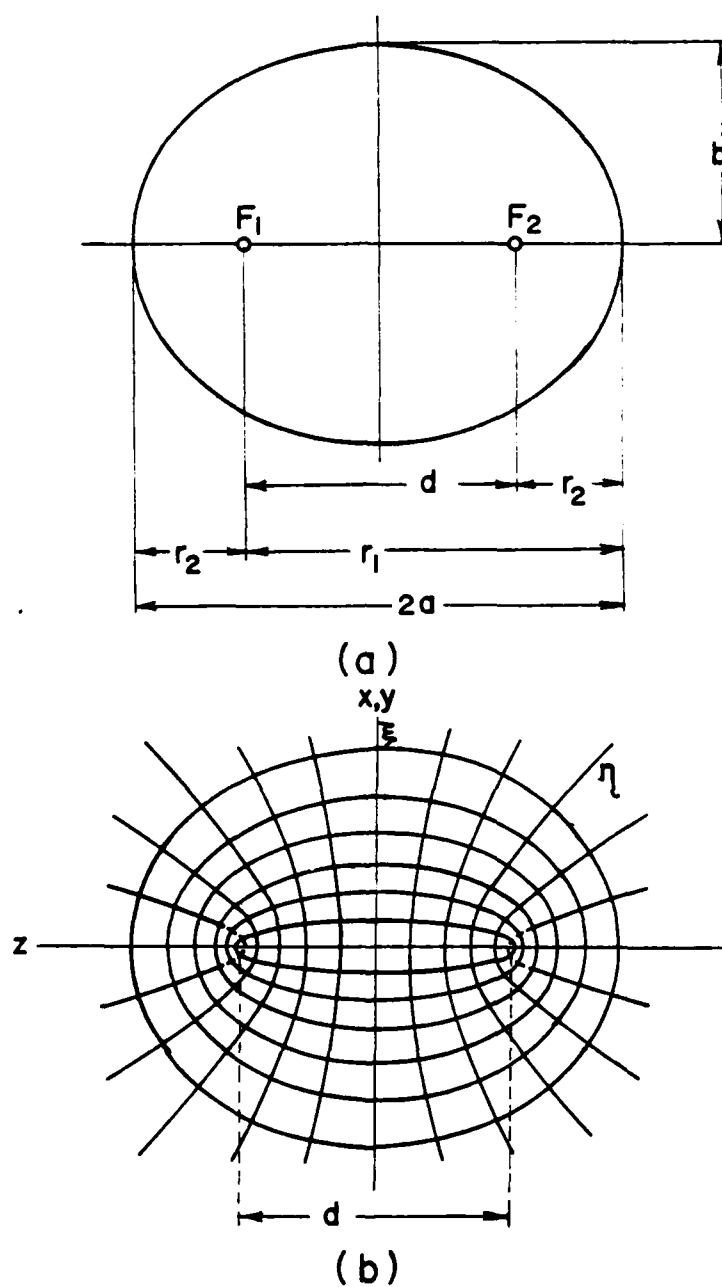


Figure 4.1 Geometry used to describe prolate spheroids, including (a) the dimensions of the ellipse of revolution and (b) the associated orthogonal coordinate surfaces.

where

$$\xi_0 = \frac{2a}{d} = \frac{a}{(a^2 - b^2)^{1/2}} = \frac{\epsilon}{(\epsilon^2 - 1)^{1/2}} \quad (4.3)$$

for

$$\epsilon = \frac{a}{b} \quad (4.4)$$

The value of  $\xi_0$  for the 7:1 spheroids used in this study is 1.01. Note that the definition of a particular spheroid requires both a radial-type parameter  $\xi$  and an interfocal distance  $d$ , whereas a single radius parameter is sufficient to define a particular sphere.

To further standardize the spheroid parameters, a new frequency that is normalized to the interfocal distance is commonly defined as

$$h = \frac{kd}{2} \quad (4.5)$$

This definition leads to a frequency/radius parameter  $h\xi_0 = ka$ , which corresponds precisely to that of a sphere with the same major radius. The nondimensional parameter  $h\xi_0$  is thus useful for fat (slightly eccentric) spheroids at any incidence angle and for all spheroids at broadside incidence, but its intuitive value for thin spheroids at or near axial incidence is somewhat questionable. This dilemma of finding suitable normalized parameters to describe the scattering from thin spheroids reappears when trying to interpret many of the results of this chapter.

## 4.2 Backscattering from Prolate Spheroids

### 4.2.1 Backscattered Frequency Response from a Prolate Spheroid

One of the first experiments performed in this study involved a determination of the frequency dependence of the backscatter from a prolate spheroid. The data were obtained on a point-by-point basis by reading the peak value of the received signal from an oscilloscope at discrete settings of the frequency and incidence angle. The values are plotted as a function of the normalized frequency  $h\xi_0$  in Figure 4.2. For purposes of comparison, all amplitudes have been normalized to the backscatter from a sphere with the same diameter as the major axis of the spheroid (42 inches in this case). Note that the reference (sphere) scattering value was actually obtained by first measuring the backscattered amplitude from a 6-inch-diameter sphere and then multiplying that result by the appropriate ratio between the desired and measured sphere radii. Although the reference sphere is not constructed of the same material as the spheroid model, both are essentially rigid scatterers (refer to Section 3.3).

The results of Figure 4.2 show that the backscattered pressure at different angles of incidence varies over a range of about 30 dB for this 7:1 prolate spheroid in the frequency range given. The values are reasonably uniform with respect to frequency for broadside ( $90^\circ$ ) and axial ( $0^\circ$ ) incidence, but some variability is observed in the angular range between these extremes. In particular, a dip at about  $h\xi_0 = 320$  is noted. There is also a rapid change in amplitude over the angular range of  $30^\circ - 75^\circ$ . The sensitivity of this data to small angular

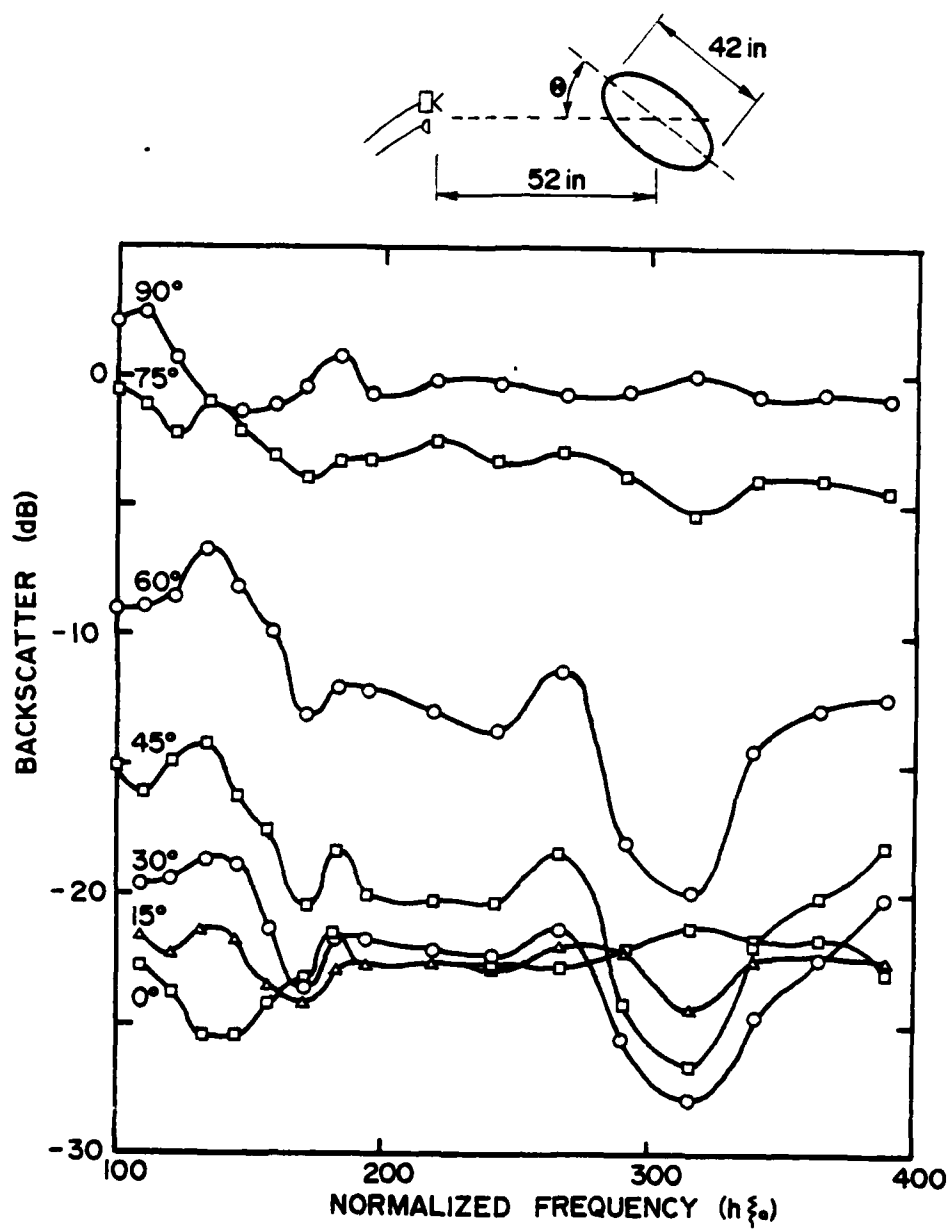


Figure 4.2 Backscatter versus normalized frequency from the 42-inch prolate spheroid at several incidence angles.

changes at any point in the angular range is actually more pronounced than may appear. In taking these measurements, a critical alignment of the scatterer, source, and receiver had to be maintained to insure repeatability of the results. This requirement resulted from the highly directional nature of the backscattered field at many incidence angles, including both axial and broadside incidence. Note that the full extent of the spheroid model could not be kept within the main radiation lobe of the speaker used for these measurements.

The experience gained in gathering these data led to several changes in technique for future experiments. First, a receiver-gate module was designed and built to provide a virtually continuous density of data values with respect to the parameter under consideration (either angle or frequency). Second, an alignment procedure based on leveling with an optical telescope was adopted. Finally, the receiver was moved from beside the source to directly in front of it. This latter arrangement more closely approximated the coincident transducers assumed for backscattering, and it reduced the difficulties experienced in trying to measure highly directive returns.

#### 4.2.2 Backscattered Directivity from a Prolate Spheroid

In order to better analyze the angular dependence of the spheroid backscatter, directivity curves were taken at several discrete frequencies within the range of 130 - 260 in  $h\xi_0$ . Three of these curves are plotted in Figure 4.3. After the values are normalized to the backscattered pressure from a sphere with the same major radius, the curves are identical within experimental accuracy. The spheroid

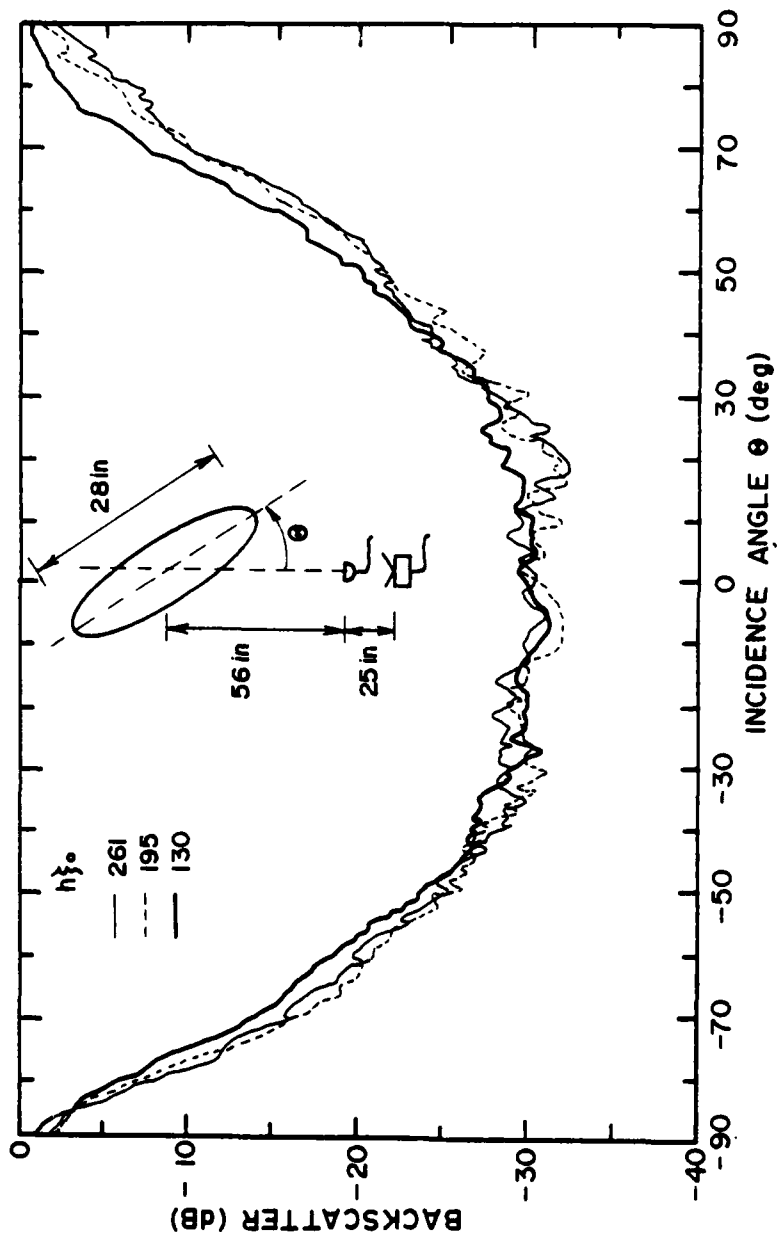


Figure 4.3 Directivity of the backscatter from the 28-inch prolate spheroid for normalized  $h\xi_0$  values of 130, 195, and 261.

backscatter is seen to vary rapidly in amplitude over the angular range of  $30^\circ - 75^\circ$  but remain basically stable in the range  $0^\circ - 30^\circ$ . Because the curvature of the body varies rapidly near the tip but becomes spherical at the tip, one expects that the region just beyond the tip governs the scattering from  $30^\circ - 75^\circ$  and that the region at the tip governs the scattering for  $0^\circ - 30^\circ$ . The lack of any noticeable change in directivity over the 2:1 frequency range indicates that the effective high-frequency limit has been reached, even in the axial direction where the radius of curvature at the specular point is of the order of a wavelength. The high sensitivity to alignment errors observed previously (Section 4.2.1) was also noted here. In this case, symmetric curves could only be obtained when the rotational axis of the spheroid was accurately maintained in the same horizontal plane as the source and receiver.

#### 4.2.3 Backscattered Directivity from Partially Damped Spheroids

While collecting the data reported in the previous two sections, a consistently close resemblance between the waveforms of the scattered and incident pulses was noted that indicated a simple scattering process. In order to gain information about the locations of the important scattering sources, an experiment was devised to selectively damp various portions of the spheroid surface and to compare the backscatter results with those from a plain spheroid. The frequency used, which corresponds to an  $h\bar{\xi}_0$  of 223, was selected primarily to obtain a good dynamic range in the measurement chamber because the backscattered directivity does not vary with frequency in the range under consideration.



The first requirement for the damped-spheroid investigation was a suitable absorbing material. After evaluating many samples of various fabrics, a heavy corduroy material was selected. The backscattering characteristics of this fabric when applied to a flat baffle about 2-feet square are plotted in Figure 4.4. All amplitudes in this figure have been normalized to the level of the reflection from the plain baffle at normal incidence. The weave of the fabric includes a series of parallel ribs in one direction. These ribs generate a peak in the backscatter results as a result of constructive interference when the ribs are positioned parallel to the baffle's rotation axis (vertical axis) and the proper angle is set. The peak is noted when the fabric is mounted with the ribs facing either toward or away from the baffle. However, no such peak is found when the ribs are rotated to any other position. In the latter case, the corduroy material provides an attenuation of about 7.5 dB at normal incidence, and it has only a small additive effect on the backscatter at other angles (refer to Figure 4.4).

Using the 28-inch spheroid as the model, portions of the spheroid were covered with a single layer of the corduroy fabric applied in variable-width strips, starting at the center of the spheroid and working outward in steps. Each strip was carefully fastened with double-sided tape so that the cloth adhered tightly to the spheroid's surface, and the ribs in the material were kept parallel to the spheroid's major axis. The tips of the spheroid were covered with fabric sections cut to a measured pattern and sewn together. A photograph of the spheroid with some damping material on its surface is shown in Figure 4.5.

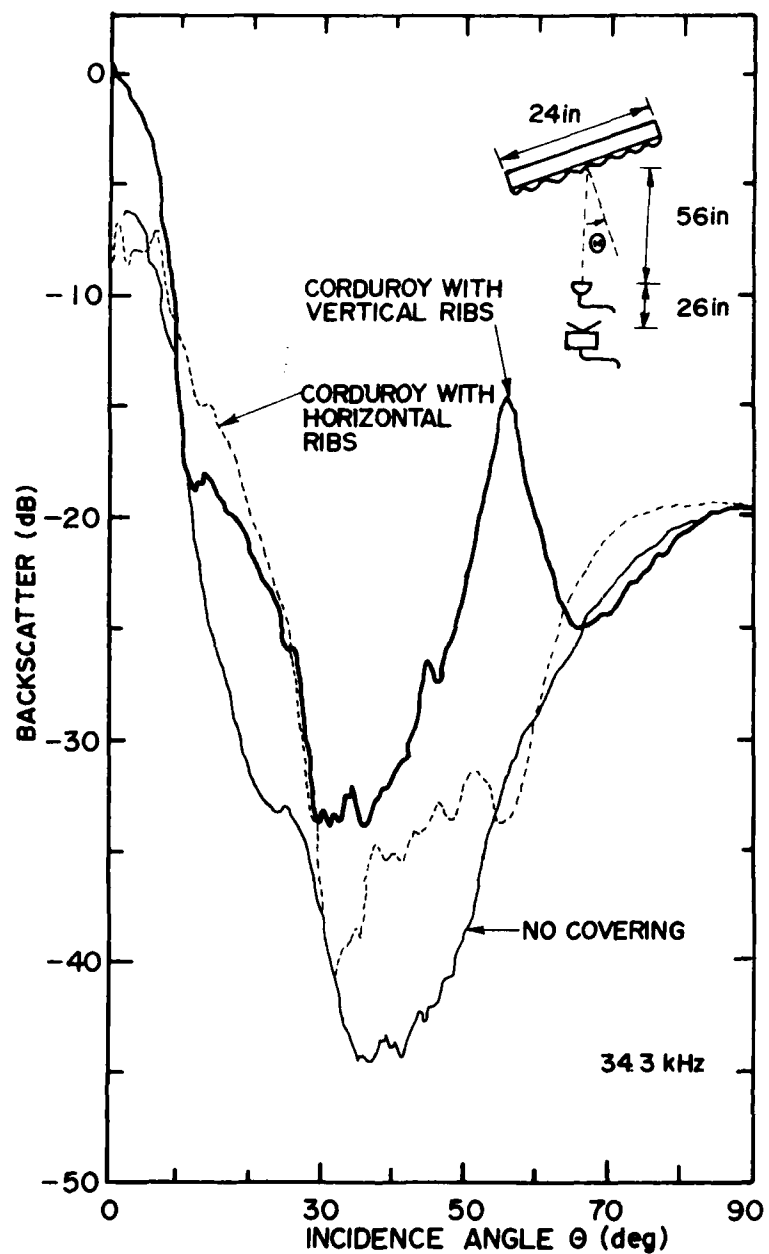


Figure 4.4 Test of the backscattering properties of the corduroy damping material in two orientations, as applied to a flat rectangular baffle at 34.3 kHz.



Figure 4.5 Photograph of the 28-inch prolate spheroid with a portion of its surface covered in a corduroy damping material.

Backscattered-directivity curves were recorded for six different percentages of the surface of the spheroid covered at both ends. The results are summarized in the curves of Figure 4.6. The backscattering from the damped spheroids is not as simple as that for plain spheroids (Section 4.2.2); it now includes interference effects and some rough-surface scattering. However, the backscattering from the totally damped spheroid is generally about the same as that for the plain spheroid reduced by the 7.5-dB normal-incidence damping factor. Note, in addition, that damping only small areas near the tips of the spheroid produces an attenuation equal to that of the totally damped spheroid over the majority of the angular range. This result indicates that the primary scattering component for about 70% of the range of incidence angles originates near the illuminated tip of the spheroid.

When more than just the ends of the spheroid is covered, the backscatter data correspond closely to the data for the end-damped case except that attenuation is observed for a slightly larger angular range. Figure 4.7 shows curves obtained for four different percentages of damping. Note that the region in which all four of the damped-spheroid plots are similar has been darkened between the extremes to reduce clutter in the graph. In these and other cases not shown, the incidence angle at which the plot for the damped spheroid begins to exhibit attenuation over that of the plain spheroid corresponds approximately to the angle at which the specular point of the spheroid falls at the edge of the damping fabric. For example, the angles at which the edge of the fabric in cases A - C of Figure 4.7 corresponds to the specular reflection point are  $65^\circ$ ,  $77^\circ$ , and  $82^\circ$ , respectively. There is a

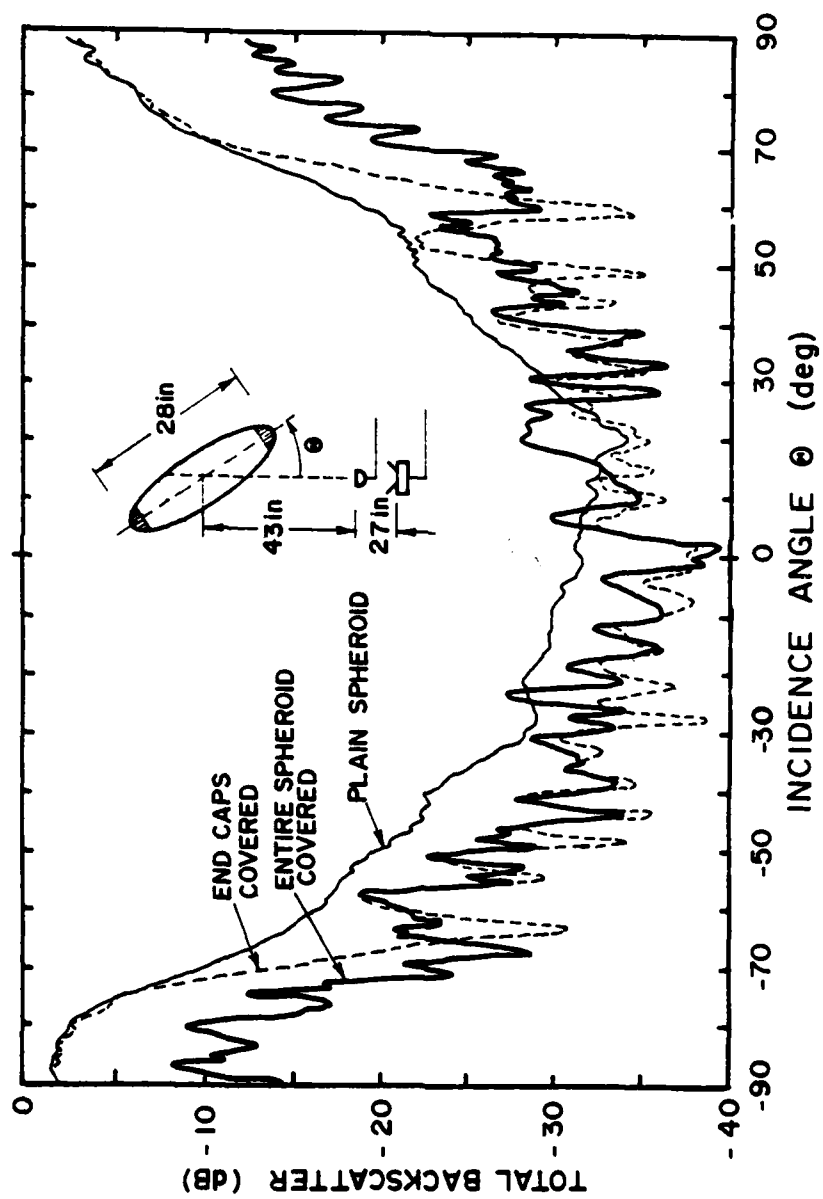


Figure 4.6 Directivity of the backscatter from plain, end-damped, and totally damped prolate spheroids. ( $h\xi_0 = 223$ )

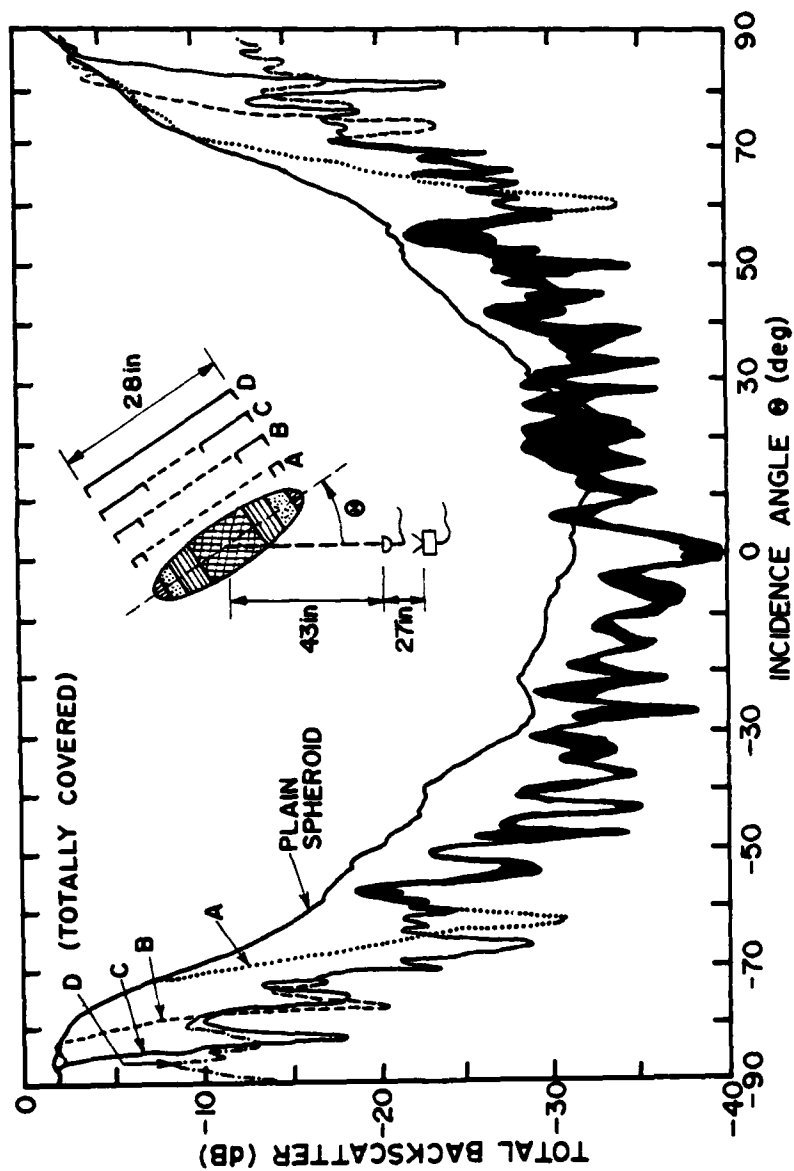


Figure 4.7 Directivity of the backscatter from a prolate spheroid with various degrees of damping material applied at both ends.  
( $h\epsilon_0 = 223$ )

definite relationship between these three angles and the curves of the figure, although the influence of the damping fabric appears to extend somewhat beyond the physical edge of the material.

When the spheroid is damped in the center instead of the ends, a complementary effect is observed. This effect is summarized in the curves of Figure 4.8. In this case, all of the spheroid except the very ends (i.e., last 2 inches of the major radius) is covered with the damping fabric, but attenuation of the backscatter is noted only for angles of incidence greater than about  $70^\circ$ . Furthermore, the backscatter near axial incidence in this case is worse because of an additional contribution from the thickness of the fabric (about  $\lambda/6$ ) at its leading edge. Figure 4.9 shows that similar results are obtained when a smaller portion of the spheroid's center is damped, except that attenuation is observed for an even smaller range of angles near broadside incidence. Once again, the transition to attenuated values is associated with the angle at which the specular points fall near the edge of the damping material (angular values of  $65^\circ$ ,  $77^\circ$ , and  $82^\circ$  for cases A - C of Figure 4.9). In fact, additional tests showed that dips could be introduced in the directivity curve near any desired angle by applying a thin fabric strip to the spheroid model at the location of the corresponding specular point.

When interpreting the results of this section, one should keep the type of receiving technique utilized in mind. The receiver-gate module is set to include returns from anywhere on the spheroid, and it detects the amplitude of the largest return in that window. Thus, when there are two separated returns, such as from the tip of the spheroid and the

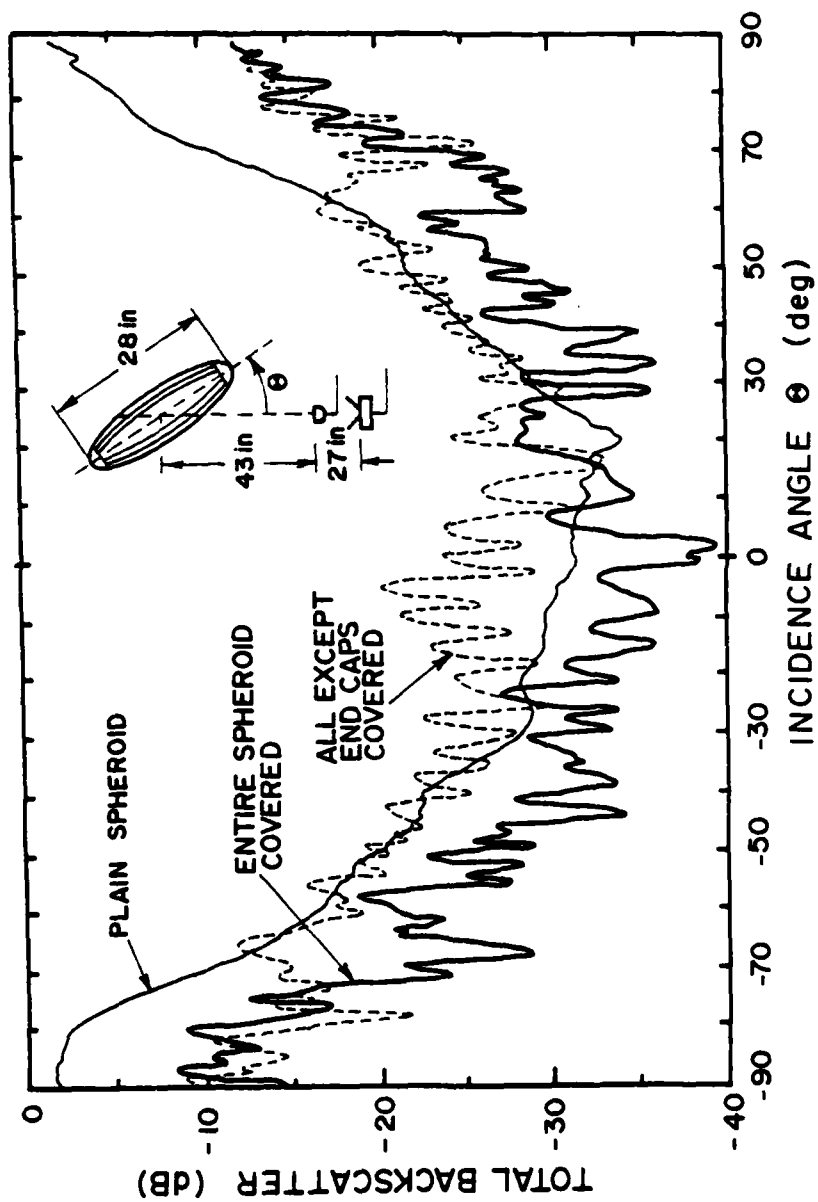


Figure 4.8 Directivity of the backscatter from plain, center-damped, and totally damped prolate spheroids. ( $h\xi_0 = 223$ )



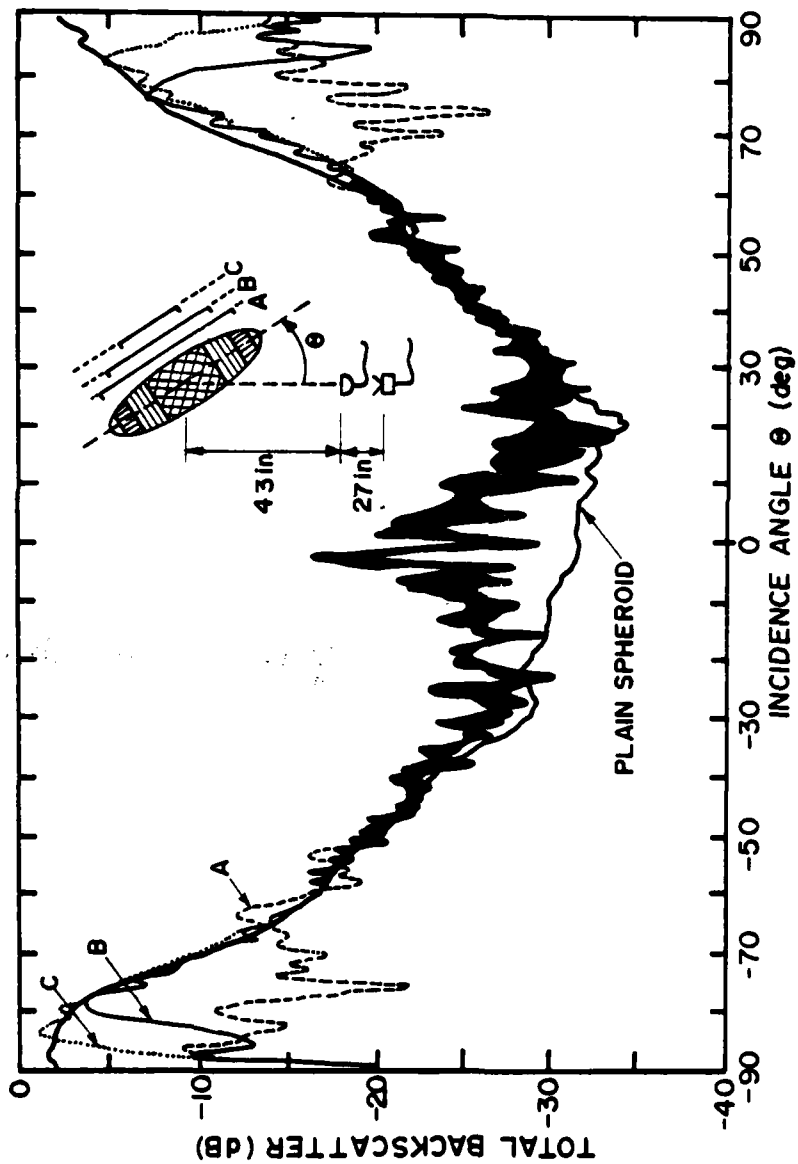


Figure 4.9 Directivity of the backscatter from a prolate spheroid with various degrees of damping material applied at the center. ( $h\xi_0 = 223$ )

damping-fabric edge, the largest of the two returns determines the plotted amplitude. The curves shown in the figures have been traced from the actual plotted results. No data smoothing or other processing has been performed except a shift of the amplitude scale to normalize the values to a sphere with the same major radius as the spheroid. The slight asymmetries in the data are related primarily to the directivity of the source used in the experiments.

#### 4.2.4 Geometric Calculations for a Prolate Spheroid

The results of the investigations for both plain and partially damped spheroids (Sections 4.2.2 and 4.2.3) strongly suggest that only specular reflection is being observed. Because this scattering mechanism is associated with tangents to the surface, it is useful to examine the geometry of the spheroid. Refer to Figure 4.10. From the figure, it is obvious that specular points for various spheroid orientations cluster near the tips because of the rapid changes in curvature there--especially in the case of thin spheroids. This explains why damping only the tips is so effective over a wide range of incidence angles (see Section 4.2.3). To compute the specular point, it is convenient to express the generating ellipse of the spheroid in terms of the parameter  $\phi$  as

$$\begin{aligned} x' &= a \cos \phi \\ y' &= b \sin \phi \quad , \end{aligned} \tag{4.6}$$

where  $2a$  and  $2b$  are the major and minor axes, respectively. Similarly, let the field point be defined by its position on a circle of radius  $r_0$

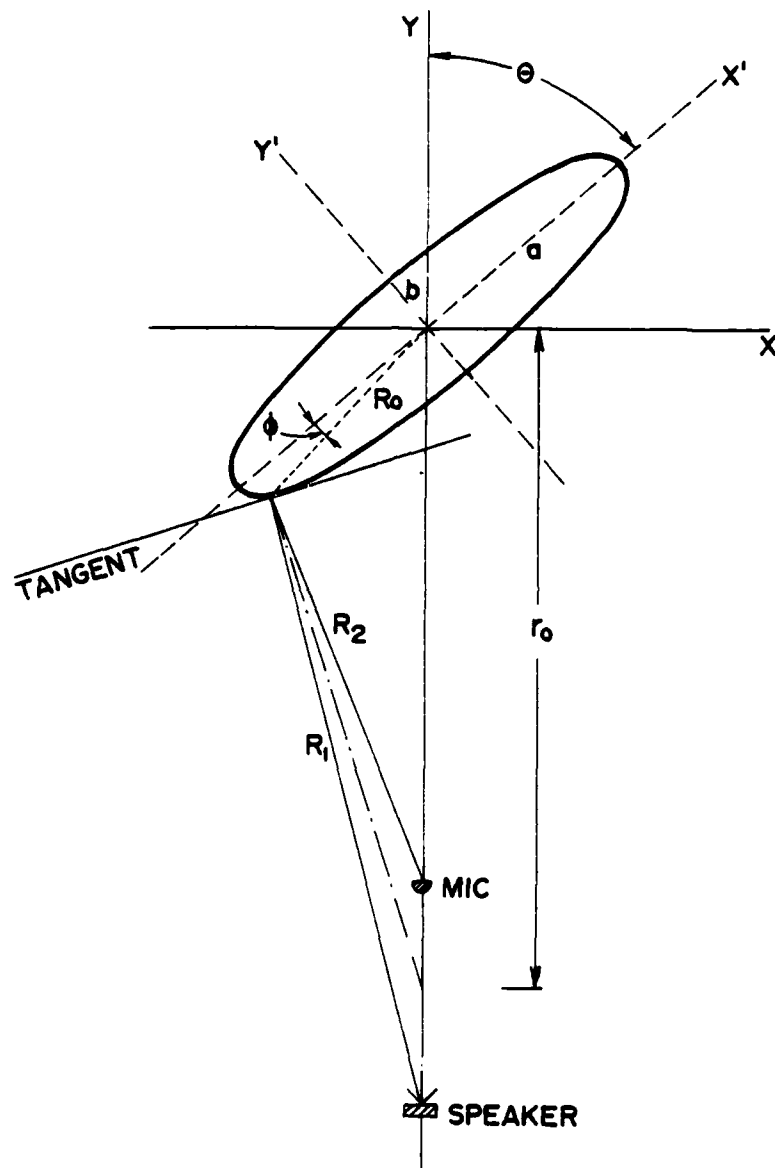


Figure 4.10 Geometry used for the calculation of backscattering from a prolate spheroid.

as

$$\begin{aligned} x &= r_0 \cos \theta \\ y &= r_0 \sin \theta \end{aligned} \quad (4.7)$$

The radius  $r_0$  is the distance from the center of the spheroid to the transducers. This distance can be approximated by the distance from the center of the spheroid to the microphone. Using elementary relations from analytic geometry for parametric curves, one can compute the equation of the normal to the ellipse and the intersection of this normal with the field-point circle. The resulting expression is

$$r_0 \sin \theta = \left( \frac{b^2 - a^2}{b^2} \right) \sin \phi + \left( \frac{r_0 a}{b} \right) \tan \phi \cos \theta \quad (4.8)$$

Equation 4.8 relates the specular point on the ellipse given by the angle  $\phi$  (Figure 4.10) with the angle of incidence  $\theta$  for a given  $r_0$ . A numerical solution of this relation was used to locate the specular points associated with the damped-spheroid directivities presented in Section 4.2.3.

The influence of surface curvature on the scattered field  $I_f$  can be expressed in terms of geometric spreading from the surface field  $I_s$  as (Figure 1.1)

$$I_f = \frac{I_s(\rho_1 \rho_2)}{(\rho_1 + s)(\rho_2 + s)} \quad (4.9)$$

The values  $\rho_1$  and  $\rho_2$  are the two principal radii of curvature of the surface, and  $s$  is the distance from the surface to the field point. If

s is large, Equation 4.9 reduces to

$$I_f = \frac{I_S}{Gs^2} \quad , \quad (4.10)$$

where  $G = 1/\rho_1\rho_2$  is called the Gaussian curvature. Equations 4.9 and 4.10 can be used to predict the scattering at a field point if  $I_S$  is assumed to be equal to the incident intensity (i.e., total reflection, such as at a rigid plane baffle).

Calculation of the Gaussian curvature for a prolate spheroid using the methods of differential geometry (see Salmon; 1927, p. 411) is somewhat lengthy but straightforward. If the spheroid is assumed to have its major axis oriented along the z direction in an  $r, \varphi_0, \theta_0$  spherical coordinate system, the resulting expression is

$$G = \frac{a^2(\sin \theta_0 \cos^2 \varphi_0 - \cos \theta_0 \sin \varphi_0 \cos \varphi_0)}{\sin \theta_0 (b^2 \cos^2 \theta_0 + a^2 \sin^2 \theta_0)^2} \quad . \quad (4.11)$$

All the experimental data of this chapter are recorded in a single plane containing the major axis. Thus, one can assume that the rotation angle  $\phi_0$  is zero, reducing the previous expression to

$$G = \frac{a^2}{[(b \cos \theta_0)^2 + (a \sin \theta_0)^2]^2} \quad . \quad (4.12)$$

Note that  $\theta_0$  now corresponds to the  $\phi$  of Figure 4.10.

Evaluation of Equation 4.9 with the dimensions used in some of the spheroid experiments indicates that s is not large enough to permit the

use of the simplified expression for large ranges (Equation 4.10). Consequently, it is necessary to obtain the two principal radii of curvature independently. One of these radii for all the cases under consideration is just the radius of curvature of the ellipse, which is easily calculated from the parametric form of the ellipse in Equation 4.6 (see, for example, Buck, 1965, p. 318):

$$\rho_1 = \frac{((b \cos \phi)^2 + (a \sin \phi)^2)^{3/2}}{ab} \quad (4.13)$$

The other principal radius of curvature can then be obtained from the Gaussian curvature:

$$\rho_2 = \frac{b((b \cos \phi)^2 + (a \sin \phi)^2)^{1/2}}{a} \quad (4.14)$$

A purely geometric prediction of the backscattered directivity from a spheroid was obtained by computing the specular points for a group of incidence angles, finding the two principal radii of curvature at those points, and substituting into Equation 4.9. The result for  $h\xi_0 = 176$  is plotted in Figure 4.11 along with the equivalent experimental curve. Note that the geometric curve has been normalized by matching with the backscattering from a reference sphere that has the same Gaussian curvature. The agreement between the curves of Figure 4.11 is quite good, and it would be even better if the geometric curve were lowered about 2 dB relative to the experimental curve. (Accumulated experimental errors in the normalization could account for this discrepancy.)

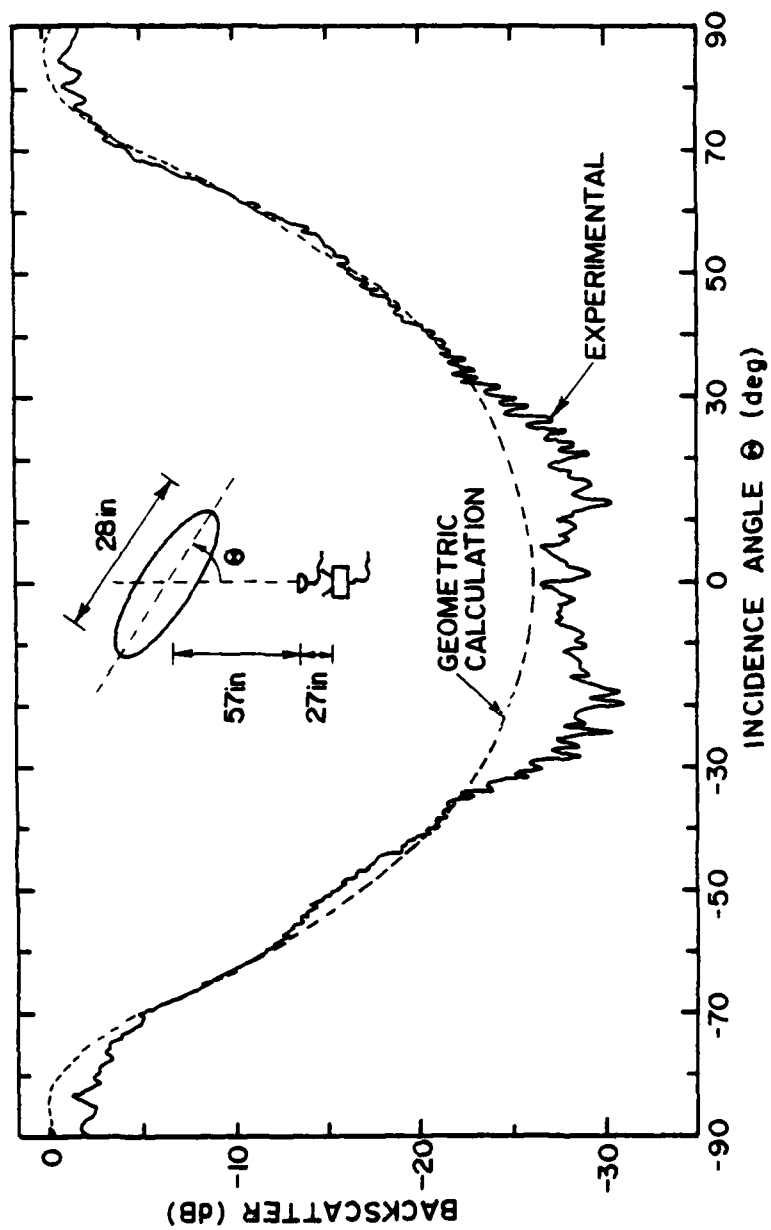


Figure 4.11 Backscattered directivity from the 28-inch prolate spheroid at 27 kHz compared to a simple geometric calculation.  
( $h\xi_0 = 176$ )

Interpretation of the agreement in the data of Figure 4.11 is not straightforward because of the difficulty of finding a typical dimension for a thin spheroid. At broadside incidence, the two principal radii of curvature are 98 inches and 2 inches; and, using them as a characteristic dimension  $R$ , one obtains  $kR$ 's of 1230 and 25, respectively. The choice of which (or what combination) of the two dimensions to use is not obvious, but both quantities are fairly large. Because the geometric prediction represents the high-frequency limit, the good agreement between theory and experiment is not surprising. However, at axial incidence, the two principal radii both become .29 inch, leading to a  $kR$  of 3.6. In this case, the single radius of curvature is only about half of a wavelength in dimension. To add to the confusion, theoretical computations by New, Andrews, Brill, Eisler, and Uberall (1974) have shown that the predictions for thin spheroids from the geometrical theory of diffraction (an extension of geometrical optics) are valid only at very high frequencies (i.e.,  $h\xi_0 \geq 575$  for a 10:1 prolate spheroid).

Figure 4.12 is a comparison of the geometric and experimental backscatter from a larger prolate spheroid ( $h\xi_0 = 261$ ). In this case, the two principal radii of curvature at broadside incidence are 147 inches and 3 inches ( $kR$ 's of 1847 and 38), and the radius at the tip is .43 inch ( $kR = 54$ ). The agreement between theory and experiment is slightly worse than the previous result (Figure 4.11) in the rapid transition region, but it is better at both broadside and axial incidence.



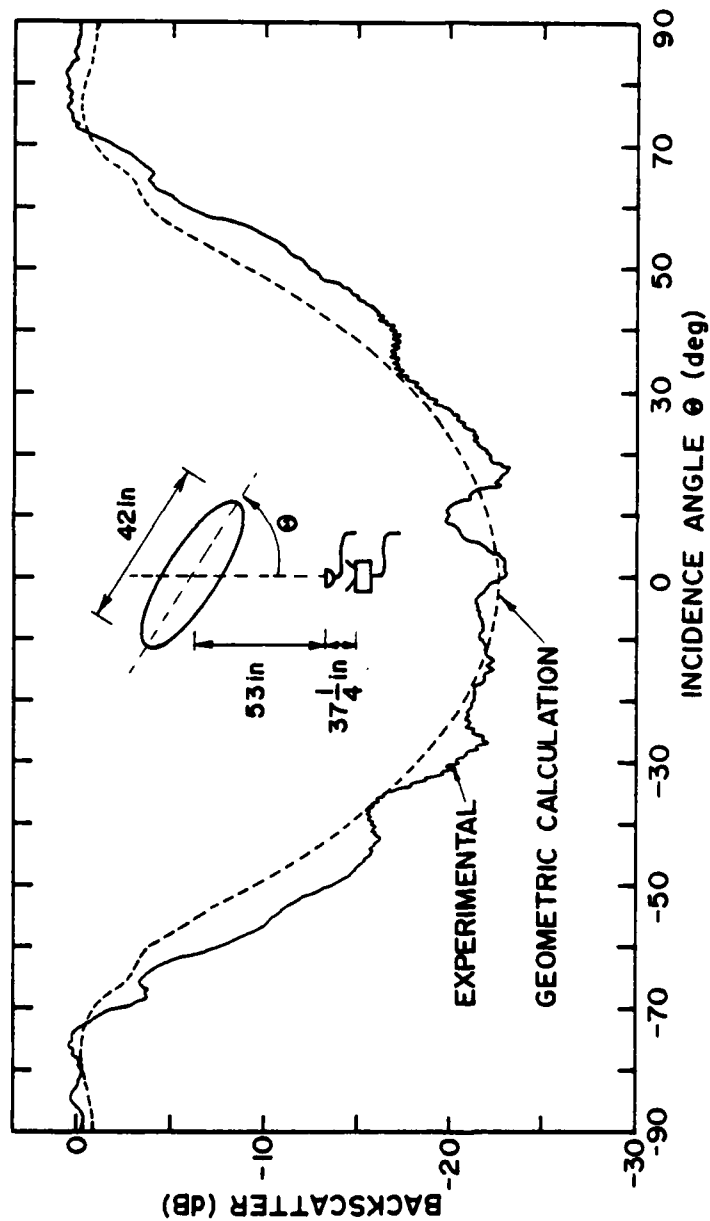


Figure 4.12 Backscattered directivity from the 42-inch prolate spheroid compared to a simple geometric calculation. ( $h\xi_0 = 261$ )

One should remember that experimental constraints limited the spacing between the transducers and the model, especially when using the large (42-inch) spheroid. Thus, the geometric prediction is sensitive to the choice of a separation distance  $r_0$  that is used in the specular-point calculation of Equation 4.8. The true surface normal in Figure 4.10 intersects the source-receiver axis between the source and receiver such that the angles between the normal and both the incident ( $R_1$ ) and reflected ( $R_2$ ) paths are equal. The results shown in the two previous figures assume that the normal intersects a point that is centered between the source and receiver. A preliminary analysis of the data showed that predictions utilizing this last approximation came as much as 3 dB closer to the experimental curve in the regions of maximum slope than results which assumed that the normal passed through the receiver. To further improve the prediction, the change in total propagation path that occurs when the specular point gets closer to the transducers was also considered. In addition, a correction was added to compensate for the directivity of the source, but this factor never exceeded 1 dB.

#### 4.3 Prolate Spheroid with Small Surface Discontinuities

##### 4.3.1 Effect of Surface Imperfections

The prolate spheroid is an interesting model because of its smooth contours and its double variation in surface curvature. Data already presented in this chapter have shown that this combination of factors leads to relatively little backscattering at all incidence angles differing from broadside incidence. In order to test the importance of

this smooth curvature, it is useful to examine the effect of small surface anomalies and discontinuities on the backscattered directivity.

One example of a surface anomaly can be seen in the oscilloscope trace that is shown in Figure 3.5 (on page 92). In the group of three returns following pulse B, the center return originates at a 3/4-inch-diameter mounting hole cut partway through the center of the spheroid along the minor axis of the generating ellipse. From a geometrical-optics point of view, this hole should have no effect because the incident field cannot "see" it. Despite this fact, a return from the hole is clearly distinguishable; but its amplitude is about 10 dB below the already small specular return from the spheroid (pulse B). Consequently, the contribution of this hole to the spheroid's backscattering can be neglected. The hole does appear to have a more prominent effect on the local surface field, which is discussed in the following section on cylinder obstructions (Section 4.4).

The effect of a surface anomaly in the illuminated area at the critical tip region is illustrated in Figure 4.13. Because of repeated use over a long period, the 28-inch wooden spheroid has acquired a dent approximately 1/8-inch deep near one tip. Thus, the backscattered directivities from both the good and dented noses of this model were compared. Even though the dent is small in relation to the dimensions of the model, it has a major effect on the backscattering at incidence angles as large as  $50^\circ$ . This result again shows the importance of the surface curvature, especially the curvature in the tip region. It also indicates that great care must be taken in constructing and handling spheroid models, and that spheroid results should only be applied to objects of very similar shape.

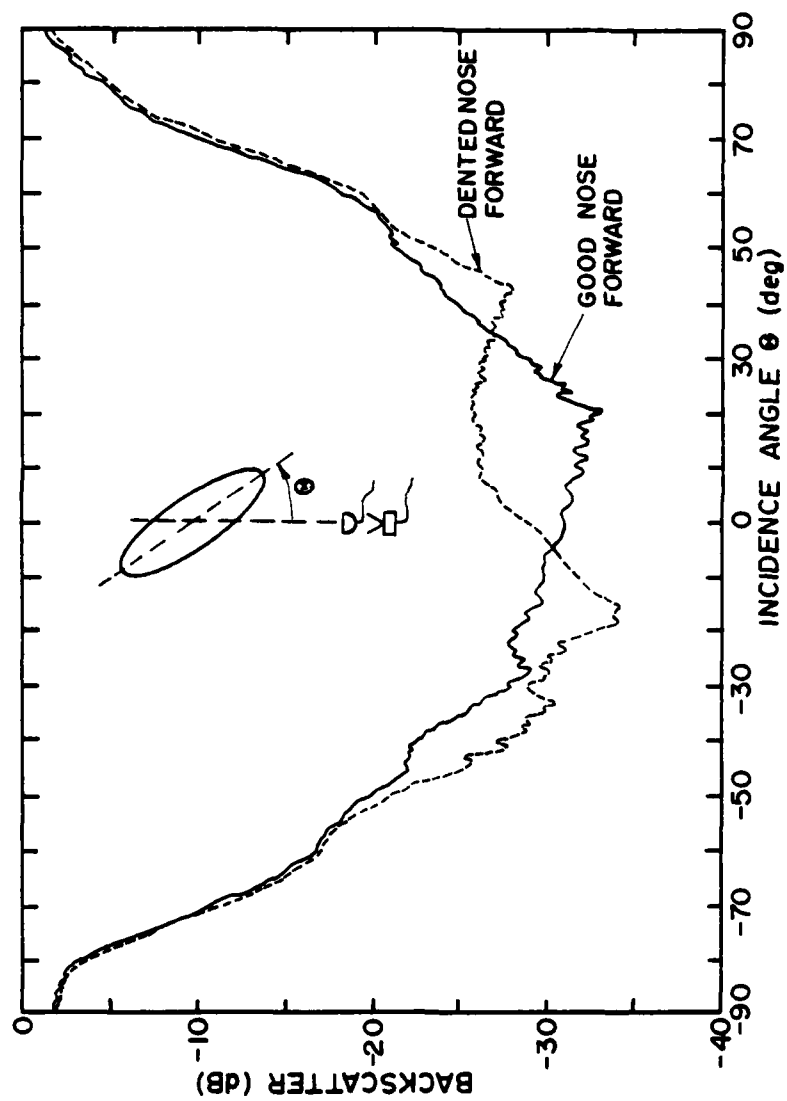


Figure 4.13 Backscattered directivity from the 28-inch prolate spheroid at 34.3 kHz with both a good nose and a slightly dented nose illuminated. ( $h\xi_0 = 223$ )

#### 4.3.2 Effect of Thin Band Obstructions

As a further investigation of anomalies on the surface of a spheroid, it is interesting to examine the effect of thin bands on the surface in a plane perpendicular to the axis of revolution. Figure 4.14 shows the result from a band of corduroy damping material about  $.25\lambda$  thick placed around the 28-inch spheroid. The position and width (about 1 inch) of the band make its absorptive effect on the backscattered directivity very small. However, the band does produce an additional scattering component from the leading edge of the fabric, as was seen in the previous data for damped spheroids (see Section 4.2.3). This additional component peaks at axial incidence, the point at which the band forms a scattering surface that is parallel to the wavefront but also of rather small thickness. The large amplitude of the peak lends support to the notion that the length dimension of a long thin scatterer largely compensates for the small thickness dimension in determining the backscattering. Recall that a similar conclusion was drawn about the support wires used to suspend the models (see Section 3.3).

Because the illuminated surface of the band of Figure 4.14 is parallel to the incident wavefront, a specular scattering mechanism cannot be ruled out--even when the small thickness dimension is considered. Thus, a smooth sloping section was carefully formed in front of the band using a dense modeling clay, and the backscattered directivity was measured again (see Figure 4.15). In this case, any specular component should be directed away from the receiver. The plot indicates a reduction of about 3 dB in the scattering by the band at axial incidence. At other angles, however, the scattering is about the

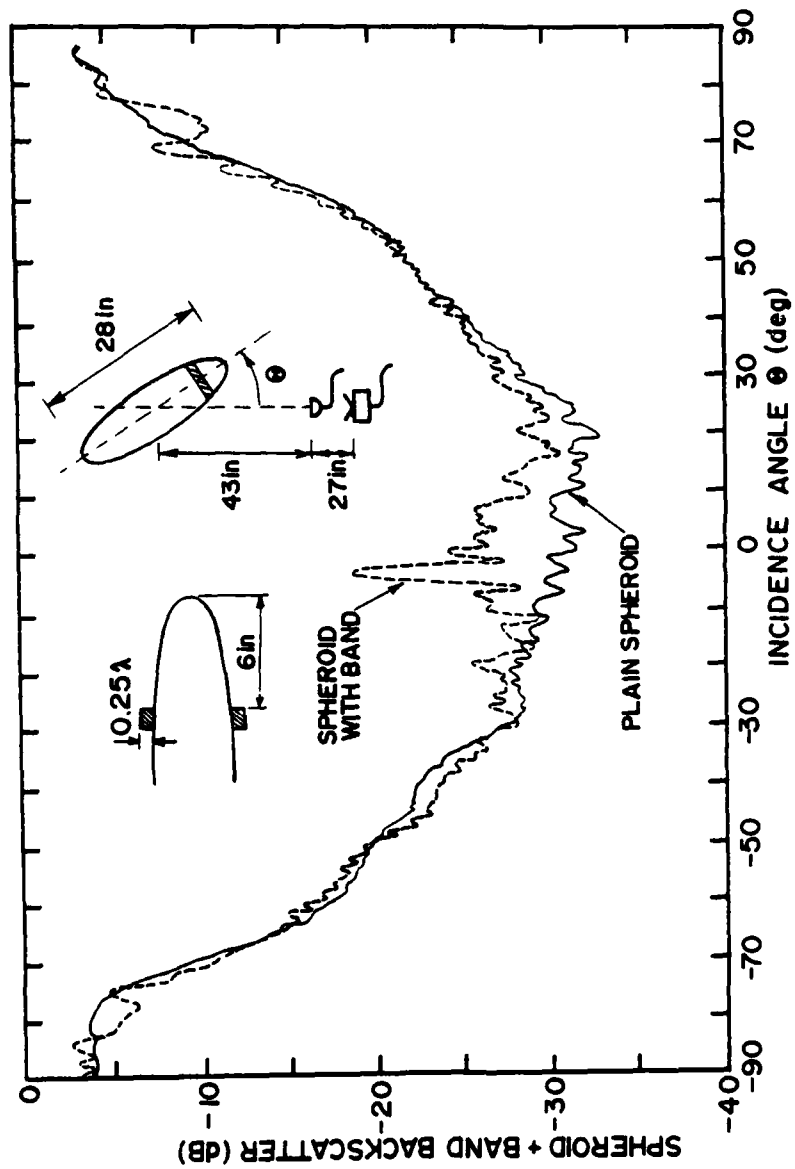


Figure 4.14 Backscattered directivity from a prolate spheroid with a band of corduroy damping material around the nose.  
( $h\xi_0 = 223$ )

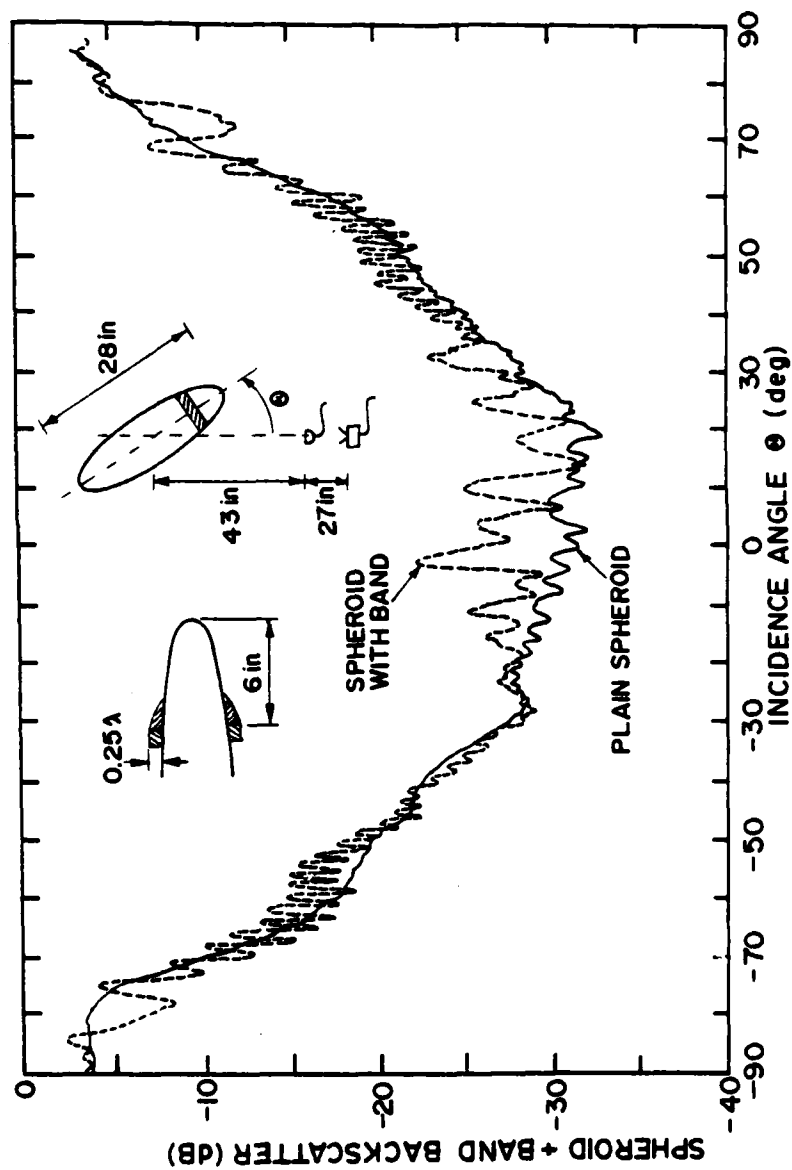


Figure 4.15 Backscattered directivity from a prolate spheroid with a smoothly preceded cloth band around the nose. ( $h\epsilon_0 = 223$ )

same as that of Figure 4.14. A different result was observed when the damping strip was removed to leave only the clay sloping section, as is shown in Figure 4.16. In this case, the scattering by the remaining clay band is significantly worse than that observed from the corduroy strip in the range of  $0^\circ - 30^\circ$ , apparently because of the sharp rigid termination of the remaining section of the band. (This is similar to results obtained with cone models discussed in Section 5.4.1.)

An investigation into the effect of the band's thickness was also performed by wrapping various numbers of rubber bands around the surface of the 42-inch spheroid. Figures 4.17, 4.18, and 4.19 show the results of bands with thicknesses of  $.063\lambda - .25\lambda$  placed around the nose of the spheroid. The thinnest band ( $.063\lambda$ ) has very little effect on the backscattered directivity except for a 5 dB peak close to axial incidence (Figure 4.17). The bands having the next two graduated thicknesses ( $.13\lambda$  and  $.19\lambda$ ), however, add substantially to the backscattering by the spheroid over a wide range of incidence angles (Figure 4.18). Finally, the thickest band ( $.25\lambda$ ) produces only a small additional increase (Figure 4.19). The smallest band appears to be so thin that it is partially hidden by the surface field on the spheroid; however, the rapid increase in scattering caused by the bands seems to have stabilized to perhaps an area-proportional increase at the thickness of the largest band. Note that, even though the largest band is only  $.25\lambda$  in thickness, the resulting backscattered directivity for a broad angular range near axial incidence is increased (over that of the plain spheroid) to almost the level from the spheroid at broadside incidence.



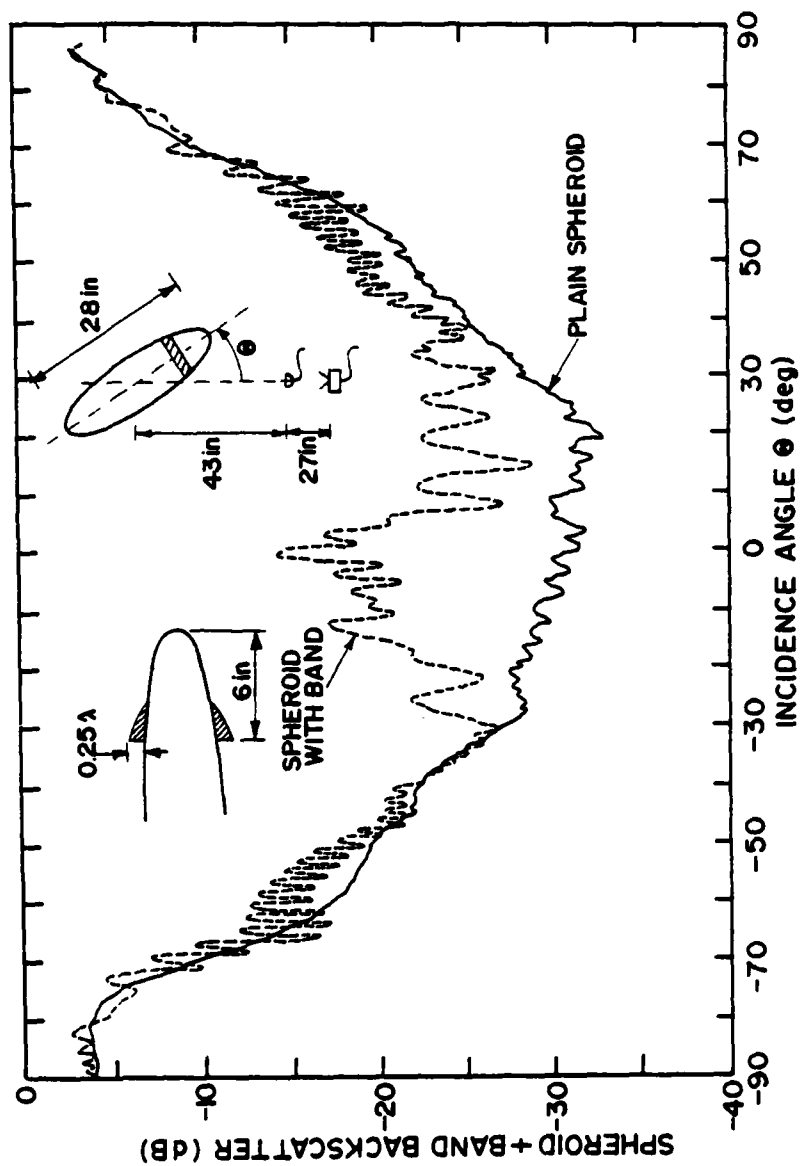


Figure 4.16 Backscattered directivity from a prolate spheroid with a sloped clay band around the nose. ( $h\xi_0 = 223$ )

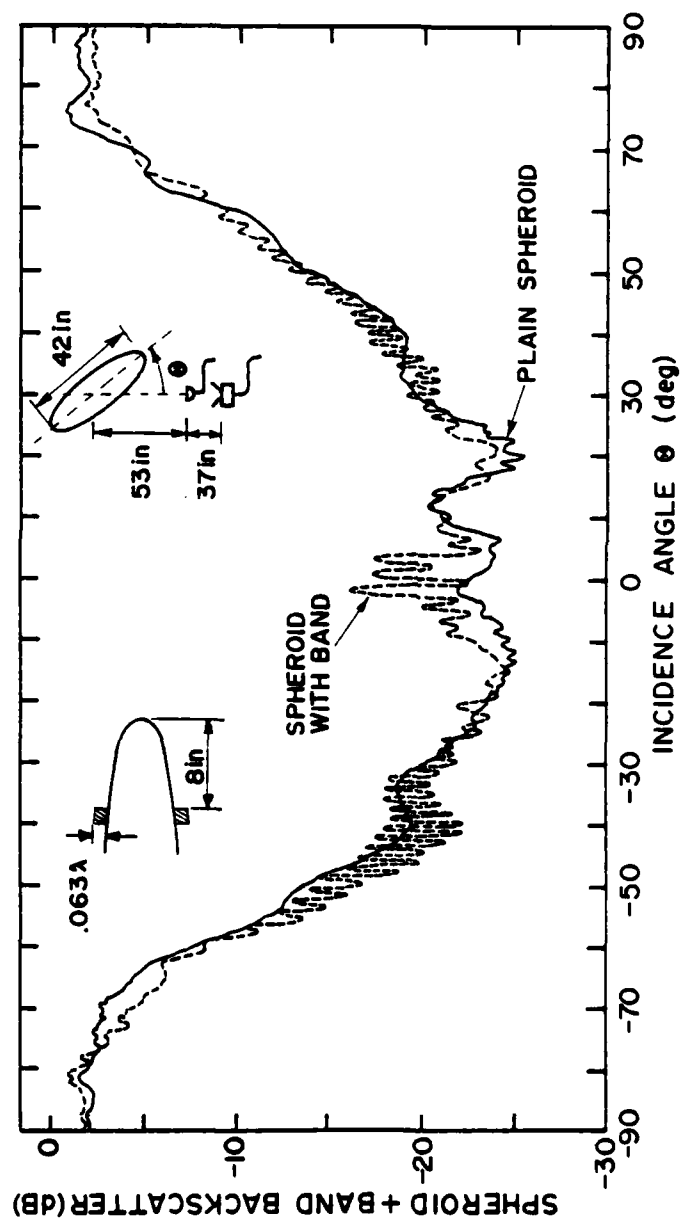


Figure 4.17 Backscattered directivity from a prolate spheroid with and without a thin rubber band around its nose. ( $h\xi_0 = 264$ )

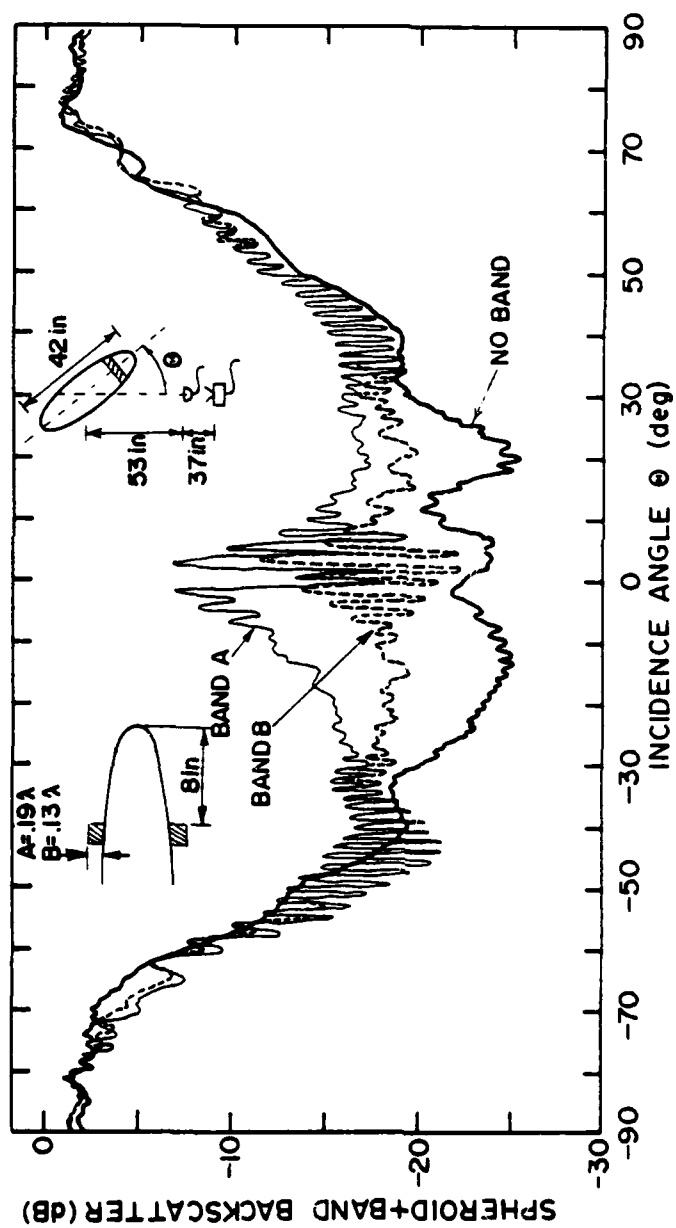


Figure 4.18 Backscattered directivity from a prolate spheroid with and without medium-thick rubber bands around its nose.  
( $h\epsilon_0 = 264$ )

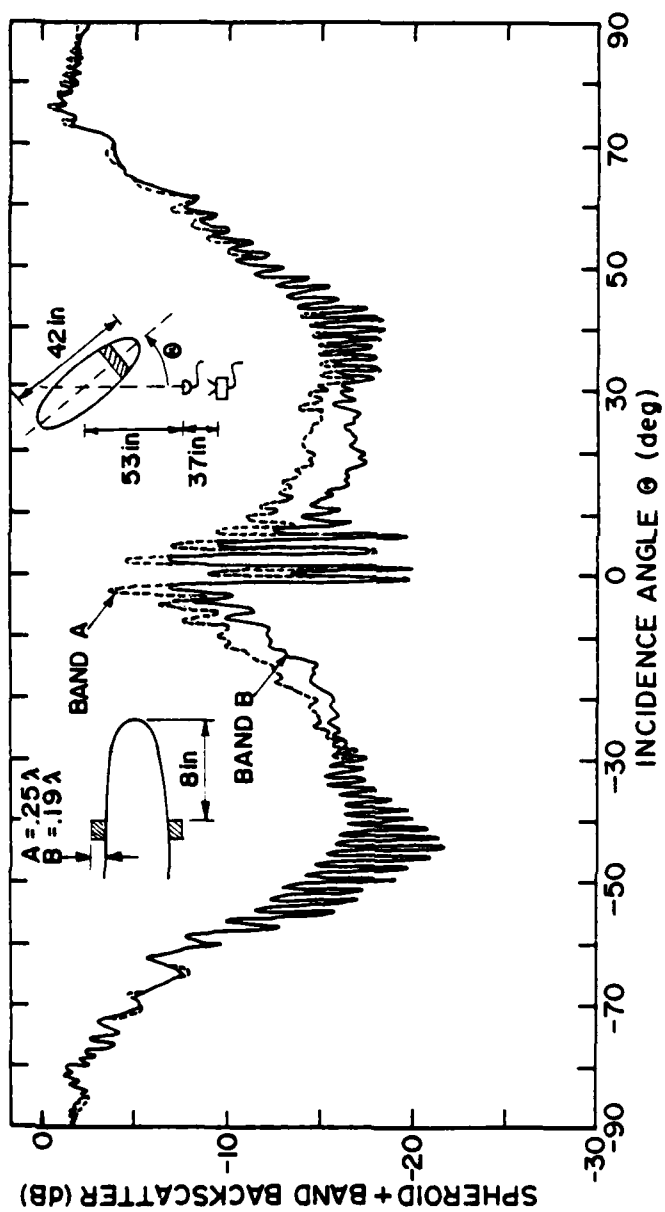


Figure 4.19 Backscattered directivity from a prolate spheroid with and without various thick rubber bands around its nose.  
( $h\epsilon_0 = 264$ )

The same group of bands was also applied to the spheroid at its center to see if the effect of the spheroid is the same there. In comparing these results with the previous examples of bands near the tip of the spheroid, one must remember that the different location of the band relative to the source and receiver can be expected to reduce the backscattering levels by about 4.5 dB because of additional propagation losses. Figure 4.20 shows that the thinnest center-located band ( $.063\lambda$ ) again has no additive effect on the backscatter from the spheroid except for the peak at axial incidence. Figure 4.21 shows that the next two sizes of bands ( $.13\lambda$  and  $.19\lambda$ ) produce a substantial increase in the scattering, while the thickest band ( $.25\lambda$ ) produces an asymmetric effect that may indicate a somewhat larger increase than that observed in the equivalent case with the bands at the spheroid tip. Note that only the distinct portions of the curve associated with the thickest band have been plotted to reduce clutter in the figure. Allowing some margin for slight positioning errors with the bands, the backscatter results for center-located and end-located bands are about the same. The differing angular ranges over which the bands increased the backscattering from the spheroid indicate that the band return is probably present as a distinct echo over a wide angular range; however, the echo from the band is only evident when the amplitude of this return exceeds that of the return from the spheroid itself. (The largest return at a given incidence angle is detected by the receiving circuitry.)

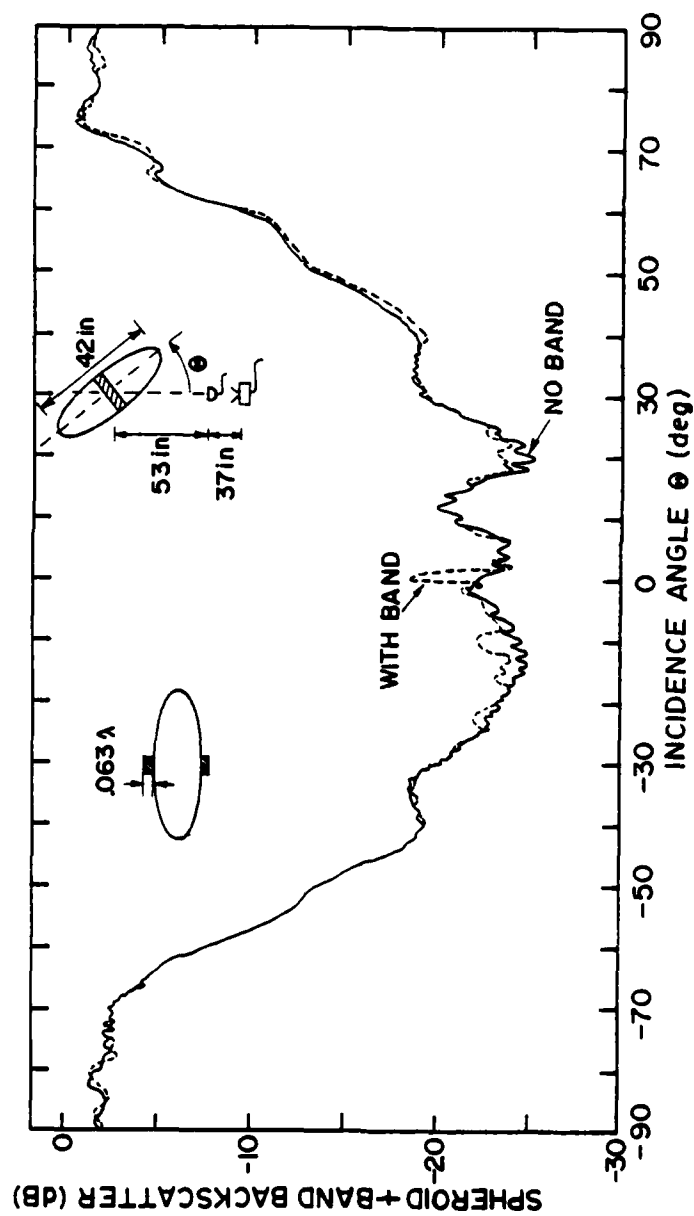


Figure 4.20 Backscattered directivity from a prolate spheroid with and without a thin rubber band around its center. ( $h_{f,0} = 264$ )

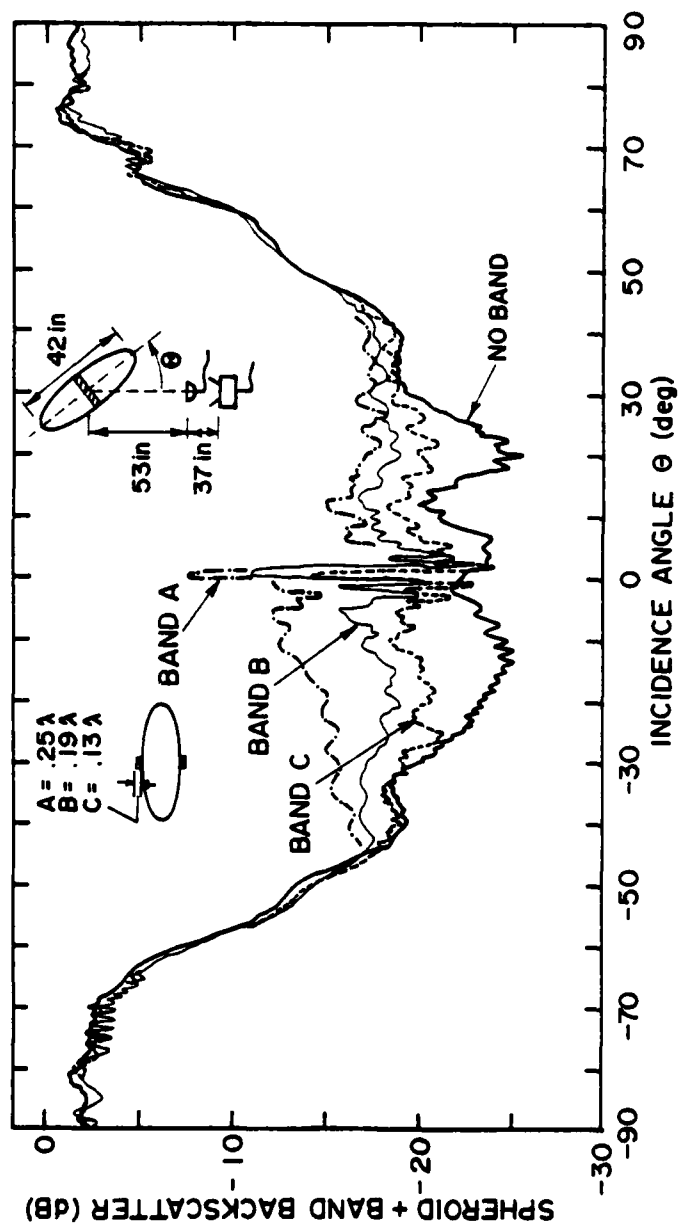


Figure 4.21 Backscattered directivity from a prolate spheroid with various rubber bands around its center. ( $h\xi_0 = 264$ )

#### 4.4 Prolate Spheroid with Cylinder Obstructions

The results of the previous section for bands around a prolate spheroid illustrate, at least qualitatively, the dramatic effect that discontinuous obstructions on the smooth surface of a spheroid can have on the backscattered pressure. In order to get a more complete quantitative view of the phenomena, an investigation of small cylinders placed on a spheroid was also performed. The cylinders are useful because both their length and diameter can be varied. They can also be easily studied both on and off the spheroid for comparison. The cylindrical models used in this investigation consist of a set that includes all combinations of the lengths of  $1/8$ ,  $1/4$ ,  $1/2$ ,  $3/4$ , and 1 inch and the diameters of  $1/8$ ,  $1/4$ ,  $1/2$ , and  $3/4$  inch. The cylinders are all machined to high precision ( $\pm .001$  inch) out of drill rod.

The cylinders were positioned in a vertical orientation along the top of the horizontally suspended spheroid with the circular base of the cylinders against the spheroid's surface. A line indicating the linear distance from the center of the spheroid along the major axis was drawn on the surface as a guide. For those cases in which the cylinders were placed near the ends of the spheroid, the cylinders were tilted somewhat from the vertical because of the curvature of the surface. This tilt only affected the data for the longest cylinders, for which the microphone was no longer centered in the main vertical-plane lobe of the cylinder scattering pattern. A gating technique was used to separate and record only the component scattered by the cylinder. This procedure was straightforward for cylinder positions away from the spheroid nose because the spheroid's backscattering component came exclusively from



the specular point at or near the nose. For comparison, data was recorded with the cylinders suspended at the same position without the spheroid present. Support in these cases was provided by two fine nylon threads (removed from a piece of braided fishing line) passed through a tiny hole coincident with the axis of the cylinder. Again, a slight but inconsequential tilt from the vertical was present with the longer cylinders.

A fairly extensive investigation was performed of both monostatic and bistatic scattering at 23 kHz from the cylinders themselves and from the cylinders at various positions on top of the 28-inch prolate spheroid. The data are summarized in the following sections. Unless otherwise stated, the curves are normalized to the return from a sphere with the same major radius as the spheroid (14 inches). Because the wavelength at the frequency used is about .6 inch, the cylinders are all of the order of a wavelength in dimension. Note that the backscatter data from the 1/8-inch-diameter cylinders have been omitted because they were too close to the background noise level to provide any useful information. A more complete study of the cylinders themselves (reported in Section 5.3) was also made at a slightly higher frequency.

#### 4.4.1 Total Backscatter from Cylinders and Spheroid

Before examining the effects of the spheroid on the scattering from cylinders, it is interesting to note the added effect of the cylinder contributions to the pressure backscattered by the spheroid. Figure 4.22 shows the results obtained when 3/4-inch-diameter ( $1.3\lambda$ ) cylinders with lengths of 1/4, 1/2, and 1 inch ( $.4\lambda$ ,  $.85\lambda$ ,  $1.7\lambda$ ) were placed at

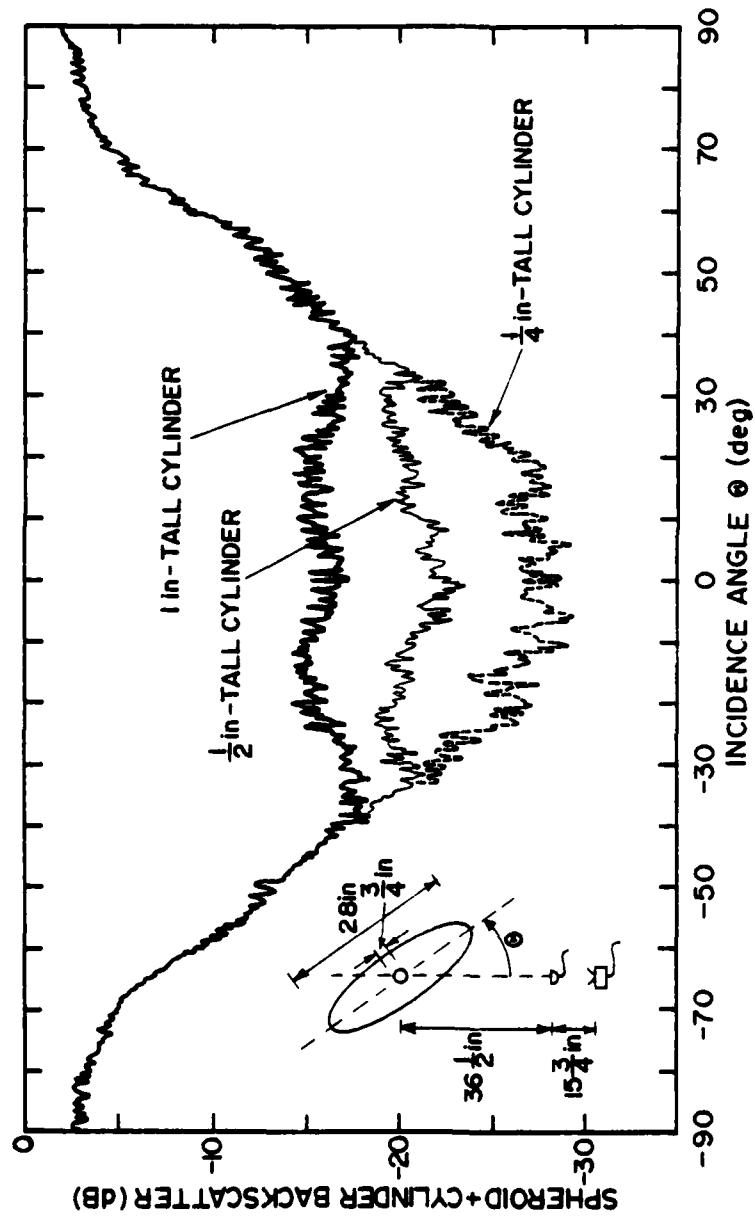


Figure 4.22 Backscatter versus angle of incidence from a prolate spheroid with  $3/4$ -inch-diameter cylinders on top at its center. ( $h\xi_0 = 150$ ,  $\lambda = .6$  inch)

the center of the 28-inch 7:1 spheroid. The 1/4-inch-tall cylinder has a return that is below that of the spheroid, even at axial incidence. Thus, this curve is the same as that from the spheroid alone. The two larger cylinders, however, backscatter more than the spheroid for incidence angles as large as  $30^\circ$ . Their echo component dominates in this angular range, increasing the total backscatter by as much as 10 dB over that from the plain spheroid. This result is contrary to one's initial intuition because the cylinders are so small relative to the size of the spheroid. Furthermore, the cylinder return would increase another 7 dB if the cylinders were placed at the illuminated tip of the spheroid (the origin of the spheroid component) because of the smaller propagation-path losses.

#### 4.4.2 Effect of Cylinder Location

Figure 4.23 illustrates the effect that a spheroid oriented at axial incidence has on the backscatter from a cylinder placed at various positions along the spheroid surface. The abscissa of the graph is the distance in inches from the center of the spheroid to the cylinder axis (with positive values toward the source and receiver), measured along a line parallel to the major axis of the spheroid. Data are presented for cylinders 3/4-inch ( $1.3\lambda$ ) in diameter and 1/4-, 1/2-, and 1-inch ( $.4\lambda$ ,  $.85\lambda$ ,  $1.7\lambda$ ) in length. Note that offsets have been applied to the data in two of the curves to separate them on the graph.

All three cylinders of Figure 4.23 backscatter significantly more pressure (than the cylinder alone) when placed on the spheroid forward of a point about 4 inches behind the spheroid's center. The relative

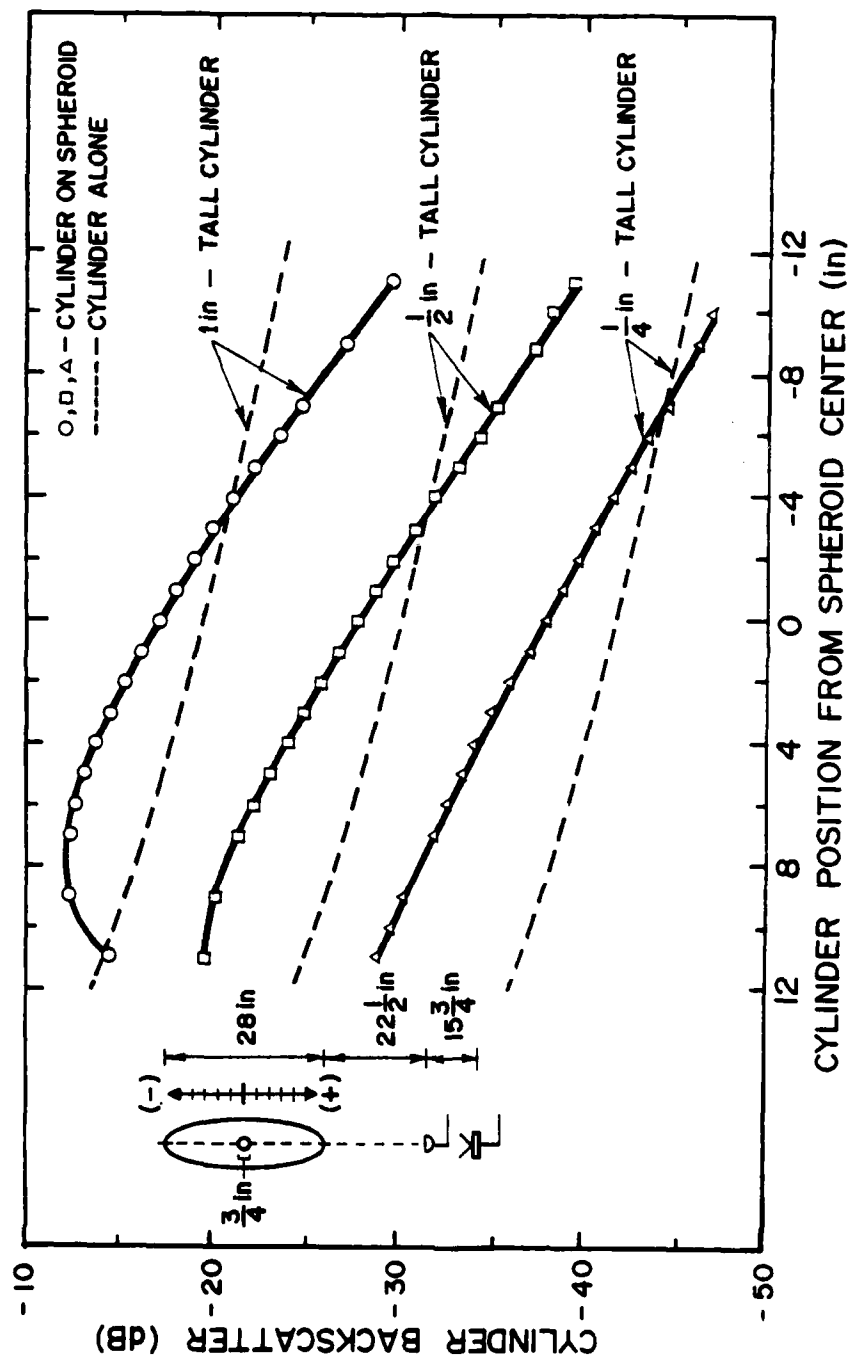


Figure 4.23 Backscatter from 3/4-inch-diameter cylinders along the top of the 28-inch prolate spheroid (axial incidence) compared to backscatter from the cylinders suspended alone. ( $h\epsilon_0 = 150$ ,  $\lambda = .6$  inch)

increase (compared to the cylinders alone) appears to be greater for the shorter cylinders. As the cylinders are moved further away from the illuminated tip of the spheroid, the backscatter drops below that of the freely suspended cylinders. The downturn in the curves for the 1-inch-tall and, to some extent, the 1/2-inch-tall cylinders at positions near the front of the spheroid is caused by the tilting of the cylinders and their scattering pattern as they rest on the steeply curved surface. The lines representing the backscatter from the freely suspended cylinders are actually matched to experimental data only at the center position along the spheroid. At other positions, they are computed using the ratio of the distances to the measured and computed points from the source and receiver. The validity of this approach was verified experimentally for several of the cylinders, including the largest and smallest (see, for example, Figure 4.24).

The differences noted in the backscatter data from one cylinder to another are related primarily to the variation in the length of the cylinders, as can be seen in Figure 4.25. The situation examined in this case is identical to that of Figure 4.23 except that 1/4-inch-diameter ( $.4\lambda$ ) cylinders were used. Results from these two cases compare closely except for a drop of about 5 dB in the returns from the thinner cylinders. One is therefore led to postulate the occurrence of a partial baffling effect caused by a surface field that forms at or near the illuminated tip of the spheroid. In other words, the intensity of the incident field that occupies the area of the spheroid projected toward the transducers appears to be deflected and concentrated around the surface of the model.

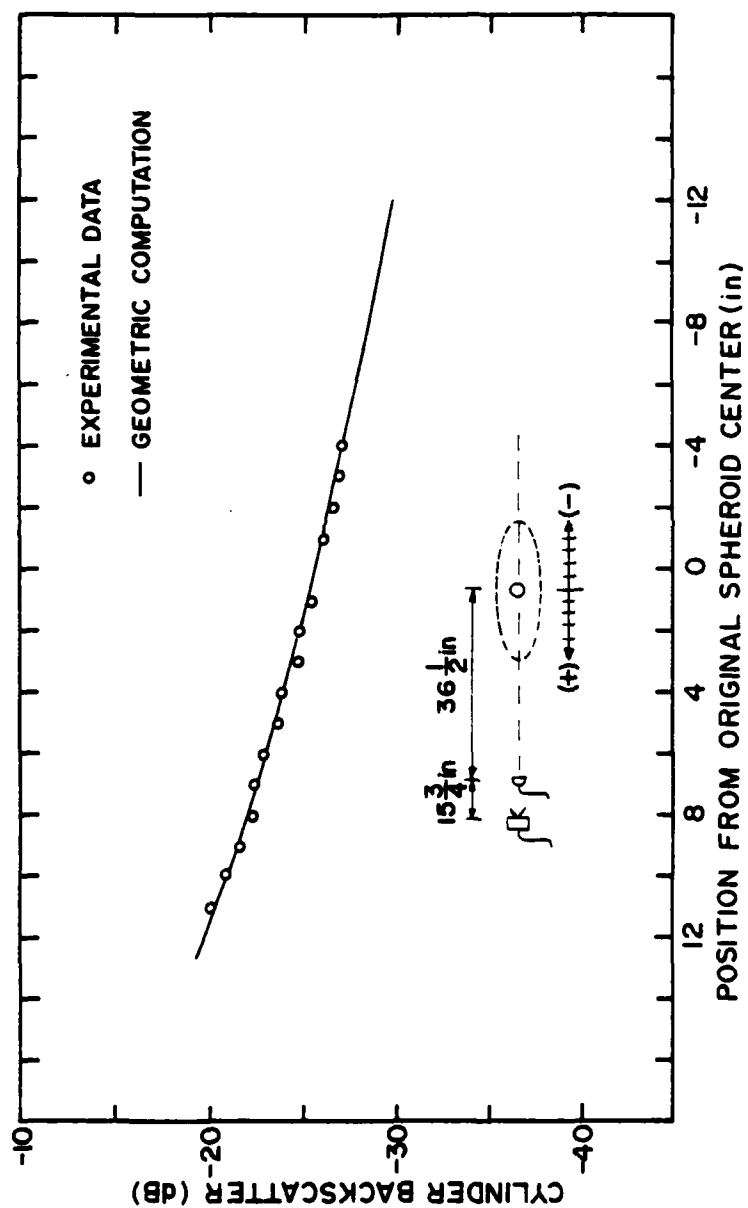


Figure 4.24 Plot of the actual backscatter from a 3/4-inch-diameter by 1/2-inch-tall cylinder versus distance compared to the geometric computation. ( $\lambda = .6$  inch)

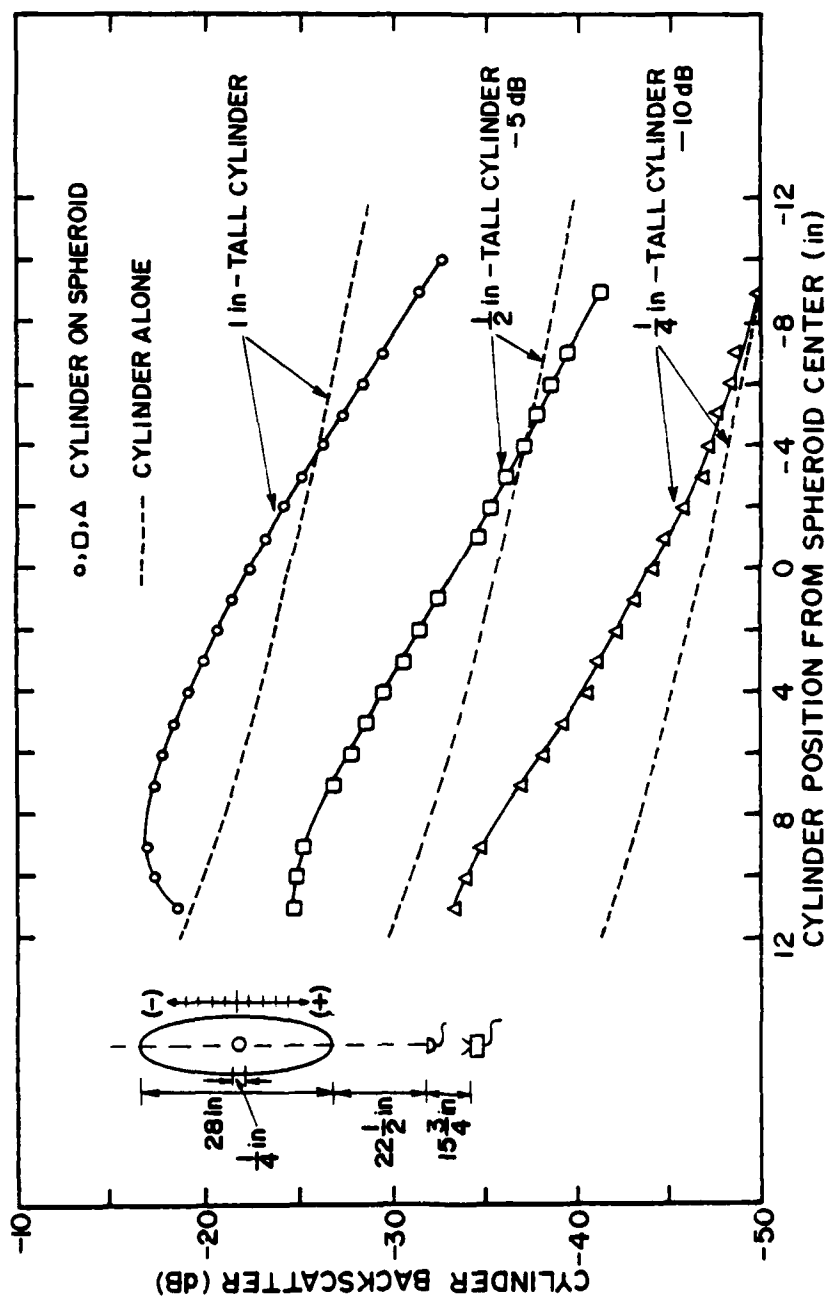


Figure 4.25 Backscatter from 1/4-inch-diameter cylinders along the top of the 28-inch prolate spheroid (axial incidence) compared to backscatter from the cylinders suspended alone. ( $h\epsilon_0 = 150$ ,  $\lambda = .6$  inch)

As a further investigation, the effect of cylinders on a spheroid that is oriented for incidence  $20^\circ$  from the axial position was examined. The results for 3/4-inch-diameter cylinders are shown in Figure 4.26. In this case, the boost in the cylinders' backscatter caused by the spheroid is still observed. However, the slope of the scattering level in relation to the position on the spheroid is noticeably less than it was for the case of axial incidence. The curves for cylinders on the spheroid now almost parallel the curves for freely suspended cylinders. Thus, a partial baffling effect is noted even for cylinders positioned near the rear of the spheroid. Again, the corresponding results for 1/4-inch-diameter cylinders were the same except for an overall decrease in amplitude of about 5 dB.

One other effect that appears to support the idea of a surface phenomenon was noted during this investigation. A few results were obtained using the 42-inch spheroid, such as the plot of Figure 4.27. This result is similar to that obtained with the smaller (28-inch) spheroid, and backscattered returns from both the spheroid and the cylinder were clearly observed at all measured positions. Nevertheless, because of the large size of this model and the close microphone spacing, the cylinder is completely hidden (in a geometrical sense) from the microphone for all spheroid positions behind the one at -3 inches. It is also completely hidden from the speaker for positions behind about -10 inches. The spheroid surface appears to direct both the incident and reflected fields into the respective shadow regions. Note that the reference level (0 dB) used in Figure 4.27 is the backscattering by a 14-inch cylinder instead of that by the 21-inch cylinder appropriate for



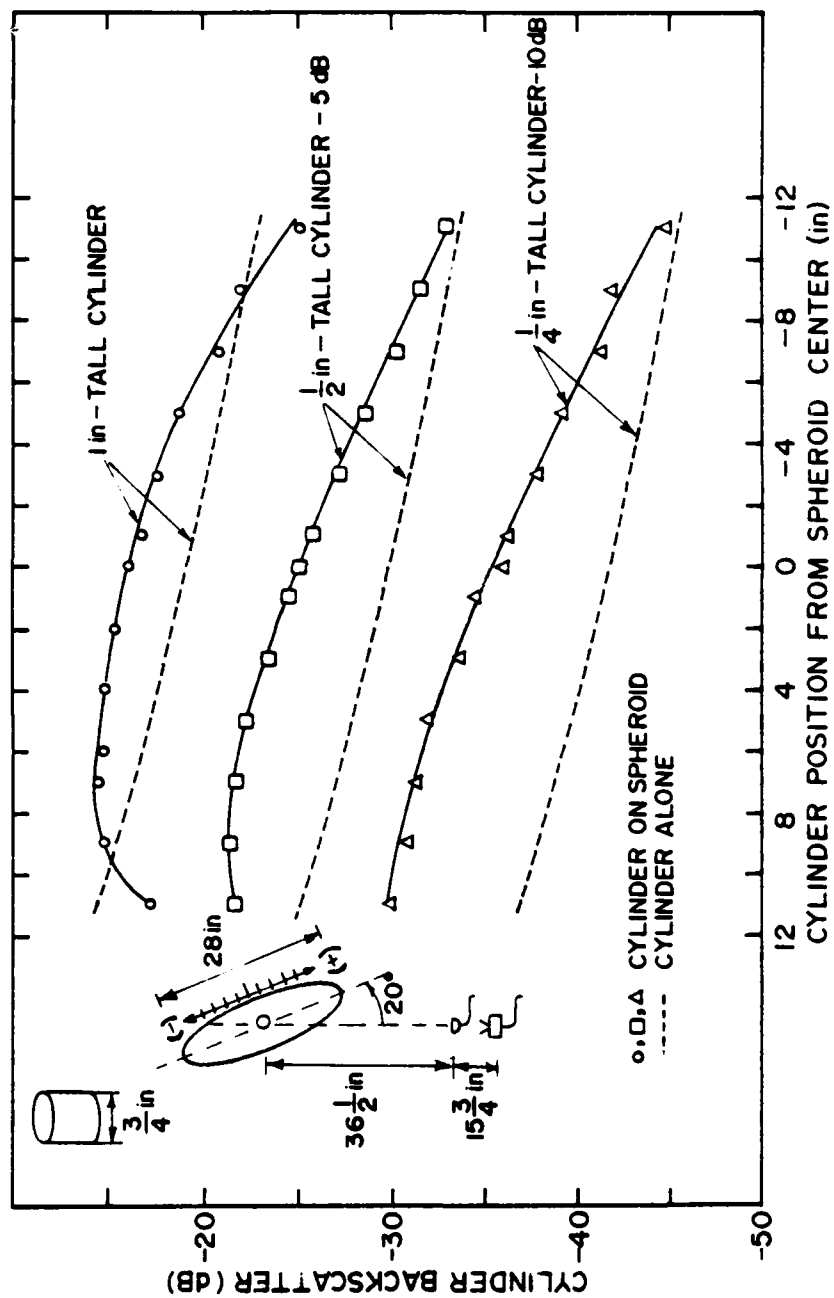


Figure 4.26 Backscatter from 3/4-inch-diameter cylinders along the top of the 28-inch prolate spheroid (20° incidence) compared to the backscatter from the cylinders suspended alone. ( $h\zeta_0 = 150$ ,  $\lambda = .6$  inch)

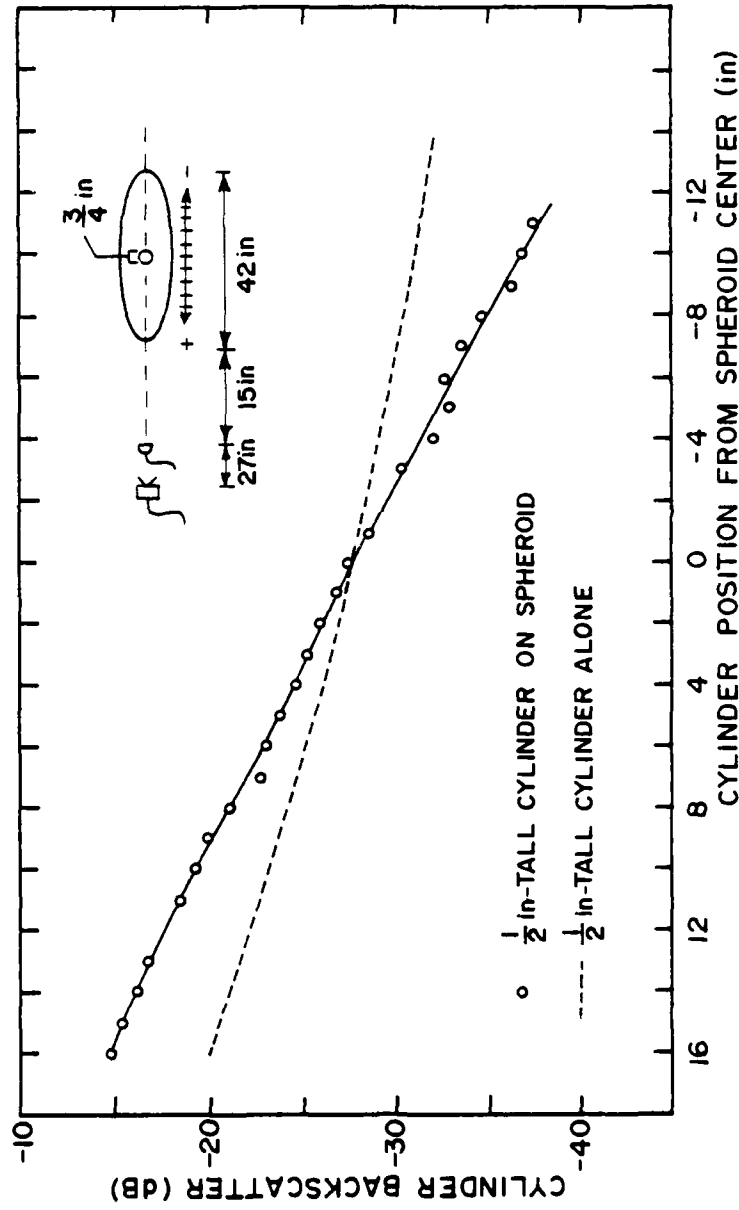


Figure 4.27 Backscatter from a 3/4-inch-diameter by 1/2-inch-tall cylinder along the top of the 42-inch prolate spheroid (axial incidence) compared to backscatter from the cylinder suspended alone. ( $h\epsilon_0 = 225$ ,  $\lambda = .6$  inch)

this spheroid; this reference was chosen to match the other results of this section. The configuration for the 28-inch spheroid was selected to insure that even the smallest cylinders were not hidden except at the most extreme rear positions on the spheroid.

#### 4.4.3 Effect of Spheroid Incidence Angle

Another parameter that might be expected to influence the scattering from obstructions on a spheroid is the incidence angle on the spheroid. Figure 4.28 shows the effect of this parameter on the backscatter from 3/4-inch-diameter ( $1.3\lambda$ ) cylinders with lengths of 1/4, 1/2, and 1 inch ( $.4\lambda$ ,  $.85\lambda$ ,  $1.7\lambda$ ) placed on top of the 28-inch prolate spheroid at its center. Just as was done in the previous section, the curves for the two smaller cylinders have been offset by 5 dB and 10 dB, respectively. An increase in the backscattered pressure over that of the freely suspended cylinders is noted for all the cylinders at axial incidence, and an even greater boost is noted as the incidence angle moves from axial incidence to about  $20^\circ$  incidence. At larger incidence angles, the level of the backscatter from the 1-inch cylinder on the spheroid dips toward the corresponding level of the freely suspended cylinder; the results from both shorter cylinders on the spheroid maintain the relative gain in level for angles as large as  $50^\circ$ . An identical trend is found in the corresponding data for the 1/4-inch-diameter ( $.4\lambda$ ) cylinders of Figure 4.29. All the curves in Figures 4.28 and 4.29 exhibit a noticeable dip (actually a smaller increase in level over that from the cylinder alone) at axial incidence, and the relative difference between the levels at  $0^\circ$  incidence and, for example, at  $20^\circ$

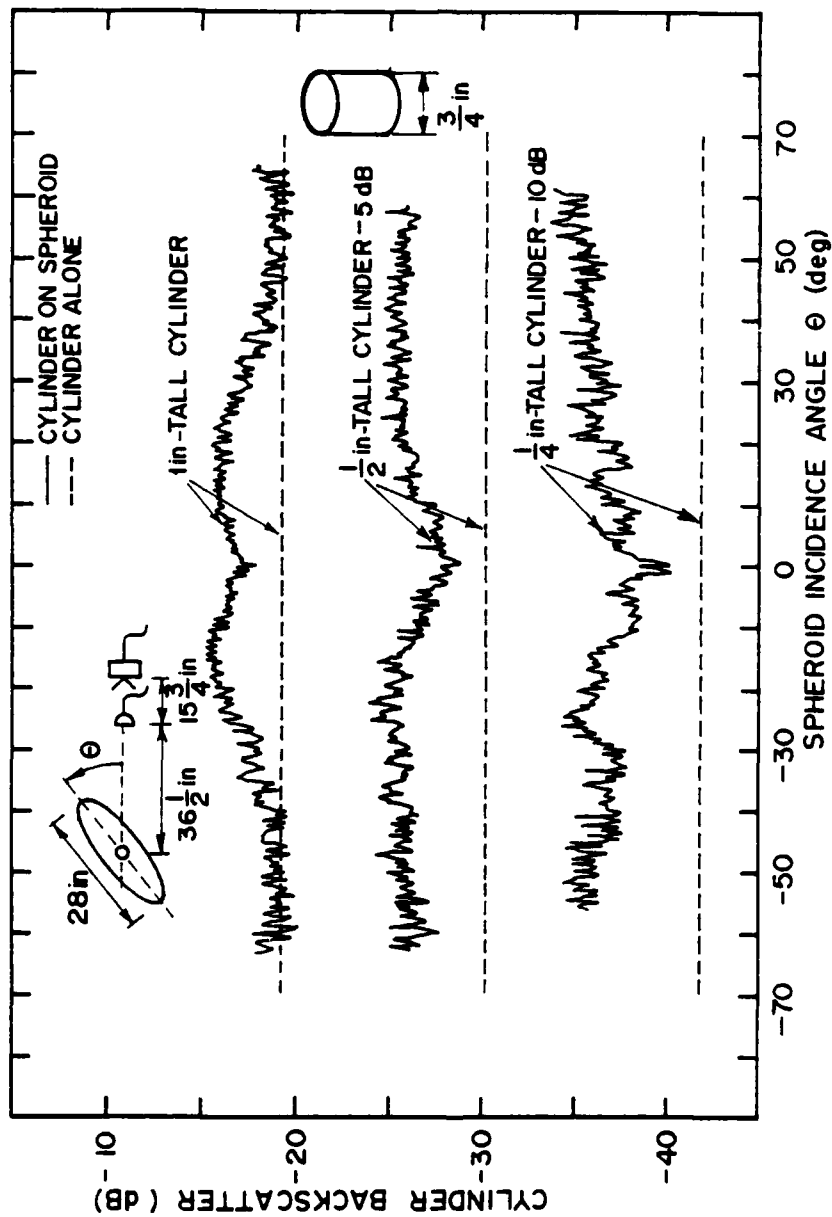


Figure 4.28 Backscatter from 3/4-inch-diameter cylinders centered on the 28-inch prolate spheroid versus spheroid incidence angle compared to backscatter from the cylinders suspended alone. ( $h\epsilon_0 = 150$ ,  $\lambda = .6$  inch)

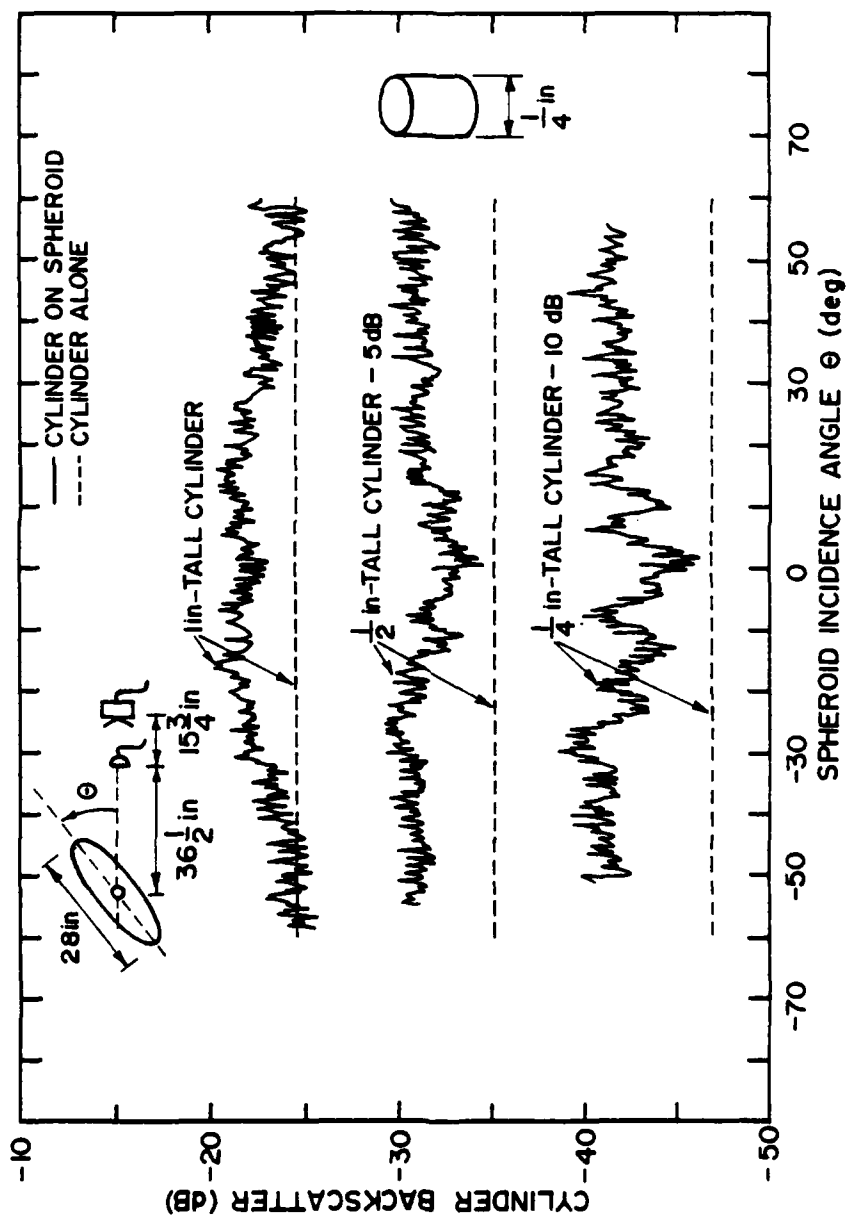


Figure 4.29 Backscatter from 1/4-inch-diameter cylinders centered on the 28-inch prolate spheroid versus spheroid incidence angle compared to backscatter from the cylinders suspended alone. ( $h\xi_0 = 150$ ,  $\lambda = .6$  inch)

incidence appears to increase as the length of the cylinder decreases. This may be caused by a damping effect at axial incidence that works against the baffling effect but adheres more closely to the spheroid surface.

The situation changes when the cylinder is moved closer to the front of the spheroid, as is illustrated in Figures 4.30 and 4.31. In these cases, little or no dip is noted in the level of the backscatter from the cylinders on the spheroid at axial incidence. The relative difference between the levels for cylinders on and off the spheroid is about equal to the maximum difference attained for cylinders at the spheroid center (Figures 4.28 and 4.29) over a wide range of spheroid incidence angles. Again, this difference tends toward zero at angles of about  $10^\circ$  or larger with the 1-inch-tall cylinder only. On the contrary, the dip in the level of backscattering noted in the previous example at axial incidence is exaggerated when the cylinder is moved closer to the rear of the spheroid (see Figures 4.32 and 4.33). In fact, the backscatter at axial incidence is now less than that for the freely suspended cylinders. At other angles, a substantial increase in the level is noted for all but the 1-inch-tall cylinder. There are some differences in this case between the data for the 3/4-inch-diameter cylinders (Figure 4.32) and the data for the 1/4-inch-diameter cylinders (Figure 4.33). However, these differences are small and may be partially caused by the poor signal-to-noise ratio experienced in this case with the smaller cylinders.

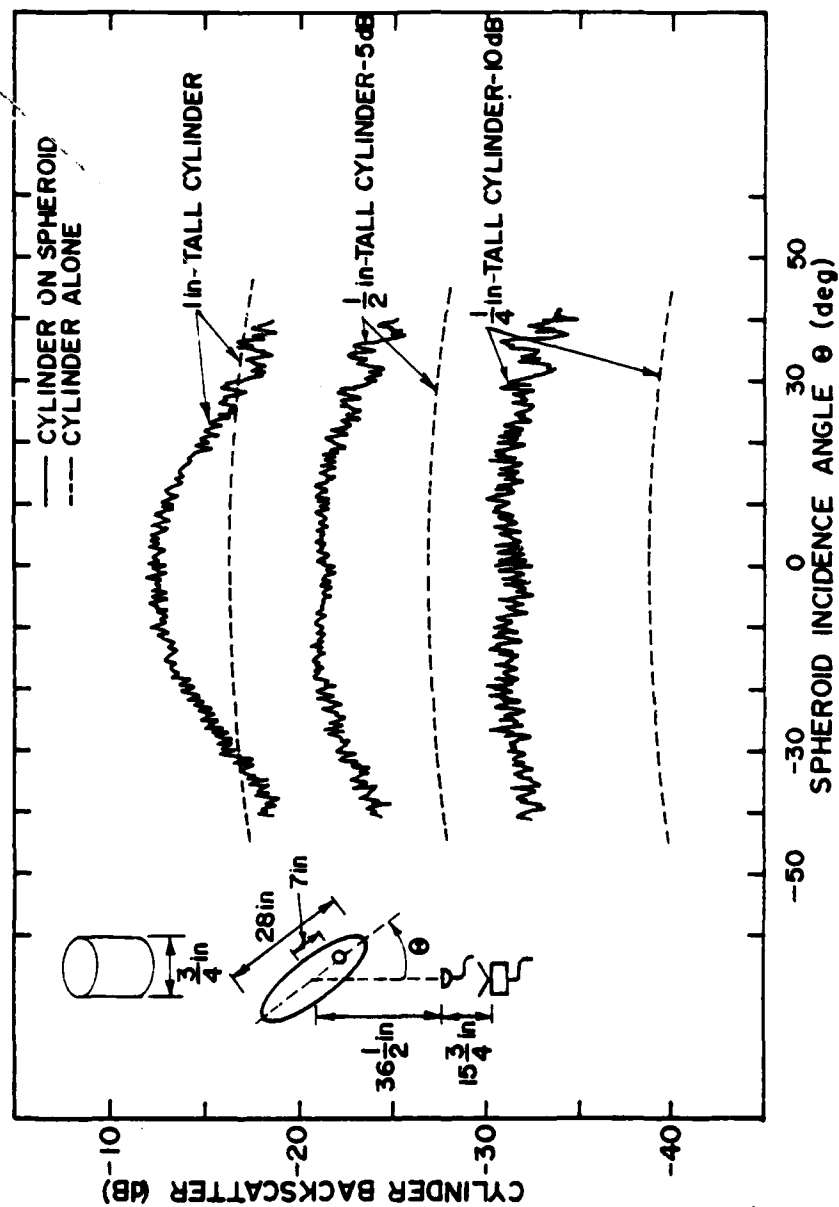


Figure 4.30 Backscatter from 3/4-inch-diameter cylinders on the 28-inch prolate spheroid 7 inches forward of center versus spheroid incidence angle compared to backscatter from the cylinders suspended alone. ( $h\xi_0 = 150$ ,  $\lambda = .6$  inch)

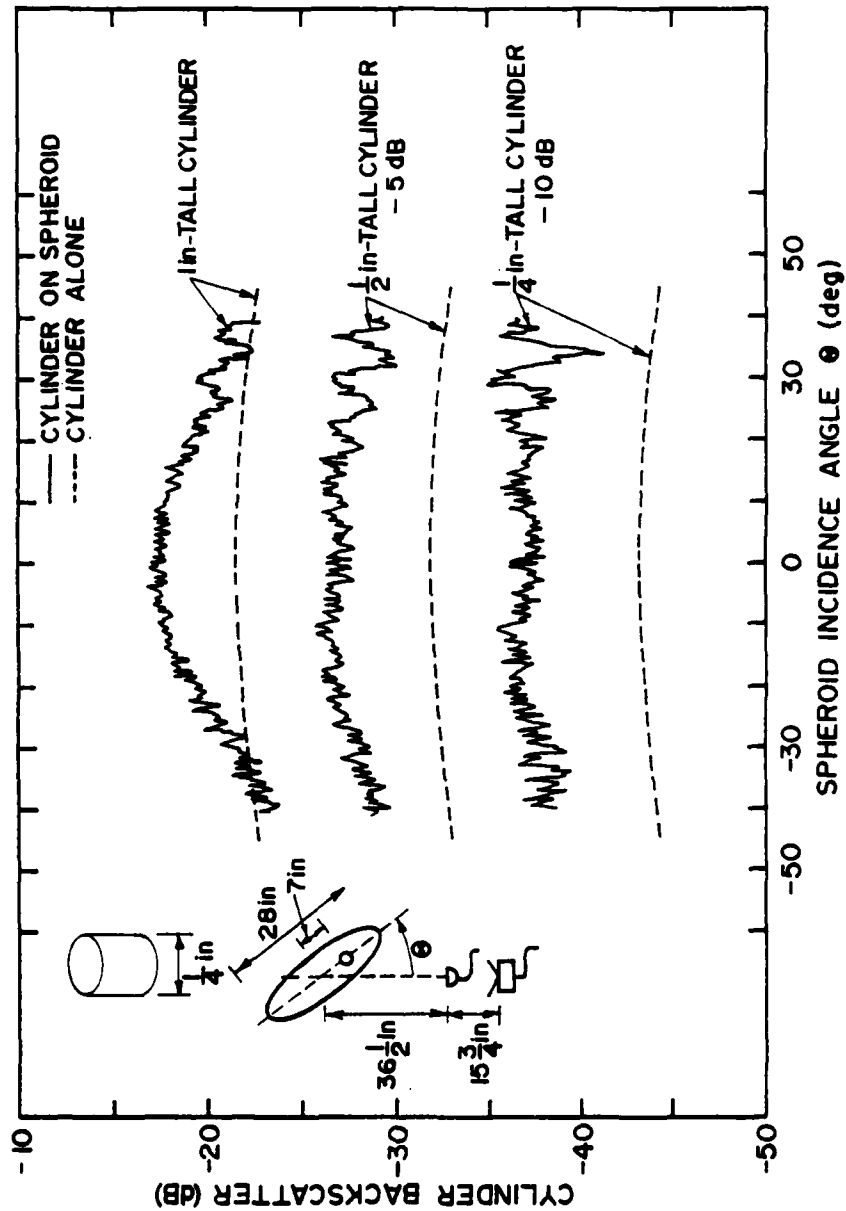


Figure 4.31 Backscatter from 1/4-inch-diameter cylinders on the 28-inch prolate spheroid 7 inches forward of center versus spheroid incidence angle compared to the backscatter from the cylinders suspended alone. ( $h\epsilon_0 = 150$ ,  $\lambda = .6$  inch)



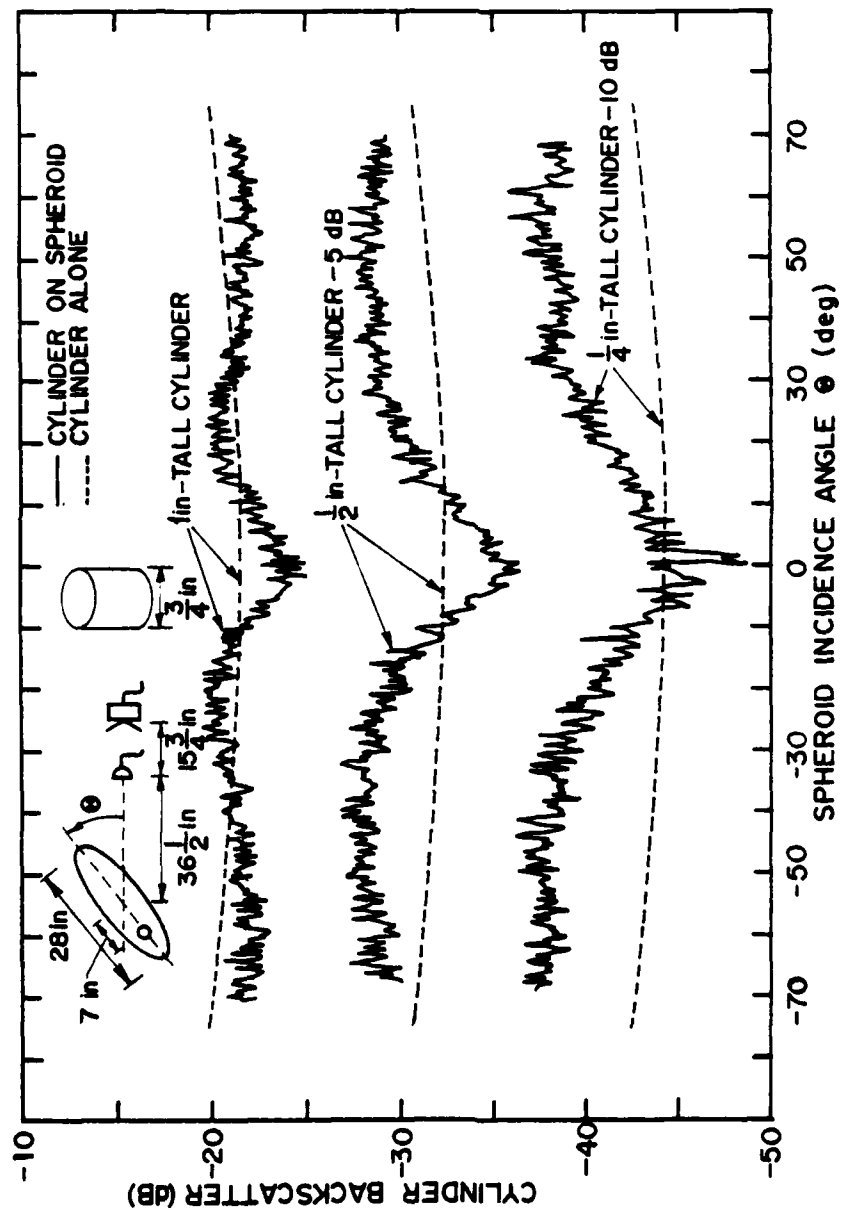


Figure 4.32 Backscatter from 3/4-inch-diameter cylinders on the 28-inch prolate spheroid 7 inches back of center versus spheroid incidence angle compared to the backscatter from the cylinders suspended alone. ( $h\xi_0 = 150$ ,  $\lambda = .6$  inch)

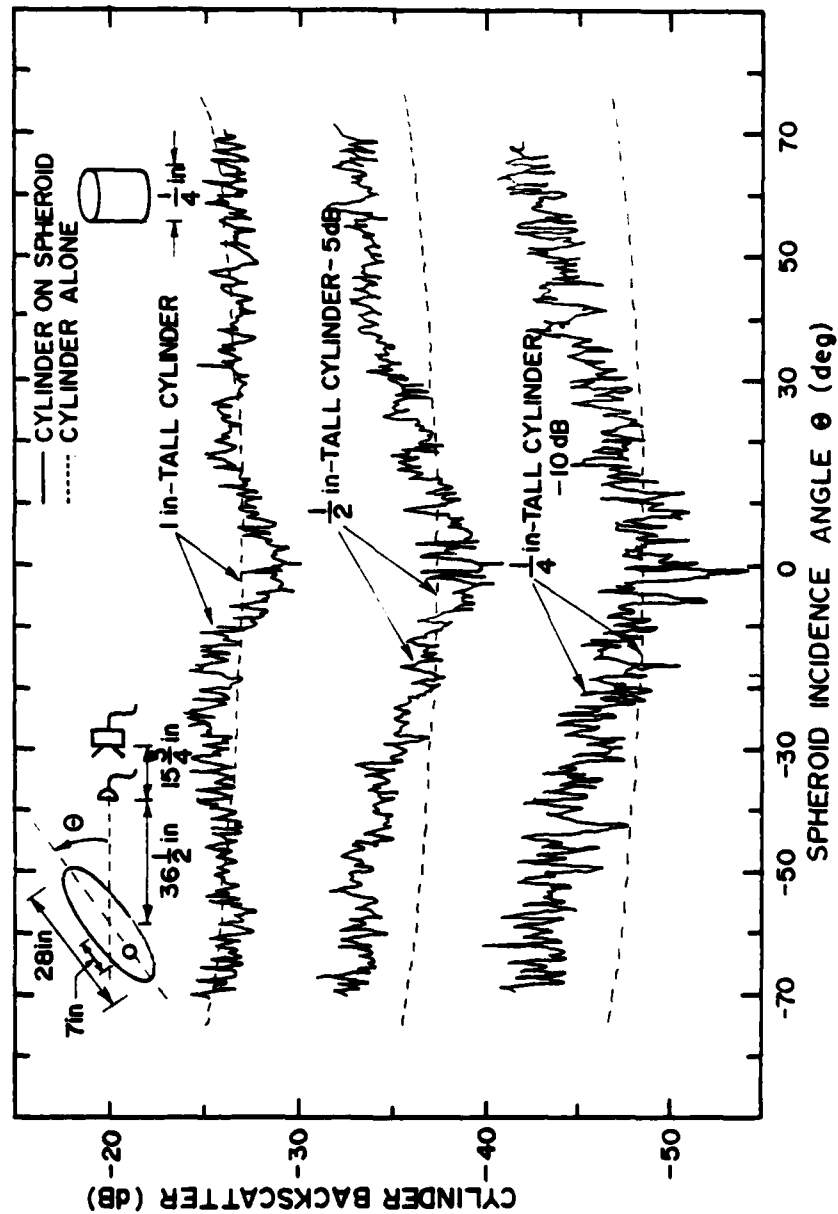


Figure 4:33 Backscatter from 1/4-inch-diameter cylinders on the 28-inch prolate spheroid 7 inches back of center versus spheroid incidence angle compared to the backscatter from the cylinders suspended alone. ( $h\epsilon_0 = 150$ ,  $\lambda = .6$  inch)

#### 4.4.4 Effect of Spheroid on Cylinder Bistatic Scattering

The final variable investigated in this study of cylinders on spheroids is the change in the bistatic scattering pattern. Figure 4.34 shows the results obtained from three of the 3/4-inch-diameter ( $1.3\lambda$ ) cylinders, and Figure 4.35 shows the results from the corresponding 1/4-inch-diameter ( $.4\lambda$ ) cylinders. In both cases, the sound field is incident axially on the spheroid, and the cylinders are on top of the spheroid at its center. The scattering from the freely suspended cylinders is uniform over the entire angular range, as would be expected from the circular symmetry in the measurement plane. The scattering from the cylinders on the spheroid is slightly larger, not only for backscatter, but over most of the angular range. Note that a small dip is indicated in the backscatter direction ( $0^\circ$ ). In general, the uniform increase in scattering by the cylinders with the spheroid present supports the idea of an increased incident-pressure level near the surface of the spheroid. The effective increase in level exhibited by the tallest (1-inch) cylinder is diminished at angles greater than about  $30^\circ$ . Finally, the results for both 3/4-inch- and 1/4-inch-diameter cylinders are largely the same, just as was found in Section 4.4.3.

Similar effects are noted for the bistatic scattering from cylinders on a spheroid at other incidence angles. Figure 4.36 presents results for three 3/4-inch-diameter cylinders on a spheroid at  $20^\circ$  incidence, and Figure 4.37 gives similar results for  $45^\circ$  incidence on the spheroid. The increase in the cylinder scattering provided by the spheroid in both of these cases is somewhat larger than that noted in the previous paragraph at axial incidence. In addition, the dip in the

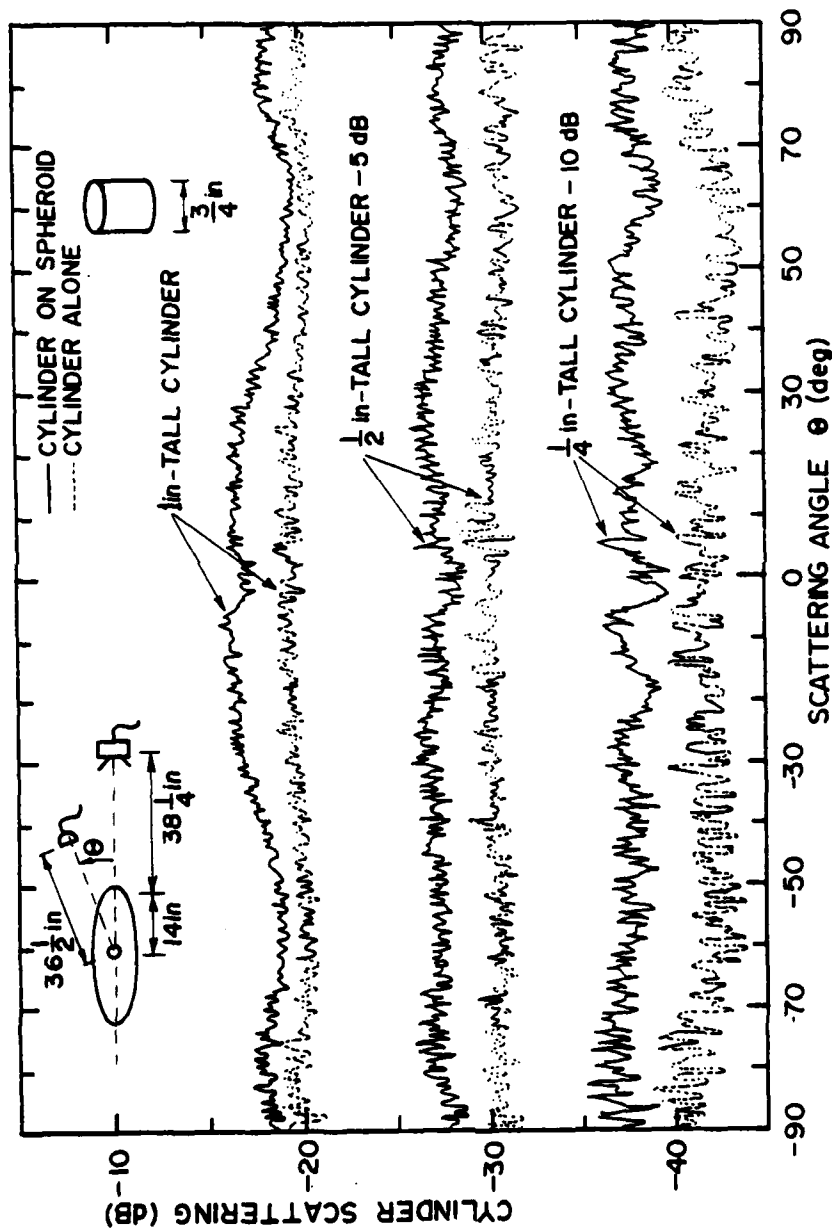


Figure 4.34 Bistatic scattering from 3/4-inch-diameter cylinders centered on top of the 28-inch spheroid (axial incidence) compared to that from the cylinders alone. ( $h\epsilon_0 = 150$ ,  $\lambda = .6$  inch)

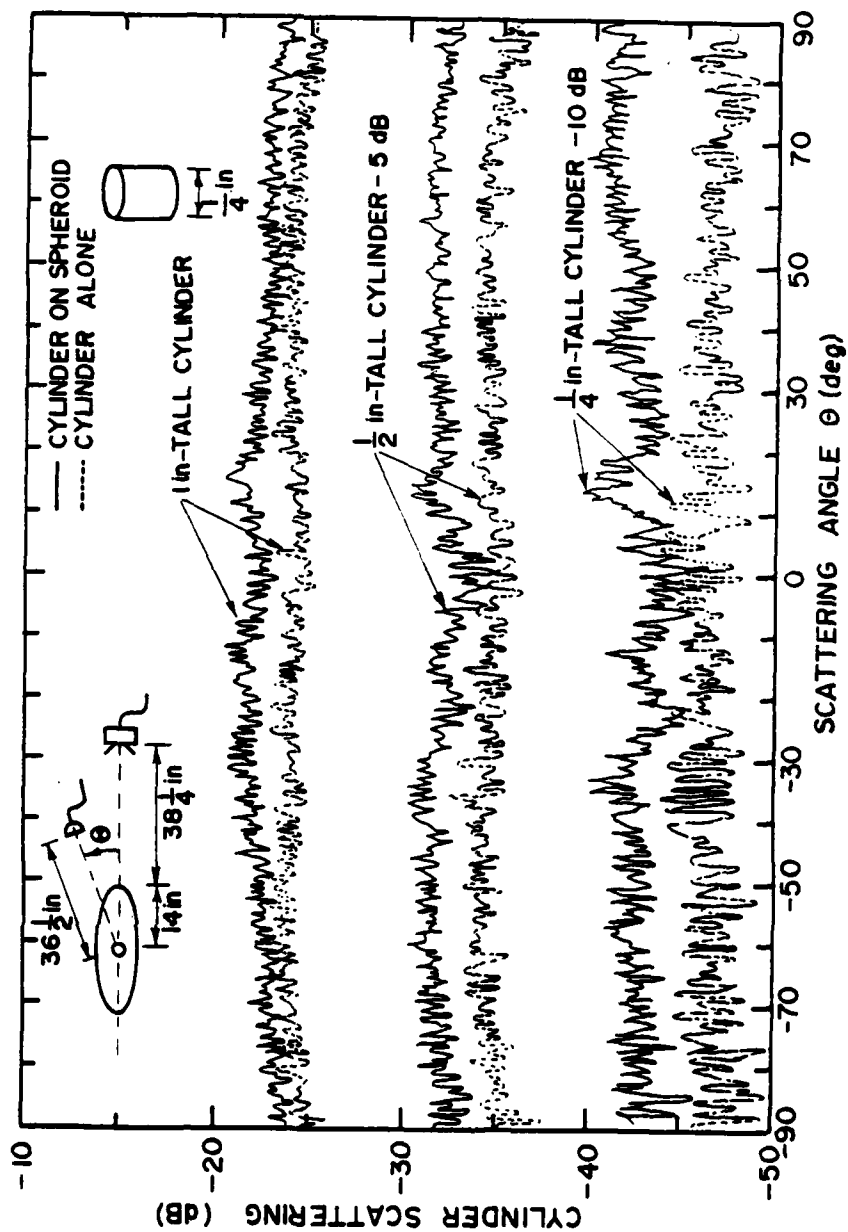


Figure 4.35 Bistatic scattering from 1/4-inch-diameter cylinders centered on top of the 28-inch prolate spheroid (axial incidence) compared to that from the cylinders alone. ( $h\xi_0 = 150$ ,  $\lambda = .6$  inch)

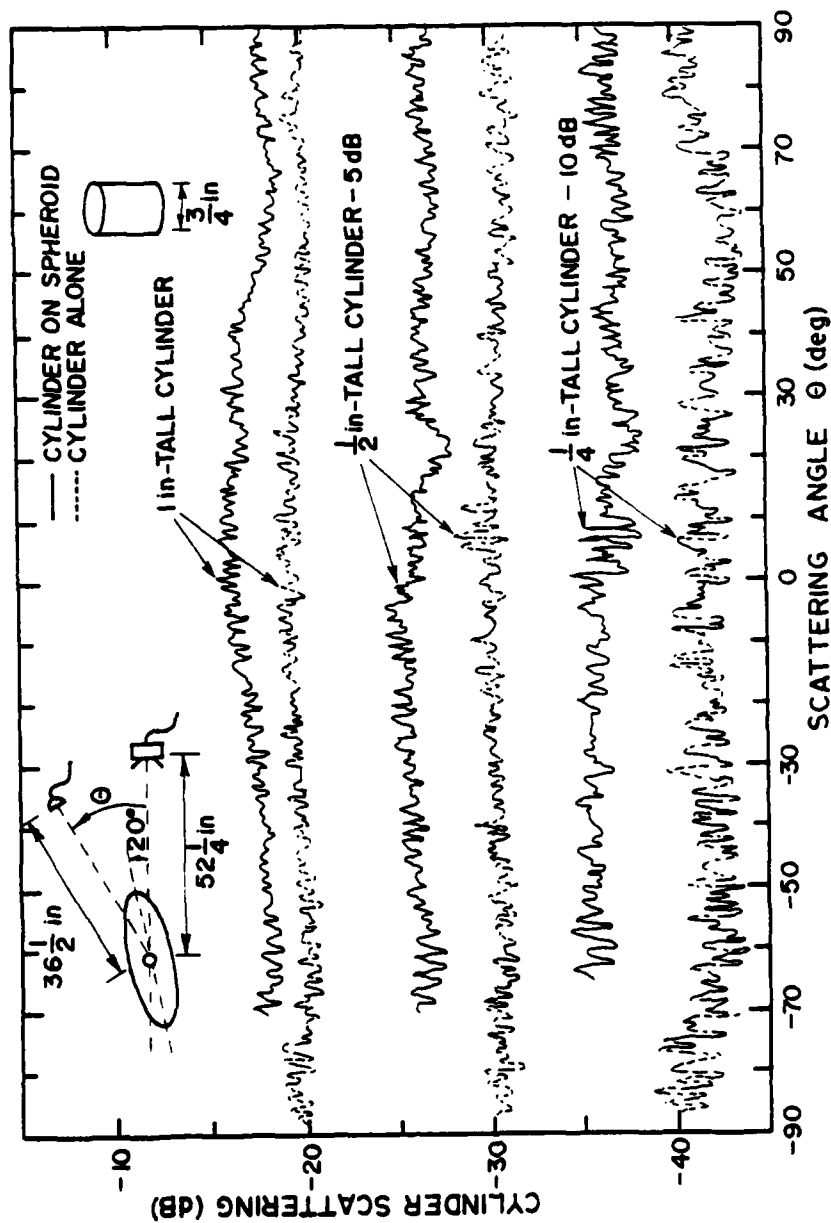


Figure 4.36 Bistatic scattering from 3/4-inch-diameter cylinders centered on top of the 28-inch prolate spheroid ( $20^\circ$  incidence) compared to that from the cylinders alone. ( $h_{c_0} = 150$ ,  $\lambda = .6$  inch)

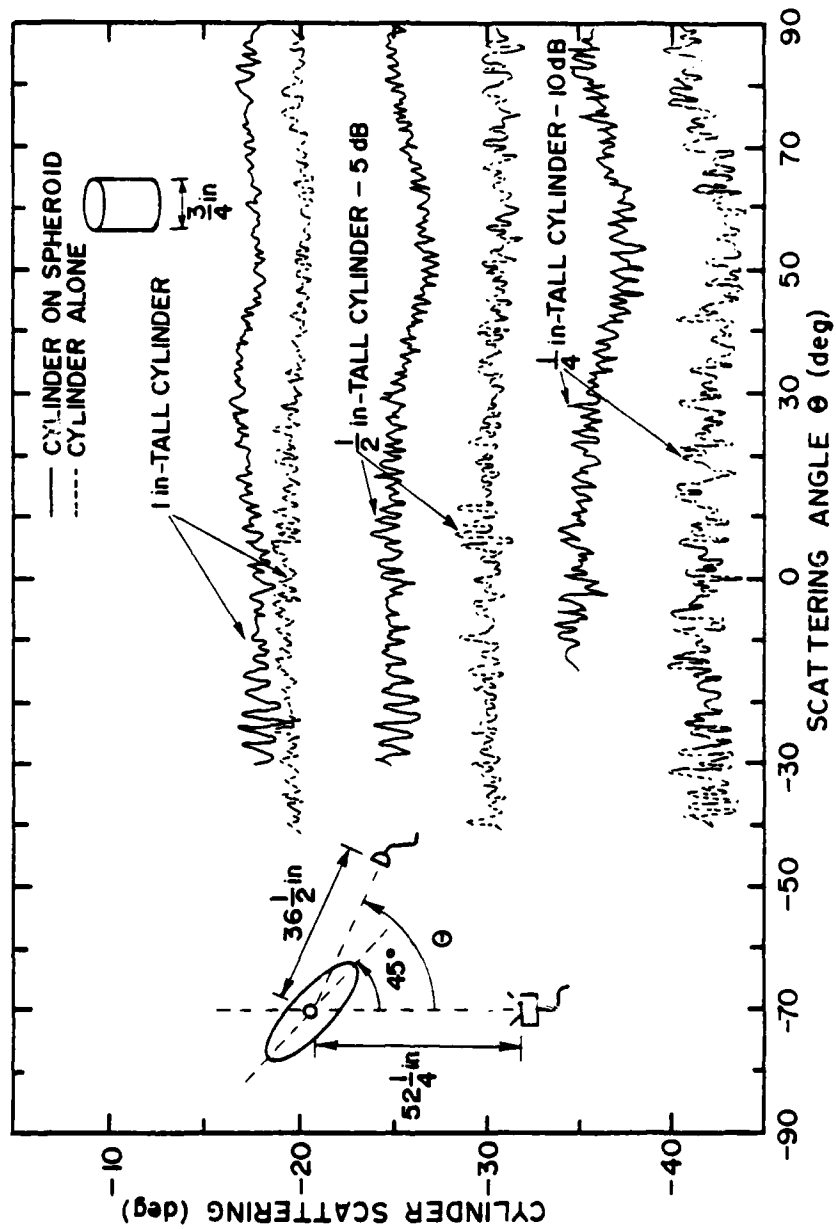


Figure 4.37 Bistatic scattering from 3/4-inch-diameter cylinders centered on top of the 28-inch prolate spheroid (45° incidence) compared to that from the cylinders alone. ( $h\epsilon_0 = 150$ ,  $\lambda = .6$  inch)

curve has moved to approximately the angular position of the spheroid axis (i.e.,  $20^\circ$  or  $45^\circ$ ). This last observation indicates that the physical phenomenon that causes the dip takes effect after the pulse is reflected by the cylinder.

#### 4.4.5 Effect of Hole in Surface of Spheroid

When the investigation of cylinder obstructions on a prolate spheroid was first performed, a significant amount of unplanned effort went into the study of a 3/4-inch-diameter hole at the center of the spheroid along the top. This hole served originally as part of the support for the spheroid model. Because it had no significant effect on the backscatter (see Section 4.3.1), the hole was left open for many of the early experiments. The cylinder obstruction tests, however, showed that the hole has a significant effect on the surface field in its neighborhood.

Figure 4.38 is a sample of the results obtained for backscatter from cylinders (3/4-inch in diameter) at positions along the top of a prolate spheroid, both with and without the hole at the center of the spheroid. The hole has very little effect on the data for the 1-inch-tall cylinder. However, for both shorter cylinders, a significant dip appears in the curve at a position just behind the hole; at positions even further behind the hole, the curve returns approximately to the level observed without the hole (see Figure 4.23). When smaller diameter cylinders are used, the effect is even more dramatic, as Figure 4.39 shows for 1/4-inch-diameter cylinders. In this last case, the dip is present even with the 1-inch-tall cylinder, and it exists over a



AD-A084 937

PENNSYLVANIA STATE UNIV UNIVERSITY PARK APPLIED RESE--ETC F/O 20/1  
AN EXPERIMENTAL ANALYSIS OF THE BASIC PHENOMENA INVOLVED IN MOO--ETC(U)  
JAN 80 M S LANG  
N00024-79-C-6043  
ARL/PSU/TH-80-43

UNCLASSIFIED

NL

31-5

AD  
ADDRESS





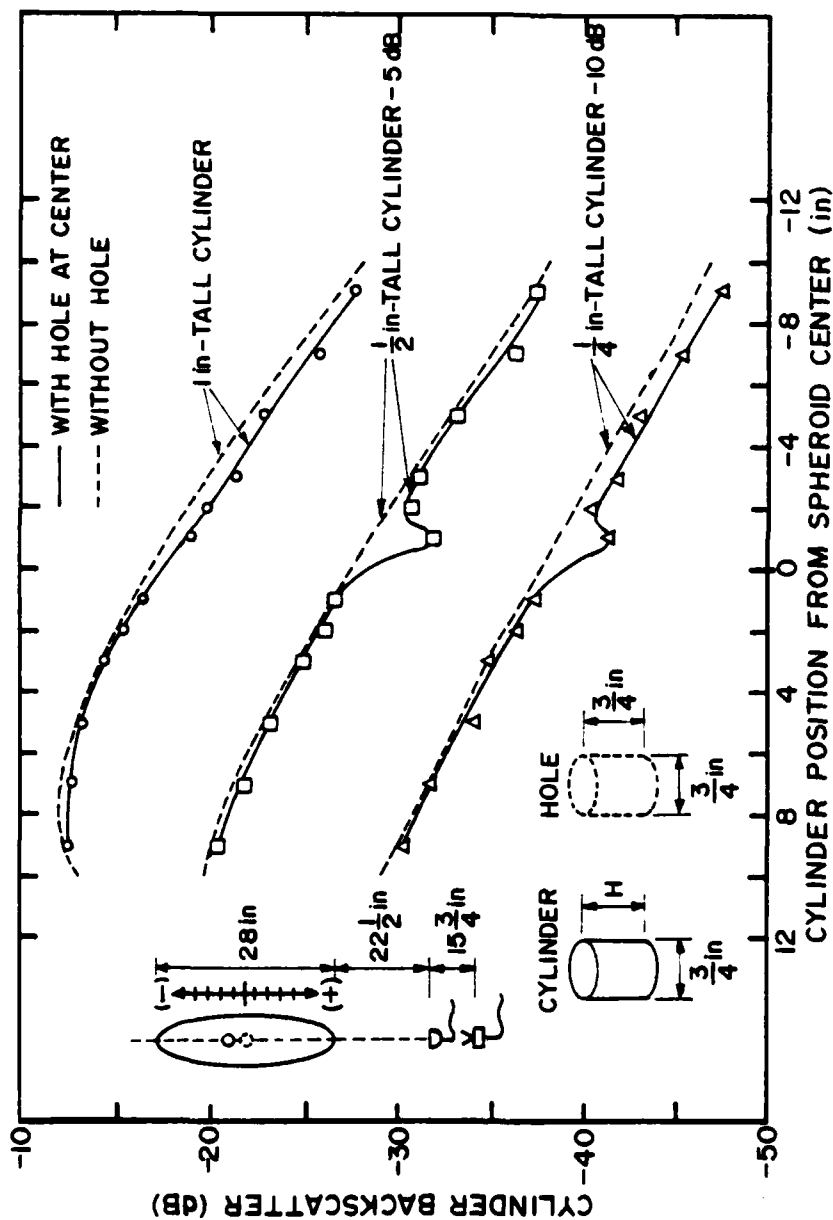


Figure 4.38 Backscatter from 3/4-inch-diameter cylinders along the top of the 28-inch prolate spheroid (axial incidence) with a hole at its center compared to the same case without the spheroid hole. ( $h\xi_0 \approx 150$ ,  $\lambda = .6$  inch)

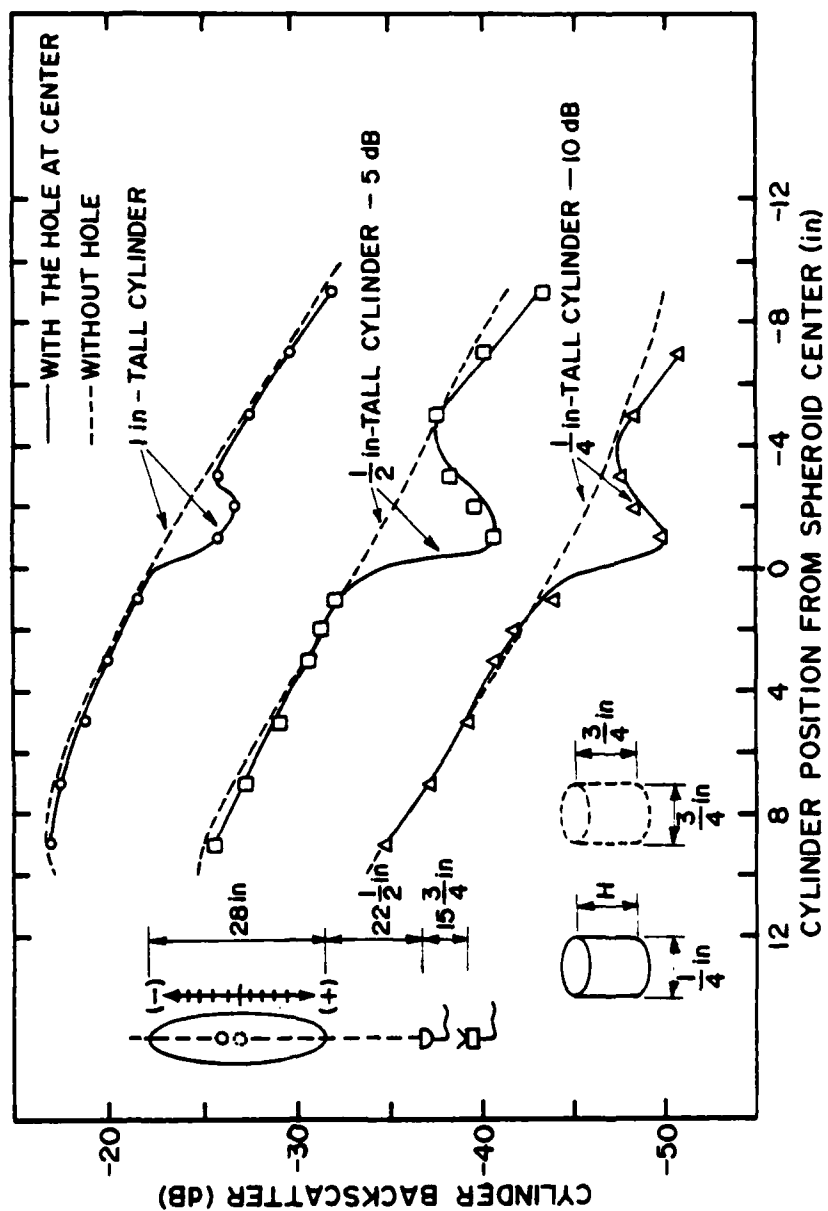


Figure 4.39 Backscatter from 1/4-inch-diameter cylinders along the top of the 28-inch prolate spheroid (axial incidence) with a hole at its center compared to the same case without the spheroid hole. ( $h/\xi_0 = 150$ ,  $\lambda = .6$  inch)

larger range of cylinder positions than was observed with 3/4-inch-diameter cylinders.

The effect of the hole is not fully understood. The strong dependence on cylinder diameter may indicate that the width of the hole's influence is fairly narrow along the surface of the spheroid. There is also evidence that a resonance phenomenon is involved. For example, Figure 4.39 indicates that the hole exerts its strongest influence with a 1/2-inch-tall cylinder. Also, Figure 4.40 shows that the depth of the hole must be considered. Despite these indications, no definitive relationship could be found between the dimensions of the hole and a simple numerical factor of a wavelength. Plots of cylinder backscatter at various spheroid incidence angles (Figures 4.41 and 4.42) show that the influence of the hole is apparently limited to axial or near-axial incidence. The hole's effect is definitely localized in the nearfield, at which the pressure distribution is known to take on complex forms. Unfortunately, this effect must apparently be considered even when evaluating the farfield results if there is an obstruction or other feature of the model near the hole.

#### 4.5 Bistatic Scattering from Prolate Spheroids

Although this investigation focused on the backscattering at spheroids and spheroids with projections, it is sometimes useful, at least in an intuitive sense, to examine the field scattered in other directions. The spheroid is interesting in this respect because its backscatter varies significantly with the aspect angle. In addition, the backscattered returns are known to be highly collimated in some

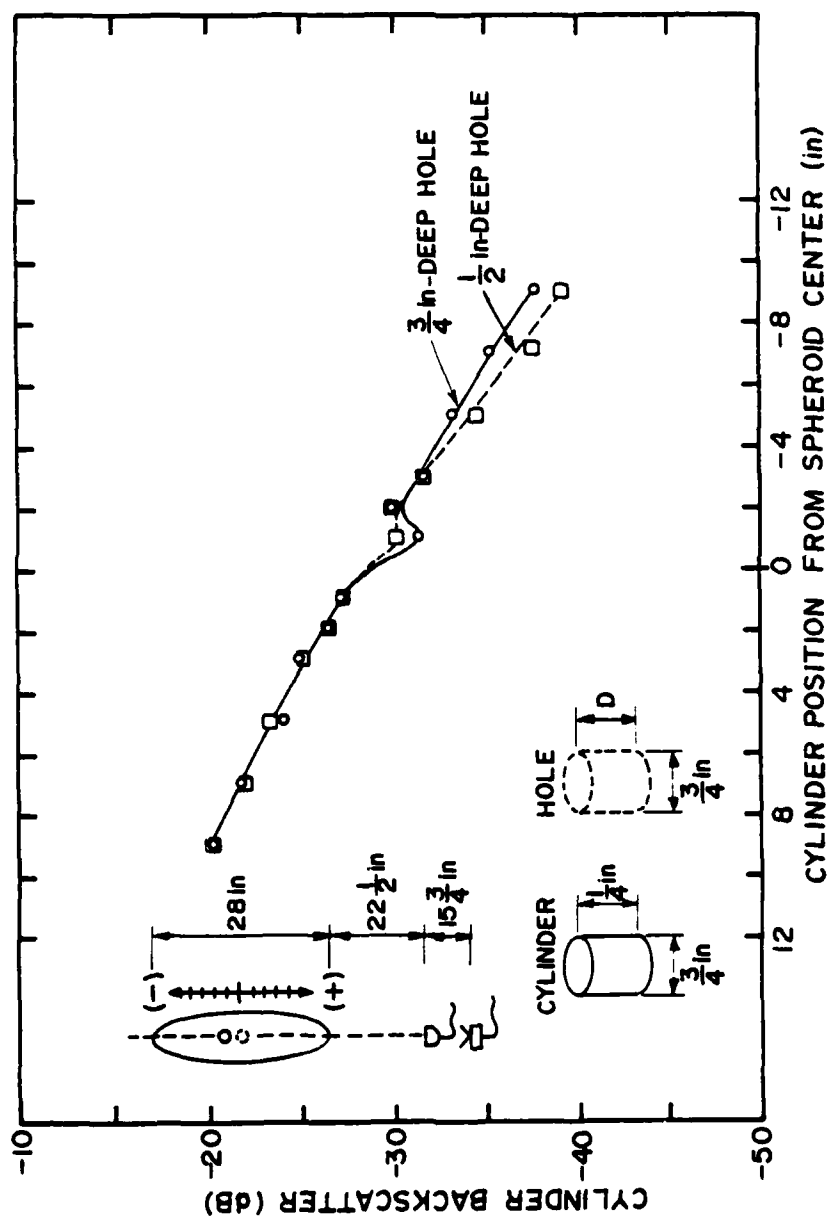


Figure 4.40 Backscatter from a cylinder along the top of the 28-inch prolate spheroid (axial incidence) with both 1/2-inch- and 3/4-inch-deep holes at its center. ( $h\xi_0 = 150$ ,  $\lambda = .6$  inch)

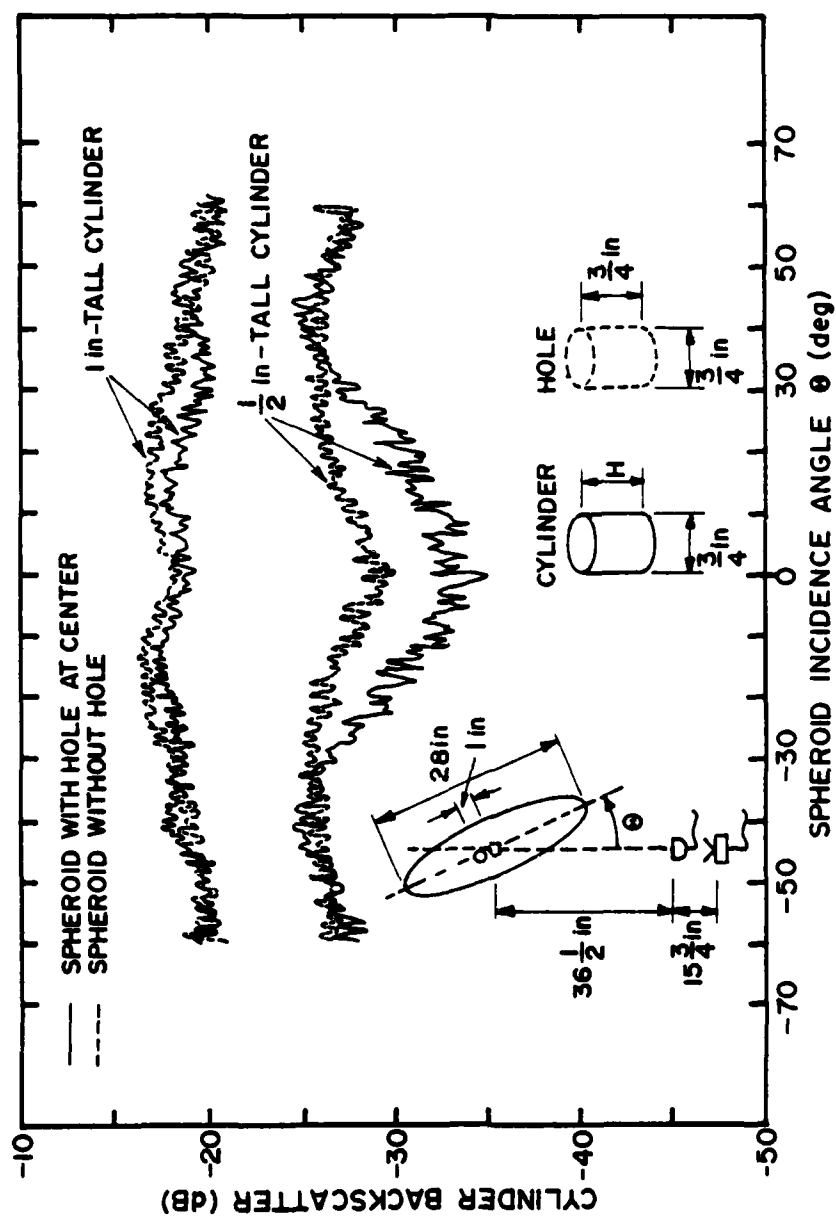


Figure 4.41 Backscatter at various spheroid incidence angles from 3/4-inch-diameter cylinders on the 28-inch prolate spheroid just behind the center, both with and without a hole at the spheroid's center. ( $h\epsilon_0 = 150$ ,  $\lambda = .6$  inch)

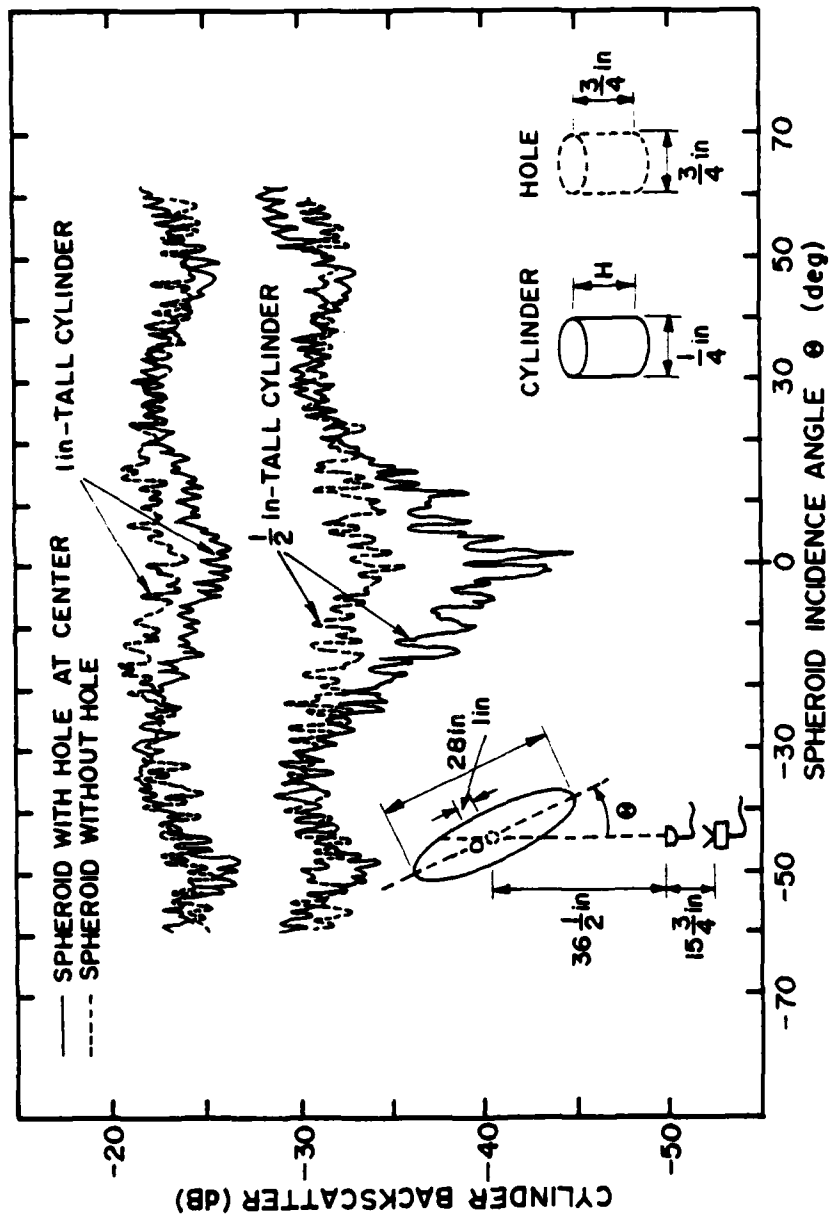


Figure 4.42 Backscatter at various spheroid incidence angles from 1/4-inch-diameter cylinders on the 28-inch prolate spheroid just behind the center, both with and without a hole at the spheroid's center. ( $h\xi_0 = 150$ ,  $\lambda = .6$  inch)



directions. The observation of these phenomena provided the impetus for a brief study of the bistatic scattering from a spheroid in a plane containing the spheroid axis, the receiver, and the source. In all cases, only a specular-type of echo return was observed. Note that the origin of the scattering angle in the plots is the direction of the backscatter, as opposed to the more common forward-scattering reference.

Figure 4.43 presents the results of the bistatic scattering by a spheroid at axial incidence. Except for some variation near  $0^\circ$ , the pattern has the uniform shape expected from a sphere. This is not unusual because the spheroid surface at the tip has two equal principal radii of curvature just like a sphere. However, the similarity is evident for fairly large angles. The variation near  $0^\circ$  is similar to the corresponding backscattering data obtained with this same spheroid model (see Figure 4.12); thus, it may be caused by slight imperfections in the model itself.

Figure 4.44 gives the bistatic scattering results for the opposite extreme of broadside incidence. The pattern consists of a single broad lobe. This pattern is somewhat unusual because the model is over 80 wavelengths long. A flat radiator with this large extent would have a much narrower center lobe. Despite the large eccentricity, however, the prolate spheroid still possesses much of the same circular symmetry as its near cousin, the sphere. In addition, the spheroid has no abrupt edges like those found on a flat radiator.

Figures 4.45, 4.46, and 4.47 complete the picture by showing the bistatic scattering from the spheroid at every  $10^\circ$  increment between the extremes of axial and broadside incidence. There are no surprises in

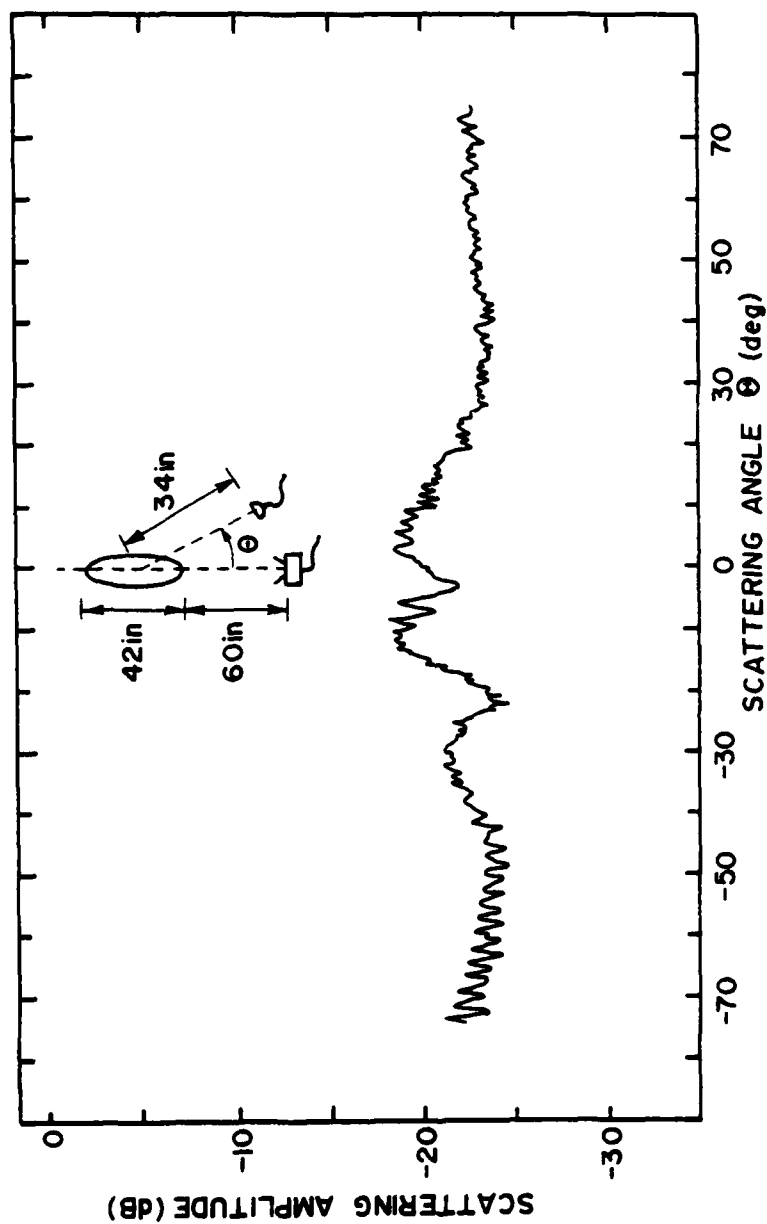


Figure 4.43 Bistatic scattering from a prolate spheroid at axial incidence. ( $h\xi_0 = 166$ ,  $\lambda = 1/2$  inch)

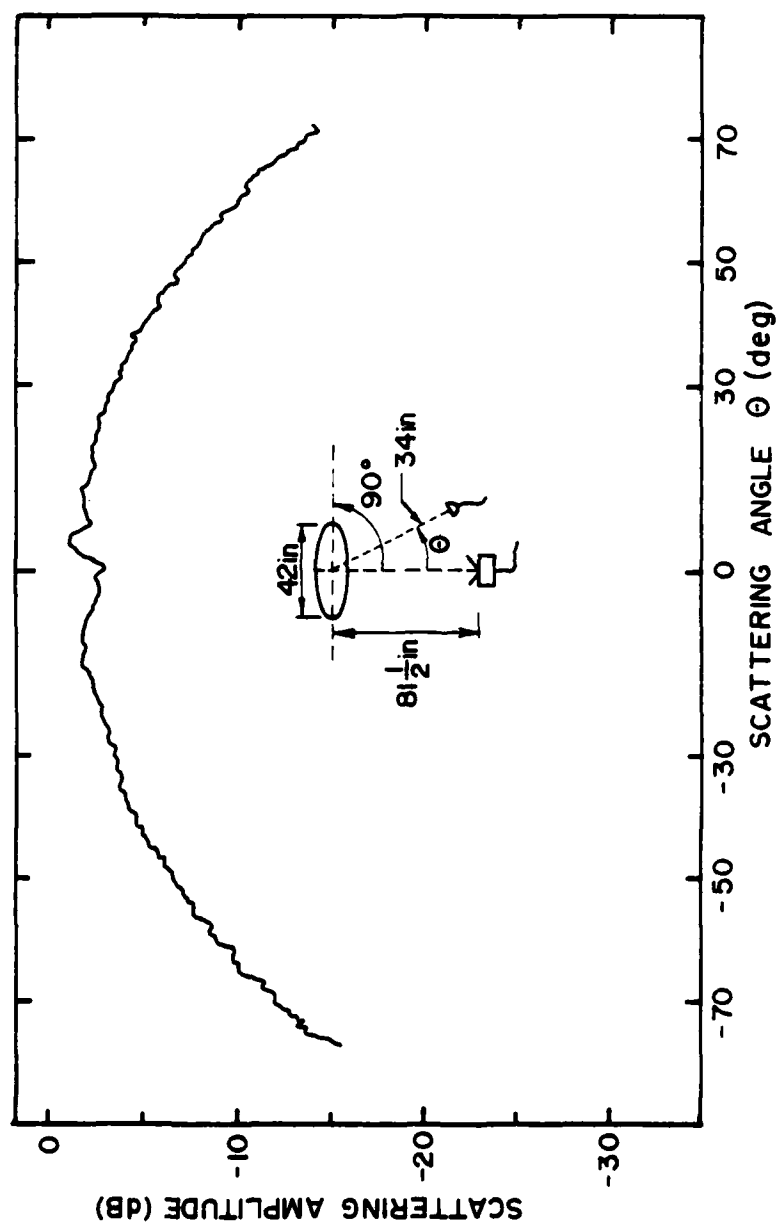


Figure 4.44 Bistatic scattering from a prolate spheroid at broadside incidence in the plane of its axis. ( $h\xi_0 = 166$ ,  $\lambda = 1/2$  inch)

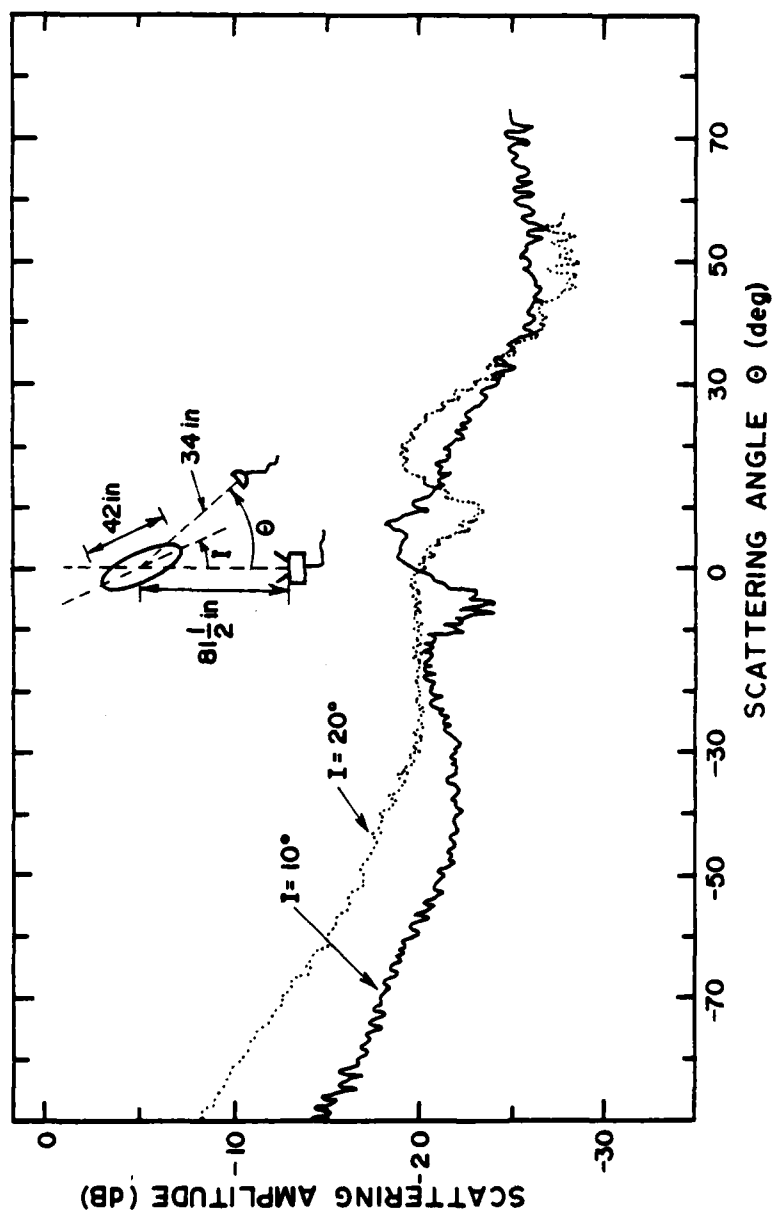


Figure 4.45 Bistatic scattering from a prolate spheroid at  $10^\circ$  and  $20^\circ$  incidence in the plane of its axis. ( $h\xi_0 = 166$ ,  $\lambda = 1/2$  inch)

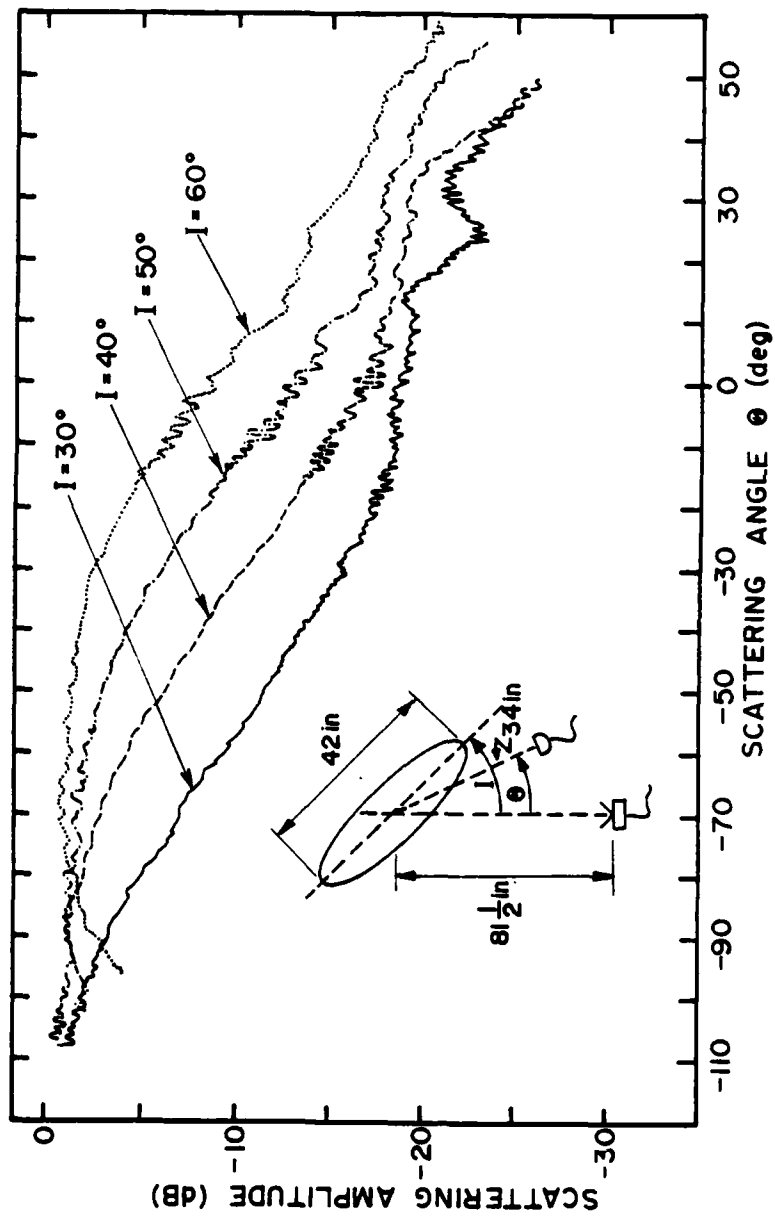


Figure 4.46 Bistatic scattering from a prolate spheroid at  $30^\circ$ ,  $40^\circ$ ,  $50^\circ$ , and  $60^\circ$  incidence in the plane of its axis.  
( $h\epsilon_0 = 166$ ,  $\lambda = 1/2$  inch)

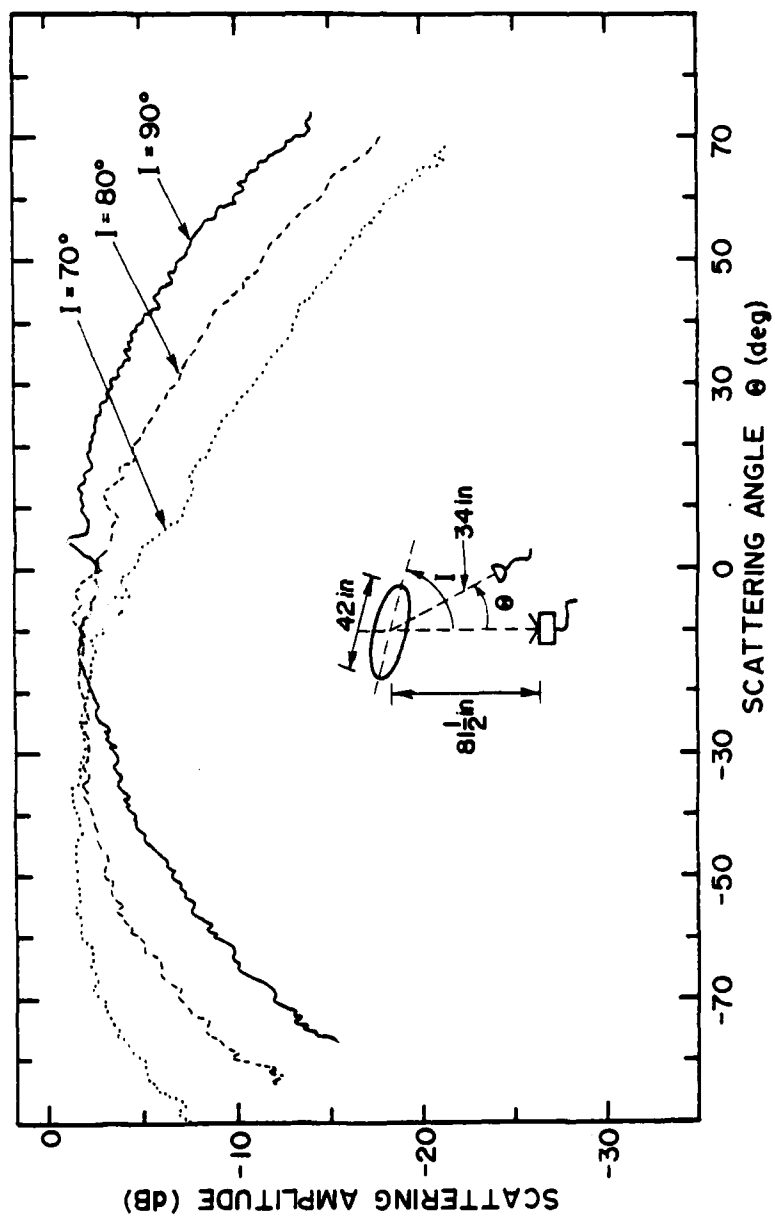


Figure 4.47 Bistatic scattering from a prolate spheroid at  $70^\circ$ ,  $80^\circ$ , and  $90^\circ$  incidence in the plane of its axis. ( $h_{\xi_0} = 166$ ,  $\lambda = 1/2$  inch)

these data. As the incidence angle is increased, the pressure scattered on the shadowed side of the spheroid decreases, while the broad lobe seen at broadside incidence appears at the position predicted by specular scattering considerations. The reason for the rapid shift in the backscatter from a spheroid (noted in Section 4.2.2) for the range of  $30^\circ - 60^\circ$  is seen in Figure 4.46. In this figure, the large lobe moves rapidly toward the  $0^\circ$  direction as the incidence angle approaches  $90^\circ$ . When interpreting these results, one should note that experimental considerations (mostly restricted space in the measurement chamber) limited the model-to-receiver separation. The simplicity of the effects observed at this close spacing, however, implies that the farfield results are not too much different. The lack of evidence of collimated returns is merely an indication that this effect is only observed in planes other than the one containing the spheroid axis.

#### 4.6 Creeping Waves

The only scattering phenomenon that has been observed with smooth bodies in the results described in previous sections is specular scattering. In particular, there has been no evidence of the Franz-type creeping waves that figure prominently in many theoretical formulations. Because of the importance of these creeping waves to diffraction theory and because of the controversy over their existence, a highly targeted effort was mounted to study these effects.

For the creeping-wave experiments, it was necessary to compute the predicted time and amplitude relationships of the creeping-wave return and then to manipulate the instrument configuration until an adequate

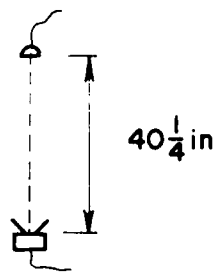
signal-to-noise ratio was obtained in that time window. This verification technique can, unfortunately, lead to self-fulfilling predictions while missing unexpected effects; but the possible difficulties were minimized as much as possible by using the knowledge of scattering effects reported in previous sections of this chapter. The results of the investigation generally support the concept of a scattering component that circumnavigates the surface of the scatterer. However, some of the observed occurrences are difficult to relate in terms of the properties customarily assigned to creeping waves (see, for example, Levy & Keller, 1959). In every case examined, the significance of the creeping-wave effects is small in comparison with other scattering phenomena.

Note that all the data values presented in this section were obtained by reading the height of the positive peak of the received pulses directly from an oscilloscope. Since slight changes in waveform, nearby returns, and background noise complicated this procedure, an error of 2 dB or more in the amplitude of the effects may be present at some points.

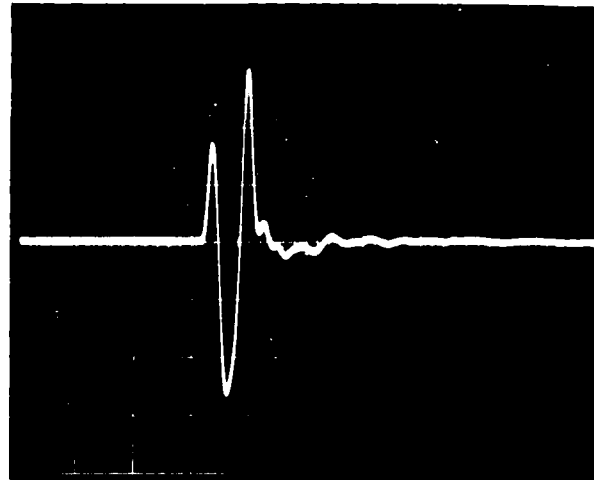
#### 4.6.1 Creeping Waves on Smooth Spheres and Spheroids

Figure 4.48 shows an oscilloscope trace of both the incident and backscattered pulses from a sphere at  $ka = 6$ . The waveform is limited to a single sine-wave cycle in order to isolate the different backscatter components in time. The specular return and a small (about 10% of the specular return) creeping-wave return about 400 microseconds later can be seen. Both the amplitude and time relationships between



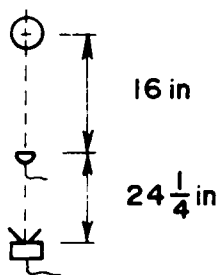


SCALE + 30 dB

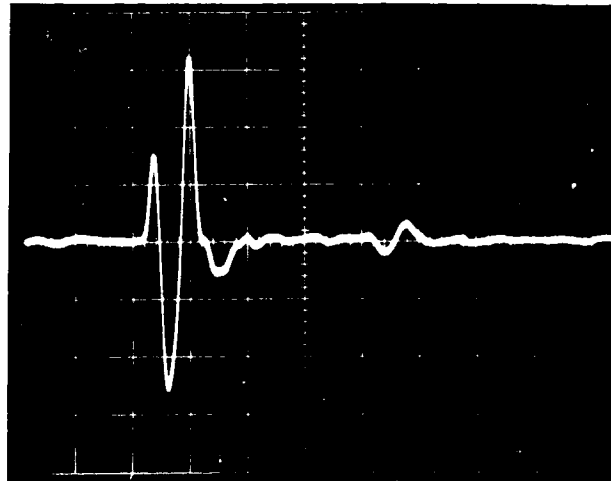


.1 msec/div. →

(a)



SCALE 0 dB



.1 msec/div. →

(b)

Figure 4.48 Oscilloscope trace of the backscattering from a sphere at  $ka = 6$ , including (a) the incident pulse at the sphere and (b) the specular and creeping-wave returns.

the two backscattered returns are consistent with predictions of the Keller theory if the creeping wave is assumed to travel at about 95% of the wave speed in air. Note, however, that the relative amplitude of the creeping-wave component is very small--so small that it adds only an insignificant contribution to the total backscattered field on a decibel scale. This relationship is also evident in Figure 4.49, which is a plot of the experimental backscattered returns from a sphere over a range of  $ka$ 's near 6. The data are normalized to the level incident at the center of the sphere with the sphere not present. As can be seen, the specular returns are about 30 dB below the incident pulse, and the creeping-wave returns are lower than the specular returns by 20 - 30 dB. Even though theory predicts that the creeping-wave returns will be somewhat larger for lower values of  $ka$ , their influence on backscattering appears to be minimal in practical situations.

Figure 4.50 presents results of the specular and creeping-wave returns from a sphere at other scattering angles. Data obtained at two different frequencies are shown, and the angle is measured from the forward direction. The focusing effect of the geometric caustic at  $180^\circ$  is clearly evident. Once again, however, the creeping-wave return is very small. Even at the forward scattering angle of  $80^\circ$ , at which the creeping wave presumably travels only a small distance on the sphere's surface, the creeping-wave term is still 10 dB below the specular term.

Creeping waves are predicted to play a major role in the scattering from thin prolate spheroids. Before moving to the thin spheroids of interest in this study, however, an examination was performed with a slightly eccentric 2:1 prolate spheroid. Figure 4.51 shows oscilloscope

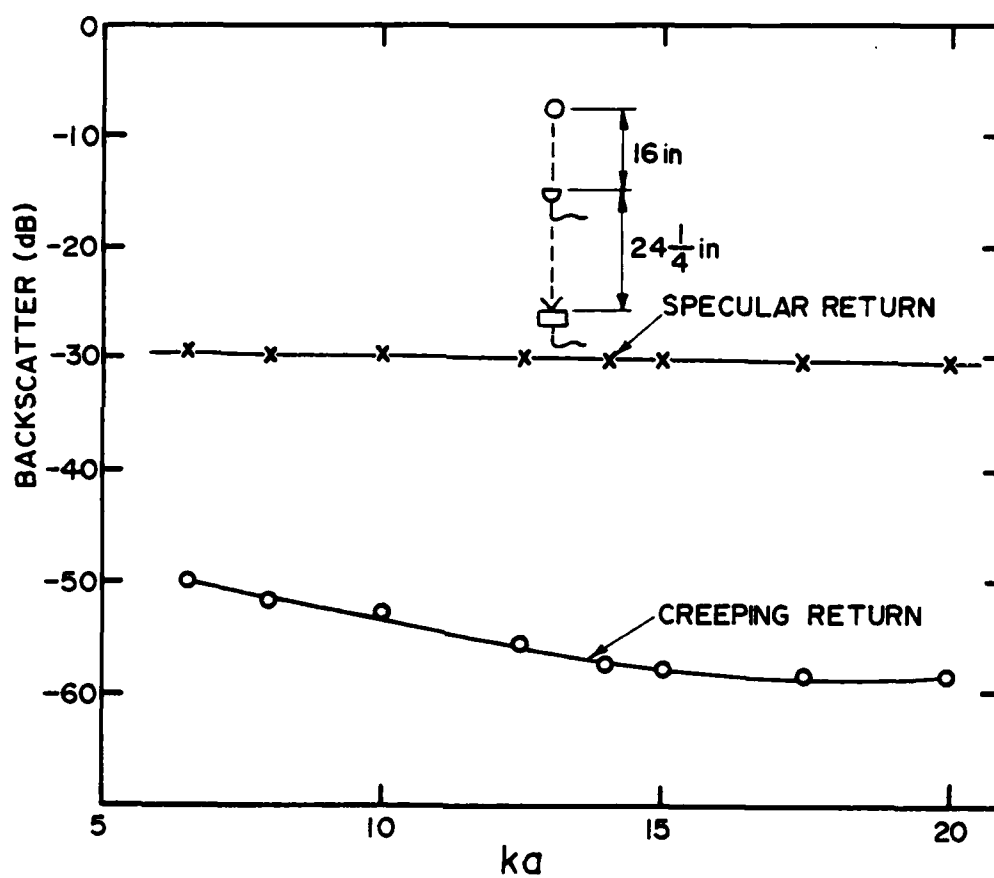


Figure 4.49 Plot of the specular (X) and creeping-wave (O) returns in the backscatter from a sphere normalized to the pulse incident on the sphere.

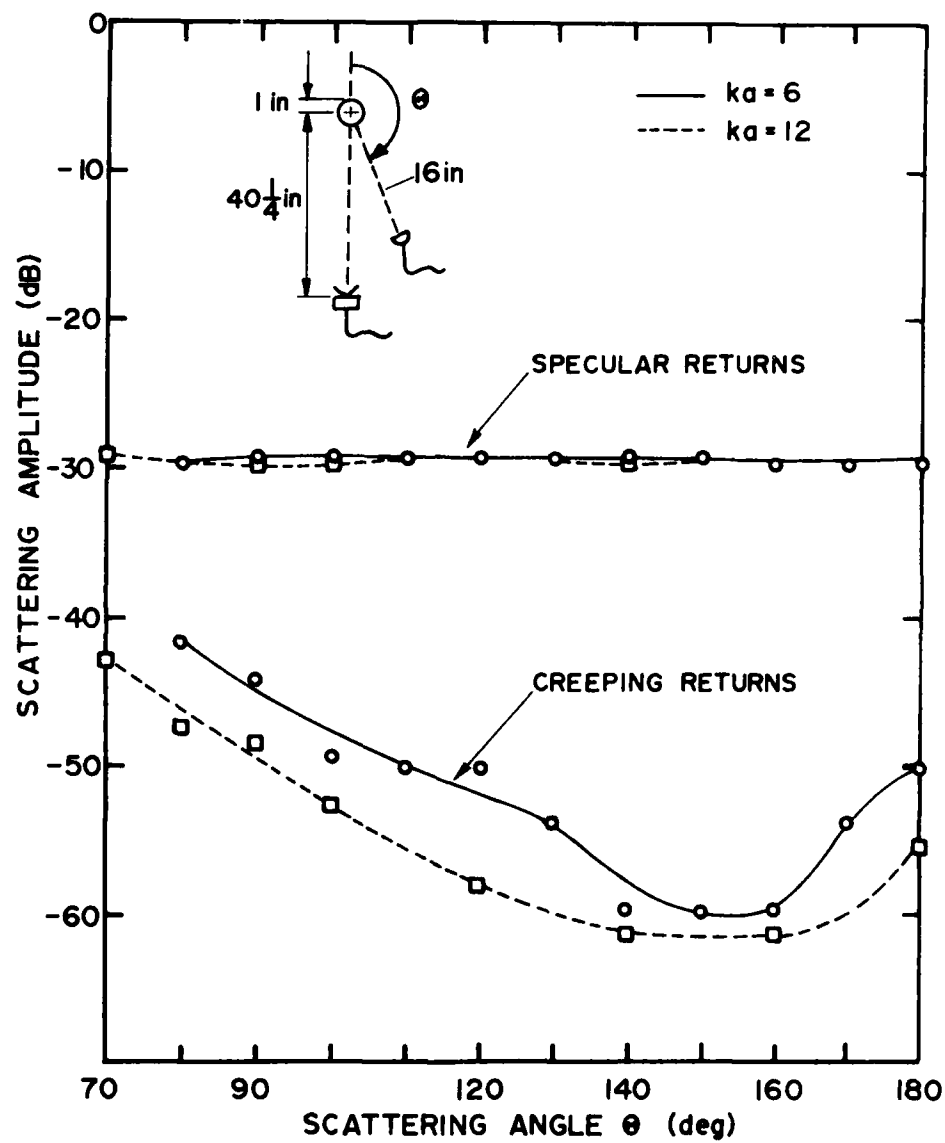
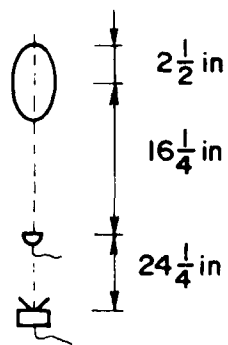
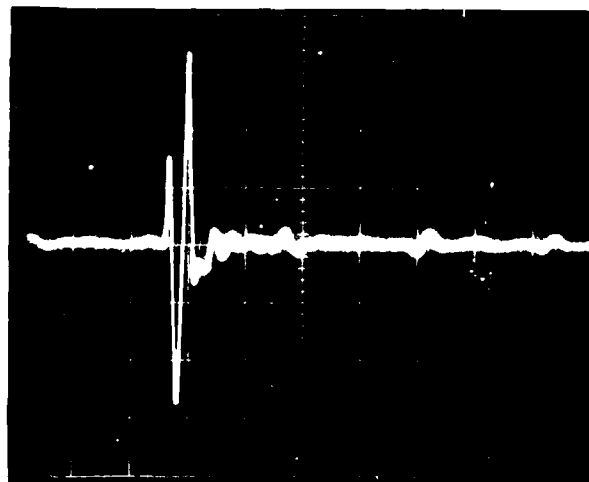


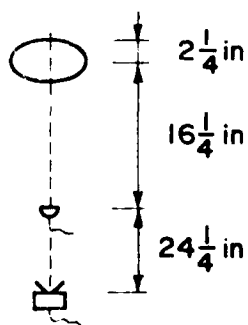
Figure 4.50 Plot of the bistatic specular and creeping-wave returns from a sphere at  $ka$ 's of 6 and 12 normalized to the pulse incident on the sphere.



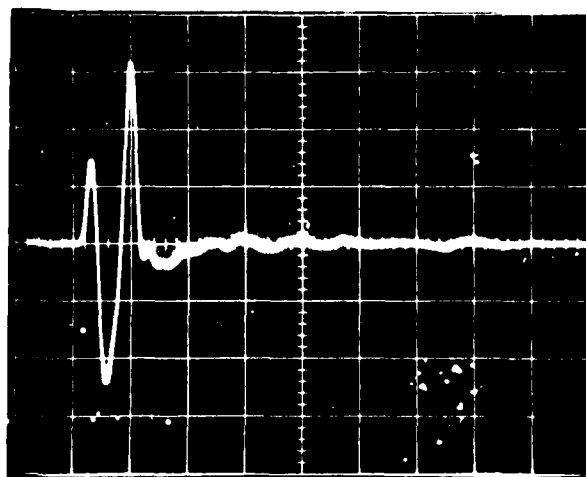
SCALE  $\times 1$



.2 msec/div.  $\rightarrow$   
(a)



SCALE  $\times 2.5$



.1 msec/div.  $\rightarrow$   
(b)

Figure 4.51 Oscilloscope trace of the backscattered specular and creeping-wave returns from a 2:1 prolate spheroid ( $h\epsilon_0 = 13.5$ ) at (a) axial and (b) broadside incidence.

traces of the backscatter at both axial and broadside incidence on this spheroid. The dimensions of the spheroid are such that  $h\bar{\epsilon}_0 = 13.5$  and  $kR = 6.7$  (where  $R$  is the minor radius). The creeping-wave return for broadside incidence is just barely visible about 600 microseconds after the specular return. At axial incidence, the creeping-wave return comes later (about 800 microseconds after the specular return), but it is also much stronger due to the axial focusing effect. The results at other scattering angles for the case of axial incidence are plotted in Figure 4.52. Similar results for the sphere ( $ka = 6$ ) described earlier in this section are also included in the figure for comparison. The specular return from the spheroid is virtually identical to that for the sphere, but the creeping-wave return is lower (6% of the specular return). This slightly eccentric spheroid has an interfocal distance that is close to the diameter of the sphere used for comparison; and the spheroid's creeping-wave return was expected to be larger than that for the sphere, based on the size of low-frequency oscillations in the frequency-response curves of Hickling (1958). Note that, when the spheroid model was rotated from axial to broadside incidence, a single (backscattered) creeping-wave return was observed that began as the axial return (Figure 4.51a) and gradually shifted in time and amplitude to the broadside return (Figure 4.51b). No change in waveform due to multiple path lengths on the surface of the spheroid was observed at any angle.

Attempts to observe the creeping-wave return from a 7:1 prolate spheroid proved to be very difficult, as is shown in Figure 4.53. Here, one sees the incident pulse and the barrage of backscattered returns that were observed with the best instrument configuration found. This

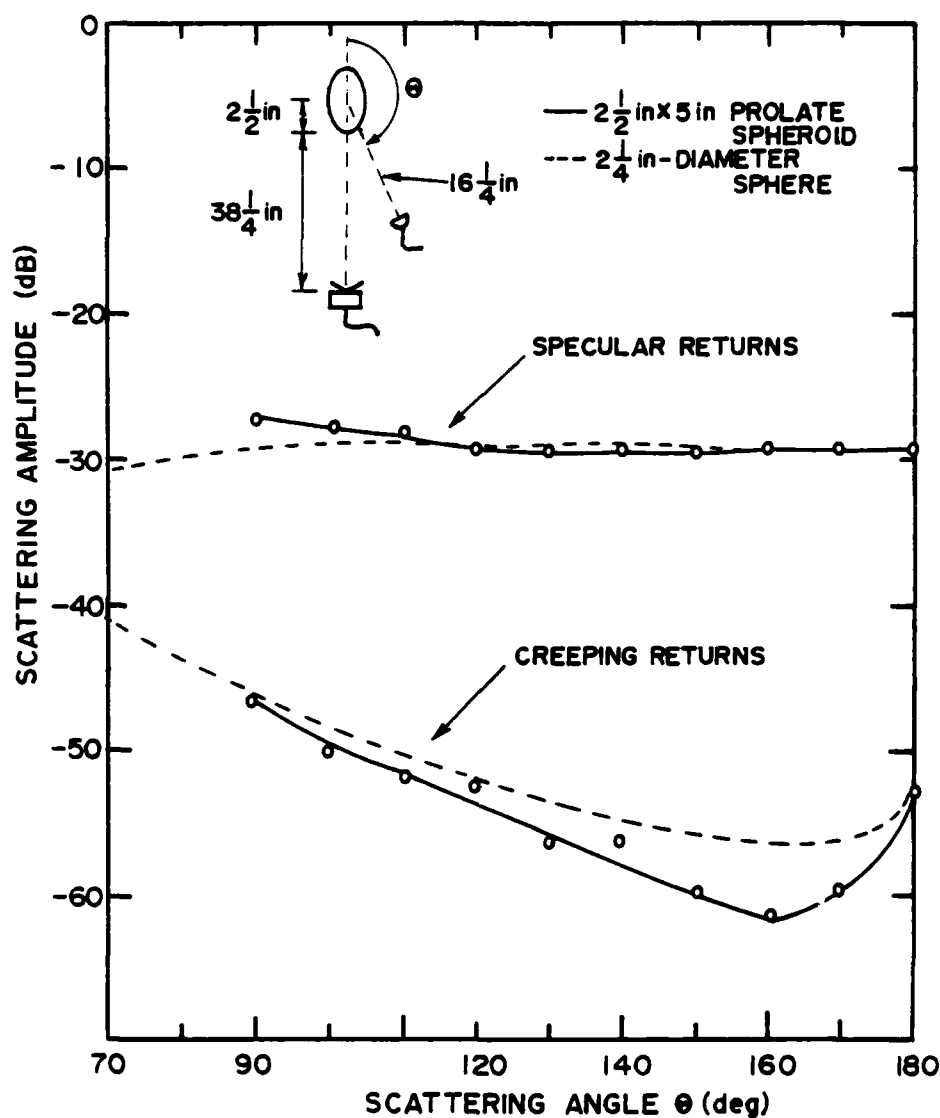
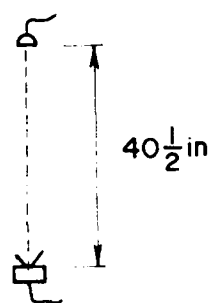
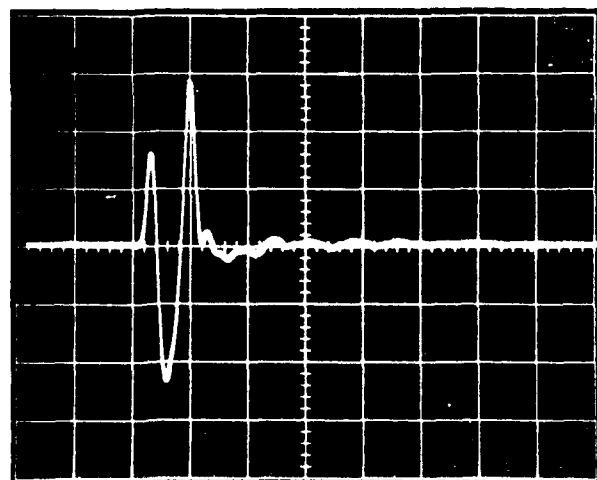


Figure 4.52 Comparison of the bistatic specular and creeping-wave returns from a 2:1 prolate spheroid ( $h\xi_0 = 13.5$ ) and a similar sphere ( $ka = 6$ ).

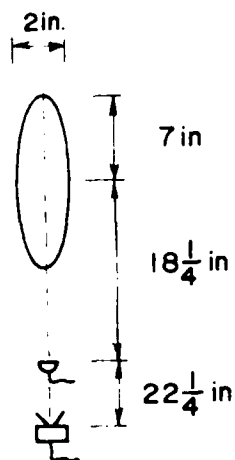


SCALE +30 dB



.1 msec/div. —

(a)



SCALE ÷ 4



SP CRP  
1 msec/div. —  
(b)

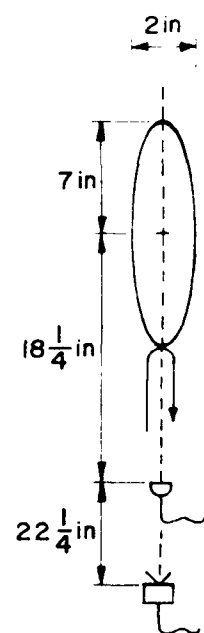
Figure 4.53 Oscilloscope traces of (a) the incident pulse and (b) the backscattered returns from a 7:1 prolate spheroid and surrounding room reflectors at  $h\xi_0 = 38$ .



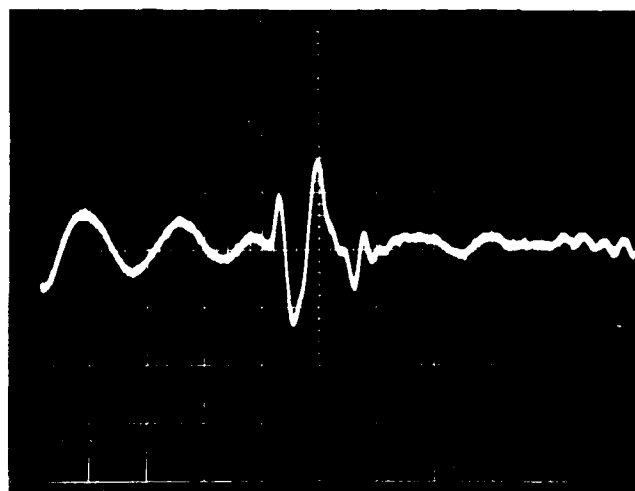
case is particularly difficult because the returns from this thin spheroid at axial incidence are very small and because the creeping-wave return follows the specular return by over 2 milliseconds. Despite the large extraneous reflections, the two desired spheroid components were effectively isolated in time (see Figure 4.54). A summary of the component amplitudes at several scattering angles is plotted in Figure 4.55. Both the specular and creeping-wave returns are lower in amplitude than those for the 2:1 spheroid, but the creeping-wave return is still about 12 dB lower in amplitude than the specular return. Theoretical results for this case indicate that larger creeping-wave effects are expected. For example, the computations of Lauchle (1975b) predict nulls of over 90 dB in the backscattered frequency response for a thin (22:1) prolate spheroid; these nulls are generally thought to be caused by interferences between specular and creeping-wave returns that are virtually identical in level.

#### 4.6.2 Creeping Waves on Spheres with Bands

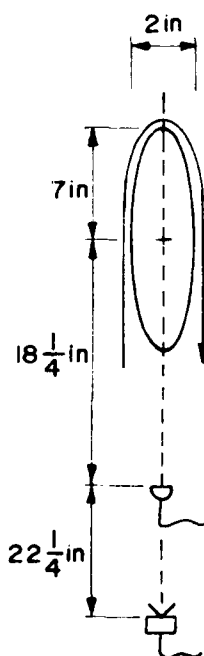
In order to evaluate the surface-hugging properties of creeping waves, an examination was made using spheres with bands applied to their surfaces. For example, Figure 4.56 shows oscilloscope traces of the backscattered specular and creeping-wave components from the sphere ( $ka = 6$ ) of Section 4.6.1 with two thicknesses of bands on its surface. The bands are constructed of one or more rubber bands stretched around the circumference of the sphere along the axis containing the source and receiver. These bands effectively form a small, rigid, reflecting wall on the surface of the sphere that intercepts all the surface rays at some orientation.



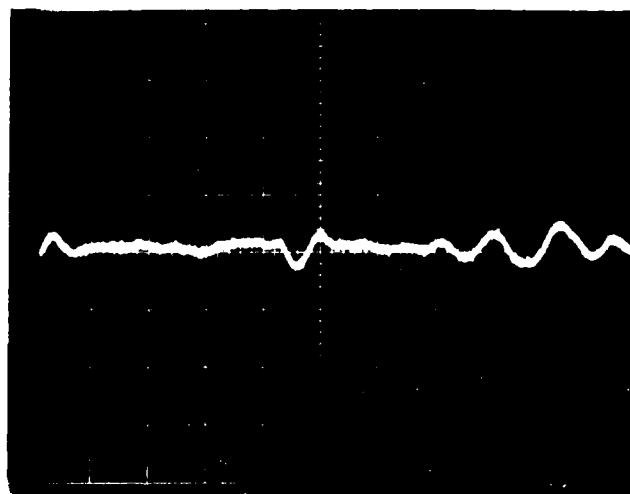
SCALE  $\div 4$



.1 msec/div  $\rightarrow$   
(a)



SCALE  $\div 4$



.1 msec/div  $\rightarrow$   
(b)

Figure 4.54 Oscilloscope trace of the backscattered (a) specular and (b) creeping-wave returns from a 7:1 prolate spheroid at  $h\tilde{c}_0 = 38$ .

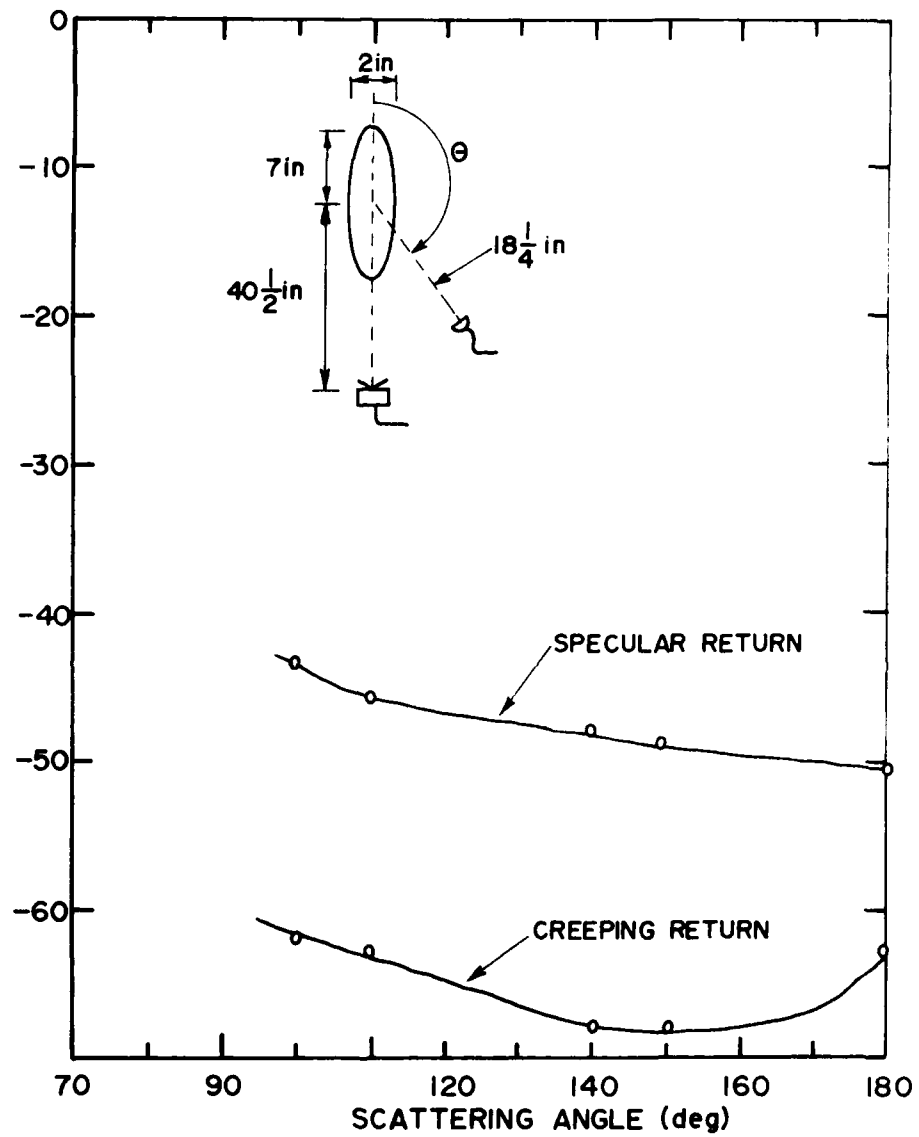
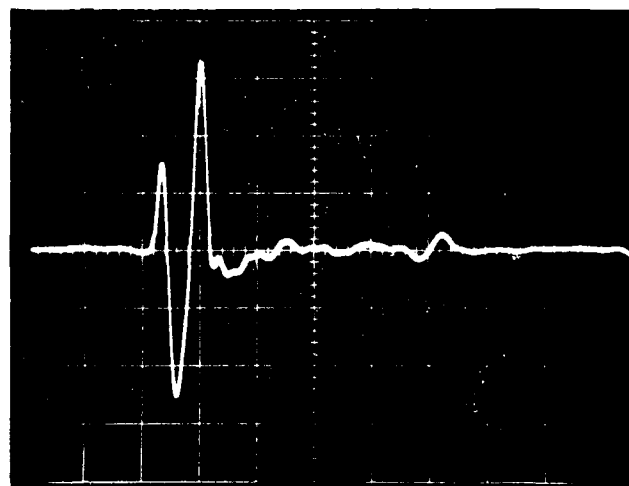
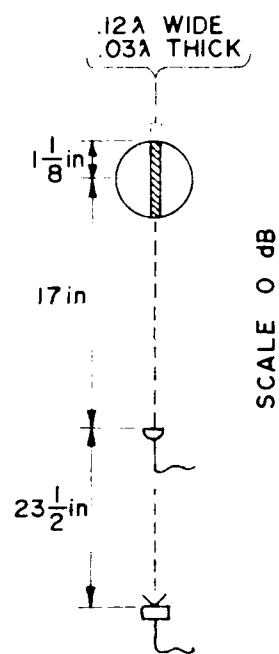
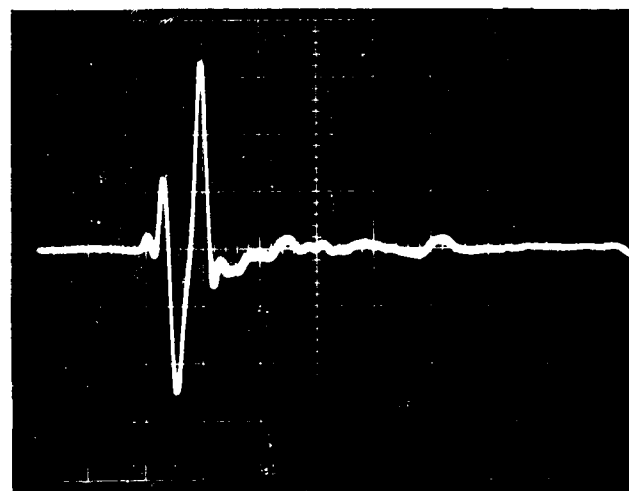
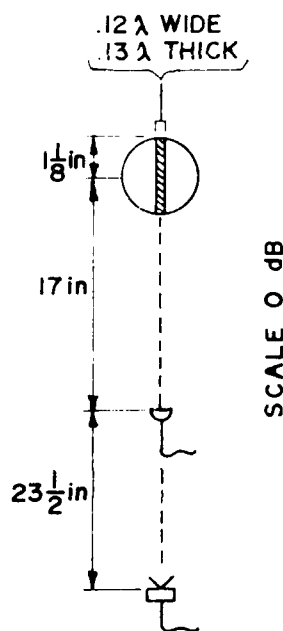


Figure 4.55 Bistatic specular and creeping-wave returns from a 7:1 prolate spheroid. ( $h\epsilon_0 = 38$ )



$.1\text{msec/div} \rightarrow$   
(a)



$.1\text{msec/div} \rightarrow$   
(b)

Figure 4.56 Oscilloscope trace of the backscattered specular and creeping-wave returns from a sphere at  $ka = 6$  with bands having thicknesses of (a)  $.03\lambda$  and (b)  $.13\lambda$  oriented along the source/receiver axis.

A single rubber band ( $.03\lambda$  thick), shown in Figure 4.56a, has virtually no effect on the backscattered returns. However, four stacked rubber bands (total  $.13\lambda$  thick) do attenuate the creeping-wave component by about 2 dB (Figure 4.56b), as well as change its waveform somewhat. These results are expanded in the plot of Figure 4.57. The figure shows that even two rubber bands ( $.07\lambda$  thick) have little or no effect on either the specular or creeping-wave returns. However, the  $.13\lambda$ -thick band (four rubber bands) does attenuate the creeping-wave component over all the angular range examined.

Figure 4.58 shows that the effect of the axial bands depends on more than their height off the surface. The upper trace shows the backscattered creeping-wave component attenuated to about half of the level observed on the plain sphere by a  $.2\lambda$ -thick band in the source/receiver axis. However, if the sphere and band are rotated by as little as  $10^\circ$ , the attenuation disappears. In fact, as is shown in Figure 4.59, the creeping-wave component is then boosted by about 3 dB over that from the plain sphere for scattering angles as large as  $70^\circ$ . Furthermore, this effect is not sensitive to the band's incidence angle because a change in angle from  $10^\circ - 40^\circ$  shows no change in the backscattered returns. Note that the band still intercepts all the surface rays, just as it did when oriented on axis. Additional tests with partial bands have led to the conclusion that the band must be present at the antipole (focus point) on the sphere's surface in order for attenuation to occur. Figure 4.60 shows that an axial band that surrounds the sphere as in Figure 4.58a with the addition of a 1/2-inch gap at the antipole has no effect on the creeping-wave component.

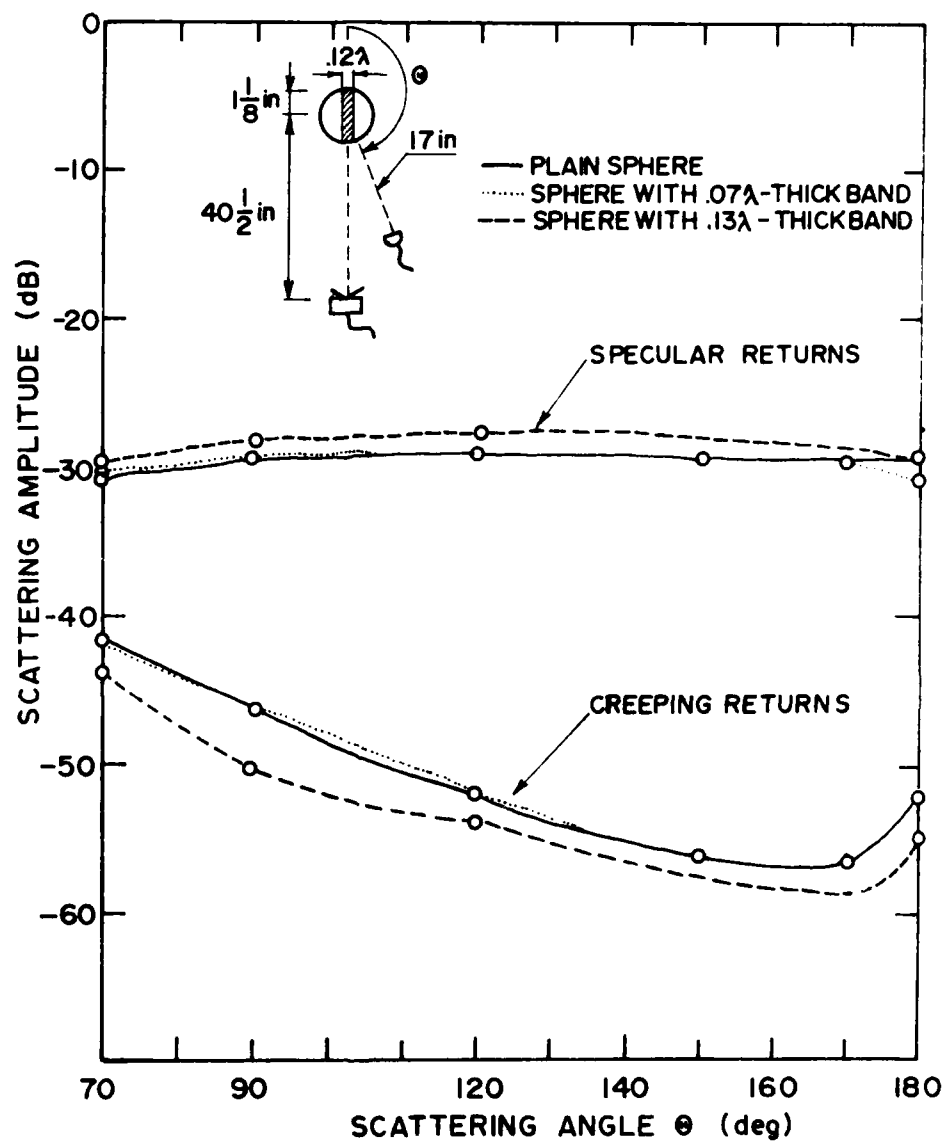


Figure 4.57 Bistatic specular and creeping-wave returns from a plain sphere and a sphere with two thicknesses of rubber bands around its surface in the source/receiver axis. ( $ka = 6$ )

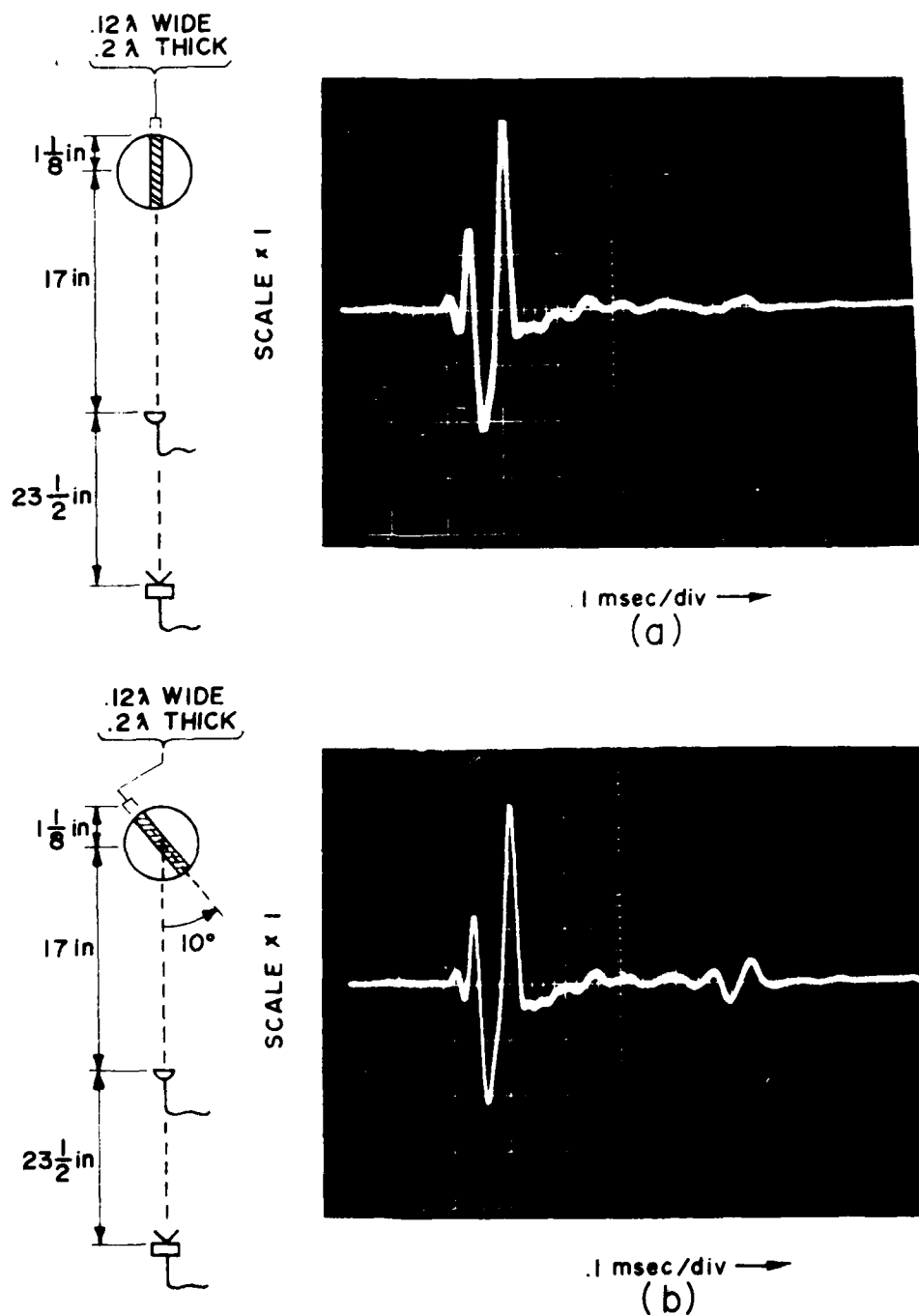


Figure 4.58 Oscilloscope trace of the backscattered specular and creeping-wave returns from a sphere at  $ka = 6$  with a band oriented (a) in the source/receiver axis and (b)  $10^\circ$  off the source/receiver axis.

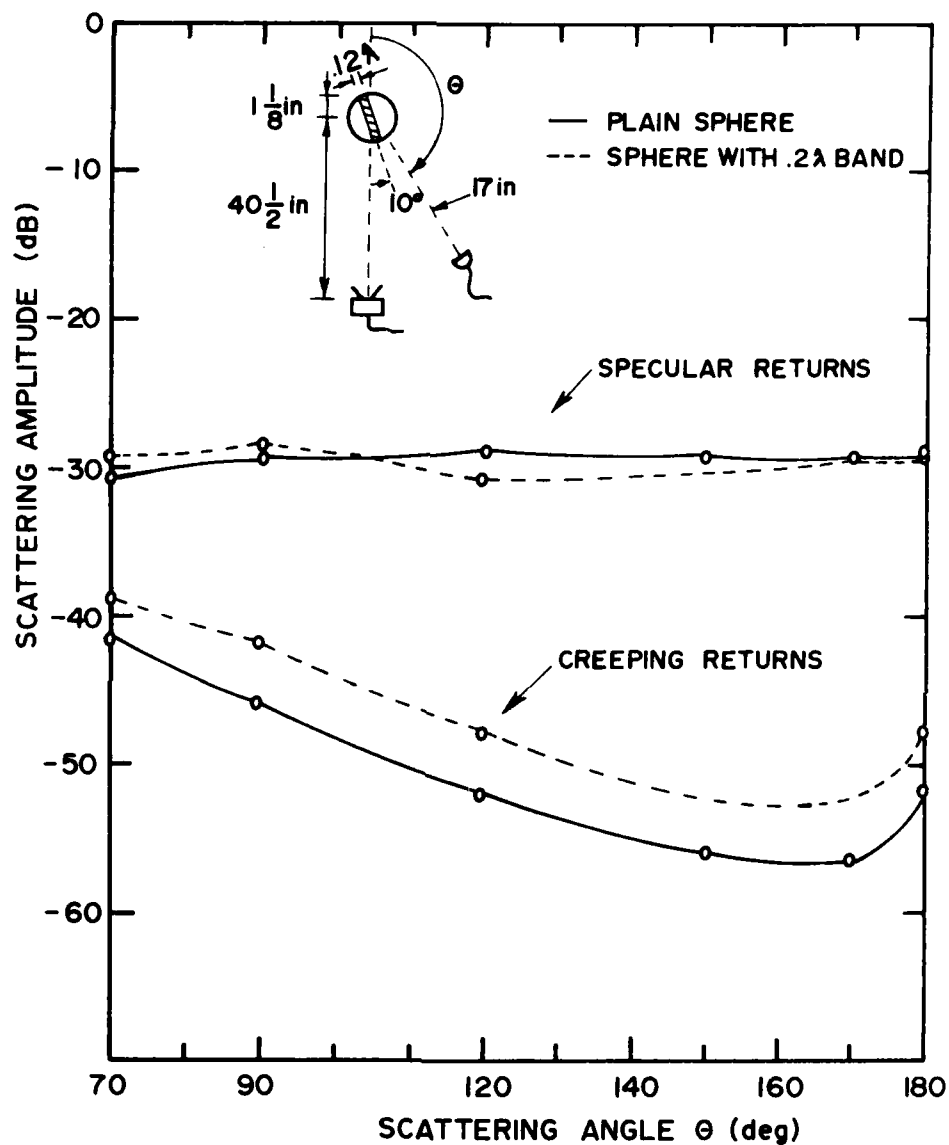
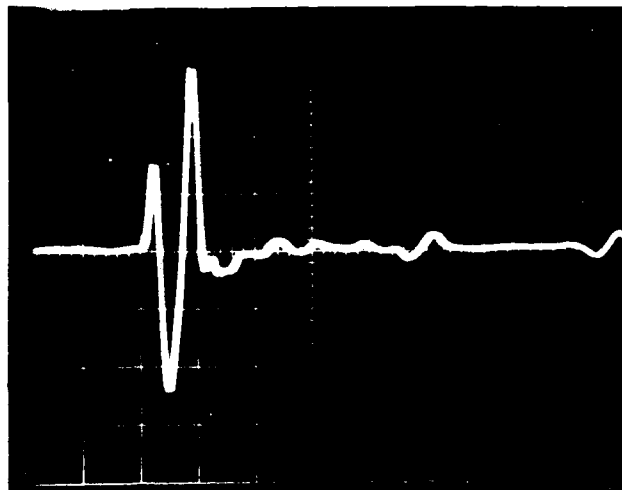
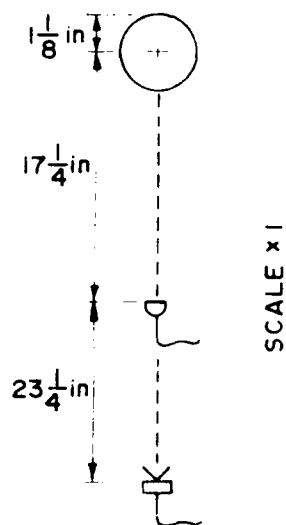
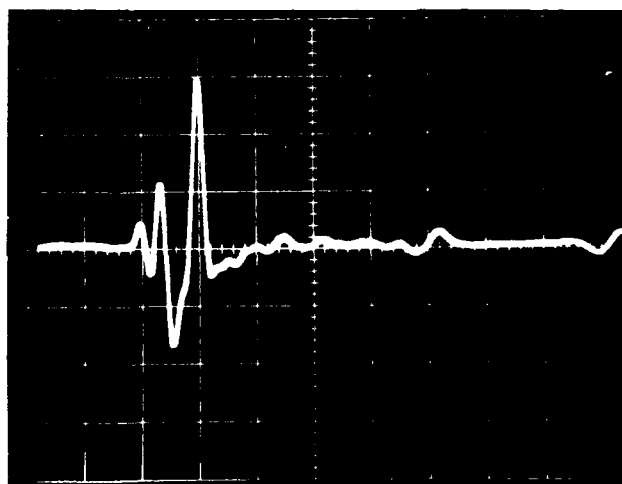
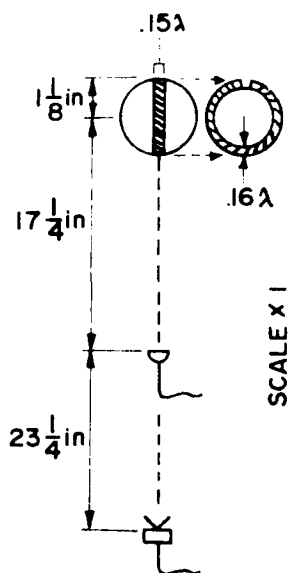


Figure 4.59 Bistatic specular and creeping-wave returns from a sphere with a band around its surface slightly out of the source/receiver axis compared to the returns from a plain sphere. ( $ka = 6$ )





.1 msec/div —  
(a)

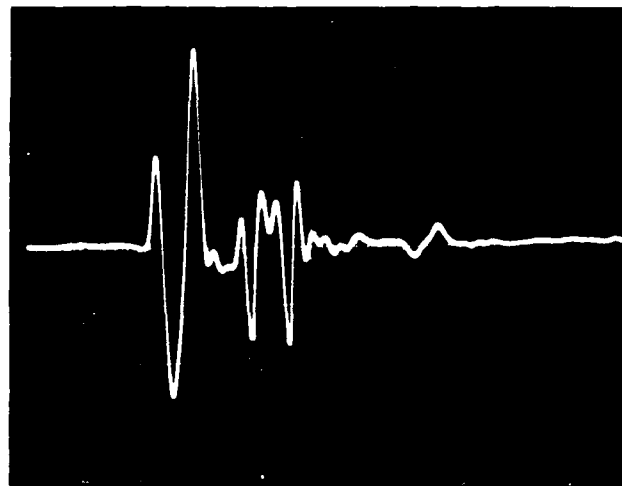
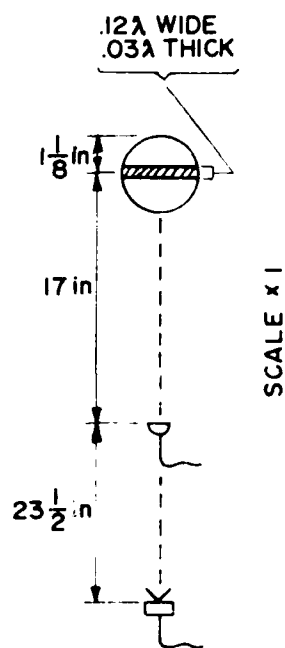


.1 msec/div —  
(b)

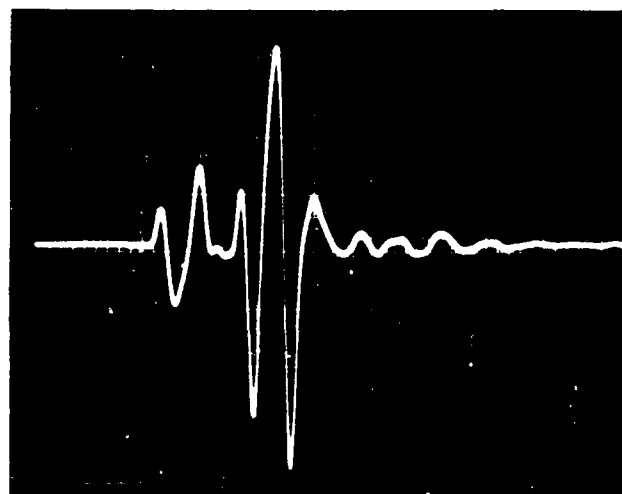
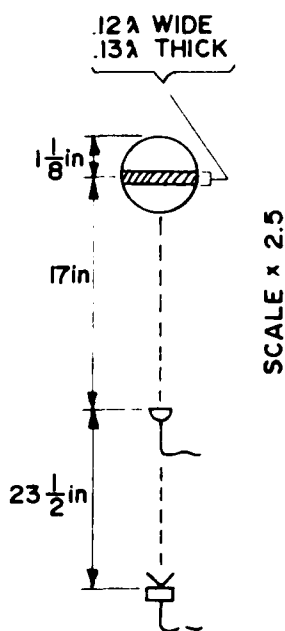
Figure 4.60 Oscilloscope trace of the backscattered returns from (a) a plain sphere and (b) a sphere with a band along the source/receiver axis open slightly at the antipole. ( $ka = 6$ )

Correspondingly, a 3/4-inch-long ( $.65\lambda$ ) band of  $.16\lambda$  thickness at the antipole attenuates the creeping-wave component by about 6 dB, while a 3/8-inch-long ( $.32\lambda$ ) section of this band still manages a 4-dB attenuation relative to the level observed with the plain sphere. Similar effects have been noted with the 2:1 spheroid at axial incidence; the 7:1 spheroid could not be tested in this manner because of an insufficient signal-to-noise ratio.

Circumferential bands on a sphere have an even more dramatic effect on the backscattered field when oriented parallel to the incident wavefront. Figure 4.61 illustrates these results for the same two thicknesses of bands as in Figure 4.56. Even though the single axial rubber band at the antipole had no noticeable effect on the creeping-wave component, the same band does generate a major specular return in this perpendicular orientation (Figure 4.61a). The band's return takes the form of two closely spaced components that are  $180^\circ$  out of phase with each other. In the case of four rubber bands (Figure 4.61b), the bands' specular return is substantially larger than the sphere's specular return. A summary of the data at this perpendicular orientation of the band is presented in Figure 4.62. The major effect of the bands' specular returns is clearly evident. In addition, one can see that the creeping-wave component is actually increased for angles near that for backscattering. Because the increase is not present at wider angles, it must occur, not at the point of creeping-wave formation, but rather at its reradiation point.



.1 msec/div  $\rightarrow$   
(a)



.1 msec/div  $\rightarrow$   
(b)

Figure 4.61 Oscilloscope trace of the backscattered specular, band, and creeping-wave returns from a sphere at  $ka = 6$  with bands having thicknesses of (a)  $.03\lambda$  and (b)  $.13\lambda$  oriented perpendicular to the source/receiver axis.

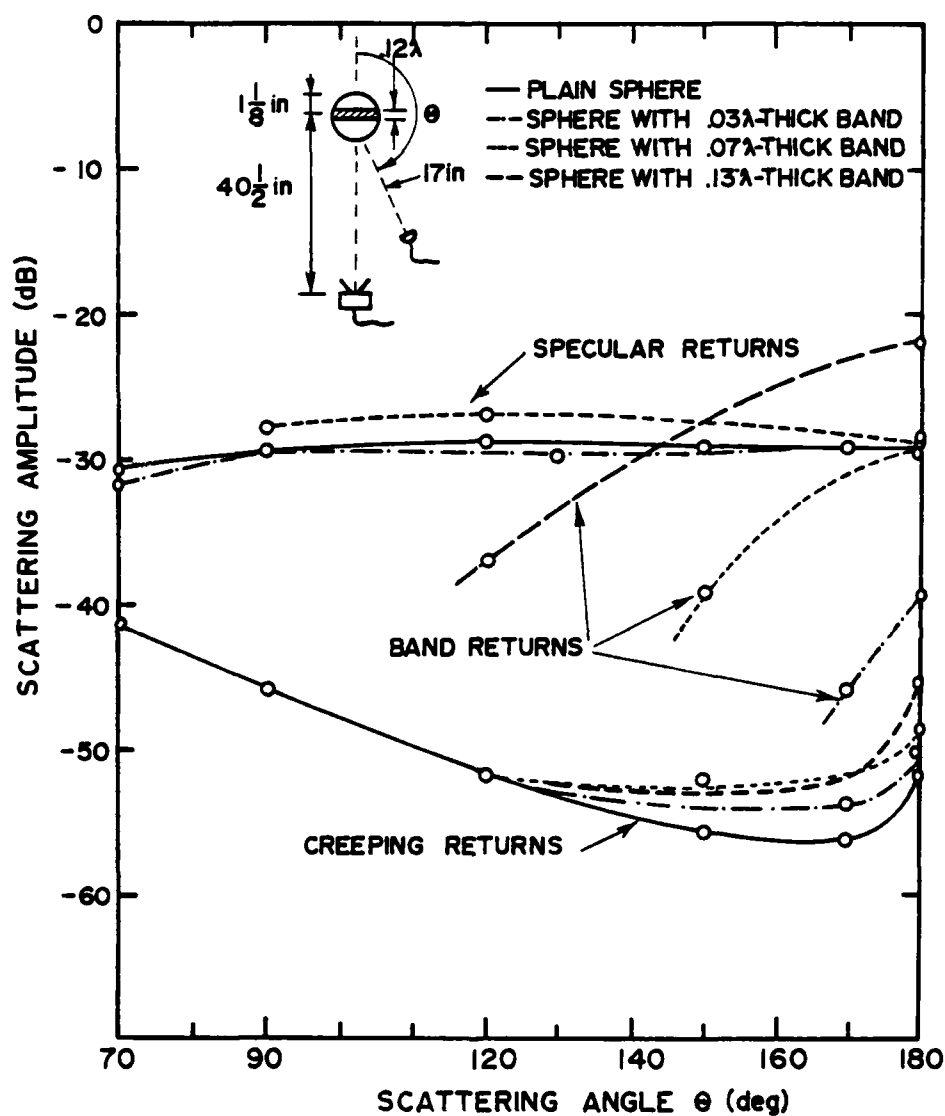
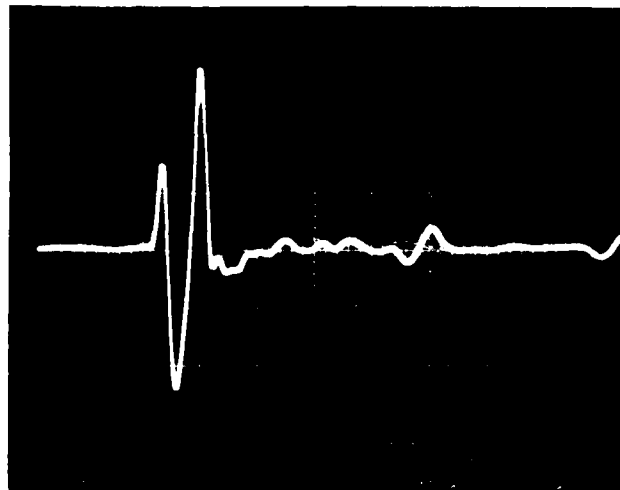
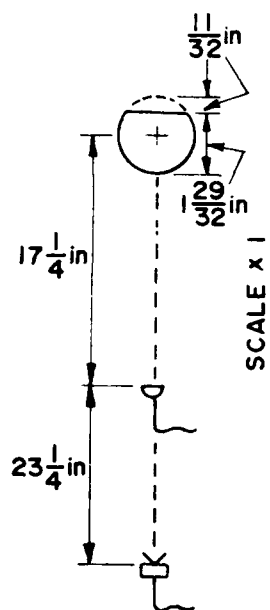


Figure 4.62 Bistatic specular and creeping-wave components from a sphere with various circumferential bands oriented parallel to the incident wavefront.

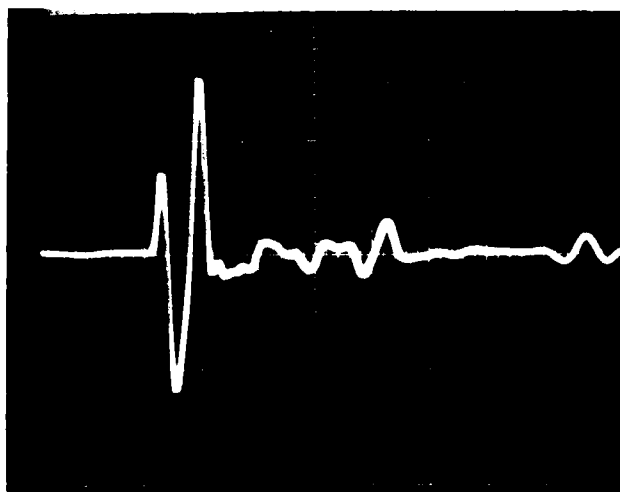
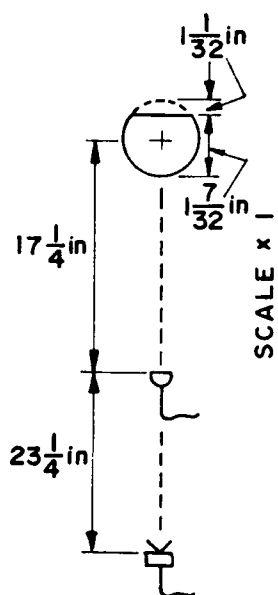
#### 4.6.3 Creeping Waves on Flattened Spheres

As a final test of the properties of creeping waves, a series of experiments was performed using spheres that were cut to produce flat surfaces on one side. This procedure was made feasible by the ready availability of models that could be destructively modified--namely, pool balls. The tests were designed to provide additional evidence (see Section 4.6.2) of how closely the creeping waves follow the surface geometry. Three different models were used, ranging from a sphere with a slight depression to a model that was almost a hemisphere. They were examined in four orientations, with the flat at the front, back, right, and left as viewed from the microphone. Note that, because the single model-support point was centered on the original sphere, the flattened spheres did not always hang with their flat surfaces oriented at a true vertical.

Oscilloscope traces of the backscattered specular and creeping-wave components from the flattened sphere oriented with the flat opposite the microphone are shown in Figure 4.63. The creeping-wave returns are increased over those from the plain sphere without a noticeable change in their waveform. In addition, components originating at the edges of the flat are visible. A summary of the complete series of backscatter data with both back and front orientations of the flat is presented in Figures 4.64, 4.65, and 4.66. With the flat oriented toward the microphone, the specular returns are boosted near  $180^\circ$  and reduced at wider angles by the effect of the flat surface. The creeping-wave component is also boosted by an amount proportional to the depth of the flat, but only for angles in the vicinity of  $180^\circ$ . With the flat



.1 msec/div →  
(a)



.1 msec/div →  
(b)

Figure 4.63 Oscilloscope trace of the backscattered returns from a flattened sphere with two different degrees of flatness. ( $ka = 6$ )

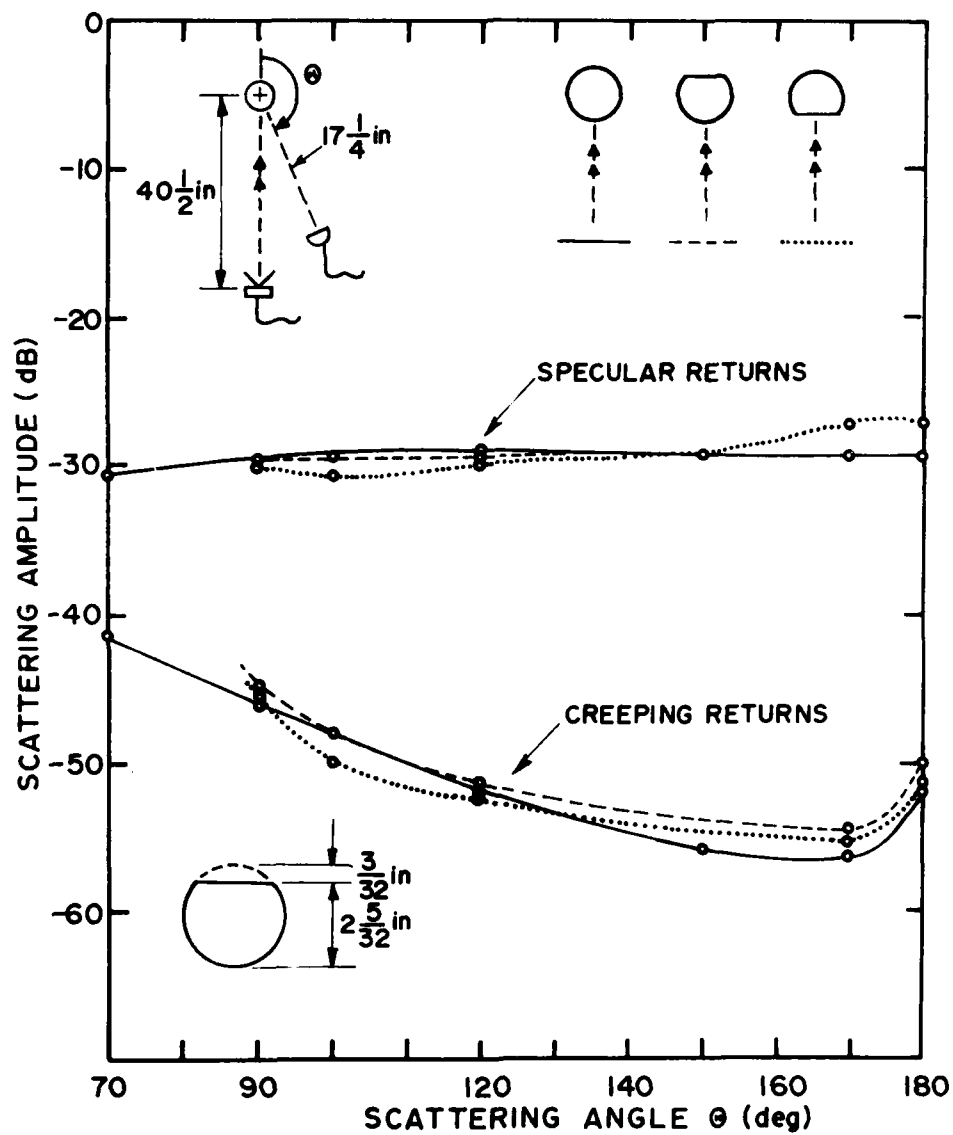


Figure 4.64 Bistatic specular and creeping-wave components from a slightly flattened sphere with the flat oriented at the front and back relative to the microphone. ( $ka = 6$ )

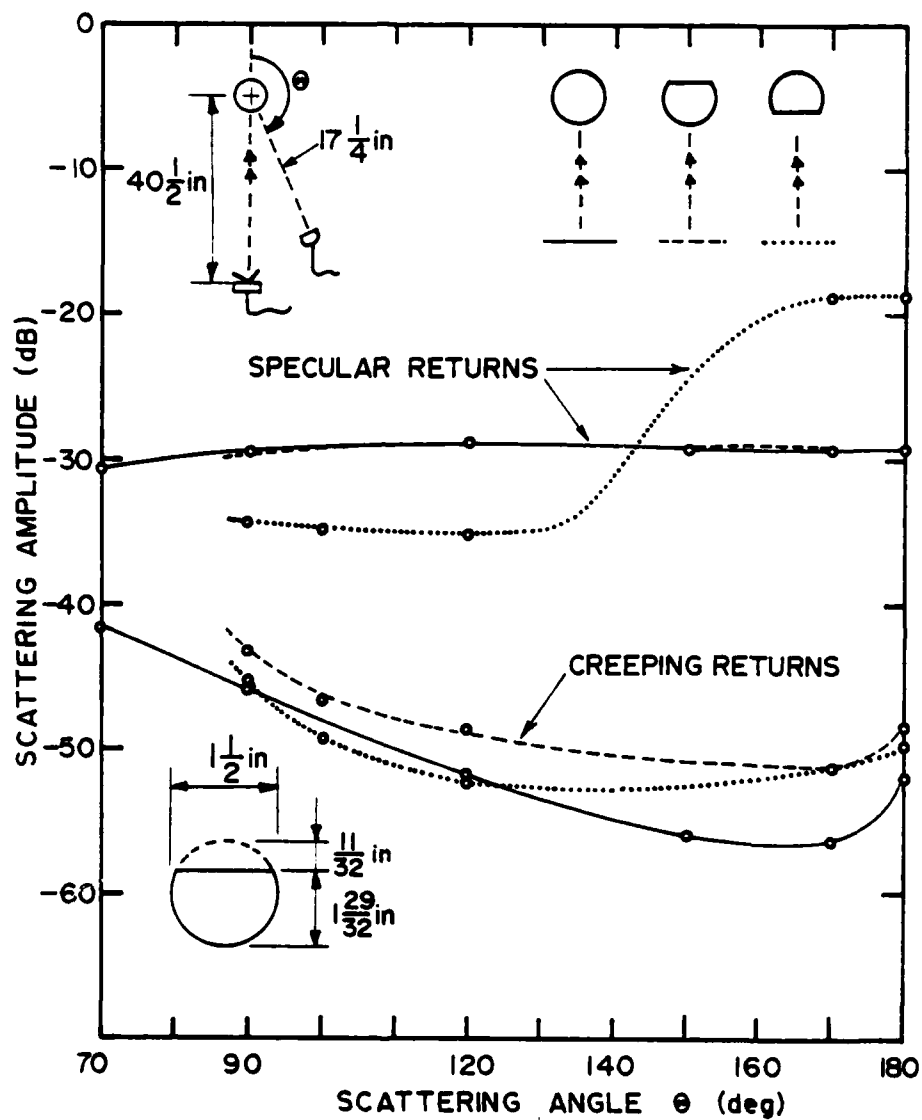


Figure 4.65 Bistatic specular and creeping-wave components from a moderately flattened sphere with the flat oriented at the front and back relative to the microphone. ( $ka = 6$ )



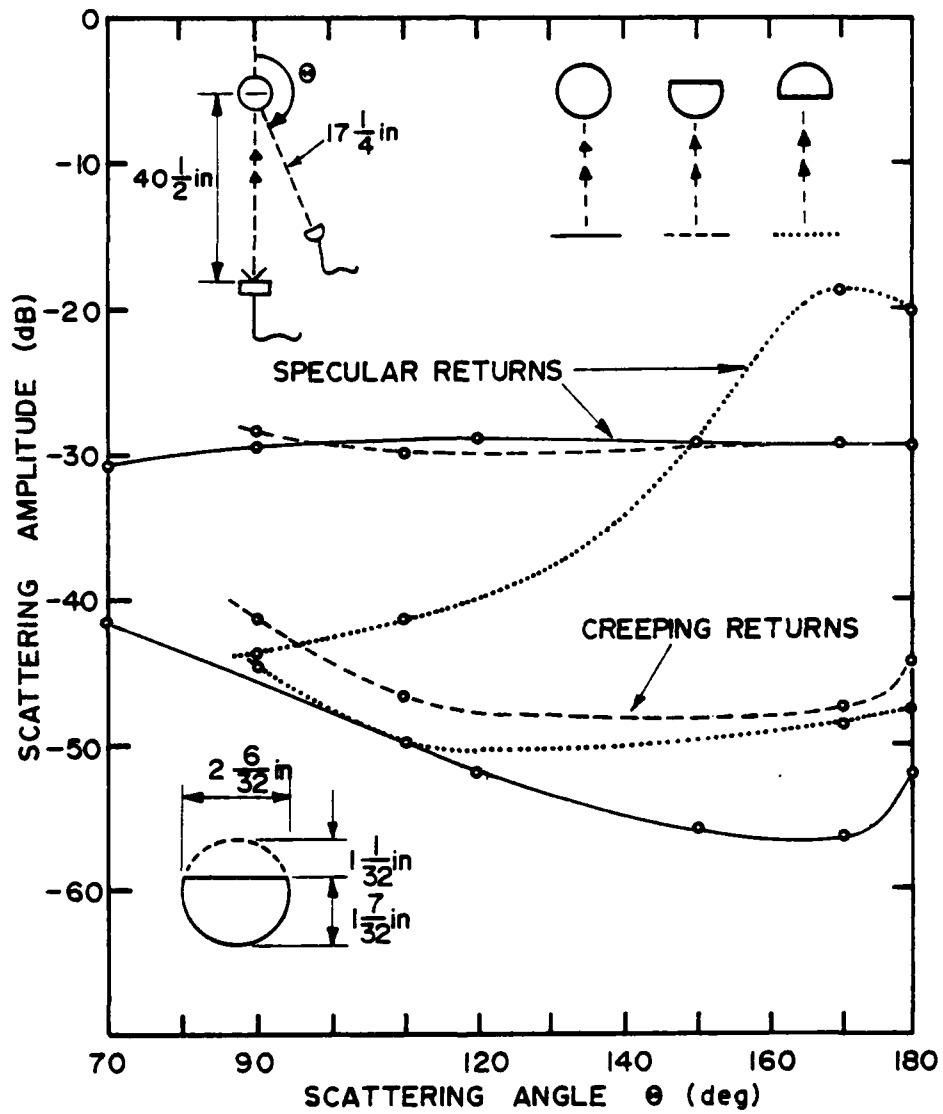


Figure 4.66 Bistatic specular and creeping-wave returns from a deeply flattened sphere with the flat oriented at the front and back relative to the microphone. ( $ka = 6$ )

oriented on the side opposite the microphone, the creeping-wave component is increased in amplitude even more than in the previous case. This increase is observed over the entire angular range. Curiously, there is no jump in the creeping-wave return near the angles at which the flat might be expected to prematurely discharge any energy in surface rays at its edge. Finally, Figure 4.67 shows that the creeping-wave component can still be attenuated in the rear-oriented flat example by placing a small band at the focus point on the model's surface.

A similar summary of the results for left and right flat orientations is plotted in Figures 4.68, 4.69, and 4.70. In these cases, the specular return is again affected at wide angles when the flat is on the side facing the microphone. However, only slight changes are noted in the creeping-wave returns. Because these creeping-wave changes are also somewhat inconsistent, they may depend on a more precise alignment of the flat relative to the incident wavefront than was maintained in this experiment.

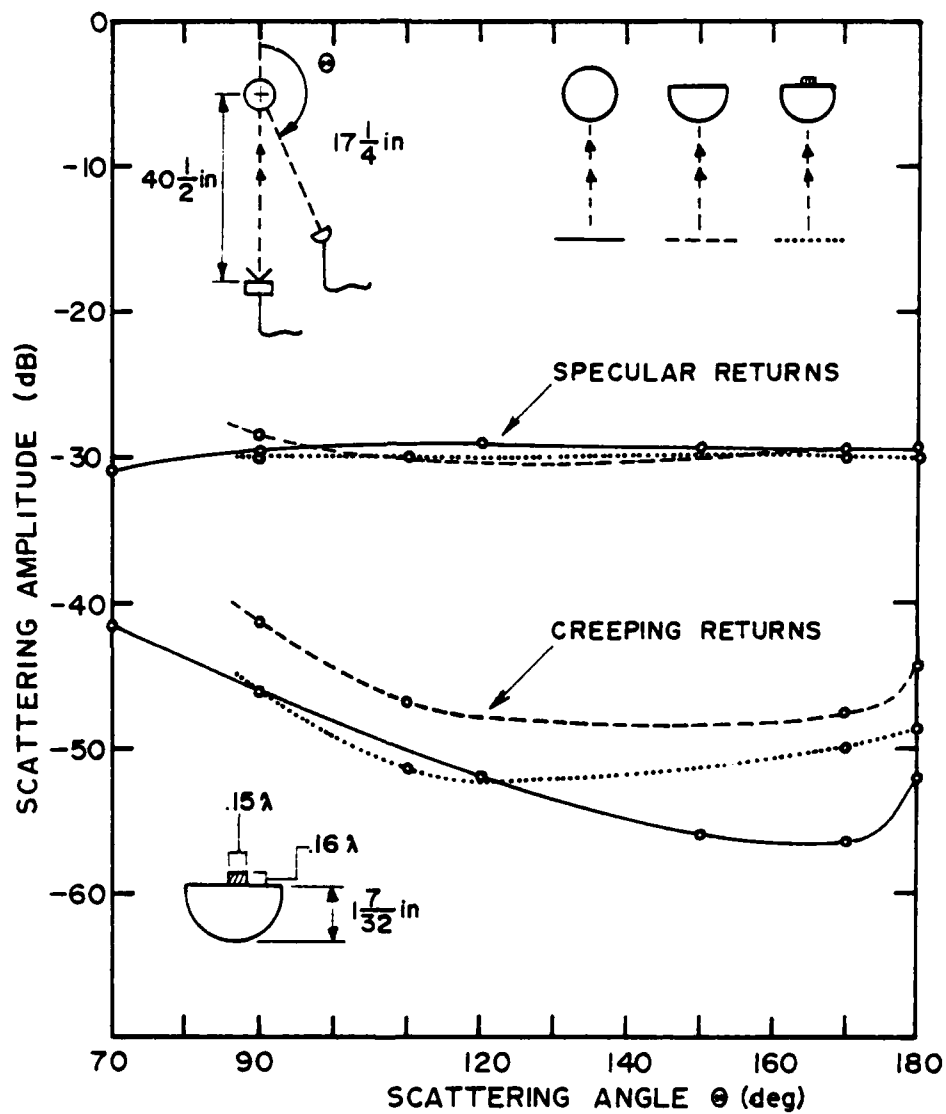


Figure 4.67 Effect of a small band at the surface focus point on the bistatic specular and creeping-wave components from a deeply flattened sphere with its flat oriented opposite the microphone. ( $ka = 6$ )

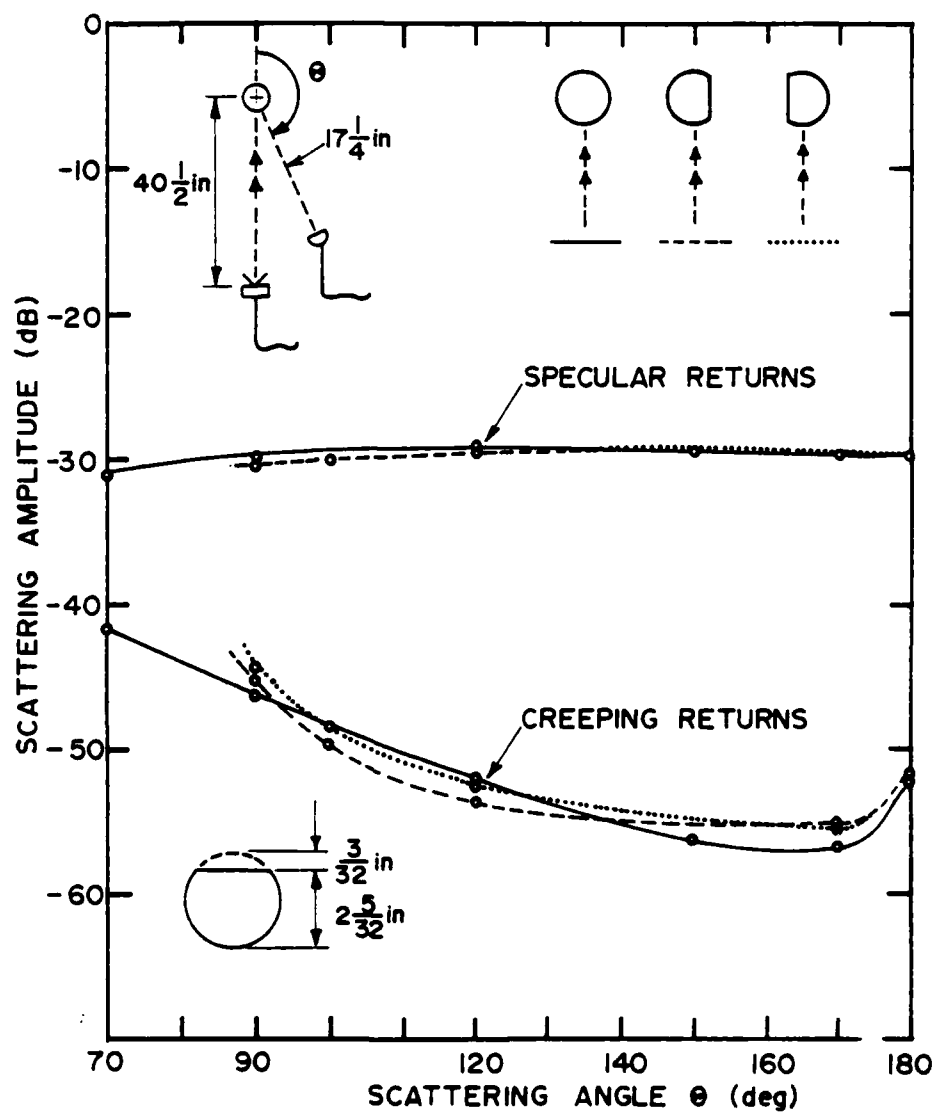


Figure 4.68 Bistatic specular and creeping-wave returns from a slightly flattened sphere with the flat oriented at the left and right relative to the microphone. ( $ka = 6$ )

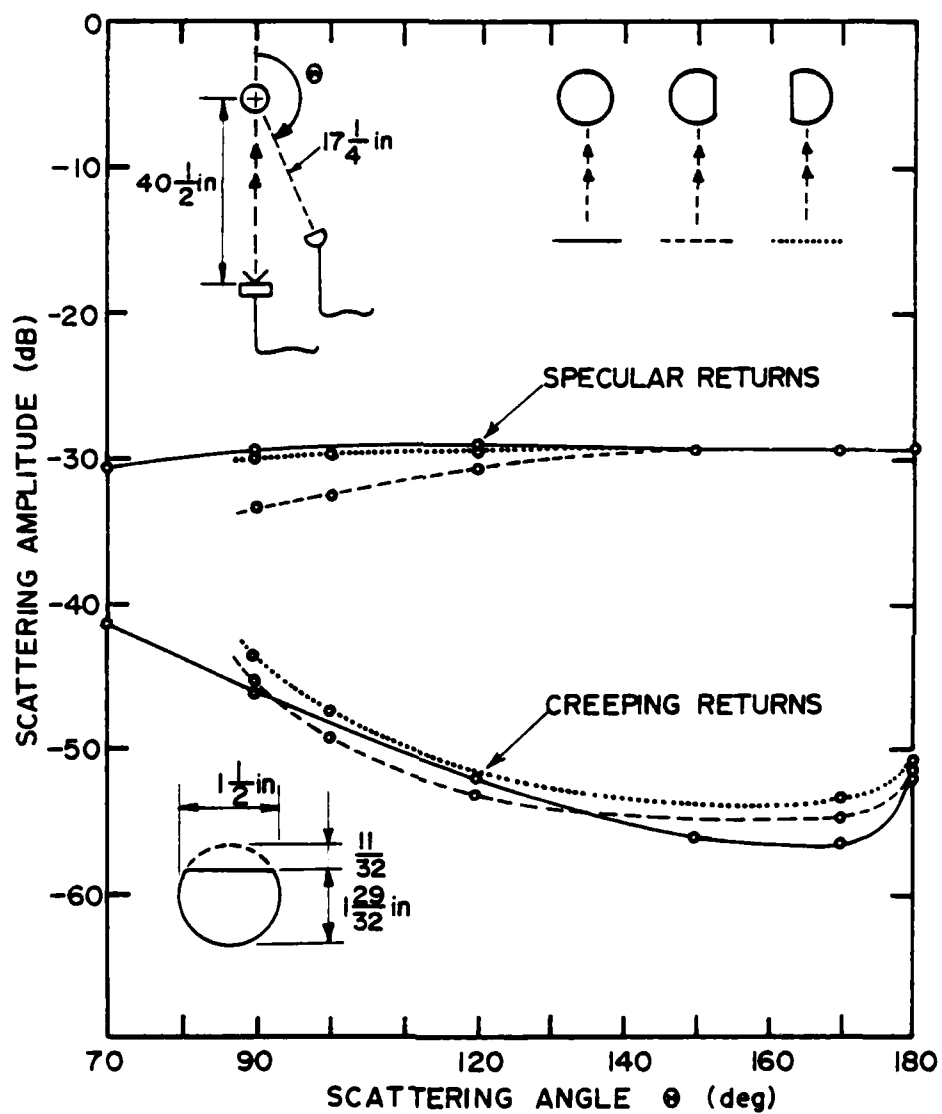


Figure 4.69 Bistatic specular and creeping-wave returns from a moderately flattened sphere with the flat oriented at the left and right relative to the microphone. ( $ka = 6$ )

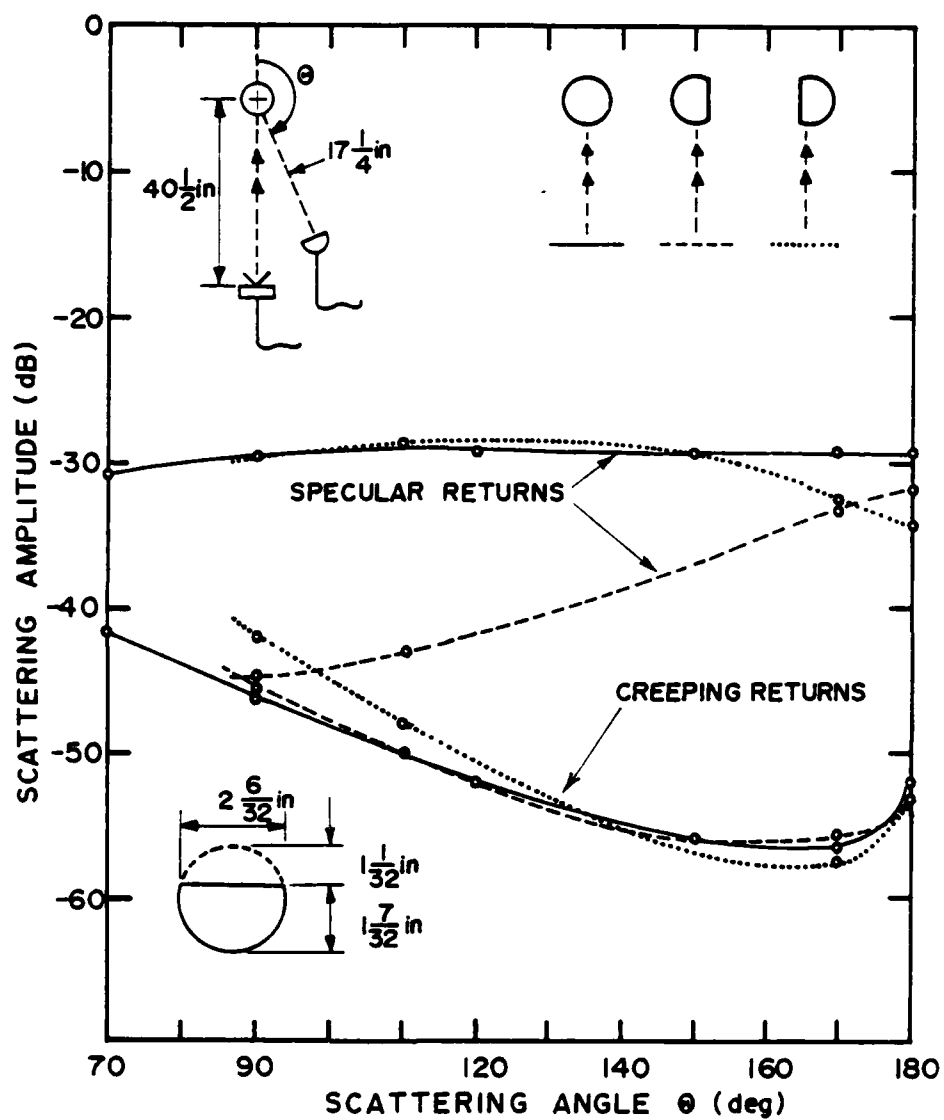


Figure 4.70 Bistatic specular and creeping-wave returns from a deeply flattened sphere with the flat oriented at the left and right relative to the microphone. ( $ka = 6$ )

## CHAPTER 5

## EDGE DIFFRACTION MEASUREMENTS AND THE FREEDMAN THEORY

The backscattering of sound by smooth bodies is dominated by simple specular effects for wavelengths near and smaller than the scatterer dimensions (see Section 4.2). Any other disturbance of the incident field is apparently minimized by the smooth curvature. This fact, coupled with observations of the dramatic effect of small obstructions on a smooth body (Sections 4.3 and 4.4), has led to an experimental investigation of discontinuous surface structures such as edges and tips. This chapter presents the results of that investigation.

Three basic categories of models were examined in this part of the study. First, scattering from the edge of plane baffles was examined, as was the field along the shadowed side of such baffles (with both damped and undamped surfaces). Second, small cylinders were used to observe the interaction of specular and edge contributions. Finally, an adaptable cone that includes both spherical caps and spherical and hemispherical terminations (see Section 3.3) was examined. This last model exhibits surface discontinuities of several different orders for examination.

A specific effort was made to choose models that test the validity of the Freedman echo-formation theory. The Freedman prediction for specular returns from a smoothly curved body has already implicitly been verified in Section 4.2.4; the Freedman result corresponds to the geometrical-optics prediction multiplied by  $(1 + 1/4k^2a^2)^{1/2}$ , and data in Section 4.2.4 show that geometrical optics accurately predicts the

backscattering by smooth bodies. (Note that  $ka$  must be less than .7 for this multiplicative factor to differ from unity by at least 10% or 1 dB.) However, the Kirchhoff assumptions, on which the Freedman theory is based, are physically plausible in the case of smooth bodies. The assumptions are questionable in the case of abrupt surface discontinuities. The results of this chapter indicate that the nonspecular Freedman predictions (and, by analogy, those of physical optics) should be used only with care.

### 5.1 Scattering at the Edge of a Plane Baffle

The first model examined in the edge-diffraction studies was one end of a large rectangular baffle. The baffle was a 3 x 5-foot section of 1/2-inch plywood suspended in the measurement chamber with its long side vertical. The one vertical edge under study was carefully filled with wood putty and sanded to eliminate most imperfections. It was long enough to allow any end effects to be separated from the desired data by time gating. This particular edge configuration is useful as a basic indicator of all edge-type scattering phenomena. The frequency used for the experiments was 21 kHz, giving a wavelength of .643 inch. Thus, the edge was about  $3/4\lambda$  in thickness. Note that, in order to avoid directivity problems and perturbation of the field, a 1/8-inch Bruel & Kjaer microphone was utilized for all the measurements.

#### 5.1.1 Angular Distribution of the Field

The first sequence of baffle experiments measured the directivity of the field scattered by an edge. The edge of the baffle was



irradiated from a direction perpendicular to the baffle, and a microphone was swept radially about the edge at separation distances from 6 inches to 30 inches in 4-inch steps. Figures 5.1, 5.2, and 5.3 summarize the angular results in the incident half-space. These curves are normalized to the field at the microphone in the direct forward direction ( $\theta = 180^\circ$ ) without the baffle present. The curves show a strong return that is slightly oscillatory for angles near and below  $0^\circ$ . The amplitude then drops rapidly as  $\theta$  takes on larger positive values. In this case, the incident pulse was eliminated by time gating. However, the baffle generated a specular contribution at angles near and below  $0^\circ$  that could not be isolated from the edge contribution at the shortest practical pulse length (.3 milliseconds). Based on the amplitude of the oscillations in the data, the edge contribution must be no more than 8 - 12 dB below the specular contribution. The edge contribution decreases for angles away from  $0^\circ$  and also for larger edge-to-receiver separations. The period of the oscillations in the backscatter curve also changes with receiver separation because of the different path lengths that are created between the interfering returns. Note that the apparent decrease in received amplitude observed for large negative angles at the widest separation (Figure 5.3) is a result of the loudspeaker's directivity characteristics. In order to better compare the data in the positive angular range, the curves have been plotted together in a smoothed form in Figure 5.4. This figure shows some evidence that the data approach a uniform level at large separation distances.

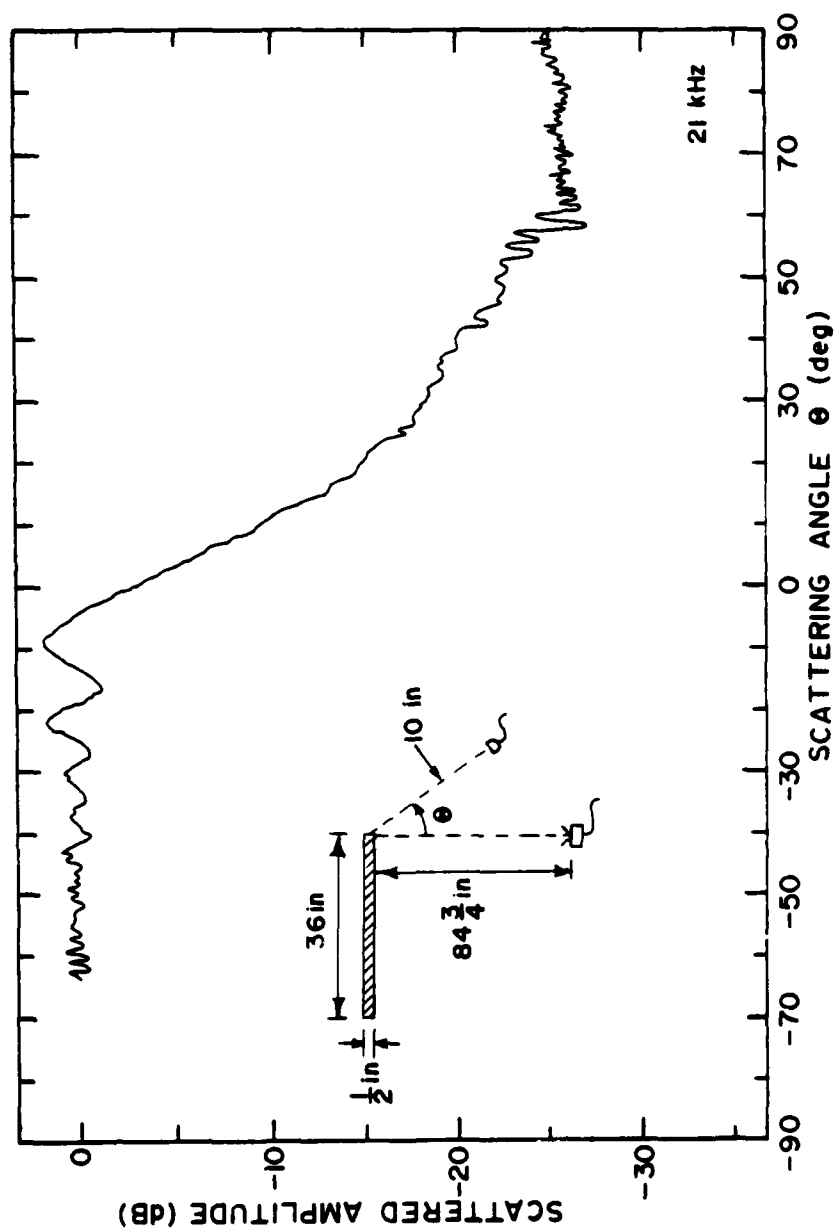


Figure 5.1 Angular distribution of the field scattered by the edge of a baffle into the incident half-space at a distance of 10 inches from the edge. ( $\lambda = .643$  inch)

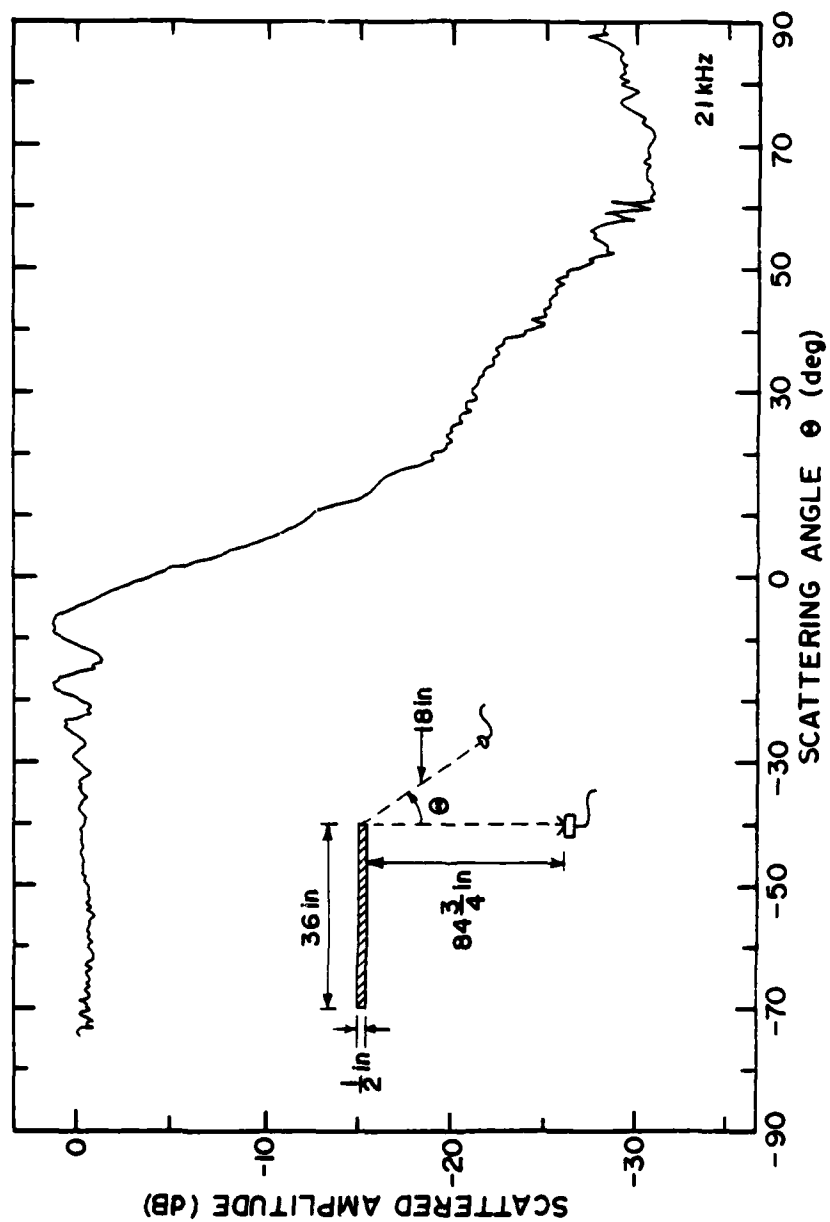


Figure 5.2 Angular distribution of the field scattered by the edge of a baffle into the incident half-space at a distance of 18 inches from the edge. ( $\lambda = .643$  inch)

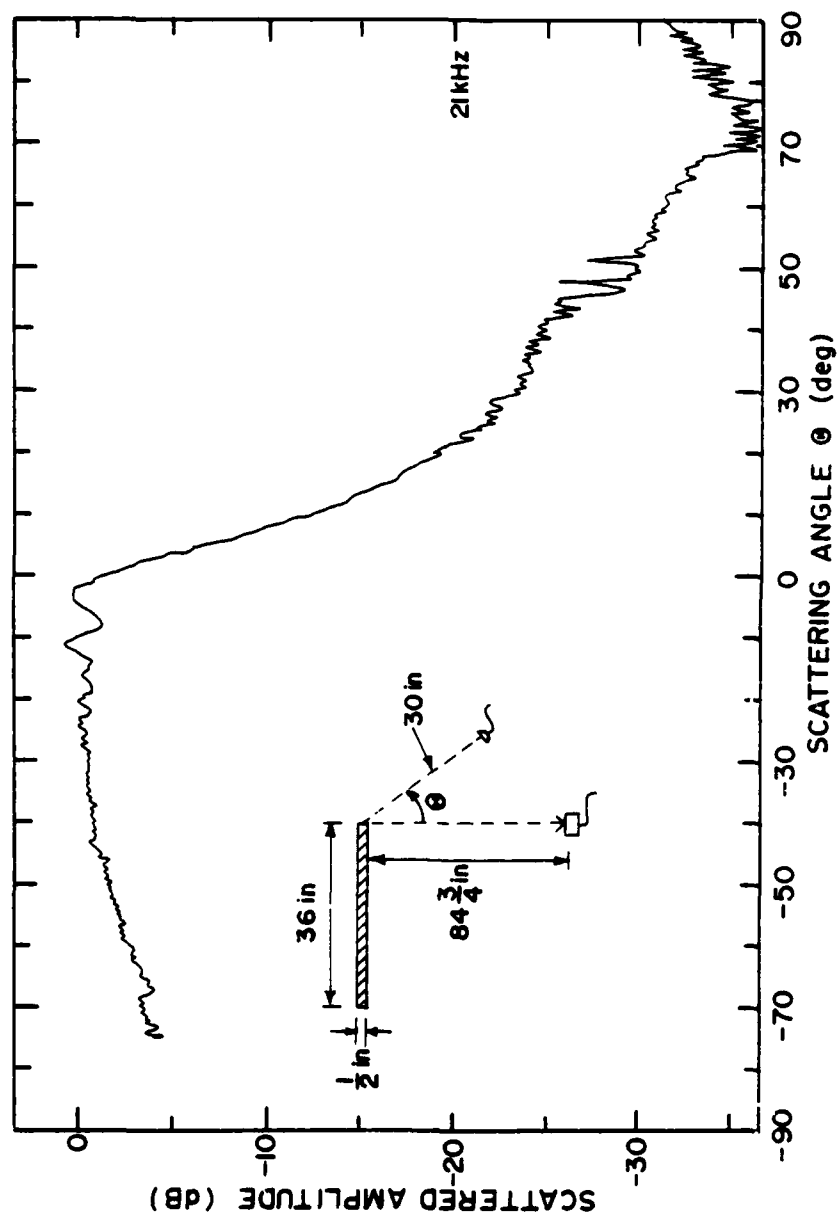


Figure 5.3 Angular distribution of the field scattered by the edge of a baffle into the incident half-space at a distance of 30 inches from the edge. ( $\lambda = .64$  inch)

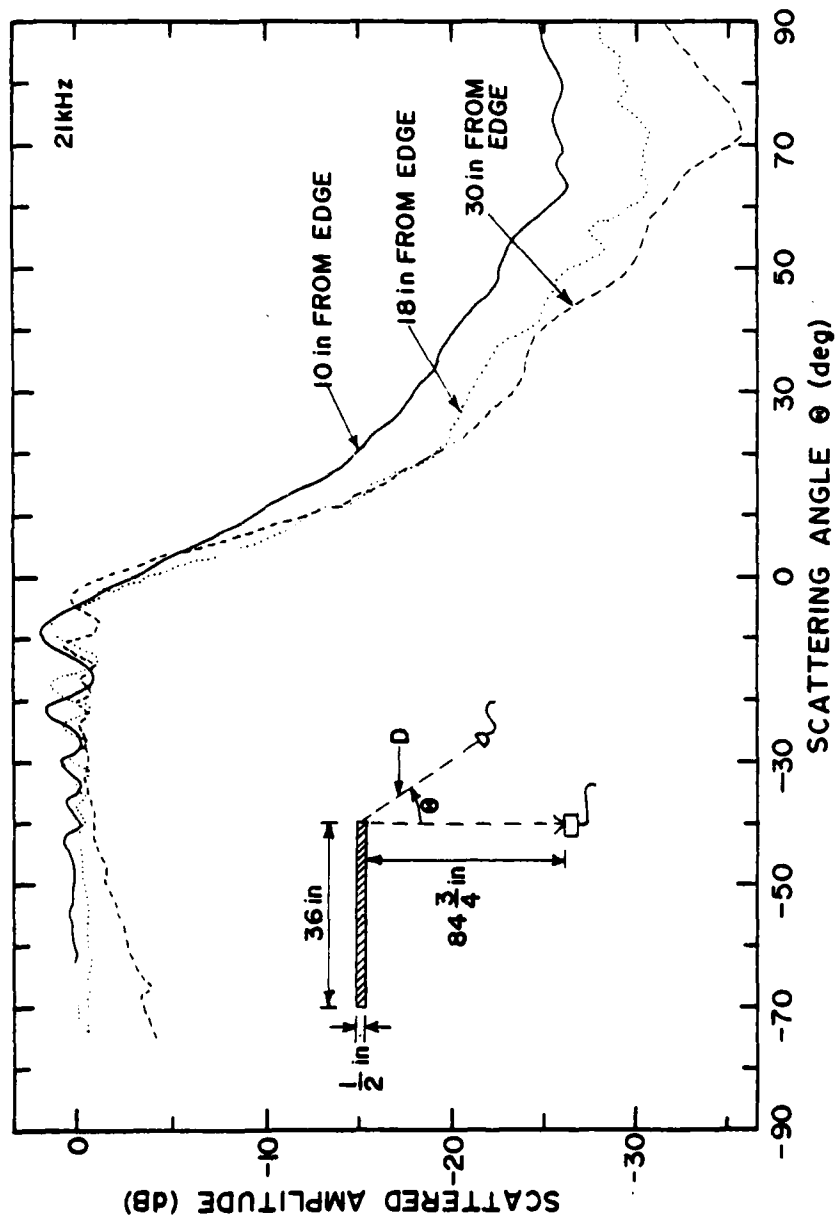


Figure 5.4 Angular distribution of the field scattered by the edge of a baffle into the incident half-space at distances of 10, 18, and 30 inches from the edge. ( $\lambda = .643$  inch)

Figures 5.5, 5.6, and 5.7 summarize the directivity results from the edge in the forward half-space. These curves look very similar to the corresponding curves in the incident half-space, but they nevertheless represent different physical effects. In the angular range of  $90^\circ - 180^\circ$ , the data represent the sum of an incident component and an edge component, while the data in the shadowed region ( $180^\circ - 270^\circ$ ) are defined to be diffraction effects. The similarity between the curves taken in the two half-spaces indicates that the specular reflection from the baffle on the incident side is acting approximately like the incident pulse on the forward-scattering side.

As a further evaluation of the field diffracted by an edge, Figures 5.5 - 5.7 compare the directivities obtained with and without a damping material applied to the shadowed surface of the baffle. The material used is the same ribbed corduroy that was used in the damped-spheroid experiments with the ribs oriented horizontally (see Section 4.2.3). Little or no effect from the damping material is observed until the microphone gets fairly close to the surface of the baffle (i.e., for angles in the vicinity of  $270^\circ$ ). Note that the oscillations in Figure 5.7 at about  $220^\circ$  are caused by interferences with a pulse originating at the opposite edge of the baffle from the tested edge. Finally, the three damped-baffle curves are shown together (in a smoothed form) in Figure 5.8. The steep transitions observed in this figure as the shadow boundary is crossed are very similar to those noted earlier in this section, which occurred on the incident side of the baffle when the reflected shadow boundary was crossed (Figure 5.4).

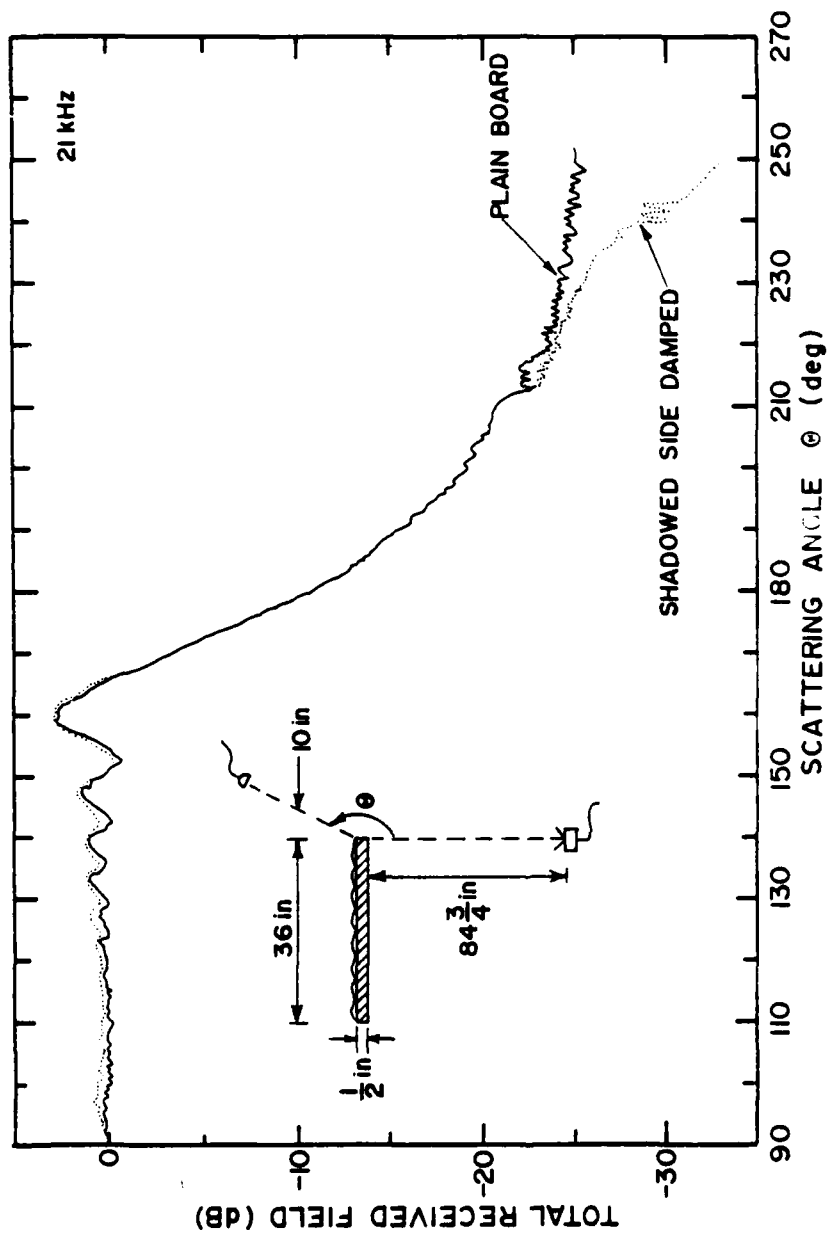


Figure 5.5 Total received field angularly distributed about the edge of a rectangular baffle in the forward half-space at 10 inches from the edge, both with and without damping material on the shadowed side of the baffle. ( $\lambda = .643$  inch)

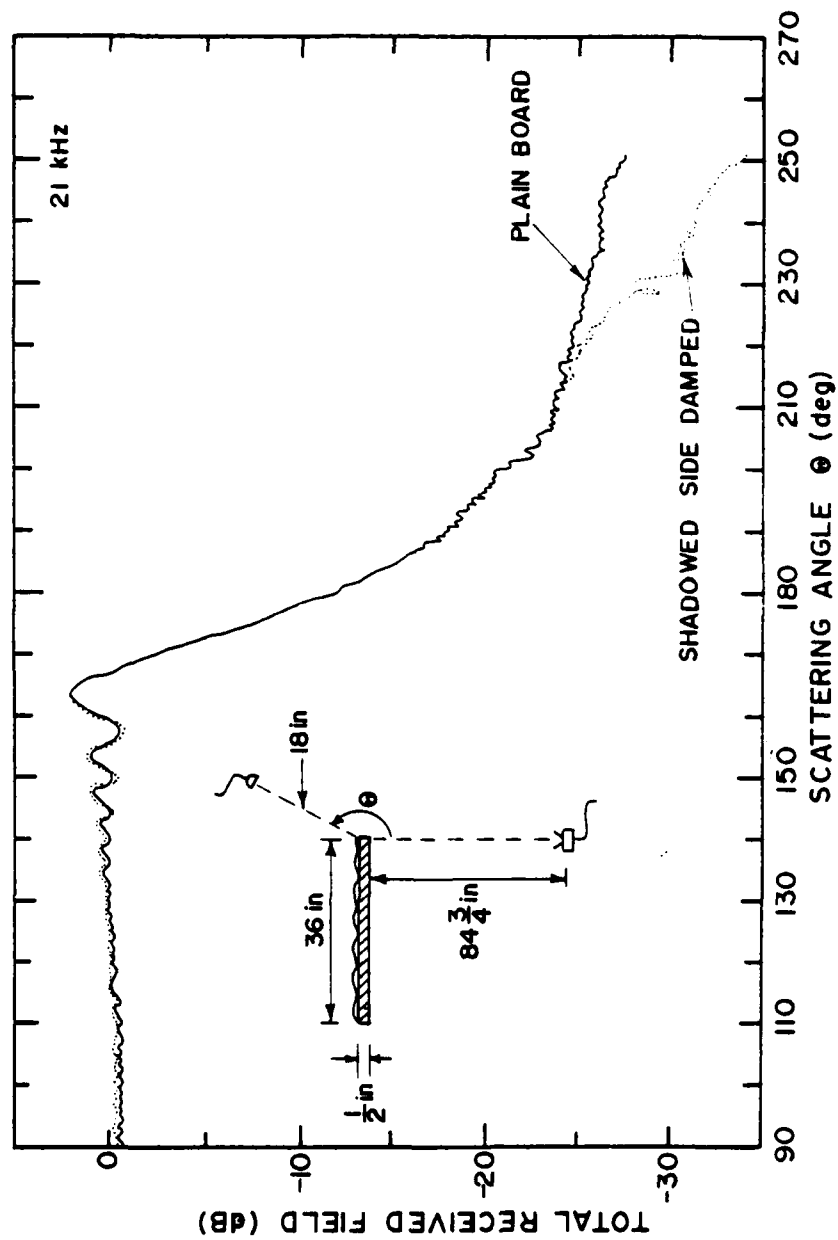


Figure 5.6 Total received field angularly distributed about the edge of a rectangular baffle in the forward half-space at 18 inches from the edge, both with and without damping material on the shadowed side of the baffle. ( $\lambda = .643$  inch)



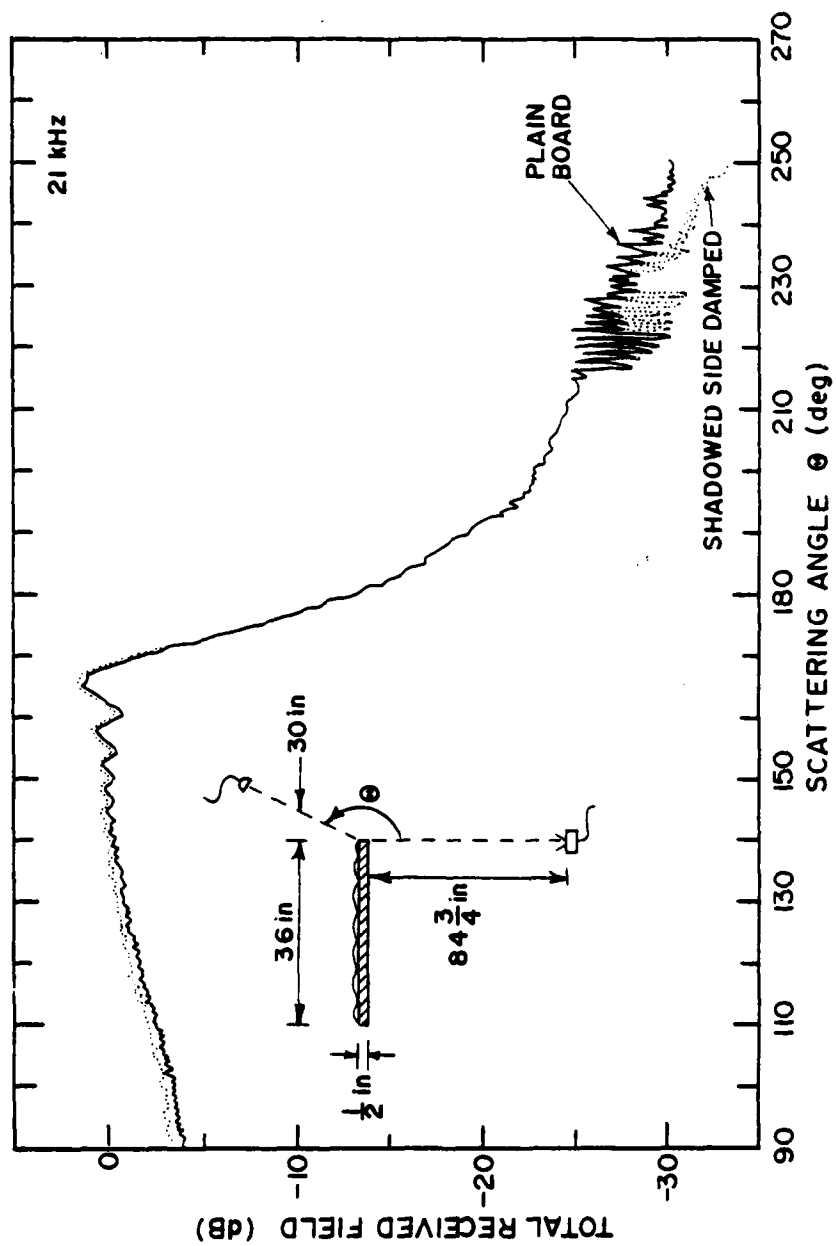


Figure 5.7 Total received field angularly distributed about the edge of a rectangular baffle in the forward half-space at 30 inches from the edge, both with and without damping material on the shadowed side of the baffle. ( $\lambda = .643$  inch)

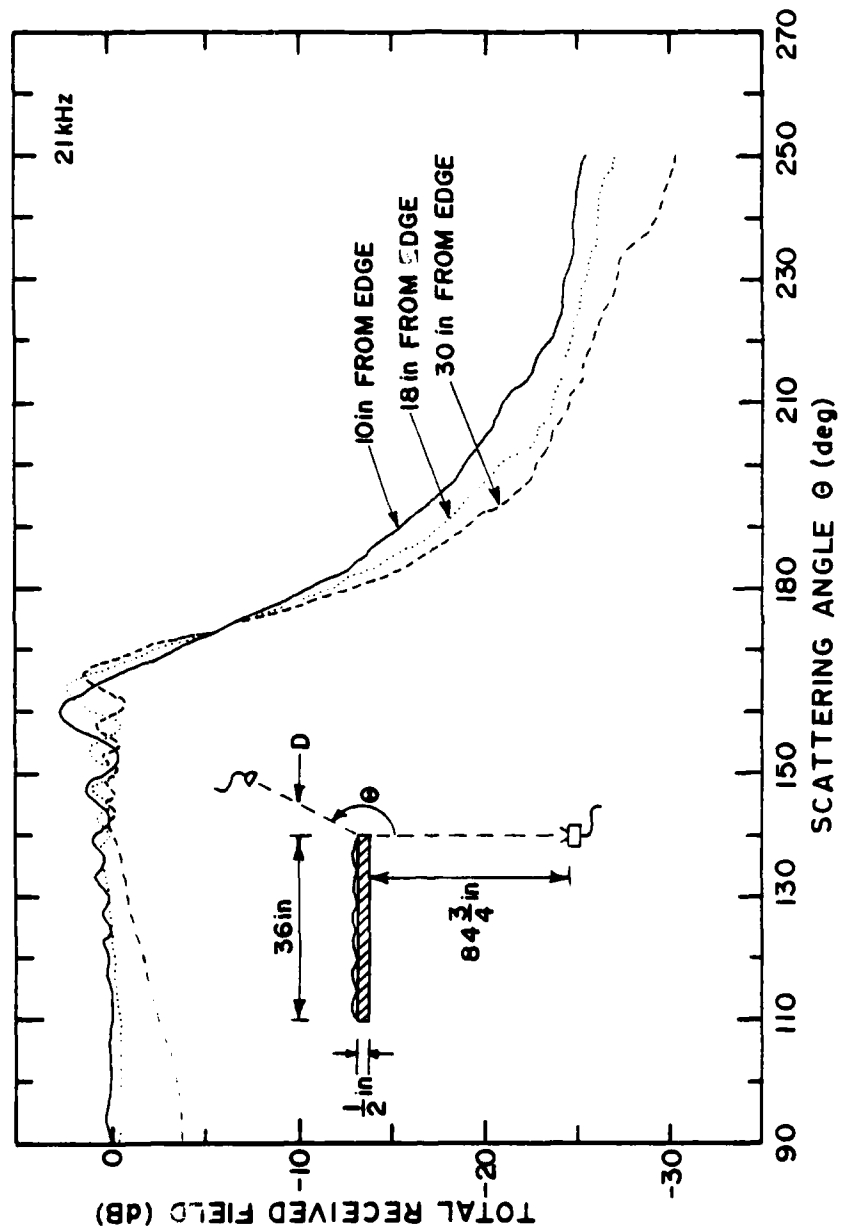


Figure 5.8 Total received field angularly distributed about the edge of a rectangular baffle in the forward half-space at 10, 18, and 30 inches from the edge with damping material on the shadowed side of the baffle. ( $\lambda = .643$  inch)

### 5.1.2 Field Along the Shadowed Side of the Baffle

Based on the results of the previous section, a decision was made to investigate the propagation of both incident and edge-generated fields along the surface of the baffle. Such results are intuitively useful for understanding the effects of surface impedance on diffraction phenomena. They are also important, for example, to aid the interpretation of the Malyuzhinets (1958) stationary-phase solution. This solution vanishes for grazing propagation when even a small amount of absorption is present along an infinite surface.

To perform the measurements, a translating device was rigged to scan the 1/8-inch microphone parallel to the surface of the baffle at a fixed distance. Figure 5.9 shows the results obtained for grazing incidence on the rigid baffle. The curves are all normalized to the field incident at the edge, and they have been offset in 5 dB steps in order to plot all on the same graph. As a reference, the field present without the baffle (obtained by applying spherical spreading losses to the field incident at the edge) is also included. The data obtained with the baffle in place generally follow the slope of the data determined without the baffle, but there are small shifts in the relative levels at the smaller microphone-to-baffle separations. It is interesting that this separation distance must approach 6 inches (approximately 9 wavelengths) before the effect of the baffle is no longer visible.

Figures 5.10 - 5.14 present the data obtained for the field along the baffle when different incidence angles were used. The results for  $180^\circ$  (grazing incidence) are the same as those of Figure 5.9. The

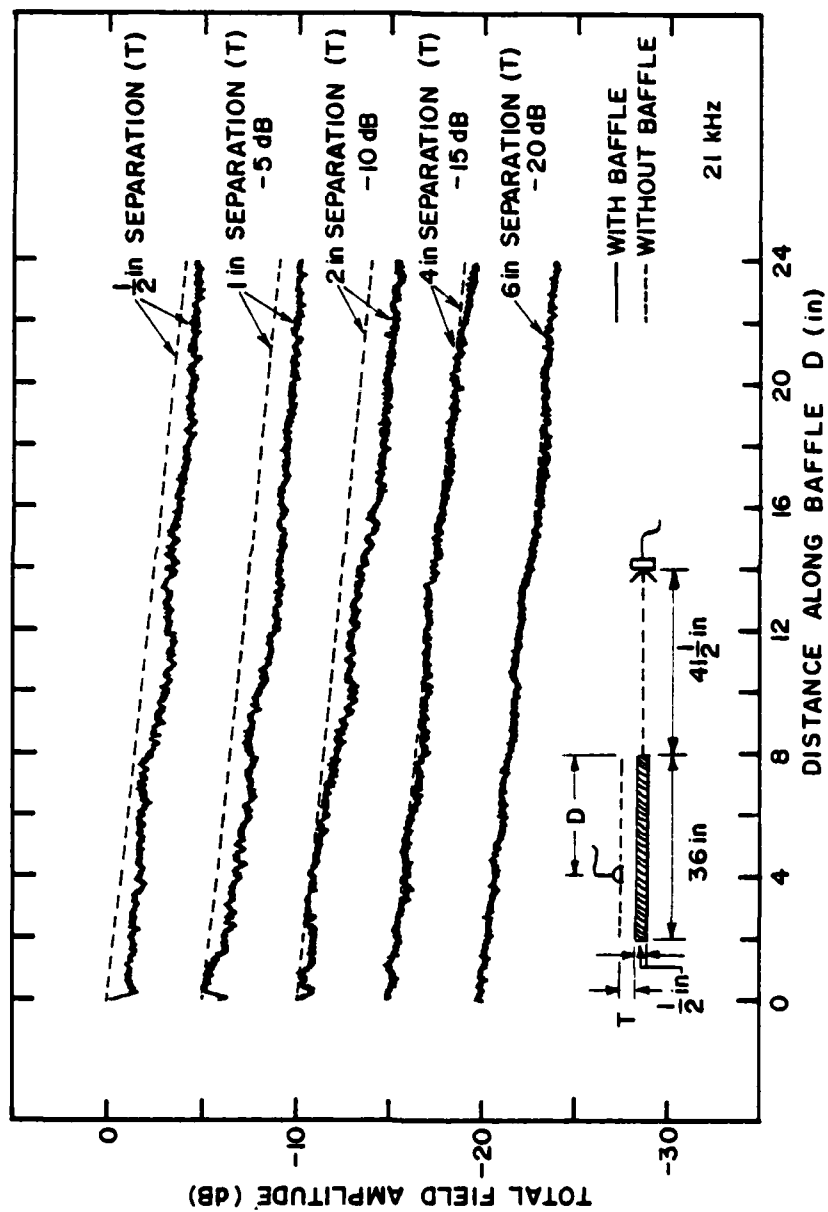


Figure 5.9 Field measured parallel to a rigid finite baffle for grazing incidence.

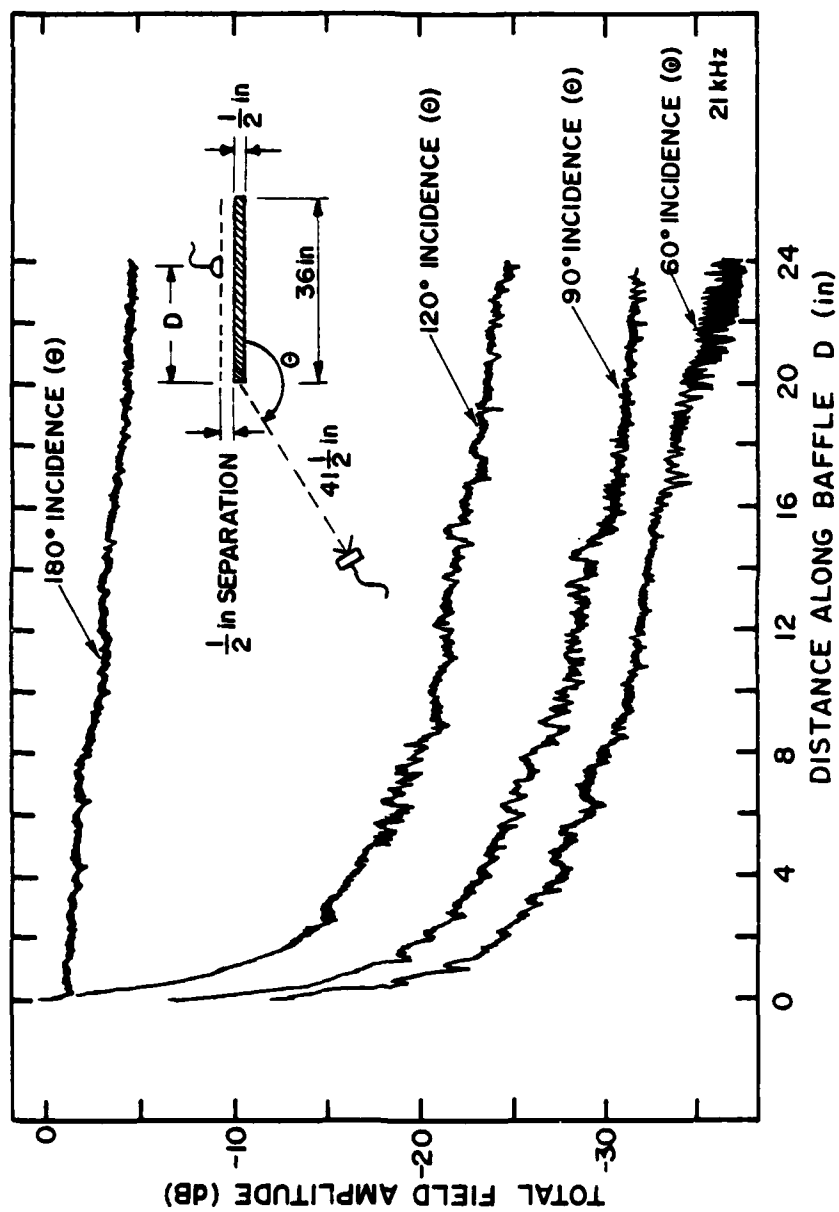


Figure 5.10 Field measured parallel to a rigid finite baffle at a distance of 1/2 inch for several angles of incidence on the edge.

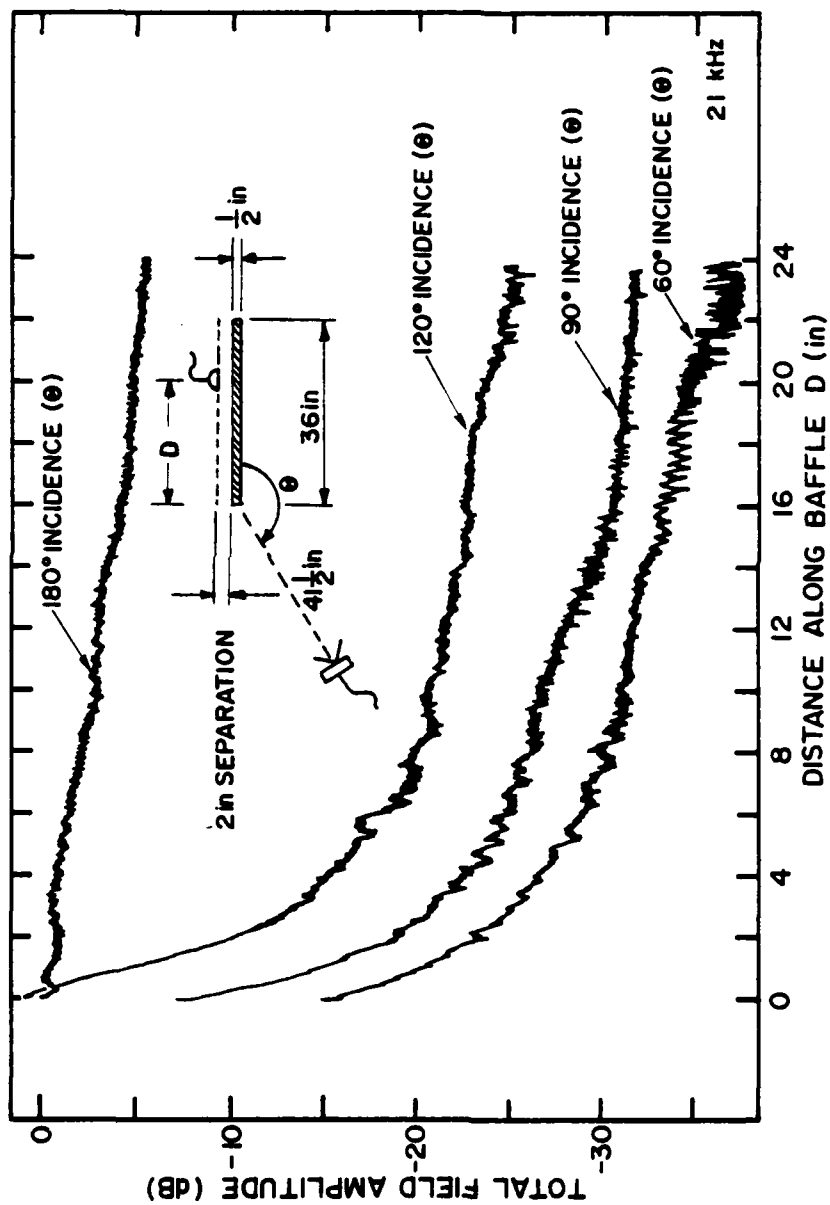


Figure 5.11 Field measured parallel to a rigid finite baffle at a distance of 2 inches for several angles of incidence on the edge.

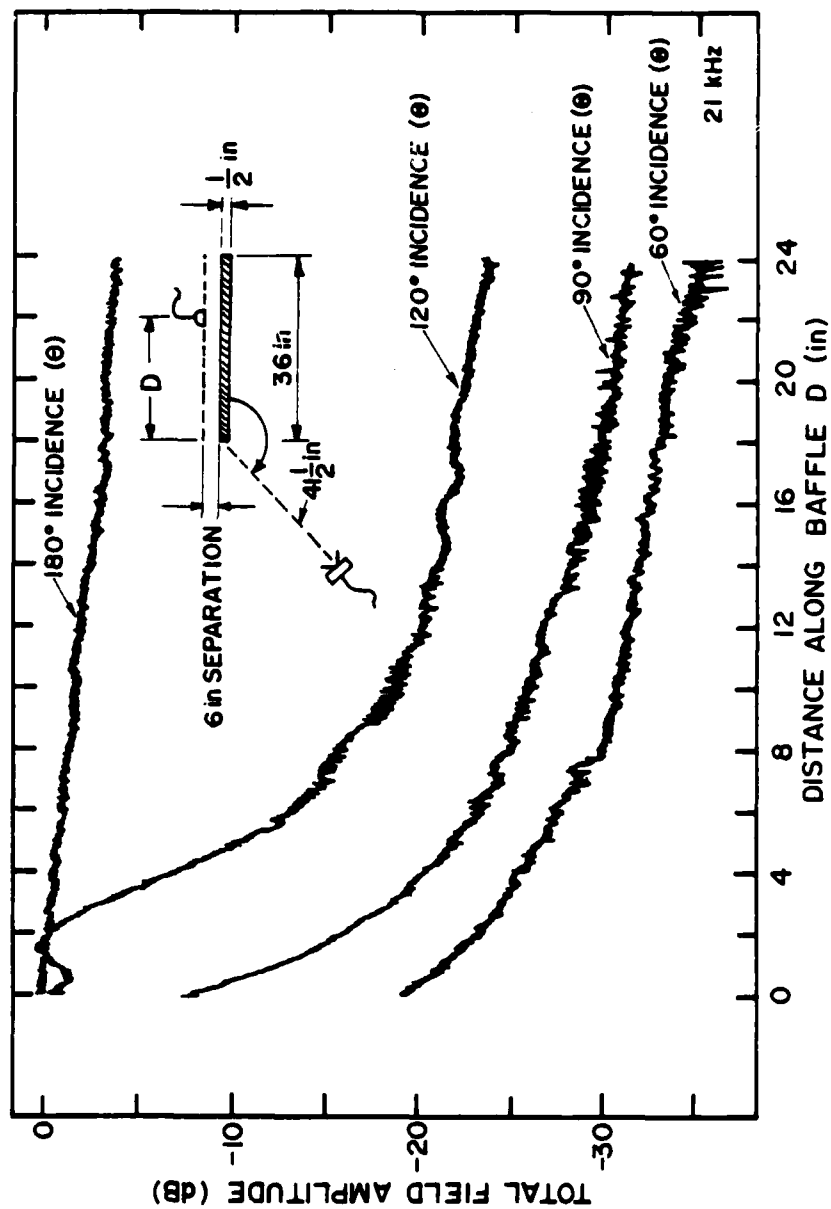


Figure 5.12 Field measured parallel to a rigid finite baffle at a distance of 6 inches for several angles of incidence on the edge.

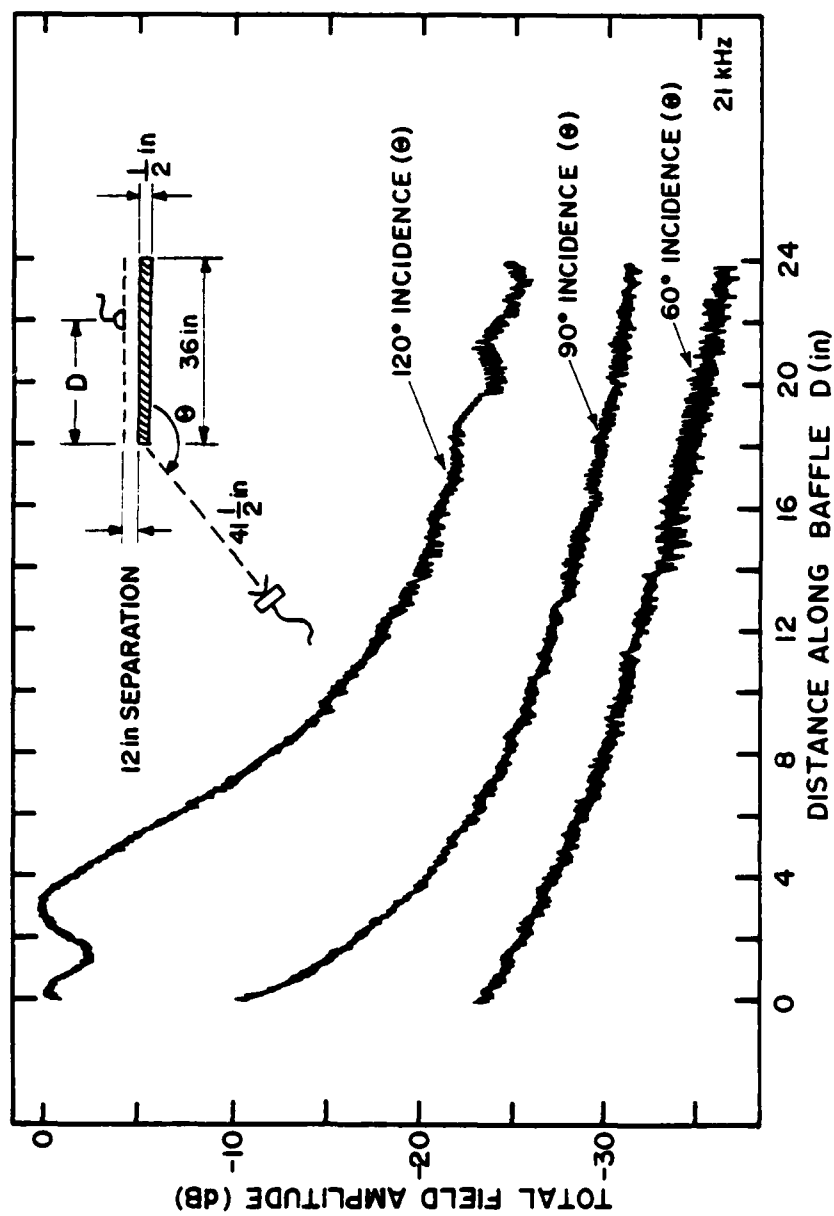


Figure 5.13 Field measured parallel to a rigid finite baffle at a distance of 12 inches for several angles of incidence on the edge.



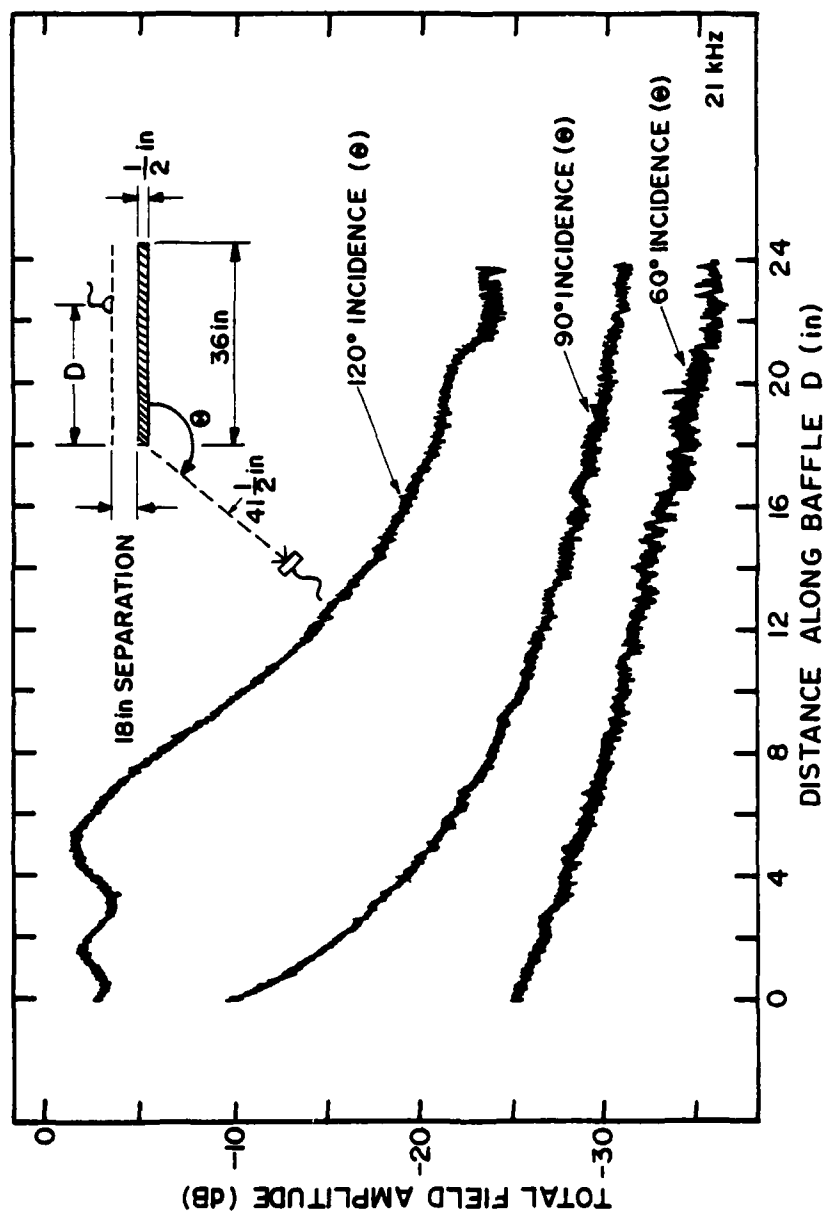


Figure 5.14 Field measured parallel to a rigid finite baffle at a distance of 18 inches for several angles of incidence on the edge.

results at the other three incidence angles were recorded in the geometrical shadow region and are thus associated with an edge-diffracted field. The variations in incidence angle appear to impart constant shifts in the field amplitude that are essentially determined very near the edge. Even at the largest distance away from the baffle (Figure 5.14), the recorded curves appear to approach a common asymptote, determined only by the incidence angle, as the receiver moves deeper into the shadow and away from the vicinity of the edge. The transition region near the edge grows larger as the microphone gets further from the baffle because the pressure has more time to diffuse into the shadowed region. At the larger microphone-to-baffle separations and  $120^\circ$  incidence, interferences are observed because the incident field (as well as the edge field) reaches the microphone at locations near the edge.

When the shadowed side of the baffle is treated with damping material, the field along the baffle is substantially different than that described in the previous paragraph for the rigid baffle. Figures 5.15 - 5.17 show results obtained for grazing incidence at various microphone-to-baffle separations. The damping material is the same as that used with the damped spheroids (see Section 4.2.3). For reference, a smoothed plot of the corresponding plain-baffle results is included for each case presented. A significant attenuation (over the plain-baffle case) is noted for a separation of  $1/2$  inch (Figure 5.15), with somewhat less attenuation observed at a 1-inch separation (Figure 5.16). However, the field amplitudes are actually increased in some cases at the larger separations of 2, 4, and 6 inches (Figure 5.17). The latter

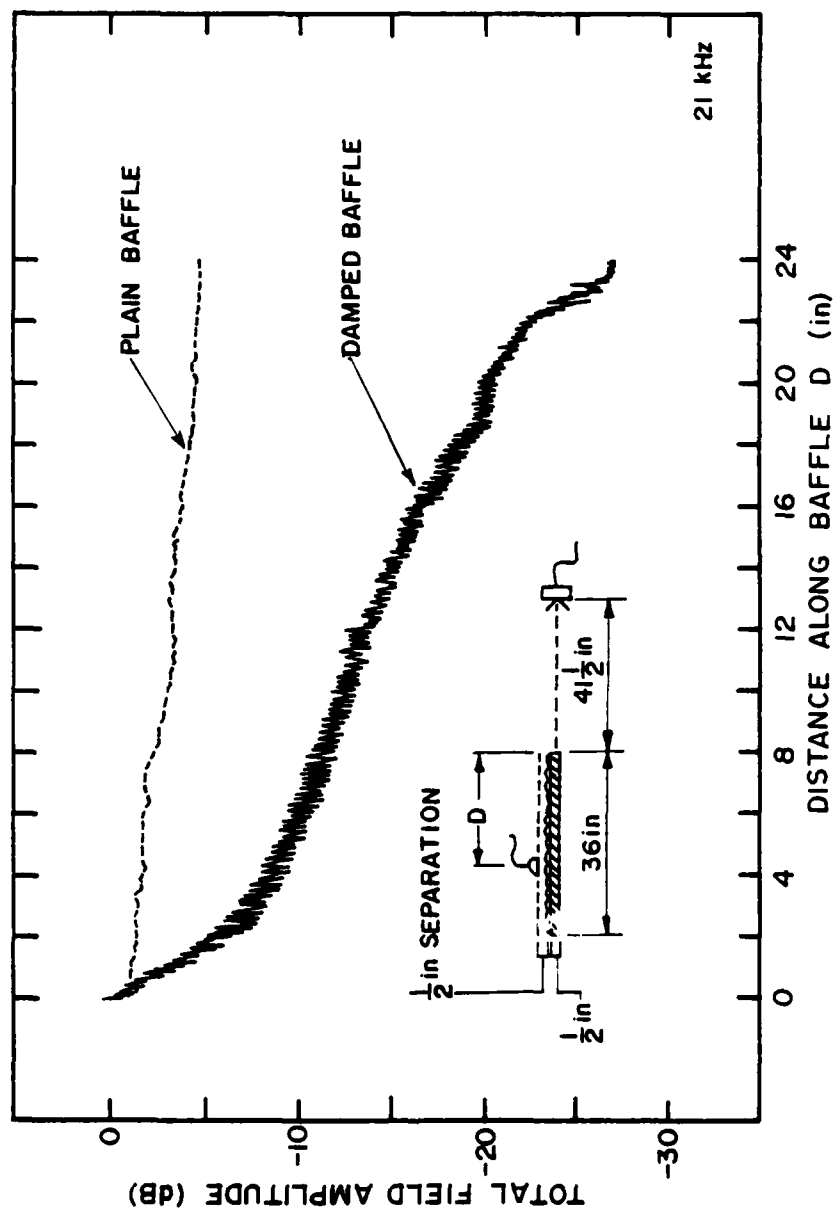


Figure 5.15 Field measured parallel to both rigid and damped baffles at a distance of 1/2 inch for grazing incidence.

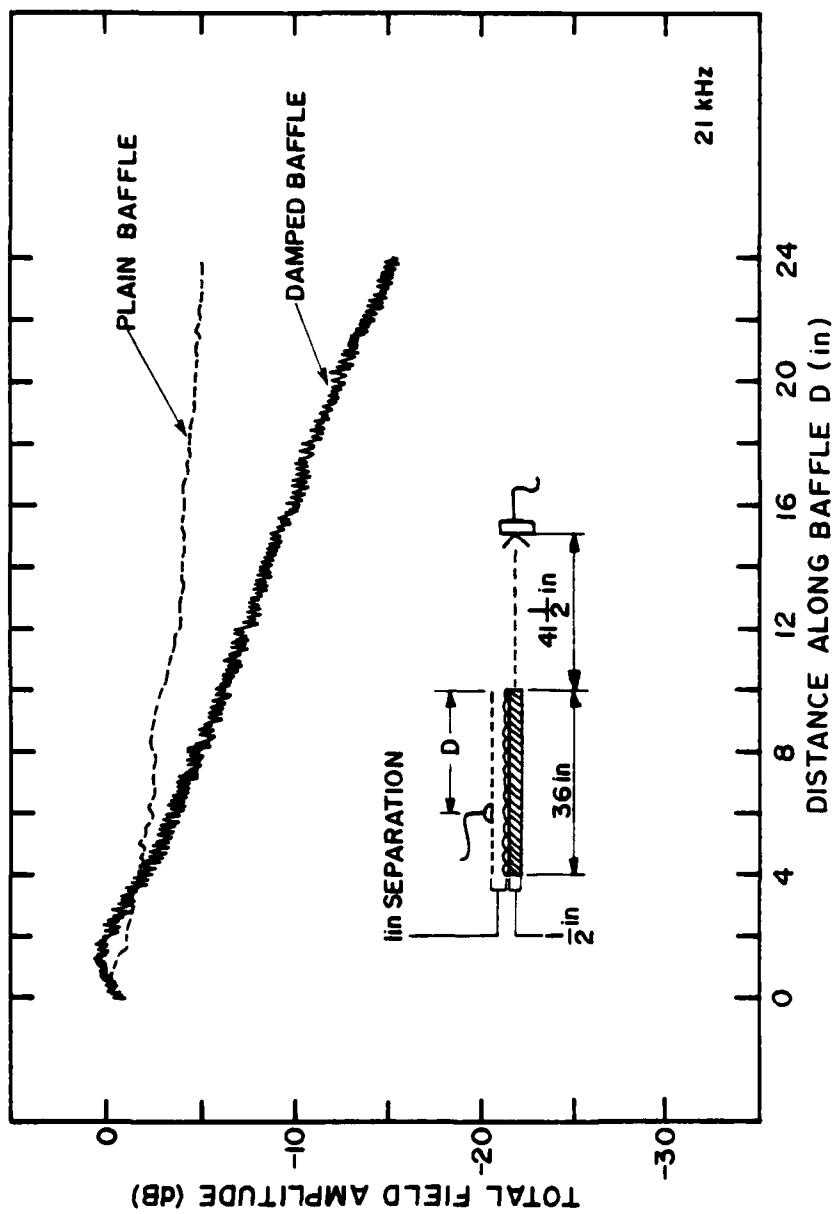


Figure 5.16 Field measured parallel to both rigid and damped baffles at a distance of 1 inch for grazing incidence.

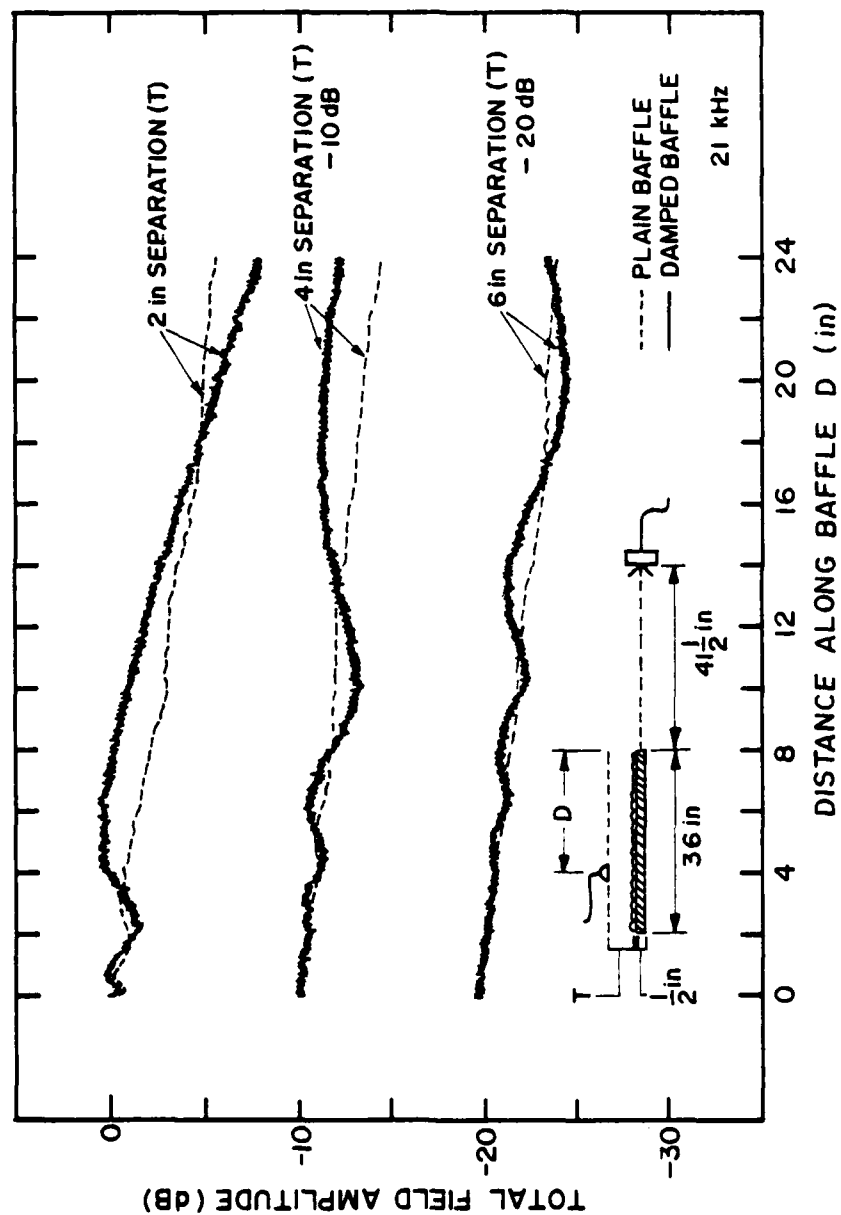


Figure 5.17 Field measured parallel to both rigid and damped baffles at distances of 2, 4, and 6 inches for grazing incidence.

trend may be related to the fact that the damping material makes the surface somewhat rougher than the surface of the plain baffle. Note that the effect of the damping material does accumulate as the field propagates over a greater length of material, but this accumulation does not begin precisely at the edge.

The attenuation caused by surface damping is greater than any presented yet for the edge-generated fields arising from incidence at angles of less than  $180^\circ$ . Figures 5.18 - 5.23 compare the data for damped and undamped baffles at  $120^\circ$  incidence and at various microphone-to-baffle separation distances. The relative attenuation at the 1/2-inch distance (Figure 5.18) is more than double that discussed in the previous paragraph for the corresponding grazing-incidence case. Furthermore, this attenuation is noted at much larger distances from the baffle. A sizeable attenuation is observed at a distance as large as 6 inches (Figure 5.21), and a slight effect is noted even at an 18-inch distance (Figure 5.23). The boost observed at some microphone-to-baffle distances in the grazing-incidence case has no counterpart in this series of data. Note that, for  $120^\circ$  incidence, the effect of the damping material is noted much closer to the edge than was observed for grazing incidence. In general, the effect of surface damping on a diffracted field appears to extend out from the surface considerably more than a wavelength.

The effect of different incidence angles on the attenuation of the diffracted field along the baffle is presented in Figures 5.24 - 5.29 in comparison with that presented previously for  $120^\circ$  incidence. Note that, while the degree of attenuation in the data does change with the

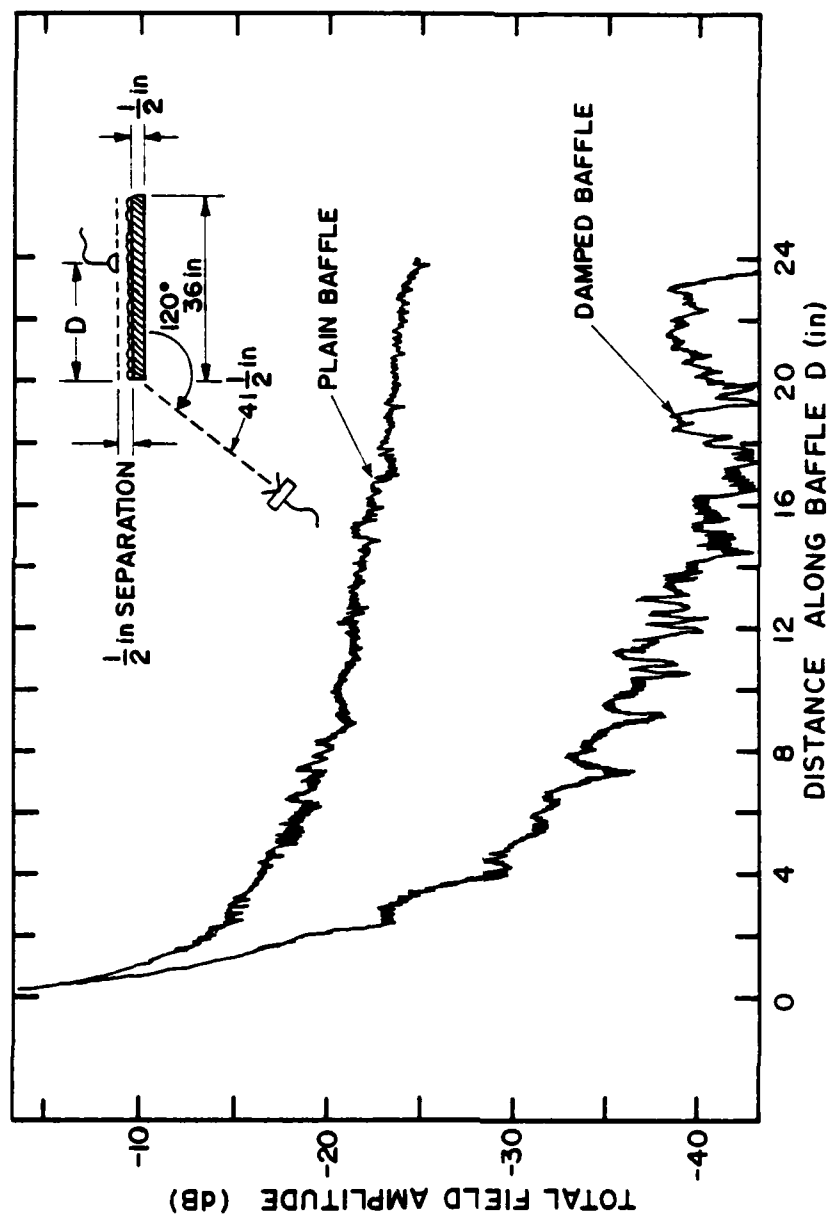


Figure 5.18 Field measured parallel to both rigid and damped baffles at a distance of 1/2 inch for 120° incidence.

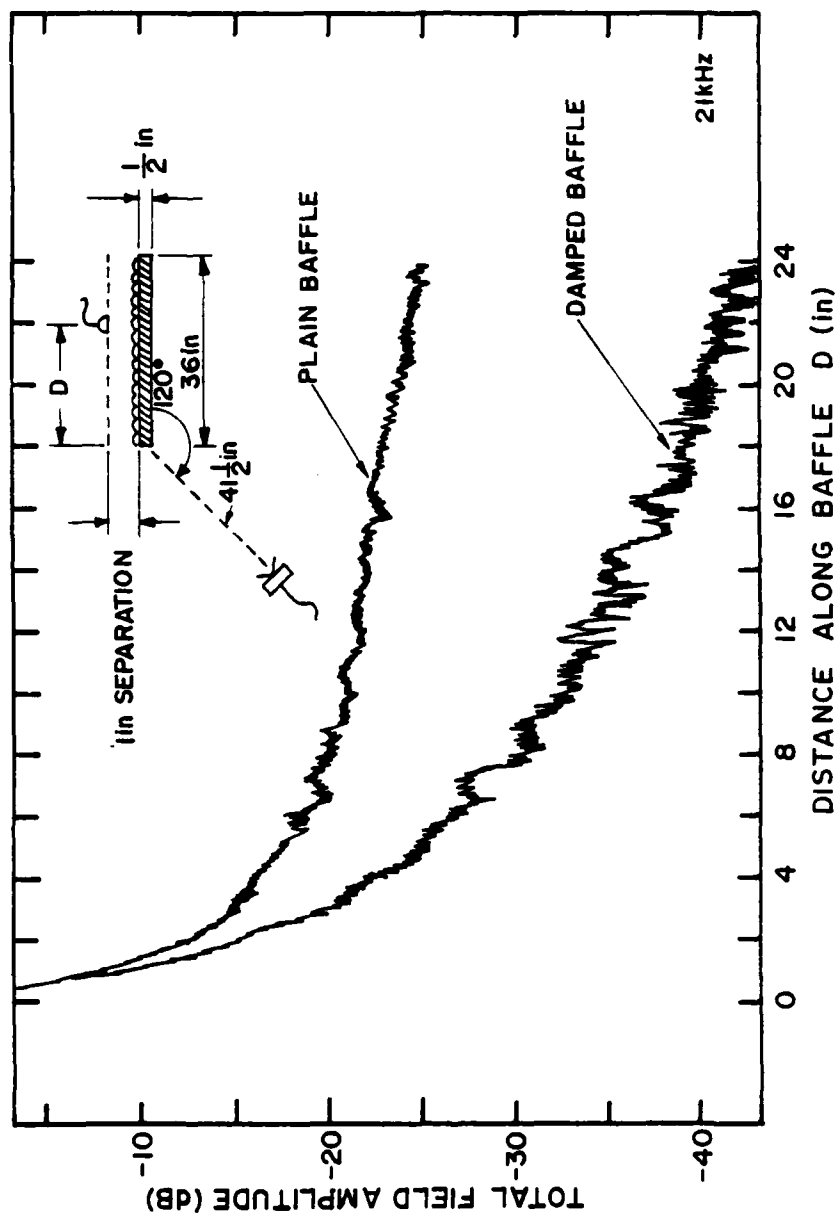


Figure 5.19 Field measured parallel to both rigid and damped baffles at a distance of 1 inch for 120° incidence.



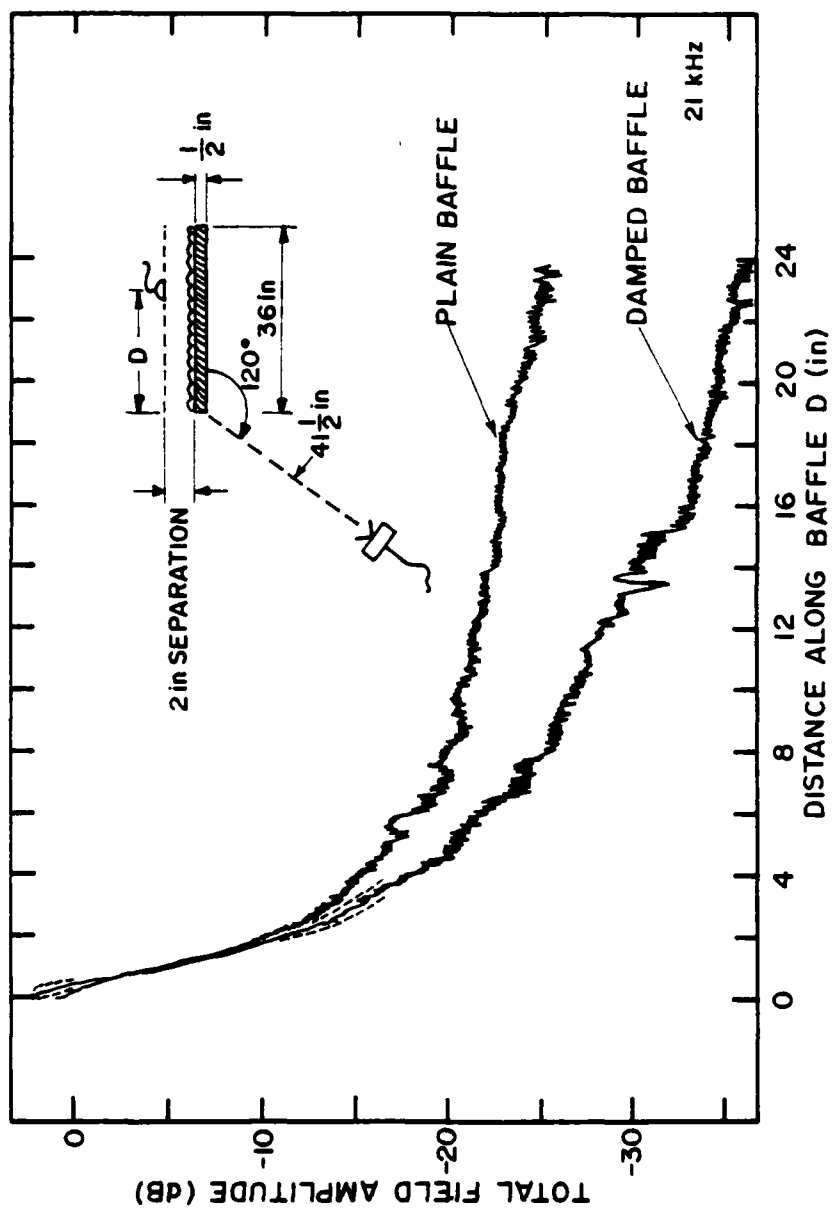


Figure 5.20 Field measured parallel to both rigid and damped baffles at a distance of 2 inches for  $120^\circ$  incidence.

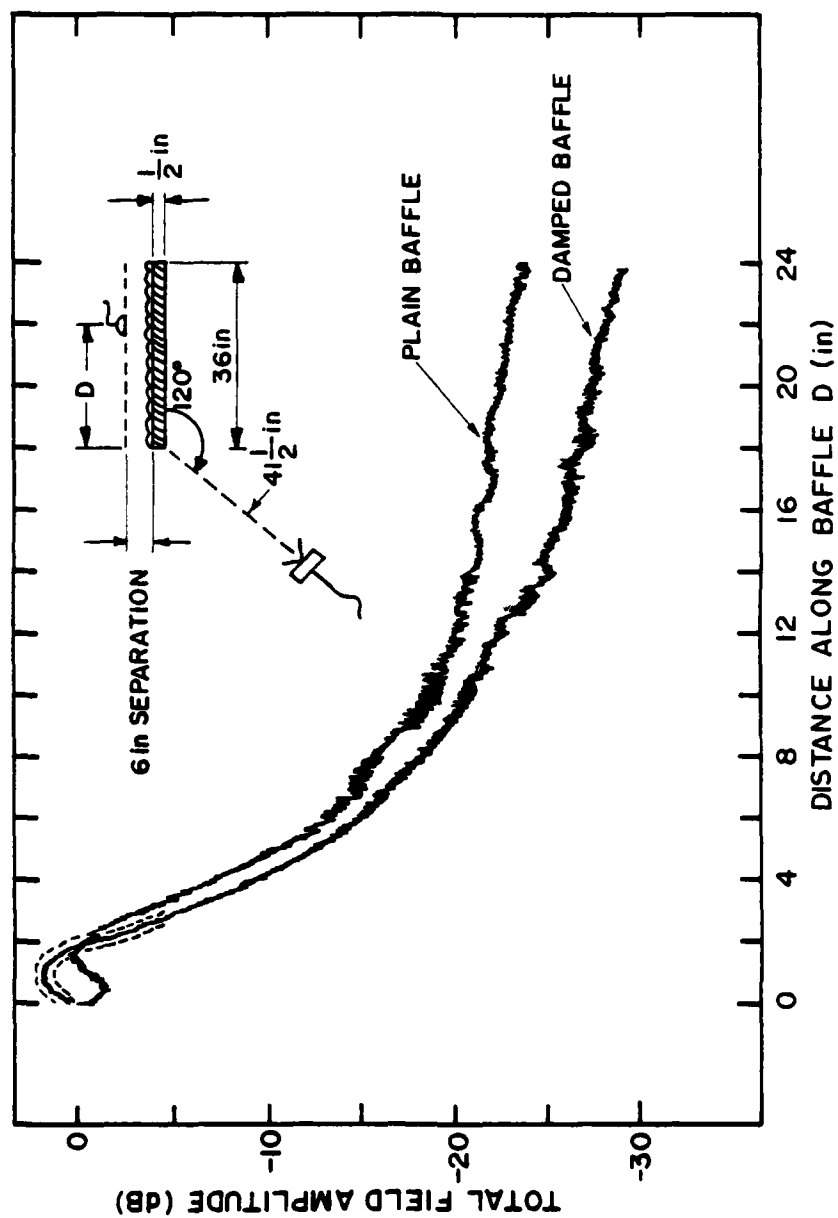


Figure 5.21 Field measured parallel to both rigid and damped baffles at a distance of 6 inches for 120° incidence.

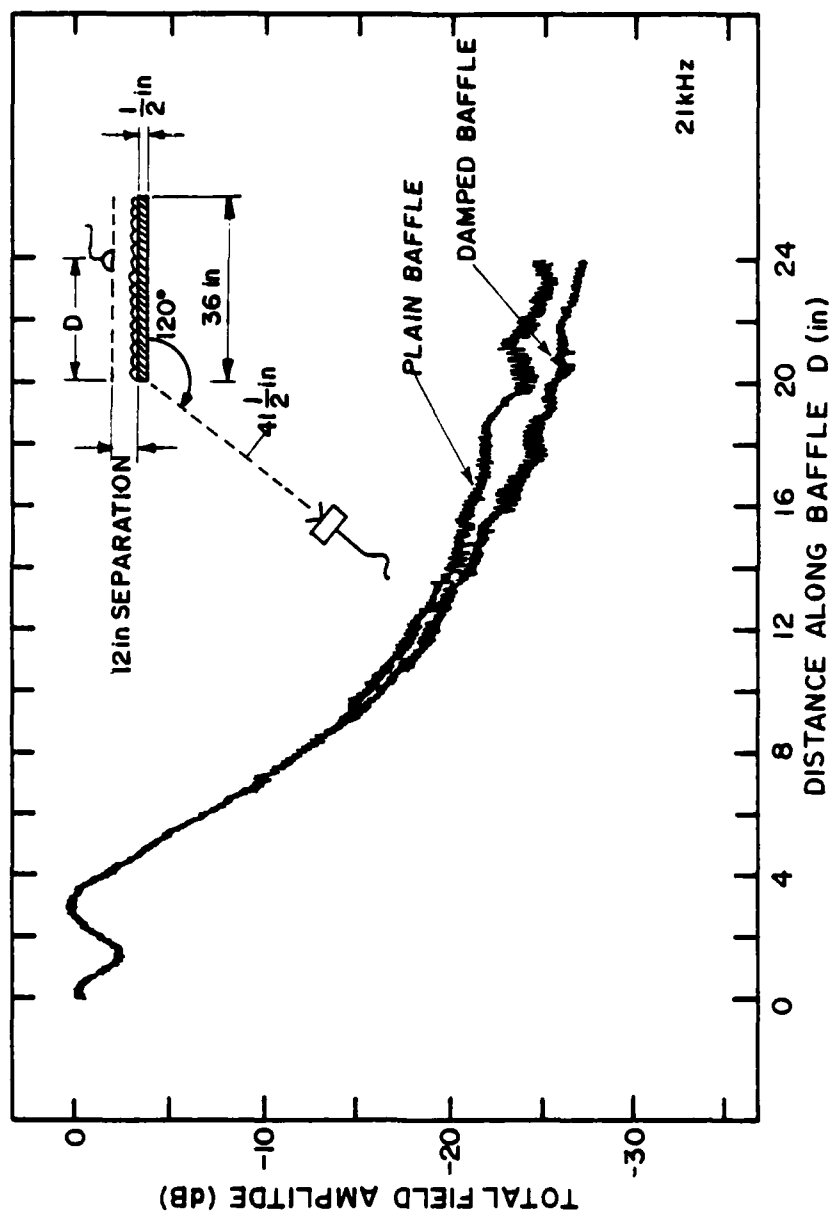


Figure 5.22 Field measured parallel to both rigid and damped baffles at a distance of 12 inches for 120° incidence.

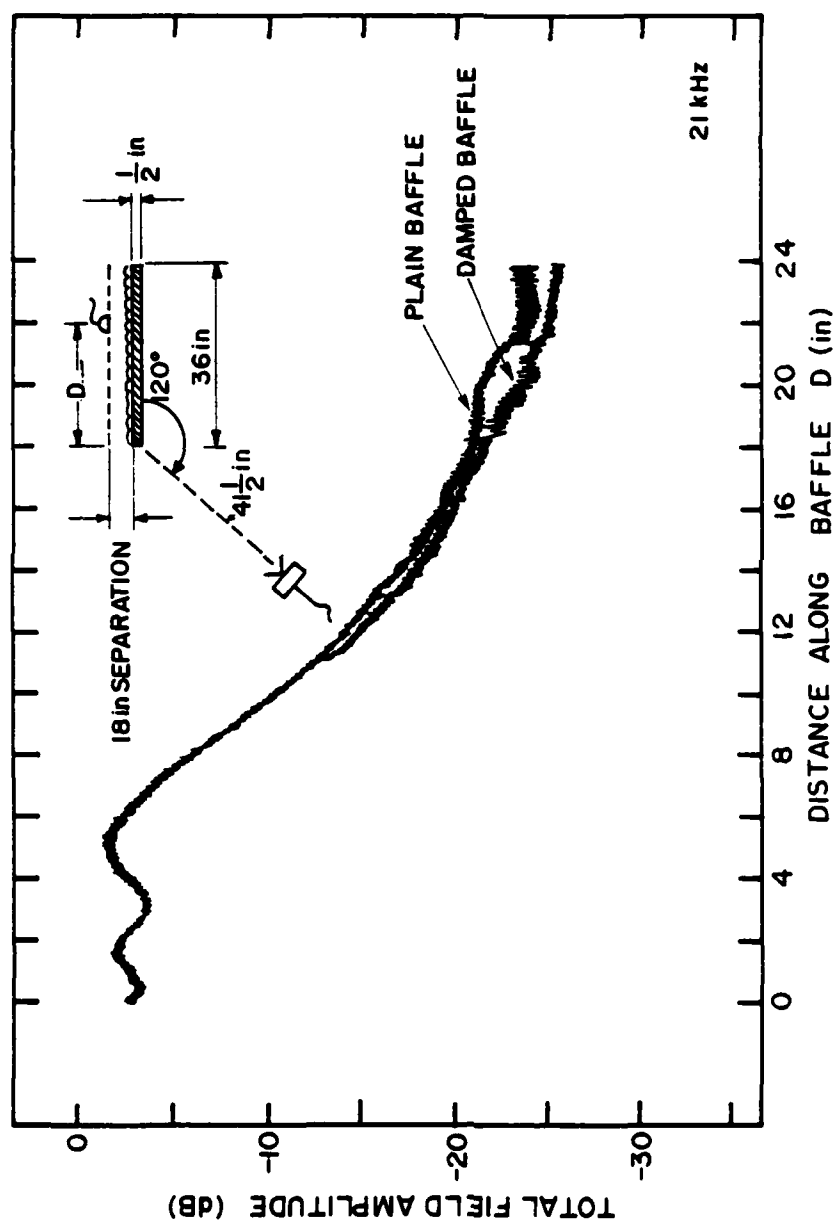


Figure 5.23 Field measured parallel to both rigid and damped baffles at a distance of 18 inches for 120° incidence.

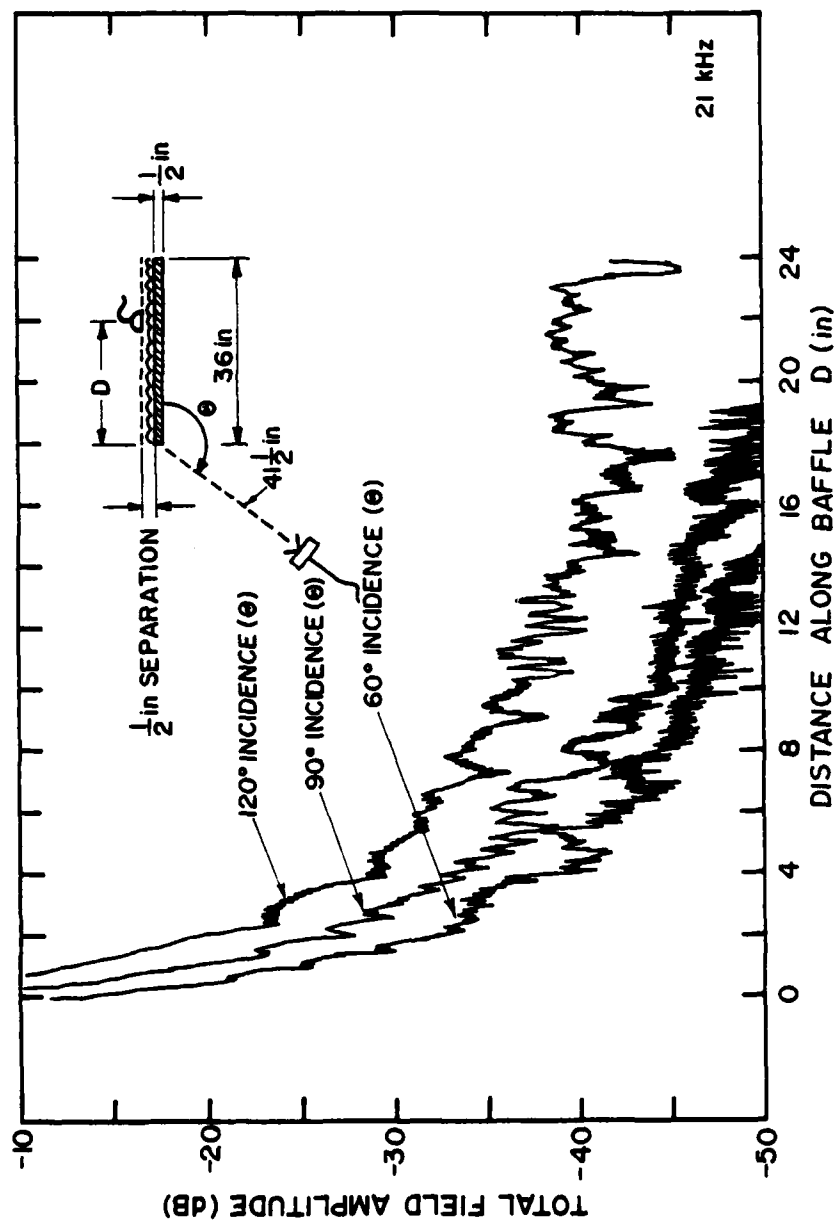


Figure 5.24 Field measured parallel to a damped baffle at a distance of  $\frac{1}{2}$  inch for incidence angles of  $60^\circ$ ,  $90^\circ$ , and  $120^\circ$ .

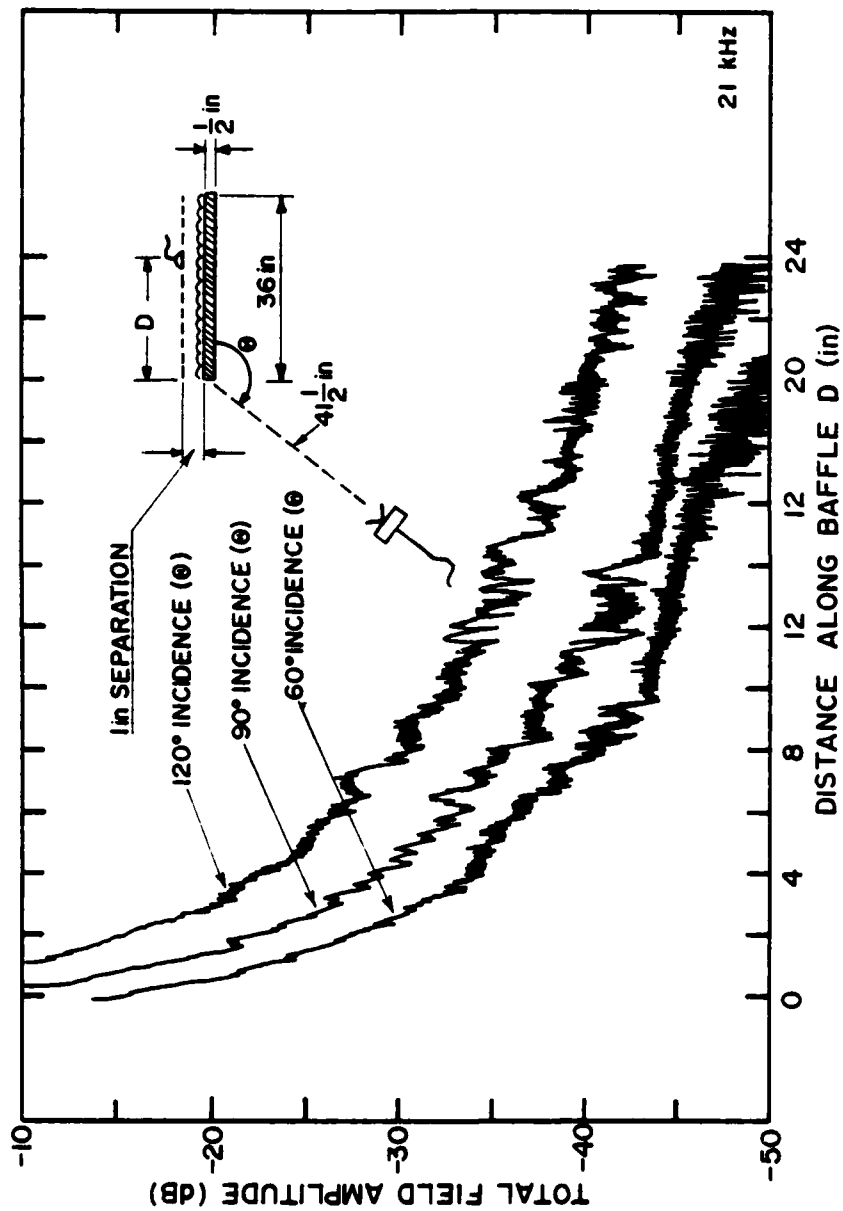


Figure 5.25 Field measured parallel to a damped baffle at a distance of 1 inch for incidence angles of 60°, 90°, and 120°.

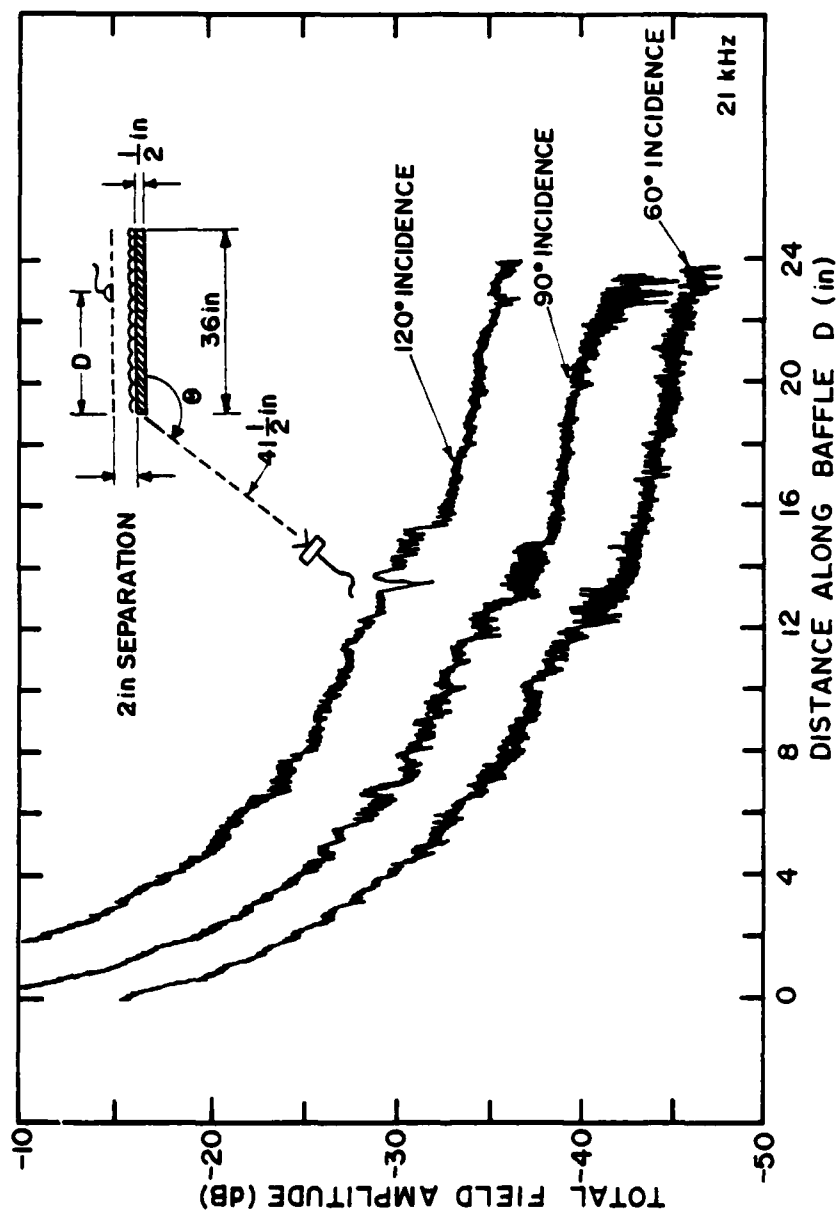


Figure 5.26 Field measured parallel to a damped baffle at a distance of 2 inches for incidence angles of 60°, 90°, and 120°.

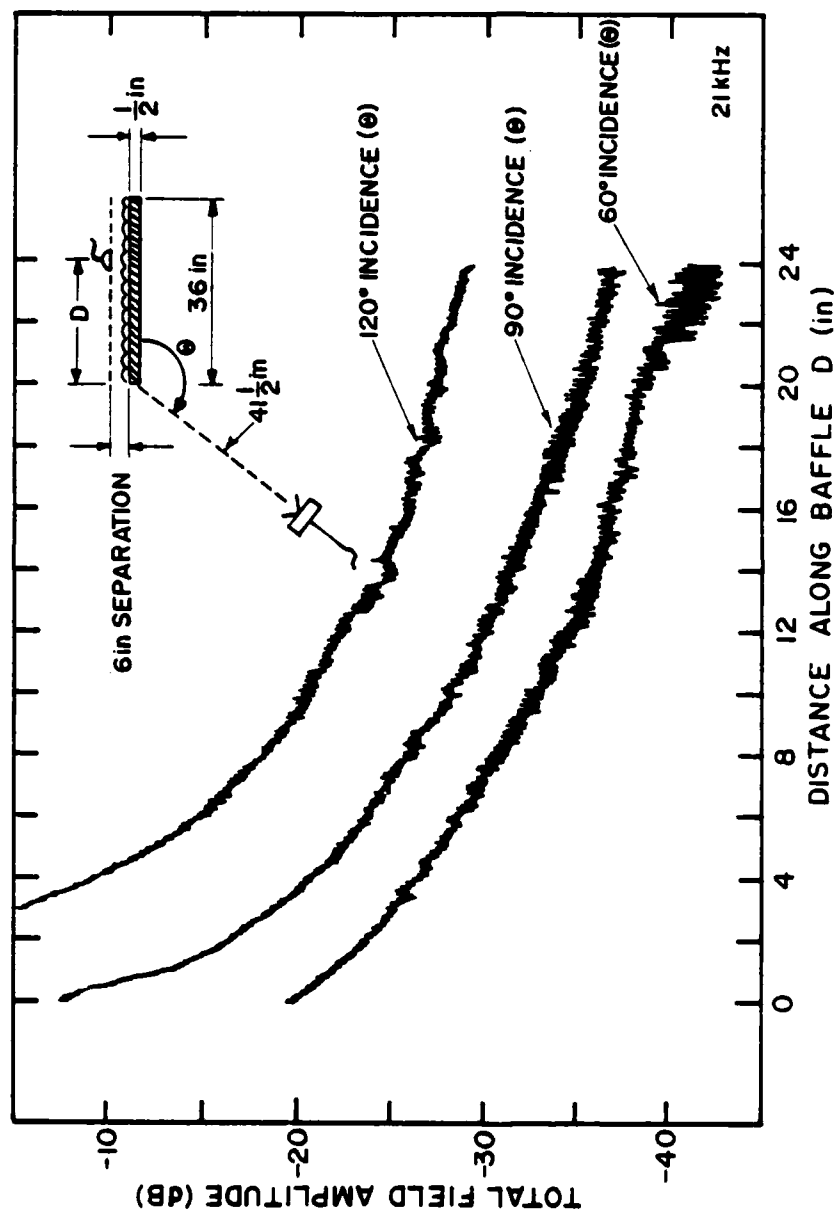


Figure 5.27 Field measured parallel to a damped baffle at a distance of 6 inches for incidence angles of 60°, 90°, and 120°.



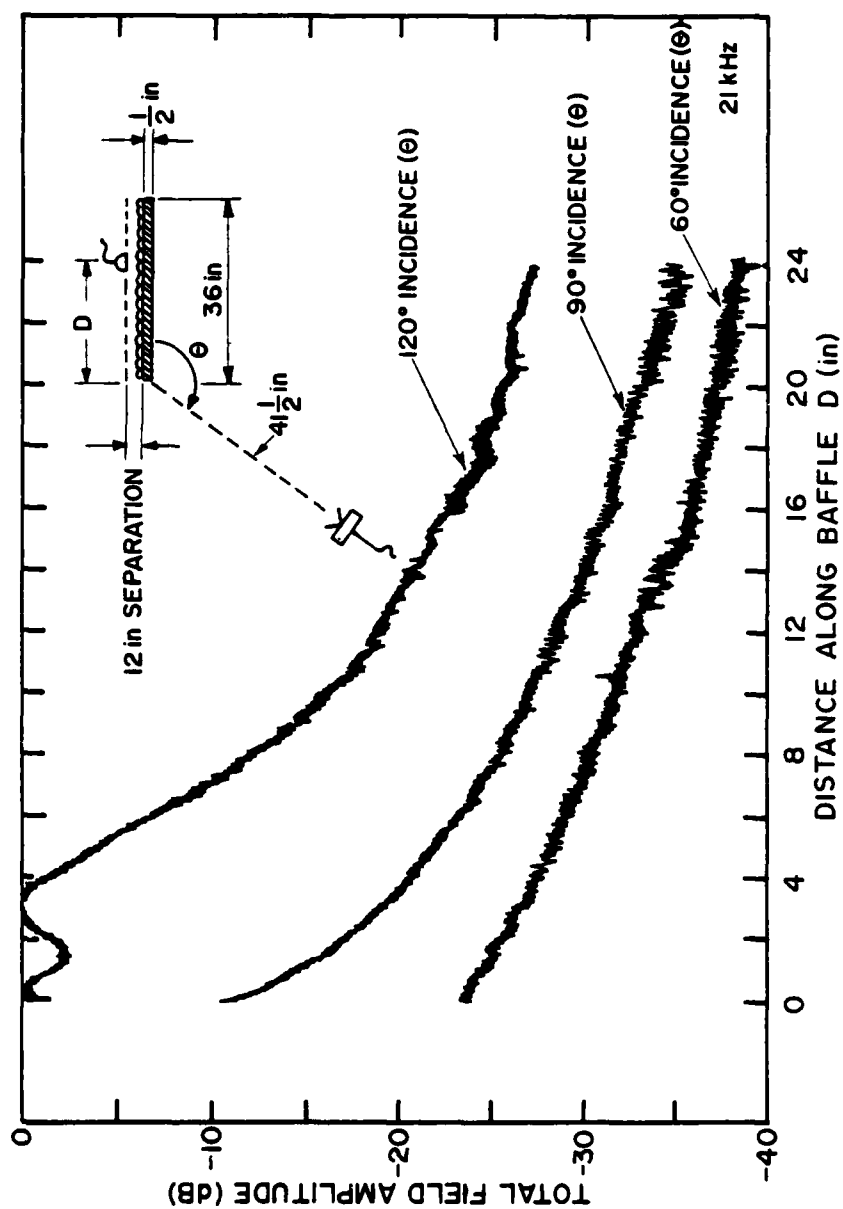


Figure 5.28 Field measured parallel to a damped baffle at a distance of 12 inches for incidence angles of 60°, 90°, and 120°.

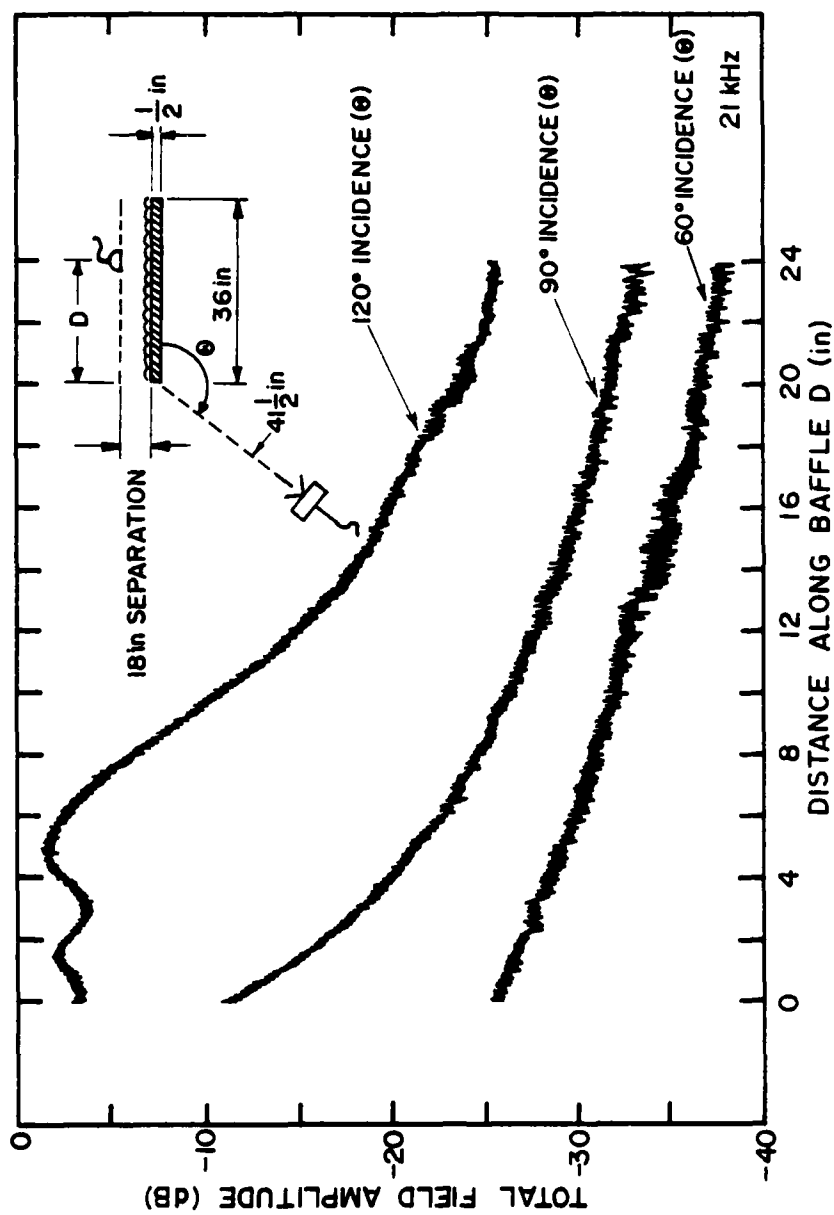


Figure 5.29 Field measured parallel to a damped baffle at a distance of 18 inches for incidence angles of 60°, 90°, and 120°.

separation distance, the relative differences between the data at the three angles shown ( $60^\circ$ ,  $90^\circ$ , and  $120^\circ$ ) remains essentially the same. Furthermore, these constant amplitude differences are the same as those observed previously with the plain baffle (Figure 5.14). It appears that the distribution of the diffracted field that is generated at the edge is not sensitive to the incidence angle, except for a constant multiplicative factor applied to the diffracted field at the moment of its generation. This fact provides some justification for the use of an edge diffraction factor that is not angularly dependent, for example, with the Keller diffraction theory.

## 5.2 Backscattering from Rounded and Square Edges

The data to be described in this section resulted from an investigation into the effect of edge width and shape on the field backscattered by one edge of a large baffle. Two rectangular plywood baffles with dimensions of 20 x 24 inches and thicknesses of  $3/8$  and 2 inches were constructed, in addition to a  $1/8$ -inch-thick fiberboard panel of the same size. One of the 24-inch edges of each baffle was cut and treated to form a square end; the other edge was either machined or fitted with a half-cylinder to form a rounded edge. The baffles were then suspended in the measurement chamber with the 24-inch edges vertical in a manner that permitted rotating the baffles about a vertical line through their centers. For purposes of comparison, three 24-inch-long cylinders with the same diameters as the edge widths were also obtained. Most of the data collected involved backscattered directivities for the two types of edges (i.e., rounded and square) and the cylinders at a frequency of 27 kHz ( $\lambda = 1/2$  inch).

Figure 5.30 is a plot of the directivities obtained from the thinnest edge ( $.25\lambda$ ). The data have been normalized to the broadside return from a 20 x 24-inch baffle (i.e., a large flat baffle). The curve shown for the cylinder was measured at an incidence angle of  $0^\circ$  (for the baffle) and then adjusted for the change in propagation paths from the transducers to the baffle's edge as the baffle is rotated. Spherical spreading on the incident path and cylindrical spreading on the return path were assumed, but the corrections were small enough to be insensitive to any inaccuracies in these assumptions. Note that the returned levels from the rounded edge and the cylinder are essentially the same at all the measured angles (i.e., at all angles for which the edge contribution could be distinctly separated from any others). For this edge thickness, the square edge also produces similar results.

As the edge approaches the size of the wavelength, changes are observed in the directivity. Figure 5.31 presents the results for a  $.76\lambda$ -thick edge. Here, the square edge behaves quite differently from the rounded edge. Moving to the largest edge ( $4\lambda$  in thickness, Figure 5.32), the square edge then exhibits the lobed pattern that is expected when interferences occur between returns from multiple scattering points (in this case, the two parallel edges). On the contrary, the results from the rounded edge and the corresponding cylinder are about the same for all three thicknesses of edge. This probably results from the fact that a specular mechanism, depending only on the local curvature at the specular point, is dominant. The data of Figure 5.33 show that this cylinder/rounded-edge similarity is present, at least for  $0^\circ$  incidence, over a wide range of frequencies. The combination of the three curves

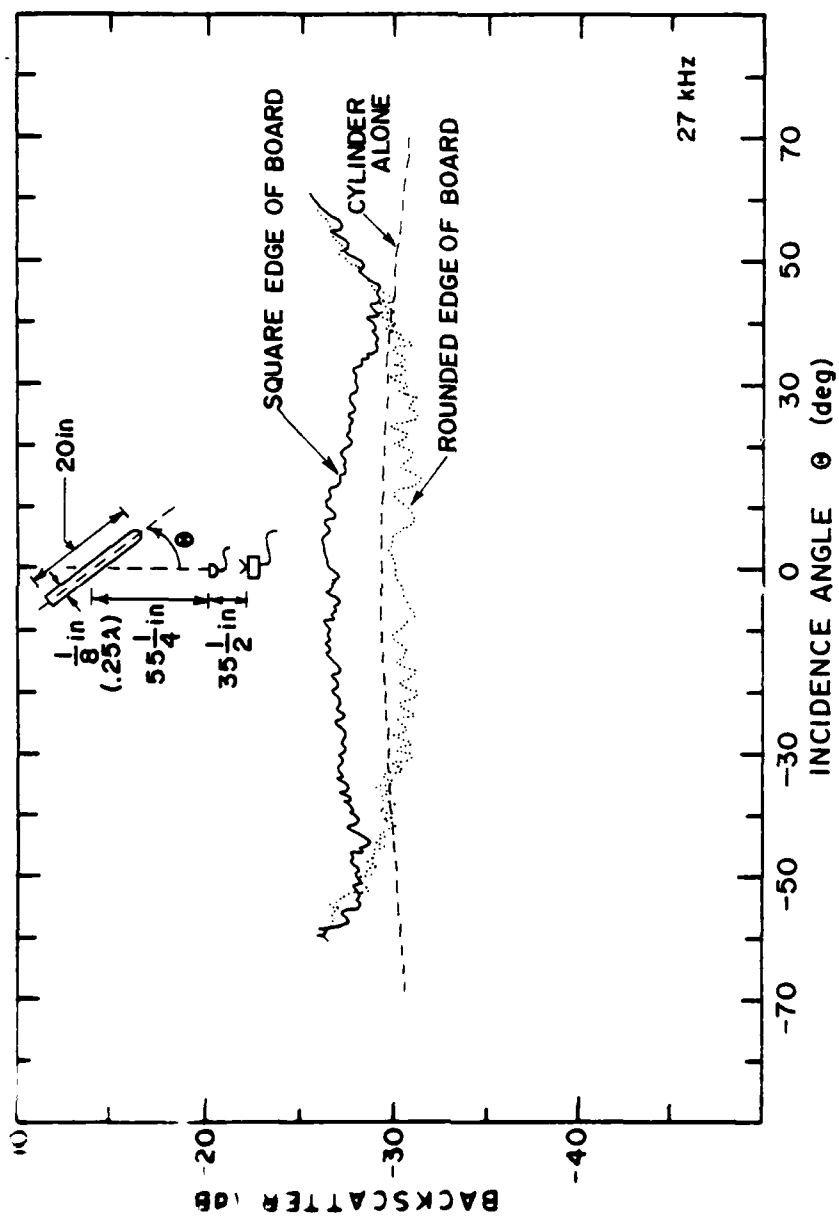


Figure 5.30 Comparison of the backscattered directivities from a square edge, a rounded edge, and a cylinder with a 1/8-inch width. ( $\lambda = 1/2$  inch)

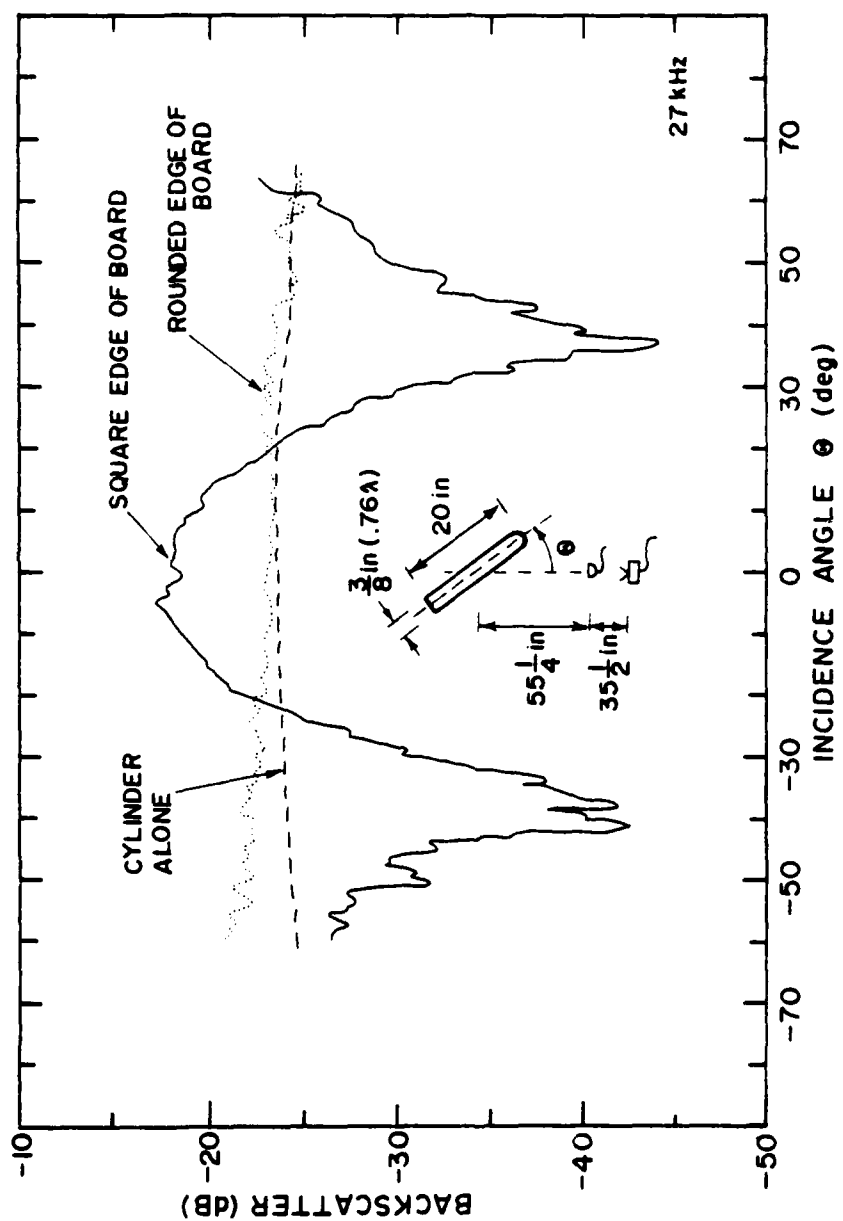


Figure 5.31 Comparison of the backscattered directivities from a square edge, a rounded edge, and a cylinder with a 3/8-inch width. ( $\lambda = 1/2$  inch)

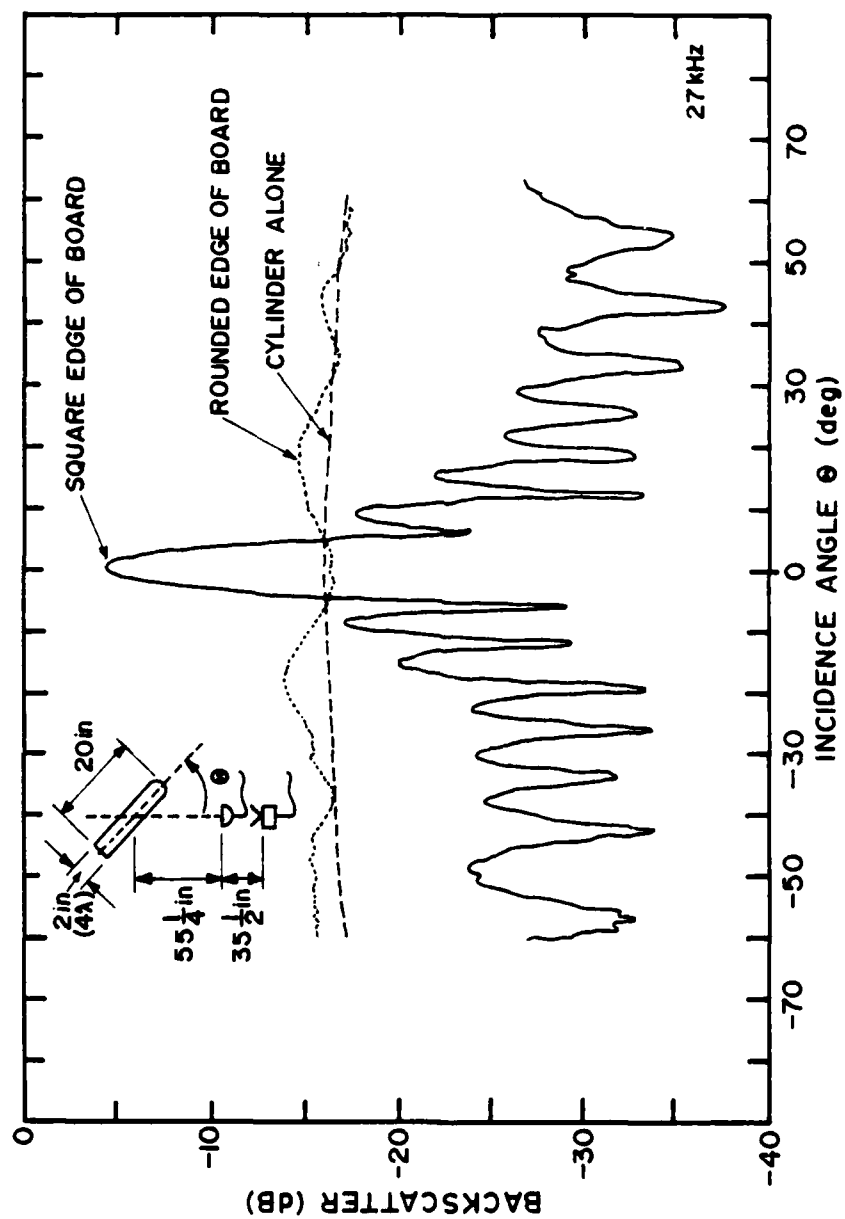


Figure 5.32 Comparison of the backscattered directivities from a square edge, a rounded edge, and a cylinder with a 2-inch width. ( $\lambda = 1\frac{1}{2}$  inch)

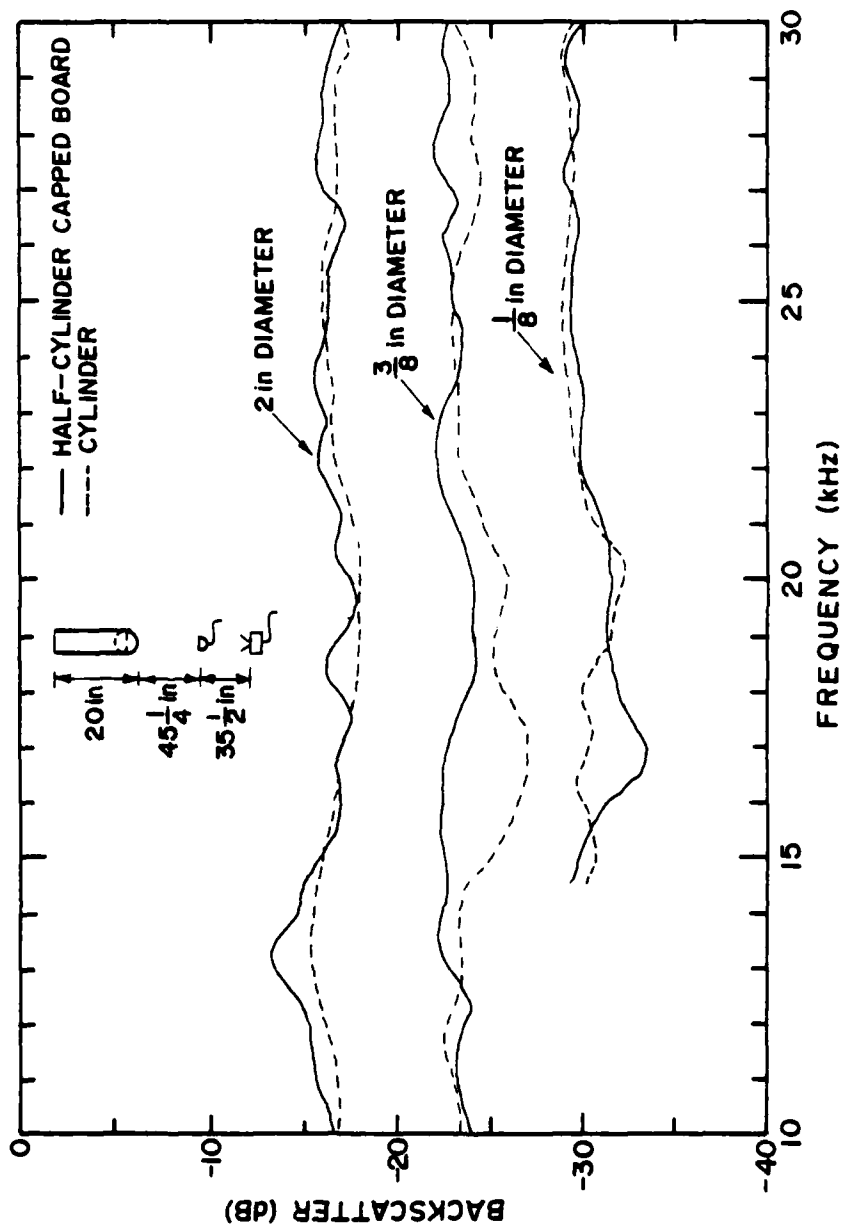


Figure 5.33 Comparison of the backscattered frequency response from a half-cylinder-capped board and a cylinder for cylinder diameters of 1/8, 3/8, and 2 inches.



in the plot shows good agreement over a  $kd$  ( $d$  = diameter) range of about .9 to 28.

The Freedman theory provides a formal method for separating the individual scattering features of a particular body and for predicting how they will interact. Thus, while theoretical examination of the specular-dominated, rounded-edge case will provide little new intuitive information about this theory, the square-edge case is ideal for study. A Freedman analysis was performed for the square edge, treating it as a thin rectangular baffle (see Section 2.4.3). The results are plotted in Figures 5.34 - 5.36. Note that the shape of the predicted directivities agrees very well with the experimental results, even for the thinner edges. This agreement is excellent at  $0^\circ$  incidence but deteriorates somewhat as the incidence angle increases. However, the relative level of the predicted values have had to be adjusted upward by 13 - 15 dB in order to obtain this agreement.

There are several possible explanations for the discrepancies in the absolute levels of the predicted and experimental data. First, as mentioned near the beginning of this section, the data were all normalized to the field backscattered by a large rectangular baffle. This is probably not the best choice for a reference. A Freedman computation of the directivity from the reference baffle indicates a primary lobe with a 3-dB width of less than  $1^\circ$  and a first side lobe about 14.5 dB lower in amplitude than the main lobe. Even though the baffle was manipulated for the peak return, an experimental error in the measurement of this highly directive return cannot be ruled out. Second, a problem with the Freedman predictions at close ranges may be

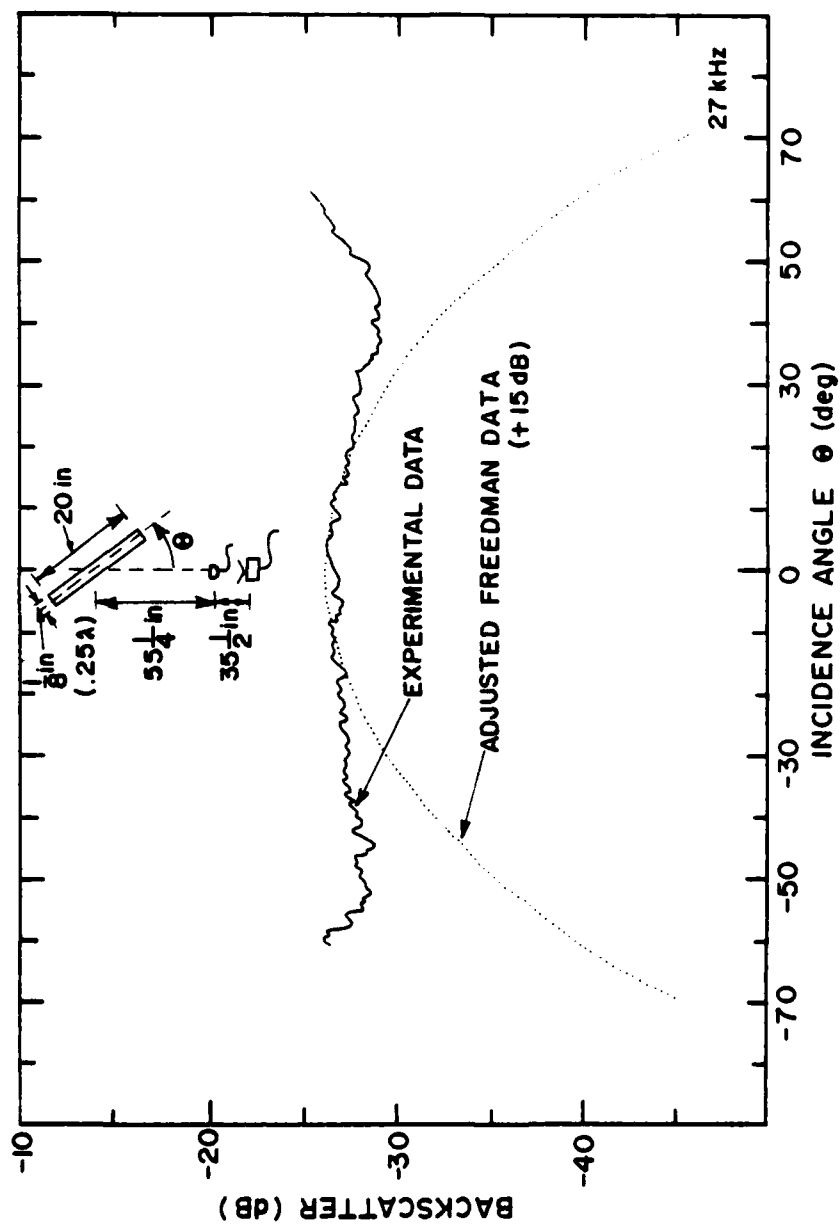


Figure 5.34 Backscattered directivity from a 1/8-inch edge, as measured experimentally and as computed using the Freedman method.

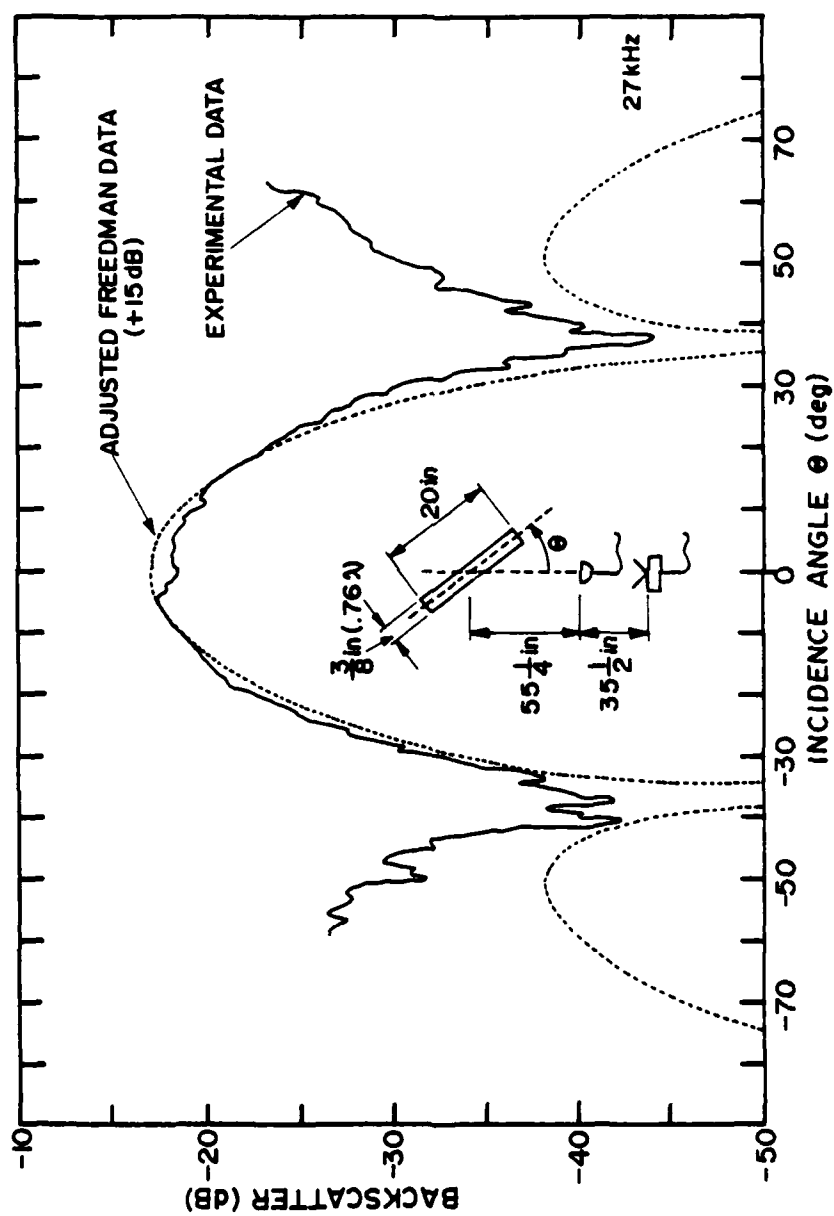


Figure 5.35 Backscattered directivity from a 3/8-inch edge, as measured experimentally and as computed using the Freedman method.

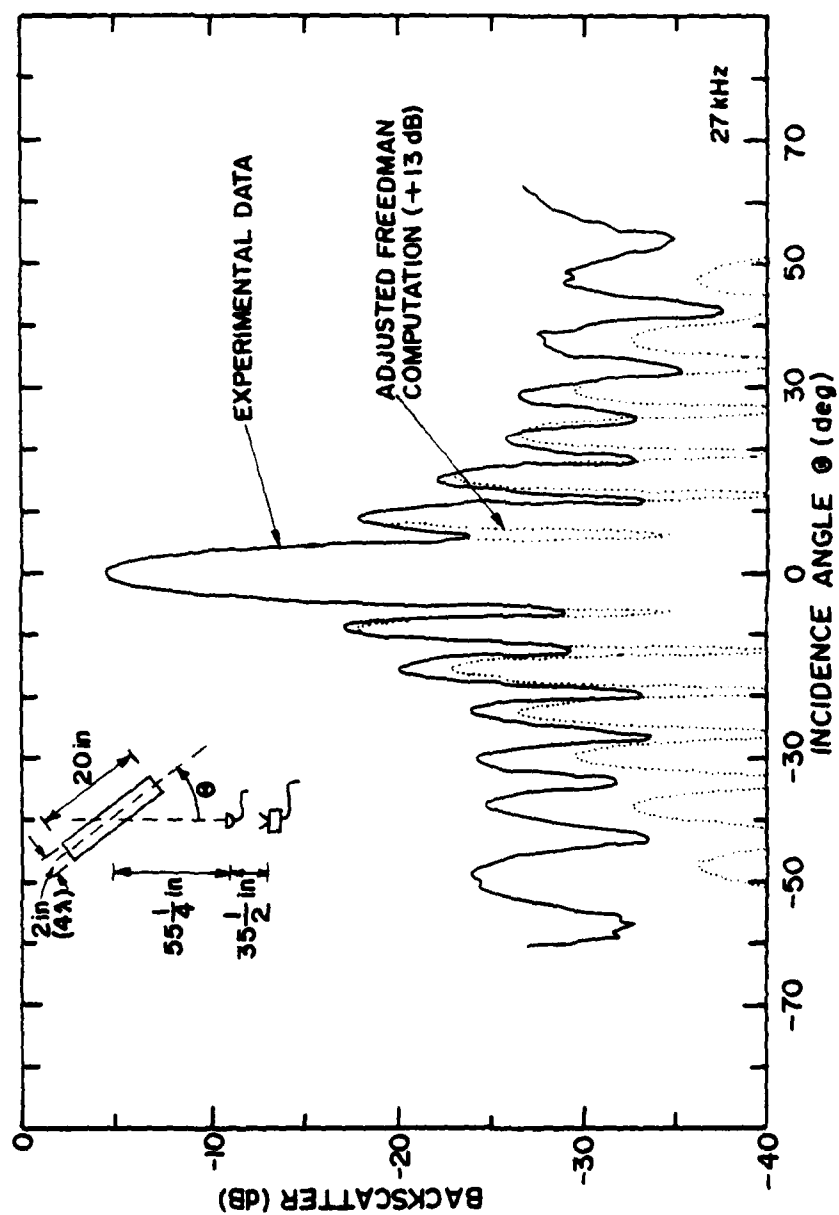


Figure 5.36 Backscattered directivity from a 2-inch edge, as measured experimentally and as computed using the Freedman method.

indicated. The computed values for backscatter from the edge rise in direct proportion to the frequency, but this rise is inconsistent with the experimental data plotted in Figure 5.37. The edge in this case is 5-feet long and 1/2-inch wide. Note that little variation with frequency is observed over a 5-to-1 change in  $ka$ . This time the data are normalized to the field incident at the edge with the edge not present. The Freedman predictions for this edge are larger than the scale of the figure, ranging from 4 dB at  $ka = 1$  to 18 dB at  $ka = 5$ ; the predicted backscattered returns are now greater than the incident field. Similar errors in the Freedman predictions have been observed in other experiments in this study when the dimensions of the scatterer are equal to or greater than the scatterer-to-microphone separation, but reasonable predictions are obtained when the scatterer is much smaller (see, for example, the data from small cylinders in the following section).

### 5.3 Backscattering from Small Cylinders

The finite cylinder is a simple but intuitively interesting scatterer. Its scattered field can be logically divided into two contributions: an end component and a side component. Both of these components generate fields similar to that of the rectangular edge examined in the previous section, and these two fields interact to form the final result. The side component is dependent largely on the length of the cylinder, while the end component depends on the area of the circular disk. For these reasons, a fairly extensive investigation into the backscatter from small cylinders was performed.

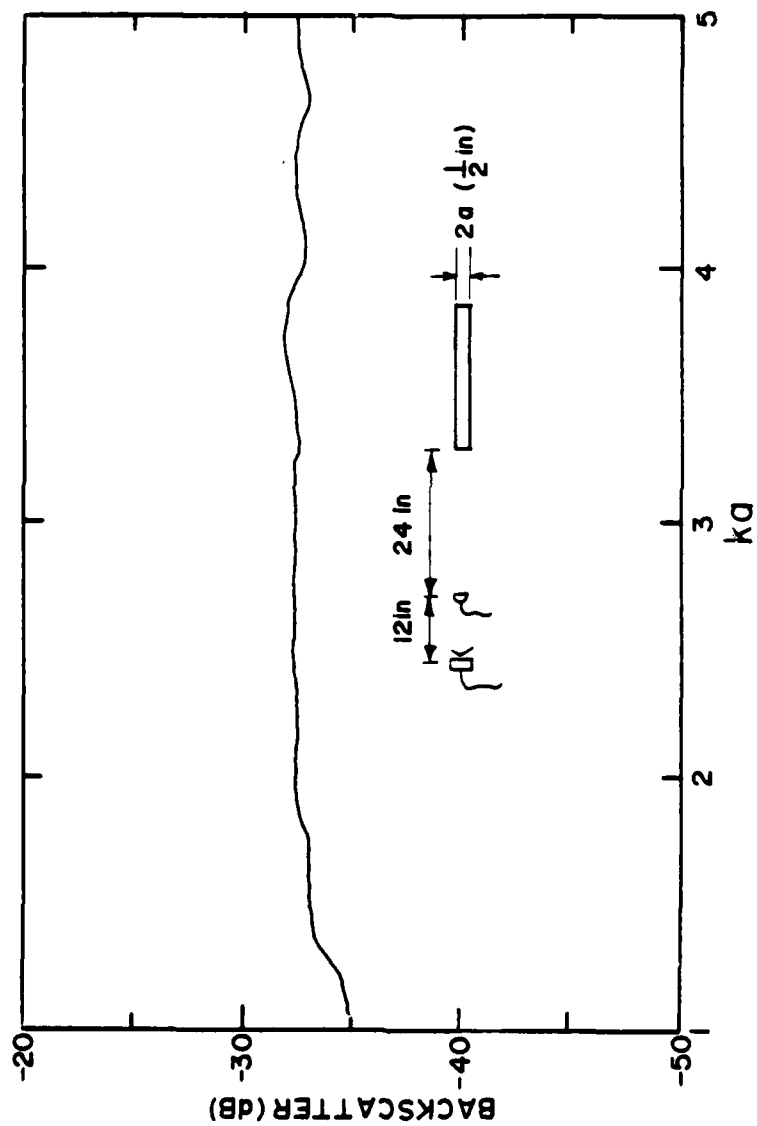


Figure 5.37 Backscatter from a thin edge at various frequencies.

The models were high-precision, rigid cylinders made out of machined drill rod. Twenty individual models in lengths of 1/8 to 1 inch and diameters of 1/8 to 3/4 inch were made. For the measurements reported in this section, the cylinders were suspended horizontally by a nylon thread through a small hole in the center axis of the cylinder. The thread consisted of two strands from a piece of braided fishing line. A frequency of 27.6 kHz ( $\lambda = 1/2$  inch) was used for most of the data, making all of the cylinders close to a wavelength in dimension. Since the data in this transition region do not vary consistently as the data in either high- or low-frequency regions, a significant portion of the measured data have been included here. The pulse length of .8 milliseconds was relatively long for these small cylinders. Note that the same cylinders were examined as obstructions on the surface of a prolate spheroid (see Section 4.4).

Figures 5.38 and 5.39 present the results obtained for the backscattered directivity from 3/4-inch-diameter cylinders in five separate lengths from 1/8 to 1 inch. The data are normalized to the field incident at the center of the cylinder without the cylinder present (as are all the data of this section). For angles near axial incidence, where the end component common to all of the cylinders can be expected to dominate, all the curves overlap. However, for angles greater than about  $20^\circ$ , the influence of the different side lengths can be seen. The number of nulls visible in the backscattering patterns ranges from two with the 1/8-inch-long cylinder to five with the 1-inch-long cylinder. Note that the curve for the 1/8-inch-long cylinder is asymmetric for angles close to broadside incidence. The absolute level

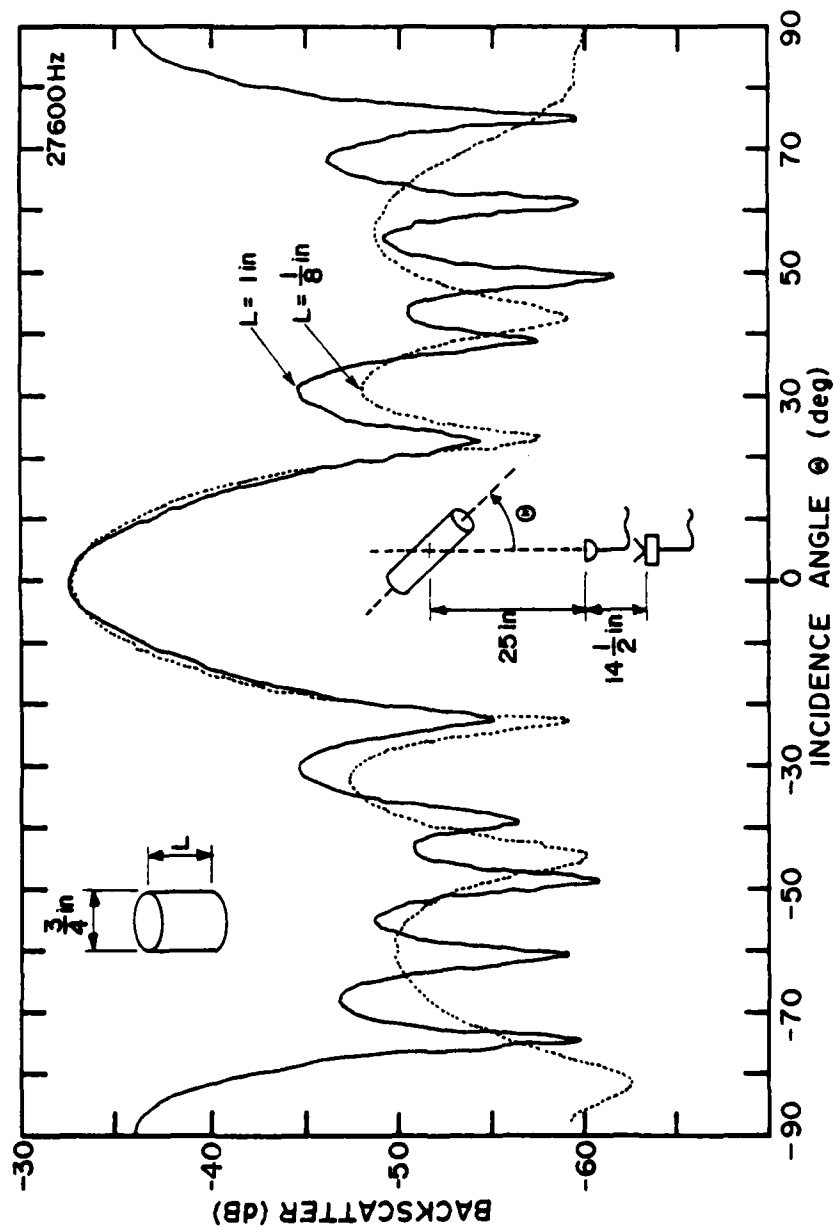


Figure 5.38 Directivity of the backscatter from  $\frac{3}{4}$ -inch-diameter cylinders with lengths of  $\frac{1}{8}$  and 1 inch. ( $\lambda = \frac{1}{2}$  inch)



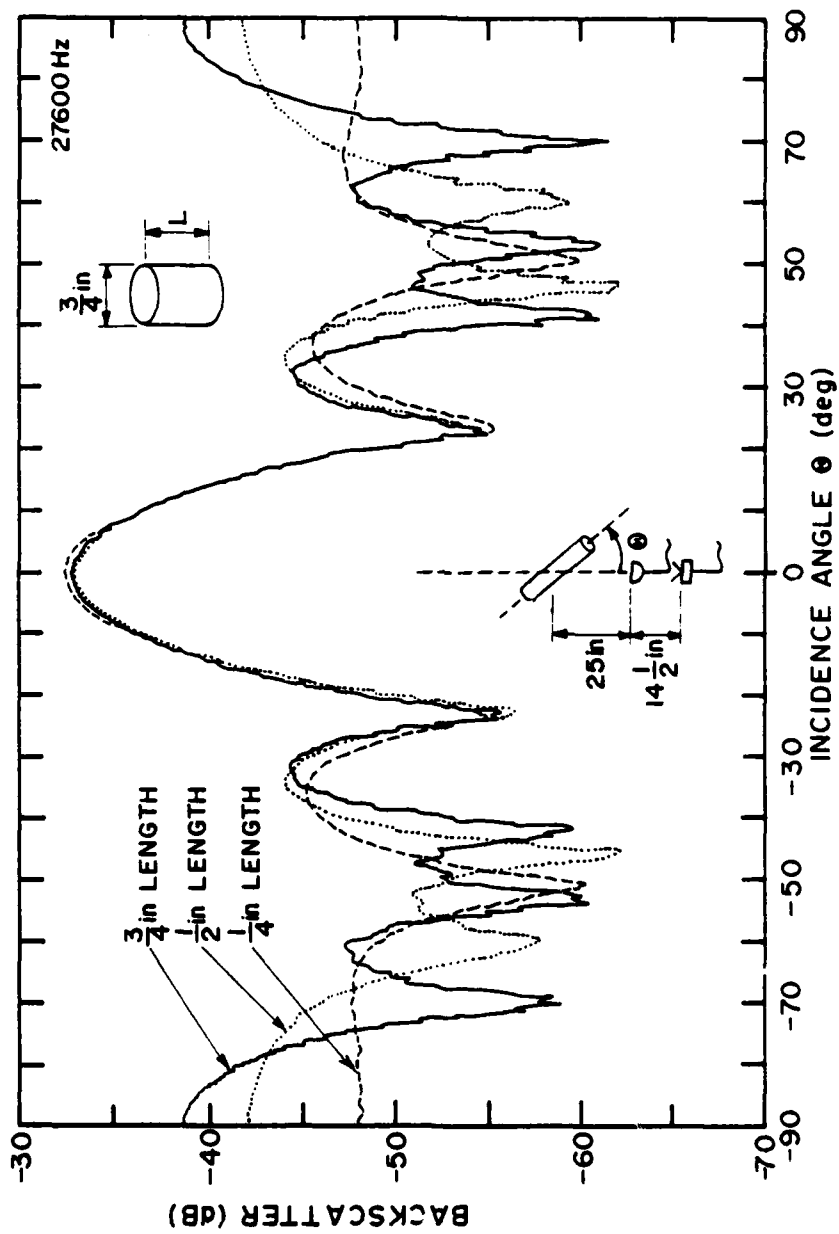


Figure 5.39 Directivity of the backscatter from  $\frac{3}{4}$ -inch-diameter cylinders with lengths of  $\frac{1}{4}$ ,  $\frac{1}{2}$ , and  $\frac{3}{4}$  inch. ( $\lambda = \frac{1}{2}$  inch)

of the return in this latter case is so small that it is very sensitive to any extraneous reflections or electrical noise.

Similar data for five cylinders of 1/2-inch diameter are presented in Figures 5.40 and 5.41. The curves for cylinders of different lengths are still the same for angles within about  $30^\circ$  of axial incidence. Thus, a cylinder endcap that is approximately one wavelength in diameter is sufficient to dominate the backscattering process near axial incidence. The relative separations between the curves in Figures 5.40 and 5.41 at broadside ( $90^\circ$ ) incidence are about the same as those described in the previous paragraph, but the absolute levels are somewhat lower because of the smaller diameter of the cylinders. The number of nulls visible in the curves for both the 1/8- and 1-inch-long cylinders has also changed.

Backscattered-directivity data for various cylinders of 1/4-inch diameter are presented in Figures 5.42 and 5.43, and similar data for various 1/8-inch-diameter cylinders are shown in Figures 5.44 and 5.45. (The results from the 1/8-inch-long cylinders are not presented because the returned levels were too small relative to the background noise.) In these cases, the endcap returns no longer dominate the scattering process (relative to the side returns) when the longer cylinders are examined, even though the absolute levels of the broadside returns are less than those seen earlier in this section with cylinders of larger diameter. Note that, for the 1/8-inch-diameter cylinders, the axial return is considerably less than the broadside return even for the 1/4-inch-long cylinder.

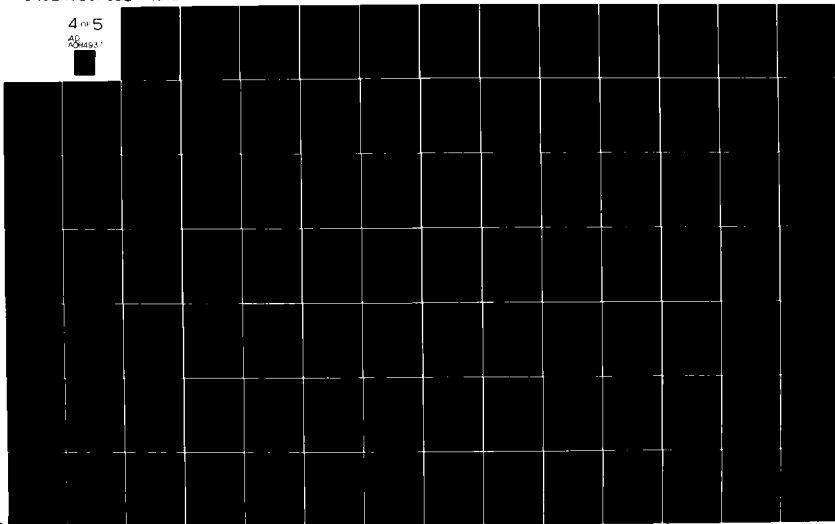
AD-A084 937

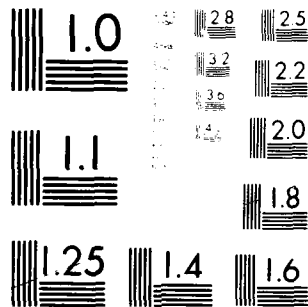
PENNSYLVANIA STATE UNIV UNIVERSITY PARK APPLIED RESE--ETC F/O 20/1  
AN EXPERIMENTAL ANALYSIS OF THE BASIC PHENOMENA INVOLVED IN MOD--ETC(U)  
JAN 80 M S LANG N00024-79-C-6043  
ARL/PSU/TN-80-43 NL

UNCLASSIFIED

4 of 5

AD-A084 937





MICROCOPY RESOLUTION TEST CHART  
NATIONAL BUREAU OF STANDARDS-1963-A

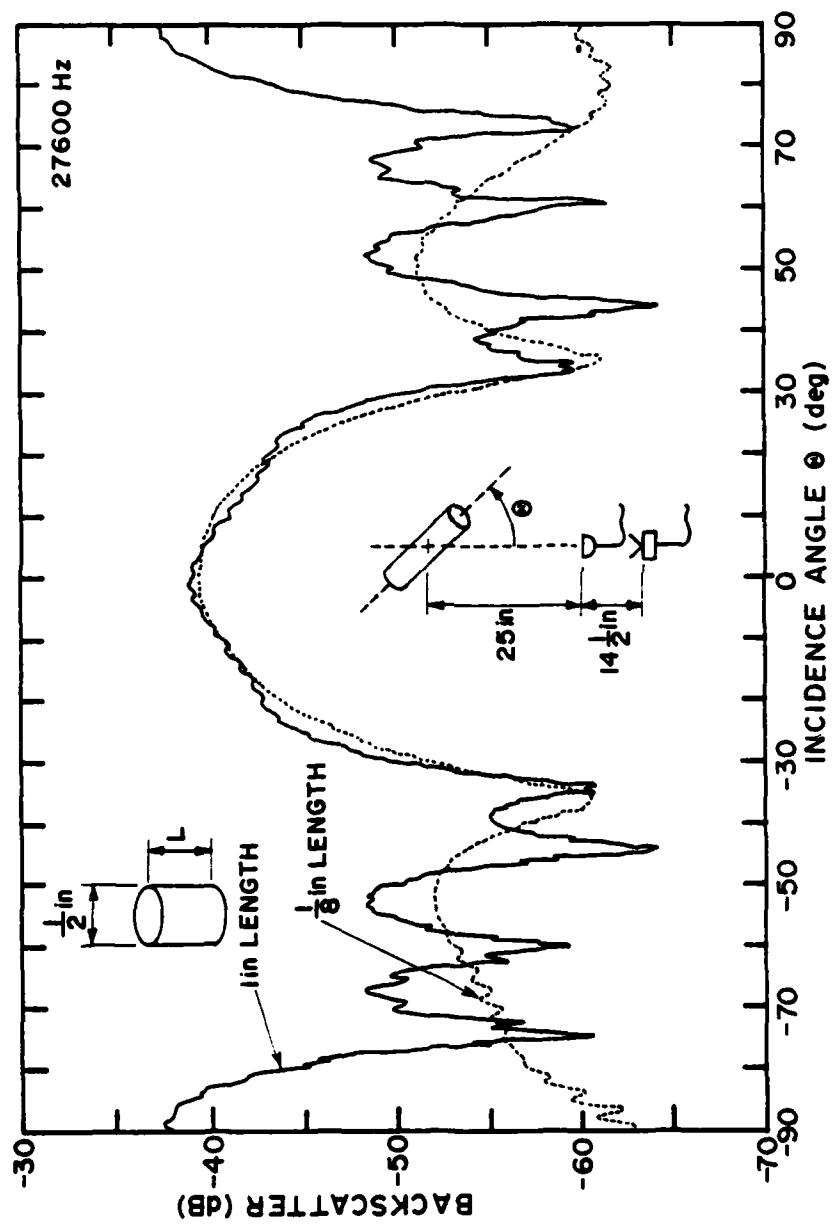


Figure 5.40 Directivity of the backscatter from 1/2-inch-diameter cylinders with lengths of 1/8 and 1 inch. ( $\lambda = 1/2$  inch)

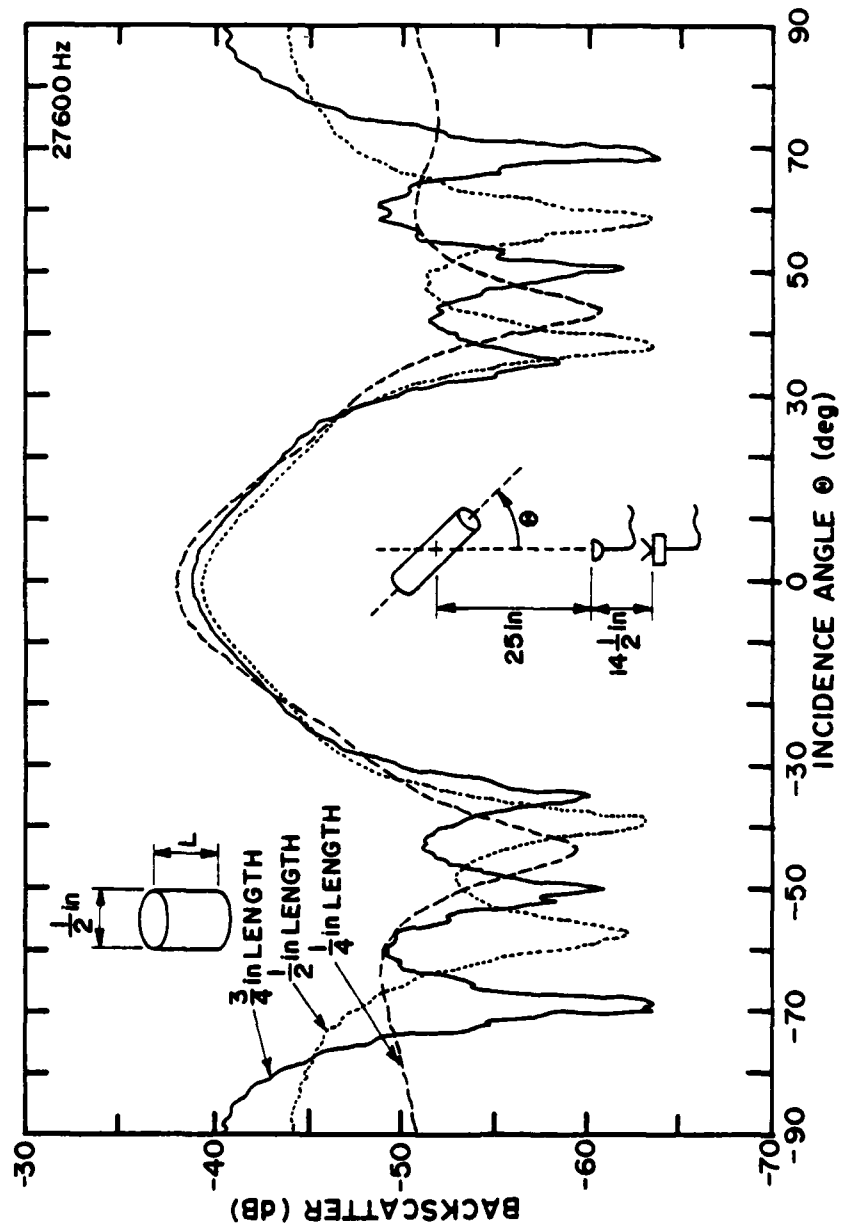


Figure 5.41 Directivity of the backscatter from 1/2-inch-diameter cylinders with lengths of 1/4, 1/2, and 3/4 inch. ( $\lambda = 1/2$  inch)

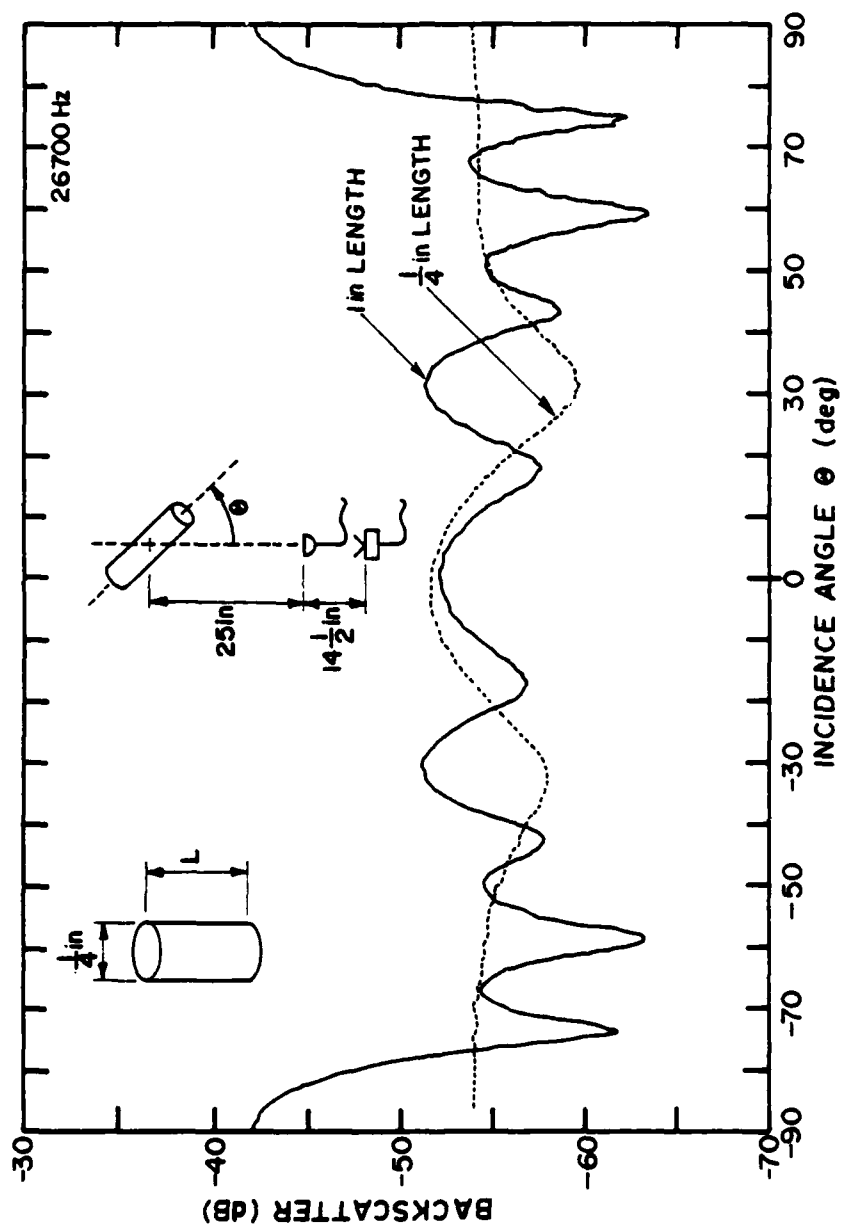


Figure 5.42 Directivity of the backscatter from 1/4-inch-diameter cylinders with lengths of 1/4 and 1 inch. ( $\lambda = 1/2$  inch)

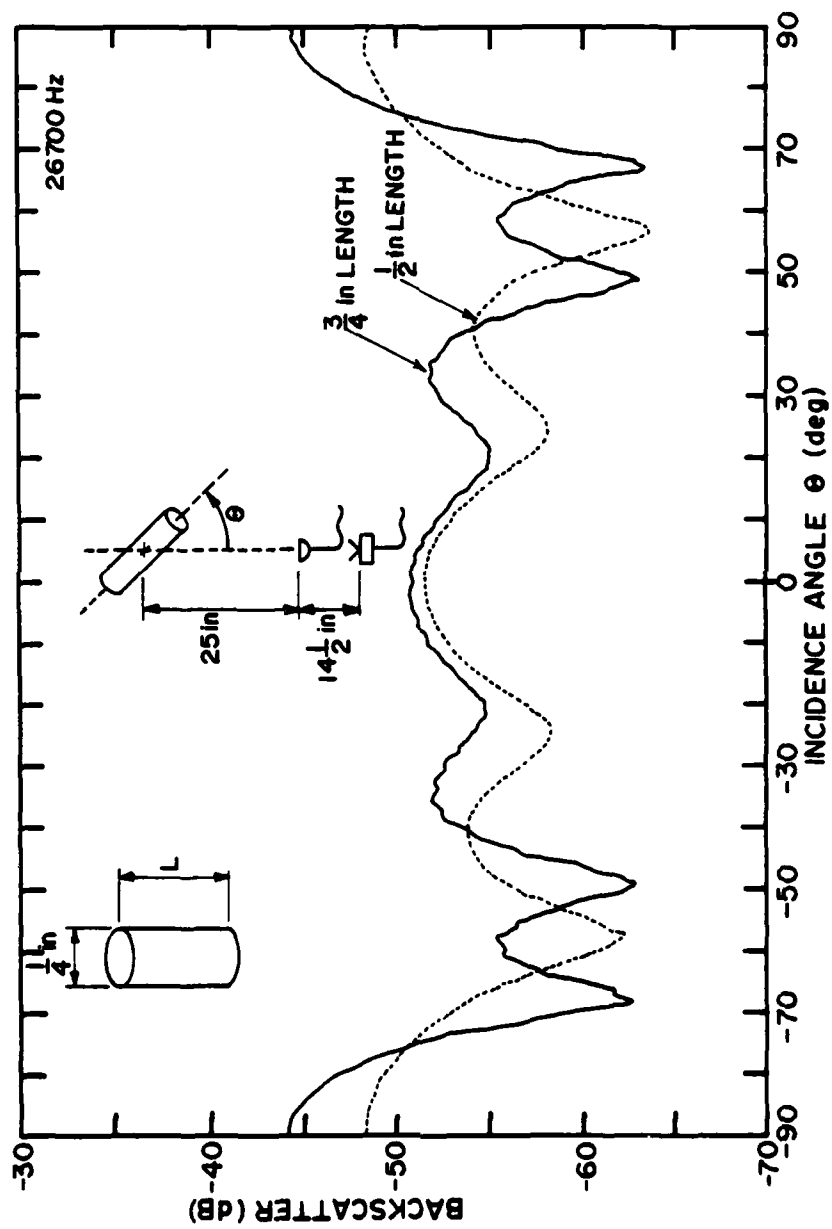


Figure 5.43 Directivity of the backscatter from 1/4-inch-diameter cylinders with lengths of 1/2 and 3/4 inch. ( $\lambda = 1\frac{1}{2}$  inch)



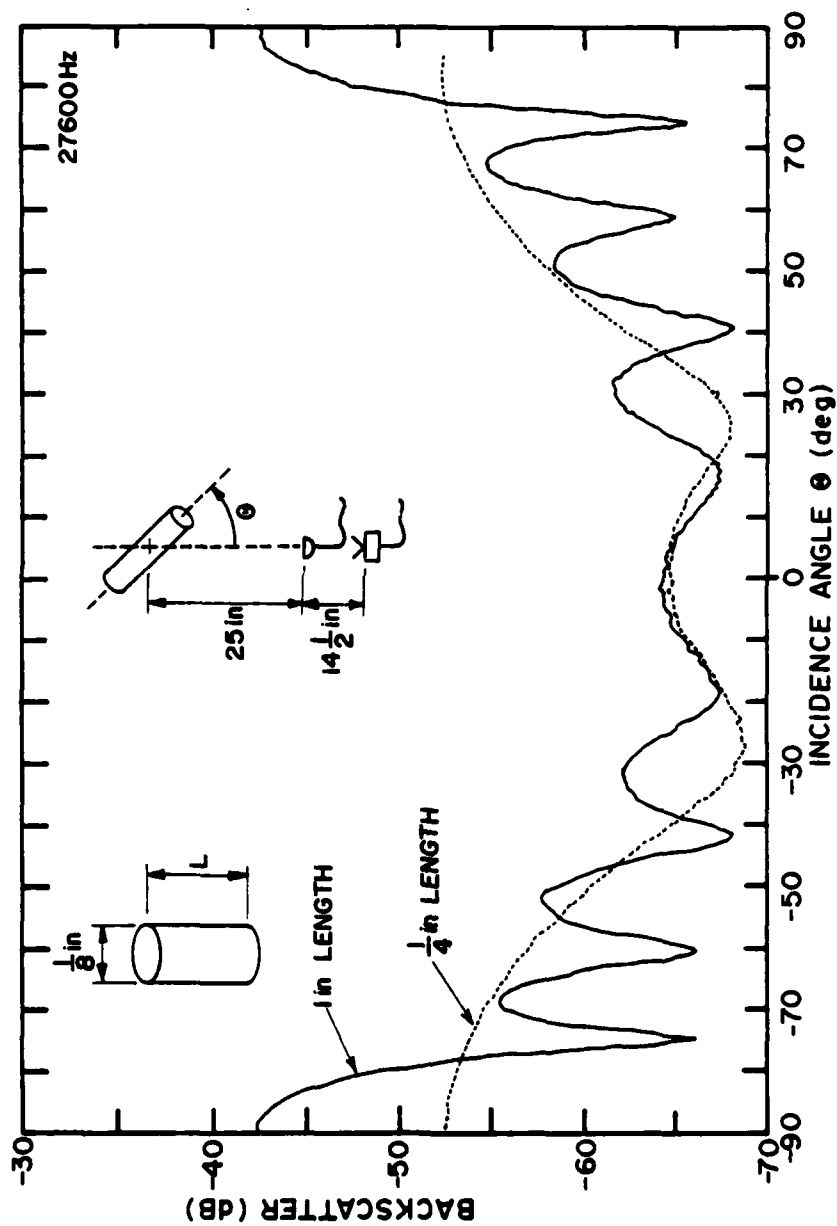


Figure 5.44 Directivity of the backscatter from 1/8-inch-diameter cylinders with lengths of 1/4 and 1 inch. ( $\lambda = 1/2$  inch)

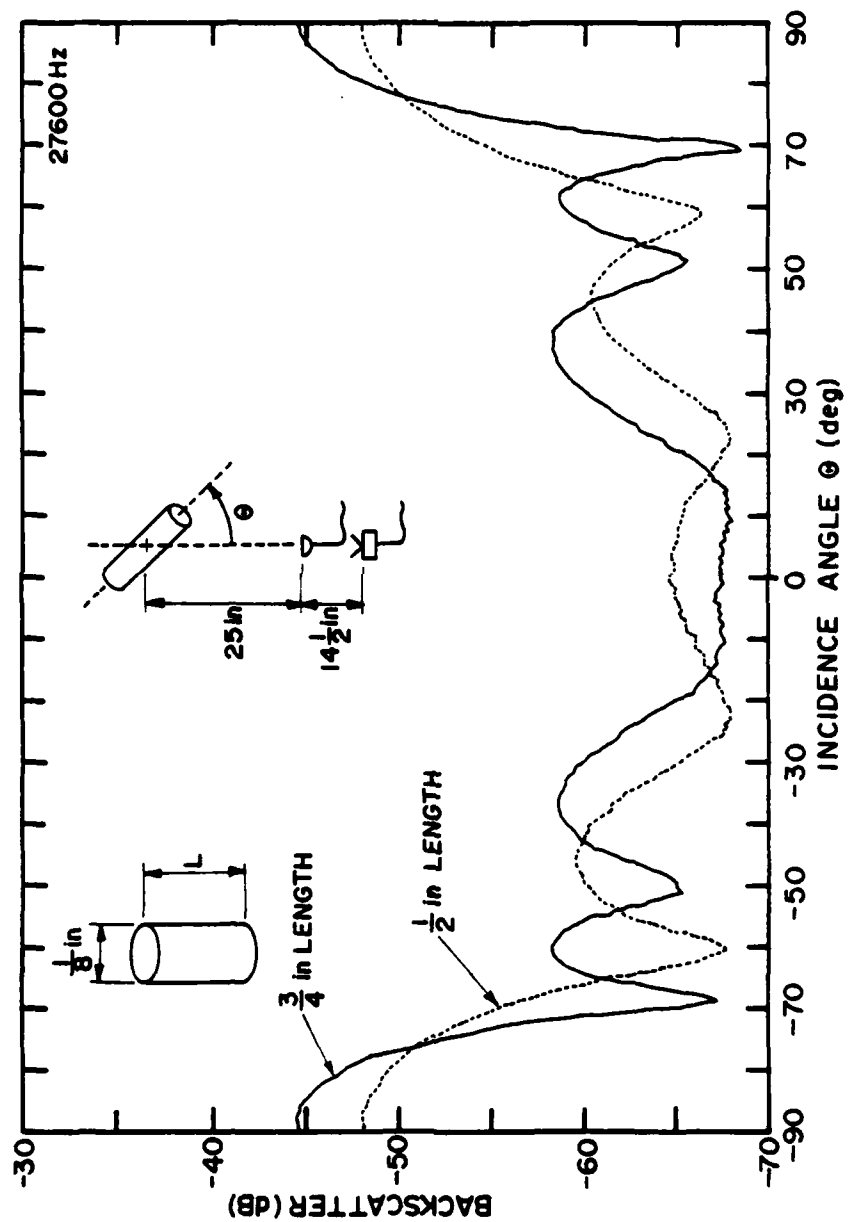


Figure 5.45 Directivity of the backscatter from 1/8-inch-diameter cylinders with lengths of 1/2 and 3/4 inch. ( $\lambda = 1/2$  inch)

To better examine the influence of the cylinders' lengths, some of the previous data have been plotted again in Figures 5.46 and 5.47 with the length of the cylinders held constant on each plot. The powerful influence of the change in diameter is clear. Just as the endcap return dominated the scattering near axial incidence, the side (length-dependent) return dominates the scattering near broadside incidence for the 1-inch-long cylinders. The side return of the 1/4-inch-long cylinders, however, does not dominate to the same degree. The total number of nulls present in the latter curves appears to be more strongly influenced by the length of the cylinder than the diameter.

The Freedman theory cannot be used directly as a theoretical comparison because it breaks down for cylinders at nonaxial incidence (see Section 2.4.2). However, the closely related physical-optics approach can provide some interesting information. For example, Figure 5.48 is a plot of the measured data for the 3/4-inch-diameter by 1-inch-long cylinder along with the corresponding physical-optics computation. The agreement between theory and experiment is good at both axial and broadside incidence, but wide discrepancies are noted at some ranges in between these extremes. Figure 5.49 shows the reason for the discrepancies. In the figure, the side and end contributions of the cylinder are plotted separately. At both axial and broadside incidence, either the side or end component dominates, so that the total result matches the physical-optics prediction reasonably well. However, at some angles between the two extreme positions, the two scattering components become very close in magnitude, and the resulting vector sum is very sensitive to small errors in either component's prediction.

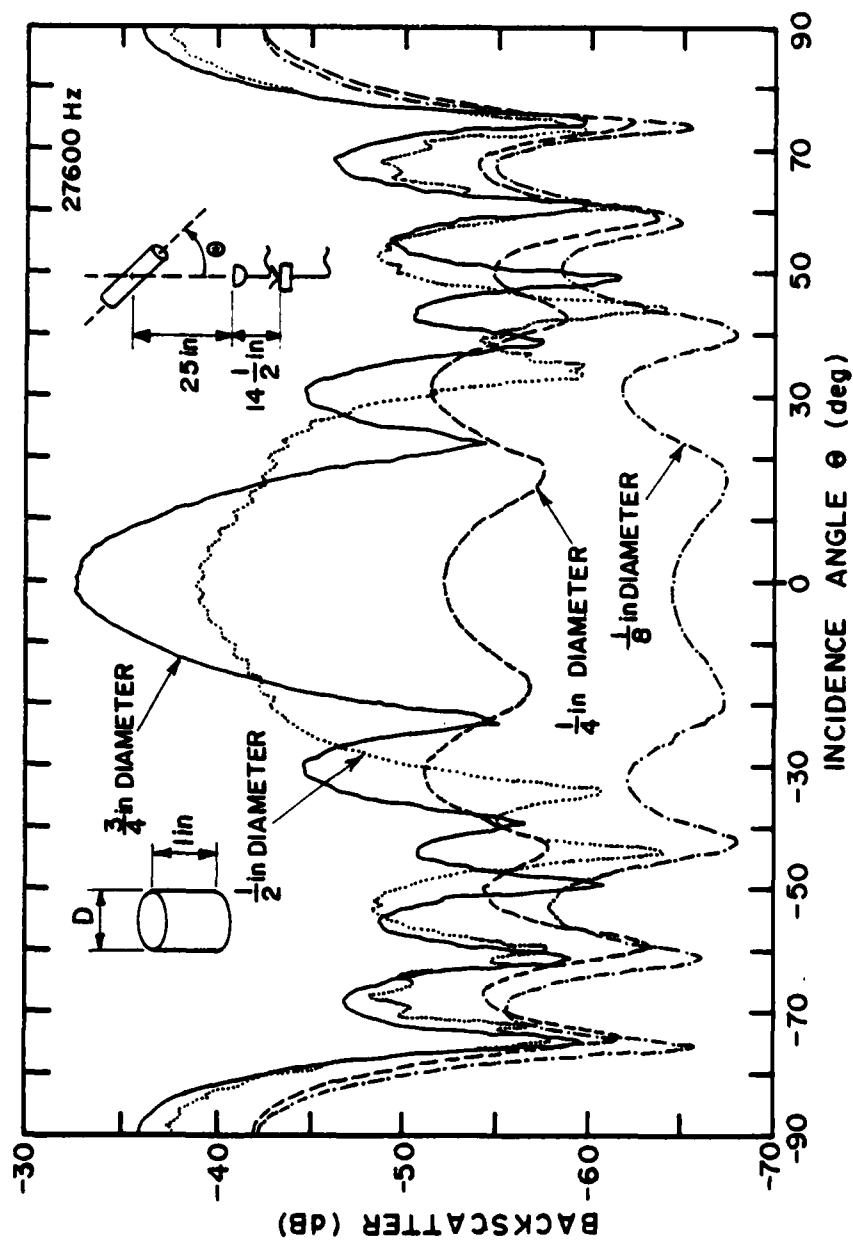


Figure 5.46 Directivity of the backscatter from 1-inch-long cylinders with diameters of  $\frac{1}{8}$ ,  $\frac{1}{4}$ ,  $\frac{1}{2}$ , and  $\frac{3}{4}$  inch. ( $\lambda = 1/2$  inch)

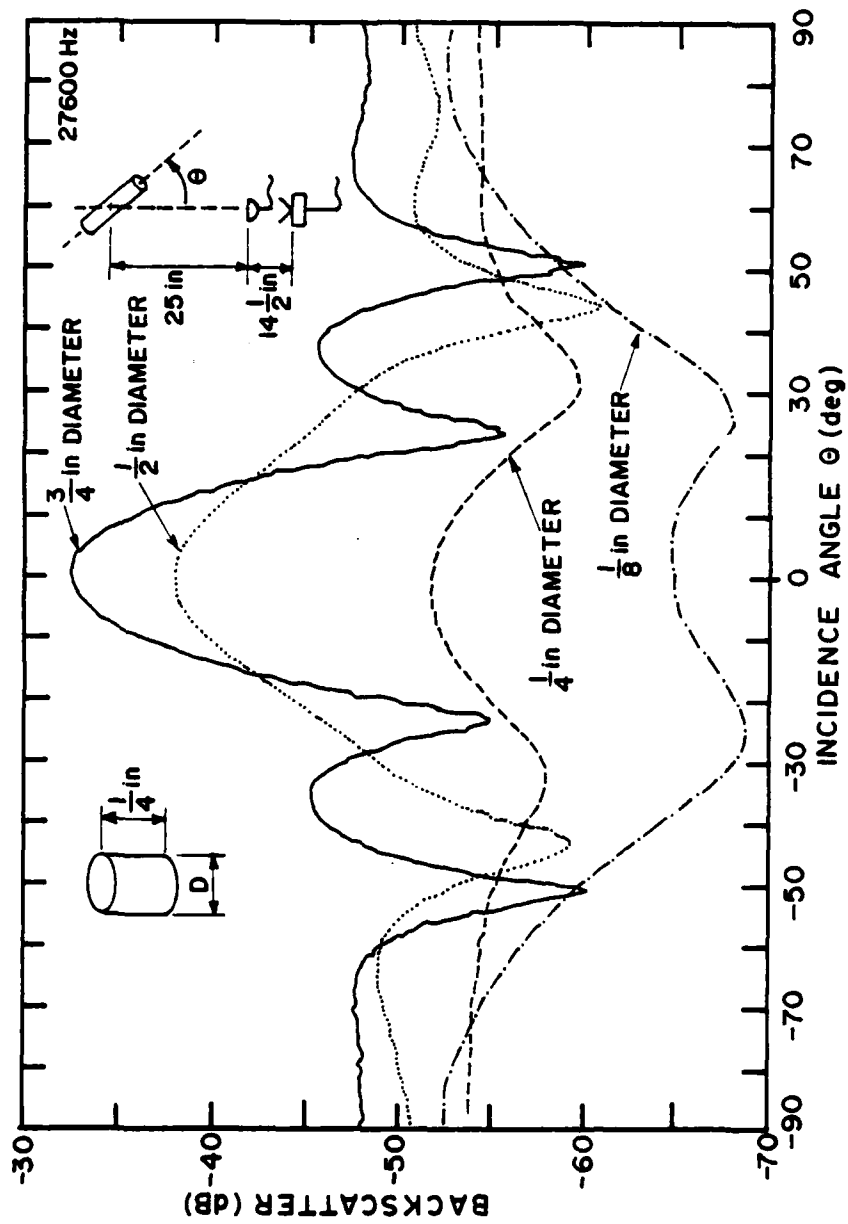


Figure 5.47 Directivity of the backscatter from 1/4-inch-long cylinders with diameters of 1/8, 1/4, 1/2, and 3/4 inch. ( $\lambda = 1/2$  inch)

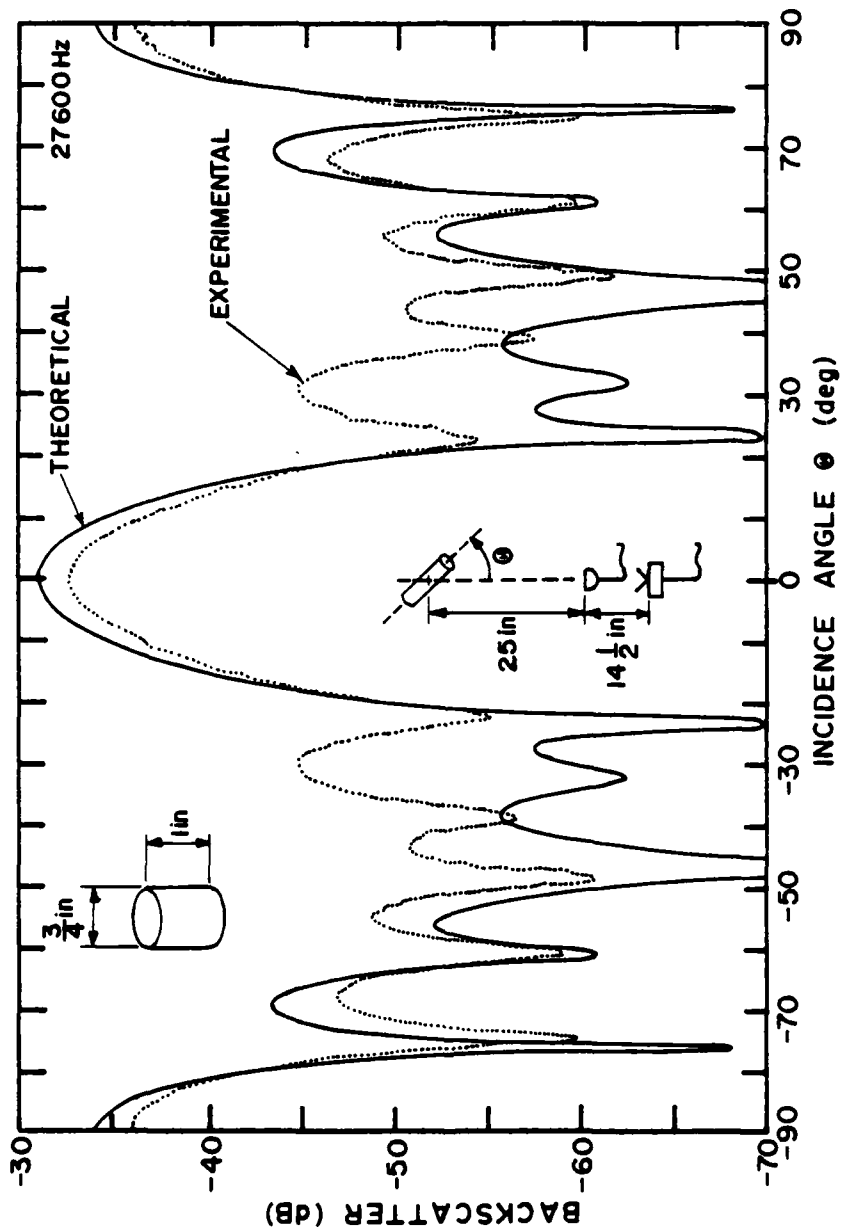


Figure 5.48 Comparison of measured and predicted values for the backscattered directivity from a  $\frac{3}{4}$ -inch-diameter by 1-inch-long cylinder. ( $\lambda = \frac{1}{2}$  inch)

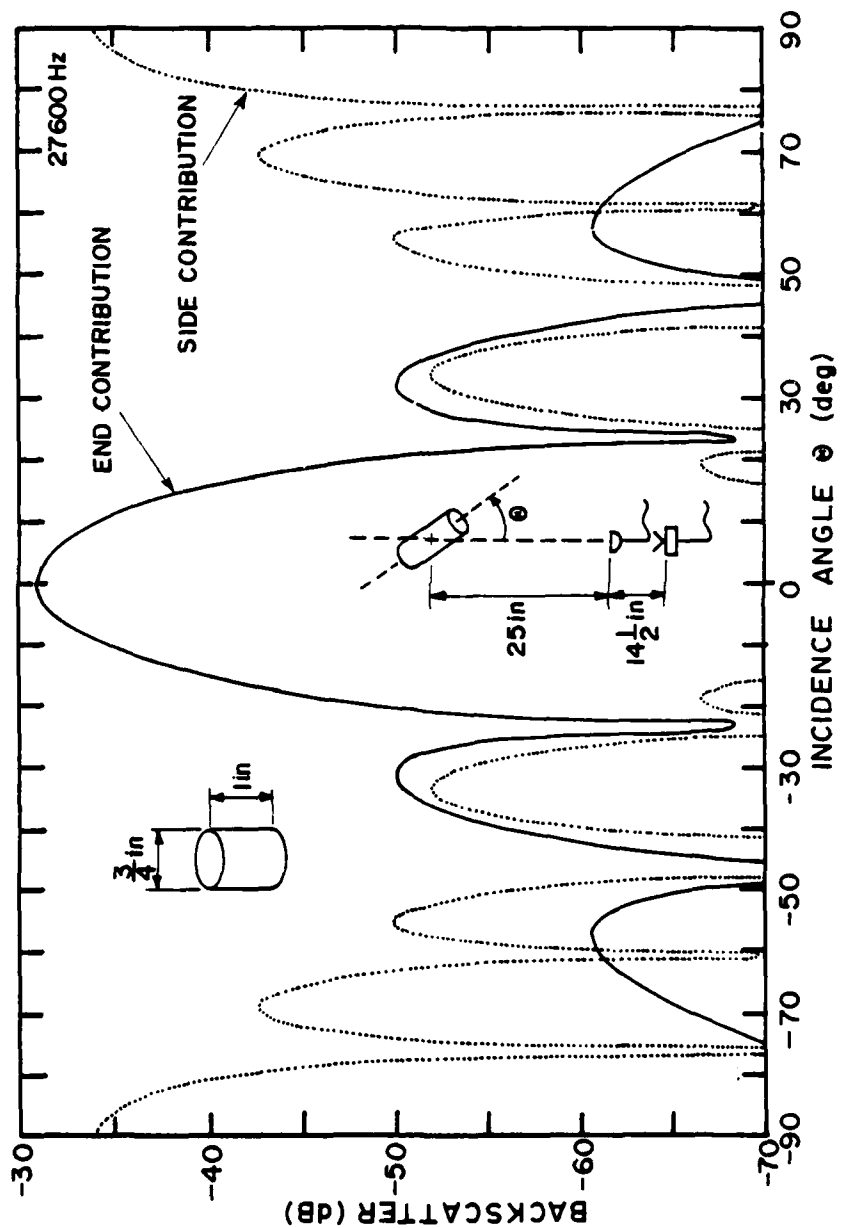


Figure 5.49 Physical-optics computation for the backscattered end and side contributions from a  $\frac{3}{4}$ -inch-diameter by 1-inch-long cylinder. ( $\lambda = 1\frac{1}{2}$  inch)

Another comparison between theory and experiment is shown in Figure 5.50 (1/4-inch-diameter by 1-inch-long cylinder). In this case, the length of the cylinder is much larger than the diameter, and the resulting theoretical prediction agrees with the experimental data only near broadside incidence. Referring to the predictions for the individual components plotted in Figure 5.51, one can see that the end contribution is so broad that it generates a very large overlap region in which the side and end components interact. The resultant interaction between the backscattering components for this cylinder is significant enough to shift the location of the nulls in the total-backscattering pattern.

Theoretical predictions for two additional examples are given in Figures 5.52 and 5.53. Again, the predictions are better at axial and broadside incidence, but there is enough variability to limit any further conclusions. In general, while the predictions for structures such as the rectangular strip and the disk (end of cylinder) are surprisingly accurate on their own, the result of two or more of these components interacting can be very wrong. The inaccuracies in the absolute levels of the Freedman predictions noted in Section 5.2 with the rectangular strip were not present in the cylinder examples of this section. All the theoretical data in this section is plotted exactly as computed (i.e., no offset in the absolute level was necessary). Note, however, that these cylinders probably satisfy the farfield assumptions of the theoretical method better than any other models used in this investigation.



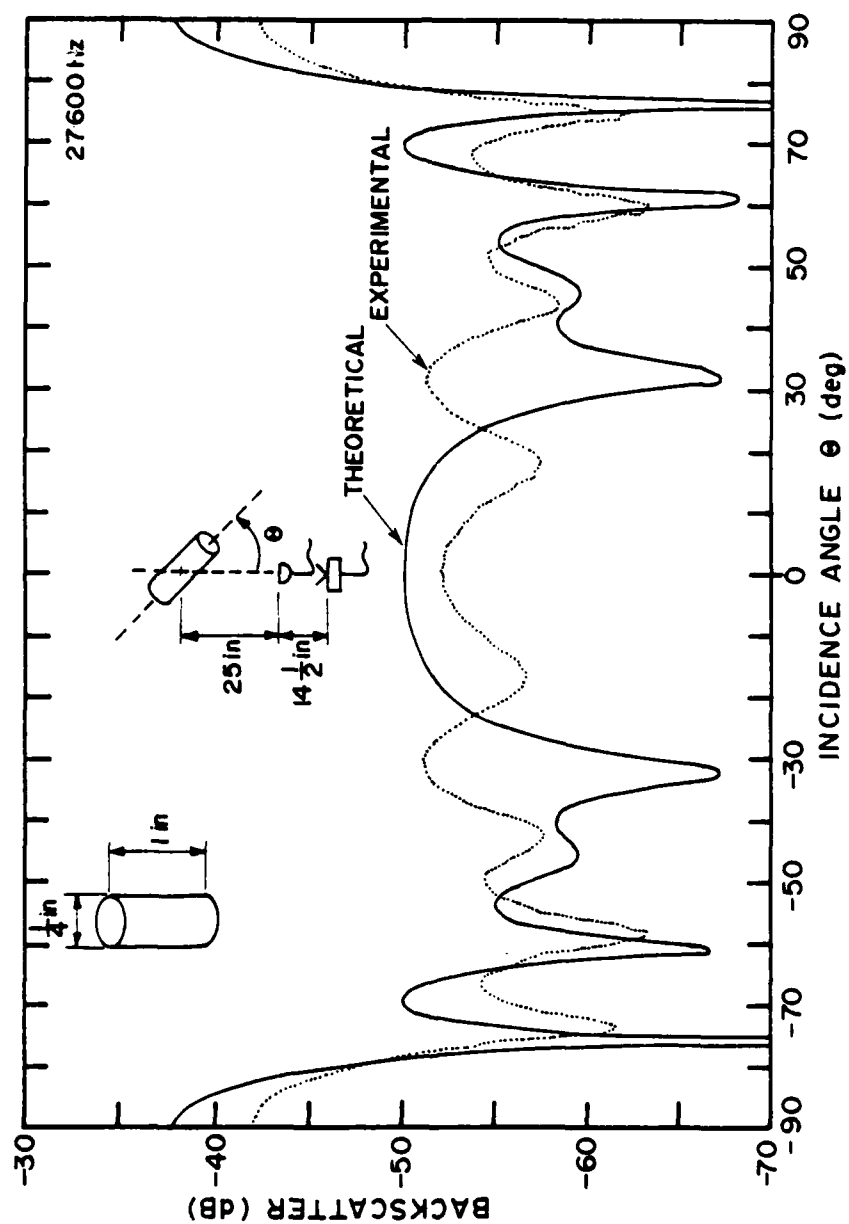


Figure 5.50 Comparison of measured and predicted values for the backscattered directivity from a  $1/4$ -inch-diameter by 1-inch-long cylinder. ( $\lambda = 1/2$  inch)

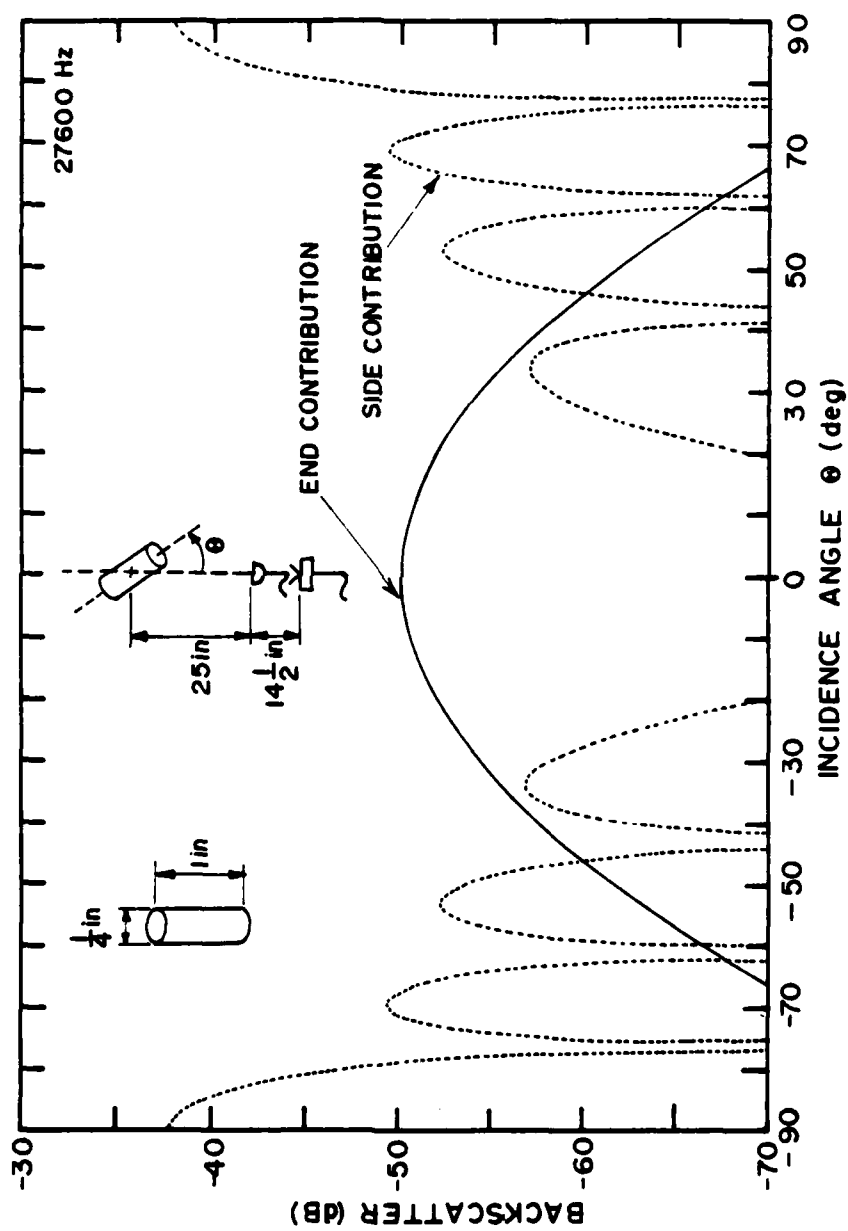


Figure 5.51 Physical-optics computation for the backscattered end and side contributions from a 1/4-inch-diameter by 1-inch-long cylinder. ( $\lambda = 1/2$  inch)

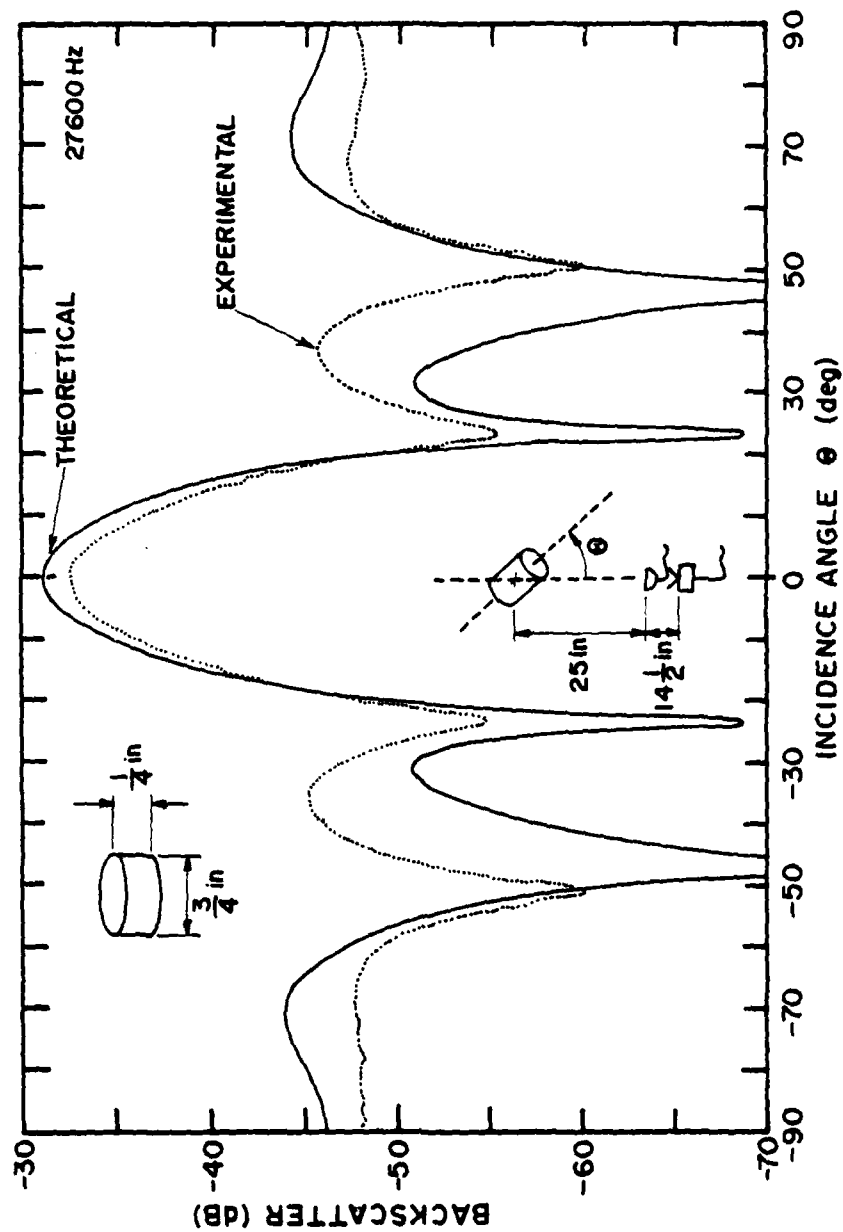


Figure 5.52 Comparison of measured and predicted values for the backscattered directivity from a  $\frac{3}{4}$ -inch-diameter by  $\frac{1}{4}$ -inch-long cylinder. ( $\lambda = 1\frac{1}{2}$  in)

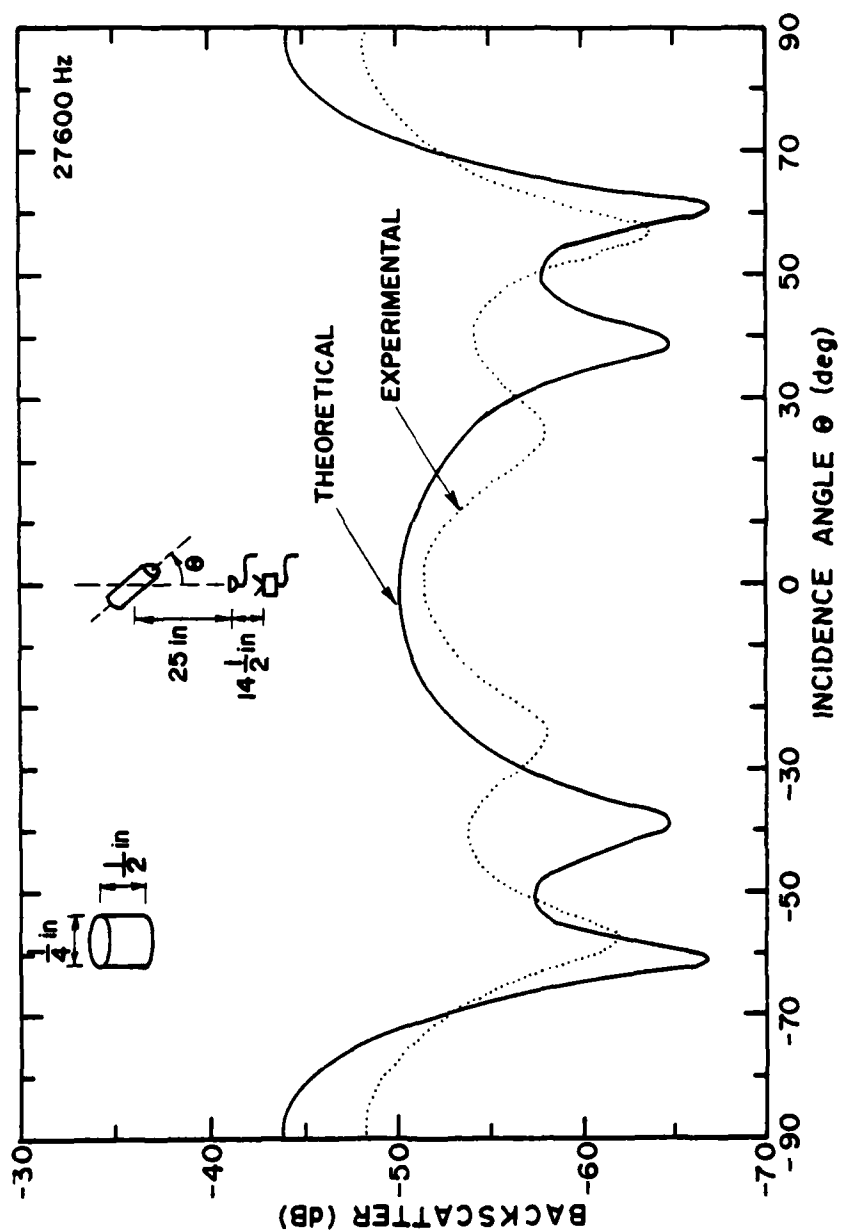


Figure 5.53 Comparison of measured and predicted values for the backscattered directivity from a 1/4-inch-diameter by 1/2-inch-long cylinder. ( $\lambda = 1/2$  inch)

#### 5.4 Scattering from Cones and Modified Cones

The data on scattering from edges discussed in previous sections has been useful for developing an intuitive understanding of the physical processes involved. However, there are other types of edges (i.e., discontinuities in slope or curvature) that are commonly found on three-dimensional bodies. For that reason, a special model based on a finite cone 18 inches in length with a  $20^\circ$  half-angle was constructed. The basic cone shape was chosen because it exhibits both tip and edge diffraction, and it generates no specular returns to mask these components. Removable caps that could substitute for the normal tip of the cone were also constructed to change the tip into smoothly joined spherical caps of 1/2-, 1-, and 2-inch radii and into a 2-inch hemisphere. In addition, both a hemisphere and a smoothly joined spherical termination were fabricated for attachment to the rear of the cone. The resulting combinations of caps and terminations on the model exhibit several types of first- and second-order discontinuities for investigation. (See Section 3.3 for a more complete description of the model.)

The design of the cone model also considered a secondary goal: to evaluate the predictions of the Freedman echo-formation theory. Basic to this theory's formulation are the Kirchhoff assumptions, one of which treats each element of a scatterer's surface as a small area radiator in an infinite baffle. This assumption is plausible for specular returns, but there is little reason to believe that it holds at edges. An experimental investigation is the best method for checking the applicability and validity of this prediction method.

Because the Freedman method only produces predictions for the cone at axial incidence (see Section 2.4.5), a detailed investigation of the frequency response of the cone at axial incidence was included in this study. The range of frequencies used was 10 - 40 kHz, which corresponds to a range in  $kh$  ( $h$  = height of the cone) of 83 - 335. These values are large enough to meet the conditions for the validity of a short-wavelength theory. In addition, experimental constraints, involving the dynamic range in the measurement chamber and the model size, essentially dictated the chosen frequency range. In addition to the frequency-response data, directivity data for both scattering and backscattering were collected at several discrete frequencies within the given range. Most of the results shown in this section have been normalized to the field incident at the center line about which the cone model rotated, but additional adjustments have been made for those curves that are compared with Freedman predictions in an attempt to better approximate farfield conditions.

Great care was expended in supporting and aligning the models because of difficulties experienced in the early cone experiments of this study. The attachment points of the supporting wires were countersunk totally into the model's surface, and the mounting holes were filled with clay after hanging the model. The smallest diameter wire that could support the weight of the models was used to suspend them. The data proved to be very sensitive to the model's alignment, especially at axial incidence. Thus, a telescope and level were used for a basic alignment, followed by peaking the actual acoustic return from the rear edge of the cone at axial incidence. A pulse length of

.28 milliseconds (slightly shorter in a few cases) was used so that most of the individual returns could be separated. Note that the cone rotated only about its center of mass because of the method of suspension. The location of this center point could not be controlled, but its approximate position was noted during each experiment. The separation distances between the models and the source/receiver were set at the maximum practical values, although these values were much too small to guarantee farfield conditions.

#### 5.4.1 General Discussion of Experimental Concerns

Before looking at the final results of the cone study, it is interesting to examine some of the experimental difficulties and observations. Figure 5.54 is a plot of the frequency response of all the backscattered returns that were observed in a time window encompassing the cone-model responses. The strongest return in all cases, except those in which the model had either the hemispherical or spherical terminations (not shown in this figure), came from the rear edge of the cone. The weakest return came from the tip region. In fact, no identifiable echo was observed from the tip above the general noise level. The data for the tip in Figure 5.54 were obtained by setting the receiver gate's window at the predicted time of the tip return and plotting the background level there. In addition to the rear-edge and tip-region returns, one or two echoes were generally observed in the region between the physical joint at which the model's removable caps were attached and the rear edge. The cone had no features in this region that might generate these additional scattered

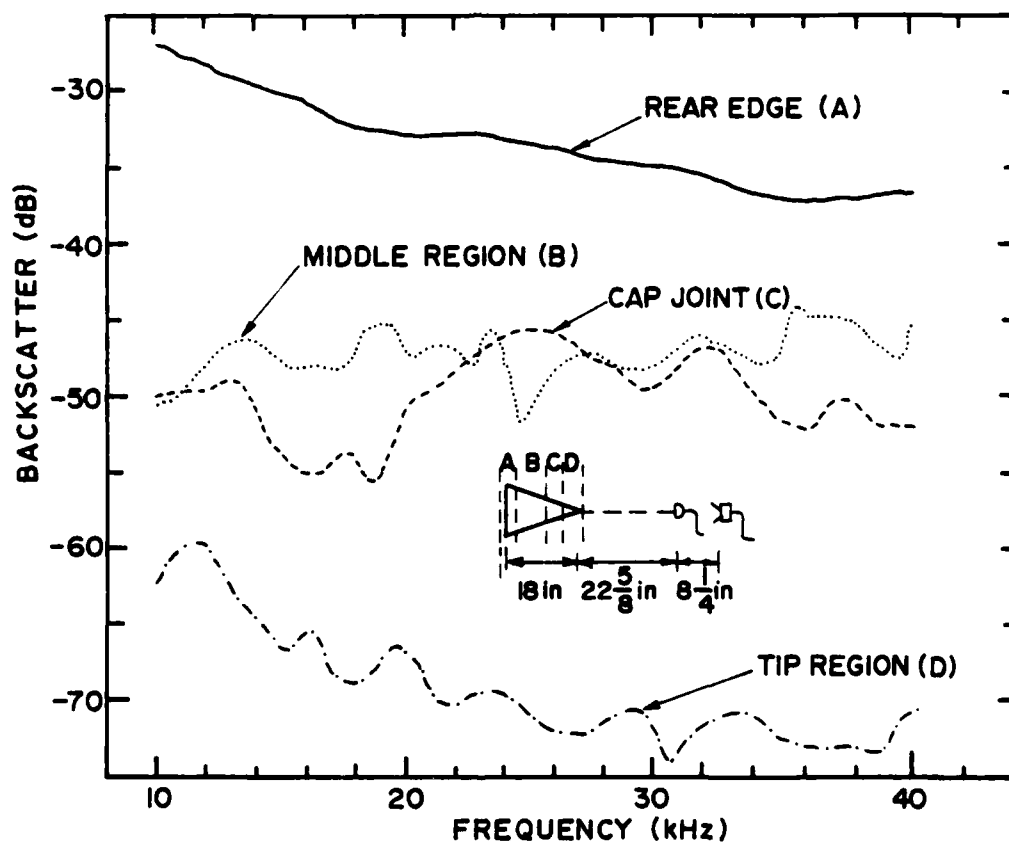


Figure 5.54 Frequency dependence of all the returns backscattered by the cone model at axial incidence.



returns. The origin of these echoes was never positively identified, but extensive experimentation led to the conclusion that they were either secondary returns (for example, cone to speaker to microphone) or were coming from the support wires at a distance somewhat above the cone's surface. Finally, a return was observed from the joint between the removable caps and the basic model. Both the joint return and the middle-region returns were considered extraneous to the information desired, and any effect of these components on the final results was carefully eliminated by time gating.

Although extraneous from the point of view of the planned experiments, the backscattered return from the cap attachment (joint) line provided useful intuitive information about the scattering process. The model and its various caps were all constructed with relatively high precision for a wooden structure. The error in the matching of the cap and cone-body cross sections along the joint circle was never more than  $1/32$  inch (usually much less), which is less than  $.1\lambda$  at the highest frequency used. Furthermore, the matching error was always such that the cap portion was larger in diameter, which resulted in a small shadow at the joint rather than a small specular area. From a visual perspective, the error in cross sectional matching appeared to be miniscule compared to the size of the model. However, it did represent a zeroth-order discontinuity in the surface, which is the most prominent edge-type scattering source. Based on this reasoning, the joint region of the cone model was carefully filled with modeling clay to form a smooth transition between the edge of the cap and the surface of the cone body. The results are shown in Figure 5.55. The return from the

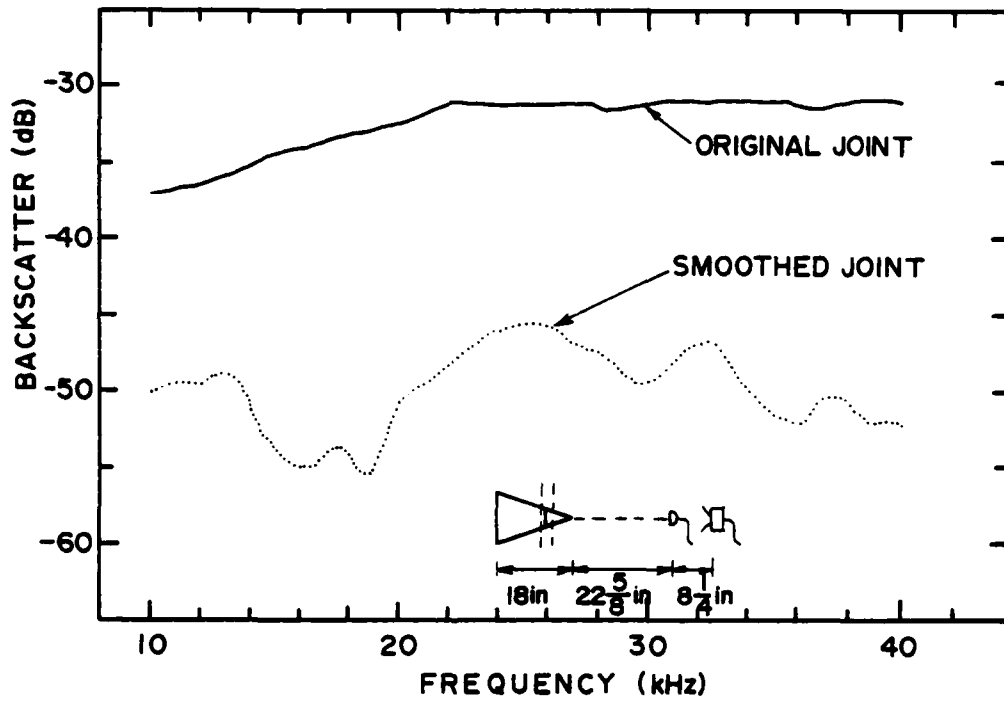


Figure 5.55 Frequency response of the backscattered return from the cap joint of the the cone model, both before and after smoothing with modeling clay.

cap joint has not been eliminated, but it has been reduced by almost 15 dB over the entire frequency range. A view of the directivity of the joint component at 20 kHz, both before and after smoothing the mismatch at the joint, is presented in Figure 5.56. The original joint acts much like the rear edge of the cone, while the directivity of the smoothed joint exhibits both a reduced amplitude and a change in form. This smoothing procedure was used with all the various caps and terminations of the model. The resulting cap-joint returns were thus reduced to the approximate level of the one just shown (see Figure 5.57). In fact, the agreement between the returns from the joint region among all the various caps is remarkable when one considers that each corresponding joint mismatch is different. These results point to an extreme sensitivity of the backscattering to small changes in the surface and surface curvature that makes experimental studies very difficult and that reduces the practical value of detailed considerations of the various types of edges.

#### 5.4.2 Backscattering at Axial Incidence

The frequency response of the cone model at axial incidence with each of the five caps and with the combination of the normal tip and the two terminations was examined. Theoretical predictions using the Freedman equations derived in Sections 2.4.5 and 2.4.6 were also computed and plotted. Because the measurements had to be made with the transducers relatively close to the scatterer, each backscattered component was individually normalized to the field incident at the point of its origin on the cone model. This eliminated any differences among

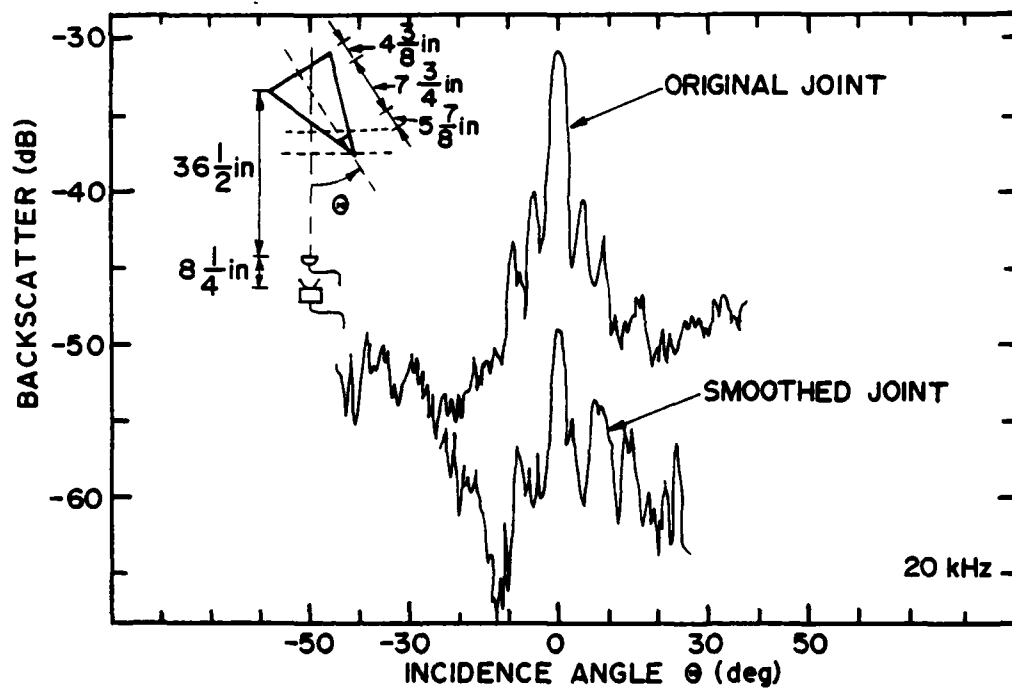


Figure 5.56 Directivity of the backscatter from the cap joint of the cone model, both before and after smoothing with modeling clay.

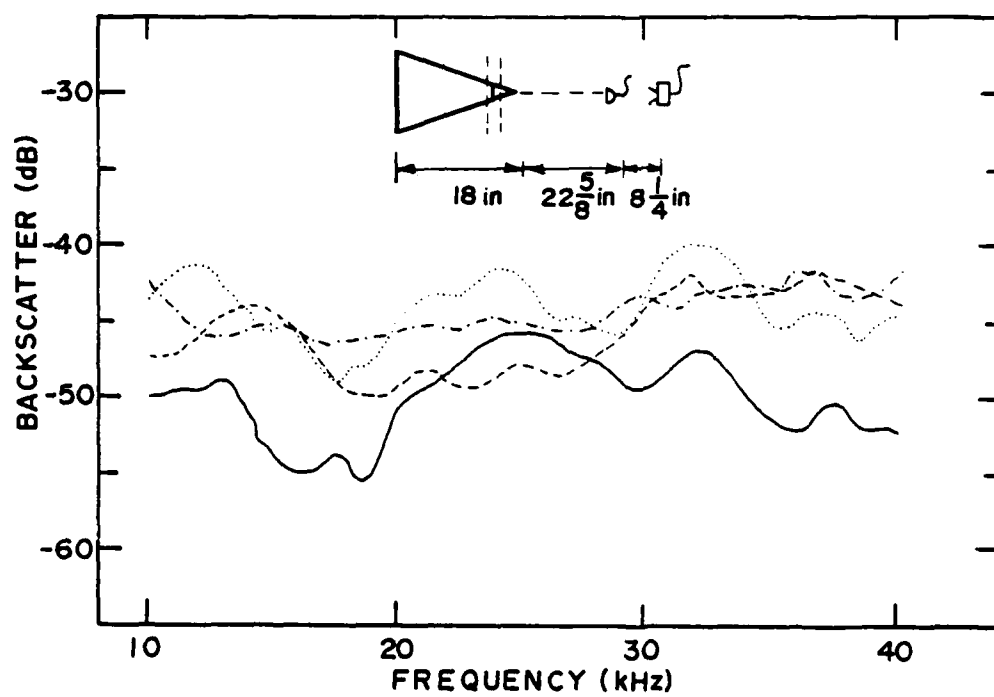


Figure 5.57 Frequency response of the backscatter from the smoothed cap joint of the cone model with several different caps attached.

the component returns that could be attributed to propagation losses over different path lengths. In the theoretical calculations, the  $r_m^2$  occurring in the denominator of all the terms was treated as the product of the distances from the source and receiver to the actual scattering feature on the model.

Figure 5.58 presents the results for backscattering obtained from the normal cone configuration. The agreement between experimental and theoretical data for the tip region is remarkable. Recall, however, that no distinct echo was observed experimentally at the tip. Thus, this agreement could be purely coincidental. The Freedman prediction for the rear edge, while in the general ballpark of the experimental results, has a distinctly different frequency dependence. In fact, the prediction has essentially reached its high-frequency limit. Based on the trend observed in Figure 5.58, the agreement between theory and experiment for the rear-edge return can be expected to get worse in frequency ranges both above and below that used for these experiments.

Changes observed in the cone model's backscattering when spherical caps with radii of 1/2, 1, and 2 inches are smoothly joined to the end of the cone are plotted in Figures 5.59 - 5.61. The rear-edge returns are essentially the same as those from the normal cone discussed in the previous paragraph, because this part of the model has not changed. However, the tip return has been replaced by a specular return from the spherical cap; and a new return from the second-derivative discontinuity, at which the spherical cap meets the cone outline, is predicted. The agreement between theory and experiment for the specular components from the cap is generally good, although the 1/2- and 2-inch

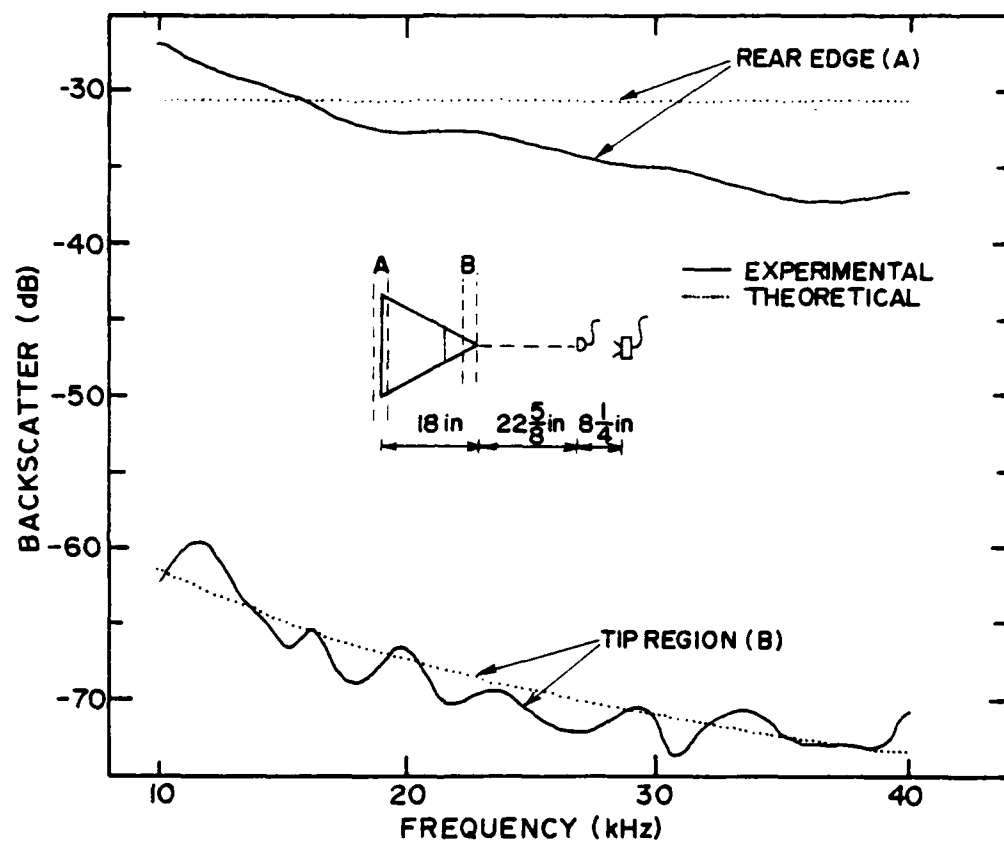


Figure 5.58 Frequency response of the backscattered returns from the cone model.

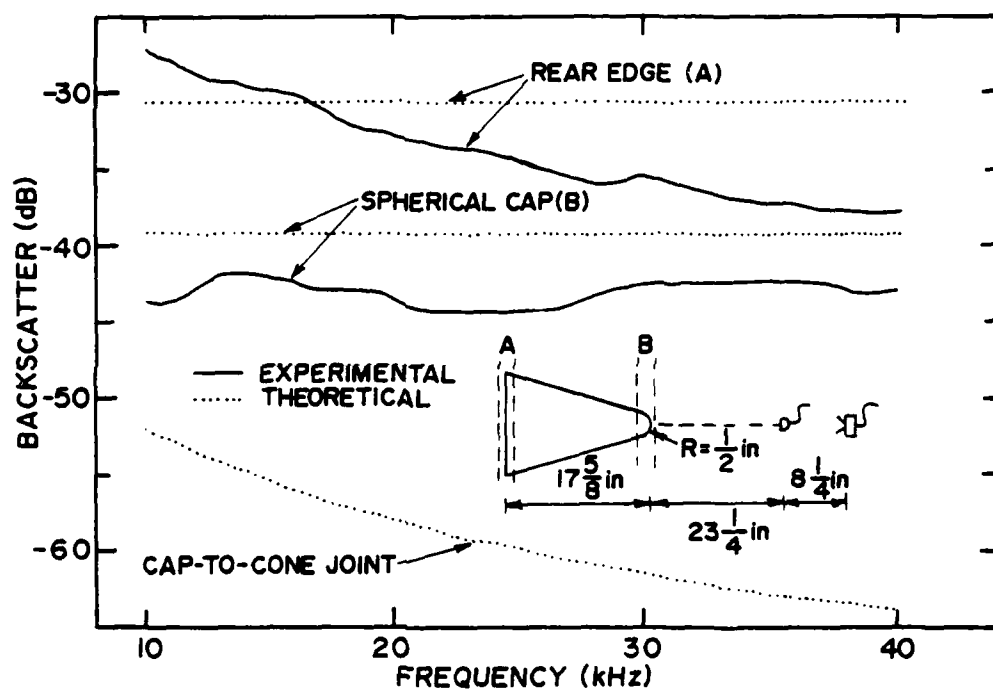


Figure 5.59 Frequency response of the backscattered returns from the cone with a spherical cap of 1/2-inch radius.



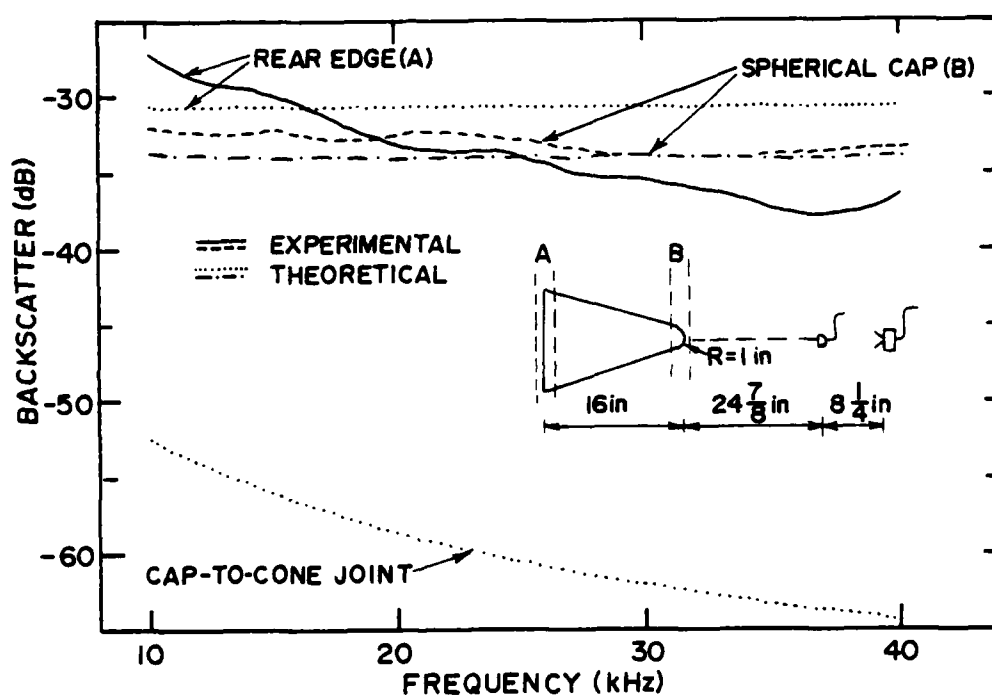


Figure 5.60 Frequency response of the backscattered returns from the cone with a spherical cap of 1-inch radius.

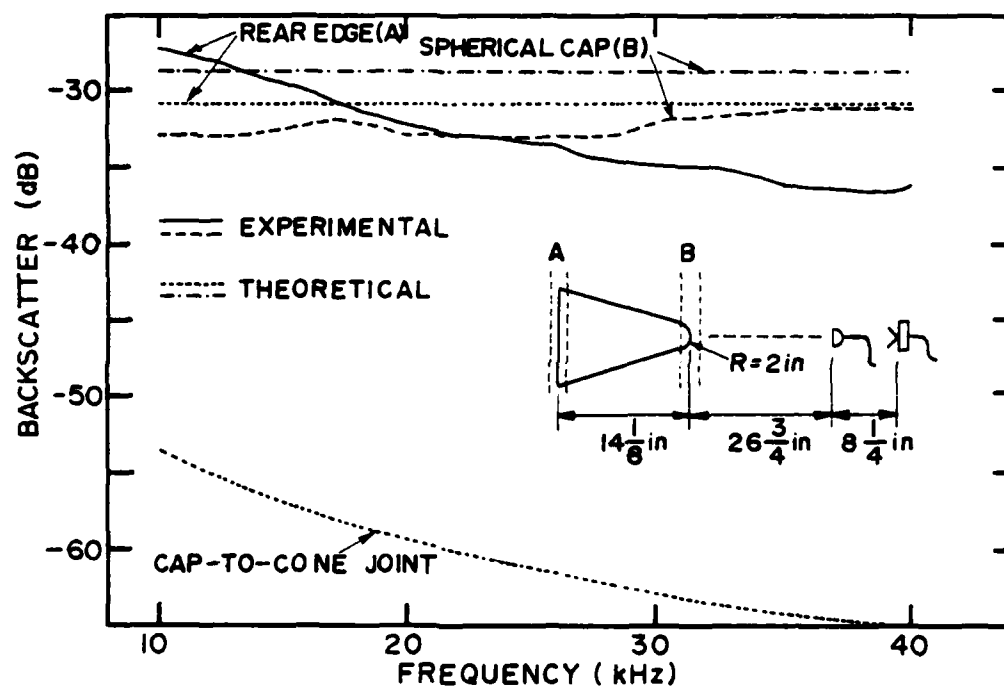


Figure 5.61 Frequency response of the backscattered returns from the cone with a spherical cap of 2-inch radius.

caps appear to be too small relative to the wavelength to generate the full amplitude of the predicted return. The slightly different trend observed with the 1-inch cap is more than likely caused by an imperfection in the cap itself. (This cap appears to be more blunt than it should be.) Any experimental return from the second-derivative joint is too close to the specular cap return to be observed separately, but it is apparently small enough to prevent noticeable interference oscillations in the frequency response of the cap return. This result is consistent with the prediction but not sufficient to judge the agreement with experiment.

Figure 5.62 shows the results obtained when the hemispherical cap of 2-inch radius is used with the basic cone. The specular return from the cap agrees well with the predicted value, possibly because of the much larger spherical area compared to that of the 2-inch smoothly joined cap. Good agreement is also noted between the experimental and predicted returns from the joint line between the hemisphere and the cone outline, which exhibits discontinuities in both slope and curvature. Note that, in this case, the surface discontinuity at the cap joint corresponds to the physical joint between the basic cone model and the removable cap. The physical match between this particular cap and the basic cone was probably the best of any of the removable caps. However, given the sensitivity of the data to small imperfections in the model at this joint (noted in Section 5.4.1), the agreement between theory and experiment for the joint component is remarkable.

Returning to the model with a normal tip, Figure 5.63 shows what happens when a hemisphere is attached to the rear of the cone. Since

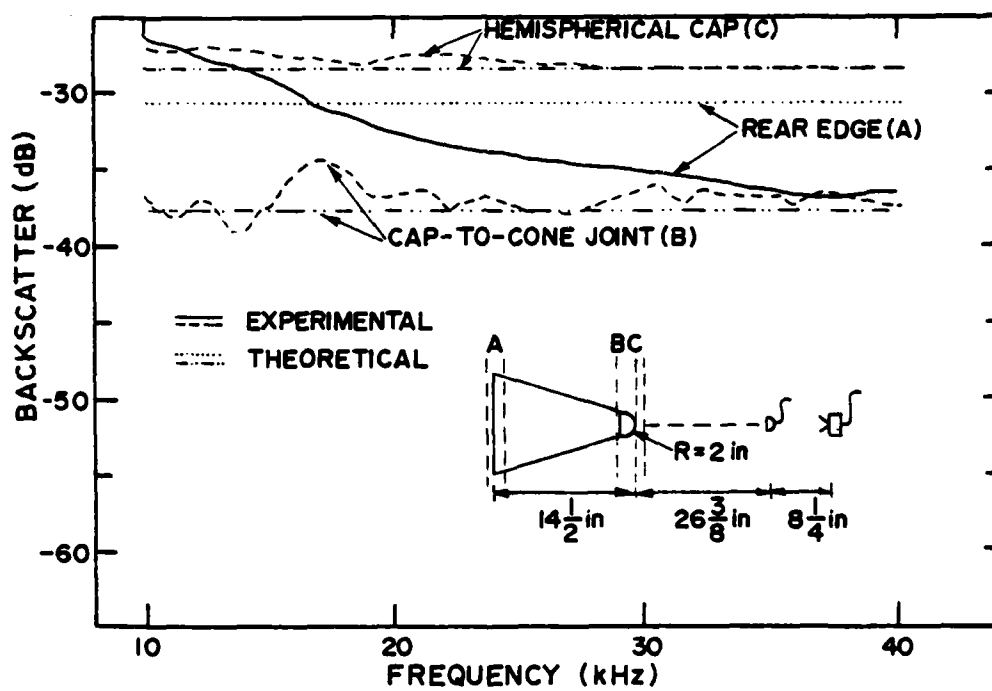


Figure 5.62 Frequency response of the backscattered returns from the cone with a hemispherical cap of 2-inch radius.

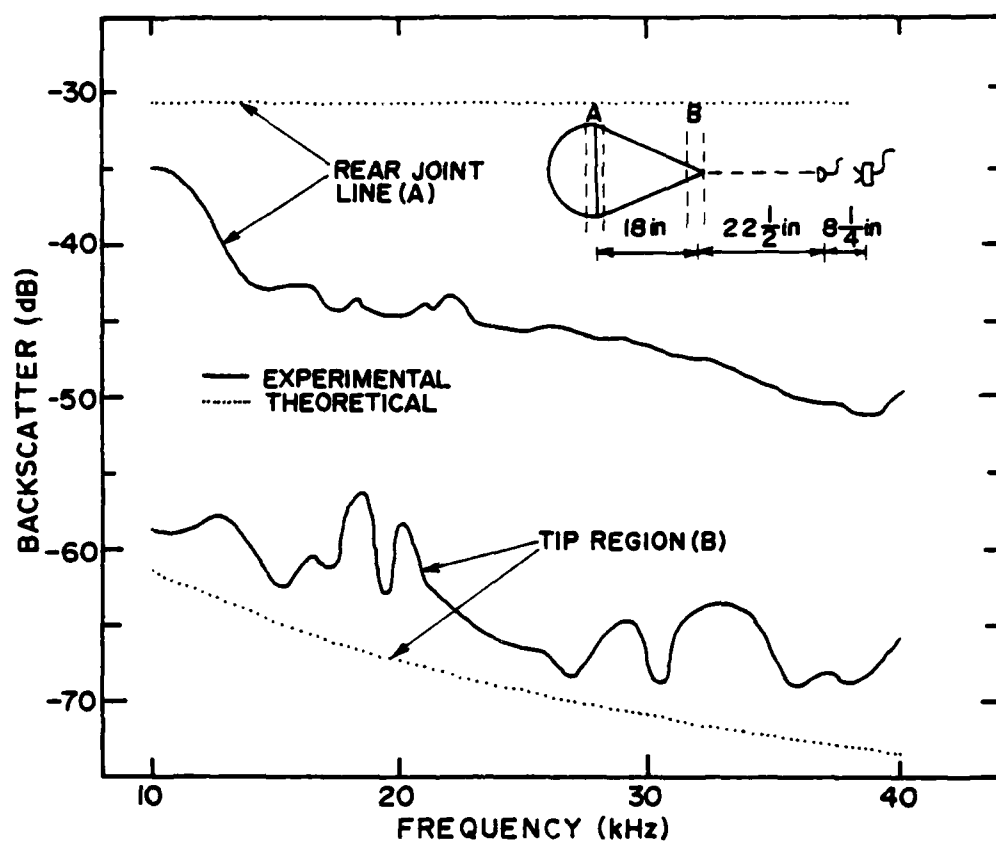


Figure 5.63 Frequency response of the backscattered returns from the cone with a hemispherical termination.

the only change in the model (compared to a normal cone) occurs in the geometrical shadow, the Freedman prediction is the same as that for the unterminated cone. However, the experimental data for the rear-edge component have changed considerably, and the agreement between theory and experiment is even poorer than noted previously with the normal cone. The tip of this model configuration is the same as that for the normal cone, but the experimental values associated with the tip region are now larger than the predicted values. It is difficult to draw any conclusions about this last fact, however, because there was still no distinct echo observed from the tip.

Figure 5.64 is a plot of the results that were obtained with a smooth spherical termination. The rear edge of the cone now exhibits only a second-order discontinuity. The experimental results from this edge are lower than those for the hemispherical termination, but not nearly as low as the predicted values. For comparison, the rear-edge returns from the unterminated, hemispherically terminated, and spherically terminated cone are plotted in Figure 5.65. The greatest change occurs between the unterminated and hemispherically terminated cones--the very cases that are indistinguishable to the Freedman theory. With the spherical termination, a return from the shadow boundary is also predicted, but no such component was observed. (This fact has been noted by other researchers as a fault of physical-optics approaches.) An additional return, however, was observed at some frequencies, apparently originating at the antipole in the shadow of the spherically terminated cone. This barely perceptible component may have been caused by the suspension-point anchor countersunk into the model in that vicinity.

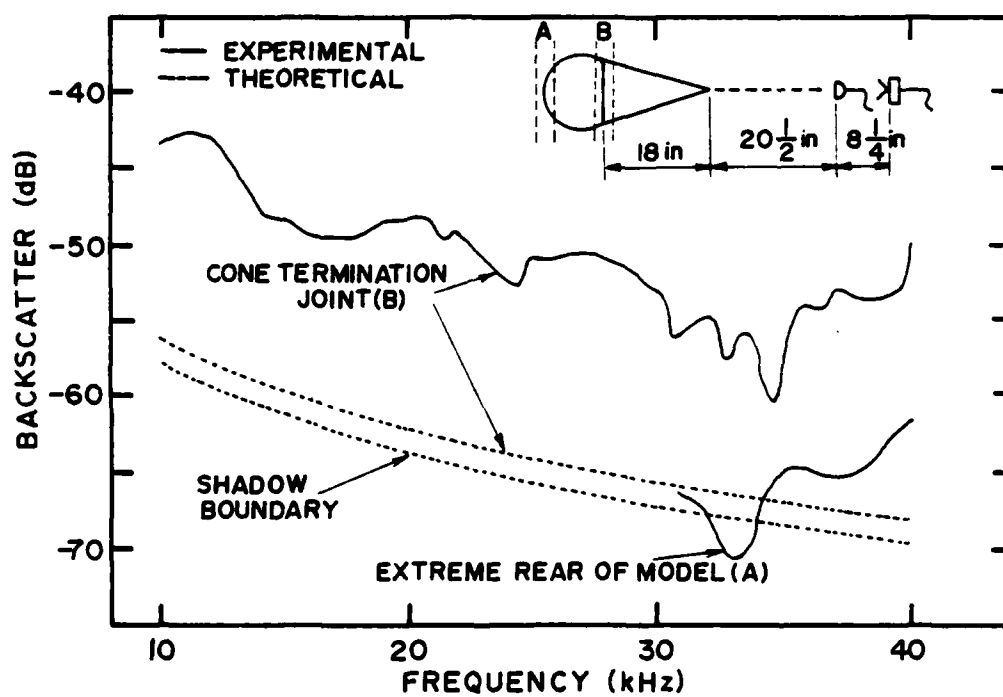


Figure 5.64 Frequency response of the backscattered returns from a cone with a smooth spherical termination.

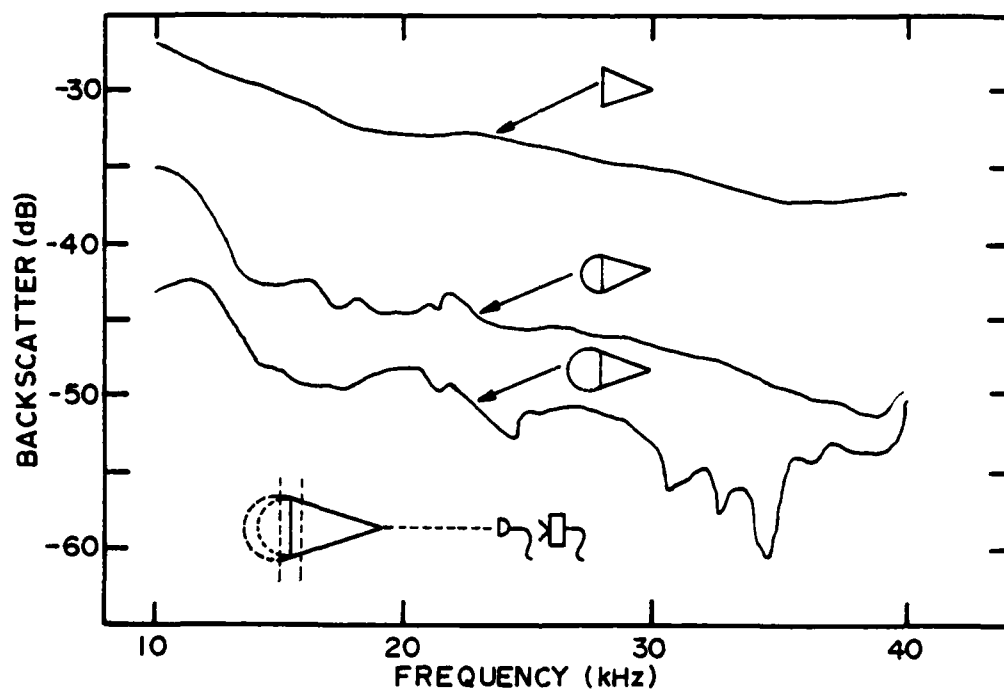


Figure 5.65 Frequency response of the backscatter from the rear edge of the cone model with no termination, a hemispherical termination, and a smooth spherical termination.



### 5.4.3 Scattering by a Normal Cone

Although the Freedman theory cannot provide predictions for the backscattering from a cone at other than axial incidence, this intuitive investigation has moved on to examine both backscattering and scattering from a cone at other incidence angles. For example, directivities of the backscatter from the 18-inch-long,  $20^\circ$ -half-angle cone at frequencies of 10, 20, 30, and 40 kHz are shown in Figures 5.66 - 5.69, respectively. Observations made during these experiments showed that, in the angular range of about  $0^\circ - 40^\circ$ , the data are dominated by the return from the rear edge. The characteristic peak at axial incidence, at which the edge is parallel with the incident wavefront, is seen at all frequencies. A lobe structure similar to that associated with extended radiating sources is also observed in the curves. As the frequency increases, the lobes in this rear-edge pattern get closer together, the edge contribution decreases in importance, and the overall dynamic range increases as all reflections become more directional. Note that the rear-edge return is really only prominent near axial incidence. However, it still dominates over a fairly wide angular range because there are no other contributing sources of any significance. For angles off axial incidence, the rear-edge return appears as a distinct echo originating at the nearest point on the illuminated portion of the edge. In the vicinity of  $70^\circ$ , a strong specular return from the side of the cone dominates all others.

Some data of backscattering from the base of the cone were also collected, and this information is summarized in Figures 5.70 - 5.73. The model in this orientation was expected to act essentially like a

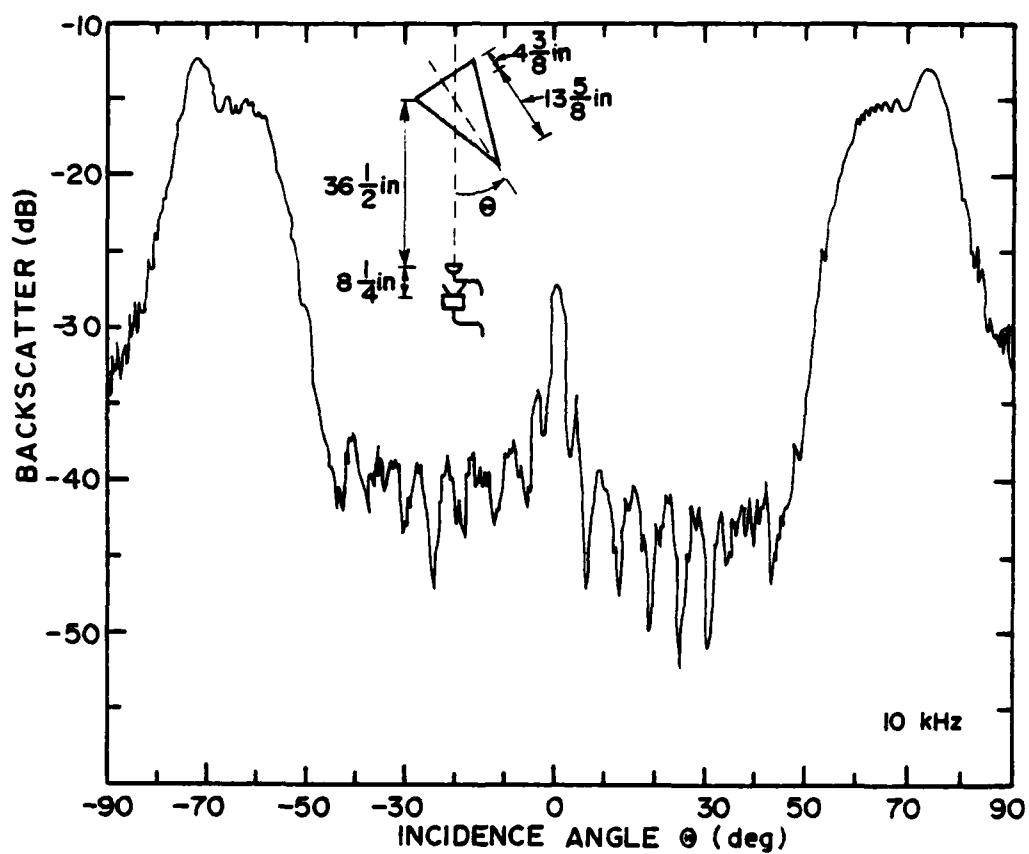


Figure 5.66 Directivity of the backscatter from the 18-inch cone model at 10 kHz. ( $kh = 84$ )

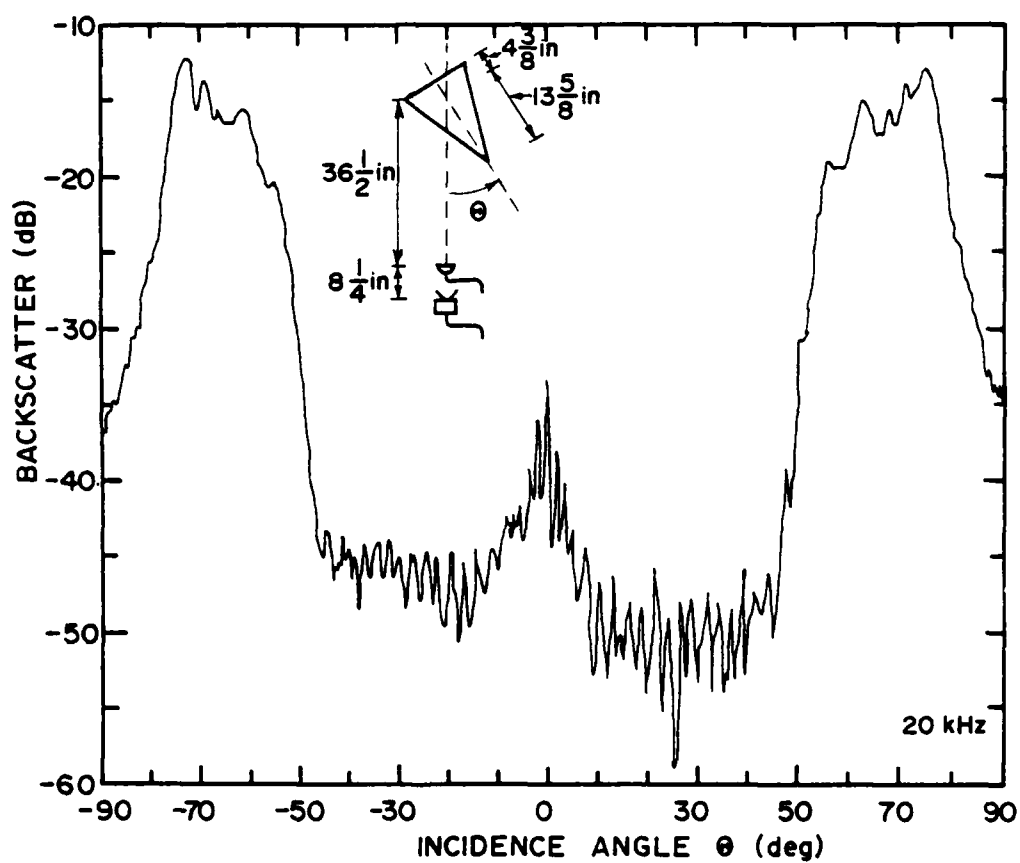


Figure 5.67 Directivity of the backscatter from the 18-inch cone model at 20 kHz. ( $kh = 168$ )

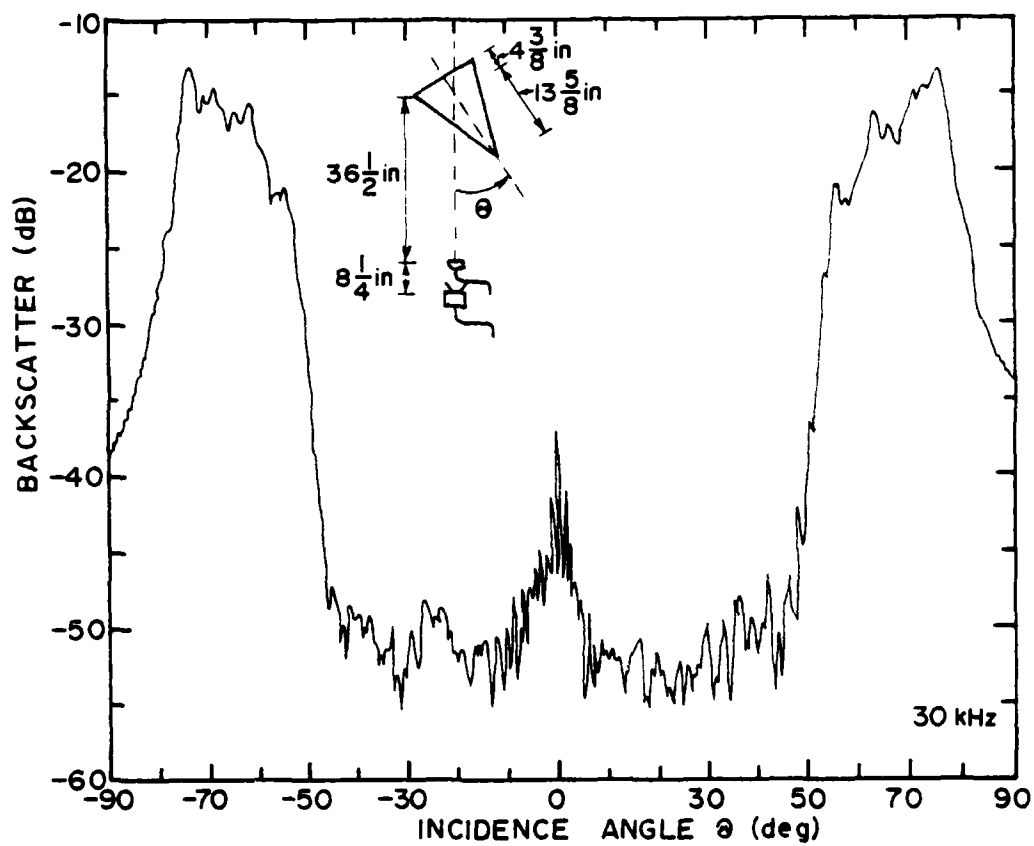


Figure 5.68 Directivity of the backscatter from the 18-inch cone model at 30 kHz. ( $kh = 251$ )

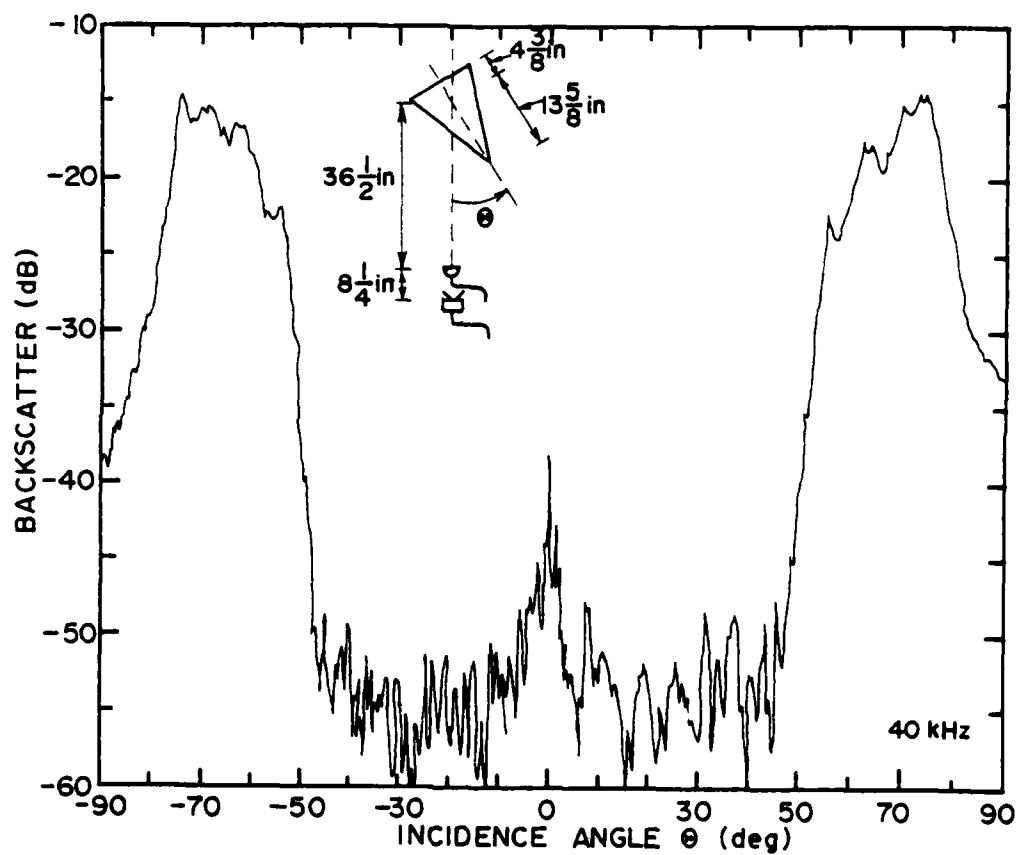


Figure 5.69 Directivity of the backscatter from the 18-inch cone model at 40 kHz. ( $kh = 335$ )

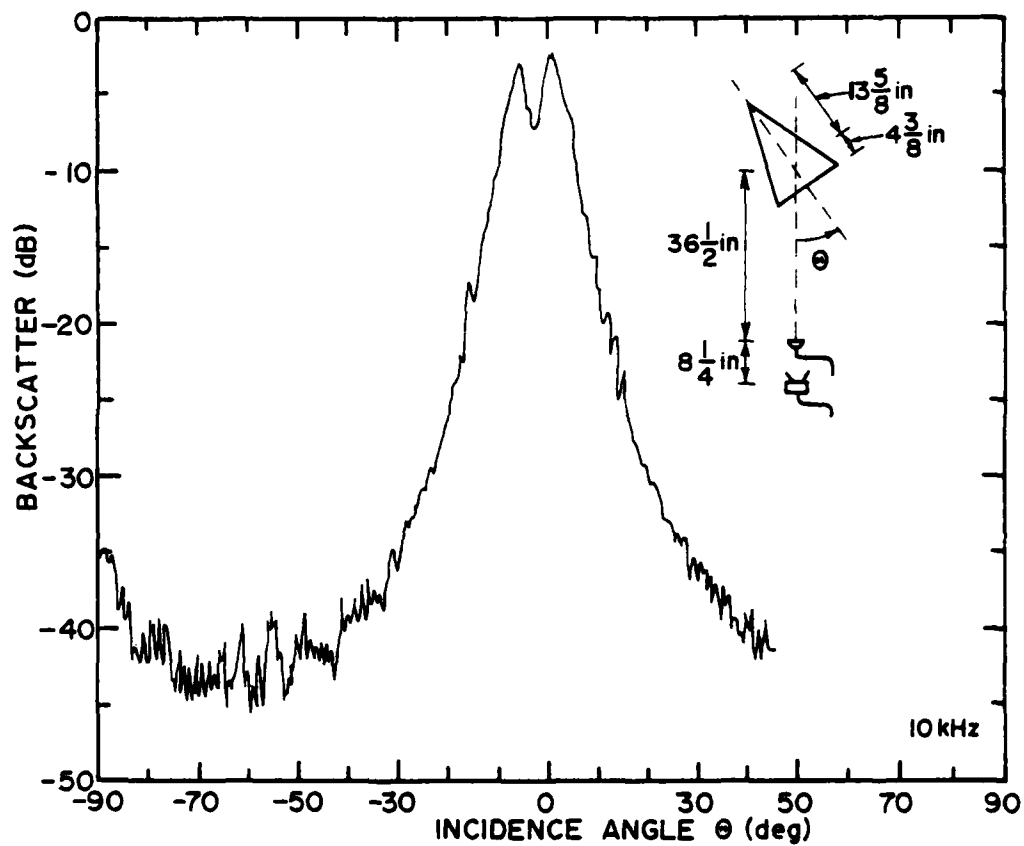


Figure 5.70 Directivity of the backscatter from the rear disk of the 18-inch cone model at 10 kHz. ( $kr = 30$ )

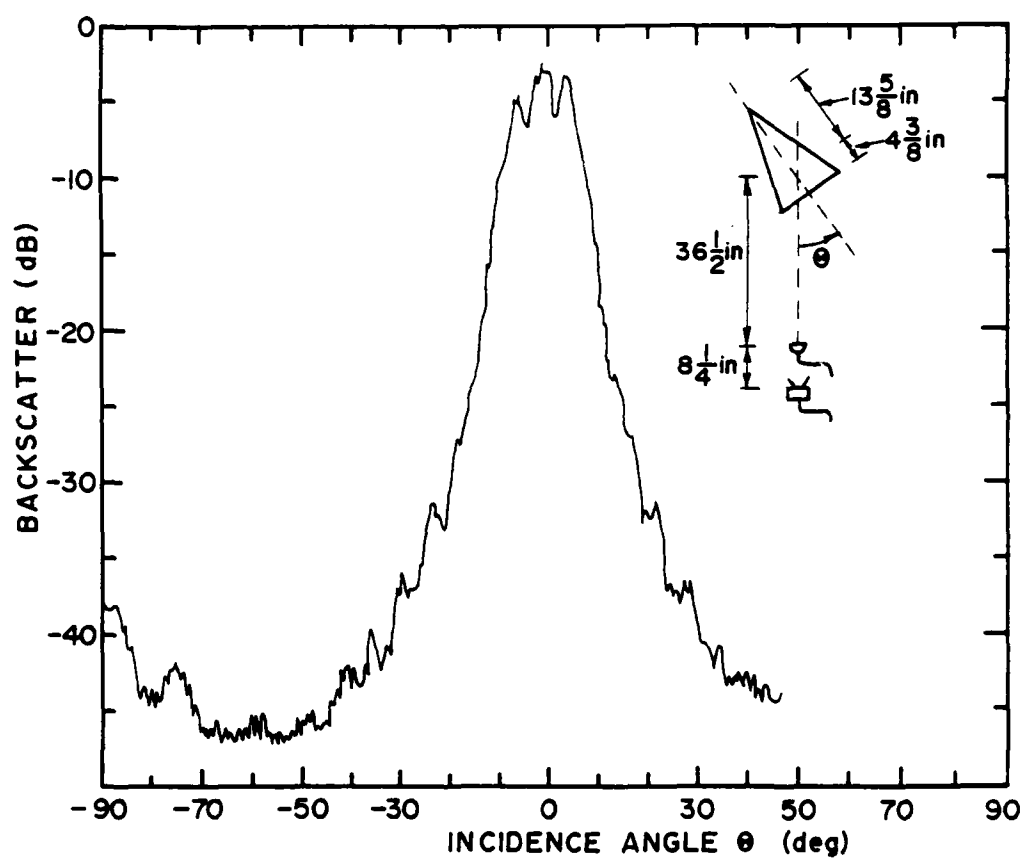


Figure 5.71 Directivity of the backscatter from the rear disk of the 18-inch cone model at 20 kHz. ( $kr = 61$ )

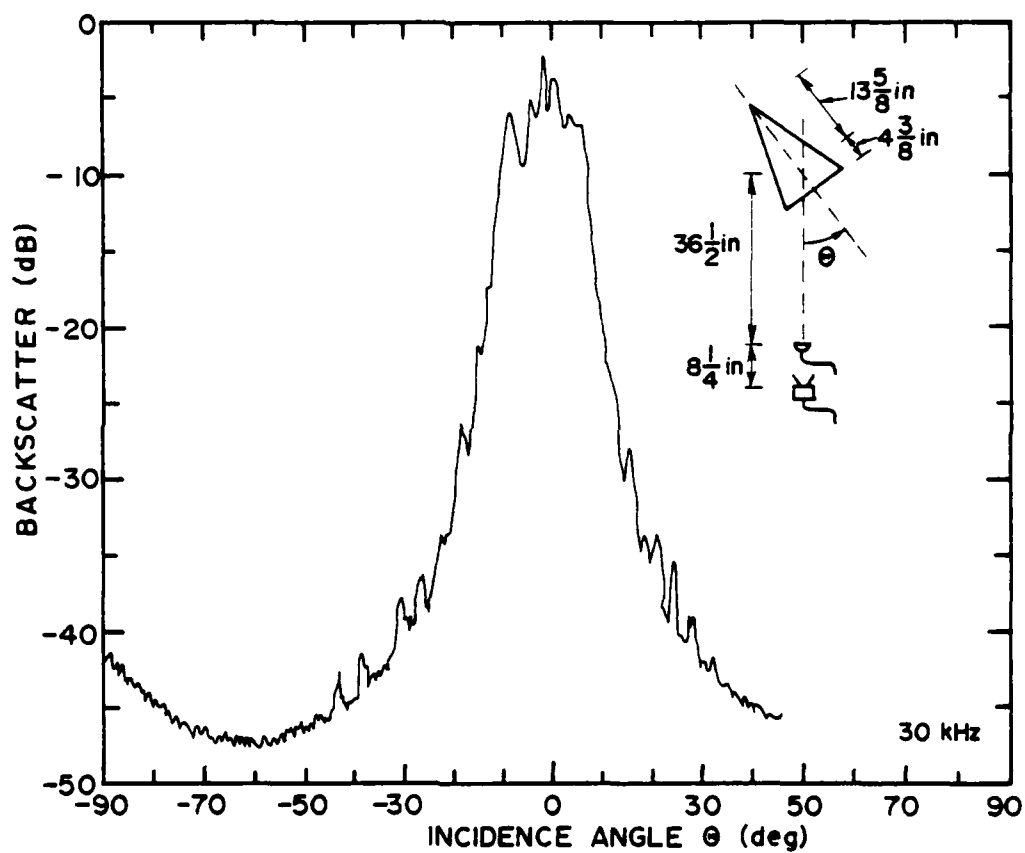


Figure 5.72 Directivity of the backscatter from the rear disk of the 18-inch cone model at 30 kHz. ( $kr = 91$ )



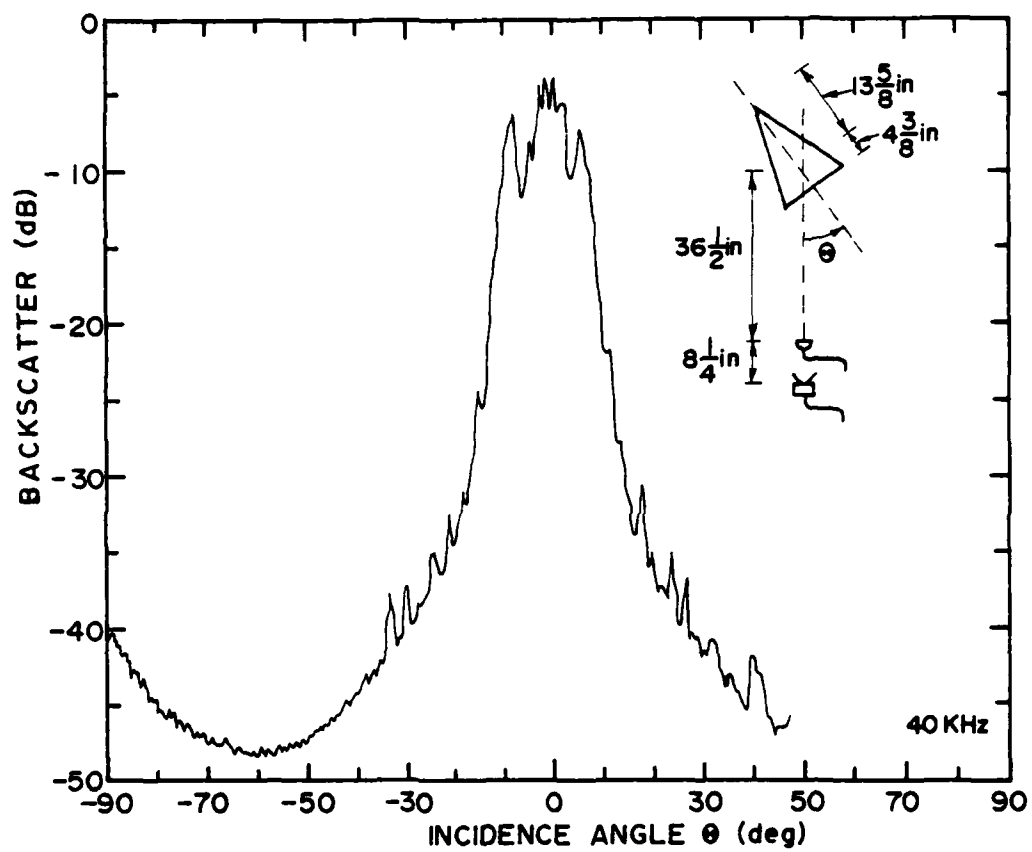


Figure 5.73 Directivity of the backscatter from the rear disk of the 18-inch cone model at 40 kHz. ( $kr = 122$ )

disk or the end of a cylinder. However, unlike the cylinder data presented in Section 5.3, the echoes from the individual edges of the disk were resolved in time. At axial incidence (on the rear of the cone), a strong specular return was observed. As the model was then rotated, this single return split into components from the points along the edge that were nearest and furthest from the microphone. This verified that a disk does produce two distinct echoes, just as predicted by the Freedman formulation. Additional returns between these two echoes were observed at some incidence angles, but these were probably caused by the mounting plate for the model's rear terminations that is countersunk into the base of the cone model. It is interesting to note the relative insensitivity of the backscattering data from the disk to a change in frequency--not only the specular level, but also the width of the axial peak and the level at angles other than axial incidence.

As an adjunct to the data already discussed, the bistatic scattering of the 18-inch cone model was measured at frequencies of 10, 20, 30, and 40 kHz. These data are presented in Figures 5.74 - 5.77. The prominent lobe structure near axial incidence, as well as the remainder of the data plotted, can all be attributed to the rear edge. The axial lobes are similar to those observed with the backscattered data discussed in the previous paragraph. However, the widths of the lobes are approximately doubled because, in this case, the paths followed by the two edge returns (whose interference generates the oscillations) are different only on the return path. It is interesting to note that the basic shape of the bistatic curves at different frequencies remains the same, even though the absolute levels do decrease with increasing frequency.

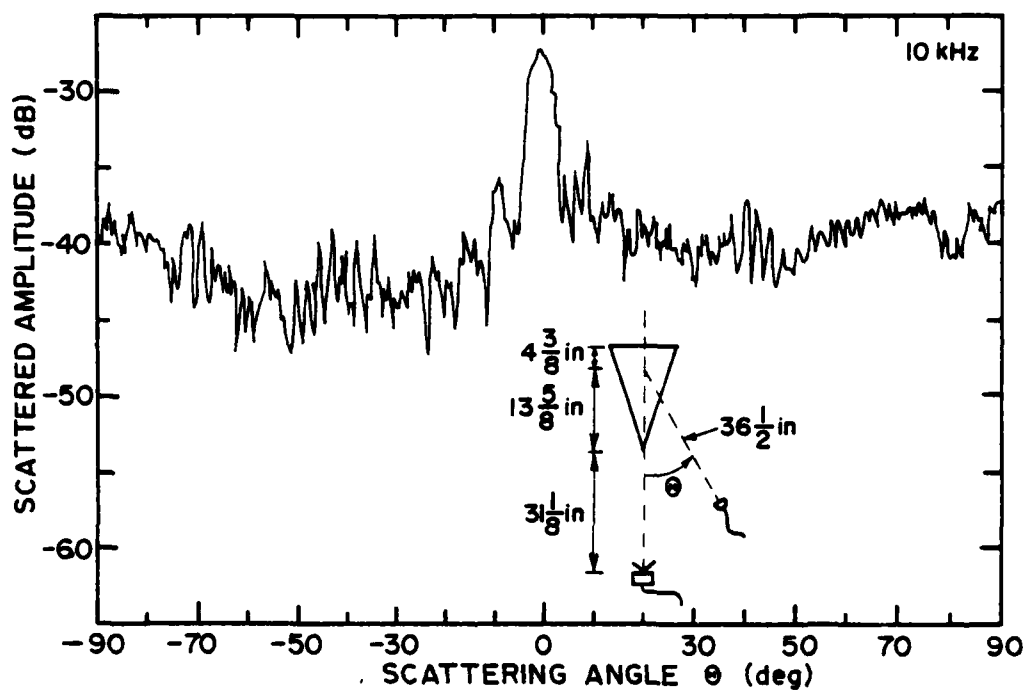


Figure 5.74 Bistatic scattering from the 18-inch cone model for axial incidence at 10 kHz. ( $kh = 84$ )

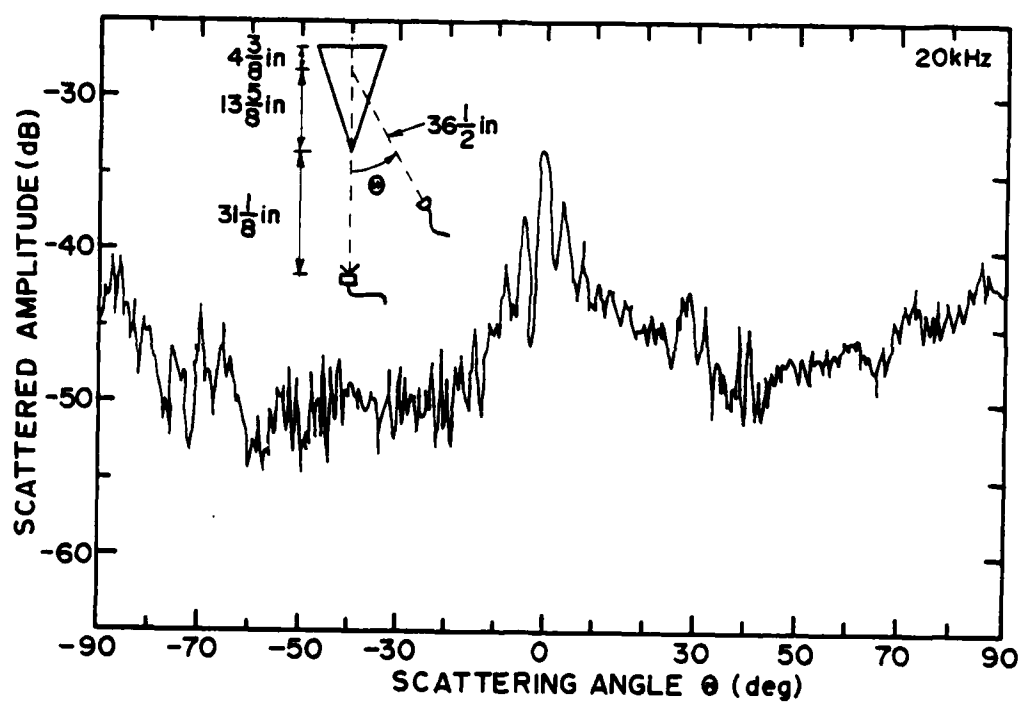


Figure 5.75 Bistatic scattering from the 18-inch cone model for axial incidence at 20 kHz. ( $kh = 168$ )

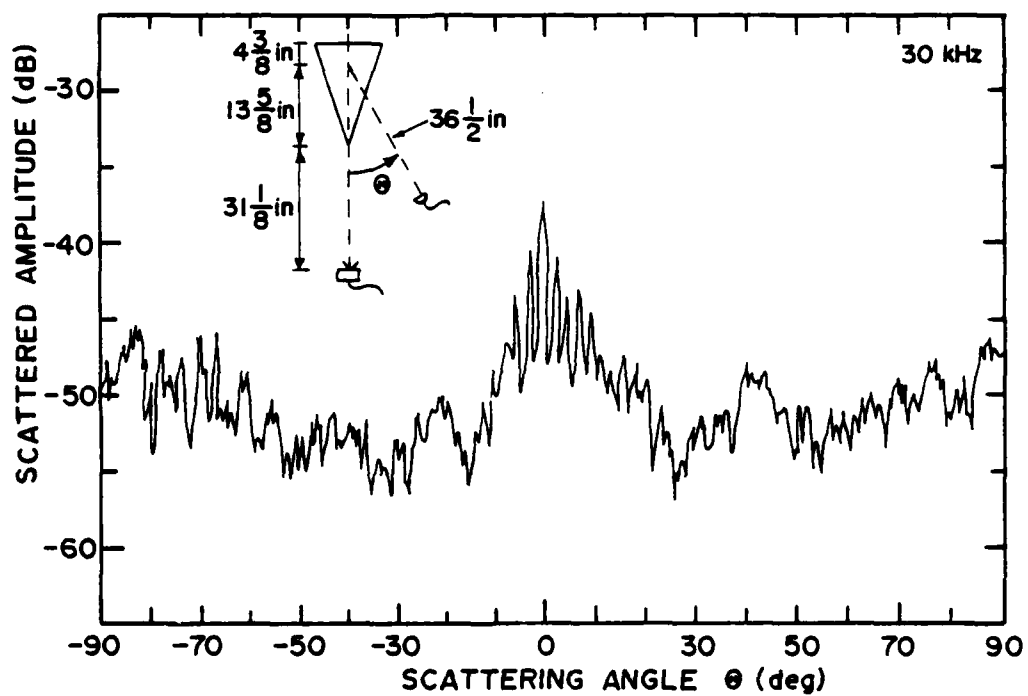


Figure 5.76 Bistatic scattering from the 18-inch cone model for axial incidence at 30 kHz. ( $kh = 251$ )

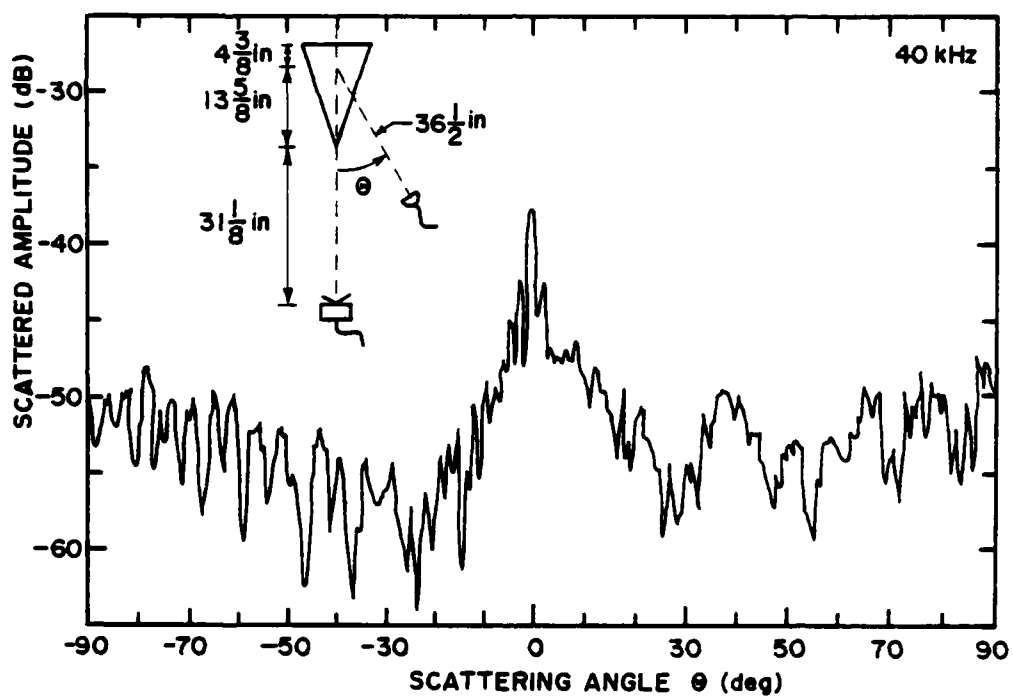


Figure 5.77 Bistatic scattering from the 18-inch cone model for axial incidence at 40 kHz. ( $kh = 335$ )

The bistatic scattering from the model at  $20^\circ$  incidence is presented in Figures 5.78 and 5.79 for frequencies of 20 and 40 kHz, respectively. At all angles plotted to the right of  $-50^\circ$ , the returns originate at the rear edge. Note that, in the 20-kHz plot (Figure 5.78), a peak in the scattered return is visible at twice the angle of incidence. This angle is at a point that corresponds to a direct reflection from the cone's tip. A similar peak is not observed at 40 kHz. The large peak at the left side of the figures is a specular return reflected from the side of the cone at the normal reflection angle. Figures 5.80 and 5.81 show what happens to the bistatic scattering at the same two frequencies for  $45^\circ$  incidence. These results are similar to the previous results taken at  $20^\circ$  incidence. It is now possible, however, to see that the specular return from the side of the cone extends over a fairly broad angular area. Looking at the data for both  $20^\circ$  and  $45^\circ$  incidence, very little difference with respect to frequency is noted in the scattering, except for a slightly lower amplitude in the regions dominated by rear-edge components at the higher frequency.

#### 5.4.4 Scattering by Cones with Spherical and Hemispherical Caps

One method for comparing the relative influence of specular and edge-generated scattering components is to modify the tip of a cone so that it becomes a spherical surface. By choosing how this spherical surface is joined to the cone outline, an additional first- or second-order edge can also be created. It has already been mentioned (see the beginning of Section 5.4) that four such tip modifications were

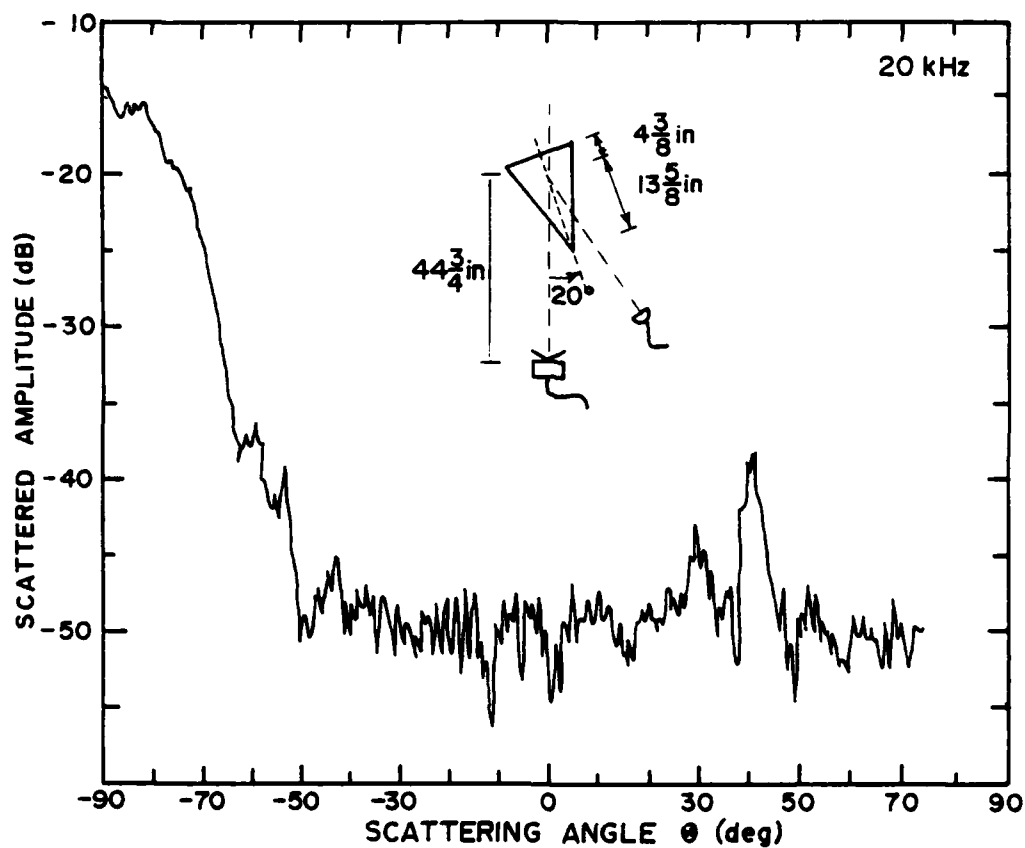


Figure 5.78 Bistatic scattering from the 18-inch cone model for  $20^\circ$  incidence at 20 kHz. ( $kh = 168$ )



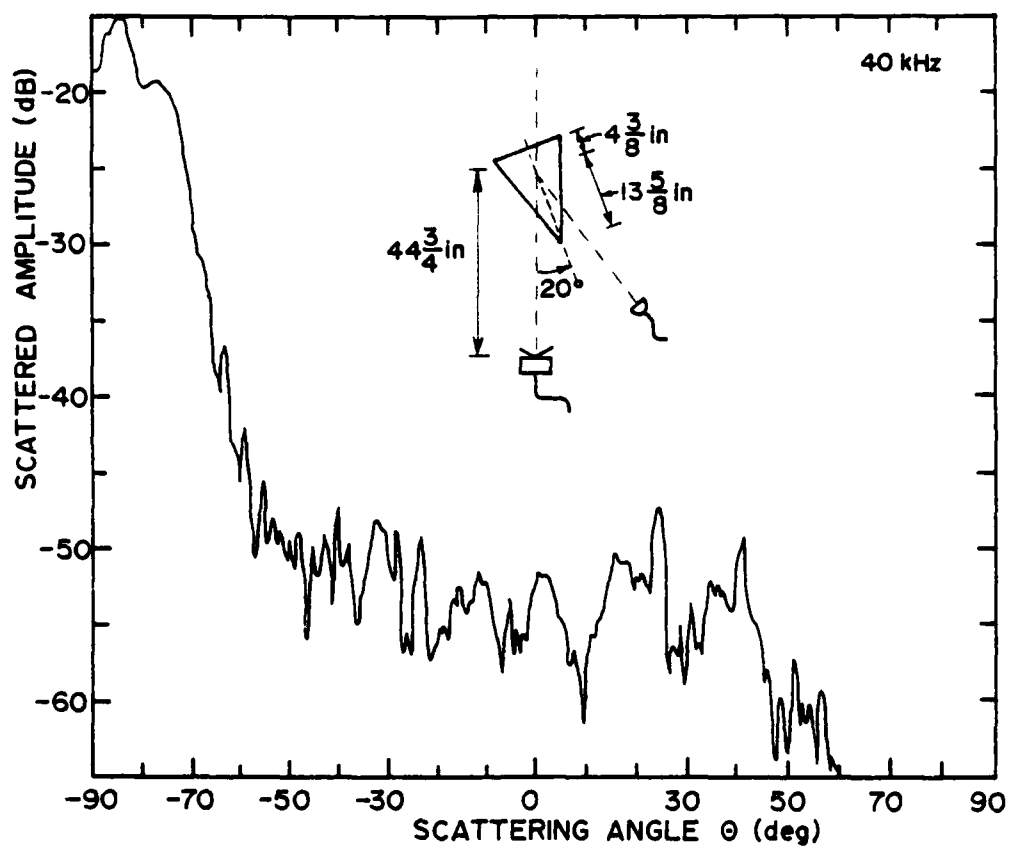


Figure 5.79 Bistatic scattering from the 18-inch cone model for  $20^\circ$  incidence at 40 kHz. ( $kh = 335$ )

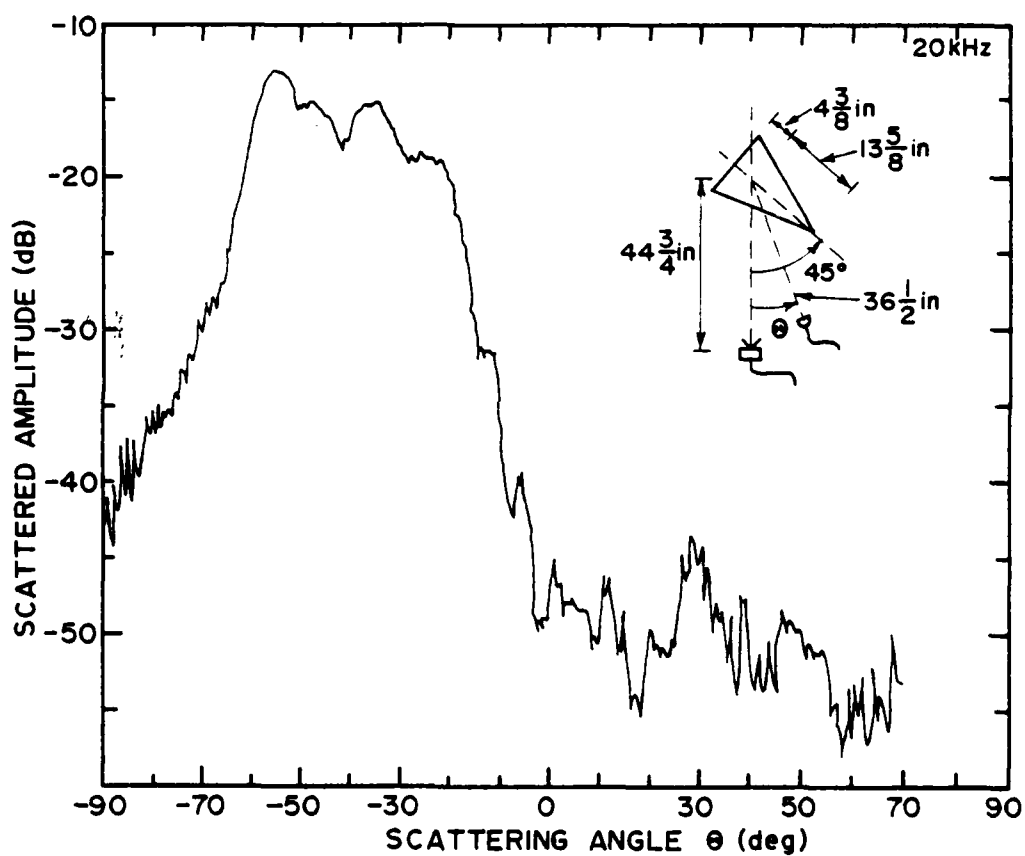


Figure 5.80 Bistatic scattering from the 18-inch cone model for  $45^\circ$  incidence at 20 kHz. ( $kh = 168$ )

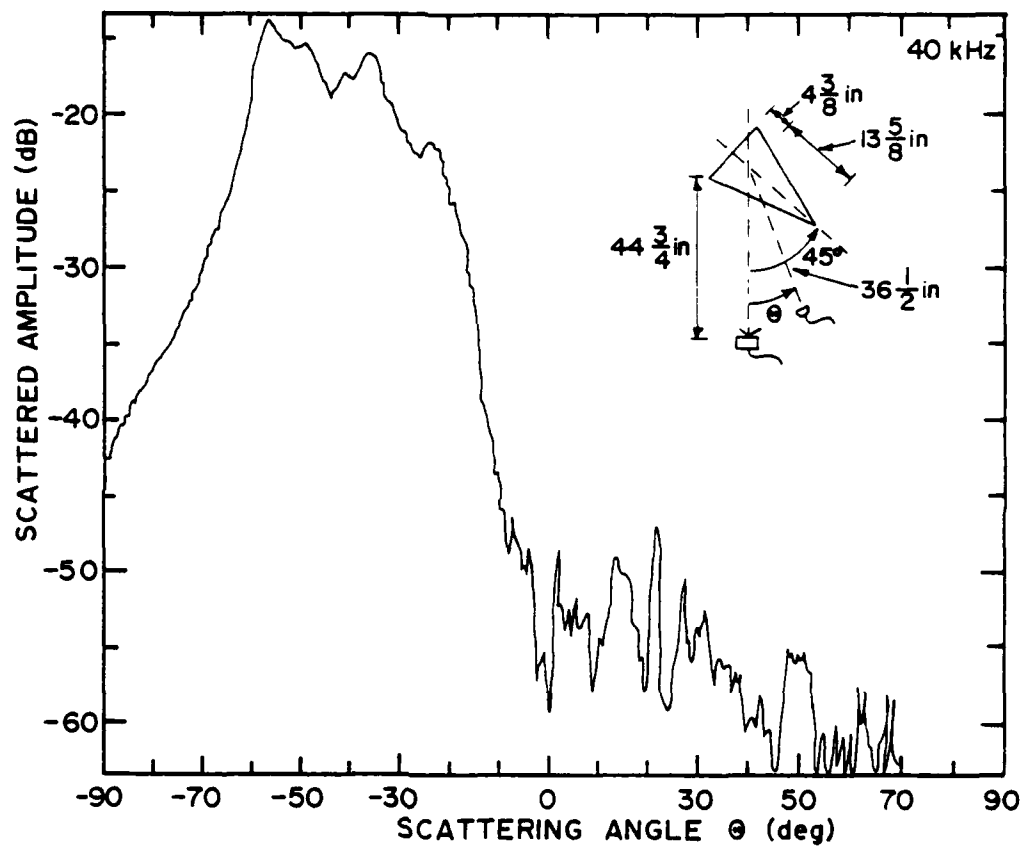


Figure 5.81 Bistatic scattering from the 18-inch cone model for  $45^\circ$  incidence at 40 kHz. ( $kh = 335$ )

constructed and used in this investigation: three smoothly joined spherical tips of 1/2-, 1-, and 2-inch radii and a hemisphere of 2-inch radius. Except for the hemisphere, the edges created at the discontinuity between the spherical cap and the cone did not scatter enough to be visible over the nearby specular return. However, some interesting comparisons of specular and rear-edge returns were possible.

Figures 5.82 - 5.84 are directivity plots of the backscattering from the cone with the three different spherical caps at 10 kHz. The data for the 1/2-inch-capped model are essentially the same as those for a normal cone because the rear-edge contribution dominates at all angles except the angle of the specular region near  $70^\circ$ . The spherical surfaces of the other two caps, however, generate echoes that are strong enough to dominate the shape of the curves over all the central angular range (about  $\pm 40^\circ$ ) except right at  $0^\circ$ . Any comparison between the cap and rear-edge components must take into account the fact that the rear-edge component suffers a propagation loss of about 8 dB greater than that of the cap. (Recall that the frequency-response data for axial incidence presented in Section 5.4.2 were compensated for the different propagation paths, while the present data have not been compensated.) However, it is clear that the amplitude of the edge component falls somewhere between the amplitude of the specular components from the 1/2-inch cap ( $kR = 2.3$ ) and the 1-inch cap ( $kR = 4.6$ ). Note also that, as the radius of the cap gets larger, its directivity begins to look more and more like the uniform pattern associated with a sphere (see Figure 5.84).

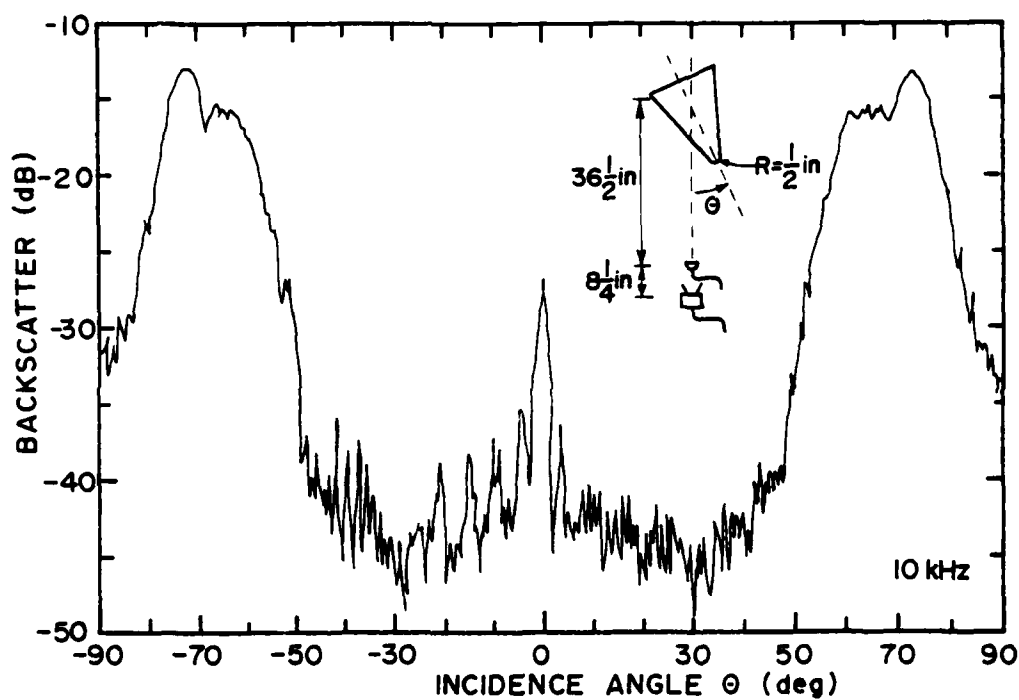


Figure 5.82 Directivity of the backscatter at 10 kHz from the cone model with a spherical cap of  $\frac{1}{2}$ -inch radius. ( $\lambda = 1.35$  inch)

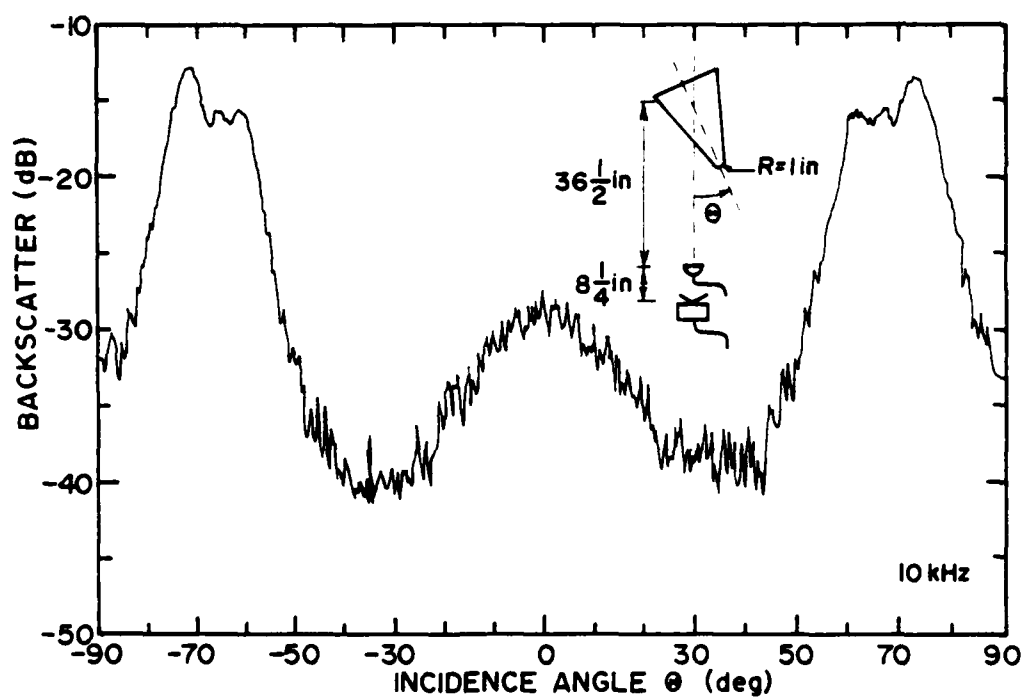


Figure 5.83 Directivity of the backscatter at 10 kHz from the cone model with a spherical cap of 1-inch radius. ( $\lambda = 1.35$  inch)

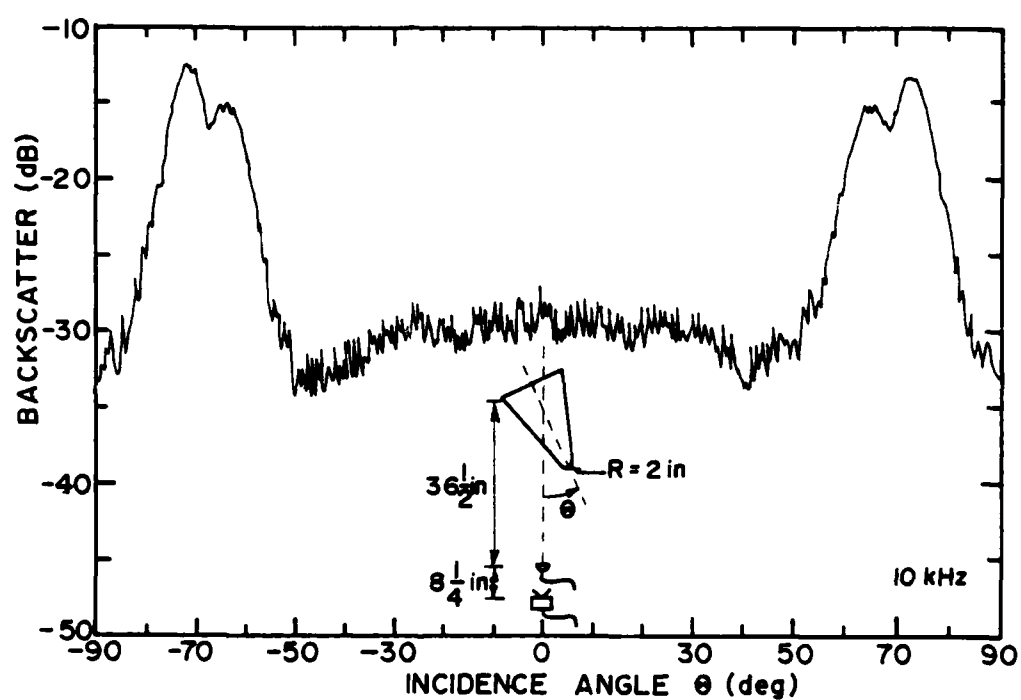


Figure 5.84 Directivity of the backscatter at 10 kHz from the cone model with a spherical cap of 2-inch radius. ( $\lambda = 1.35$  inch)

Figure 5.85 is a plot of the backscattered directivities at 20 kHz from the cone models with all three spherical caps, and Figures 5.86 and 5.87 present similar data at 30 and 40 kHz. At these frequencies, the specular return from the 1/2-inch cap is strong enough to dominate the total backscattering except for the peak at axial incidence from the rear edge. A comparison of the absolute levels between these cases and the 10-kHz case discussed in the previous paragraph shows that this specular domination is caused more by the decline with increasing frequency of the rear-edge component than any increase in the tip's specular component. The levels of the specular returns, in fact, remain fairly constant with frequency. The shape of the curves near axial incidence, however, does become more uniform at higher frequencies, probably because the smaller effective (specular) scattering area remains on the spherical cap over a larger range of incidence angles.

Results for bistatic scattering from the three spherically capped models at 10 kHz are presented in Figure 5.88. Just as for backscattering, the rear-edge component dominates the curve for the 1/2-inch-capped model, but it affects the curves for the other two models only near axial incidence. The scattered returns that are determined by specular effects are considerably different in form from those attributable to edge effects. The specular returns approximate the uniform result of a sphere to a degree that is dependent on the size of the cap's radius. As an additional comparison, a plot of the bistatic scattering from only the cap of the 1/2-inch-capped model is shown in Figure 5.89. This curve has roughly the same form as the specular curves for the caps of larger diameter, but it occurs at a



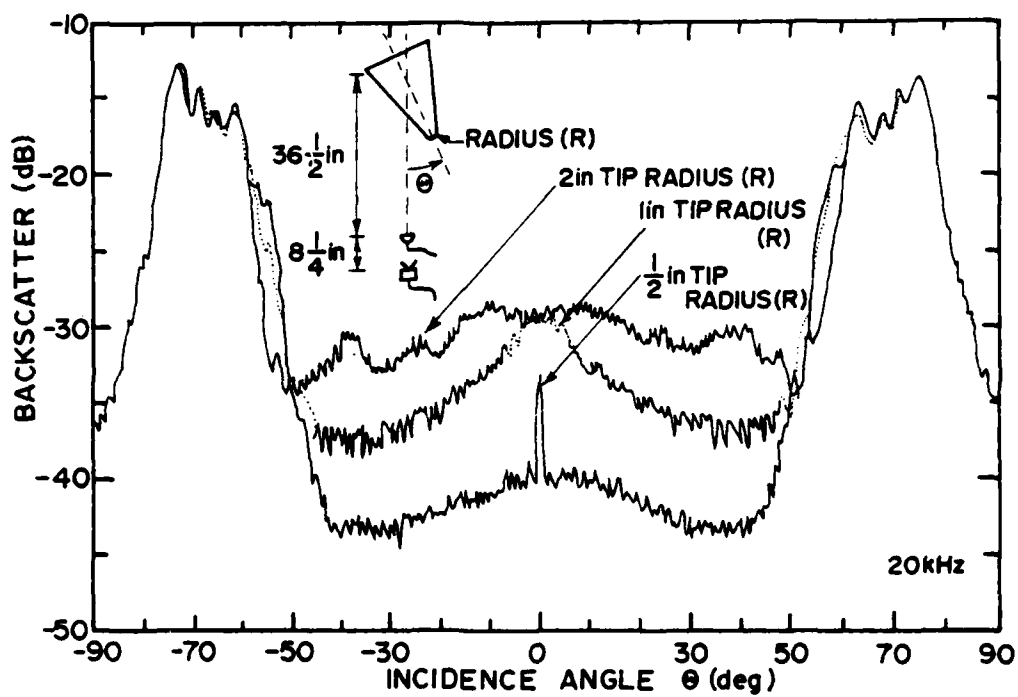


Figure 5.85 Directivity of the backscatter at 20 kHz from the cone model with spherical caps having radii of 1/2, 1, and 2 inches. ( $\lambda = .675$  inch)

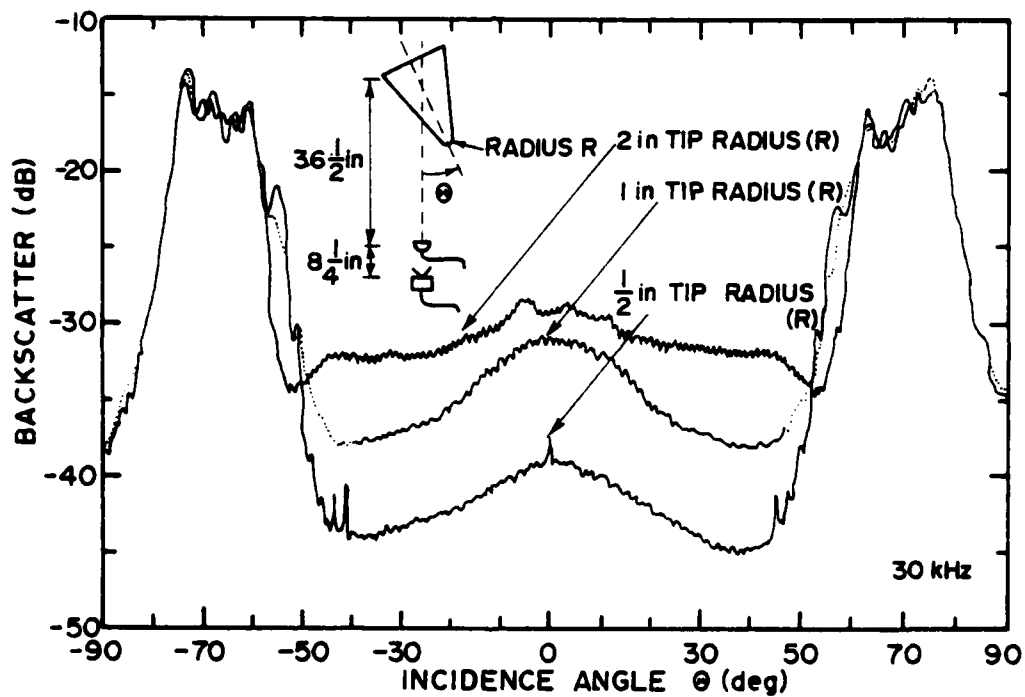


Figure 5.86 Directivity of the backscatter at 30 kHz from the cone model with spherical caps having radii of 1/2, 1, and 2 inches. ( $\lambda = .45$  inch)

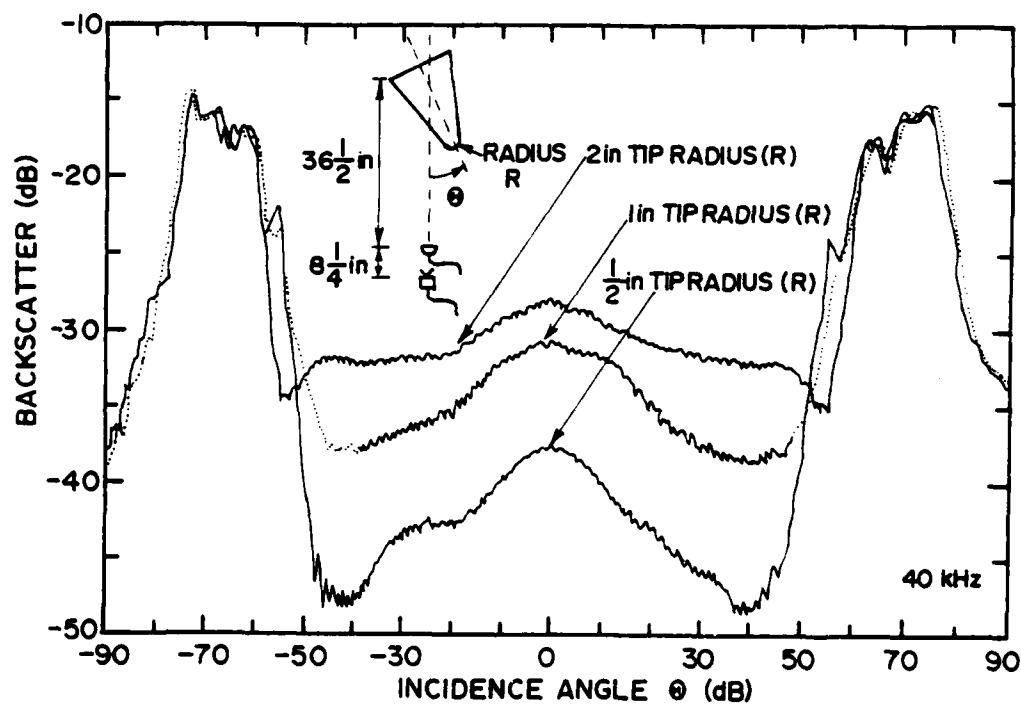


Figure 5.87 Directivity of the backscatter at 40 kHz from the cone model with spherical caps having radii of 1/2, 1, and 2 inches. ( $\lambda = .34$  inch)

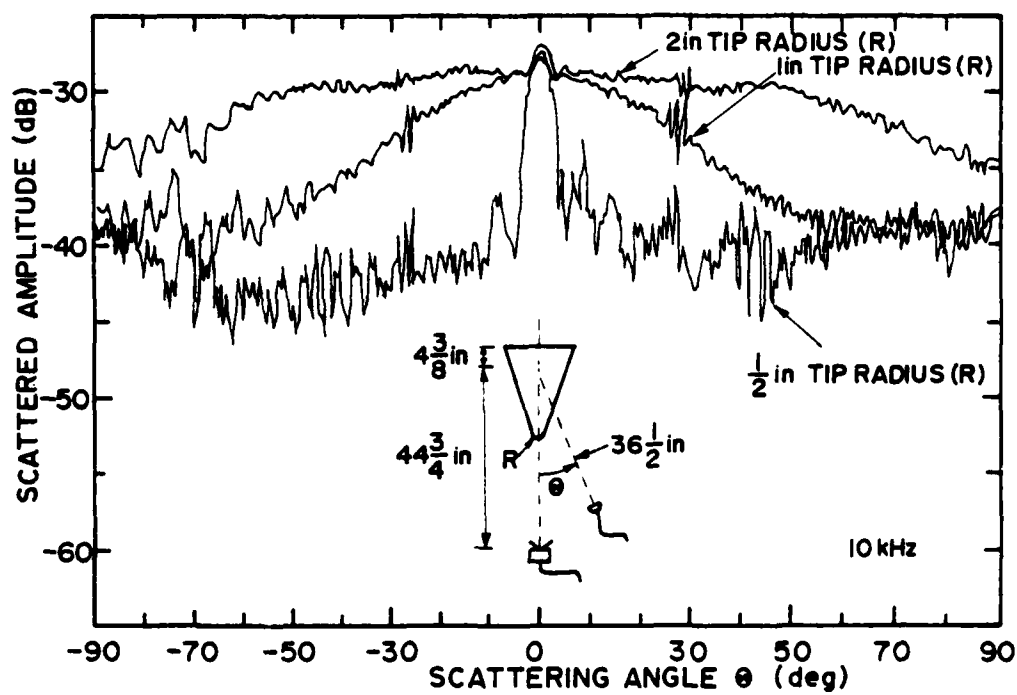


Figure 5.88 Bistatic scattering at 10 kHz from the cone model with spherical caps having radii of 1/2, 1, and 2 inches. ( $\lambda = 1.35$  inch)

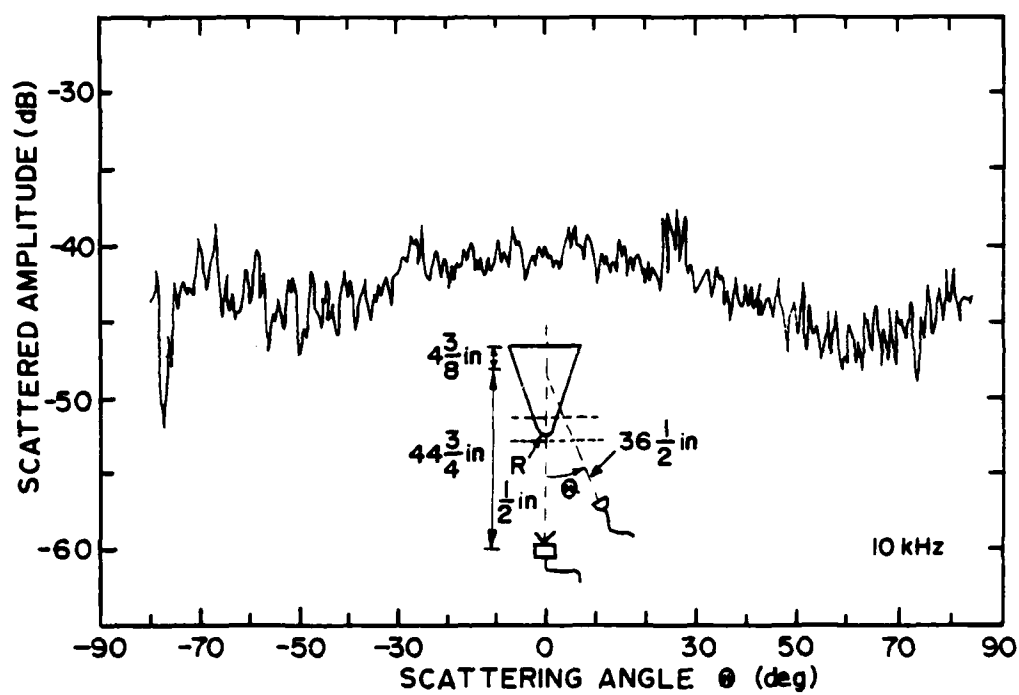


Figure 5.89 Bistatic scattering at 10 kHz from only the tip of the cone model with a spherical cap of 1/2-inch radius. ( $\lambda = 1.35$  inch)

level that is too low to noticeably influence the total scattering curve. Note that the extra activity evident in all the bistatic plots at about  $28^\circ$  was caused by an extraneous return.

Similar bistatic scattering data for the three models at 20, 30, and 40 kHz are presented in Figures 5.90 - 5.92. The trends noted at 10 kHz are also evident in this data. In addition, just as was found with the backscattering data, the specular return from the 1/2-inch cap now has a greater influence on the total scattering results than it had at 10 kHz because of the decreased amplitude of the rear-edge component. In a slight departure from the backscattering results, however, the shape of the bistatic curves does not seem to change (i.e., become more uniform) with increasing frequency. This last result is not unreasonable since the incident field remains fixed along the cone axis.

Although similar at axial incidence to the 2-inch spherically capped model, the 2-inch hemispherically capped model exhibits noticeable differences in its directivities for both scattering and backscattering. Figures 5.93 and 5.94 show the results of the backscattered directivities at the four usual frequencies. The levels near axial incidence are larger than those for the equivalent spherically capped model primarily because of the distinct bulge in the middle of the curves. A slight oscillatory pattern, possibly caused by interferences of some kind, is also evident. (The cap-joint return is not interfering because it has been effectively removed by time gating.) Note that the bulge in the curve that was just mentioned gets noticeably narrower as the frequency increases. This result is unusual because the hemispherical cap is a much better model of a sphere than any of the

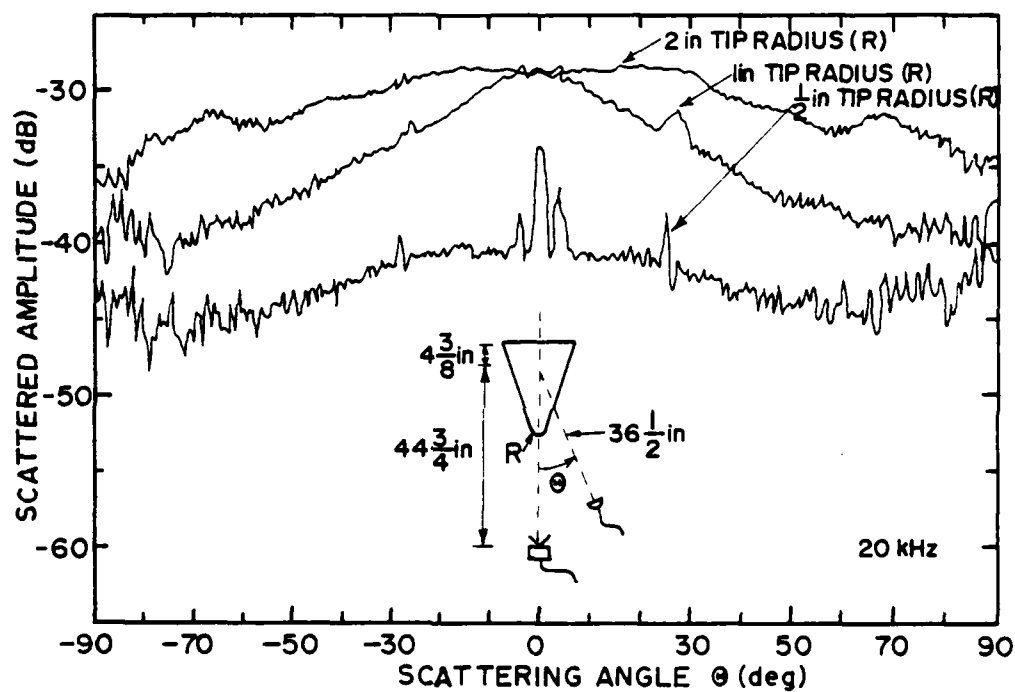


Figure 5.90 Bistatic scattering at 20 kHz from the cone model with spherical caps having radii of 1/2, 1, and 2 inches. ( $\lambda = .675$  inch)

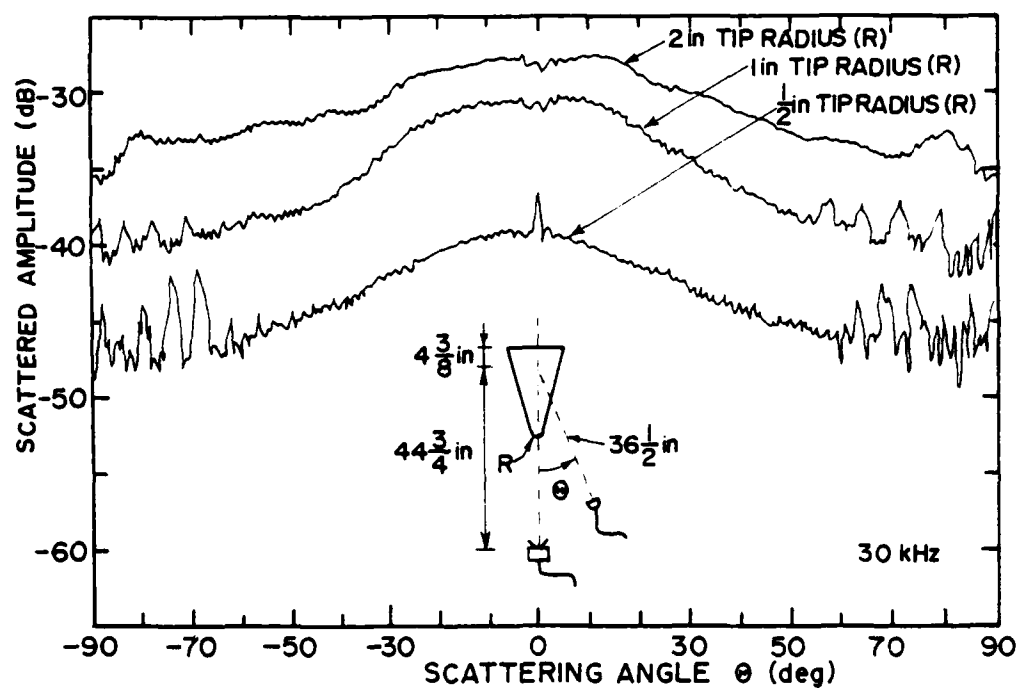


Figure 5.91 Bistatic scattering at 30 kHz from the cone model with spherical caps having radii of 1/2, 1, and 2 inches. ( $\lambda = .45$  inch)



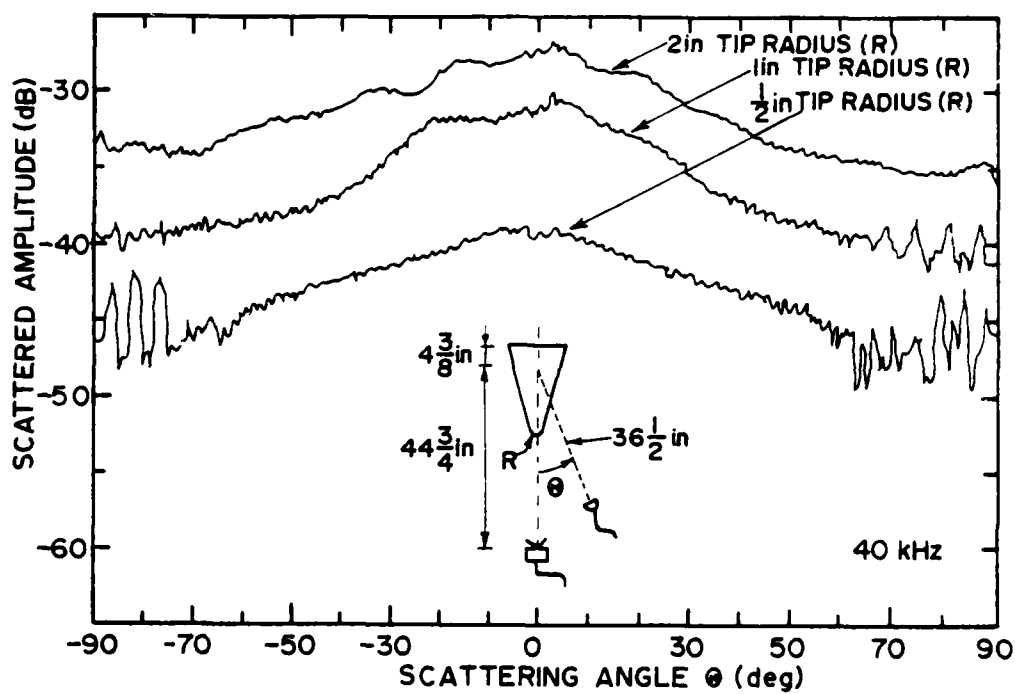


Figure 5.92 Bistatic scattering at 40 kHz from the cone model with spherical caps having radii of 1/2, 1, and 2 inches. ( $\lambda = .34$  inch)

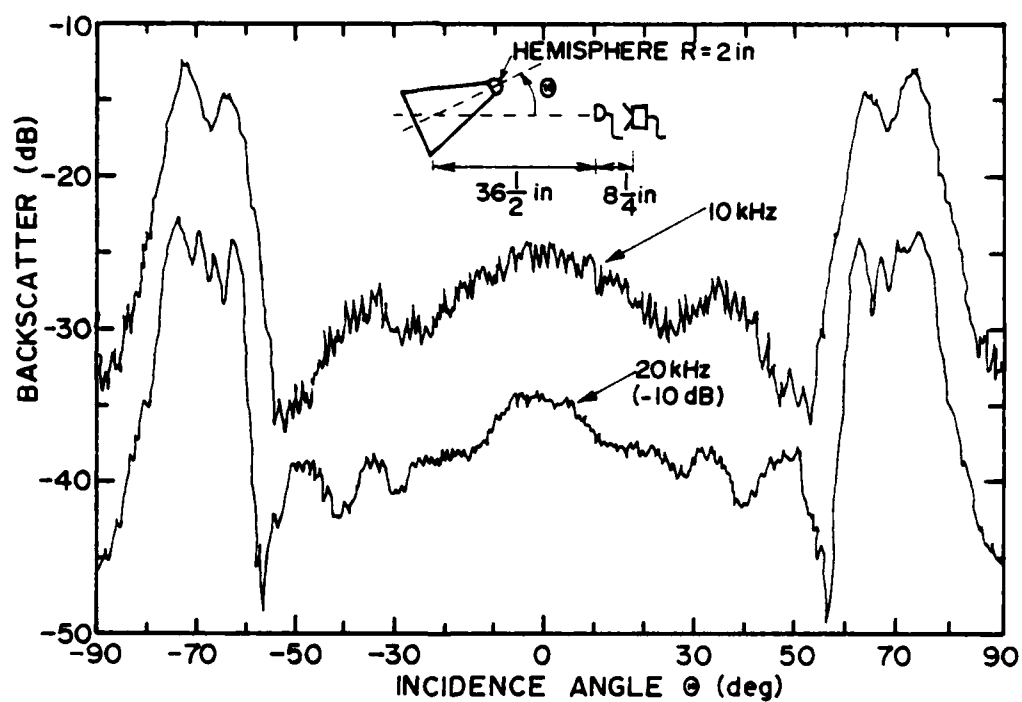


Figure 5.93 Directivity of the backscatter at 10 kHz and 20 kHz (-10 dB) from the cone model with a 2-inch hemispherical cap. ( $\lambda = 1.35, .675$  inch)

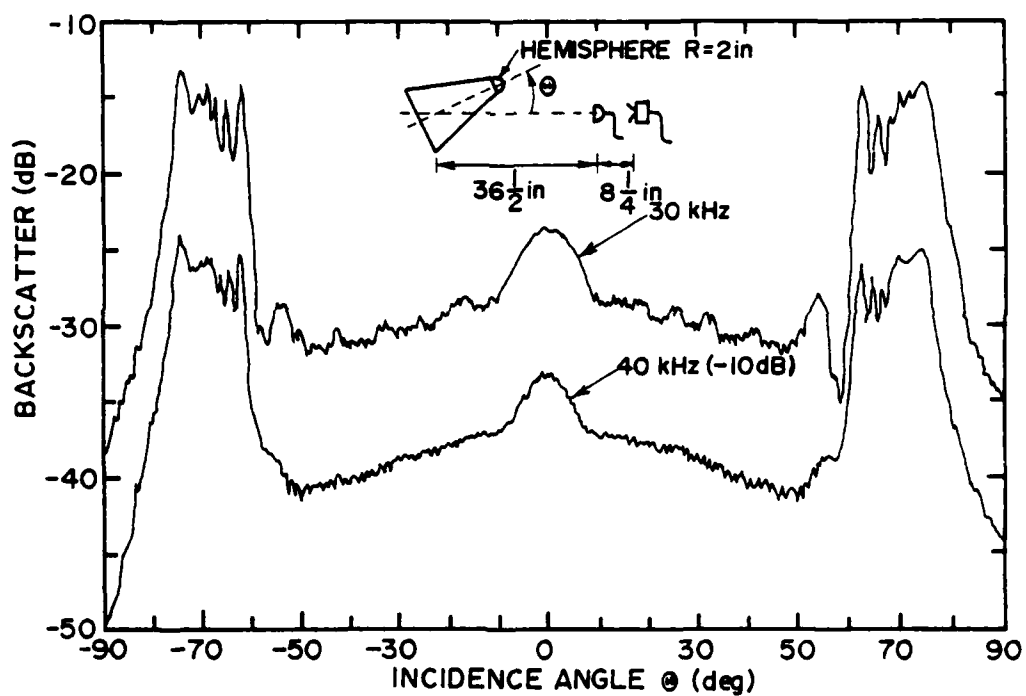


Figure 5.94 Directivity of the backscatter at 30 kHz and 40 kHz (-10 dB) from the cone model with a 2-inch hemispherical cap. ( $\lambda = .45, .34$  inch)

spherical caps, although it does join to the cone outline in a more abrupt manner. The bistatic scattering results at all four frequencies for the hemispherically capped model are plotted in Figure 5.95. Again, the levels are somewhat larger than those for the corresponding spherically capped model, and the bistatic curves exhibit a noticeable bulge in the center. The bulges in this case, however, appear to be about twice as wide as those in the backscattering case.

#### 5.4.5 Scattering by Cones with Terminations

Because the scattering by a cone is so heavily dominated by returns from the rear edge, an examination of various modifications to this edge is perhaps the most interesting aspect of these cone studies. The addition of a hemispherical termination with the same radius as the base of the cone reduces the severity of the edge considerably. It does not affect the illuminated portion of the cone model, however, for a reasonably large range of incidence angles near the axial direction. Alternately, a section of a sphere that joins the rear of the cone in a manner that preserves the slope there can be added to form a cone-sphere. This will add considerably to the size of the model, including an additional extension in the illuminated region. It will also move the shadow boundary away from the location of the former rear edge and leave a smooth surface instead of an edge at the new shadow boundary. Both types of terminations were investigated in this study. It should be noted, however, that the data in these cases were much more difficult to take than any of the previously discussed cone data. The scattering from the modified rear edges was reduced to an amplitude that was well

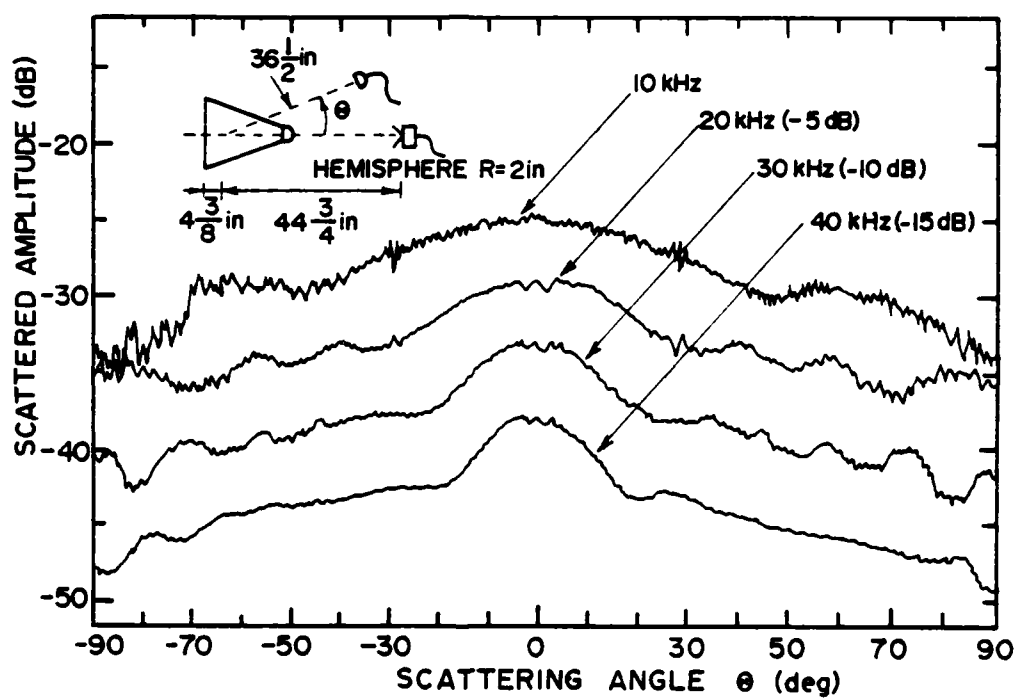


Figure 5.95 Bistatic scattering from the cone model with a 2-inch hemispherical cap at frequencies of 10 kHz, 20 kHz (-5 dB), 30 kHz (-10 dB), and 40 kHz (-15 dB).

below the scattered amplitude from some of the extraneous features mentioned at the beginning of this section (such as the physical cap joint); thus, a careful procedure of gating various returns and matching similar plots was required to arrive at the final results. Although data were recorded at 10, 20, 30, and 40 kHz, the data at 30 kHz were never successfully isolated from the extraneous returns. Note that most of the curves presented in this section are plotted separately because they overlap in a manner that is too complicated to permit viewing on a single plot. However, the data from the two different terminations should be compared among themselves and with the normal cone results shown in Section 5.4.3.

Figures 5.96 - 5.98 present the directivities of the backscatter from the hemispherically terminated cone at frequencies of 10, 20, and 40 kHz. Comparing these results with the equivalent normal-cone data in Figures 5.66 - 5.69, one notes that the specular returns from the side of the cone at angles near  $70^\circ$  are about the same. However, the region near  $0^\circ$ , at which the rear-edge return dominates the backscattering, is much lower (about 10 dB) in amplitude. The total dynamic range is thus larger, approaching 60 dB in the 40-kHz case. Note also that the lobe structure near axial incidence is different. The peak-to-sidelobe level for the terminated cone is less than that for the normal cone, and the widths of the maxima appear to be somewhat different. This change in the form of the edge-backscattering plots is similar to that observed when the surface discontinuity at the physical joint of the cone model's caps was smoothed with modeling clay (see Section 5.4.1).

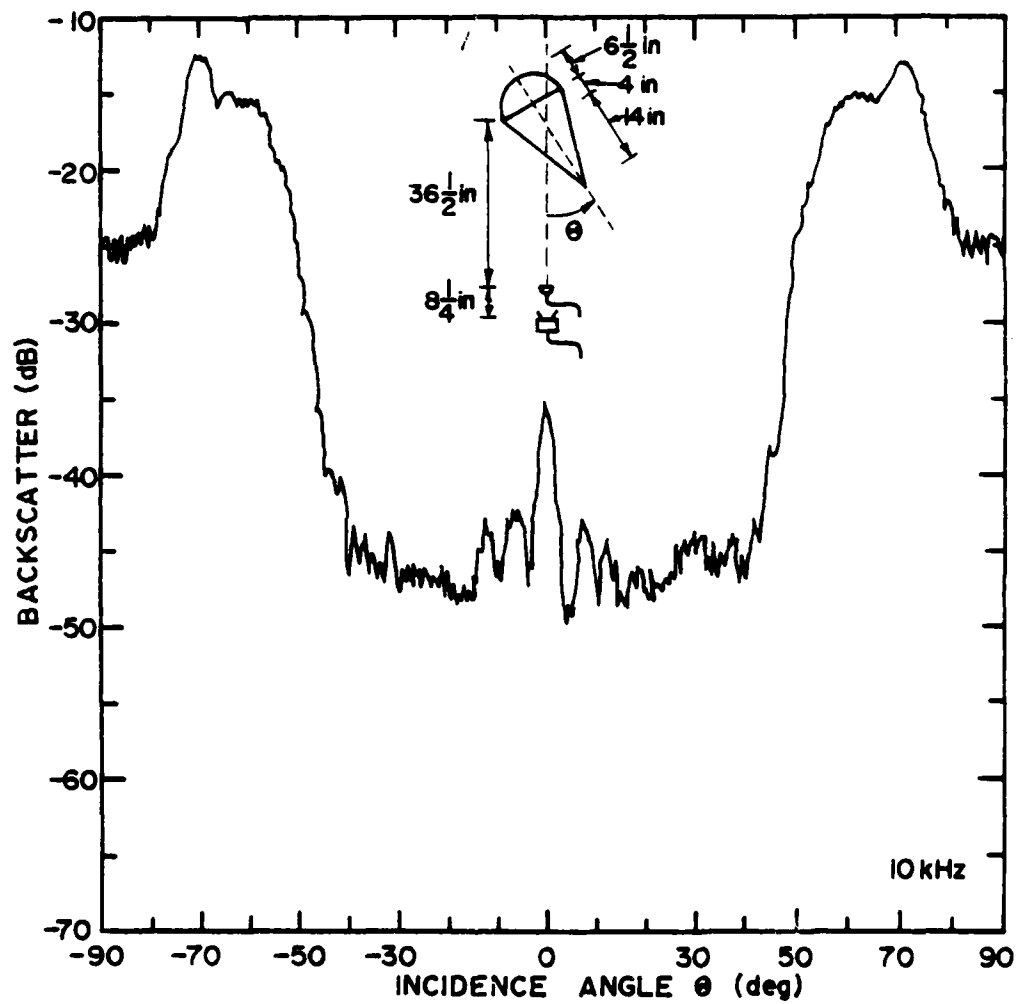


Figure 5.96 Directivity of the backscatter at 10 kHz from the cone model with a hemispherical termination.

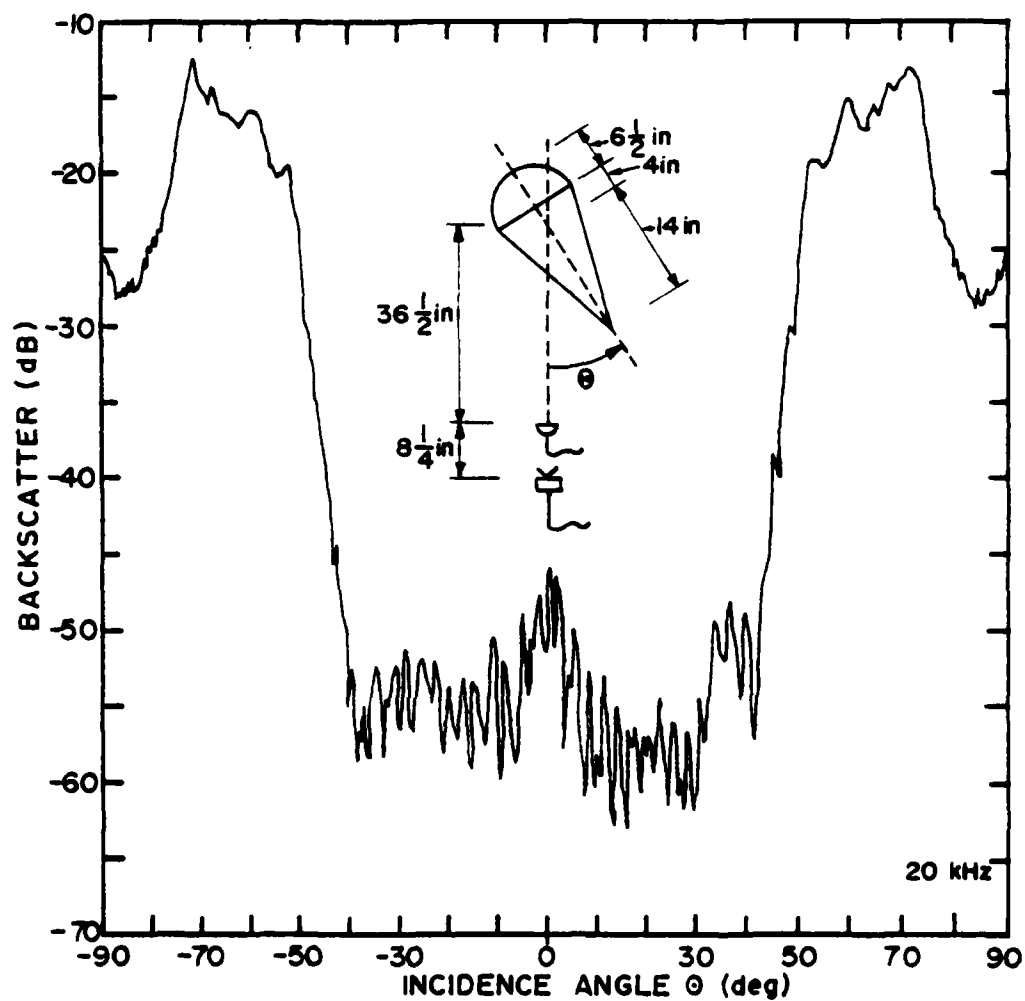


Figure 5.97 Directivity of the backscatter at 20 kHz from the cone model with a hemispherical termination.



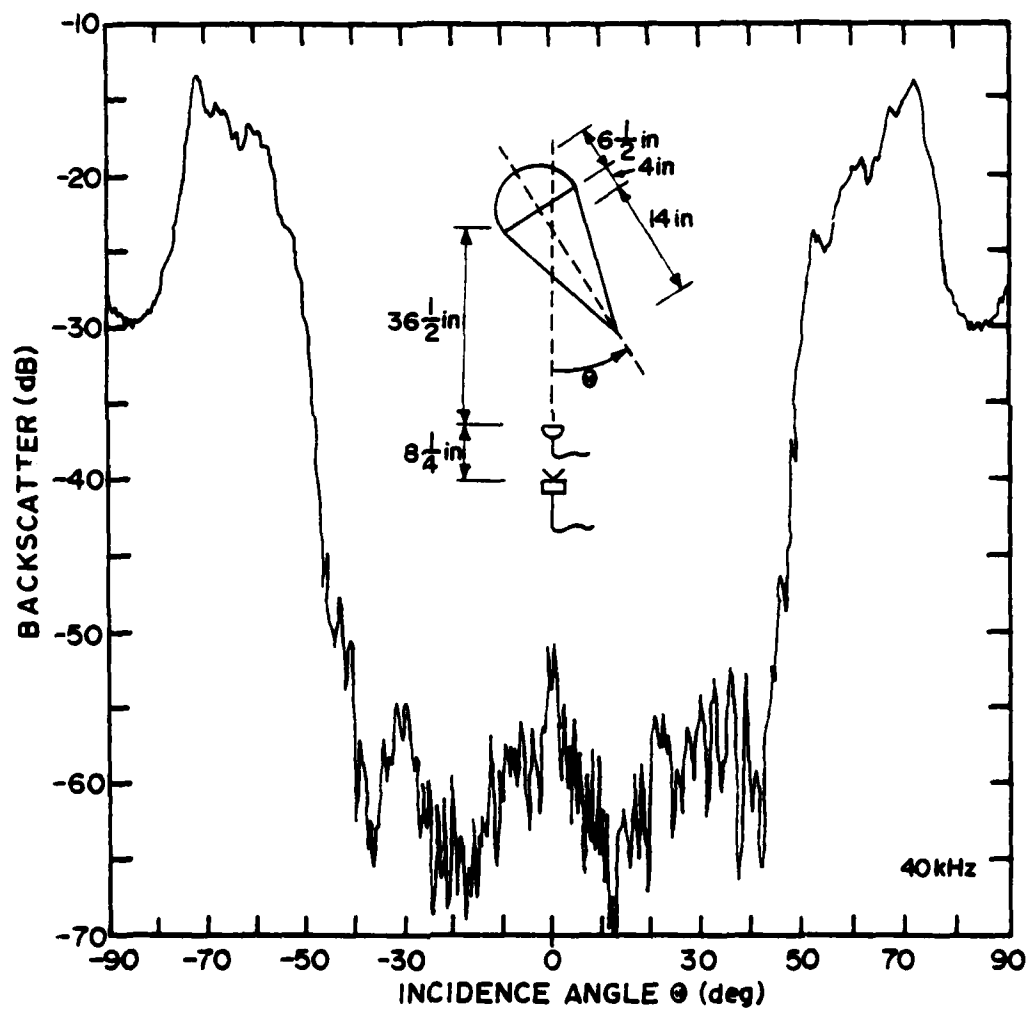


Figure 5.98 Directivity of the backscatter at 40 kHz from the cone model with a hemispherical termination.

The same conclusions are applicable in a slightly exaggerated form when the spherical termination (as opposed to the hemispherical termination) is applied to the cone model. This can be seen in Figures 5.99 - 5.101. Again, the side returns for both the normal and terminated cones are very similar except for a broadening in width, this time near  $90^\circ$ . At other angles, these curves are very similar to those for the hemispherically capped cone except at axial incidence. Especially at 10 kHz, the edge return for the cone-sphere at axial incidence seems to be lower than that for the hemispherically terminated cone because of a reduction in the central peak relative to the side lobes. Assuming that these results are not invalidated by slight discrepancies in the models, it appears that going from a slight discontinuity in the first derivative (i.e., hemispherically terminated cone) to one in the second derivative (i.e., cone-sphere) at the edge reduces the backscattered return only at axial incidence. This is contrary to Freedman's general formulation, in which reduction by an additional factor of  $k$  is predicted when the order of the discontinuity is increased.

The bistatic scattering results at 10, 20, and 40 kHz for both the hemispherically and spherically terminated cones are shown in Figures 5.102 and 5.103, respectively. In the case of the hemispherical termination, the curves are reduced in amplitude but changed very little in shape from those for the normal cone in Figures 5.74 - 5.77. The data obtained with the spherical termination are similar to those from the hemispherical termination except at axial incidence, at which the central peak is compressed at least at the lower frequencies. In

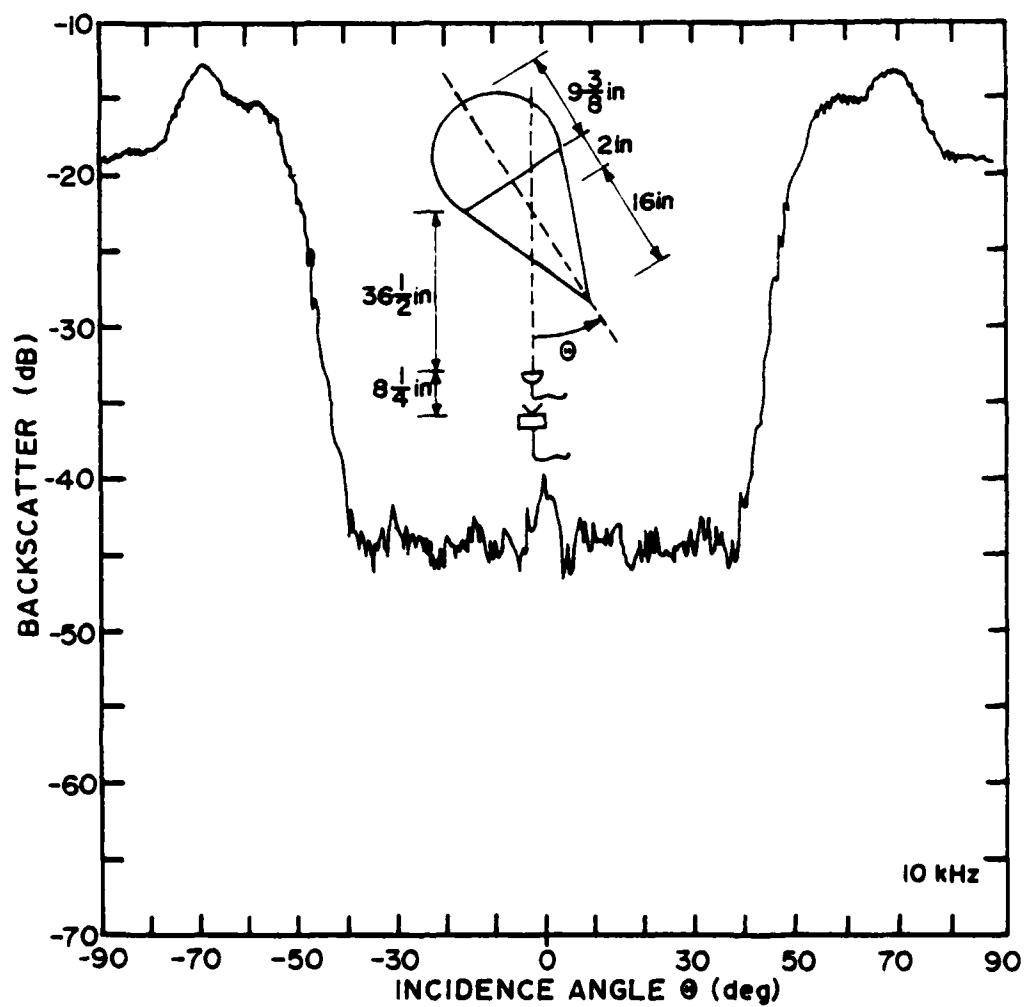


Figure 5.99 Directivity of the backscatter at 10 kHz from the cone model with a spherical termination.

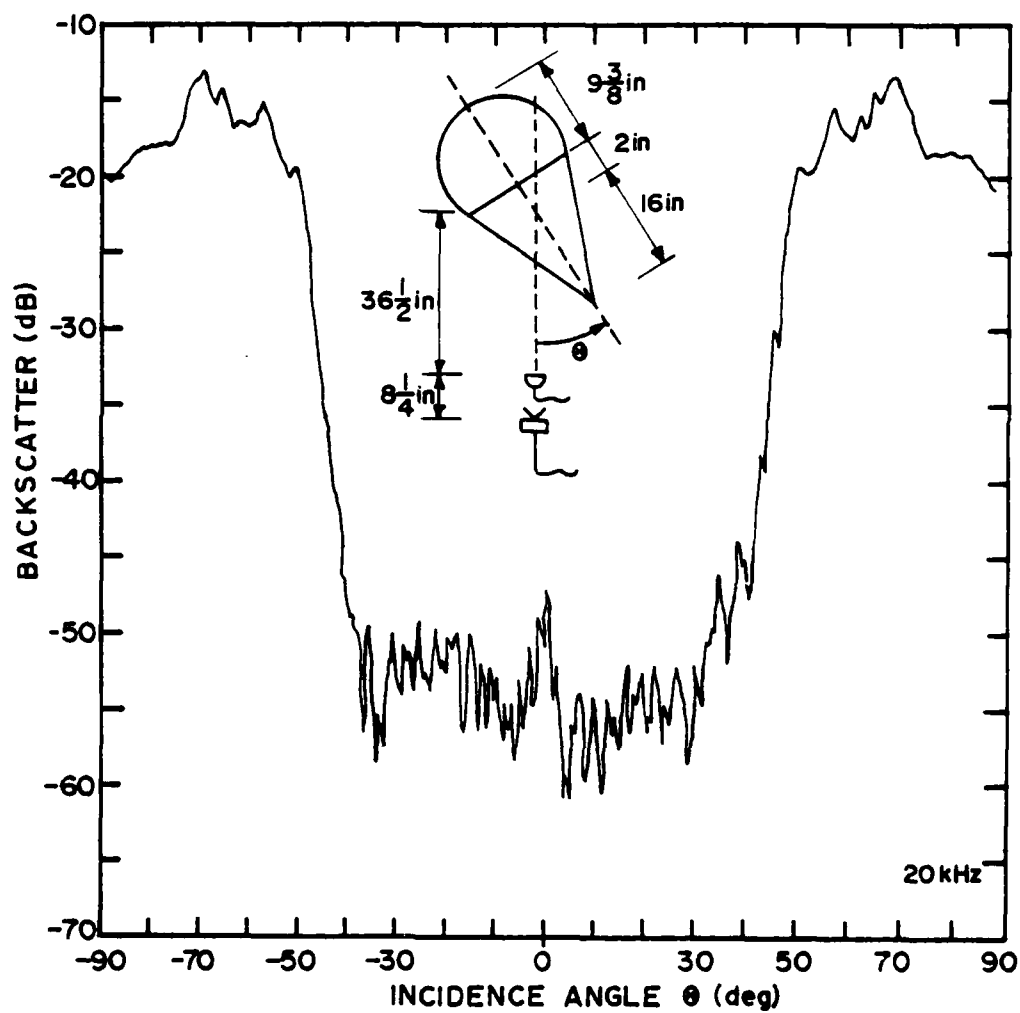


Figure 5.100 Directivity of the backscatter at 20 kHz from the cone model with a spherical termination.

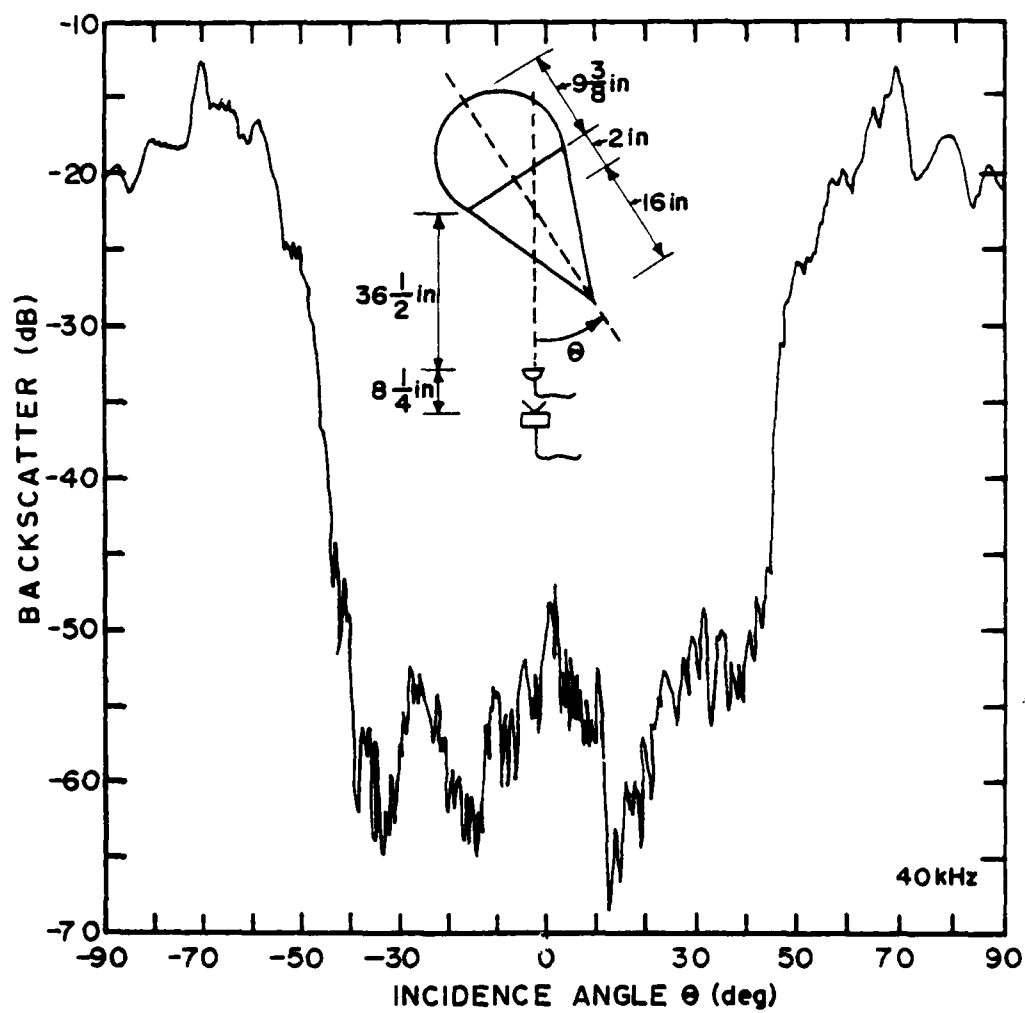


Figure 5.101 Directivity of the backscatter at 40 kHz from the cone model with a spherical termination.

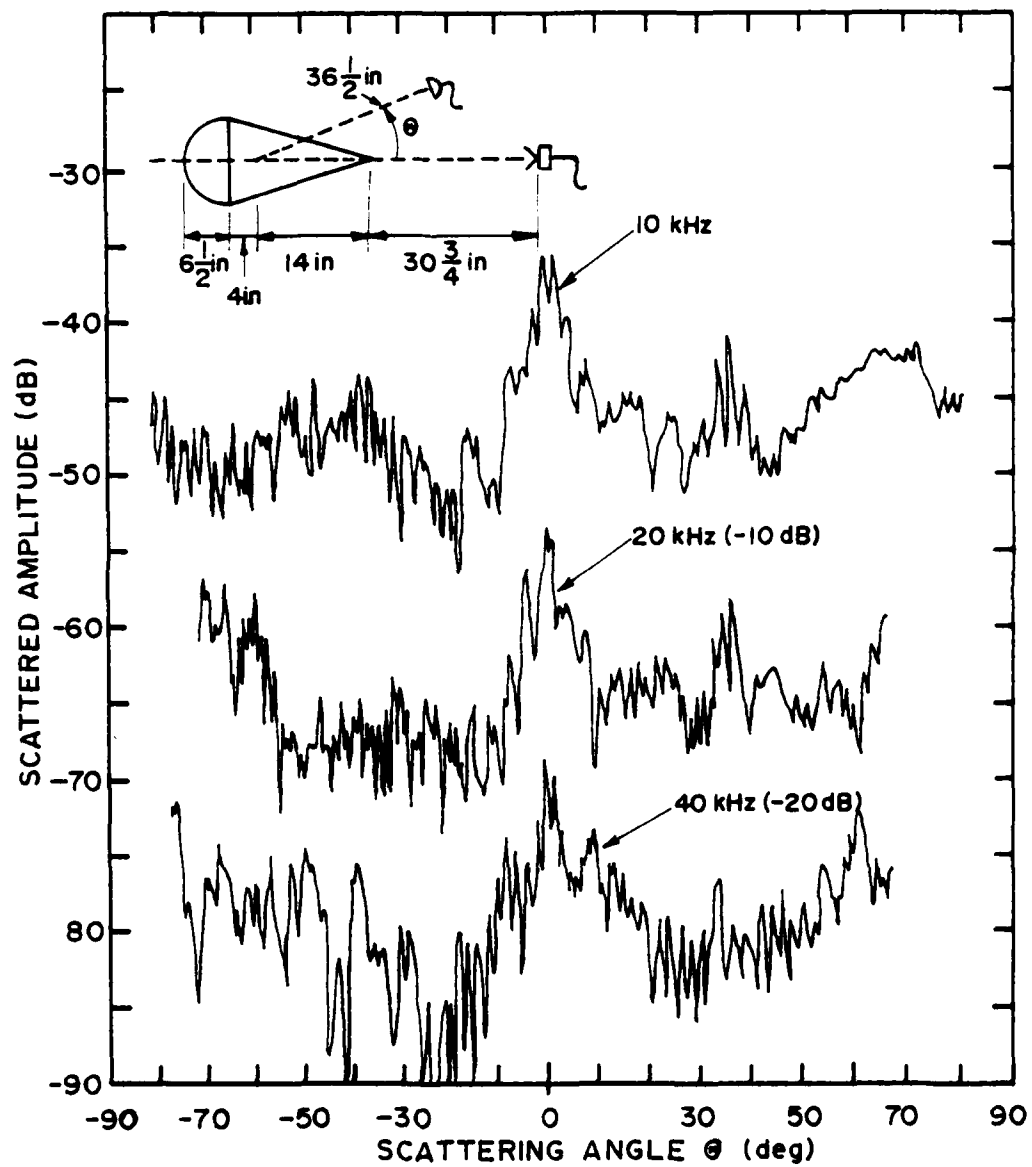


Figure 5.102 Bistatic scattering from the cone model with a hemispherical termination at 10, 20, and 40 kHz.

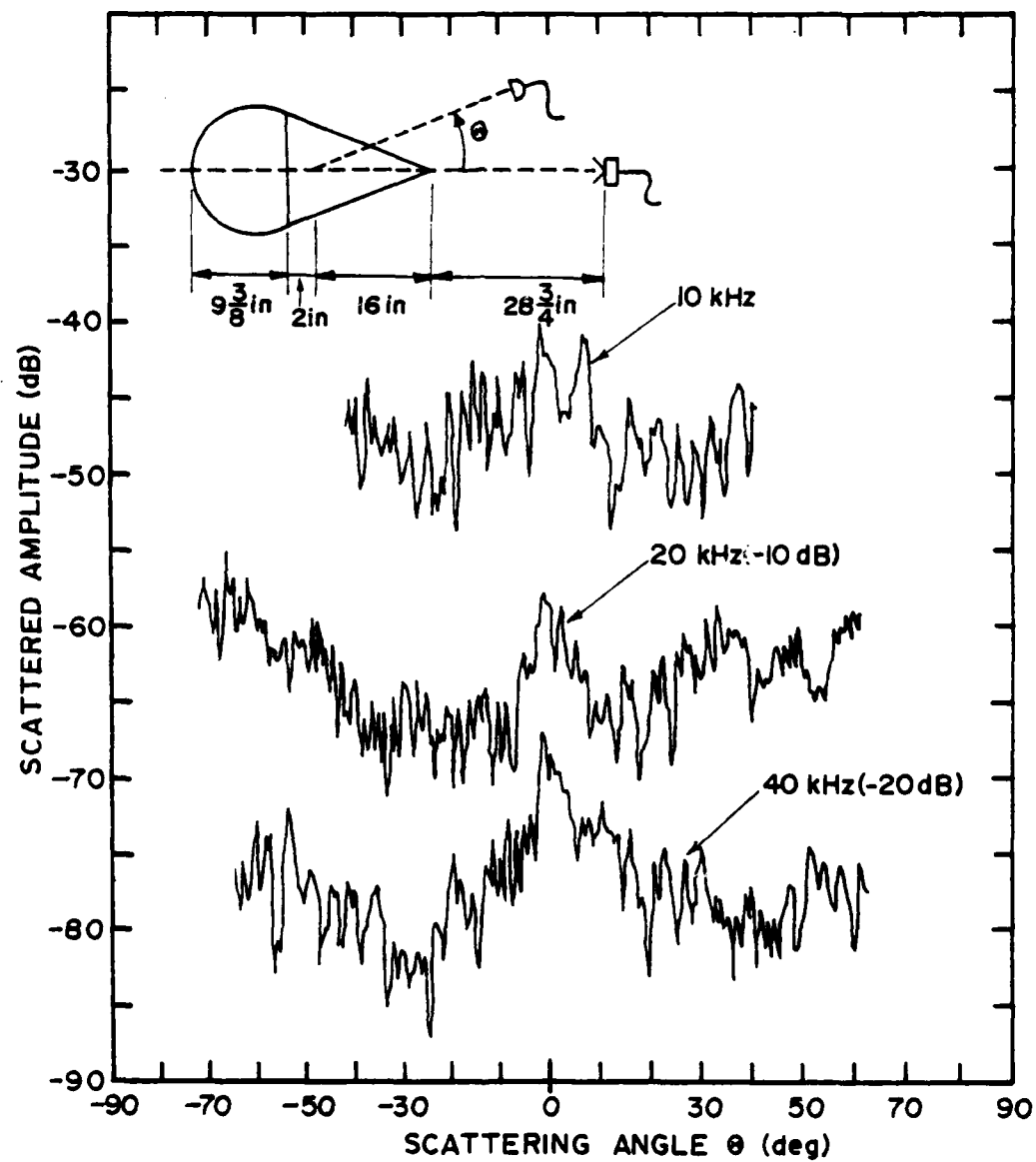


Figure 5.103 Bistatic scattering from the cone model with a spherical termination at 10, 20, and 40 kHz.

general, the same conclusions given in the previous paragraph with regard to backscattering apply here. Because of variabilities in the data, however, it is difficult to draw any conclusions about changes in the lobe structure of the curves.



## CHAPTER 6

### HOLOGRAPHIC IMAGING TECHNIQUES

The primary goal of this investigation is to examine the scattering of sound by three-dimensional bodies into the farfield. However, an adequate understanding of this physical process may require knowledge of the acoustic field near the scattering body. For example, the backscattering from a small cylindrical obstruction on the surface of a spheroid is modified by the local field near the spheroid (see Section 4.4). Unfortunately, this local field is very difficult to measure because it is distributed in a complex manner and because it is easily distorted by any measurement sensor.

During the course of this investigation, the author was introduced to a relatively new measurement technique called long-wavelength acoustic imaging or holography. This procedure uses data collected in the farfield to determine the nonevanescient components of the local field near a radiator or scatterer. In short, by determining both the amplitude and phase of the harmonic field scattered by an object into the farfield, the propagating portion of the acoustic pressure (or velocity) can be determined at the object by back propagating the field to that location. As might be expected, there are limitations to the procedure, as well as a considerable number of unresolved questions in the associated theory. The method, however, has demonstrated a remarkable ability to produce useful results despite poor experimental conditions and violations of the theoretical assumptions. For that reason, the author decided to experimentally investigate the usefulness

of this imaging technique for diffraction studies as a part of this thesis effort.

The following sections briefly review the efforts that were carried out within the scope of this scattering investigation in the area of wavefront imaging. The topics include a description of the complex equipment developed for the study, as well as a presentation of the results obtained to date. There is also a brief overview of the theoretical foundations of the procedure; this overview is intended to provide assistance in applying physical interpretations to the results. Note that these efforts have been performed in conjunction with Cohen (1979) and K. E. Eschenberg, and they represent an extension of earlier work by Graham (1969) and Watson (1971).

#### 6.1 Theoretical Basics

The technique of wavefront reconstruction or holography is based on well-known concepts in scalar wave theory. However, both the procedures used in processing the measured data and the interpretation of the results are unusual enough to cause many misunderstandings. The following discussion provides a general theoretical explanation of the technique using the interpretations provided by pioneers in the field of optical holography (for example, Lalor, 1968; Wolf & Shewell, 1967). Because this author has been concerned primarily with the experimental aspects of the measurement procedure, many important (and largely unresolved) considerations such as finite aperture size, resolution, multiple scatterers, etc. have been omitted from the discussion. The reader is referred to papers by Cohen (1979) and Van Roy (1971), as well

as the book by Goodman (1968), for a more complete treatment of wavefront-reconstruction theory.

For purposes of this study, a hologram is a recording of the amplitude and phase of a pressure wavefront at a large number of points within a designated plane. The task of reconstruction is to compute the form of that same wavefront at some other plane, in particular, the plane that contained the original source (object plane). This reconstruction procedure is derived by first computing the recorded wavefront in terms of the source distribution (forward propagation), and then inverting the equation to effectively backward propagate the wave to its source.

The forward-propagation solution is determined from the Helmholtz-Huyghens radiation integral (Skudrzyk, 1971, p. 492; also see Appendix A):

$$V(R_H) = \iint_S \left\{ G(|R_H - R_0|) \left( \frac{\partial V(R_0)}{\partial n} \right) - V(R_0) \left( \frac{\partial G(|R_H - R_0|)}{\partial n} \right) \right\} dS \quad (6.1)$$

This expression relates the velocity potential  $V$  at any field point  $R_H$  to both the velocity potential and its normal derivative at points  $R_0$  on a surface  $S$ . The surface  $S$  must be a closed boundary surrounding a sourceless region containing the field point. The function  $G$  is the Green's function of the form

$$G(r) = \left( \frac{\exp(-ikr)}{4\pi r} \right) + G_0(r) \quad (6.2)$$

where  $r$  is measured from an origin inside the surface  $S$  and where  $G_0(r)$  is any function analytic within  $S$ . Both derivatives are taken with respect to the outward normal of the surface  $S$ . The orientation of the source point, field point, and integration surface to be considered is shown in Figure 6.1. Note that the source point ( $R_S$ ) and the field point ( $R_H$ , or hologram point) are separated by the planar surface of integration  $S_0$  (object plane). This surface is closed around the field point by a hemisphere whose radius tends to infinity.

Equation 6.1 can be simplified in two ways. First, the integral over the infinite hemisphere contributes nothing to the solution because both the pressure field and the Green's function tend to zero at infinity. Thus, this portion of the integral can be ignored. Second, the analytic part of the Green's function  $[G_0(r)]$  can be chosen in a manner that makes the total Green's function zero at all points on the boundary  $S_0$ . The function becomes

$$G(r) = \left( \frac{\exp(-ikr)}{4\pi r} \right) - \left( \frac{\exp(-ikr')}{4\pi r'} \right), \quad (6.3)$$

where  $r' = |R_H' - R_0|$  and  $R_H'$  is a point located symmetrically across the plane  $S_0$  from  $R_H$  at an equal distance from the plane (see Figure 6.1). Note that it is not necessary for this Green's function to have a physical meaning as long as the function satisfies the mathematical requirements that have been stated. However, if a physical interpretation is desired, the reader should consider the equivalent reciprocal case, which has a field point at  $R_0$  and two source points at  $R_H$  and  $R_H'$ . If the Green's function chosen in Equation 6.3 is used in Equation 6.1, the first term under the integral sign is eliminated,



leaving

$$v(R_H) = \iint_{S_0} v(R_0) \left( \frac{\partial G(|R_H - R_0|)}{\partial n} \right) dS \quad (6.4)$$

This equation can be expressed in terms of the physical quantity of pressure by use of the relation

$$p = \rho_0 \left( \frac{\partial v}{\partial t} \right) = i\omega \rho_0 v \quad (6.5)$$

where  $\rho_0$  is the density of the medium and  $\omega$  is the angular frequency.

The result is

$$p(R_H) = - \iint_{S_0} p(R_0) \left( \frac{\partial G(|R_H - R_0|)}{\partial n} \right) dS_0 \quad (6.6)$$

The choice of how to solve Equation 6.6 normally depends on the form of  $p(R_0)$ . However, because  $S_0$  is a rectangular area, a more general solution is possible. Letting  $G_n(r)$  represent the normal derivative of the Green's function,  $D = z_0 - z_H$ , and expressing all coordinates in a cartesian system, Equation 6.6 becomes

$$p(x_0, y_0, z_0) = - \iint_{S_0} p(x_0, y_0, z_0) G_n(x_H - x_0, y_H - y_0, D) dx_0 dy_0 \quad (6.7)$$

This integral is in the form of a two-dimensional convolution in  $x_0$  and

$y_0$ , which in shorthand notation can be written as

$$p(R_H) = p(R_0) * G_n(r) \quad . \quad (6.3)$$

Using the properties of Fourier transforms and the convolution theorem (see, for example, Skudrzyk, 1971, pp. 99-100), Equation 6.8 can be written in frequency space as

$$\hat{p}(k_x, k_y, z_H) = \hat{p}(k_x, k_y, z_0) \cdot \hat{G}_n(k_x, k_y, D) \quad . \quad (6.9)$$

The symbol " $\hat{\phantom{x}}$ " denotes the two-dimensional spatial Fourier transform defined by the equations

$$\hat{a}(k_x, k_y) = \iint_{-\infty}^{\infty} a(x, y) e^{i(k_x x + k_y y)} dx dy \quad (6.10)$$

and

$$a(x, y) = \left(\frac{1}{2\pi}\right)^2 \iint_{-\infty}^{\infty} \hat{a}(k_x, k_y) e^{-i(k_x x + k_y y)} dk_x dk_y \quad . \quad (6.11)$$

The frequency-space parameters  $k_x$  and  $k_y$  (sometimes called spatial frequencies) are spatial wave numbers (with units of 1/length) defined by the Fourier transform. They can be related to an effective wave number  $K$  in the plane by

$$K = (k_x^2 + k_y^2)^{1/2} \quad . \quad (6.12)$$

Note that  $K$  is essentially a parameter of the Fourier transform that can

assume any required value. When propagation of this planar two-dimensional field is considered, a new wave number  $k_z$  is also needed. However, the wave numbers in the plane are now related to the wave number  $k$  in the acoustic medium by

$$k = (K^2 + k_z^2)^{1/2} = (k_x^2 + k_y^2 + k_z^2)^{1/2} \quad (6.13)$$

As is shown later, this last relationship is of profound significance to the reconstruction process.

Equation 6.9 is a purely algebraic expression. Thus, it can easily be inverted to show that

$$\hat{p}(k_x, k_y, z_0) = \frac{\hat{p}(k_x, k_y, z_H)}{\hat{G}_n(k_x, k_y, D)} \quad (6.14)$$

This equation (or its inverse two-dimensional transform) is the fundamental relation on which wavefront reconstruction is based. Notice that it gives the pressure field at an assumed planar source distribution (object plane) as a function of the pressure measured on a field plane (hologram plane). The function  $1/\hat{G}_n(k_x, k_y, D)$  can be identified as the frequency-domain backward-propagation function.

In order to study the characteristics of the process of wavefront reconstruction, it is necessary to find the functional form of the backward propagator (i.e.,  $\hat{G}_n$ ). Refer again to Figure 6.1. For source points  $R_s$  on the surface  $S_0$  (as assumed in the reconstruction process), the magnitudes of  $r$  and  $r'$  in the Green's function (Equation 6.3) are equal, and the normal derivatives of the two terms in the Green's



function differ only in sign. Thus,

$$G_n(r) = \frac{\partial G(r)}{\partial n} = 2 \left( \frac{\partial (e^{-ikr}/4\pi r)}{\partial n} \right) \quad (6.15)$$

Noting that the surface normal is in the direction of the  $z$  coordinate, the transform of the Green's function becomes

$$\hat{G}_n(\hat{r}) = \iint_{-\infty}^{\infty} 2 \left( \frac{d(e^{-ikr}/4\pi r)}{dz} \right) e^{i(k_x x_0 + k_y y_0)} dx_0 dy_0 \quad (6.16)$$

where  $\hat{r} = (k_x, k_y, z)$ . To simplify this discussion, assume that the origin of the coordinates is at the field point ( $R_H = 0$ ) so that

$$r = |R_H - R_0| = (x_0^2 + y_0^2 + z_0^2)^{1/2} \quad (6.17)$$

It is now convenient to transform both the space and frequency coordinates from a rectangular to a polar coordinate system using

$$K = (k_x^2 + k_y^2)^{1/2}, \quad k_x = K \cos \phi, \quad k_y = K \sin \phi \quad (6.18)$$

and

$$R = (x^2 + y^2)^{1/2}, \quad x = R \cos \theta, \quad y = R \sin \theta \quad (6.19)$$

Substituting these relations into the integral expression for the frequency-domain Green's function (Equation 6.16) and exchanging the

order of differentiation and integration, one obtains

$$\begin{aligned} \hat{G}_n(\hat{r}_0) = & 2 \frac{d}{dz} \int_0^\infty \int_0^{2\pi} \left( \frac{e^{-ik(R^2+z_0^2)^{1/2}}}{4\pi(R^2+z_0^2)^{1/2}} \right) \\ & \cdot e^{-iKR(\cos \phi \cos \theta + \sin \phi \sin \theta)} \\ & \cdot R d\theta dR \quad . \end{aligned} \quad (6.20)$$

Next, a simple trigometric identity simplifies the relation to

$$\hat{G}_n(\hat{r}_0) = \frac{1}{2\pi} \frac{d}{dz} \int_0^\infty \int_0^{2\pi} \left( \frac{e^{-ik(R^2+z_0^2)^{1/2}}}{(R^2+z_0^2)^{1/2}} \right) e^{-iKR \cos(\theta-\phi)} R d\theta dR \quad . \quad (6.21)$$

The integral over  $\theta$  represents a Bessel function of order zero (Skudrzyk, 1971, p. 697). Thus, Equation 6.21 can be written as

$$\hat{G}_n(\hat{r}_0) = - \frac{d}{dz} \int_0^\infty \left( \frac{e^{-ik(R^2+z_0^2)^{1/2}}}{(R^2+z_0^2)^{1/2}} \right) J_0(KR) R dR \quad . \quad (6.22)$$

This integral is in the form of a Hankel transform, and the result is given by Erdelyi (1954, p. 9) as

$$\hat{G}_n(\hat{r}_0) = - \frac{d}{dz} \left\{ \left( \frac{-1}{(k^2 - K^2)^{1/2}} \right) e^{-iz_0(k^2 - K^2)^{1/2}} \right\} \quad . \quad (6.23)$$

Finally, the derivative with respect to the  $z$  coordinate can be applied

to yield

$$\hat{G}_n(\hat{r}_0) = -e^{-iz_0(k^2 - K^2)^{1/2}} \quad (6.24)$$

The function of interest here, the backward propagator, is thus given by

$$\frac{1}{\hat{G}_n(\hat{r}_0)} = -e^{iz_0(k^2 - K^2)^{1/2}} \quad (6.25)$$

The backward-propagation function given by Equation 6.25 takes the form of the phase delay of a plane wave traveling in the  $z$  direction, as can be seen by using the relationship between  $k$  and  $K$  (Equation 6.13) to show that

$$\frac{1}{\hat{G}_n(\hat{r}_0)} = -e^{iz_0 k_z} \quad (6.26)$$

This last fact explains why the function is called a propagation function, and it leads to an interesting physical interpretation. The wavefront-reconstruction process generates an inverse-propagation solution expressed by Equation 6.14 and Figure 6.1. The pressure field measured at the hologram plane is used to construct an equivalent distribution of (monopole) sources in the object plane that will produce the measured field. Furthermore, the constructed source distribution is always equivalent to the field at the hologram plane after propagation back to the object plane. Note that the geometrical relationship between the hologram plane and the object plane is not fixed. Once the field is known in the hologram plane, it can be backward propagated to

any other object plane. The information provided by wavefront reconstruction is particularly useful when the object plane is coincident with (or an infinitesimal distance in front of) the radiating and/or diffracting surface that generated the measured field. However, the result is mathematically valid for an object plane anywhere between the hologram plane and the closest source, with the only requirement being that the region inside the entire closed surface  $S$  (refer to Figure 6.1) contain no sources. Thus, by measuring both the amplitude and phase of a harmonic field (or the harmonic components of any field) at the hologram plane, the complete three-dimensional structure of this field (reconstructed one plane at a time) has been determined.

The actual propagation process involved with wavefront reconstruction requires more explanation. The pressure-field representation in the basic reconstruction equation (Equation 6.14) is a two-dimensional spatial transform of the pressure in the hologram. Thus, the distribution of the field in this plane is described mathematically as a continuous sum of two-dimensional plane waves of various amplitudes and frequencies. In a manner analogous to the description of a time waveform by a frequency spectrum, Fourier-transform theory shows that any functional distribution that is well-behaved at infinity can be represented by an equivalent frequency-domain spectrum of adequate bandwidth. Thus, a spectrum of three-dimensional plane waves whose traces on both the hologram and object planes sum to produce the respective field distributions can be used to represent the backward propagation. In addition, the individual spectral waves must physically propagate in the medium between the hologram and object

AD-A084 937

PENNSYLVANIA STATE UNIV UNIVERSITY PARK APPLIED RESE--ETC F/O 20/1  
AN EXPERIMENTAL ANALYSIS OF THE BASIC PHENOMENA INVOLVED IN MOD--ETC(U)

JAN 80 M S LANG

N00024-79-C-6043

UNCLASSIFIED

ARL/PSU/TM-80-43

ML

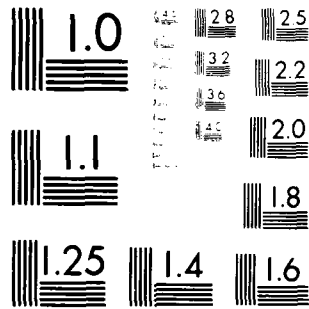
5115

AD

5000347

■

END  
DATE  
FILMED  
7-80  
DTIC



MICROCOPY RESOLUTION TEST CHART  
NATIONAL BUREAU OF STANDARDS - 1963-A

planes at a characteristic sound speed. The resulting bandwidth limitation on the backward-propagated field is evident in the two forms of the backward propagator (Equation 6.25):

$$\frac{1}{\hat{G}_n(\hat{r}_0)} = \begin{cases} -e^{-iz_0kz} & \text{for } K < k \\ -e^{z_0kz} & \text{for } K > k \end{cases}, \quad (6.27)$$

In this relation,  $k_z = (k^2 - K^2)^{1/2}$ . When the effective wave number in the hologram plane ( $K$ ) is less than that in the medium ( $k$ ), the spectral waves whose traces match the corresponding components in the hologram are backward propagated by inverting their phase. However, in the opposite case ( $K > k$ ), the spectral waves must be exponentially amplified to account for the rapid exponential decrease that occurs when high-spatial-frequency components near the object attempt to radiate into the surrounding medium. In a real experiment, any exponentially attenuated components will rapidly drop below the background noise level, making it impractical to boost them by the required amount. Consequently, a modified backward propagator that substitutes an exponential attenuation for  $K > k$  is normally used. In this way, the field is reconstructed as if the higher-spatial-frequency components never existed, and a resolution limitation close to the wavelength in the acoustic medium is introduced. This field resulting from the latter reconstruction procedure is very useful, however, for many types of studies because only the components that radiate into the farfield are imaged.

The resolution limitation (or advantage) of wavefront reconstruction is an inherent part of the physical process of wave

propagation, and it makes the interpretation of holographic results difficult. In addition, there are variations from the ideal situation presented in the previous discussion that result from practical considerations. For example, a real hologram plane is finite in dimension. This limitation degrades the image somewhat due to diffraction effects at the edges of the hologram, and it results in the hologram intercepting only a portion of the sound radiated or scattered by the structure under investigation. However, the reconstruction process proceeds blindly according to the simple conditions assumed during the derivation. Thus, the process predicts a directed source distribution, i.e., a distribution of sources that correctly reproduces the field originally measured at the hologram but may generate a different field at points outside the hologram. The same type of result occurs when examining either multiple objects at different  $z$  distances or an extended, three-dimensional object. The reconstruction is technically invalid for all but the nearest object because additional sources appear inside the surface of integration (recall the surface  $S$  in Figure 6.1) in the other cases. The result observed, however, can be described as showing the sources in the current reconstruction plane "in focus" and the others as "out-of-focus" noise terms.

Detailed treatment of these theoretical questions, as well as others relating to the process of wavefront reconstruction, is beyond the scope of this study. The technique is interesting, however, because previous investigators have shown that it produces very useful results, even under less than ideal experimental conditions that violate some of the underlying assumptions (Graham, 1969; Watson, 1971). The wavefront-



reconstruction process has been used in this investigation for two reasons. First, it was desired to experimentally evaluate the applicability and usefulness of this imaging technique in studies of scattering. Second, an effort was made to use this technique to provide additional clues about the physical diffraction mechanisms associated with the nearfield of a scatterer.

## 6.2 Experimental Apparatus

The studies of wavefront-reconstruction techniques performed in this investigation are an extension of work done by Graham (1969) and Watson (1972) at this laboratory. These and other researchers demonstrated the fundamental utility of the procedures for highlighting primary sources of farfield sound on radiating and scattering bodies. However, their results indicated that more accurate techniques (where the "more" was undefined) would be required to obtain reliable quantitative information and to relate the data directly to physical parameters. Consequently, early in the planning stages of this study, it was decided to devise a measurement capability with sufficient versatility to implement suggested experimental improvements and to adapt to new changes in technique that might be required. As a result of this decision, a considerable amount of effort was devoted to development of the required apparatus and processing techniques over a span of several years. However, the effort has been justified as the completed system has easily adapted to required methodology changes that were not even considered at the beginning.

The experimental requirements can be divided into three broad steps: (1) measurement of the field scattered or radiated by an object over an entire rectangular plane, (2) reconstruction of the field at the object by backward propagation, and (3) examination and analysis of the results. The most important component of the field to be measured is, unfortunately, the most difficult to measure: the phase. The importance of the phase information is dramatically illustrated by Watson's (1971) excellent results, which were derived solely from measurements of the phase expressed with a binary resolution (i.e., in phase or out of phase). Traditional holographic methods used the interference between the field of the scattering object and a reference field to indicate the phase; then, they tapped the Fourier-transform abilities of lenses to reconstruct the image. For this study, however, the amplitude and phase were measured directly. This measurement is feasible at the long wavelengths used, and it allows the elimination of several spurious interference terms that would otherwise be present in the reconstruction. In order to study scattering effects, the equipment was designed to operate with sine-wave pulses of short duration. The microphone scanning system was required to accurately and repeatably position sensors at up to 256 sampling positions along both vertical and horizontal axes (the finest sampling used by Watson in his investigations). Finally, both the reconstruction process and the interpretation of the results were performed on a digital computer. This allowed the emulation and study of any real or imagined (within practical limits) propagation process, as well as the utilization of available digital processing techniques.

A block diagram of the data-acquisition and control system that was developed to meet the specified requirements is shown in Figure 6.2. In order to implement the required versatility of the system, most of the component devices are operated under the control of a programmable microprocessor. Budget limitations ruled out the acquisition of a complete minicomputer. Thus, a basic microprocessor board (Texas Instruments TM990/100M) was purchased, and the resident monitor program that came with this board was modified to permit edit, compile, load, and file-storage operations to be performed by The Pennsylvania State University's central computer system via a dial-up phone link. Because the average hologram contains over 16,000 data values (128 x 128 grid locations) and the phone link is relatively slow (1200 baud), the phone link was not used to transmit the recorded data. Instead, an old 9-track digital tape drive was acquired, repaired, and interfaced to the microprocessor for data storage.

When recording holograms, the acoustic pressure is sampled over an entire rectangular area, approximately 73 x 88 inches in dimension, by the microphone scanning system shown in Figure 6.3. Four small electret microphones (Knowles BT-1759) move up and down on carriages that are attached to vertical rods via slide bearings and are interconnected via a cable and pulley arrangement. (Four additional microphones can be attached to the other ends of the carriage assemblies to record field data originating on the other side of the scanner.) In addition, the entire assembly moves horizontally on tracks on the floor. Both the vertical and horizontal motion are precisely driven, with proper acceleration and deceleration, by stepper motors under the control of

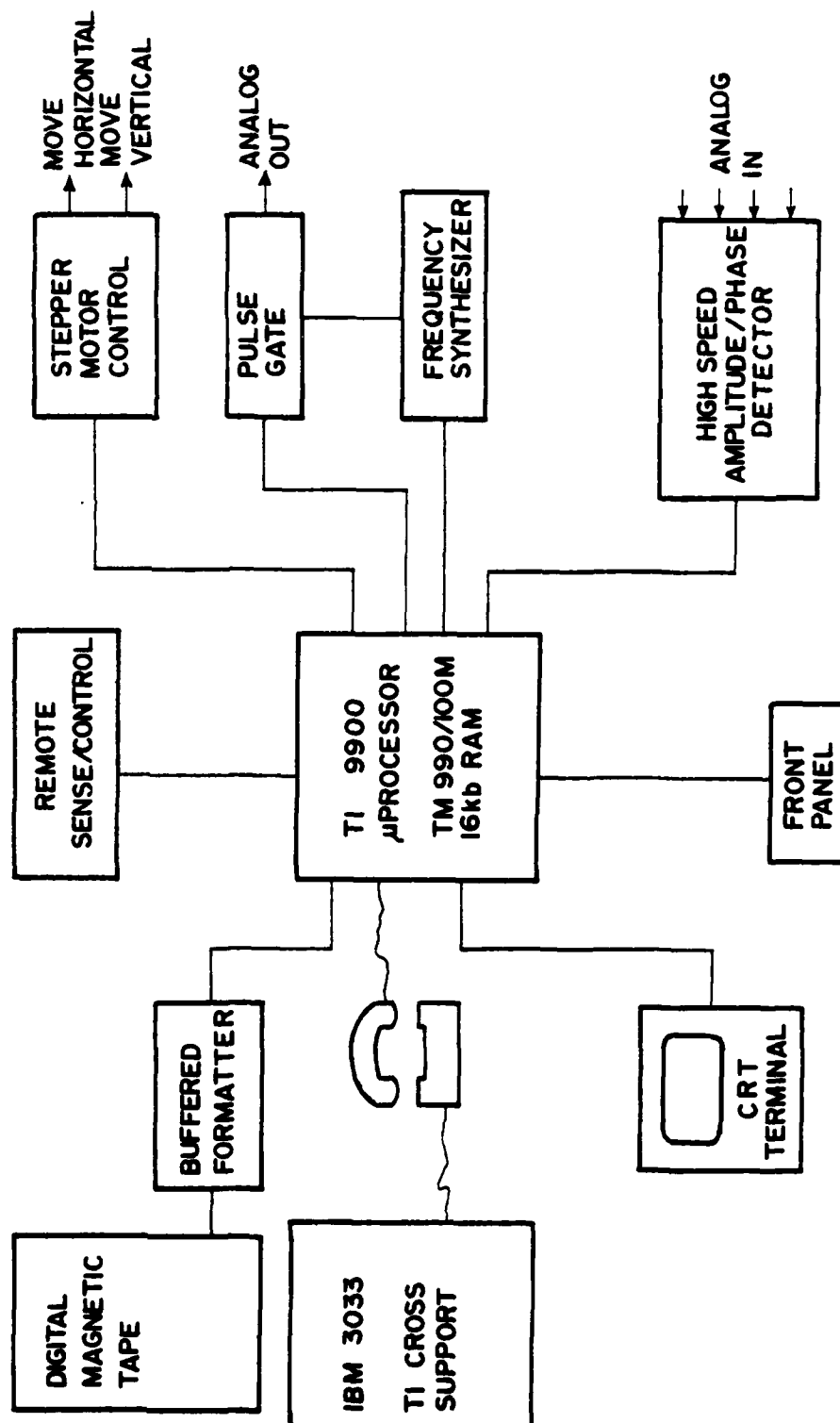


Figure 6.2 Block diagram of the control and data-acquisition electronics used for recording acoustic holograms.



Figure 6.3 Photograph of the microphone scanning system used for holographic measurements.

the microprocessor. Four microphones are used instead of one for the simple purpose of reducing the required scanning time by a factor of 4. Note that this particular scanning system has evolved through several modifications of previous designs, and it has several faults that should be corrected in any new designs. In particular, the uneven motion delivered by the vertical-axis stepper motor induces a severe vibration into the cable used in the drive system. Also, a structure with fewer or smaller support members that can distort the acoustic field would be desirable, but the focusing effect of the reconstruction process helps to eliminate spurious reflections from the scanner.

The microphone signals are preamplified, filtered, and then passed to a special amplitude/phase detection subsystem. The latter subsystem deserves special attention because it provides the capability to operate with pulses. A block diagram of its major functional elements is presented in Figure 6.4. In operation, the reference signal (which is continuous, not pulsed) is squared off at its zero crossings and passed to a phase-locked loop circuit acting as a frequency multiplier. This circuit creates a signal that corresponds to the reference signal multiplied by 720 (or any other desired count); the multiplied signal is, in turn, digitally counted in synchronization with the reference signal. As a result, a running tally of the phase delay from the start of the reference cycle is available in half-degree increments. Sometime after a cycle of the reference signal begins, the unknown signal will begin its next cycle (defined as a zero crossing of positive slope). This point is precisely detected by a trigger circuit; and the running phase tally at that point is saved in a holding register, providing a

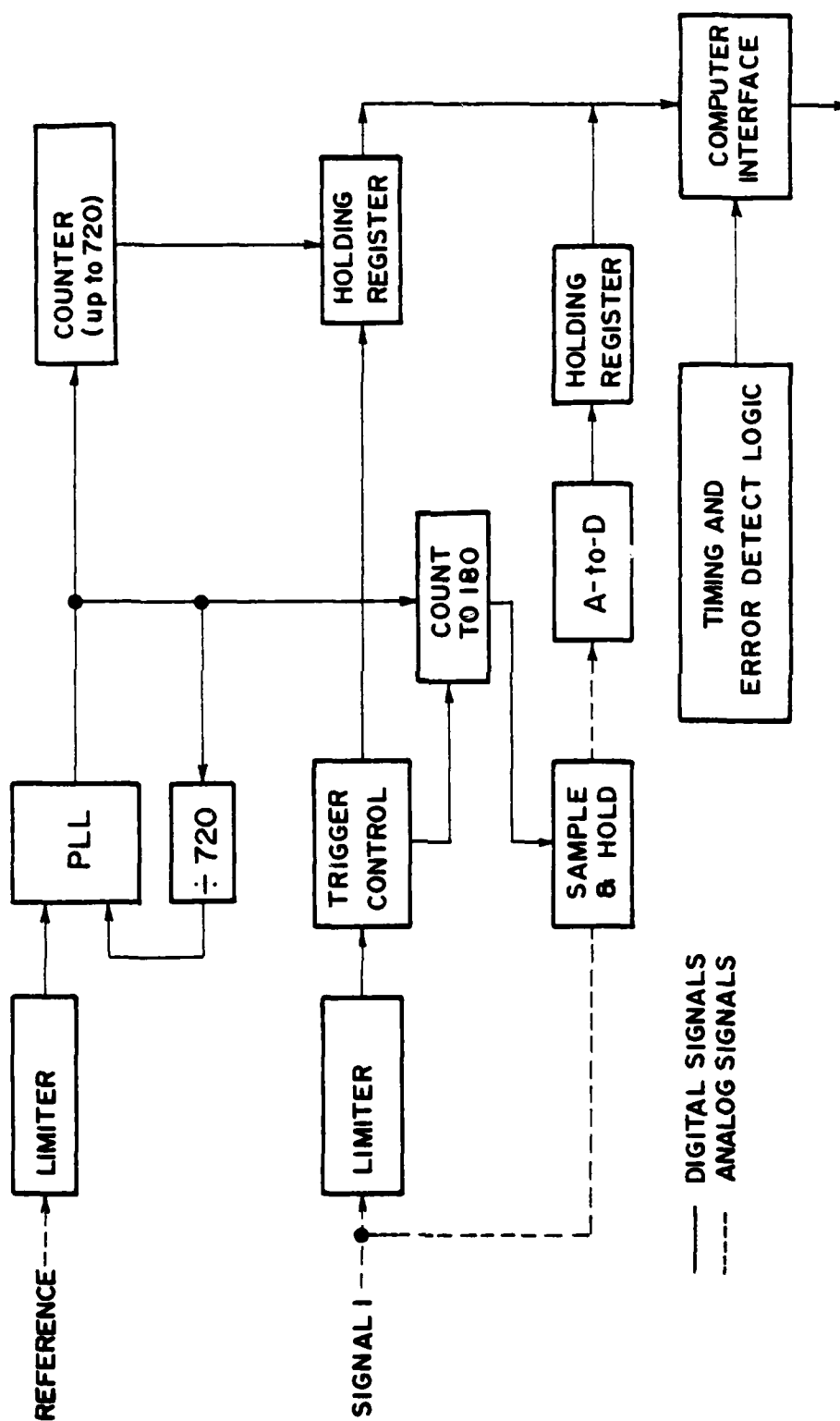


Figure 6.4 Block diagram of one channel of the high-speed amplitude/phase detection system.

digital count of the phase delay in the range of 0 - 720 half-degrees. Simultaneously, a separate counter, which is set to count down from 180, is started. When this second counter reaches zero, the sinusoid is at its maximum value ( $90^{\circ}$ ); and this peak value is read through an analog-to-digital convertor into another holding register. Both the amplitude and phase of the unknown are now available in digital form.

Because no commercial device could be found, this very fast amplitude/phase detector was designed and constructed as part of this thesis effort. The actual prototype contains four sets of trigger circuits and holding registers so that all four microphone signals from the scanner can be processed simultaneously. The detection procedure takes a maximum of  $2\frac{1}{4}$  cycles of the input wave, plus about 50 microseconds (including initial synchronization with the reference signal). The detection device operates with half-degree resolution over a frequency range of about 1 - 20 kHz. Because of the sophisticated nature of the device's operation and the variable quality of input signals, extensive error-checking circuitry was included to look for missing- or multiple-phase detections, phase-locked-loop tracking errors, etc.

The timing of the hologram recording process is handled by the microprocessor program. This function includes generating a pulse (or continuous wave) of preset length and starting the amplitude/phase detection during a central portion of the desired echo from the scatterer. The data values, which are normally recorded on a 128 x 128 grid, are transferred to a large IBM computer for numerical reconstruction at any selected plane. The program for the



reconstruction task was developed by Cohen (1979), and it implements the modified backward-propagation procedure [which attenuates high spatial frequencies (see Section 6.1)] using fast-Fourier-transform algorithms. The resulting grid of reconstruction values (also containing 128 x 128 elements) is analyzed interactively using a high-performance graphics system (Adage AGT-30) at the The Pennsylvania State University's Computation Center. The graphics system and supporting software (also developed as part of this project) allow a user to interactively manipulate and analyze the pressure plotted as a three-dimensional surface in a reconstructed plane. This capability proved extremely valuable because of the large quantity of data in each reconstruction and because of the complex nature of many of the reconstructions. The plots shown in the following section are all projected views of the reconstructed-pressure surface that have been selected through interactive analysis to emphasize individual points about the data.

### 6.3 Experimental Results

This section presents holographic reconstructions of the scattered sound field near the surface of four basic bodies: a square baffle, a sphere, a prolate spheroid, and a cone. The results are best described as preliminary because they were selected primarily to test the performance of the measurement technique. As a group, the experiments have done a good job of bringing out many of the advantages and limitations of the procedure. However, they have not provided as much information about the nearfield of three-dimensional scatterers as had been hoped. Note that all the reconstructions are plotted as three-

dimensional surfaces in the object (scatterer) plane, with height above the plane representing the reconstructed pressure amplitude. All data points are normalized to the peak value in each plot.

#### 6.3.1 Backscattering at a Flat Baffle

The previous holographic work at this laboratory (Graham, 1969; Watson, 1971) examined the sound field radiated by plates driven into continuous mechanical vibration. Thus, the earliest scattering experiments were performed using flat baffles as scatterers and continuously driven sources. For example, Figure 6.5 is a reconstruction of a 12-inch square baffle positioned parallel to the microphone scanner at a separation distance of  $77\frac{5}{8}$  inches. The incident wave is produced by a horn tweeter that is directed at the baffle from just in front of the scanner. The outline of the baffle is distinguishable in the upper-right portion of the figure, but there is also a fairly strong return just below and to the left of the baffle.

Because there were no other objects near the baffle, the extra returns indicated in Figure 6.5 were presumed to be an out-of-focus contribution from a table about 3 feet behind the baffle. In order to test this hypothesis, the baffle experiment was repeated using a pulsed source and the shortest allowable pulse length. The resulting reconstruction is shown in Figure 6.6. In this case, the field on the baffle is the only visible component. Note that the form of this field is different from that in the previous reconstruction, indicating that the field in the previous example had been distorted by out-of-focus terms. Holography is known to have very good directivity in the plane

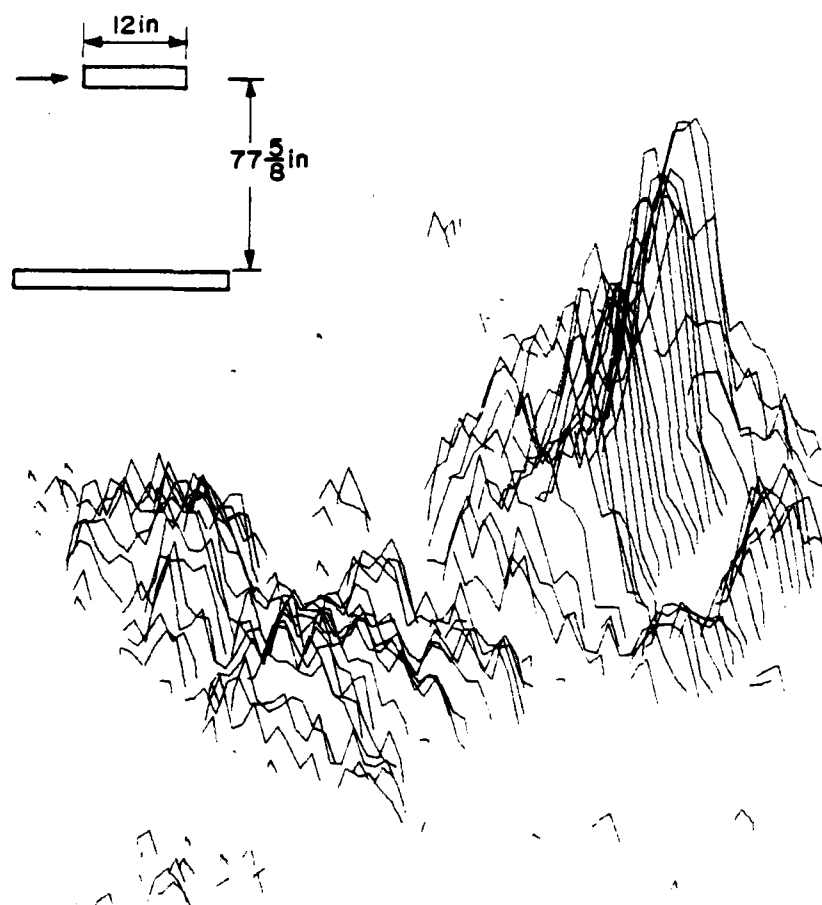


Figure 6.5 Reconstruction of a 12-inch square baffle at 8 kHz taken with a continuous source.

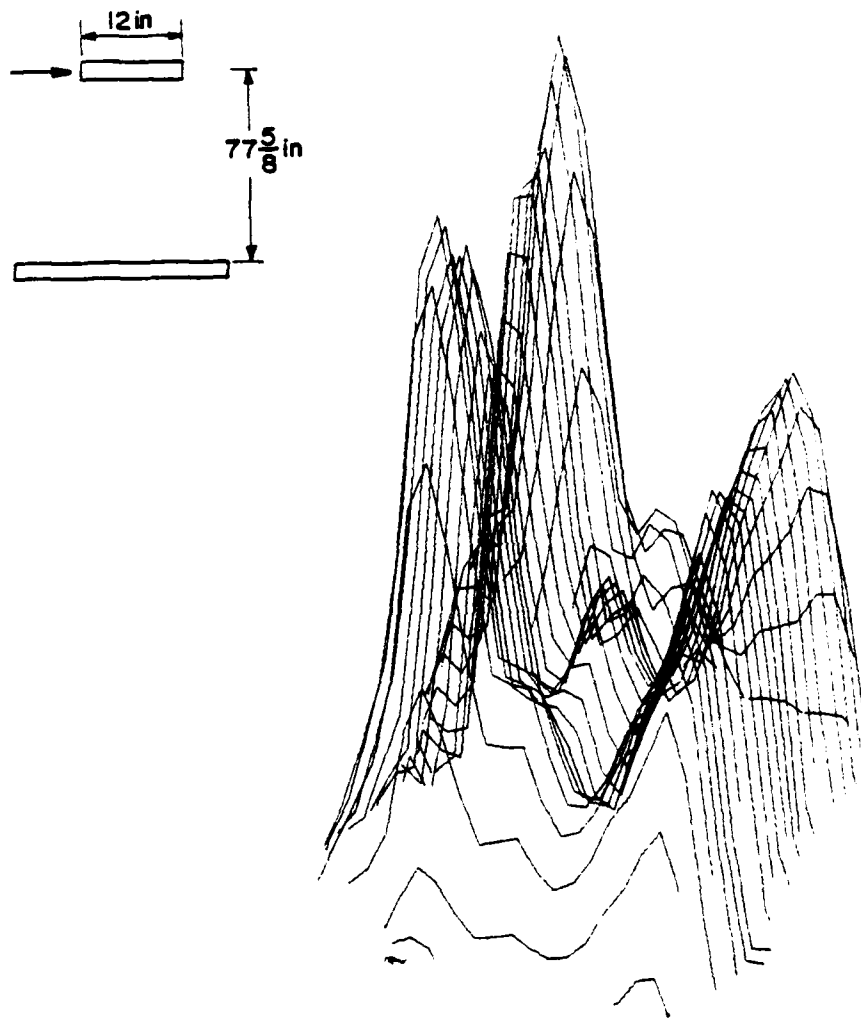


Figure 6.6 Reconstruction of a 12-inch square baffle at 8 kHz taken with a pulsed source.

parallel to the hologram (as is evident in the figure), and it also exhibits focusing effects along the  $z$  axis (line perpendicular to the hologram). However, the resolution provided in the  $z$  axis is apparently very poor. For this reason, all future holograms were taken using a pulsed source.

The reconstruction of Figure 6.6 indicates that the scattered field on a baffle is more prominent near the edges. This result is very similar to the data obtained from vibrating plates, but it was not expected in this case. Consequently, a thorough checkout of the recording procedure was carried out immediately after the results were discovered. This checkout showed that a random background was being created in the hologram by the measurement system. Whenever the detection device had tried three times unsuccessfully to obtain a valid phase reading on a low-level signal, the system accepted the last erroneous reading. After modifying the electronics to force a zero amplitude in this situation, the experiment was repeated to obtain the result shown in Figure 6.7. The reconstruction now shows a fairly uniform pressure distribution over the surface of the baffle. The latter result is the correct one; in the previous result, random phase errors were introducing spurious high-spatial-frequency components that accentuated the reconstructed field at the edges of the baffle. In contrast, other studies showed that amplitude errors in the hologram caused by calibration problems have little effect on the reconstructions.

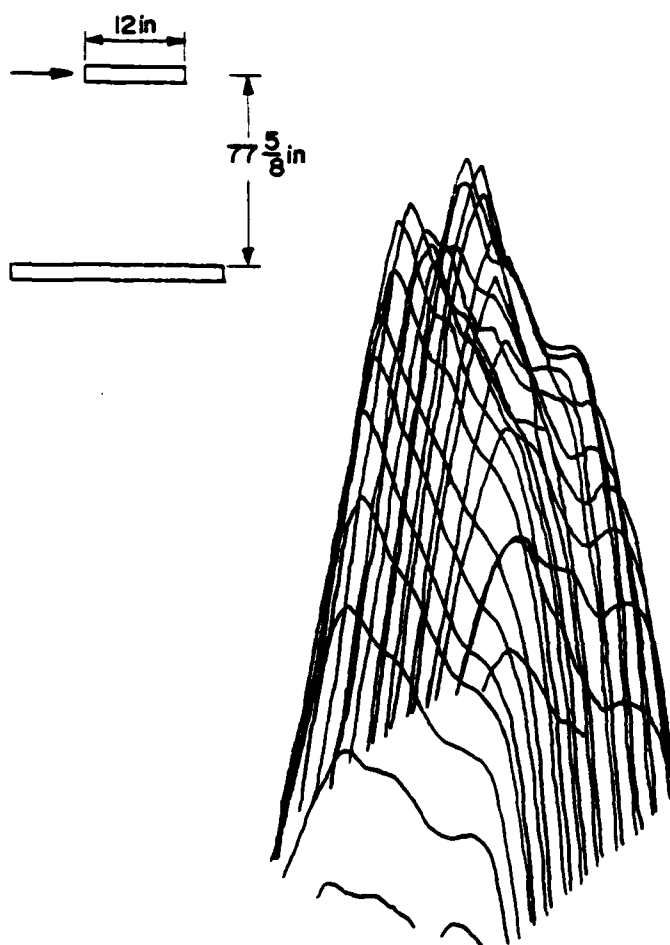


Figure 6.7 Reconstruction of a 12-inch square baffle at 8 kHz after modifying the phase-error electronics.

### 6.3.2 Backscattering at Spheres of Different Sizes

The next series of tests examined the scattering from two spheres with diameters of 2-1/4 and 6 inches that were suspended with their centers in the same object plane. A reconstruction of the surface scattering at 17 kHz is shown in Figure 6.8. The reconstruction shows a much broader return for the larger sphere, indicating that the surface field is fairly uniform over most of the illuminated area (similar to the baffle discussed in the previous section). Because the relative amplitudes of the data in the figure are distorted by the viewing angle of the plot, a side view of the same reconstruction is shown in Figure 6.9. The relative ratio between the two peaks in the reconstruction is about 2.1, while the expected ratio between the backscattering by the two spheres is about 2.7. However, if a more accurate estimate is made by reconstructing each sphere at its leading surface (specular point), the amplitude ratio of the reconstructed components from the spheres matches the expected result very closely. This agreement gives one some confidence that the amplitudes, at least among different portions of the same reconstruction, are accurate. (This is not true of many holographic techniques.)

As a further test of the focusing effect of the imaging technique, the smaller sphere used in the previous experiment was moved into another object plane about 13 inches behind the first object plane. Figure 6.10 shows the resulting reconstruction in the plane of the closest sphere, and Figure 6.11 shows the result in the plane of the furthest sphere. In both cases, a well-defined component is observed at the location of the sphere that is in the corresponding reconstruction

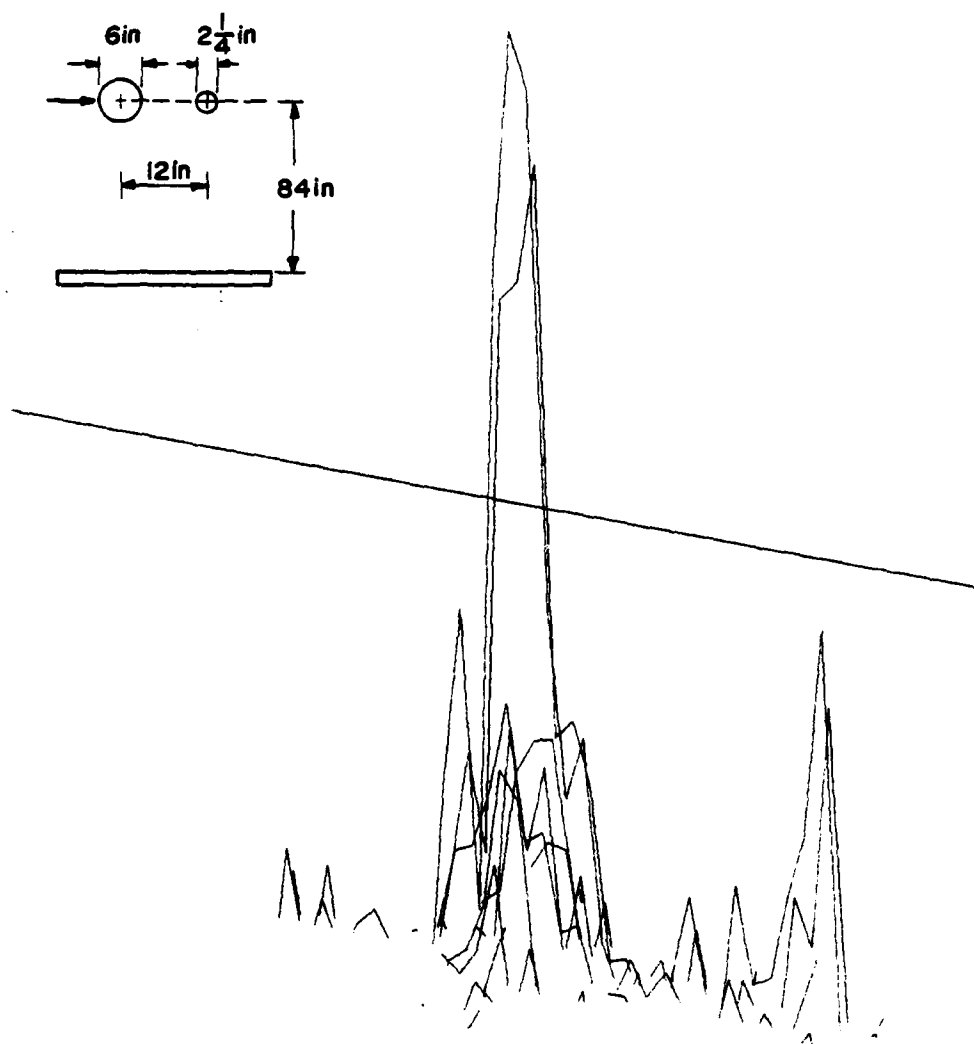


Figure 6.8 Reconstruction at 17 kHz of two spheres of different diameters in the same object plane.



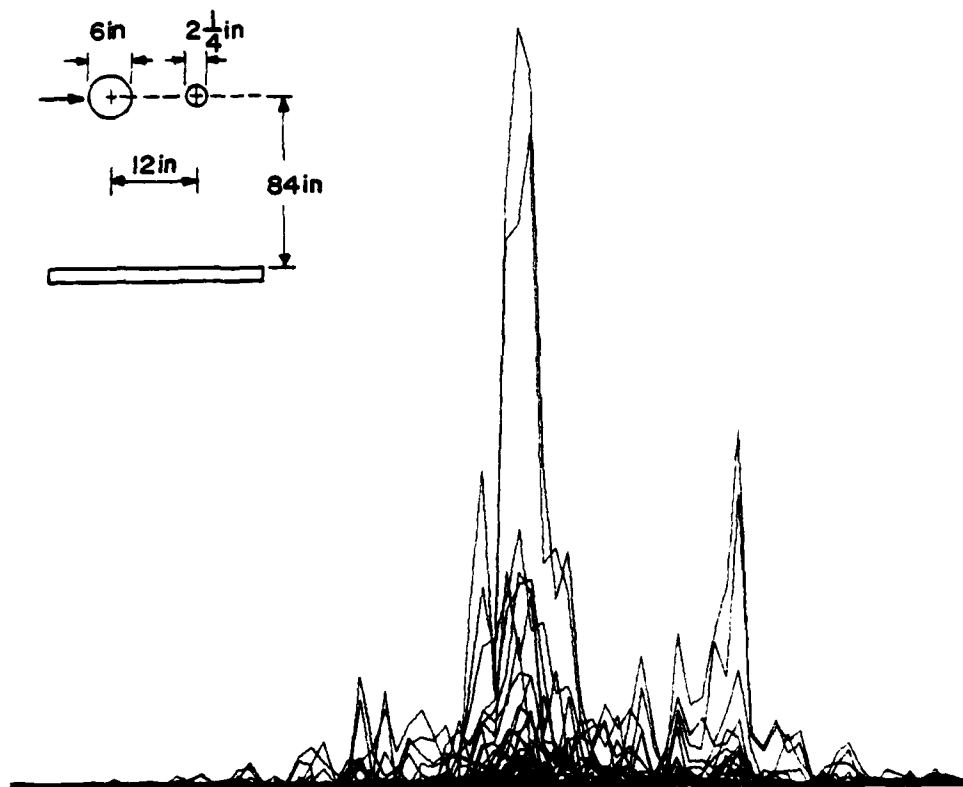


Figure 6.9 Reconstruction (side view) at 17 kHz of two spheres of different diameters in the same object plane.

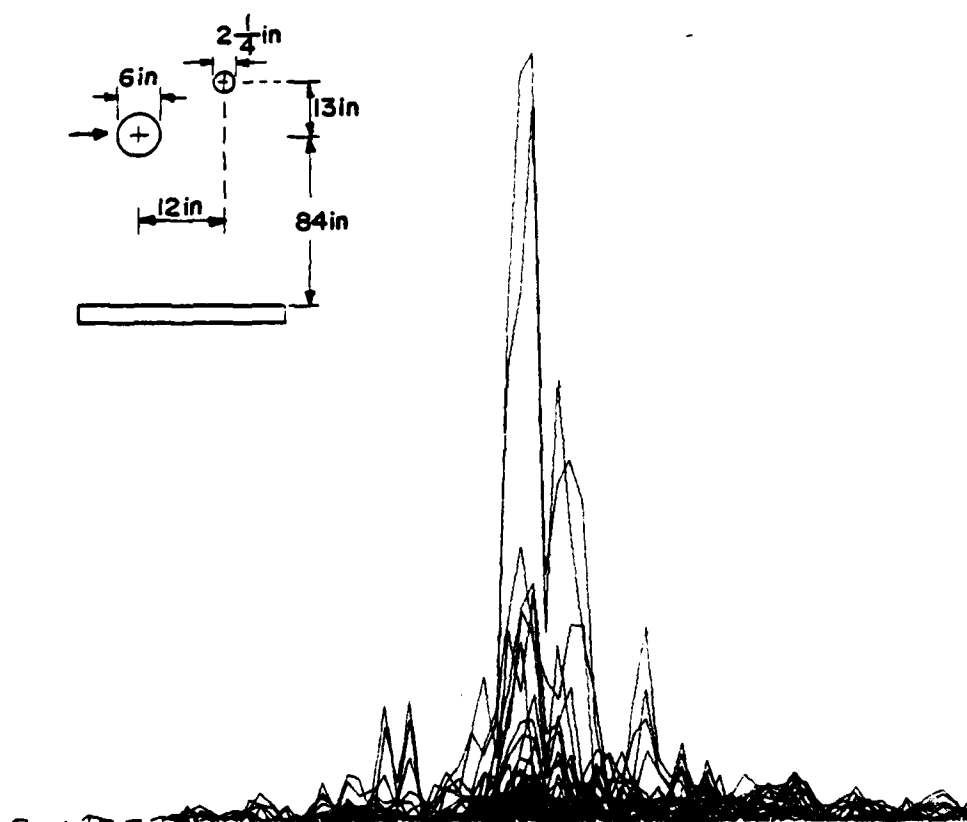


Figure 6.10 Reconstruction (side view) at 17 kHz of two unequal spheres in different object planes, as viewed in the plane of the closest sphere.

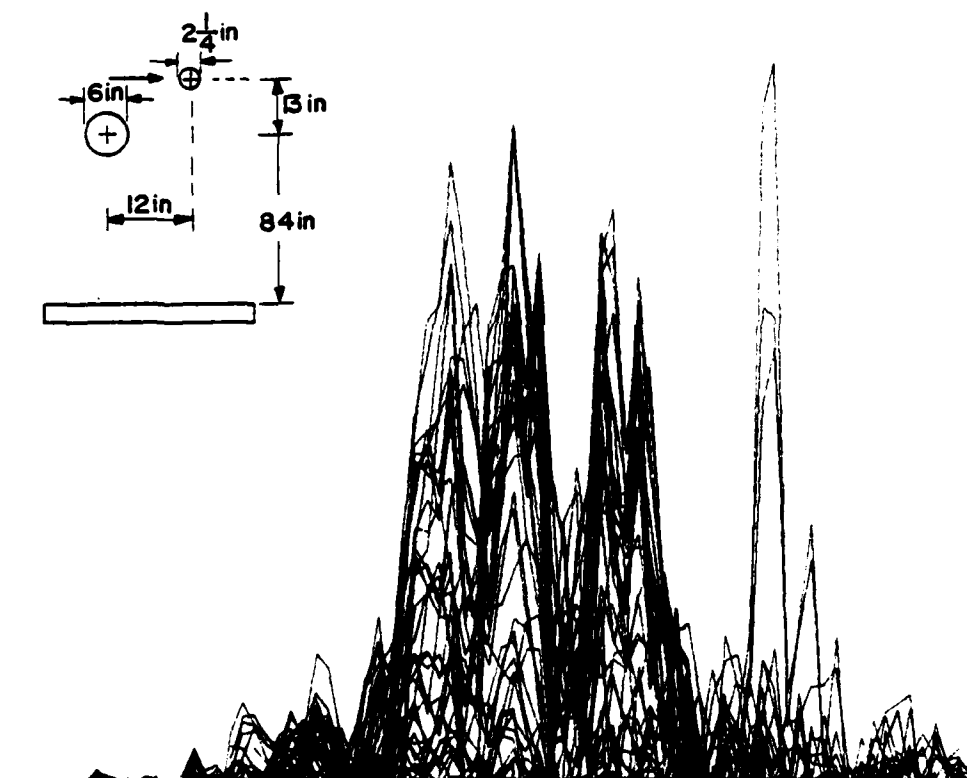


Figure 6.11 Reconstruction (side view) at 17 kHz of two unequal spheres in different planes, as viewed in the plane of the furthest sphere.

plane. In addition, an out-of-focus component from the other sphere is noted in Figure 6.11. The out-of-focus component in Figure 6.10 is apparently too small to be visible. Note that, in comparing the latter two figures, one must remember that the data are rescaled to the local maximum in each plot. Thus, the peak values in the two plots actually differ by an absolute ratio of 3.5. A comparison of the reconstructions of the larger sphere in the two figures gives one an idea of the meaning of the term "out of focus." When this condition exists, the reconstructed field is lower in amplitude, broader in area, and has no prominent peaks. When separated from other returns, this out-of-focus component is easily found by visual inspection; and Powers and Mueller (1974) indicate that the slope of the field can be used as a numerical indicator of the degree of focus achieved in some cases.

### 6.3.3 Backscattering at a Prolate Spheroid

Having developed some intuitive feel for the results of a wavefront reconstruction, attention next turned to extended, three-dimensional scatterers. The first model examined was the 42-inch-long, 7:1 prolate spheroid. Figure 6.12 shows the reconstruction obtained for broadside incidence in the plane of the leading side. Just as was noted in both of the previous sections, the field on the spheroid is evenly distributed over most of the surface, although somewhat lower values are noted near the ends. The corresponding reconstruction for axial incidence is shown in Figure 6.13 (viewed in the plane of the tip). In this case, the reconstructed field is broader than the physical dimensions of the tip, which may indicate the size of the surface field

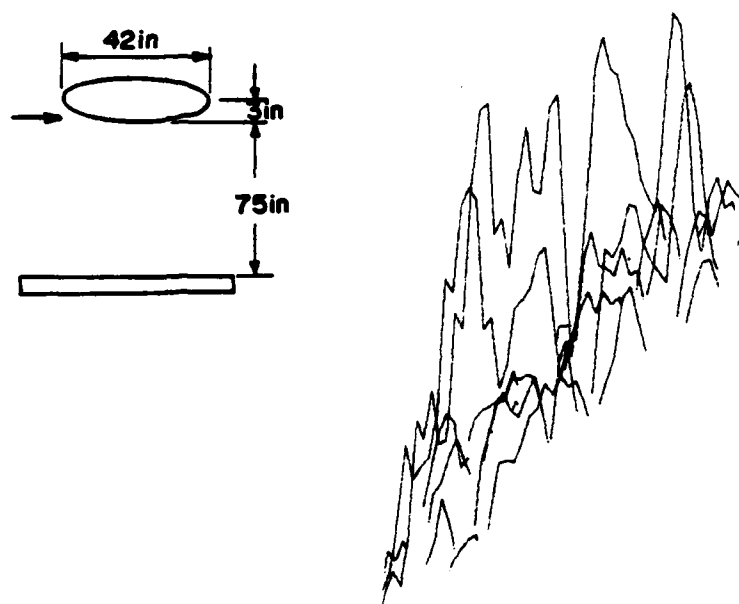


Figure 6.12 Reconstruction at 17 kHz from a 7:1 prolate spheroid for broadside incidence.

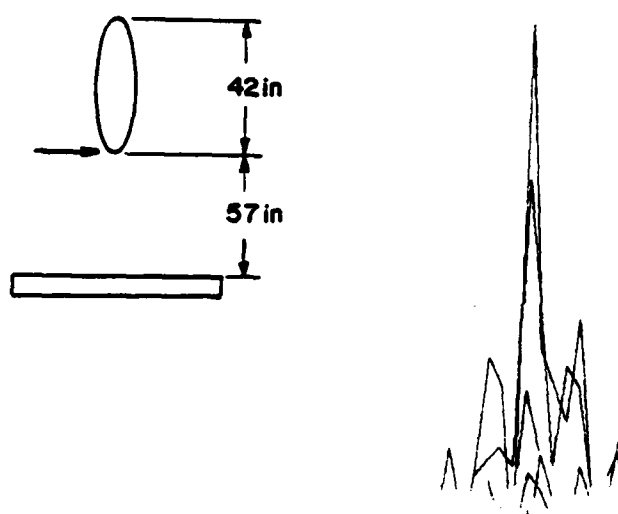


Figure 6.13 Reconstruction at 17 kHz from a 7:1 prolate spheroid at axial incidence, viewed in the plane of the tip.

or may indicate out-of-focus contributions from points further down the length of the model. For the axial incidence case, a reconstruction that was made at the center of the spheroid is shown in Figure 6.14. In this result, there are no individual components evident above the general background level. The final experiment in this series involved a small cylinder that was centered on top of the axially directed spheroid. In the resulting reconstructions, a cylinder contribution is observed in the center plane, and some additional contributions to the background level at the tip are also noted.

#### 6.3.4 Backscattering at a Finite Cone

The other three-dimensional scatterer examined was the 18-inch cone model (described in Section 3.3), with either the usual pointed tip or a spherical cap of 2-inch radius. The reconstruction of the pointed-tip cone was examined both at the tip (Figure 6.15) and at the rear edge (Figure 6.16). The component indicated at the rear edge is a circle along the outline of the base, as might be expected. This reconstruction also has a peak in the center, which may be an out-of-focus component. At the tip, a reasonably well-defined component is also evident. However, because this tip component is almost as large as the rear component in absolute magnitude, it must be an out-of-focus term. (Data of Section 5.4.2 show that the tip return is much smaller than the rear-edge return.) This last result shows that reconstructions must be interpreted very carefully. Turning to the spherically capped cone, the reconstructions at the cap and at the rear edge are shown in Figures 6.17 and 6.18, respectively. A distinct specular return is

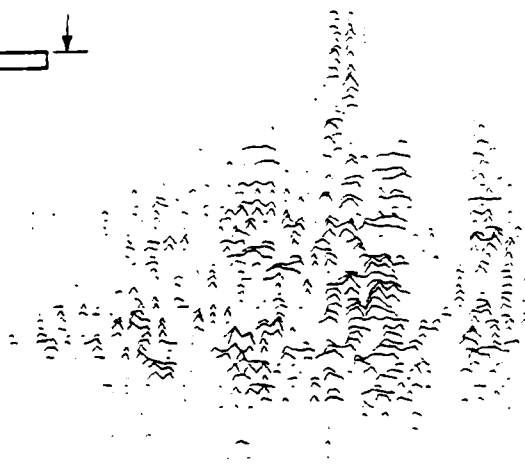
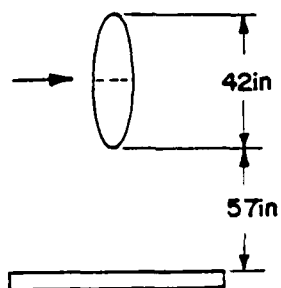


Figure 6.14 Reconstruction at 17 kHz from a 7:1 prolate spheroid at axial incidence, viewed in the plane at the spheroid center.



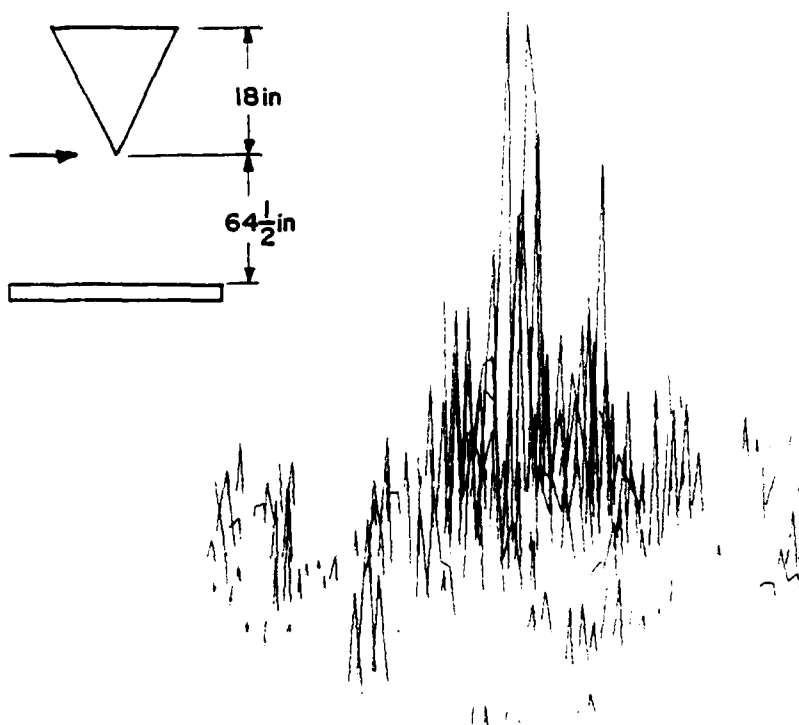


Figure 6.15 Reconstruction at 17 kHz from a finite cone, viewed in the plane of the tip.

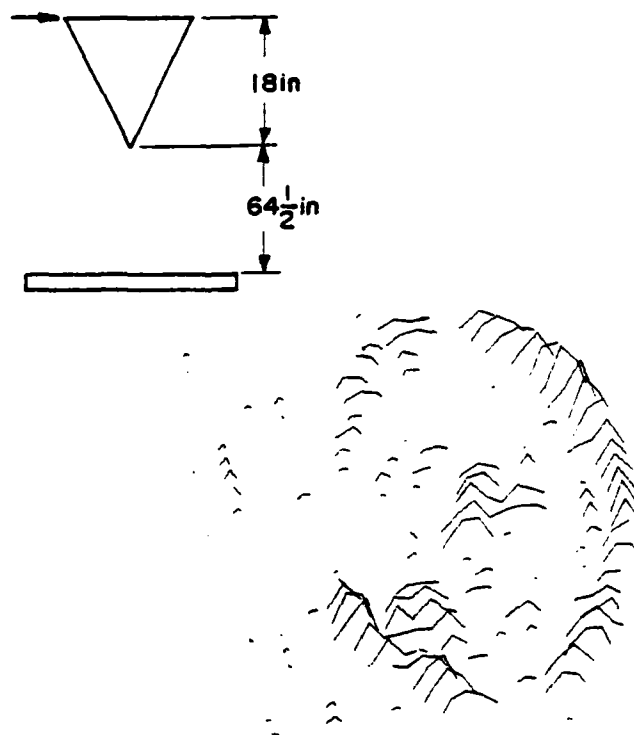


Figure 6.16 Reconstruction at 17 kHz from a finite cone, viewed in the plane of the rear edge.

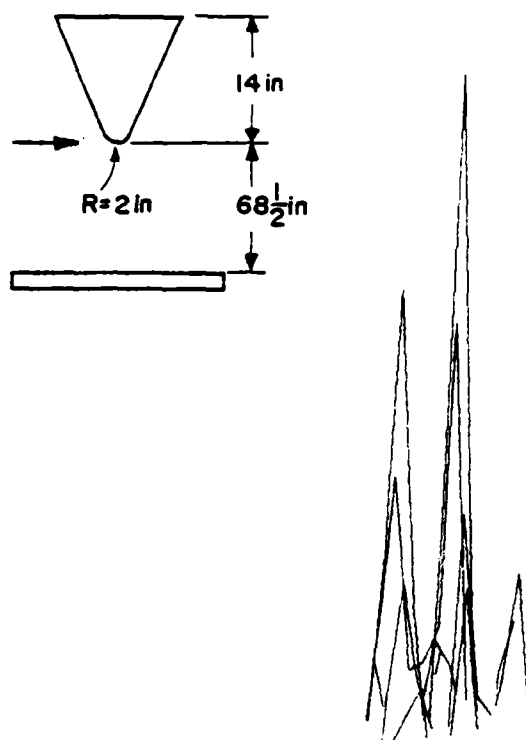


Figure 6.17 Reconstruction at 17 kHz from a spherically capped cone, viewed in the plane of the tip.

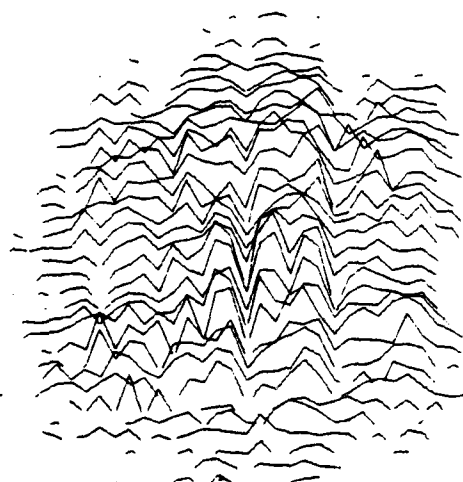
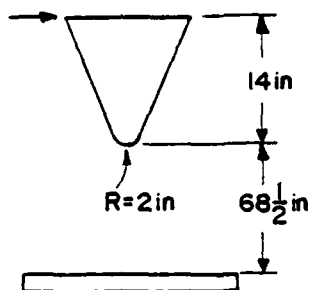


Figure 6.18 Reconstruction at 17 kHz from a spherically capped cone, viewed in the plane of the rear edge.

noted at the cap. At the rear edge, however, the expected ring-shaped return is not observed. One must conclude that the rear-edge (ring) return is being masked by an out-of-focus component from the cap.

#### 6.4 General Conclusions About the Technique

The results described in Section 6.3 have pointed out both good and bad features of the technique of wavefront reconstruction. There is at least some evidence that accurate quantitative values of the equivalent surface fields on a scatterer can be obtained. However, the lack of resolution in the  $z$  direction is a serious problem for studies of three-dimensional scatterers. It is possible that either a more accurate pulse system or the addition of several frequencies can aid in the solution of this problem. Only more work will tell. There are also unresolved questions about the interpretation of the equivalent surface fields. However, when the difficulties encountered in trying to measure surface fields by traditional sensing methods are considered, the imaging technique shows enough merit to justify more studies.

## CHAPTER 7

## SUMMARY AND CONCLUSIONS

The previous chapters have summarized in detail the individual results of a fairly extensive series of scattering experiments. The primary purpose of these experiments has been to examine the physical diffraction mechanisms that are important in modern diffraction theories. In addition, both theoretical and experimental analyses of the Freedman theory of echo formation have been included to supplement the sparse amount of information in the literature about this theory. Because of the large amount of data presented, it is easy to lose sight of the many similarities and relationships among the data from various experiments. This is unfortunate because the results are probably most valuable when taken as a whole in order to develop one's physical intuition. Consequently, this chapter places an overall perspective on the results of the study by describing the major conclusions derived by the author. Wherever possible, brief references to other sections of this thesis are included to direct the reader to additional pertinent information. Note, however, that it will generally be necessary to refer to several different experiments to evaluate all the information relating to any individual conclusion.

The backscattering from a prolate spheroid appears to be governed almost exclusively by specular effects (see Section 4.2). The directivity results of the spheroid match simple geometric predictions very closely, even though the specular points on the spheroid for much of the angular range fall near a tip of relatively small radius (Section

4.2.4). There is evidence, though, that these results are very sensitive to small changes in the model's shape that are caused either by surface anomalies (Section 4.3.1) or small obstructions on the surface (Sections 4.3.2 and 4.4.1). Thus, it appears that predictions based only on specular effects will work reasonably well (although the predicted amplitudes may be a little too large); this is true even for bodies whose radii of curvature are relatively small in relation to a wavelength, if the scattering surface is smoothly curved. This conclusion is reinforced by results from modified cones having spherical surfaces at the tip (Section 5.4.2). Although they possess only a small fraction of the total surface area of a sphere at their tip, the cones with smoothly joined spherical caps exhibit very uniform scattering patterns that are similar in both directivity and absolute level to those of a sphere. In contrast, the cone with a hemispherical cap, which possesses a much larger spherical area, exhibits distinct bulges in both its backscattered and bistatic directivity results (Section 5.4.4). This last result may be attributed to the more abrupt transition between the sphere and cone outlines that is present with the hemispherical cap. Note that the relatively small spacing between the models and the transducers in the experiments may have exaggerated all the relationships described in this paragraph.

The curved symmetry of the thin prolate spheroid also points out the fundamental differences between the scattering from flat and slightly curved bodies. Although the long dimension of the thin spheroid is almost flat (at least near the center), the body continues to behave more like a sphere than a cylinder. For example, at broadside

incidence, the bistatic scattering pattern for the spheroid is very broad in the plane of the spheroid's major axis (Section 4.5), while a cylinder of much smaller dimensions exhibits prominent lobes (similar to the backscatter data of Section 5.3). This result is certainly related to the fact that the surface of the cylinder is terminated at both ends by abrupt edges. However, the strong geometrical similarity between the sphere and spheroid (described in Section 4.1) should be noted as an additional consideration. In fact, the Gaussian curvature of the spheroid at its specular point for broadside incidence is exactly the same as the Gaussian curvature of a sphere with the same major radius; and this relation is always true despite the large differences in the principal radii of curvature between a thin spheroid and an equivalent sphere. As a corollary to the conclusion about bistatic scattering, the backscatter from the thin spheroid is also relatively smooth (Section 4.2.2). In this case, the specular points shift rapidly to the sphere-like tip region as the body is rotated from broadside incidence to axial incidence. Because the radii of curvature at the specular point change rapidly as the incidence angle is varied, it is difficult to describe the backscattering by a thin spheroid in terms of a characteristic dimension (see Section 4.2.4).

Several of the smooth-body studies produced evidence of surface fields, but the properties of the fields differ from those normally attributed to so-called creeping waves. A component that closely matches the Franz-type creeping waves (see Deppermann & Franz, 1954) is observed for the simple case of a sphere (Section 4.6.1), but this return depends only loosely on the shape of the model's surface. For



example, a band placed around the surface of a sphere to block the creeping-wave component has no effect unless the band passes through the antipole (focus point) on the rear side of the sphere (Section 4.6.2). In addition, the amplitude of the creeping-wave component is increased at all measured scattering angles by cutting a flat surface into one side of the sphere (Section 4.6.3). This increase is observed even when the flattened portion is oriented toward the transducers, an orientation in which the assumed path of the creeping waves around the rear of the body is unchanged from that on the unmodified sphere. These results are best explained as a continuous manifestation of the diffraction model that postulates a diffusion of sound energy into the shadow at a shadow boundary (described in Malyughinets, 1959).

Other surface effects, possibly related to the creeping waves, were observed with small obstructions on the prolate spheroid. For example, the scattering by small cylinders is enhanced when the cylinders are placed on the spheroid surface (Section 4.4.2). This baffle-like effect appears to be localized to an area located no more than one wavelength from the surface; and it is formed (in fact, is most prominent) at the illuminated tip of the spheroid, which is different than the formation point postulated for creeping waves. Although this second surface phenomenon exhibits certain properties only at axial incidence, the basic baffle effect is evident for incidence angles on the spheroid as large as  $50^\circ$  from axial incidence (Section 4.4.3).

The studies of edges on rectangular baffles led to two major conclusions. First, the shape of an edge (i.e., flat or round) must be considered in scattering predictions, even when the thickness of the

edge is no more than  $\lambda/4$ . A comparison of backscattering by rounded and by square edges shows distinct differences for edges of this small dimension (Section 5.2). In addition, there is evidence that the angular distribution of the field scattered by a small but finite edge is very directive (Section 5.1.1). The second major conclusion relates to the effect of surface absorption on a field propagating at the grazing angle. The results show that a significant attenuation of the grazing field is observed. This attenuation is present not only near the baffle but out to a distance of several wavelengths when the field is generated by edge diffraction (i.e., on the shadowed side of a baffle, as in Section 5.1.2). A surprisingly large attenuation of the grazing field is also observed when the source field is incident at the grazing angle (Section 5.1.2). Thus, there is evidence that surface fields on fairly long bodies can be effectively attenuated by a small amount of surface absorption.

The most important intuitive conclusion drawn from the studies of cone models is the importance of scattering from edges that represent a discontinuity in the cross section of a surface. The prominence of the rear-edge contribution from a finite cone is well known. However, the results of this study show that the backscattering by a similar surface discontinuity of less than 10% of the wavelength (at the points where the removable caps attach to the cone model) has an amplitude within a few decibels of that from the rear edge (Section 5.4.1). Thus, the existence of a surface discontinuity appears to be more important as a determinant of scattering levels than is the actual size of the discontinuity. As a corollary to this conclusion, the scattering from

an abrupt edge can be significantly reduced (10 - 15 dB) by making the edge discontinuous only in slope, as was demonstrated by smoothing the surface of the cone model at the cap joint (Section 5.4.1) and by attaching a hemisphere to the rear of the cone (Section 5.4.2). Some additional improvement is also gained by reducing the discontinuity at the edge from first to second order (i.e., using the spherical cone termination instead of the hemispherical termination), but the change in scattering level that occurs in this case is not as great as the change observed in going from the zero-order to the first-order discontinuity (Section 5.4.2).

The various types of edges that were examined on the cone models also exhibit interesting differences in their directivities for both backscattering and bistatic scattering. First, when the cone is illuminated from the front, the directivity of the backscatter from the rear edge exhibits the distinctly lobed pattern that is characteristic of the interference between two similar returns (at least for angles where returns from both edges are visible, as in Section 5.4.3). However, when the cone is illuminated from the rear (i.e., onto the circular base), only a single broad peak is noted (Section 5.4.3). In the latter case, there is a strong specular contribution from the disk itself that dominates any edge contributions for angles near axial incidence. Then, as the cone is rotated, the specular component decreases in amplitude and appears to split into returns from each edge; but the two edge returns are separated enough in time that they do not interfere. Second, when the rear edge of the cone is modified with either the hemispherical or spherical termination, the shape of the

directivity changes in a manner that reduces the difference between the central peak and the sidelobes (Section 5.4.5). As a consequence, the reduction in scattering associated with the change in the order of discontinuity at the edge (see Section 5.4.2) is observed only for axial incidence. Note that the directivity of the bistatic scattering for the rear edge of the cone-sphere is essentially uniform in level (it does oscillate slightly)--in stark contrast to that from the normal cone, which exhibits a large central peak (see Section 5.4.5).

At the current stage of development, it is difficult to draw any firm conclusions from the experimental results obtained by wavefront reconstruction. It is tempting, for example, to compare the distribution of the surface fields on the spheroid (Section 6.3.3) and the square baffle (Section 6.3.1) and then to look for a result that explains the differences observed between their farfield scattering patterns. However, sufficient understanding of the method's details has not been developed (see Section 6.4). The wavefront-reconstruction technique, in general, looks very promising if the problems of resolution in the  $z$  axis can be adequately resolved.

Finally, a few conclusions can be drawn about the Freedman theory. First, the theoretical analysis (Section 2.2) shows that it is a variant solution of physical optics rather than an asymptotic theory as described by Freedman (1962a). Second, just as with physical optics, the Freedman method appears to provide good predictions (at least at large ranges) for two-dimensional objects, such as rectangular edges, at angles not too far from the surface normal (Section 5.2). However, for three-dimensional objects, where more than one surface may contribute to

the scattering, serious problems are noted. The cylinder examples of Section 5.3 indicate that the problems found in the theory for three-dimensional scatterers are caused by the sensitivity of the vector sum of multiple scattering components to small errors in the predictions of the individual components. Third, problems with the Freedman theory are also noted at abrupt surface discontinuities where the assumptions of the theory are questionable (Section 5.4.2). For example, the prediction for the backscattering by the rear edge of a cone exhibits the wrong frequency dependence. In addition, the theory fails to account for the nature of the edge at the cone's shadow boundary, which the experimental results show to be very important. Fourth, there is evidence that the Freedman predictions for first- and second-order edges and tips on the surface of a cone are relatively accurate, but the results are inconclusive on this point because of the extreme sensitivity of the data to minor imperfections in the model (see Section 5.4.1) and/or because of marginal signal-to-noise ratios in the experiments.

From a qualitative point of view, the Freedman predictions are generally very good; that is, the backscattered returns generally do originate where predicted, even on three-dimensional bodies. The only major problem that has been encountered occurs at the shadow boundary (final range point of the body). The Freedman theory always predicts a scattering component from this boundary, but none is experimentally observed if the surface of the scatterer is smooth at the boundary (such as occurs, for example, with the spheroid or the cone-sphere). It is possible to argue that the quantitative successes of the Freedman theory

are tied very strongly to its ability to predict the locations of scattering components. Because the predicted locations of these components are accurate, their phases are also correct; and holography studies (for example, Watson, 1971) have shown that the phase carries the dominant information about the basic form of the scattering pattern, such as the locations of maxima and minima.

When examined in detail, the previous conclusions are merely an indication of the complexity of the scattering process. There is evidence that small variations of simple scatterers can significantly affect the scattering results. Thus, from a practical point of view, one must be very careful in using simple examples to model related shapes, and realistic expectations on the accuracy of the results should be assumed. On the other hand, there are enough similarities in the results to postulate that adequate predictions can be made if sufficient insight into the physical mechanisms can be developed and formulated into prediction methods. This study represents only a small contribution toward that goal. It is hoped, however, that the effort has demonstrated the usefulness of exploratory experimentation as a means for both understanding the physical phenomena and helping to direct the development of better techniques for predicting the scattering from three-dimensional bodies.

## REFERENCE LIST

- Albers, V. M. (Ed.). Benchmark papers in acoustics: Underwater sound. Stroudsburg, Pa.: Dowden, Hutchinson & Ross, 1972.
- Albertsen, N. C., & Christiansen, P. L. Hybrid diffraction coefficients for first and second order discontinuities of two-dimensional scatters. SIAM Journal of Applied Mathematics, 1978, 34, 398-414.
- Andebura, V. A., & Ostashevskii, A. P. Sound scattering by rigid prolate spheroids. Soviet Physics-Acoustics, 1974, 20, 112-114.
- Barakat, R. Diffraction of plane waves by an elliptic cylinder. The Journal of the Acoustical Society of America, 1963, 35, 1990-1996.
- Barnard, G. R., & McKinney, C. M. Scattering of acoustic energy by solid and air-filled cylinders in water. The Journal of the Acoustical Society of America, 1961, 33, 226-238.
- Bayliss, A., & Maestrello, L. Measurements and analysis of farfield scattering from a prolate spheroid. The Journal of the Acoustical Society of America, 1978, 64, 896-900.
- Bechtel, M. E. Application of geometric diffraction theory to scattering from cones and disks. Proceedings of the IEEE, 1965, 53, 877-882.
- Becknell, G. G., & Coulson, J. An extension of the principle of the diffraction evolute, and some of its structural detail. Physics Review, 1922, 20, 607-612.
- Berger, R. L., & Ackerman, E. The Penn State anechoic chamber. Noise Control, 1956, 2(5), 16-21.
- Blake, W. K., & Wilson, G. A. Short-wavelength diffracted surface pressures on a rigid prolate spheroid. The Journal of the Acoustical Society of America, 1977, 61, 1419-1426.
- Blore, W. E. Experimental measurements of the radar cross section of a cone sphere. Proceedings of the IEEE, 1963, 51, 1263-1264.
- Bolomey, J. C., & Wirgin, A. Numerical comparison of the Green's function and the Waterman and Rayleigh theories of scattering from a cylinder with arbitrary cross-section. Proceedings of the IEE, 1974, 121, 794-804.
- Born, M., & Wolf, E. Principles of optics. New York: MacMillan, 1959.
- Bowman, J. J., Senior, T. B. A., & Uslenghi, P. L. E. (Eds.). Electromagnetic and acoustic scattering by simple shapes. Amsterdam: North-Holland, 1969.

- Brown, W. P., Jr. On the asymptotic behavior of electromagnetic fields scattered from convex cylinders near grazing incidence. Journal of Mathematical Analysis and Applications, 1966, 15, 355-385.
- Buchal, R. N., & Keller, J. B. Boundary layer problems in diffraction theory. Communications on Pure and Applied Mathematics, 1960, 13, 85-114.
- Buck, R. C. Advanced calculus (2nd ed.). New York: McGraw-Hill, 1965.
- Chen, P., & Pao, Y. The diffraction of sound pulses by a circular cylinder. Journal of Mathematical Physics, 1977, 18, 2397-2406.
- Christiansen, P. L. Comparison between edge diffraction processes. Proceedings of the IEEE, 1974, 62, 1462-1468.
- Cohen, R. L. Digital wavefront reconstruction for acoustical applications (Doctoral dissertation, The Pennsylvania State University, 1979).
- Copley, L. G. Fundamental results concerning integral representations in acoustic radiation. The Journal of the Acoustical Society of America, 1968, 44, 28-32.
- Crispin, J. W., & Siegel, K. M. (Eds.). Methods of radar cross-section analysis. New York: Academic Press, 1968.
- Dardy, H. D., Bucaro, J. A., Schuetz, L. S., & Dragonette, L. R. Dynamic wide-bandwidth acoustic form-function determination. The Journal of the Acoustical Society of America, 1977, 62, 1373-1376.
- Darling, D. A., & Senior, T. B. A. Low-frequency expansions for scattering by separable and non-separable bodies. The Journal of the Acoustical Society of America, 1965, 37, 228-234.
- Deppermann, K., & Franz, W. Theorie der Beugung an der Kugel unter Berücksichtigung der Kriechwelle. Annalen der Physik, 1954, 14, 253-264.
- Doolittle, R. D., McNicholas, J. V., & Uberall, H. Circumferential sound pulses on elastic cylinders. The Journal of the Acoustical Society of America, 1967, 42, 522-523.
- Dragonette, L. R. Evaluation of the relative importance of circumferential or creeping waves in the acoustic scattering from rigid and elastic solid cylinders and from cylindrical shells (NRL Report 8216). Washington, D. C.: Naval Research Laboratory, September 1978. (NTIS No. AD-A060 836)
- Dunsiger, A. D. A study of acoustic echoes from solid cylindrical targets of square and circular section. Journal of Sound and Vibration, 1968, 8, 229-239.



- Dunsiger, A. D. High-frequency acoustic echoes received from simple geometric shapes with possible applications to target recognition. Journal of Sound and Vibration, 1970, 13, 323-345.
- Erdelyi, A. (Ed.). Tables of integral transforms (Vol. 2, Bateman Manuscript Project). New York: McGraw-Hill, 1954.
- Fock, V. A. Electromagnetic diffraction and propagation problems. New York: Pergamon, 1965.
- Foxwell, J. H. The diffraction of sound round a rigid sphere from a point source on the sphere. Journal of Sound and Vibration, 1970, 11, 103-113.
- Franz, W. Über die Greenschen Functionen des Zylinders und der Kugel. Zeitschrift für Naturforschung, 1954, 9a, 705-716.
- Franz, W., & Deppermann, K. Theorie der Beugung am Zylinder unter Berücksichtigung der Kriechwelle. Annalen der Physik, 1952, 10, 361-373.
- Franz, W., & Klante, K. Diffraction by surfaces of variable curvature. IRE Transactions on Antennas and Propagation, 1959, AP-7, S68-S70.
- Freedman, A. A mechanism of acoustic echo formation. Acustica, 1962, 12, 10-21. (a)
- Freedman, A. The high frequency echo structure of some simple body shapes. Acustica, 1962, 12, 61-70. (b)
- Freedman, A. An experimental examination of acoustic echo structure. Acustica, 1964, 14, 89-104.
- Freedman, A. Sound field of plane or gently curved pulsed radiators. The Journal of the Acoustical Society of America, 1970, 48, 221-227. (a)
- Freedman, A. Transient fields of acoustic radiators. The Journal of the Acoustical Society of America, 1970, 48, 135-138. (b)
- Freedman, A. Farfield of pulsed rectangular acoustic radiator. The Journal of the Acoustical Society of America, 1971, 49, 738-748.
- Freedman, A. Sound field of a pulsed, planar, straight-edged radiator. The Journal of the Acoustical Society of America, 1972, 51, 1624-1639.
- Freedman, A. The use of linear system theory in acoustic radiation and scattering analysis. Journal of Sound and Vibration, 1977, 52, 265-276.
- Gatkin, N. G., Paramonova, S. N., & P'yanov, V. M. Sound scattering by rigid prolate spheroids. Soviet Physics-Acoustics, 1972, 17, 313-318.

- Goodman, J. W. Introduction to Fourier optics. New York: McGraw-Hill, 1968.
- Goodman, R. R., Bunney, R. E., & Marshall, S. W. Observation of circumferential waves on solid aluminum cylinders. The Journal of the Acoustical Society of America, 1967, 42, 523-524.
- Goodrich, R. F., & Kazarinoff, N. D. Scalar diffraction by prolate spheroids whose eccentricities are almost one. Proceedings of the Cambridge Philosophical Society, 1963, 59, 167-183.
- Graham, T. S. Long wavelength acoustic holography (Doctoral dissertation, The Pennsylvania State University, 1969). Dissertation Abstracts International, 1970, 30, 3319B. (University Microfilms No. 70-674)
- Hampton, L. D., & McKinney, C. M. Experimental study of the scattering of acoustic energy from solid metal spheres in water. The Journal of the Acoustical Society of America, 1961, 33, 664-673.
- Harbold, M. L., & Steinberg, B. N. Direct experimental verification of creeping waves. The Journal of the Acoustical Society of America, 1969, 45, 592-603.
- Hickling, R. Frequency dependence of echoes from bodies of different shapes. The Journal of the Acoustical Society of America, 1958, 30, 137-139.
- Hickling, R. Analysis of echoes from a solid elastic sphere in water. The Journal of the Acoustical Society of America, 1962, 34, 1582-1592.
- Hickling, R. Analysis of echoes from a hollow metallic sphere in water. The Journal of the Acoustical Society of America, 1964, 36, 1124-1137.
- Hong, S. Asymptotic theory of electromagnetic and acoustic diffraction by smooth convex surfaces of variable curvature. Journal of Mathematical Physics, 1967, 8, 1223-1232.
- Hong, S., & Borison, S. L. Short-pulse scattering by a cone--direct and inverse. IEEE Transactions on Antennas and Propagation, 1968, AP-16, 98-102.
- Horton, C. W., & Karal, F. C., Jr. On the diffraction of a plane sound wave by a paraboloid of revolution. The Journal of the Acoustical Society of America, 1950, 22, 855-856.
- James, G. L. Geometrical theory of diffraction for electromagnetic waves. London: The Institution of Electrical Engineers, 1976.
- Karal, F. C., Jr., & Keller, J. B. Geometrical theory of elastic surface-wave excitation and propagation. The Journal of the Acoustical Society of America, 1964, 36, 32-40.

- Kay, I., & Keller, J. B. Asymptotic evaluation of the field at a caustic. Journal of Applied Physics, 1954, 25, 876-883.
- Kazarinoff, N. D., & Ritt, R. K. On the theory of scalar diffraction and its application to the prolate spheroid. Annals of Physics, 1959, 6, 277-299.
- Keller, J. B. Diffraction by a convex cylinder. IRE Transactions on Antennas and Propagation, 1956, AP-4, 312-321.
- Keller, J. B. Diffraction by an aperture. Journal of Applied Physics, 1957, 28, 426-444.
- Keller, J. B. A geometrical theory of diffraction. In L. M. Graves (Ed.), Calculus of variations and its applications: Proceedings of the symposium on applied mathematics (Vol. 8). New York: McGraw-Hill, 1958.
- Keller, J. B. Backscattering from a finite cone. IRE Transactions on Antennas and Propagation, 1960, AP-8, 175-182.
- Keller, J. B. Backscattering from a finite cone--comparison of theory and experiment. IRE Transactions on Antennas and Propagation, 1961, AP-9, 411-412.
- Keller, J. B. Geometrical theory of diffraction. The Journal of the Optical Society of America, 1962, 52, 116-130.
- Keller, J. B., & Hansen, E. B. Survey of the theory of diffraction of short waves by edges. Acta Physica Polonica, 1965, 27, 217-234.
- Keller, J. B., & Karal, F. C., Jr. Surface wave excitation and propagation. Journal of Applied Physics, 1960, 31, 1039-1046.
- Keller, J. B., & Levy, B. R. Decay exponents and diffraction coefficients for surface waves on surfaces of nonconstant curvature. IRE Transactions on Antennas and Propagation, 1959, AP-7, S52-S61.
- Keller, J. B., Lewis, R. M., & Seckler, B. D. Asymptotic solution of some diffraction problems. Communications on Pure and Applied Mathematics, 1956, 9, 207-265.
- Kendig, R. P. Acoustic diffraction by an impedance covered half-plane (Doctoral dissertation, The Pennsylvania State University, 1977). Dissertation Abstracts International, 1977, 38, 2264B-2265B. (University Microfilms No. 77-23, 246)
- Kennaugh, E. M., & Moffatt, D. L. On the axial echo area of the cone-sphere shape. Proceedings of the IRE, 1962, 50, 199.
- Kleshchev, A. A. Sound scattering by ideal spheroids in the high-frequency limit. Soviet Physics-Acoustics, 1974, 19, 447-449.

- Kleshchev, A. A., & Sheiba, L. S. Scattering of a sound wave by ideal prolate spheroids. Soviet Physics-Acoustics, 1970, 16, 219-222.
- Kline, M. An asymptotic solution of Maxwell's equations. Communications on Pure and Applied Mathematics, 1951, 4, 225-262.
- Knott, E. F., & Senior, T. B. A. Comparison of three high-frequency diffraction techniques. Proceedings of the IEEE, 1974, 62, 1468-1474.
- Kouyoumjian, R. G., & Pathak, P. H. A uniform geometrical theory of diffraction for an edge in a perfectly conducting surface. Proceedings of the IEEE, 1974, 62, 1448-1461.
- Kraus, L., & Levine, L. M. Diffraction by an elliptic cone. Communications on Pure and Applied Mathematics, 1961, 14, 49-68.
- Lalor, E. Inverse wave propagator. Journal of Mathematical Physics, 1968, 9, 2001-2006.
- Lauchle, G. C. Short-wavelength acoustic diffraction by prolate spheroids. The Journal of the Acoustical Society of America, 1975, 58, 568-575. (a)
- Lauchle, G. C. Short-wavelength acoustic backscattering by a prolate spheroid. The Journal of the Acoustical Society of America, 1975, 58, 576-580. (b)
- Lee, S. W. Uniform asymptotic theory of electromagnetic edge diffraction: A review. In P. L. E. Uslenghi (Ed.), Electromagnetic scattering. New York: Academic Press, 1978.
- Leitner, A. Diffraction of sound by a circular disk. The Journal of the Acoustical Society of America, 1949, 21, 331-334.
- Leizer, I. G. Applicability of the methods of geometric acoustics for the calculation of sound reflection from plane surfaces. Soviet Physics-Acoustics, 1966, 12, 180-184.
- Leppington, F. G. Creeping waves in the shadow of an elliptic cylinder. Journal of the Institute of Mathematics and its Applications, 1967, 3, 388-402.
- Levy, B. R., & Keller, J. B. Diffraction by a smooth object. Communications on Pure and Applied Mathematics, 1959, 12, 159-209.
- Levy, B. R., & Keller, J. B. Diffraction by a spheroid. Canadian Journal of Physics, 1960, 38, 128-144.
- Ludwig, D. Boundary layers in the field scattered by a convex object at high frequencies. Communications on Pure and Applied Mathematics, 1969, 22, 715-736.

- Malyuzhinets, G. D. The excitation, reflection, and emission of surface waves on a wedge with given impedances of the faces. Doklady Akademii Nauk S.S.S.R., 1958, 121(3), 436-439.
- Malyuzhinets, G. D. Developments in our concepts of diffraction phenomena. Uspelchi Fizicheskikh Nauk, 1959, 69(5), 321-334.
- Malyuzhinets, G. D. Das Sommerfeldsche Integral und die Losung von Beugungsaufgaben in Winkelgebeiten. Annalen der Physik, 1960, 7(6), 107-112.
- Mie, G. Beitrage zur Optik truber Medien, speziell kolloidaler Metallosungen. Annalen der Physik, 1908, 25, 377-445.
- Moore, W. E. Recovery of acoustic pulse waveforms using calculator-controlled signal processing (NRL Report 7658). Washington, D. C.: Naval Research Laboratory, March 1974. (NTIS No. AD-777 717)
- Morse, P. M., & Feshbach, H. Methods of theoretical physics. New York: McGraw-Hill, 1953.
- Neubauer, W. G. A summation formula for use in determining the reflection from irregular bodies. The Journal of the Acoustical Society of America, 1963, 35, 279-285.
- Neubauer, W. G. Experimental measurement of "creeping" waves on solid aluminum cylinders in water using pulses. The Journal of the Acoustical Society of America, 1968, 44, 298-299.
- Neubauer, W. G., Vogt, R. H., & Dragonette, L. R. Acoustic reflection from elastic spheres. I. Steady-state signals. The Journal of the Acoustical Society of America, 1974, 55, 1123-1129.
- New, R., Andrews, F. A., Brill, D. W., Eisler, T. J., & Uberall, H. M. Technology transfer/A case study: Target strength (Technical Report Aug 73 - Mar 74). Washington, D. C.: Catholic University of America, Acoustics Group, March 1974. (NTIS No. AD-A012 871)
- Pathak, P. H., & Kouyoumjian, R. G. An analysis of the radiation from apertures in curved surfaces by the geometrical theory of diffraction. Proceedings of the IEEE, 1974, 62, 1438-1447.
- Powers, J. P., & Mueller, D. E. A computerized acoustic imaging technique incorporating automatic object recognition. In P. S. Green (Ed.), Acoustical holography (Vol.5). New York: Plenum Press, 1974.
- Rayleigh, J. W. S. On the electromagnetic theory of light. Philosophical Magazine and Journal of Science, 1881, 12, 81-101.
- Rayleigh, J. W. S. The theory of sound. New York: Dover, 1945.
- Ross, R. A. Radar cross section of rectangular flat plates as a function of aspect angle. IEEE Transactions on Antennas and Propagation, 1966, AP-14, 329-335.

- Rubinowicz, A. Zur Kirchhoffschen Beugungstheorie. Annalen der Physik, 1924, 73, 339-364.
- Rudgers, A. J. Acoustic pulses scattered by a rigid sphere immersed in a fluid. The Journal of the Acoustical Society of America, 1969, 45, 900-910.
- Salmon, G. A treatise on the analytic geometry of three dimensions (7th ed.). New York: Chelsea, 1927.
- Schenck, H. A. Improved integral formulation for acoustic radiation problems. The Journal of the Acoustical Society of America, 1968, 44, 41-58.
- Senior, T. B. A. The backscattering cross section of a cone-sphere. IEEE Transactions on Antennas and Propagation, 1965, AP-13, 271-277.
- Senior, T. B. A. The scattering from acoustically hard and soft prolate spheroids for axial incidence. Canadian Journal of Physics, 1966, 44, 655-667.
- Senior, T. B. A. The diffraction matrix for a discontinuity in curvature. IEEE Transactions on Antennas and Propagation, 1972, AP-20, 326-333.
- Senior, T. B. A., & Uslenghi, P. L. E. Comparison between Keller's and Ufimtsev's theories for the strip. IEEE Transactions on Antennas and Propagation, 1971, AP-19, 557-558.
- Senior, T. B. A., & Uslenghi, P. L. E. Experimental detection of the edge-diffraction cone. Proceedings of the IEEE, 1972, 60, 1448.
- Siegel, K. M., Crispin, J. W., & Schensted, C. E. Electromagnetic and acoustical scattering from a semi-infinite cone. Journal of Applied Physics, 1955, 26, 309-313.
- Skudrzyk, E. J. The foundations of acoustics. Wein: Springer-Verlag, 1971.
- Skudrzyk, E. J., Hayek, S. I., & Stuart, A. D. Acoustic diffraction: Part I - Plane diffractors and wedges (TM 73-109). State College, Pa.: The Pennsylvania State University Applied Research Laboratory, May 1973. (NTIS No. AD-A040 668)
- Spence, R. D. The diffraction of sound by circular disks and apertures. The Journal of the Acoustical Society of America, 1948, 20, 380-386.
- Spence, R. D. A note on the Kirchhoff approximation in diffraction theory. The Journal of the Acoustical Society of America, 1949, 21, 98-100.
- Spence, R. D., & Granger, S. The scattering of sound from a prolate spheroid. The Journal of the Acoustical Society of America, 1951, 23, 701-706.

- Spiegel, M. R. Theory and problems of vector analysis and an introduction to tensor analysis (Schaum's Outline Series). New York: McGraw-Hill, 1959.
- Uberall, H., Doolittle, R. D., & McNicholas, J. V. Use of sound pulses for a study of circumferential waves. The Journal of the Acoustical Society of America, 1966, 39, 564-578.
- Ufimtsev, P. Ia. Secondary diffraction of electromagnetic waves by a strip. Soviet Physics-Technical Physics, 1958, 3, 535-548.
- Ufimtsev, P. Ia. Asymptotic investigation of the problem of diffraction on a strip. Radio Engineering and Electronic Physics, 1969, 14, 1014-1025.
- Uslenghi, P. L. E. (Ed.). Electromagnetic scattering. New York: Academic Press, 1978.
- Van Roy, D. L. Digital ultrasonic reconstruction in the near field (No. 320.2402). Houston: I.B.M. Scientific Center, May 1971.
- Varadan, V. V. Scattering matrix for elastic waves. II. Application to elliptic cylinders. The Journal of the Acoustical Society of America, 1978, 63, 1014-1024.
- Varadan, V. V., & Varadan, V. K. Scattering matrix for elastic waves. III. Application to spheroids. The Journal of the Acoustical Society of America, 1979, 65, 896-905.
- Varatharajulu, V., & Pao, Y. Scattering matrix for elastic waves. I. Theory. The Journal of the Acoustical Society of America, 1976, 60, 556-566.
- Voltmer, D. R. Diffraction by doubly curved convex surfaces (Doctoral dissertation, The Ohio State University, 1970). Dissertation Abstracts International, 1971, 31, 4061B. (University Microfilms No. 70-26,382)
- Waterman, P. C. Matrix formulation of electromagnetic scattering. Proceedings of the IEEE, 1965, 53, 805-812.
- Waterman, P. C. New formulation of acoustic scattering. The Journal of the Acoustical Society of America, 1969, 45, 1417-1429.
- Watson, E. E. Detection of sound radiation from plates using long wavelength acoustical holography (Doctoral dissertation, The Pennsylvania State University, 1971). Dissertation Abstracts International, 1972, 32, 6560B. (University Microfilms No. 72-13,951)
- Watson, G. N. The diffraction of electric waves by the earth. Proceedings of the Royal Society, 1918, A95, 83-99.

- Weston, V. H. The effect of a discontinuity in curvature in high-frequency scattering. IRE Transactions on Antennas and Propagation, 1962, AP-10, 775-780.
- Weston, V. H. Effect of a discontinuity of curvature in high-frequency scattering, part II. IEEE Transactions on Antennas and Propagation, 1965, AP-13, 611-613.
- Wiener, F. M. Sound diffraction by rigid spheres and circular cylinders. The Journal of the Acoustical Society of America, 1947, 19, 444-451.
- Wiener, F. M. Notes on sound diffraction by rigid circular cones. The Journal of the Acoustical Society of America, 1948, 20, 367-369.
- Wiener, F. M. The diffraction of sound by rigid disks and rigid square plates. The Journal of the Acoustical Society of America, 1949, 21, 334-347.
- Wolf, E., & Shewell, J. R. The inverse wave propagator. Physics Letters, 1967, 25A, 417-418.



APPENDIX A  
DERIVATION OF THE KIRCHOFF SCATTERING INTEGRAL

For purposes of notation in the following derivation, an underscore represents a vector ( $\underline{r}$ ); the same letter symbol without an underscore represents the vector's magnitude ( $r = |\underline{r}|$ ); and a caret represents the corresponding unit vector ( $\hat{r} = \underline{r}/r$ ).

Let  $p(\underline{r}')$  be a solution of the Helmholtz equation (Morse & Feshbach, 1953, pp. 804-807) at a field point  $\underline{r}'$  in a region containing the source distribution  $f(\underline{r}')$ :

$$(\nabla^2 + k^2)p(\underline{r}') = f(\underline{r}') \quad . \quad (A.1)$$

Also, let  $G(\underline{r}, \underline{r}')$  be a solution of the Helmholtz equation with a unit point source located at  $\underline{r}$ :

$$(\nabla^2 + k^2)G(\underline{r}, \underline{r}') = \delta(\underline{r}' - \underline{r}) \quad . \quad (A.2)$$

The function  $\delta(\underline{r}' - \underline{r})$  is the standard delta function, and the  $\nabla^2$  operator is applied to the primed coordinate system. The function  $G(\underline{r}, \underline{r}')$  is frequently called the free-space Green's function, and it is given as (Skudrzyk, 1971, pp. 641-642)

$$G(\underline{r}, \underline{r}') = \frac{\exp(-ikR)}{4\pi R} \quad , \quad (A.3)$$

where  $\underline{R} = \underline{r} - \underline{r}'$  and  $R = |\underline{r}' - \underline{r}|$ . If Equation A.1 is multiplied by  $G(\underline{r}, \underline{r}')$ , Equation A.2 is multiplied by  $p(\underline{r}')$ , and the results of these

two operations are subtracted, one obtains

$$p(\underline{r}') \nabla^2 G(\underline{r}, \underline{r}') - G(\underline{r}, \underline{r}') \nabla^2 p(\underline{r}') = p(\underline{r}') \delta(\underline{r}' - \underline{r}) - G(\underline{r}, \underline{r}') f(\underline{r}') \quad . \quad (A.4)$$

Since the delta function is only defined in terms of an integration, this last equation is now integrated over a volume  $V$  that contains the source distribution  $f(\underline{r}')$  (i.e., a region where Equations A.1 and A.2 are valid) to obtain

$$\begin{aligned} \iiint_V (p(\underline{r}') \nabla^2 G(\underline{r}, \underline{r}') - G(\underline{r}, \underline{r}') \nabla^2 p(\underline{r}')) dV \\ = p(\underline{r}) - \iiint_V G(\underline{r}, \underline{r}') f(\underline{r}') dV \quad . \end{aligned} \quad (A.5)$$

Finally, Green's theorem (Morse & Feshbach, 1953, pp. 803-804) is used to convert the volume integral into the corresponding surface integral. Letting  $S$  represent the closed surface bounding the volume  $V$  and  $\underline{n}$  represent the outward unit normal vector, one obtains

$$\begin{aligned} p(\underline{r}) = \iint_S (p(\underline{r}') \underline{\nabla} G(\underline{r}, \underline{r}') - G(\underline{r}, \underline{r}') \underline{\nabla} p(\underline{r}')) \cdot \hat{n} dS \\ + \iiint_V G(\underline{r}, \underline{r}') f(\underline{r}') dV \quad . \end{aligned} \quad (A.6)'$$

This equation relates the pressure at a field point to both the pressure and its normal derivative on the enclosing surface  $S$  and also the pressure due to the specified source distribution. The point  $\underline{r}$  must be

inside  $S$  in order for the integration of the delta function in Equation A.4 to yield a nonzero value. Note that Equation A.6 takes the form of an integral equation with the pressure appearing on both sides of the equal sign. This fact is very important when sources of energy outside the surface of integration must be considered.

Equation A.6 can now be applied to the case of interest, that of a rigid body subjected to an incident field from a single point source at location  $\underline{r}_2$  (Figure A.1). The surface  $S$  is chosen as the sum of the scatterer surface  $S_0$  and the surface of a sphere of infinite radius  $S_\infty$ , and the integration volume thus includes all of space outside the scatterer. The source distribution  $f(\underline{r})$  is that of a point source of strength  $P$  at  $\underline{r}_2$  which is radiating into a space angle of  $4\pi$ :

$$f(\underline{r}') = 4\pi P \delta(\underline{r}' - \underline{r}_2) \quad . \quad (A.7)$$

On the surface of the scatterer, the normal velocity is zero (Neumann boundary condition), and thus

$$\hat{n} \cdot \underline{\nabla} p = 0 \quad \text{on} \quad S_0 \quad . \quad (A.8)$$

Using Equation A.8 to simplify the integral over the scatterer surface (does not apply for  $S_\infty$ ) and substituting Equation A.7 for the source

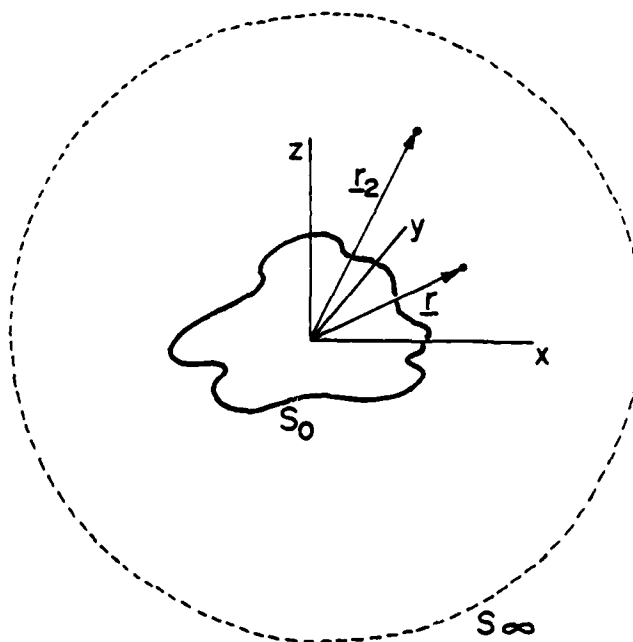


Figure A.1 Geometry showing a rigid body subjected to an incident acoustic wave from a point source at  $\underline{r}_2$ , as viewed at a field point at  $\underline{r}$ .

distribution, one obtains

$$\begin{aligned}
 p(\underline{r}) = & \iint_{S_{\infty}} (p(\underline{r}') \underline{\nabla} G(\underline{r}, \underline{r}') - G(\underline{r}, \underline{r}') \underline{\nabla} p(\underline{r}')) \cdot \hat{n} dS_{\infty} \\
 & + \iint_{S_0} (p(\underline{r}') \underline{\nabla} G(\underline{r}, \underline{r}')) \cdot \hat{n} dS_0 + \frac{P \exp(-ik|\underline{r}_2 - \underline{r}|)}{|\underline{r}_2 - \underline{r}|} .
 \end{aligned} \tag{A.9}$$

It is now convenient to decompose the field pressure into incident and scattered components denoted as

$$p(\underline{r}) = p_i(\underline{r}) + p_s(\underline{r}) , \tag{A.10}$$

and then to examine the form of each of these components. Since all energy comes from the point source at  $\underline{r}_2$ , the incident field is given by

$$p_i(\underline{r}) = \frac{\exp(-ik|\underline{r}_2 - \underline{r}|)}{|\underline{r}_2 - \underline{r}|} . \tag{A.11}$$

Note that this corresponds exactly to the last term on the right side of Equation A.9, and thus that equation reduces to

$$\begin{aligned}
 p_s(\underline{r}) = & \iint_{S_{\infty}} (p(\underline{r}') \underline{\nabla} G(\underline{r}, \underline{r}') - G(\underline{r}, \underline{r}') \underline{\nabla} p(\underline{r}')) \cdot \hat{n} dS_{\infty} \\
 & + \iint_{S_0} (p(\underline{r}') \underline{\nabla} G(\underline{r}, \underline{r}')) \cdot \hat{n} dS_0 .
 \end{aligned} \tag{A.12}$$

Although only the scattered pressure remains on the left side of the

equation, the total pressure still appears under both integral signs on the right side. At large distances from the scatterer, the scattered field will assume the characteristics of spherical divergence, and thus can be represented as

$$p_s(\underline{r}) \rightarrow \left(\frac{P}{r}\right) f(\vartheta, \varphi) \exp(-ikr) \quad , \quad (\text{A.13})$$

where  $f(\vartheta, \varphi)$  is sometimes called the form function. Note that this field is similar to the incident field in dependence on range.

Turning now to the integral in Equation A.12 over  $S_\infty$ , it is first necessary to investigate the asymptotic forms of the functions  $G(\underline{r}, \underline{r}')$  and  $dS_\infty$ . In the limit as  $r' \rightarrow \infty$ , then  $R \rightarrow r'$ . In addition,

$$\begin{aligned} \nabla G(\underline{r}, \underline{r}') &= \hat{R} \left\{ \frac{d(\exp(-ikR)/4\pi R)}{dR} \right\} \\ &= \left(\frac{\hat{R}}{4\pi}\right) \left\{ \left(\frac{-ik}{R}\right) - \left(\frac{1}{R^2}\right) \right\} \exp(-ikR) \\ &\rightarrow \left(\frac{\hat{R}}{4\pi}\right) \left(\frac{-ik}{R}\right) \exp(-ikR) \\ &\rightarrow -ik\hat{R}G(\underline{r}, \underline{r}') \quad . \end{aligned} \quad (\text{A.14})$$

Because  $S_\infty$  is a sphere, one can say that

$$dS_\infty \rightarrow R^2 \sin \vartheta d\vartheta d\varphi = R^2 da \quad . \quad (\text{A.15})$$

Substituting these asymptotic relations into the integral, one obtains

$$\begin{aligned} I_{\infty} &= \iint_{S_{\infty}} - \{G(\underline{r}, \underline{r}') \underline{\nabla} p(\underline{r}') + ikR \hat{r} p(\underline{r}') G(\underline{r}, \underline{r}')\} \cdot \hat{n} R^2 da \\ &= \iint_{S_{\infty}} \{-RG(\underline{r}, \underline{r}')\} R \{\underline{\nabla} p(\underline{r}') + \hat{r}' p(\underline{r}')\} \cdot \hat{n} da \quad . \quad (A.16) \end{aligned}$$

In the asymptotic limit, the function  $R G(\underline{r}, \underline{r}')$  is bounded. Thus,  $I_{\infty}$  will tend to zero if

$$\lim_{r' \rightarrow \infty} R \{\underline{\nabla} p(\underline{r}') + \hat{r}' p(\underline{r}')\} \cdot \hat{n} \rightarrow 0 \quad . \quad (A.17)$$

This condition is known as the Sommerfeld radiation condition (Skudrzyk, 1971, pp. 493-494), and it must be satisfied in order for this derivation to be valid. Because both the incident and scattered components of the pressure vary as  $1/R$ , it is reasonable to assume that the radiation condition does hold if even a small amount of damping is included. Having shown that the integral over  $S_{\infty}$  vanishes, Equation A.12 is reduced to

$$p_s(\underline{r}) = \iint_{S_0} \{p(\underline{r}') \underline{\nabla} G(\underline{r}, \underline{r}')\} \cdot \hat{n} dS_0 \quad . \quad (A.18)$$

Thus, for a rigid body, the scattered field is related solely to the total pressure evaluated on the surface of the scatterer. If sources of energy outside the surface of integration had been allowed in the previous derivation, the result would have been identical to Equation

A.18. In that case, the integral over  $S_\infty$  would have exactly reproduced the incident field from the external sources, and this term would have canceled with the incident component on the left side of Equation A.9.

Equation A.18 is actually a specific form of the Helmholtz-Huyghens radiation integral (Skudrzyk, 1971, pp.491-496), with no approximations on the field having been made. To evaluate this relation for the case of interest, the Kirchhoff assumptions must be applied. Thus, it will be assumed (1) that every point on the illuminated portion of the scatterer surface  $S_I$  acts as if it were a plane in an infinite rigid baffle and (2) that the pressure on the shadowed portions of the scatterer surface is identically zero. The surface pressure can be obtained by examining the scattering from a rigid plane. Figure A.2 illustrates the case of an incident wave of form  $p_i(\underline{r}) = P \exp(-ik \cdot \underline{r})$  reflected from a plane boundary in a form  $p_r(\underline{r}) = R \exp(-ik' \cdot \underline{r})$ . At the boundary, the total pressure given by  $p(\underline{r}) = p_i(\underline{r}) + p_r(\underline{r})$  is subject to the Neumann boundary condition of Equation A.8. Thus,

$$-ik \cdot \hat{n} P \exp(-ik \cdot \underline{r}) - ik' \cdot \hat{n} R \exp(-ik' \cdot \underline{r}) = 0 \quad . \quad (A.19)$$

In order to examine the relationships determined by Equation A.19, it is helpful to remove the vector representations by assuming that the point of reflection is at the origin of a rectangular coordinate system. Equation A.19 becomes (see Figure A.2)

$$\begin{aligned} -ik \cos \theta P \exp(-ikx \cos \theta - iky \sin \theta) \\ -ik' \cos \theta' R \exp(-ik'x \cos \theta' - ik'y \sin \theta') = 0 \quad . \end{aligned} \quad (A.20)$$



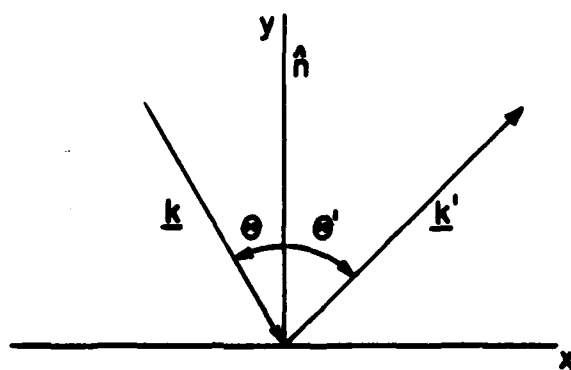


Figure A.2 Scattering of a plane wave at a plane boundary.

It is clear that  $k = k'$  because the frequency of the wave does not change on reflection. In addition, because Equation A.20 must hold at the boundary ( $x = 0$ ) for all values of  $y$ , one finds that  $\theta = \theta'$ . This observation, when applied to Equation A.20, leads further to the fact that  $R = P$ . The incident and reflected rays are thus identical in form and

$$\begin{aligned} p(\underline{r}) &= p_i(\underline{r}) + p_r(\underline{r}) \\ &= P \exp(-ik \cdot \underline{r}) + P \exp(-ik \cdot \underline{r}) \\ &= 2p_i(\underline{r}) \end{aligned} \quad (A.21)$$

For the case presented in Chapter 2, that of backscattering from a rigid body, the incident pressure is

$$p_i(r') = \frac{P \exp(ikr')}{r'} \quad (A.22)$$

The scalar notation can now be used because the source is a point source at the origin of the coordinate system. For backscattering, the receiver is also at the source location, making  $\underline{r} = 0$ . Substituting this information into Equation A.18, one obtains

$$p_s(0) = \iint_{S_I} \left( \frac{2P \exp(-ikr')}{r'} \right) \left( \frac{-ik\hat{r}' \exp(-ikr')}{4\pi r'} \right) \cdot \hat{n} dS \quad (A.23)$$

If  $\psi$  is taken as the angle between the incident radius vector  $\underline{r}'$  and the

surface normal  $\underline{n}$ , the result finally becomes

$$\begin{aligned}
 p_s(0) &= \left(\frac{-i2kP}{4\pi}\right) \iint_{S_I} \left(\frac{\exp(-i2kr')}{r'^2}\right) \cos \psi dS_I \\
 &= \left(\frac{-iP}{\lambda}\right) \iint_{S_I} \left(\frac{\exp(-i2kr')}{r'^2}\right) \cos \psi dS_I \quad . \quad (A.24)
 \end{aligned}$$

Note that this is the same equation as that obtained by more heuristic means in Section 2.1 (Equation 2.6).

## APPENDIX B

## RECEIVER-GATE MODULE

The primary function of the receiver-gate module is to measure the highest peak of all received signals within a preset time window and to hold that value until another measurement can be made. The slowly varying output of this device is then used to obtain a smooth plot of any desired component that can be isolated within the window. The actual unit designed for this project provides a useful dynamic range of at least 40 dB over frequencies of 1 - 40 kHz. Just as with any commercial product, it must be used with caution to insure that the data provided are what is actually desired.

Figure B.1 is a schematic of the first two stages of the receiver-gate module. The incoming signal is first amplified by a factor of 10 to bring it up to a level of about 5 volts. The input preamplifier stage is also designed to blank any signals that occur before the measurement window in order to prevent strong incident pulses from overdriving the following stages. The amplified signal is then passed through an active, full-wave rectifier whose final stage includes a small amount of signal averaging. The averaging is used to smooth out any undesirable transients before they reach the peak detector. The averaging time constant is set by substitution of the 450-picofarad capacitor, and the symmetry of the rectifier is adjusted via the 5000-ohm potentiometer. Note that the HA-2535 operational amplifier is an extremely fast device because it must swing a large voltage range at twice the input frequency. This device can be replaced by a less

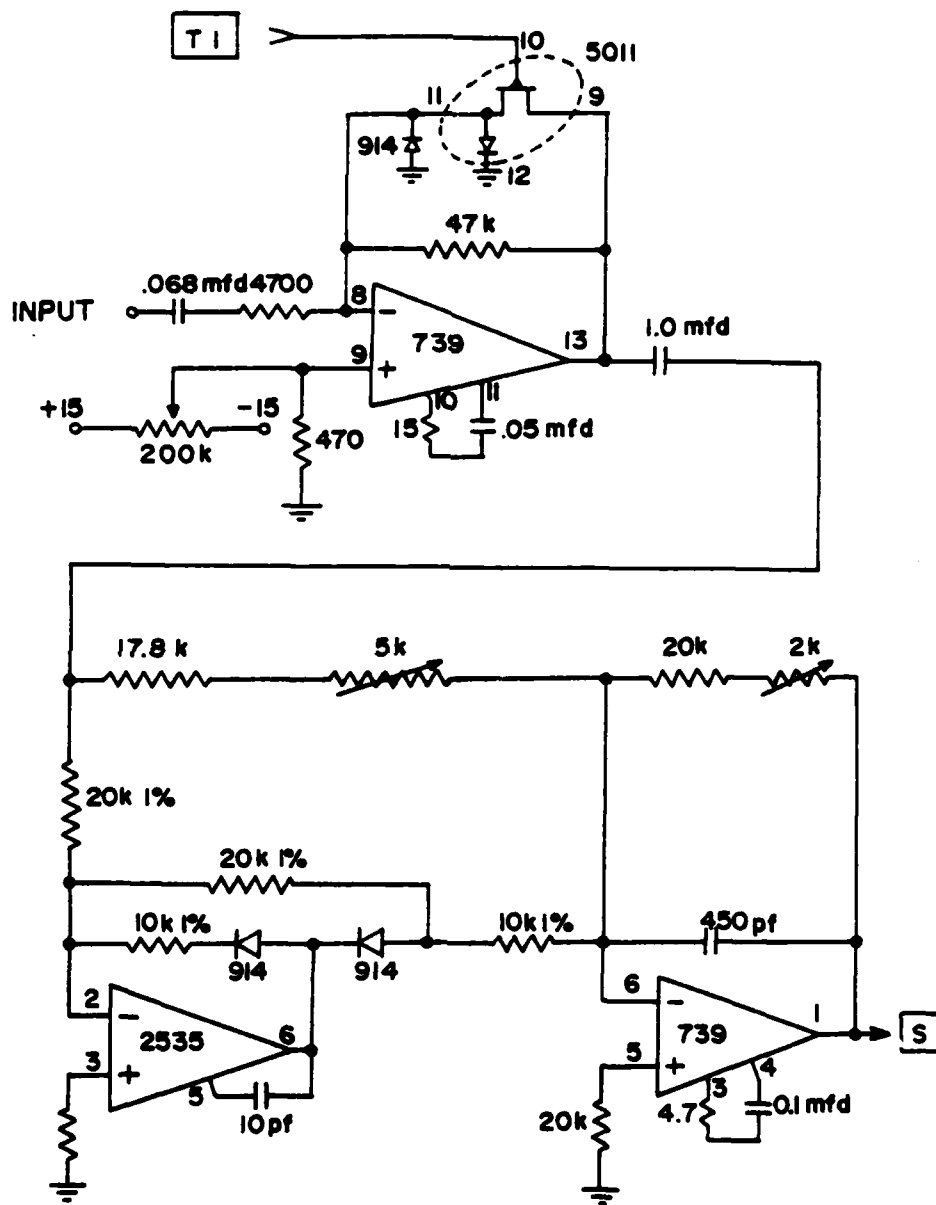


Figure B.1 Schematic of the preamplifier and full-wave rectifier elements of the receiver-gate module.

expensive operational amplifier if the maximum (40 kHz) frequency used for this study is not required.

The rectified signal is passed to a peak detector (Figure 3.2). This stage is reset prior to the time window and then holds the peak value attained until reset again. The peak voltage is converted to a decibel scale by the 8048 temperature-compensated logarithmic convertor. The frequency of the peak-detected signal is low enough to be accurately tracked by this device. Finally, near the end of the time window, the logarithmic peak value is sampled and held by the final stage until the next time window.

The logic circuits that provide the timing signals are shown in Figure B.3. There are three simple monostable multivibrators implemented in CMOS logic and connected in series. The delay from the initial sync pulse to the window, the width of the window, and the width of the sampling time at the end of the window are all adjustable. A separate monitor output, which can be used to observe the relation between the three time settings and the received signal by means of an oscilloscope, is also provided. Note that the feedback capacitors in the multivibrators must be modified if times significantly different from those used in this study are desired.

Finally, a list of the full identifiers of all semiconductor components is shown in Table B.1. All the operational amplifiers are operated at voltages of +15 volts. The CMOS logic is driven from the same +15 volt power supply. Resistors can have a 1/4-watt power rating. Note that new components that could improve the performance of the module and/or reduce its cost have become available since its design.

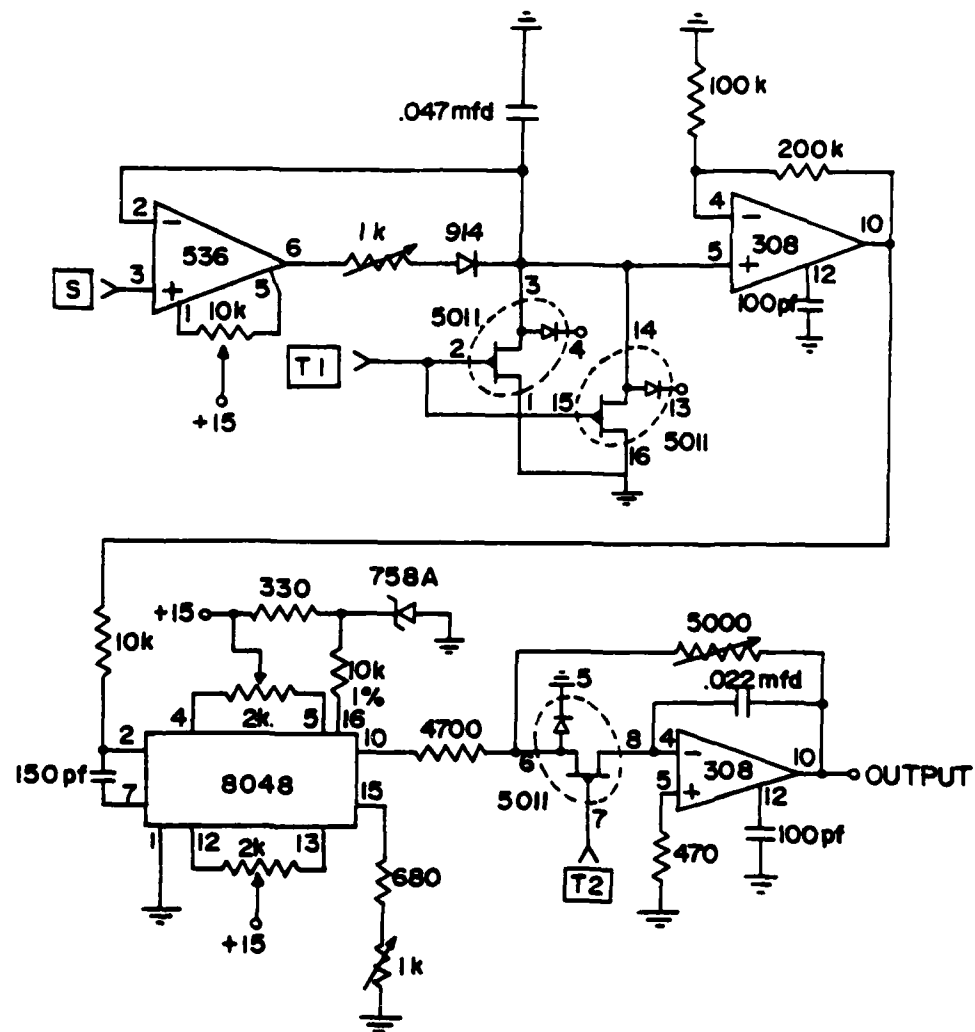


Figure B.2 Schematic of the peak detector, log convertor, and sample-hold elements of the receiver-gate module.

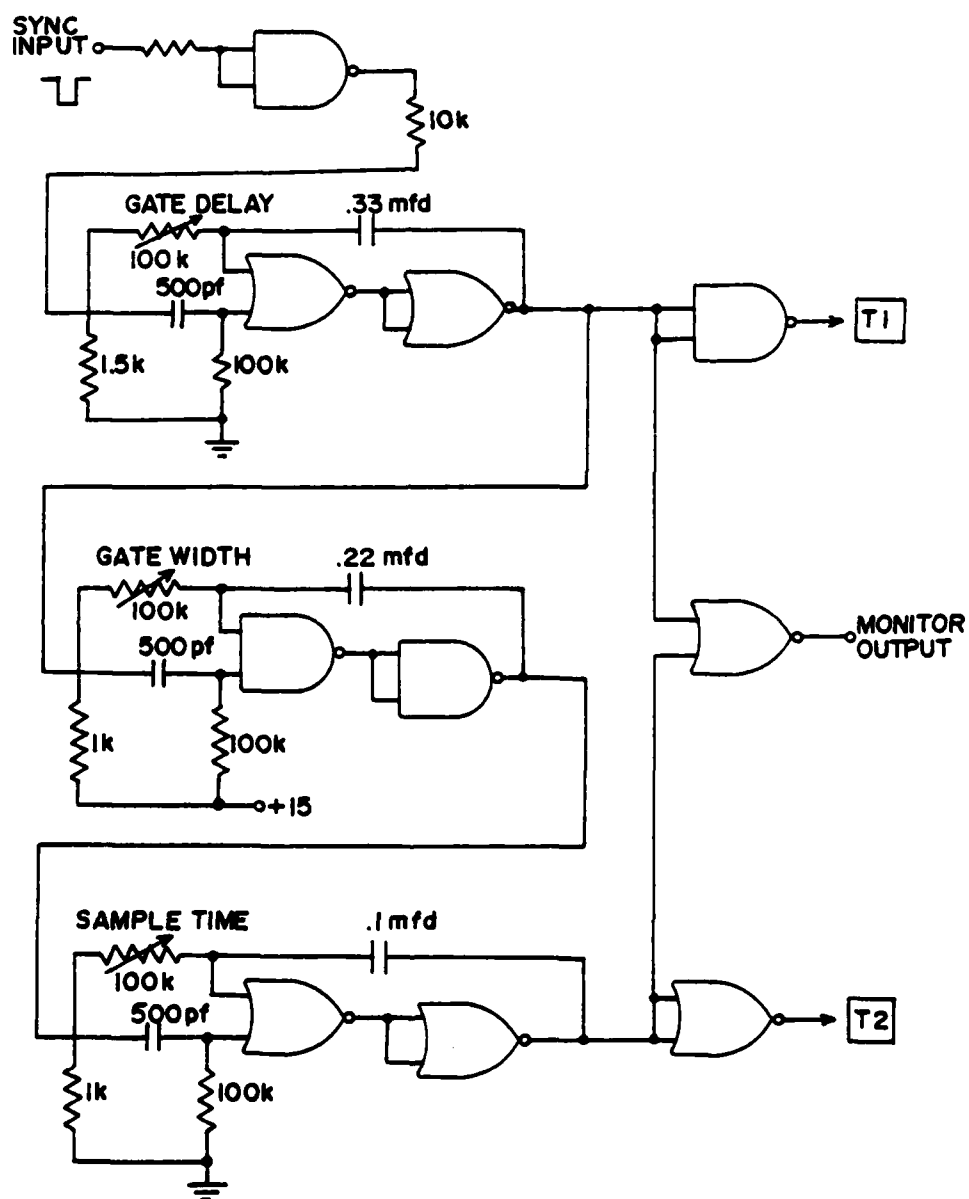


Figure B.3 Schematic of the timing elements of the receiver-gate module.



Table B.1

List of Semiconductor Components  
Used in the Receiver-Gate Module

Signal Diode 1N914

Zener Diode 1N758A (10 volts)

Operational Amplifier  $\mu$ A739

Operational Amplifier HA-2535

Operational Amplifier NE536T

Operational Amplifier LM308D

Analog Gate IH5011PE

Log Amplifier 8048BC

CMOS NOR Gate CD4001A

CMOS NAND Gate CD4011A

In particular, the operational amplifiers in most cases could be replaced with bipolar-FET-type devices such as the LF356N.

#### VITA

Mark Stiles Lang was born December 25, 1950, in Lubbock, Texas. He graduated from Rockport-Fulton High School, Rockport, Texas, as the class valedictorian in May 1969. In May 1973, he received a B.S. degree (with highest honors) in Physics from Texas Tech University. From June 1973 to the present he has been a Graduate Assistant at the Applied Research Laboratory of The Pennsylvania State University, performing research relating to the areas of acoustic diffraction, acoustical holography, and computer graphics. Following graduation, he will remain at the Applied Research Laboratory as a Research Associate. He is a member of the Acoustical Society of America, the Audio Engineering Society, and the Special Interest Group on Graphics (SIGGRAPH) of the Association for Computing Machinery, as well as the honor societies of Phi Kappa Phi and Sigma Pi Sigma.

DISTRIBUTION

Commander (NSEA 09G32)  
Naval Sea Systems Command  
Department of the Navy  
Washington, DC 20362

Copies 1 and 2

Commander (NSEA 0342)  
Naval Sea Systems Command  
Department of the Navy  
Washington, DC 20362

Copies 3 and 4

Defense Technical Information Center  
5010 Duke Street  
Cameron Station  
Alexandria, VA 22314

Copies 5 through 16

